

UNCLASSIFIED

AD NUMBER
AD881744
NEW LIMITATION CHANGE
TO Approved for public release, distribution unlimited
FROM Distribution authorized to U.S. Gov't. agencies and their contractors; Administrative/Operational Use; Jan 1971. Other requests shall be referred to Air Force Rocket Propulsion Lab., Attn: DOG/STINFO, Edwards AFB, CA 93523.
AUTHORITY
Air Force Rocket Propulsion Lab ltr dtd 29 Sep 1971

THIS PAGE IS UNCLASSIFIED

AD881744

AD No. _____
L. _____

230

AIR FORCE REUSABLE ROCKET ENGINE PROGRAM

**XLR129-P-1
FINAL REPORT
AFRPL-TR-71-1 VOL I
JANUARY 1971**

**Robert R. Atherton, et. al.
Pratt & Whitney Aircraft
Division of United Aircraft Corporation
Florida Research and Development Center**

**Prepared Under
Contract F04611-68-C-0002 for
Air Force Rocket Propulsion Laboratory
Edwards Air Force Base, California 93523**

OK

AIR FORCE REUSABLE ROCKET ENGINE PROGRAM

XLR129-P-1

FINAL REPORT

AFRPL-TR-71-1 VOL I

JANUARY 1971

THIS DOCUMENT IS UNCLASSIFIED
EXCEPT WHERE SHOWN OTHERWISE
AND IS SUBJECT TO THE AUTOMATIC
DOWNGRADING AND DECLASSIFICATION
SCHEDULES OF THE EXECUTIVE ORDER
11652 OF OCTOBER 12, 1976
AND OF THE EXECUTIVE ORDER
11734 OF APRIL 12, 1977
UNLESS INDICATED OTHERWISE
ONLY WITH PRIOR APPROVAL OF _____

Prepared Under
Contract F04611-68-C-0002 for
Air Force Rocket Propulsion Laboratory
Edwards Air Force Base, California 93523

attn: DOG/ST/NEO

D D C
[Stamp]

FOREWORD

This final report describes the Air Force XLR129-P-1 Reusable Rocket Engine Program conducted during the period 6 November 1967 to 15 August 1970, and is submitted in accordance with the requirement of Contract F04611-68-C-0002.

This effort was the second phase of the Air Force Cryogenic Rocket Engine Advanced Development Program, Project 2 of the Program Element 63408F.

This publication was prepared by the Pratt & Whitney Aircraft Florida Research and Development Center as report PWA FR-3832.

This Technical Report has been reviewed and is approved.

Robert E. Probst
Captain, USAF
Program Manager
Air Force Rocket Propulsion Laboratory

ABSTRACT

The objective of this program was to demonstrate the performance and mechanical integrity of a 250,000 lb thrust reusable rocket engine designated the XLR129-P-1. The program, sponsored by the Air Force Rocket Propulsion Laboratory, was accomplished by Pratt & Whitney Aircraft at the Florida Research and Development Center and consisted of design and analysis of all engine components and the demonstrator engine. Fabrication and testing of the critical major components was also accomplished. This effort was the second phase of the Air Force Cryogenic Rocket Engine Advanced Development Program, Project 2 of Program Element 63048F. During the first year, experimental evaluation was conducted in the areas of a fixed fuel area preburner injector, hydrogen cooled roller bearings, compact pump inlets, lightweight nozzle fabrication techniques and selected control valves. These tests provided the background needed for the design of these particular components. During the second year, the design of all components and the demonstrator engine was completed. The engine was designed to operate with liquid oxygen and liquid hydrogen propellants, uses the staged combustion cycle, includes a variable thrust, and a variable mixture ratio capability. During the third year, fabrication and testing of certain components such as the preburner injector, transition case, and fuel turbopump was accomplished. Critical control system components such as the preburner oxidizer valve, the preburner fuel valve and static seals were also tested and evaluated. These tests demonstrated the feasibility of these components. The program commenced 6 November 1967, and ended on 15 August 1970.

CONTENTS

Section	Page
Illustrations	xv
Tables	lxxiii
Abbreviations and Symbols	lxxx
I. INTRODUCTION	1
A. General	1
B. Program Tasks	3
II. SUMMARY, CONCLUSIONS, AND RECOMMENDATIONS	5
A. Demonstrator Engine	5
B. Preburner Injector	5
C. Transition Case	7
D. Main Burner Injector	11
E. Main Burner Chamber	13
F. Nozzles	13
G. Fuel Turbopump	15
H. Oxidizer Turbopump	17
I. Low Speed Inducers	21
J. Control System	21
K. Integrated Components	23
III. ENGINE SYSTEM DESCRIPTION AND PERFORMANCE	29
A. Description	29
B. Operating Characteristics	33
1. Steady-State Operating Parameters	33
2. Start, Shutdown and Throttle Transients	41
C. Layout and Schematic	41
D. Weight	41
E. Interfaces	41
F. Systems Analysis	49
1. General	49
2. Initial System Analysis	50
3. Special Design Cycle Studies	55
G. Performance Data	65

CONTENTS (Continued)

Section	Page
IV. DESIGN SUPPORT TESTING	69
A. Fixed Fuel Area Preburner Injector	69
1. Introduction	69
2. Summary, Conclusions and Recommendations	69
3. Oxidizer Element Testing	70
4. Preburner Rig Testing	85
5. Stability Investigation	109
B. Roller Bearing Durability Tests	131
1. Introduction	131
2. Summary, Conclusions, and Recommendations	131
3. Analysis	141
4. Hardware Description	143
5. Test Results	146
C. Pump Inlet Evaluation	197
1. Introduction	197
2. Summary, Conclusions, and Recommendations	197
3. Testing	199
4. Analysis	204
D. Nozzle Fabrication Investigation	217
1. Introduction	217
2. Summary, Conclusions and Recommendations	217
3. Analysis	218
4. Fabrication Investigation	224
5. Test	226
E. Controls Component Tests	255
1. Main Chamber Oxidizer Valve	255
2. Preburner Oxidizer Valve	283
3. Translating Seal F-33435	310
4. Static Seals	336
V. COMPONENT DEVELOPMENT	347
A. Preburner Injector and Ignition System	347
1. Introduction	347
2. Summary, Conclusions and Recommendations	347

CONTENTS (Continued)

Section	Page
3. Hardware Description	349
4. Fabrication	354
5. Testing	372
6. Facilities	497
B. Transition Case	503
1. Introduction	503
2. Summary, Conclusions and Recommendations	503
3. Hardware Description	506
4. Fabrication	510
C. Main Burner Injector	553
1. Introduction	553
2. Summary, Conclusions and Recommendations	554
3. Hardware Description	554
4. Fabrication	559
D. Main Burner Chamber	575
1. Introduction	575
2. Summary, Conclusions and Recommendations	575
3. Hardware Description	576
4. Fabrication	584
E. Nozzles	589
1. Introduction	589
2. Summary, Conclusions and Recommendations	593
3. Hardware Description	593
4. Fabrication	605
5. Subcomponent Testing	608
F. Fuel Turbopump	611
1. Introduction	611
2. Summary, Conclusions and Recommendations	613
3. Hardware Description	614
4. Fabrication	641
5. Testing	665
6. Facilities	776
G. Oxidizer Turbopump	785
1. Introduction	785
2. Summary, Conclusions and Recommendations	785

CONTENTS (Continued)

Section	Page
3. Hardware Description	788
4. Operating Characteristics	810
5. Fabrication	810
H. Low Speed Inducers	813
(A) Fuel Low Speed Inducer	813
1. Introduction	813
2. Summary, Conclusions and Recommendations	815
3. Hardware Description	815
4. Operating Characteristics	820
(B) Oxidizer Low Speed Inducer	821
1. Introduction	821
2. Summary, Conclusions and Recommendations	821
3. Hardware Description	823
4. Operating Characteristics	827
5. Subcomponent Testing	827
VI. CONTROL SYSTEM	833
A. System Description	833
1. Introduction	833
2. Main Control Valves	835
B. Preburner Oxidizer Valve	837
1. Introduction	837
2. Summary, Conclusions and Recommendations	837
3. Hardware Description	837
4. Fabrication	846
5. Testing	847
C. Preburner Fuel Valve	865
1. Introduction	865
2. Summary, Conclusions and Recommendations	865
3. Hardware Description	866
4. Fabrication	868
5. Testing	871

CONTENTS (Continued)

Section	Page
D. Main Chamber Oxidizer Valve	897
1. Introduction	897
2. Summary, Conclusions and Recommendations	897
3. Hardware Description	897
4. Fabrication	901
5. Testing	901
E. Secondary Control Valves and Systems	903
1. Helium System	903
2. Vent Valves	906
3. Nozzle Coolant System	909
4. Electrical Ignition System	916
F. Engine Command Unit	921
1. Introduction	921
2. Summary, Conclusions and Recommendations	921
3. Logic Description and Operational Characteristics	924
4. Components	929
VII. INTEGRATED COMPONENTS	935
A. Hot Gas System Rig	935
1. Introduction	935
2. Summary, Conclusions and Recommendations	935
3. Hardware Description	935
4. Testing	945
B. Hot Gas Turbopump Test Rig	963
1. Introduction	963
2. Summary, Conclusions and Recommendations	963
3. Hardware Design	964
4. Assembly	964
5. Testing	964
VIII. ENGINE INTEGRATION	1033
A. Introduction	1033
B. Plumbing	1033
1. Introduction	1033
2. Summary, Conclusions and Recommendations	1037
3. Hardware Description and Fabrication	1037

CONTENTS (Continued)

Section	Page
C. Static Seals	1057
1. Introduction	1057
2. Summary, Conclusions and Recommendations . .	1058
3. Hardware Description	1058
4. Testing	1063
Appendix ENGINE CONTROL SYSTEM	1145
I CONTROL SYSTEM ANALYSIS	1149
A. Introduction	1149
B. Control System Description	1151
1. Basic Control System Philosophy	1151
2. Gross Mode Control System	1155
3. Fuel Pump Speed Loop	1156
4. Oxidizer Flow Trim Loop	1157
5. Fuel Flow Trim Loop	1158
6. LOX NPSP Protection	1159
7. Preburner Temperature Limiter Loop	1160
8. Cavitation Protection for the Main Fuel Pump . .	1161
9. Transpiration Cooling Flow Protection	1162
10. Main Turbopump Overspeed Protection	1164
11. Start and Shutdown Operation	1165
12. Prestart Logic	1167
13. Start and Shutdown Schedule Selection Logic	1168
C. Block Diagram Nomenclature	1169
II CONTROL COMPUTER	1175
A. Summary	1175
B. General	1177
1. Introduction	1177
2. Computer	1177
3. Input Circuit	1178
4. Output Subsystem	1179
5. Central Processing Unit Interface	1179
6. Central Processing Unit	1179
7. Recommendations	1180
8. Preliminary Requirements for Input/Output Processor	1180
9. Interface Description	1182
10. Power Estimate for I/O Section	1185
11. Accuracy Estimate of I/O Section	1185

CONTENTS (Continued)

Section	Page
C. Input Interface	1185
1. Multiplexer	1186
2. A/D Converter	1186
3. Speed Circuits	1187
4. Failure Input Circuits	1192
D. Output Interface	1193
1. Recommended Output Section	1193
2. Alternate Output Section	1194
3. Actuator Servos	1194
4. Solenoid Drivers	1195
E. Computer Interface	1197
1. Controller Organization	1197
2. Applications	1197
F. Central Processing Unit	1203
1. General Organization of BDX 800	1203
2. Central Processor	1203
3. Interrupts	1204
4. Input/Output Communication	1205
5. Peripheral Equipment	1206
G. Block Diagram Discussion	1207
1. General	1207
2. Scaling	1207
3. Self-Test and Monitoring	1212
4. Min/Max Limits Subroutine	1212
5. Computer Self-Test Routines	1212
6. Conclusions	1212
H. Flight Safety	1215
1. Mission Reliability	1215
2. A First Approach to Mission Reliability	1222
I. Vehicle Interface	1227
1. Signal Format	1227
2. Data Word Transmission	1228
3. Transmission System	1229

CONTENTS (Continued)

Section		Page
III	DYNAMIC MODEL RESEARCH STUDY	1231
	A. General	1231
	B. Summary of Study Results	1233
	C. Overall System	1235
	D. Start and Shutdown Logic	1235
	E. Primary Control	1235
	F. Engine Protection Loops	1241
	G. Valve Sensitivity	1241
	H. Minimum Acceptable Computation Rate for Real-Time Hardware	1243
IV	FLOWMETER STUDY PROGRAM	1245
	A. Introduction	1245
	B. Requirements	1245
	1. Flowmeter Design Requirements	1245
	C. Results of Study Program	1247
	1. Flowmeter Survey	1247
	2. General Design Evaluation	1248
	3. Evaluation of Design Concepts	1251
	4. Recommended Flowmeter Design	1251
	5. Force Screen Flow Sensor Mechanization	1254
	D. Summary, Recommendations and Conclusions	1257
V	ELECTROMECHANICAL VALVE CONTROL SYSTEM	1259
	A. Introduction	1259
	B. System Selection	1259
	C. Summary and Comparison of AC and DC Systems	1261
	D. Description of Electromechanical System	1263
	1. Reliability	1263
	2. Simplicity	1263
	3. Partitioning	1263
	4. Redundancy	1264
	5. Redundant Operational Philosophy	1265
	6. Motor Electronics Combinations	1266
	7. Monitoring	1266
	8. Maintainability	1267
	9. Repairability	1267

CONTENTS (Continued)

Section	Page
E. Development Risks	1269
1. Electronics	1269
2. Lubrication	1269
3. Position Sensor	1269
VI PNEUMATIC VALVE CONTROL SYSTEM	1271
A. Introduction	1271
B. System Selection	1271
C. Summary	1273
1. Total System Weight	1273
2. System Power Requirements	1273
3. Reliability of Components	1274
4. Cost Considerations	1274
D. Description of Pneumatic Control System	1275
1. General System	1275
2. Pneumatic System Interface With Engine	1276
3. Electrical Interface With Control Computer	1278
4. Pneumatic Actuator Assembly	1279
E. Development Areas and Further Considerations	1281
1. Lubrication	1282
2. Materials	1282
3. Seals	1282
4. Transmission Protection	1282
5. Weight Tradeoff Studies	1282
VII SENSOR STUDY	1283
A. General	1283
1. Rationale of Judgement	1283
2. Recommendations	1283
B. Rotational Speed Sensing	1285
1. General	1285
2. Speed Sensor	1285
3. Comparison of Speed Sensors	1285

CONTENTS (Continued)

Section	Page
C. Temperature Sensors	1289
1. High Temperature Sensors	1289
2. Low Temperature Sensors	1291
D. Pressure Sensors	1293
E. Median Selection Circuit	1295
DISTRIBUTION LIST	1299

ILLUSTRATIONS

Figure		Page
1	XLR129-P-1 Demonstrator Engine Program Schedule	2
2	XLR129 Demonstrator Engine	8
3	XLR129 Demonstrator Engine Preburner Injector	9
4	Transition Case With Centerbody Installed	11
5	Main Burner Injector	12
6	Main Burner Chamber Wafer Assembly	14
7	Primary Nozzle Design	14
8	Design of Two-Position Nozzle	15
9	Fuel Turbopump Assembly	18
10	Oxidizer Turbopump Assembly	19
11	Fuel Low Speed Inducer	24
12	Oxidizer Low Speed Inducer	25
13	Hot Gas System Rig Mounted in Test Stand	26
13a	Hot Turbine Rig	26
14	Operating Range for Demonstrator Engine	29
15	XLR129 Demonstrator Engine	30
16	Demonstrator Engine Propellant Flow Schematic	31
17	Demonstrator Engine Estimated Start, Shutdown, and Throttle Transient Data	41
18	Demonstrator Engine Layout	43
19	Demonstrator Engine Complete Propellant Flow Schematic	45
20	Fuel Inlet Operating Region	46
21	Oxidizer Inlet Operating Region	48
22	Propellant Temperature Limits for Fuel Trim Capability	49

ILLUSTRATIONS (Continued)

Figure		Page
23	Effect of Pump Interstage Tapoff Location on Lightweight Heat Exchanger Coolant Valve	60
24	Effect of Pump Interstage Tapoff Location on Engine Impulse Efficiency	61
25	Effect of Low Speed Inducer Tapoff Location on Lightweight Heat Exchanger Coolant Valve	62
26	Effect of Low Speed Inducer Tapoff Location on Engine Impulse Efficiency	63
27	Effect of Fuel Preburner Supply Tapoff Location on Lightweight Heat Exchanger Coolant Valve	64
28	Effect of Preburner Supply Tapoff Location on Engine Impulse Efficiency	65
29	Altitude Performance for Demonstrator Engine, Booster Application	66
30	Sea Level Specific Impulse vs Mixture Ratio, Booster Application	66
31	Vacuum Specific Impulse vs Thrust, Booster Application	68
32	Data From Prior Tangential Entry Oxidizer Element Testing	71
33	Integral Flow Block	72
34	Integral Flow Block With Optically Clear Lucite Adapter	72
35	Quick Change Flow Block	73
36	Pulse Chambers	74
37	Flow Calibrations for 0.095-Inch Tube	74
38	Flow Calibrations for 0.124-Inch Tube	75
39	Element Discharge Coefficient	76
40	Cone Angle vs Thrust for 0.124-Inch Element	76
41	Element Test Matrix Test Results	83

ILLUSTRATIONS (Continued)

Figure		Page
42	Preburner Rig Configuration	85
43	Original and Revised Oxidizer Domes	86
44	Preburner Injector Block Assembly	86
45	Cross Section of Fixed Fuel Area Preburner Injector	87
46	Plan View of E-8 Test Facility	88
47	Preburner Rig Control System	89
48	Preburner Rig Pulse Gun	90
49	Injector Face Prior to Test 1.01	95
50	Preburner Temperature Profile, Rig 35117-1, Test 1.01, 11-Inch Rake	95
51	Preburner Temperature Profile, Rig 35117-1, Test 1.01, 11-Inch Rake	96
52	Preburner Temperature Profile, Rig 35117-1, Test 2.01, 11-Inch Rake	97
53	Injector Face After Test 2.01	97
54	Injector Secondary Burned Area After Test 2.01	98
55	Face of Backup Injector Before Test 3.01	99
56	Preburner Temperature Profile With Primary-to-Total Oxidizer Flow Split Variation, Rig 35117-2, Test 3.01, 11-Inch Rake	99
57	Preburner Temperature Profile, Rig 35117-2, Test 3.01, 11-Inch Rake	100
58	Preburner Temperature Profile, Rig 35117-2, Test 4.02, 11-Inch Rake	101
59	Preburner Temperature Profile, Rig 35117-2, Test 12.01, 11-Inch Rake	103
60	Injector Face After Test 14.02	104
61	Characteristic Velocity Efficiency Based on Rig Pressures and Flowrates	104

ILLUSTRATIONS (Continued)

Figure		Page
62	Characteristic Velocity Efficiency Based on Combustion Temperatures at the 7-Inch Rake	105
63	Characteristic Velocity Efficiency Based on Combustion Temperatures at the 11-Inch Rake	105
64	Oxidizer Injector Calibration	106
65	Secondary Effective Area vs Momentum Ratio	107
66	Primary-to-Total Flow Split vs Momentum Ratio	107
67	Primary Effective Area vs Momentum Ratio	108
68	Fuel Injector Effective Area	108
69	Flow Split Variation	110
70	Oxidizer Injector Percent Pressure Drop vs Percent Thrust	110
71	Primary Pressure Drop as a Percent of Chamber Pressure	111
72	Secondary Pressure Drop as a Percent of Chamber Pressure	111
73	Effect of Fuel Injection Temperature	112
74	Effect of Fuel Injector Pressure Drop	113
75	Fuel Temperature Effect on Amplitude	114
76	Fuel Temperature Effect on Frequency	115
77	Fuel Temperature Effect on Fuel Manifold Amplitude and Frequency	116
78	Preburner injector Analog Stability Model	118
79	Oxidizer Vaporization Delay	118
80	Analog Simulation of Flow Split Variation	119
81	Analog Simulation of Fuel Temperature Variation	120
82	Predicted Volume Influence on Preburner Stability	121

ILLUSTRATIONS (Continued)

Figure		Page
83	Influence of Effective Areas on Preburner Stability	122
84	Predicted Frequency Response	123
85	Predicted Frequency Response	123
86	Oxidizer Element Slot Modifications for Water Flow Testing	125
87	Oxidizer Element Calibration for Injector Flow Tests	127
88	Effect of Momentum Ratio on Primary and Secondary Effective Area	128
89	Effect of Momentum Ratio on Fuel Effective Area	128
90	Roller Bearing Test Matrix	132
91	Roller Bearing Fatigue Life vs Radial Load (50,000 rpm)	142
92	Roller Bearing Test Rig Cutaway	144
93	250K Roller Bearing Configuration	145
94	Roller Configuration	145
95	B-13 Test Stand Schematic	147
96	Disassembly Condition of Reaction Bearing (S/N V-1) With Turbine End of Rollers Up (Build 22)	150
97	Disassembly Condition of Reaction Bearing (S/N V-1) With Rear End of Rollers Up (Build 22)	150
98	Disassembly Condition of Load Bearing (S/N V-2) With Turbine End of Rollers Up (Build 22)	151
99	Teardown Condition of Failed Roller (No. 4) and Cage From Load Bearing (S/N W-2)	152
100	Disassembly Condition of Load Bearing (S/N W-2) With Turbine End of Rollers Up (Build 24)	153
101	Disassembly Condition of Reaction Bearing (S/N W-1) With Rear End of Rollers Up (Build 24)	153

ILLUSTRATIONS (Continued)

Figure		Page
102	Inner Races of Bearings (S/N X-1 and X-2) Following Test of Build 25A	154
103	Outer Race Failure in the Onloaded Zone of Load Bearing (S/N X-2) Following Test of Build 25A	155
104	Rollers From Load Bearing (S/N X-2) Showing Impact Damage to Turbine End of Rollers (Build 25A)	155
105	Disassembly Condition of Reaction Bearing (S/N X-1) With Turbine End of Rollers Up (Build 25A)	156
106	Disassembly Condition of Reaction Bearing (S/N Y-1) Showing Skewed Position of Roller (Build 26)	157
107	Disassembly Condition of Reaction Bearing (S/N Y-1A) Showing Skewed Position of Roller (Build 27)	158
108	Disassembly Condition of Reaction Bearing (S/N Y-1A) With Turbine End of Rollers Up (Build 27)	158
109	Disassembly Condition of Load Bearing (S/N Y-2) With Turbine End of Rollers Up (Build 27)	159
110	Disassembly Condition of Reaction Bearing (S/N Z-1) Roller No. 5 (Build 28)	160
111	Disassembly Condition of Reaction Bearing (S/N Z-1) With Turbine End of Rollers Up (Build 28)	161
112	Disassembly Condition of Load Bearing (S/N Z-2) With Turbine End of Rollers Up (Build 28)	161
113	Disassembly Condition of Reaction Bearing (S/N AA-1) With Turbine End of Rollers Up (Build 29)	162
114	Disassembly Condition of Load Bearing (S/N AA-2) With Turbine End of Rollers Up (Build 29)	162
115	Disassembly Condition of Reaction Bearing (S/N X-1) With Rear End of Rollers Up (Build 30)	163
116	Disassembly Condition of Reaction Bearing (S/N X-1) With Turbine End of Rollers Up (Build 30)	164
117	Disassembly Condition of Load Bearing (S/N Z-2) With Rear End of Rollers Up (Build 30)	164

ILLUSTRATIONS (Continued)

Figure		Page
118	Disassembly Condition of Load Bearing (S/N Z-2) With Turbine End of Rollers Up (Build 30)	165
119	Rollers From Load Bearing (S/N BB-2) Showing Heavy Scoring on Turbine End of Rollers (Build 31)	166
120	Rollers From Load Bearing (S/N BB-2) Showing Heavy Scoring on Rear End of Rollers (Build 31)	166
121	Comparison of Post-Test Condition of a Typical Roller From Reaction Bearing (S/N BB-1) and Load Bearing (S/N BB-2) of Build 31	167
122	Cracked Outer Race From Reaction Bearing (S/N BB-1) of Build 31	167
123	Disassembly Condition of Load Bearing (S/N BB-2) With Turbine End of Rollers Up (Build 31)	168
124	Disassembly Condition of Reaction Bearing (S/N BB-1) With Turbine End of Rollers Up (Build 31)	168
125	View Showing Crack in Outer Race of Reaction Bearing (S/N CC-1) Build 32	169
126	Disassembly Condition of Reaction Bearing (S/N CC-1) With Rear End of Rollers Up (Build 32)	171
127	Disassembly Condition of Load Bearing (S/N CC-2) With Rear End of Rollers Up (Build 32)	171
128	View Showing Crack in Outer Race of Reaction Bearing (Build 33)	173
129	View Showing Moderate Scuffing on Turbine End of Rollers From Reaction Bearing (Build 33)	174
130	View Showing Moderate Scuffing on Turbine End of Rollers From Load Bearing (Build 33)	174
131	Disassembly Condition of Reaction Bearing (S/N EE-1) With Rear End of Rollers Up (Build 36)	175
132	Disassembly Condition of Reaction Bearing (S/N EE-1) With Turbine End of Rollers Up (Build 36)	176
133	Disassembly Condition of Lead Bearing (S/N EE-2) With Rear End of Rollers Up (Build 36)	176

ILLUSTRATIONS (Continued)

Figure		Page
134	Disassembly Condition of Load Bearing (S/N EE-2) With Turbine End Rollers Up (Build 36)	177
135	Reaction Bearing (S/N FF-1) Outer Race ID Showing Thermal Cracks (Build 38)	178
136	Load Bearing (S/N FF-2) Outer Race ID Showing Thermal Cracks (Build 38)	179
137	Condition of Load Bearing (S/N FF-2) Outer Race (Build 39)	180
138	Disassembly Condition of Reaction Bearing (S/N FF-1) With Turbine End of Rollers Up (Build 39)	181
139	Disassembly Condition of Load Bearing (S/N FF-2) With Turbine End of Rollers Up (Build 39)	181
140	View Showing Condition of Load Bearing Outer Race (S/N GG-2) After Test of Build 40.	182
141	View Showing Condition of Load Bearing Rollers (S/N GG-2) Turbine End Up (Build 40).	183
142	View Showing Condition of Load Bearing Rollers (S/N GG-2), Rear End Up (Build 40).	183
143	View Showing Condition of Load Bearing Inner Race (S/N GG-2) After Test of Build 40	184
144	View Showing Condition of Load Bearing Cage (S/N GG-2) After Test of Build 40	184
145	View Showing Overall Condition of Load Bearing (S/N GG-2), Rear End Up (Build 40).	185
146	View Showing Overall Condition of Load Bearing (S/N GG-2), Turbine End Up (Build 40).	186
147	View Showing Condition of Reaction Bearing Outer Race (S/N GG-1) After Test of Build 40	186
148	View Showing Overall Condition of Reaction Bearing (S/N GG-1) Turbine End Up (Build 40).	187
149	View Showing Skewed Position of Roller No. 7 in Reaction Bearing Cage (S/N HH-1) After Test of Build 41	188

ILLUSTRATIONS (Continued)

Figure		Page
150	View Showing Overall Condition of Reaction Bearing (S/N HH-1), Turbine End Up (Build 41)	188
151	View Showing Condition of Reaction Bearing Rollers (S/N HH-1), Turbine End Up (Build 41)	189
152	View Showing Condition of Reaction Bearing Inner Race (S/N HH-1) After Test of Build 41	189
153	View Showing Condition of Reaction Bearing Outer Race (S/N HH-1) After Test of Build 41	190
154	View Showing Overall Condition of Load Bearing (S/N HH-2), Turbine End Up (Build 41)	190
155	Enlarged View of ID of Outer Race Showing Numerous Thermal Cracks	191
156	View Showing Condition of Reaction Bearing Rollers (S/N JJ-1) With Rear End Up (Build 42)	192
157	View Showing Condition of Reaction Bearing Rollers (S/N JJ-1) With Turbine End Up (Build 42)	192
158	View Showing Condition of Load Bearing Rollers (S/N JJ-2) With Rear End Up (Build 42)	193
159	View Showing Condition of Load Bearing Rollers (S/N JJ-2) With Turbine End Up (Build 42)	193
160	View Showing Overall Condition of Reaction Bearing (S/N JJ-1), Turbine End Up (Build 42)	194
161	View Showing Overall Condition of Reaction Bearing (S/N JJ-1), Rear End Up (Build 42)	194
162	View Showing Overall Condition of Load Bearing (S/N JJ-2), Turbine End Up (Build 42)	195
163	View Showing Overall Condition of Load Bearing (S/N JJ-2), Rear End Up (Build 42)	195
164	Demonstrator Engine Showing Inlet Flow Distributors at the Fuel and Oxidizer Inlets (Circled Areas)	197
165	Candidate Inlets and Predicted Pressure Loss	198
166	Closed Loop Water Test Facility	200

ILLUSTRATIONS (Continued)

Figure		Page
167	Water Test Stand Schematic	200
168	Straight Inlet Test Installation	201
169	Short Radius Elbow With Turning Vanes Inlet Test Installation	201
170	Pancake Inlet Test Installation	202
171	Cavitation Damage on Lucite Viewing Section	202
172	Straight Inlet Test Section Pressure Tap Locations	204
173	Elbow Test Section Pressure Tap Locations	204
174	Pancake Test Section Pressure Tap Locations	205
175	Suction Specific Speed vs Unit Flow for Straight Inlet	205
176	Suction Specific Speed vs Unit Flow for Elbow Inlet	206
177	Suction Specific Speed vs Unit Flow for Pancake Inlet	206
178	Noncavitating Head vs Net Positive Suction Head (Straight Inlet)	207
179	Noncavitating Head vs Net Positive Suction Head (Straight Inlet)	207
180	Noncavitating Head vs Net Positive Suction Head (Elbow Inlet)	208
181	Noncavitating Head vs Net Positive Suction Head (Elbow Inlet)	208
182	Noncavitating Head vs Net Positive Suction Head (Pancake Inlet)	208
183	Noncavitating Head vs Net Positive Suction Head (Pancake Inlet)	208
184	Noncavitating Head vs Suction Specific Speed (Straight Inlet)	210
185	Noncavitating Head vs Suction Specific Speed (Straight Inlet)	210

ILLUSTRATIONS (Continued)

Figure		Page
186	Noncavitating Head vs Suction Specific Speed (Elbow Inlet)	211
187	Noncavitating Head vs Suction Specific Speed (Elbow Inlet)	211
188	Noncavitating Head vs Suction Specific Speed (Pancake Inlet)	212
189	Noncavitating Head vs Suction Specific Speed (Pancake Inlet)	212
190	Unit Head vs Unit Flow (Straight Inlet).	214
191	Unit Head vs Unit Flow (Elbow Inlet)	214
192	Unit Head vs Unit Flow (Pancake Inlet)	215
193	Comparison of Unit Head vs Unit Flow for All Inlets Tested	216
194	Inlet Line Wall Static Pressure Rise Because of Prerotation (Straight Inlet)	216
195	Velocity Profile at Inlet Housing Flange	217
196	Fluid Temperature vs Area Ratio	218
197	Heat Flux vs Area Ratio	219
198	Inside Film Coefficient vs Area Ratio	219
199	Coolant Passageway Area vs Area Ratio	220
200	Nozzle Configuration Comparison	224
201	Band Height vs Moment of Inertia for Several Configurations.	225
202	Gather Forming Die	225
203	Corrugation Sample Panel	226
204	Integral Band Design Sample Panel.	227
205	Hydrostatic Test Samples	227
206	Failed Hydrostatic Test Samples	228

ILLUSTRATIONS (Continued)

Figure		Page
207	Resistance Weld Examination Specimen	229
208	Resistance Weld Test Samples	230
209	Specimens After First Two Tests	231
210	Strain vs Cycle Life for Inconel 625 (AMS 5599)	233
211	Initial Thermal Fatigue Sample	233
212	ΔT Investigation With Air-Cooled Back.	234
213	ΔT Investigation With Water-Cooled Back.	235
214	ΔT Investigation With Air-Cooled Back and Insulated Weld Joint	235
215	ΔT Investigation With Water-Cooled Back and Insulated Weld Joint.	236
216	Thermal Fatigue Sample With Cooling Fins	236
217	Thermal Fatigue Cycling Set Up	237
218	Test Results of Flat Sample With Corrugations and Copper Fins	237
219	Cooling Fin Thickness Test Results	238
220	Test Results of 4-Inch Diameter Corrugated Can	239
221	Line Resistance Heating Using Proximity Effect	240
222	Line Heater Assembly	240
223	Line Heating Test Results	241
224	Thermal Fatigue Sample	241
225	Initial Test Temperatures.	242
226	Visicorder Tape of Heating Cycle Results	242
227	Initial Thermal Fatigue Specimen and Enlarged View Showing Thermal Fatigue Fractures	243
228	Crack in 0.005 Inch Thick Inconel 625 (AMS 5599) Before Etching (500X Magnification)	244

ILLUSTRATIONS (Continued)

Figure		Page
229	Crack in 0.005 Inch Thick Inconel 625 (AMS 5599) After Etching (500X Magnification)	244
230	Specimen Being Tested at Final Conditions	246
231	Final Thermal Fatigue Specimen Configuration	246
232	Thermal Fatigue Specimen Final Assembly (Top View)	247
233	Thermal Fatigue Specimen Final Assembly (Side View)	247
234	Thermal Fatigue Specimen Final Assembly (Bottom View)	248
235	ΔT vs Cycle Life for 0.005 Inch Thick Corrugations.	250
236	Photograph of Failed Corrugation With Crown Temperature at 2160° R	250
237	Photograph of Failed Corrugation With Crown Temperature at 1910° R	251
238	Thermal Fatigue of Inconel 625 (AMS 5599) Tube vs Corrugated Sheet	253
239	Main Chamber Oxidizer Valve	257
240	B-22 Cryogenic Static Cycle Test Stand	258
241	Main Chamber Oxidizer Valve Instrumentation Schematic, B-22 Stand	258
242	Laminated Kapton Shutoff Seal	259
243	Laminated Kapton F-FEP Teflon Seal Leakage vs Actuation, Shutoff, and Pressure Cycles, Rig F-33466-9	260
244	Failed Portion of Disk Seal After Test	261
245	Disk Seal Axial Supporting Ring After Test	262
246	Hoop Shutoff Seal	263
247	Lip Seal Package	263
248	Hoop-Type Disk Seal Leakage vs Time, Rig F-35106-6	264
249	Hoop-Type Disk Seal Leakage vs Actuation Cycles, Rig F-35106-6	265

ILLUSTRATIONS (Continued)

Figure		Page
250	Hoop Type Disk Seal Leakage vs Total Cycles, Rig F-35106-6	266
251	Primary and Secondary Lip Seals and Static Seals Leakage vs Actuation Cycles, Rig F-35106-6	267
252	Hoop Seal Surface After Test, Rig F-35106-6	268
253	Shaft Disk Surface After Test, Rig F-35106-6	268
254	Shutoff Seal Prior to Test, Rig F-33466-10	269
255	Strap Actuated Shutoff Seal	270
256	Strap Actuated Disk Seal Leakage vs Time, Rig F-33466-10	271
257	Strap Actuated Disk Seal Leakage vs Actuation Cycles, Rig F-33466-10	272
258	Primary Shaft Lip Seal Leakage vs Actuation Cycles, Rig F-33466-10	273
259	Static Seal Leakages vs Actuation Cycles, Rig F-33466-10 . .	274
260	Glycol Contamination on Inlet Side of Disk, Rig F-33466-10, 2.99 Inch Diameter Disk	275
261	Shutoff Seal After Endurance Test, Rig F-33644-10	275
262	Shutoff Seal After Endurance Test, Rig F-33466-10	276
263	Disk Seal Surface After Endurance Test, Rig F-33466-10 . .	276
264	Strap Actuated Disk Seal, Rig F-33466-10	277
265	Cam Actuated Shutoff Seal, Rig F-35106-17	278
266	Cam Actuated Disk Seal Leakage vs Time, Rig F-35106-7 . .	279
267	Cam Actuated Disk Seal Leakage vs Time, Rig F-35106-7 . .	279
268	Primary Shaft Lip Seal Leakage vs Actuation Cycles, Rig F-35106-7	280
269	Static Seal Leakage vs Actuation Cycles, Rig F-35106-7 . . .	281
270	Disk Seal After Test, Rig F-35106-7	282

ILLUSTRATIONS (Continued)

Figure		Page
271	Area of Seal Element Failure	282
272	Shaft Disk Sealing Surface After Test, Rig F-35106-7	282
273	Adhesion Tests of Chromium and Chromium-Molydenum Plating on Stainless Steel (AMS 5646)	285
274	Surface Characteristics of Chromium and Chromium- Molydenum Plating on Stainless Steel (AMS 5646)	286
275	Surface Characteristics of Chromium and Chromium- Molydenum Ultrasonic Plating on Stainless Steel (AMS 5646)	287
276	Chromium and Chromium-Molydenum Plated Surfaces After 250 Hours of Salt Spray Testing	287
277	Coefficient of Friction Machine	288
278	Wear Characteristics of 0.001 Inch Thick Chrome Plate (PWA 48)	292
279	Wear Characteristics of 0.001 Inch Thick Chrome Plate (PWA 48)	292
280	Wear Characteristics of 0.001 Inch Thick Chromium- Molydenum	293
281	Piston Ring Installation Configuration and Pressure Distribution	293
282	Pressure Balance Piston Ring	295
283	Preburner Oxidizer Valve Rig	296
284	Schematic of Preburner Oxidizer Valve Rig Test Stand Installation	297
285	Piston Ring Leakage on Rig F-33469-7B	298
286	Pretest and Post-test Condition of the Housing	298
287	Pretest and Post-test Views of Housing Showing Piston Ring Wear Area	299
288	Pretest and Post-test Condition of Sleeve Showing Wear From Upper Secondary Piston Ring	299

ILLUSTRATIONS (Continued)

Figure		Page
289	Pretest and Post-Test Condition of Upper Piston Ring	300
290	Pretest and Post-test Condition of Lower Piston Ring	300
291	Closeup Views of Main Housing Wear	301
292	Unbalanced Piston Rings	302
293	Piston Ring Leakage on Rig F-33469-8	302
294	Pretest and Post-test Condition of Housing, Rig F-33469-8. .	303
295	Pretest and Post-test Views of Housing Showing Piston Ring Wear Area, Rig F-33469-8	303
296	Pretest and Post-test Condition of Sleeve Showing Wear From Upper Secondary Piston Ring, Rig F-33469-8	304
297	Pretest and Post-test Condition of Upper Piston Ring, Rig F-33469-8	394
298	Pretest and Post-test Condition of Lower Piston Ring, Rig F-33469-8	305
299	Piston Ring Leakages on Rig F-33458-7	305
300	Pretest and Post-test Condition of Housing, Rig F-33458-7	306
301	Pretest and Post-test Views of Housing Showing Piston Ring Wear Area, Rig F-33458-7.	306
302	Pretest and Post-test Condition of Sleeve Showing Wear From Upper Secondary Piston Ring, Rig F-33458-7. . .	307
303	Pretest and Post-test Condition of Upper Piston Ring, Rig F-33458-7	307
304	Pretest and Post-test Condition of Lower Piston Ring, Rig F-33458-7	308
305	Rig F-33458-7 Actuation Force Requirements During Cycle Endurances	308
306	Piston Ring Leakage on Rig F-33458-8	309
307	Post-test Condition of Housing, Rig F-33458-8	310

ILLUSTRATIONS (Continued)

Figure		Page
308	Post-test View of Housing Showing Piston Ring Wear Area, Rig F-33458-8	311
309	Post-test Condition of Sleeve Showing Wear From Upper Secondary Piston Ring, Rig F-33458-8	311
310	Post-test Condition of Upper Piston Ring, Rig F-33458-8	312
311	Post-test Condition of Lower Piston Ring, Rig F-33458-8.	312
312	Rig F-33458-8 Actuation Force Requirements During Cycle Endurance	313
313	Translating Seal Test Rig Vent Shaft Seal Leakage vs Cycles	314
314	Translating Seal Test Rig Primary Shaft Seal Leakage vs Cycles	315
315	Translating Seal Test Rig Leakage vs Inlet Pressure, Stationary Shaft	316
316	Translating Seal Test Rig Leakage vs Inlet Pressure, Translating Shaft	317
317	Translating Seal Test Rig Balance Piston Seal Leakage vs Cycles	318
318	Translating Seal Test Rig	319
319	Shaft Seal Package	320
320	Lip Seal Mold	321
321	Translating Seal Test Rig Leakage vs Cycles for Build 10B	323
322	Primary Shaft Lip Seal After Test of Build 10B	324
323	Vent Shaft Lip Seal After Test of Build 10B	324
324	Balance Piston Lip Seal After Test of Build 10B	325
325	Translating Seal Test Rig Leakage vs Cycles for Build 11	326

ILLUSTRATIONS (Continued)

Figure		Page
326	Primary Shaft Lip Seal After Test of Build 11	327
327	Vent Shaft Lip Seal After Test of Build 11	328
328	Balance Piston Lip Seal After Test of Build 11	328
329	Translating Seal Test Rig Leakage vs Cycles for Build 12 . .	329
330	Primary Shaft Lip Seal After Test of Build 12	331
331	Vent Shaft Lip Seal After Test of Build 12	331
332	Balance Piston Lip Seal After Test of Build 12	332
333	Translating Seal Test Rig Leakage vs Cycles for Build 13 . .	333
334	Primary Shaft Lip Seal After Test of Build 13	334
335	Vent Shaft Lip Seal After Test of Build 13	334
336	Balance Piston Lip Seal After Test of Build 13	335
337	Plumbing Schematic for Testing Build 14	335
338	Translating Seal Test Rig Leakage vs Cycles for Build 14 . .	337
339	Primary Shaft Lip Seal After Test of Build 14	338
340	Vent Shaft Lip Seal After Test of Build 14	338
341	Balance Piston Lip Seal After Test of Build 14	339
342	Coupling Configurations	340
343	Predicted Coupling Deflection at Seal vs Weight	341
344	Flange Test Rig	342
345	Location of Strain Gage Rosettes	343
346	Magnetic Proximity Probe Locations Rig 35120-2	343
347	Finite Element Computer Program Predictions	344
348	Instrumentation Locations Rig 35120-3	345
349	Axial Deflection at ID of Flange Rig 35120-3	346

ILLUSTRATIONS (Continued)

Figure		Page
350	Comparison of Predicted and Measured Stresses on OD Wall Rig 35120-3	346
351	XLR129 Reusable Rocket Engine, Preburner Injector and Igniter Location	349
352	Demonstrator Engine Preburner Injector	350
353	Preburner Injector Face Pattern	352
354	Preburner Torch Assembly	352
355	Preburner Torch Assembly Mounting and Sealing	353
356	Injector Housing Fabricated by Vendor	355
357	Element Blank	356
358	Blanks X-ray Inspected for Wall Thinning	356
359	Preburner Injector Element Secondary Flow Area Deviations	357
360	Physical Dimensions of Elements	358
361	Physical Dimensions of Secondary Slot	358
362	Element Flowrate Distribution	359
363	Faceplate Initial Build	360
364	Normal Distribution Curve of Effective Area With a Narrow Range (8.9%) Total Band	360
365	Four Braze Joints of the Injector Assembly	362
366	(Injector Grain Structure) Microstructure of Injector Housing Before and After Solution Heat Treatment	363
367	Microstructure of Injector Housing After Faceplate Braze and Precipitation Heat Treat	364
368	Braze Material in Fuel Slots	365
369	Microstructure of Injector Housing After Final Solution Heat Treatment, Before Rebraze of Faceplate	368
370	Cross Section of New Seal Configuration	370

ILLUSTRATIONS (Continued)

Figure		Page
371	Outer Three Rows of Oxidizer Elements Scarfed On Second Injector	372
372	Preburner Test Rig	373
373	Angle-of-Turn Load Deviation vs Axial Stress	374
374	Bolt Elongation-Deviation vs Axial Stress	375
375	Bolt Torque Deviation vs Axial Stress	375
376	Preburner Rig Instrumentation	381
377	Test Sequence for Preburner Testing	384
378	Injector Face With Local Discolored Spots	387
379	Thermocouple Rakes, Viewed Upstream Through the Nozzle, Test 3.01	394
380	Temperature Distribution, 20% Thrust	395
381	Temperature Distribution, 35% Thrust	395
382	Oxidizer Flow Reached Secondary Cavity of the Injector . . .	396
383	Preburner Chamber Pressure During Pulsing, Test 1.01 . .	397
384	Preburner Scrub Liner After Test 1.01	398
385	Preburner Injector Fixed to Prevent Uncooled Liner Damage	399
386	Injector Face Showing Good Condition Without Metal Erosion	401
387	Fixed Area Preburner Temperature Profile	401
388	Scrub Liner Burning Pattern, Top Dead Center View	402
389	Scrub Liner Burning Pattern, 90 deg View	403
390	Scrub Liner Burning Pattern, 180 deg View	403
391	Scrub Liner Burning Pattern, 220 deg View	404
392	Areas of Spring Seal Leakage After Build 2 Testing	404

ILLUSTRATIONS (Continued)

Figure		Page
393	Injector Element Pattern Showing 12 Redirected Elements	405
394	Injector Thermal Relief Slots	406
395	Modifications Made to Preburner for Build 3	407
396	Rakes Added to Obtain Temperature Profile Data	407
397	Injector Face Condition After Run 5.01	409
398	Liner Damage Sustained During Test 6.01	410
399	Injector Shown After Run 6.01	411
400	Fixed Area Preburner Temperature Profile, Run 6.01	411
401	Fixed Area Preburner Temperature Profile, Run 6.01	412
402	Element Test Set Up	414
403	Elements Considered Blocked Having Ratios Below 0.92	415
404	Dual Water Flow Test Set Up	415
405	Temperature Based on Dual Flows	416
406	Cross Section of Injector With Flow Collectors	417
407	Combustion Temperature	418
408	Preburner Injector and Oxidizer Control Valve With Spacer	418
409	Combustion Temperature	419
410	Injector in Stand With Static Pressure Tool	420
411	Ratio of Individual Pressure to Average Pressure for Fuel Side GN ₂ Flow Without Close Mounted Filter	421
412	Fuel Filter Close Coupled to Fuel Inlet Horn	422
413	GN ₂ on Fuel Injector With Filter Near Injector - Ratio of Individual Pressure to Average Pressure	423
414	Shaded Areas Showing Locations Considered Blocked	424

ILLUSTRATIONS (Continued)

Figure		Page
415	Six Elements With Blocked Primaries Plugged by Welding	425
416	Preburner Discolored Area, Run 7.01	427
417	Fixed Area Preburner Temperature Profile, Run 7.01	427
418	Fixed Area Preburner Temperature Profile, Run 7.01	428
419	Preburner Scrub Liner and Average Combustion Temperatures, Test 7.01	429
420	Fixed Area Preburner Temperature Profile	430
421	Portion of Injector Face and Typical Liner Section Viewed Through Mirror	434
422	Fixed Area Preburner Temperature Profile, Test 10.02 . . .	434
423	Fixed Area Preburner Temperature Profile, Test 10.02 . . .	435
424	Preburner Scrub Liner and Average Combustion Temperatures, Test 10.02.	436
425	Injector Face Showing Eroded Areas	437
426	Fixed Area Preburner Temperature Profile, Run 11.01, Build 4	437
427	Fixed Area Preburner Temperature Profile, Run 11.01, Build 4	438
428	Preburner Scrub Liner and Average Combustion Temper- ature, Test 13.01	443
429	Fixed Area Preburner Temperature Profile, Run 13.01	447
430	Fixed Area Preburner Temperature Profile, Run 13.01	447
431	Fixed Area Preburner Temperature Profile, Run 13.01	448
432	Fixed Area Preburner Temperature Profile, Run 13.01	448
433	Fixed Area Preburner Temperature Profile, Run 13.01	449
434	Fixed Area Preburner Temperature Profile, Run 13.01	449
435	Profile Shift of PCT 301, Run 13.01	450

ILLUSTRATIONS (Continued)

Figure		Page
436	Injector Face Shown After Run 14.01	451
437	Fixed Area Preburner Temperature Profile, Run 14.01 . . .	454
438	Fixed Area Preburner Temperature Profile, Run 14.01 . . .	454
439	Uncooled and Cooled Liner Configuration	455
440	Cooled Liner Configuration With Uncooled Liner Vibration Damper	459
441	Injector Face Before Run 1.01	462
442	Liner Condition Before Run 1.01	462
443	Injector Face After Run 1.01	463
444	Liner Condition After Run 1.01	463
445	Temperature Distribution for Run 1.01	466
446	Temperature Distribution for Run 1.01	466
447	Scrub Liner Temperature	467
448	Injector Face Condition After Run 5.01	469
449	Liner Position (12 o'clock) After Run 5.01	469
450	Temperature Distribution During Run 5.01	476
451	Temperature Distribution During Run 5.01	476
452	Temperature Distribution During Run 5.01	477
453	Temperature Distribution During Run 5.01	477
454	Scrub Liner Temperature, Run 5.01	479
455	Temperature Distributions, Run 7.01	481
456	Temperature Distribution, Run 7.01	481
457	Scrub Liner Temperature, Run 7.01	482
458	Injector Face Condition After Teardown	483
459	Liner Condition After Teardown	483

ILLUSTRATIONS (Continued)

Figure		Page
460	Temperature Distribution During Run 8.01	485
461	Temperature Distribution During Run 8.01	485
462	Scrub Liner Temperature, Run 8.01	486
463	View of Large End of Liner Showing Large Circumferential Crack Along Ring Weld and Crack Branched Out Through Weld and Liner	488
464	Close-up of Fracture Through 1-1/4 In. Long Circumferential Crack Showing Fatigue Progressing From Numerous Origins on Both the ID and and OD of the Liner	489
465	Photomicrographs of Section Through 1/2 In. Long Circumferential Indication Showing a Single, Transgranular Crack Progressing Through the Liner Side Heat Affected Zone of the Liner Ring Weld	490
466	Section of Transpiration Liner Showing Where Electron Beam Missed the Land	491
467	Preburner Torch Igniter Assemblies Mounted in B-7 Test Stand	492
468	Igniter Instrumentation	493
469	Typical Igniter Firing	494
470	E-8 Test Stand Plot Plan	498
471	E-8 Control Console	499
472	E-8 Analog Computer	499
473	200-Channel Digital Data System	501
474	Preburner Rig Control System	502
475	XLR129 Reusable Rocket Engine	504
476	Plug-In Concept	505
477	Transition Case Assembly	507
478	Outer Case and Cooling Liner	508

ILLUSTRATIONS (Continued)

Figure		Page
479	Gimbal Thrust Ball Assembly	510
480	Preburner Flow Duct.	511
481	Preburner Flow Duct to Centerbody Piston Ring Connection	512
482	Details of Cooled Line Assembly	512
483	Connection of Front and Rear Sections of Hot Gas Scrub Liner	514
484	Preburner Flow Duct Front Support	515
485	Transition Case Centerbody	516
486	Sphere Welding Fixture	522
487	Sphere Showing Two Segments Welded in Position	523
488	Transition Case Bolt Hole Drilling Fixture	524
489	Transition Mockup Assembly Showing Preburner Injector and Fuel Pump Installation	525
490	Hydrostatic Proof Test of the Transition Case	525
491	Advanced Propulsion XLR129 Preburner Outer Case Showing Locations of Strain Gage Rosettes No. 1 Through No. 10. Strain Gage Rosette No. 47 Located Inside Case	526
492	Advanced Propulsion XLR129 Preburner Outer Case Showing Locations of Strain Gage Rosettes No. 12 Through No. 18, 36, and 44	527
493	Advanced Propulsion XLR129 Preburner Outer Case Showing Locations of Strain Gage Rosettes No. 11, 29 Through 33, 40, 41, and 43	527
494	Advanced Propulsion XLR129 Preburner Outer Case Showing Locations of Strain Gage Rosettes No. 20 Through 24, 37, 38, 39, and 42	528
495	Advanced Propulsion XLR129 Preburner Outer Case Showing Locations of Strain Gage Rosettes No. 19, 25, 26, and 27	528

ILLUSTRATIONS (Continued)

Figure		Page
496	Advanced Propulsion XLR129 Preburner Outer Case Showing Locations of Strain Gage Rosettes No. 26, 27, and 28	529
497	Advanced Propulsion XLR129 Preburner Outer Case Showing Locations of Strain Gage Rosettes No. 34, 35, and 36	529
498	Advanced Propulsion XLR129 Preburner Outer Case Showing Locations of Strain Gage Rosettes No. 45 and 46	530
499	Transition Case Showing Setup for Experimental Stress Analysis and Internal Pressure - Thrust Proof Test	530
500	Strain Gage Data, Gage No. 18	537
501	Biaxial Strain Data, Gage No. 20A	537
502	Strain Gage Data, Gage No. 16	538
503	Outer Case and Porous Cooling Liner Instrumentation	538
504	Formed Case Cooling Liner Segments	544
505	Transition Case With Cooling Liner	545
506	Gimbal Ball	545
507	Preburner Combustor Duct and Inner Coolant Liner	547
508	Preburner Combustor Duct Brazed Assembly	547
509	Centerbody and Formed Outer Liners	549
510	Transition Case With Centerbody Installed	549
511	Turbine Simulator Cap	550
512	Transition Case Assembly Viewed Through Main Injector Flange	551
513	Turbine Ducts Viewed Through the Main Injector Flange	551
514	Fuel Turbopump Duct and Turbine Simulator Assembly	552
515	Oxidizer Turbopump Duct and Turbine Simulator Assembly	552

ILLUSTRATIONS (Continued)

Figure		Page
516	Transition Case Mounted in E-8 Test Stand Before Test	553
517	Main Burner Injector and Torch Location	555
518	Main Burner Injector	556
519	Segmented Injector Concept	556
520	Typical Main Burner Injector Cross Section	557
521	Typical Spraybar	557
522	Main Burner Injector Spraybar Cross Section	558
523	Main Burner Torch Assembly	560
524	Main Burner Torch Assembly, Propellant Flow, Mounting and Sealing	560
525	Comparison of Predicted and Actual Flow Data	562
526	Plates of Inconel 718 Machined to Accept Medium Spraybar	571
527	Spraybar Braze Technique Substantiated	571
528	Tensile Specimen Data Plot	572
529	Cyclic Loading Tensile Specimen Data	573
530	Location of Main Burner Chamber Assembly	577
531	Main Burner Chamber Assembly, Side View	577
532	Main Chamber Assembly, View Aft	578
533	Main Burner Chamber, Side View	579
534	Forward Chamber Coolant Metering	581
535	Forward Chamber Liner Coolant Metering Installation, Side View	581
536	Rear Chamber Liner Coolant	582
537	Rear Chamber Liner Coolant Metering, Side View	582
538	Typical Cylindrical Wafer	583

ILLUSTRATIONS (Continued)

Figure		Page
539	Igniter Incorporated in Main Chamber Wall	585
540	Location of Lands on Chamber Wafer	585
541	Pulse Gun Installation in Igniter Boss	586
542	Location of Primary Nozzle	590
543	Location of Two-Position Nozzle and Translating Mechanism	591
544	Nozzle Assembly	592
545	Regeneratively Cooled Primary Nozzle	594
546	Primary Nozzle Configuration	594
547	Total Thrust vs Axial Position	595
548	Nozzle Wall Static Pressure	595
549	Preburner Supply Heat Exchanger	596
550	Preburner to Transpiration Heat Exchanger Flange	598
551	Transpiration Supply Heat Exchanger	598
552	Two-Position Nozzle	600
553	Typical Nozzle Shell Configuration	600
554	Design of Two-Position Nozzle Complete	601
555	Two-Position Nozzle Geometry	601
556	Translating Mechanism	602
557	Drive Motor, Gearbox and Locking Device for Translating Mechanism	604
558	Ball Nut Gimbal and Support	605
559	Translating Mechanism Forward Supports	606
560	Braze Peel Test Specimens	608
561	Inconel 625 Provides Highest Average Cycle Life	609

ILLUSTRATIONS (Continued)

Figure		Page
562	Primary Nozzle Meets Life Requirements	610
563	Predicted Thermal Gradient of Regenerative Nozzle Tube Nearest Throat	610
564	Fuel Turbopump Location	611
565	Fuel Turbopump Assembly	612
566	High-Speed Inducer	165
567	High-Speed Inducer Attachment	615
568	Front Bearing and Mount Assembly	616
569	Roller Bearing Configuration	617
570	Front Bearing Preloading	617
571	Front Bearing Coolant Flowpath	619
572	Rotor Assembly	619
573	Thrust Balance System	621
574	Thrust Piston Fluid Supply and Discharge	621
575	Rear Bearing and Mount Assembly	622
576	Rear Bearing Preloading	622
577	Rear Bearing Coolant Flow	623
578	Fuel Turbopump Liftoff Seal	624
579	Turbine Inlet Duct	625
580	1st-Stage Stator Installation	626
581	1st-Stage Disk, Blade, and Shroud Installation	628
582	2nd-Stage Stator Installation	629
583	2nd-Stage Stator Flow Guide	630
584	2nd-Stage Stator Seal Diaphragm	630
585	Rotor Assembly Shaft Transition Section Isotherms	631

ILLUSTRATIONS (Continued)

Figure		Page
586	Turbine Discharge Turnaround Manifold	632
587	Turbine Coolant Flows and Pressures	635
588	Rotor Assembly	638
589	Rotor Assembly Coolant Flows	639
590	Fuel Turbopump Housings	639
591	Maximum Stresses and Deflections in Critical Areas of the Housings	641
592	Fuel Turbopump Inlet Flow vs Pressure Rise	642
593	High-Speed Inducer	644
594	1st-Stage Impeller	644
595	2nd-Stage Impeller.	645
596	Thrust Balance Piston	645
597	Turbine Blades	647
598	1st-Stage Turbine Blade and Rotor Assembly	647
599	2nd-Stage Turbine Blade and Rotor Assembly	648
600	Fuel Turbopump Bearing (Typical)	648
601	Inducer Housing Assembly (View 1)	649
602	Inducer Housing Assembly (View 2)	650
603	Main Turbopump Housing Milling Operation	651
604	Main Housing After Completion of Welding and Heat Treatment	652
605	Main Turbopump Housing Machined to Dimension	653
606	2nd-Stage Housing After Machining Operations	653
607	Front Thrust Balance Piston Housing - Pump Side Up	654
608	Front Thrust Balance Piston Housing - Rear Side Up	654

ILLUSTRATIONS (Continued)

Figure		Page
609	Rear Bearing Support and Rear Thrust Piston Housing - Front Side Up	655
610	VF-47 Rear Bearing Support - Turbine Side Up.	655
611	Liftoff Seal Assembly	656
612	Turbine Inlet Duct - Inlet End at Top.	657
613	Turbine Inlet Duct - Discharge End at Top.	657
614	Turbine Inlet Duct Assembly With Heat Shields Installed - View 1	658
615	Turbine Inlet Duct Assembly With Heat Shields Installed - View 2	659
616	Turbine Inlet Cover Housing	659
617	1st-Stage Cored Stator	660
618	2nd-Stage Cored Stator	661
619	Turbine Exit Diffuser - Inlet Side	662
620	Turbine Exit Diffuser - Discharge Side	662
621	Inside Turnaround Duct	663
622	Outside Turnaround Duct	664
623	Turbine Support Ring	664
624	Turbine Outside Heat Shield	665
625	1st-Stage Turbine Blade Vibration Test Setup.	667
626	2nd-Stage Turbine Blade Vibration Test Setup	667
627	Holographic Test Schematic	668
628	Hologram Test Setup Used for Turbine Blade Mode Shape Determination	669
629	Mode Shapes at the Resonance Points of the XLR129 1st-Stage Turbine Blade	670

ILLUSTRATIONS (Continued)

Figure		Page
630	Mode Shapes at the Resonance Points of the XLR129 2nd-Stage Turbine Blade	670
631	Main Housing Proof Test Verified Design	671
632	Locations of Strain Gages Installed on the Main Fuel Turbopump Housing for Hydrostatic Proof Pressure Tests	672
633	2nd-Stage Actuator Maximum Strain Readout	674
634	Fuel Turbopump Liftoff Seal	678
635	Liftoff Seal Test Rig	679
636	Cross Section of Liftoff Seal Assembly.	680
637	Inner Bellows Section Showing Fabrication Problem Areas . .	692
638	Outer Bellows Weld Fabrication Location	682
639	Overextension of Bellows Resulting in Excessive Tensile Loads	683
640	B-21 Test Stand Station Flow Test Arrangement, Block Diagram	684
641	Fuel Turbopump Turbine Stator Flow Calibration	685
642	Rotor Support System for Fuel Turbopump Critical Speed Analysis	686
643	XLR129 Fuel Pump Rotor, Natural Frequency Test	686
644	XLR129 Fuel Pump Rotor, Second Bending Mode Predicted and Test Results	687
645	XLR129 Fuel Pump Rotor, First Bending Mode Predicted and Test Results	688
646	Front Bearing Support Spring Rate Setup	689
647	Front Bearing Support Accelerometer Mounting	689
648	Series Spring Simulation of Front Bearing Support Test Setup	690
649	Rear Bearing Support Test Setup	694

ILLUSTRATIONS (Continued)

Figure		Page
650	Rear Bearing Support Accelerometer Mounting	692
651	Inducer Housing Modifications	695
652	Significant Turbopump Parameters vs Time, Test 3.01, Sheet 1 of 3	701
653	Significant Turbopump Parameters vs Time, Test 3.01, Sheet 2 of 3	702
654	Significant Turbopump Parameters vs Time, Test 3.01, Sheet 3 of 3	703
655	Axial Thrust and Speed vs Time, Test 3.01	704
656	Significant Turbopump Parameters vs Time, Test 4.01, Sheet 1 of 3	705
657	Significant Turbopump Parameters vs Time, Test 4.01, Sheet 2 of 3	706
658	Significant Turbopump Parameters vs Time, Test 4.01, Sheet 3 of 3	707
659	Axial Thrust and Speed vs Time, Test 4.01	708
660	Fuel Pump Vibration Traces, Test Rig 35138-1, Test 5.01	709
661	Frequency Analysis of Vibration Data	709
662	Significant Turbopump Parameters vs Time, Test 5.01, Sheet 1 of 3	710
663	Significant Turbopump Parameters vs Time, Test 5.01, Sheet 2 of 3	711
664	Significant Turbopump Parameters vs Time, Test 5.01, Sheet 3 of 3	712
665	Axial Thrust and Speed vs Time, Test 5.01	713
666	Turbopump Liftoff Seal Wear Results	714
667	Turbopump Liftoff Seal Failed Bellows Convolution	715
668	Fuel Turbopump Pressure Rise, Rig 35138-1	716

ILLUSTRATIONS (Continued)

Figure		Page
669	Fuel Turbopump Overall Efficiency, Rig 35138-1	717
670	Fuel Turbopump 1st-Stage Polytropic Efficiency, Rig 35138-1	717
671	Fuel Turbopump 2nd-Stage Polytropic Efficiency, Rig 35138-1	718
672	Fuel Turbopump Overall Unit Head, Rig 35138-1	718
673	Fuel Turbopump 1st-Stage Polytropic Head Coefficient, Rig 35138-1	719
674	Fuel Turbopump 2nd-Stage Polytropic Head Coefficient, Rig 35138-1	719
675	Fuel Turbopump Turbine Efficiency, Rig 35138-1	720
676	Significant Turbopump Parameters vs Time, Test 6.01, Sheet 1 of 3	722
677	Significant Turbopump Parameters vs Time, Test 6.01, Sheet 2 of 3	723
678	Significant Turbopump Parameters vs Time, Test 6.01, Sheet 3 of 3	724
679	Axial Thrust and Speed vs Time, Test 6.01	725
680	Significant Turbopump Parameters vs Time, Test 7.01, Sheet 1 of 3	727
681	Significant Turbopump Parameters vs Time, Test 7.01, Sheet 2 of 3	728
682	Significant Turbopump Parameters vs Time, Test 7.01, Sheet 3 of 3	729
683	Axial Thrust and Speed vs Time, Test 7.01	730
684	Comparative Acceleration Vibration Traces, Test 5.01	731
685	Pump Discharge Pressure vs Flow, Tests 7.01 and 8.01	731
686	Vibration Trace, Test 8.01	732
687	Significant Turbopump Parameters vs Time, Test 8.01, Sheet 1 of 3	733

ILLUSTRATIONS (Continued)

Figure		Page
688	Significant Turbopump Parameters vs Time, Test 8.01, Sheet 2 of 3	734
689	Significant Turbopump Parameters vs Time, Test 8.01, Sheet 3 of 3	735
690	Axial Thrust and Speed vs Time, Test 8.01	736
691	Significant Turbopump Parameters vs Time, Test 9.01, Sheet 1 of 3	737
692	Significant Turbopump Parameters vs Time, Test 9.01, Sheet 2 of 3	738
693	Significant Turbopump Parameters vs Time, Test 9.01, Sheet 3 of 3	739
694	Axial Thrust and Speed vs Time, Test 9.01	740
695	Significant Turbopump Parameters vs Time, Test 10.01, Sheet 1 of 3	742
696	Significant Turbopump Parameters vs Time, Test 10.01, Sheet 2 of 3	743
697	Significant Turbopump Parameters vs Time, Test 10.01, Sheet 3 of 3	744
698	Axial Thrust and Speed vs Time, Test 10.01	745
699	Significant Turbopump Parameters vs Time, Test 11.01, Sheet 1 of 3	746
700	Significant Turbopump Parameters vs Time, Test 11.01, Sheet 2 of 3	747
701	Significant Turbopump Parameters vs Time, Test 11.01, Sheet 3 of 3	748
702	Axial Thrust and Speed vs Time, Test 11.01	749
703	F35138-2 Post-Test View Showing Moderate Rub Indications on 2nd-Stage Impeller and Pumping Shroud	750
704	Post-Test View of 2nd-Stage Impeller Showing Blade Tip Rub	750

ILLUSTRATIONS (Continued)

Figure		Page
705	F35138-2 Post-Test View of 2nd-Stage Impeller Showing Fretting Indications on the Face Splines	751
706	Post-Test View Showing Light Rub Indications on Thrust Piston Front Face Outer Seal Land and Housing Leaded Bronze Rub Face	751
707	Build 2 Post-Test View Showing Thermal Cracks in the Rear Leaded Bronze Rub Face and Rub Indications From Both Rear Thrust Piston Seal Lands	752
708	Turbine Inlet Conical Flow Duct Buckled by Excessive Pressure Transient	753
709	Rig F35138, Build 2 Post-Test View of Front Bearing Showing Good Condition of Detail Parts	754
710	Rig F35138, Build 2 Post-Test View of Rear Bearing Showing Good Condition of Detail Parts	754
711	Pump Pressure Rise vs Inlet Flow, Rig 35138-2	755
712	Overall Efficiency vs Inlet Unit Flow, Rig 35138-2	755
713	First Stage Efficiency Characteristic	756
714	Second Stage Efficiency Characteristic	756
715	Overall Unit Head vs Inlet Unit Flow, Rig 35138-2	757
716	First Stage Head Coefficient	757
717	Second Stage Head Coefficient	758
718	Turbine Efficiency	758
719	Overall Unit Pressure vs Net Positive Suction Head, Rig 35138-2	759
720	Suction Specific Speed vs Unit Flow, Rig 35138-2	759
721	Significant Turbopump Parameters vs Time, Test 1.01, Sheet 1 of 3	762
722	Significant Turbopump Parameters vs Time, Test 1.01, Sheet 2 of 3	763

ILLUSTRATIONS (Continued)

Figure		Page
723	Significant Turbopump Parameters vs Time, Test 1.01, Sheet 3 of 3	764
724	Axial Thrust and Speed vs Time, Test 1.01	765
725	Significant Turbopump Parameters vs Time, Test 2.01, Sheet 1 of 3	766
726	Significant Turbopump Parameters vs Time, Test 2.01, Sheet 2 of 3	767
727	Significant Turbopump Parameters vs Time, Test 2.01, Sheet 3 of 3	768
728	Axial Thrust and Speed vs Time, Test 2.01	769
729	Pump Total Pressure Rise vs Inlet Flow, Rig 35147-1A . . .	771
730	Overall Efficiency vs Inlet Unit Flow, Rig 35147-1A	771
731	First Stage Efficiency Characteristics	772
732	Second Stage Efficiency Characteristics	772
733	Overall Unit Head vs Inlet Unit Flow, Rig 35147-1A	773
734	First Stage Head Coefficients	773
735	Second Stage Head Coefficients	774
736	Turbine Performance	774
737	Vibration Trace, Rig 35147-1A, Tests 1.01 and 2.01	775
738	Fuel Pump Rig Instrumentation	781
739	Fuel Pump 2nd-Stage Stator Calibration Data	782
740	Test Facility Schematic	783
741	Oxidizer Turbopump Location	786
742	Oxidizer Turbopump Assembly	787
743	Oxidizer Turbopump High-Speed Inducer	788
744	Oxidizer Turbopump High-Speed Inducer Stresses	789
745	Oxidizer Turbopump Impeller	789

ILLUSTRATIONS (Continued)

Figure		Page
746	Oxidizer Turbopump Impeller Stresses	790
747	Oxidizer Turbopump Bearings and Bearing Mounts	791
748	Oxidizer Turbopump Front Bearing Coolant	792
749	Oxidizer Turbopump Rear Bearing Coolant Flow	793
750	Oxidizer Turbopump Thrust Balance System	794
751	Thrust Piston Clearance and Flowrate	795
752	Oxidizer Turbopump Thrust Piston Deflection	795
753	Oxidizer Turbopump Seal Package	796
754	Oxidizer Turbopump Bellows Actuated Lutoff Seal	797
755	Oxidizer Turbopump Turbine	798
756	Oxidizer Turbopump Turbine Inlet Duct	799
757	Oxidizer Turbopump Turbine Stages and Exhaust System . . .	800
758	Oxidizer Turbopump Turbine Hub and Tie Bolt Temperature Profile	803
759	Oxidizer Turbopump Turnaround Manifold and Exit Diffuser Temperatures	804
760	Oxidizer Turbopump Cooling System	806
761	Oxidizer Turbopump Turbine Disk Coolant Flow	807
762	Oxidizer Turbopump Turbine Support Coolant Flow	807
763	Oxidizer Turbopump Inlet Housing	808
764	Oxidizer Turbopump Impeller Housing	809
765	Oxidizer Turbopump Housing Stresses	810
766	Oxidizer Turbopump Flow vs Pressure Rise	811
767	Fuel Low-Speed Inducer Location	813
768	Fuel Low-Speed Inducer, Cross Sectional View	814

ILLUSTRATIONS (Continued)

Figure		Page
769	Fuel Low-Speed Inducer	816
770	Fuel Low-Speed Inducer Thrust Piston and Front Bearing Arrangement	817
771	Fuel Low-Speed inducer Internal Flow Systems	817
772	Fuel Low-Speed Inducer Turbine Stator Assembly	819
773	Fuel Low-Speed Inducer Pressure Rise	820
774	Oxidizer Low-Speed Inducer Location	922
775	Oxidizer Low-Speed Inducer Cross Sectional View	823
776	Oxidizer Low-Speed Inducer	824
777	Oxidizer Low-Speed Inducer Rotor Assembly	825
778	Oxidizer Low-Speed Inducer Turbine and Variable Guide Vanes	826
779	Oxidizer Low-Speed Inducer Turbine Disk	828
780	Oxidizer Low-Speed Inducer Pressure Rise	829
781	Flow Pattern Schematic, 1.5 Inch Chord Vane	830
782	Flow Pattern Schematic, 1 Inch Chord Vane	830
783	Demonstrator Engine Control System	834
784	Preburner Oxidizer Valve	838
785	Preburner Oxidizer Valve Layout	838
786	Preburner Oxidizer Valve Port Contour	839
787	Preburner Oxidizer Valve Operating Characteristics	840
788	Preburner Dome Cross Sections	841
789	Secondary Oxidizer Flow Passages	842
790	Preburner Oxidizer Valve Flow Schematic	842
791	Flow Area Error, Predicted vs Measured	843
792	Translating Shaft Lip Seal Package	844

ILLUSTRATIONS (Continued)

Figure		Page
793	Balance Piston Lip Seal Package and Upper Piston Ring . . .	844
794	Lower Piston Ring Installation	845
795	Preburner Oxidizer Valve	848
796	Preburner Oxidizer Valve Test Results.	848
797	Actuation System Linearity	849
798	Frequency Response Characteristics	850
799	Actuation System Linearity	850
800	Frequency Response Characteristics	851
801	Preburner Oxidizer Valve Instrumentation	852
802	Strain Gaged Spool Piece	853
803	Piston Ring Load	854
804	Piston Ring Leakage - Cycling	855
805	Piston Ring Static Test Leakage Data	855
806	Shaft Seal Force	856
807	Shaft Seal Leakage - Cycling (Primary).	857
808	Shaft Seal Leakage - Static (Primary)	857
809	Shaft Seal Leakage - Cycling (Secondary)	858
810	Shaft Seal Leakage - Static (Secondary)	858
811	Shaft Seal Post-Test Condition (Primary)	859
812	Shaft Seal Post-Test Condition (Secondary)	859
813	Shaft Seal in Typical Condition	860
814	Balance Piston Seal Leakage - Static	860
815	Shutoff Seal Leakage	861
816	Shutoff Seal Before Test Run	862

ILLUSTRATIONS (Continued)

Figure		Page
817	Shutoff Seal, Post-Test Condition	862
818	Preburner Dome Structural Analysis	863
819	Effect of Seal Package Reoperation	863
820	Reoperated Lower Seal Plate	865
821	Preburner Fuel Valve	866
822	Hoop Seal Cross Section	867
823	Shaft Lip Seals	867
824	Fabrication of Preburner Fuel Valve Seal Element (AKS-6754)	868
825	Lip Seal Fabrication	869
826	Assembly of Preburner Fuel Valve Shutoff Seal and Disk . . .	870
827	Results Compared to Design Prediction	872
828	Post-Test Torque	872
829	Valve Dynamic Torque	873
830	Transpiration Coolant Port Compared to the Actual Area . . .	873
831	Se. 1 Rubbing on Seal Housing Inside Diameter	874
832	Collapsed Seal Loading Nut Lock Ring	874
833	Modified Seal Loading Nut Lock Ring	875
834	Preburner Fuel Valve Housing Stress Patterns	875
835	Preburner Fuel Valve Housing Stress Patterns	876
836	Rub Marks on Seal Housing ID	877
837	Circular Rub Mark on Face of Seal Housing	877
838	Radial Marks on Seal Retaining Ring	878
839	Static Seal Support Ring Indicated Relative Motion Between Valve Housing and Seal Housing	878

ILLUSTRATIONS (Continued)

Figure		Page
840	Shutoff Seal Leakage	881
841	Drive End Shaft Lip Seal Package	883
842	Blind End Shaft Lip Seal Leakage	885
843	Total Torque Data	887
844	Amplitude Ratio and Phase Lag	887
845	Amplitude Ratio and Phase Lag	888
846	Amplitude Ratio and Phase Lag	888
847	Amplitude Ratio and Phase Lag	889
848	Plots at the 5-degree Position	889
849	Plot at the 5-degree Position	890
850	Blind End Shaft Lip Seal in the End Cover	890
851	Seal Shown After End Cover Disassembly	891
852	Drive End Cover Assembly Showing Crack in Primary Lip Seal and Frayed Secondary Lip Seal	891
853	Seals Viewed After Cover Disassembly	892
854	Severe Wear in Silver Plating at Blind End of Valve Shaft . .	893
855	Condition of Shim After Removal	893
856	End Wear on Valve Shaft	894
857	Shutoff Seal Showing Good Condition After Cycle Test	894
858	Shutoff Seal Deformations	895
859	Disk Showing Wear Pattern	896
860	Main Chamber Oxidizer Valve	896
861	Hoop Seal Cross Section	898
862	Shaft Stress Analysis Summary	899
863	Main Chamber Oxidizer Valve Shaft Lip Seals	899

ILLUSTRATIONS (Continued)

Figure		Page
864	Flange Stress Analysis Summary	902
865	Oxidizer Valve Parts Display	903
866	Helium System Schematic	904
867	Helium System, Typical Packaging	906
868	Propellant Vent Valve	907
869	Propellant Vent Valve Shutoff Seal	908
870	Triangular Transfer Tube Assembly Closed-End Trunnion . .	910
871	Two-Position Nozzle Choked Venturi Configuration	911
872	Triangular Transfer Tube Assembly Cooled Inlet Trunnion	912
873	Single Transfer Tube Assembly	913
874	Single Transfer Tube Assembly Ball Joint Passages and Shaft Retention	913
875	Two-Position Nozzle Coolant Supply System, Extended Position	914
876	Nozzle Detail Parts	915
877	Assembled Feed System Linkage	916
878	Electrical System Definition Envelope	917
879	First Benton Exciter	918
880	Electrical Components Deformed Because of Seal Failure at 1300 psig	919
881	Deformation of Electrical Components Box After Seal Failure	920
882	Second Benton Exciter	920
883	Block Diagram Defining Engine Control Task	922
884	Skin Thermocouples Installed on Inside Diameter of Main Case	936

ILLUSTRATIONS (Continued)

Figure		Page
885	Preformed, Welded, Spherical Segments	936
886	Centerbody Installed in Interior of Main Case	937
887	Centerbody Consisting of Cooling Liner and Outer Liner . . .	938
888	Preburner Flow Duct	939
889	Cooled Structural Duct	940
890	Transpiration Cooled Liner	940
891	Preburner Flow Duct Front Support	941
892	Preburner Flow Duct to Centerbody Piston Ring Connection	941
893	Knife Edge Seal of Duct Outer Heat Shield	942
894	Fuel Pumps Turbine Simulator	943
895	Oxidizer Pump Turbine Simulator	944
896	Main Burner Simulator	944
897	Gimbal Thrust Ball Attached to Outer Case Gimbal Cone . . .	945
898	Hot Gas System Rig Instrumentation	947
899	Instrumentation to Monitor Main Case Cavity Conditions . . .	949
900	Instrumentation to Monitor Main Case Cavity Conditions . . .	949
901	Rig Inspected Through Nozzle Throat	953
902	Discoloration Extending Into Uncooled Section of the Lines . .	953
903	Temperature Profile in Final Pump Simulator, Run 3.01 . . .	956
904	Total Pressure Profile in Fuel Pump Simulator Ducting, Run 3.01	956
905	Static Pressure in Oxidizer Pump Simulator Ducting, Run 3.01	957
906	Temperature Profile in Fuel and Oxidizer Pump Simulators, Run 6.01	960

ILLUSTRATIONS (Continued)

Figure		Page
864	Flange Stress Analysis Summary	902
865	Oxidizer Valve Parts Display	903
866	Helium System Schematic	904
867	Helium System, Typical Packaging	906
868	Propellant Vent Valve	907
869	Propellant Vent Valve Shutoff Seal	908
870	Triangular Transfer Tube Assembly Closed-End Trunnion . .	910
871	Two-Position Nozzle Choked Venturi Configuration	911
872	Triangular Transfer Tube Assembly Cooled Inlet Trunnion	912
873	Single Transfer Tube Assembly	913
874	Single Transfer Tube Assembly Ball Joint Passages and Shaft Retention	913
875	Two-Position Nozzle Coolant Supply System, Extended Position	914
876	Nozzle Detail Parts	915
877	Assembled Feed System Linkage	916
878	Electrical System Definition Envelope	917
879	First Benton Exciter	918
880	Electrical Components Deformed Because of Seal Failure at 1300 psig	919
881	Deformation of Electrical Components Box After Seal Failure	920
882	Second Benton Exciter	920
883	Block Diagram Defining Engine Control Task	922
884	Skin Thermocouples Installed on Inside Diameter of Main Case	936

ILLUSTRATIONS (Continued)

Figure		Page
907	Total Pressure Profile in Fuel Pump Simulator Ducting, Run 6.01	960
908	Static Pressure in Fuel Pump Simulator Ducting, Run 6.01	961
909	Partial Effectiveness of Electron Beam Weld in Uncooled Scrub Liner	961
910	Hot Turbine Test Rig Schematic	965
911	Pump Discharge Pressure vs Flow Test 1.02, Rig 35155-1..	966
912	Significant Turbopump Parameters vs Time, Test 1.02, Rig F35155-1, Sheet 1 of 4	967
913	Significant Turbopump Parameters vs Time, Test 1.02, Rig F35155-1, Sheet 2 of 4	968
914	Significant Turbopump Parameters vs Time, Test 1.02, Rig F35155-1, Sheet 3 of 4	969
915	Significant Turbopump Parameters vs Time, Test 1.02, Rig 35155-1, Sheet 4 of 4	970
916	Temperature Profile Data, Test 1.02	972
917	Pressure Profile Data, Test 1.02	972
918	Pump Discharge Pressure vs Flow, Test 3.01, Rig F35155-1	973
919	Significant Turbopump Parameters vs Time, Test 3.01, Rig F35155-1, Sheet 1 of 4	974
920	Significant Turbopump Parameters vs Time, Test 3.01, Rig F35155-1, Sheet 2 of 4	975
921	Significant Turbopump Parameters vs Time, Test 3.01, Rig F35155-1, Sheet 3 of 4	976
922	Significant Turbopump Parameters vs Time, Test 3.01, Rig F35155-1, Sheet 4 of 4	977
923	Temperature Profile Data, Test 3.01	979
924	Pressure Profile Data, Test 3.01	979

ILLUSTRATIONS (Continued)

Figure		Page
925	Pump Discharge Pressure vs Flow, Test 4.01, Rig F35155-1	980
926	Significant Turbopump Parameters vs Time, Test 4.01, Rig F35155-1, Sheet 1 of 4	981
927	Significant Turbopump Parameters vs Time, Test 4.01, Rig F35155-1, Sheet 2 of 4	982
928	Significant Turbopump Parameters vs Time, Test 4.01, Rig F35155-1, Sheet 3 of 4	983
929	Significant Turbopump Parameters vs Time, Test 4.01, Rig F35155-1, Sheet 4 of 4	984
930	Temperature Profile Data, Test 4.01	986
931	Pressure Profile Data, Test 4.01	986
932	Transition Case Inner Wall Temperature vs Time, Test 4.01, Rig F35155-1	987
933	Post-Test 4.01 View Into Transition Case Through Fuel Turbopump Port Showing Good Condition of the Ports (View 1)	988
934	Post-Test 4.01 View Into Transition Case Through Fuel Turbopump Port Showing Good Condition of the Ports (View 2)	988
935	Post-Test 4.01 View Into Transition Case Through Fuel Turbopump Port Showing Good Condition of the Ports (View 3)	989
936	Post-Test 4.01 View Into Transition Case Through Fuel Turbopump Port Showing Good Condition of the Ports (View 4)	989
937	Post-Test 4.01 View Into Transition Case Through Fuel Turbopump Port Showing Good Condition of the Ports (View 5)	990
938	Post-Test 4.01 View Into Transition Case Through Fuel Turbopump Port Showing Good Condition of the Ports (View 6)	990
939	Post-Test 4.01 View of Turbine Inlet Duct Assembly	991

ILLUSTRATIONS (Continued)

Figure		Page
940	Post-Test 4.01 View of Turbine Inlet Duct Assembly and 1st-Stage Stator (View 1)	991
941	Post-Test 4.01 View of Turbine Inlet Duct Assembly and 1st-Stage Stator (View 2)	992
942	Post-Test 4.01 View of Fuel Turbine Showing Good Condition of the Parts	992
943	Post-Test 5.02 View Into Transition Case Through Exhaust Nozzle Showing Good Condition of the Parts	994
944	Hot Turbine Test Rig Operating at the 100% $r = 6$ Level, Test 5.02	994
945	Pump Discharge Pressure vs Flow Test 5.02, Rig F35155-2	995
946	Significant Turbopump Parameters vs Time, Test 5.02, Rig F35155-2, Sheet 1 of 4	997
947	Significant Turbopump Parameters vs Time, Test 5.02, Rig F35155-2, Sheet 2 of 4	999
948	Significant Turbopump Parameters vs Time, Test 5.02, Rig F35155-2, Sheet 3 of 4	1001
949	Significant Turbopump Parameters vs Time, Test 5.02, Rig F35155-2, Sheet 4 of 4	1003
950	Temperature Profile Data, Test 5.02	1005
951	Pressure Profile Data, Test 5.02	1005
952	Pump Discharge Pressure vs Flow, Test 6.01, Rig F35155-2	1006
953	Significant Turbopump Parameters vs Time, Test 6.01, Rig F35155-2, Sheet 1 of 4	1007
954	Significant Turbopump Parameters vs Time, Test 6.01, Rig F35155-2, Sheet 2 of 4	1009
955	Significant Turbopump Parameters vs Time, Test 6.01, Rig F35155-2, Sheet 3 of 4	1011
956	Significant Turbopump Parameters vs Time, Test 6.01, Rig F35155-2, Sheet 4 of 4	1013

ILLUSTRATIONS (Continued)

Figure		Page
957	Temperature Profile Data, Test 6.01	1015
958	Pressure Profile Data, Test 6.01	1015
959	Hot Turbine Test Rig Operating at the 100% $r = 5$ Level, Test 6.01	1016
960	Hot Turbine Test Rig Major Components, Post-Test 6.01, Rig F35155-2 (View 1)	1017
961	Hot Turbine Test Rig Major Components, Post-Test 6.01, Rig F35155-2 (View 2)	1017
962	Hot Turbine Test Rig Major Components, Post-Test 6.01, Rig F35155-2 (View 3)	1018
963	Hot Turbine Test Rig Major Components, Post-Test 6.01, Rig F35155-2 (View 4)	1018
964	Hot Turbine Test Rig Major Components, Post-Test 6.01, Rig F35155-2 (View 5)	1019
965	Disassembly View of Fuel Turbopump Turbine Section Showing Deformed Centerball Seal Rings	1019
966	Disassembly View Into Transition Case Through Fuel Turbopump Port Showing Slight Ovalized Centerball	1020
967	Disassembly View of Fuel Turbine Showing Distorted Tip Shroud and Turbine Blade Dents	1020
968	Disassembly View of Fuel Turbine Showing Blade Dents and Distorted Tip Shroud	1021
969	Disassembly View of Fuel Turbine Stators and Exit Diffuser Showing the Excellent Condition	1022
970	Disassembly View of Fuel Turbine Rotors Showing Good Condition	1023
971	Disassembly View of Fuel Pump Front Bearing Showing Good Condition	1023
972	Disassembly View of Fuel Pumps Rear Bearing Showing Good Condition	1024
973	Disassembly View of Fuel Pumps Front Thrust Piston Rub Face Showing Good Condition	1024

ILLUSTRATIONS (Continued)

Figure		Page
974	Disassembly View of Fuel Pump Rear Thrust Piston Rub Face Showing Good Condition	1025
975	Disassembly View of Fuel Pump Inducer Showing Good Condition	1025
976	Disassembly View of Fuel Pump 1st-Stage Impeller Showing Good Condition	1026
977	Disassembly View of Fuel Pump 2nd-Stage Impeller Showing Good Condition	1026
978	Disassembly View of Preburner Injector Showing Good Condition	1027
979	Disassembly View of the Preburner Combustion Chamber Showing the Good Condition of the Trans- piration Cooled and Uncooled Liners	1028
980	Pump Pressure Rise vs Inlet Flow, Rig F35155	1029
981	Overall Pump Efficiency vs Inlet Flow, Rig F35155	1029
982	Overall Unit Head vs Inlet Unit Flow, Rig F35155	1030
983	Turbine Efficiency vs Velocity Ratio, Rig F35155	1030
984	Thrust Balance Margin vs Inlet Unit Flow, Rig 35155	1031
985	XLR129 Engine Plumbing, View 1	1035
986	XLR129 Engine Plumbing, view 2	1036
987	XLR129 Engine Plumbing, View 3	1036
988	Preburner Fuel Line	1038
989	Tensile Test Rings Cut From Tubing	1039
990	Tensile Test Samples Cut From Tubing	1040
991	Preburner Fuel Line, Curved Section	1041
992	Main Fuel Pump Discharge Plumbing	1044
993	General Arrangement of Oxidizer Pump Discharge Lines With Oxidizer Low-Speed Inducer	1045

ILLUSTRATIONS (Continued)

Figure		Page
994	Preburner Oxidizer Supply Line	1046
995	Main Burner Oxidizer Supply	1047
996	Fuel Pump Inlet Line	1050
997	Oxidizer Low-Speed Inducer-to-Oxidizer Turbopump	1051
998	Fuel Low-Speed Inducer Turbine Drive Fuel Supply	1052
999	Primary Nozzle Fuel Supply Line	1053
1000	Main Chamber Coolant Supply Line	1054
1001	Connector and Seal	1055
1002	Inconel 718 High-Pressure Boss Connector	1056
1003	Alternate Boss Connector	1057
1004	Static Seal Rig	1059
1005	Seal Configurations Dimensions	1060
1006	Groove Dimensions for Seal Configurations 1 Through 8	1061
1007	Groove Dimensions for Seal Configuration 9	1062
1008	Typical Seal Installations	1063
1009	Seal Nomenclature	1063
1010	Seal Test Rig	1064
1011	Strain Gage and Proximity Probe Locations	1065
1012	Proximity Probe Installation Pressure Cycle	1065
1013	Vented O-Ring, Build 5, Leakage vs Total Cycles	1066
1014	Post-Test Seal Condition, Build 5	1067
1015	Flat Flange Pivot Point Deformation	1067
1016	Vented O-Ring, Build 6, Leakage vs Total Cycles	1068
1017	Post-Test Seal Condition, Build 6	1068
1018	Flange Face Surface Damage	1069

ILLUSTRATIONS (Continued)

Figure		Page
1019	Flange Deflection, Build 7	1070
1020	Vented O-Ring, Build 8, Leakage vs Total Cycles	1071
1021	Post-Test Seal Condition, Build 8	1071
1022	Del C-Seal and Sealing Surface Conditions, Build 9	1072
1023	Del C-Seal and Sealing Conditions, Build 10	1072
1024	Del C-Seal, Build 9, Leakage vs Total Cycles	1073
1025	Del C-Seal Deformation, Build 9	1074
1026	Del C-Seal and Spacer Post Test Condition, Build 9	1074
1027	Flat Face Flange Surface, Build 9	1075
1028	Del C-Seal, Builds 9 and 10, Leakage vs Pressure	1075
1029	Del C-Seal in Groove, Build 9	1076
1030	Servotronics Omega Seal and Sealing Conditions, Builds 11 and 12	1076
1031	Servotronics Omega Seal, Build 11, Leakage vs Total Cycles	1077
1032	Servotronics Omega Seal, Build 12, Leakage vs Total Cycles	1078
1033	Typical Groove Side of Omega Seal	1078
1034	Flat Face Flange	1079
1035	Typical Flat Face Flange Side of Omega Seal	1080
1036	Cross Section of Omega Seal Through Cracked Area 35 Times Size	1080
1037	Servotronics Apex Seal and Sealing Conditions, Builds 13 and 14	1081
1038	Servotronics Apex Seal, Build 13, Leakage vs Total Cycles	1082
1039	Servotronics Apex Seal, Build 14, Leakage vs Total Cycles	1082

II ILLUSTRATIONS (Continued)

Figure		Page
1040	Apex Seal Groove Side	1083
1041	Apex Seal Flat Face Side	1083
1042	Build 14 Seal Collapse Area	1084
1043	Apex Seal Rolled Position	1084
1044	Pressure Science, Inc. C-Ring Seal and Sealing Conditions for Builds 15, 16, 17, 18, 21	1085
1045	Indium Coated C-Ring Build 15, Leakage vs Total Cycles . .	1086
1046	Silver Plated Teflon Primer Coated C-Ring, Build 16, Leakage vs Total Cycles	1086
1047	Silver Plated C-Ring, Build 17, Leakage vs Total Cycles . .	1087
1048	Lead Plated C-Ring, Build 18, Leakage vs Total Cycles . . .	1087
1049	Indium Coated C-Ring Static Seal	1088
1050	Flange Face of Indium Coated Seal	1089
1051	Silver Plated Teflon Primer Coated C-Ring Static Seal	1089
1052	Silver Plated C-Ring Static Seal	1090
1053	Silver Plated C-Ring Static Seal	1091
1054	Lead Plated C-Ring Static Seal	1092
1055	Flange Face	1092
1056	Lead-Indium Plated C-Ring Static Seal	1093
1057	Lead-Indium Plated C-Ring (Groove Side)	1093
1058	Parker V-Seal and Sealing Conditions, Builds 19, 20, 22, 23, 24, and 25	1094
1059	Proximity Probe Locations, Build 23	1095
1060	Parker V-Seal, Build 19, Leakage vs Total Cycles	1096
1061	Parker V-Seal, Build 20, Leakage vs Total Cycles	1096
1062	Parker V-Seal, Build 22, Leakage vs Total Cycles	1097

ILLUSTRATIONS (Continued)

Figure		Page
1063	Parker V-Seal, Build 24, Leakage vs Total Cycles	1097
1064	Parker V-Seal, Build 25, Leakage vs Total Cycles	1098
1065	Flange Deflection, Build 23C	1099
1066	Bolt Stress vs Pressure, Build 23	1099
1067	Parker V-Seal, Build 20 Leakage vs Time	1101
1068	Chromatograph, Gas Flow Schematic, Builds 22, 24, and 25.	1101
1069	Thermal Conductivity Detector, Balanced Bridge Circuit . . .	1102
1070	Parker V-Seal, Build 19	1102
1071	Seal Groove, Build 19	1103
1072	Parker V-Seal, Build 20	1103
1073	Seal and Support Rings, Build 24	1104
1074	Inverted C-Seal and Sealing Conditions	1105
1075	Inverted C-Seal, Build 26, Leakage vs Total Cycles	1106
1076	Inverted C-Seal, Build 28, Leakage vs Total Cycles	1106
1077	Inverted C-Seal, Build 29, Leakage vs Total Cycles	1107
1078	Inverted C-Seal, Build 30, Leakage vs Total Cycles	1107
1079	Build 26 Seal Condition	1109
1080	Build 27 Seal Condition	1109
1081	Build 27 Seal Condition, Cross Sectional View	1110
1082	Build 28 Seal Condition	1110
1083	Build 29 Seal Condition	1111
1084	Build 30 Seal Condition	1111
1085	Build 30 Seal Condition, Cross Section View	1112
1086	Air Ratchet Wrench, F-46159	1112
1087	Pivot Ring Seal and Sealing Conditions for Builds 31, 32A, 33, 34A and 35	1113

ILLUSTRATIONS (Continued)

Figure		Page
1088	Air Wrench Angle of Turn Indicator	1114
1089	Bolt Stretch vs Torque/Angle of Turn, Build 35	1115
1090	Lead-Plated Pivot Ring, Build 31 Leakage vs Total Cycles . .	1115
1091	Lead-Plated Pivot Ring, Build 32A, Leakage vs Total Cycles	1116
1092	Lead-Plated Pivot Ring, Build 33, Leakage vs Total Cycles .	1116
1093	Lead-Plated Pivot Ring, Build 34A, Leakage vs Total Cycles	1117
1094	Warmup Temperature vs Time, Build 34A During Thermal Cycling	1118
1095	Flange Temperature vs Time, Builds 34A and 35	1118
1096	Silver-Plated Pivot Ring, Build 35, Leakage vs Total Cycles	1119
1097	Thermal Cycle Test With Silver-Plated Pivot Ring, Build 35	1119
1098	Lead-Plated Pivot Ring Seal Showing Radial Scratches	1120
1099	Plating Void In Lead-Plated Pivot Ring Seal	1121
1100	Lead-Plated Pivot Ring Seal in Flange Showing Nonuniform Plating	1121
1101	Lead-Plated Pivot Ring Seal Showing Darkened Spots	1122
1102	Lead-Plated Pivot Ring Seal	1122
1103	Flange Seal Groove Showing Radial Scratches	1123
1104	Lead-Plated Pivot Ring Seal in Flange Showing Voids and Imprinted Marks	1123
1105	Silver-Plated Pivot Ring Seal	1124
1106	Silver-Plated Pivot Ring Seal, Reverse Side	1124
1107	Toroidal Segment Seal and Sealing Conditions for Builds -36, -37, -38, -39 and -40	1126

ILLUSTRATIONS (Continued)

Figure		Page
1108	Bolt Stretch vs Torque/Angle of Turn, Build 36	1127
1109	Toroidal Segment Seal, Build 36, Leakage vs Total Cycles . .	1128
1110	Toroidal Segment Seal, Build 36, Leakage vs Thermal Cycles	1129
1111	Bolt Stretch vs Torque/Angle of Turn, Build 37	1129
1112	Toroidal Segment Seal, Build 37, Leakage vs Total Cycles . .	1130
1113	Bolt Stretch vs Torque/Angle of Turn, Build 38	1131
1114	Toroidal Segment Seal, Build 38, Leakage vs Total Cycles . .	1131
1115	Toroidal Segment Seal, Build 38, Leakage vs Thermal Cycles	1132
1116	Thermal Cycles of Builds 38, 39, and 40 Using GN ₂ Through LN ₂ Heat Exchanger and Into Rig With Atmospheric Surroundings	1132
1117	Bolt Stretch vs Torque/Angle of Turn, Build 39	1133
1118	Toroidal Segment Seal, Build 39, Leakage vs Total Cycles . .	1134
1119	Toroidal Segment Seal, Build 39, Leakage vs Thermal Cycles	1134
1120	Bolt Stretch vs Torque/Angle of Turn, Build 40	1135
1121	Toroidal Segment Seal, Build 40, Leakage vs Total Cycles . .	1135
1122	Build 36 Seal Showing Post-Test Minor Edge Imperfections . .	1136
1123	Build 36 Seal Showing Post-Test, Minor Side Imperfections .	1136
1124	Build 37 Seal Showing Post-Test Metallic Contamination . . .	1137
1125	Build 37 Seal Showing Post-Test Contamination Voids	1137
1126	Build 37 Toroidal Segment Seal Cross Section	1138
1127	Build 38 Seal Edge at Post-Test Inspection	1138
1128	Build 38 Seal Side at Post-Test Inspection	1139

ILLUSTRATIONS (Continued)

Figure		Page
1129	Build 39 Seal Side at Post-Test Inspection	1140
1130	Build 39 Seal Edge at Post-Test Inspection	1140
1131	Build 39 Seal Cross Section Showing Minute, Radial ID Scratches	1141
1132	Build 40 Seal Side at Post-Test Inspection	1141
1133	Build 40 Seal Edge at Post-Test Inspection	1142
1134	Build 40 Seal Cross Section at Post-Test Inspection	1142
1135	Flange Deflection vs Pressure for Builds 36, 37 and 40	1143
1136	Complete Control System	1153
1137	Gross Control Mode	1155
1138	Fuel Pump Speed Loop	1157
1139	LOX Flow Trim Loop	1158
1140	Fuel Flow Trim Loop	1159
1141	LOX NPSP Protection Loop	1160
1142	Preburner Temperature Protection Loop	1161
1143	Fuel NPSP Protection Loop	1163
1144	Transpiration Cooling Protection Loop	1164
1145	Main Pump Overspeed Protection Loop	1165
1146	Prestart, Start and Shutdown Schedules and Logic	1166
1147	Prestart Logic	1167
1148	Start and Shutdown Schedule Selection Logic	1168
1149	J-FET Multiplexer	1187
1150	Preferred A/D Converter, Successive Approximation Type	1188
1151	Fixed Time Interval Block Diagram	1189
1152	Variable Time Interval Block Diagram, Part A	1190

ILLUSTRATIONS (Continued)

Figure		Page
1153	Variable Time Interval Block Diagram, Part B	1191
1154	Sensor Fault Detection and Selection	1192
1155	Recommended Output Section	1193
1156	Alternate Output Section	1194
1157	Pull-Hold Solenoid Drive Circuit	1195
1158	Solenoid Driver	1197
1159	Computer Interface Block Diagram	1198
1160	Signals Between the CPU and Each Controller	1198
1161	A/D Converter to Computer Interface	1199
1162	Speed Inputs to Computer Interface	1200
1163	Computer to D/A Converter Interface	1200
1164	Computer to Discrete Output Interface	1201
1165	Failure Inputs to Computer Interface	1201
1166	BDX 800 Computer Organization	1205
1167	CPU-I/O Interface Lines	1206
1168	Control System With Start, Shutdown and Pre-Start Logic . .	1209
1169	Hybrid Block Diagram Defining Engine Control Task	1217
1170	Block Diagram: Emergency Shutdown Computer	1220
1171	Actuator Servo Configuration	1221
1172	Mission Reliability Configuration	1223
1173	Failure Mode Logic Flow Diagram	1225
1174	Signal Format	1228
1175	Vehicle Interface	1229
1176	Differential Transmission System	1230

ILLUSTRATIONS (Continued)

Figure		Page
1177	Engine Control Simulated Failure of All Sensors	1236
1178	Acceleration Without Fuel Pump Speed Trim	1237
1179	Acceleration With Fuel Pump Speed Trim	1238
1180	Final Control System Acceleration	1239
1181	Engine Control Fuel Pump Overspeed Protection	1244
1182	Flowmeter Schematic	1254
1183	Force Screen Flow Sensor	1255
1184	Electro-Mechanical System Selection	1259
1185	Power Distribution	1263
1186	Fail Operative Mechanization Including Quad Feedback Provisions	1265
1187	Engine Control System	1267
1188	XLR129 Pneumatic Valve Controller System	1276
1189	Pneumatic Flow Diagram	1277
1190	Functional Block Diagram Electronic Interface of Pneumatic Controller	1278
1191	Valve Controller Unit for Preburner LOX Valve	1281
1192	Pump Speed Sensing Arrangement	1286
1193	Preburner Selection, Conversion, and Monitoring	1291
1194	Preburner Temperature Probes	1293
1195	Pressure Sensor	1296
1196	Pump Pressure Sensing	1296
1197	Cooling Pressure Sensing	1297
1198	Typical Signal Selection and Failure Rejection Process	1297

TABLES

Table		Page
I	Demonstrator Engine Characteristics	1
II	Demonstrator Engine Operating Characteristics, Booster	34
III	Demonstrator Engine Calculated Weight	46
IV	Cycle Definition Procedures	51
V	XLR129-P-1 Design Trades	57
VI	Element Dimensional Characteristics	70
VII	Test Matrix	80
VIII	Dimensional Characteristics of Elements Tested	81
IX	Test Matrix Results	82
X	Summary of Measured Parameters During Preburner Injector Testing	91
XI	Summary of Calculated Parameters During Preburner Injector Testing	93
XII	Flowrates for Tests 7.01 and 8.01	101
XIII	Preburner Test Comparison	117
XIV	Phase Angle Comparison	120
XV	Injector Water Flow Test Results	124
XVI	Nominal Test Conditions	126
XVII	Injector Area Change per Momentum Ratio Change	129
XVIII	Summary of Roller Bearing Tests	133
XIX	End Wear Summary Matrix Points 22 and 23	170
XX	Cavitation Test Data	203
XXI	Comparison of Material Candidates	220
XXII	Properties of Inconel 625 (AMS 5599)	221
XXIII	Configuration Study	221

TABLES (Continued)

Table	Page
XXIV	Resistance Weld Measurements 229
XXV	Preliminary Thermal Fatigue Cycling Test Results 245
XXVI	Thermal Fatigue Cycling Test Results 255
XXVII	Taber Abraser Wear Testing of Chromium and Chromium-Molybdenum Alloy Electroplate 286
XXVIII	Force Wear Tests 290
XXIX	Data Recorded During Tests 297
XXX	Summary of Test Results 321
XXXI	Materials Purchase Timetable 354
XXXII	First Preburner Injector 361
XXXIII	Preburner Fuel Area Calibration 367
XXXIV	Original Fabrication Sequence 369
XXXV	Bolt Loading Requirements for Preburner Rig 376
XXXVI	Preburner Instrumentation 377
XXXVII	XLR129 Preburner Injector Pretest Matrix Revision 1 383
XXXVIII	Preburner Test Results 385
XXXIX	Radial Distance of Sel Rake Thermocouples to Chamber Center Line 388
XL	Predicted vs Actual Performance for 20% Thrust Engine Mixture Ratio of 5, Rig 35131-1 Run 1.01 388
XLI	Predicted vs Actual Performance for 20% Thrust Engine Mixture Ratio of 6, Rig 35131-1 Run 1.01 390
XLII	Predicted vs Actual Performance for 20% Thrust Engine Mixture Ratio of 7, Rig 35131-1 Run 1.01 391
XLIII	Predicted vs Actual Performance for 35% Thrust Engine Mixture Ratio of 5, Rig 35131-1 Run 1.01 393
XLIV	Injector Flow Test Tabulation for Profile Correlation 413

TABLES (Continued)

Table	Page
XLV	Predicted vs Actual Performance for 50% Thrust, Engine Mixture Ratio of 5, Rig 35131-4, Run 7.01 431
XLVI	Predicted vs Actual Performance for 20% Thrust, Engine Mixture Ratio of 5, Rig 35131-4, Run 10.02 432
XLVII	Predicted vs Actual Performance for 50% Thrust, Engine Mixture Ratio of 5, Rig 35131-4, Run 11.01 439
XLVIII	Predicted vs Actual Performance for 50% Thrust, Engine Mixture Ratio of 6, Rig 35131-4, Run 11.01 440
XLIX	Predicted vs Actual Performance for 50% Thrust, Engine Mixture Ratio of 7, Rig 35131-4, Run 11.01 441
L	Predicted vs Actual Performance for 75% Thrust, Engine Mixture Ratio of 5, Rig 35131-4, Run 13.01 444
LI	Predicted vs Actual Performance for 75% Thrust, Engine Mixture Ratio of 7, Rig 35131-4, Run 13.01, Before Profile Shift 445
LII	Predicted vs Actual Performance for 75% Thrust, Engine Mixture Ratio of 7, Rig 35131-4, Run 13.01, After Profile Shift 446
LIII	Predicted vs Actual Performance for 75% Thrust, Engine Mixture Ratio of 5, Rig 35131, Run 14.01 452
LIV	Predicted vs Actual Performance for 100% Thrust, Engine Mixture Ratio of 6, Rig 35131, Run 14.01 453
LV	Engine Thrust Level 20%, Engine Mixture Ratio 5, Rig No. 35133, Run No. 1.01 464
LVI	Engine Thrust Level 50%, Engine Mixture Ratio 5, Rig No. 35133, Run No. 5.01 465
LVII	Engine Thrust Level 20%, Engine Mixture Ratio 5, Rig No. 35133, Run No. 5.01 470
LVIII	Engine Thrust Level 20%, Engine Mixture Ratio 6, Rig No. 35133, Run No. 5.01 471
LIX	Engine Thrust Level 20%, Engine Mixture Ratio 7, Rig No. 35133, Run No. 5.01 472

TABLES (Continued)

Table		Page
LX	Engine Thrust Level 50%, Engine Mixture Ratio 5, Rig No. 35133, Run No. 5.01	473
LXI	Engine Thrust Level 50%, Engine Mixture Ratio 6, Rig No. 35133, Run No. 5.01	474
LXII	Engine Thrust Level 50%, Engine Mixture Ratio 7, Rig No. 35133, Run No. 5.01	475
LXIII	Engine Thrust Level 75%, Engine Mixture Ratio 7, Rig No. 35133, Run No. 7.01	480
LXIV	Engine Thrust Level 75%, Engine Mixture Ratio 7, Rig No. 35133, Run No. 8.01	484
LXV	Summary of Igniter Test Data	495
LXVI	Component Manufacturing Timetable	517
LXVII	Machine Welded Specimens	520
LXVIII	Hand Welded Specimens	521
LXIX	Strain and Elastic Stress Data, XLR129 Transition Case Under Combined Internal Pressure and Thrust Loads (Preburner Ratio)	532
LXX	Strain and Elastic Stress Data, XLR129 Transition Case Under Combined Internal Pressure and Thrust Loads (Engine Ratio)	539
LXXI	Process Specification	561
LXXII	Braze Detail Tabulation	564
LXXIII	Fabrication Detail Tabulation	567
LXXIV	Rigmesh Material Property Program	574
LXXV	Material Delivery Dates	587
LXXVI	Translating System Weights	607
LXXVII	XLR129 Fuel Turbopump Parts Procurement Time	643
LXXVIII	Rotor Ambient Spin Test	666

TABLES (Continued)

Table	Page
LXXIX	Strain Data: XLR129 Fuel Turbopump Housing (2150805), 1 in. Cutback, Proof Pressure Test Cycle 2 674
LXXX	Elastic Stress Data: XLR129 Fuel Turbopump Housing (2150805), 1 in. Cutback, Proof Pressure Test Cycle 2 676
LXXXI	Liftoff Seal Ambient Leakage Measurements (Original Secondary Seal Location) 679
LXXXII	Liftoff Seal Leakage Measurements (Relocated Secondary Seal) 681
LXXXIII	Natural Bending Frequencies 687
LXXXIV	Predicted Critical Speeds, XLR129 Fuel Pump Assembly . . 693
LXXXV	Fuel Turbopump Test Summary 697
LXXXVI	XLR129 Fuel Turbopump F35147-1A Performance Data Summary 777
LXXXVII	XLR129 Fuel Turbopump F35138-1 and -2, Performance Data Summary 779
LXXXVIII	Mounting Effects on Oxidizer Turbopump Bearings 791
LXXXIX	Front Bearing Coolant Flow 792
XC	Rear Bearing Coolant Flow 793
XCI	Calculated and Allowable 2nd-Stage Turbine Blade and Disk Stresses 802
XCII	Oxidizer Turbopump Turbine Coolant Flow System Flowrates, Pressures, Temperatures, and Orifice Sizes 805
XCIII	Vane Streamline Deviation 831
XCIV	Preburner Oxidizer Valve Parts Lead Times 847
XCV	Preburner Fuel Valve Parts Lead Times 870
XCVI	Main Chamber Oxidizer Valve Parts Lead Times 903
XCVII	Solenoid Valve Description 905

TABLES (Continued)

Table	Page
XCVIII	Propellant Vent Valve Parts Lead Times 909
XCIX	Solenoid Valve Parts Lead Times 915
C	Design Recommendations 923
CI	Test Data Summary, Hot Firings Using Fuel Pump Simulator 952
CII	Preburner-Transition Case Test Results Rig No. 35139-1 Run No. 301 Engine Thrust Level 50% Mixture Ratio 5.0 955
CIII	Preburner-Transition Case Test Results Rig No. 35139-1 Run No. 601 Engine Thrust Level 20% Mixture Ratio 5.0 959
CIV	Hot Turbine Test Run Rig No. 35155-1 Run No. 1.02 Engine Thrust Level 50% Mixture Ratio 5.0 971
CV	Hot Turbine Test Run Rig No. 35155-1 Run No. 3.01 Engine Thrust Level 75% Mixture Ratio 5.0 978
CVI	Hot Turbine Test Run Rig No. 35155-1 Run No. 4.01 Engine Thrust Level 75% 985
CVII	Hot Turbine Test Run Rig No. 35155-2 Run No. 5.02 Engine Thrust Level 75% Mixture Ratio 5.0 100% Mixture Ratio 6.0 100% Mixture Ratio 7.0 1004
CVIII	Hot Turbine Test Run Rig No. 35155 Run No. 6.01 Engine Thrust Level 50% Mixture Ratio 7.0 100% Mixture Ratio 5.0 1014
CLX	Summary of Hot Turbine Test Rig Data 1032
CX	Tensile Strength Comparison 1039
CXI	Tubing Tensile Strength 1040
CXII	Actuator Selection Rationale 146
CXIII	Summary of Selected Sensor Types 1147
CXIV	Computer Signal Interfaces 1183
CXV	Comparison of A/D Converters 1188

TABLES (Continued)

Table		Page
CXVI	Number of Steps Used in Program	1213
CXVII	Estimates of Size of the Final Program	1213
CXVIII	Valve Sensitivity Tests, Runs 112A Through 119A, Cycle 8A	1241
CXIX	Summary of Flowmeter Survey Results	1249
CXX	Flow Sensor Tradeoff Considerations	1253
CXXI	System Weight Breakdown for Complete Engine Control System	1261
CXXII	Peak Power Summary	1262
CXXIII	Peak Start-Up Power Summary Table	1262
CXXIV	Pump Speed Sensing Arrangement	1286
CXXV	Temperature Sensor Data	1290
CXXVI	Comparison of Various Electrical Displacement Transducers	1298

ABBREVIATIONS AND SYMBOLS

Symbols	
A_{cd}	Effective flow area, in. ²
A_s	Slot area, in. ²
A_o	Element area, in. ²
A_1	Inlet flow area excluding blockage, in. ²
A_2	Exit flow area excluding blockage, in. ²
B_x	Blade angle distribution
B_2	Exit blade height, in.
C	Radial clearance, in.
C_L	Coefficient of lift
C_{M1}	Inlet meridional velocity, fps
C_{M2}	Exit meridional velocity, fps
C_r	Clearance, in.
C_{U1}	Inlet tangential velocity, fps
C_{U2}	Exit tangential velocity, fps
C_1	Inlet absolute velocity, fps
C_2	Exit absolute velocity, fps
C_3	Absolute volute velocity, fps
D_1	Diffuser inlet diameter, in.
D_2	Diffuser exit diameter, in.
D_{1h}	Inlet hub diameter, in.
D_{2h}	Exit hub diameter, in.
D_{1M}	Inlet mean diameter, in.
D_{2M}	Exit mean diameter, in.
D_{1T}	Inlet tip diameter, in.

ABBREVIATIONS AND SYMBOLS (Continued)

Symbols

D_{2T}	Exit tip diameter, in.
i	Leading edge incidence, deg
I_s	Specific impulse (instantaneous), $lb_1 - sec/lb_m$
L/R	Diffuser length to inlet radius ratio
l_x	Mean axial length, in. tip
M	Momentum, ft-lb/sec
N	Speed, rpm
S	Specific speed
$NPSH_{Fluid}$	Net positive suction head in fluid LH_2 ft required
$NPSH_{H_2O}$	Net positive suction head in H_2O ft required
P	Pressure, psi
P_c	Chamber pressure (throat total), psia
P_s	Static pressure, psi
P_{VAP}	Vapor pressure, psi/ft
P_1	Inlet pressure, psi total required
Q_1	Flow rate at inlet/exit, gpm
R_c	Cutwater radius, in.
R_{c3}	Velocity correction factor, C_3/C_2
r	Mixture ratio (oxidizer to final) by weight
S	Suction specific speed
S_{Fluid}	Suction specific speed in fluid LH_2 capability
S_{H_2O}	Suction specific speed in H_2O capability
SMD	Sauter mean diameter, in.
t_c	Cutwater thickness, in.
t_h	Hub thickness, in.

ABBREVIATIONS AND SYMBOLS (Continued)

Symbols	
T_{H1}	Inlet hub blade thickness, in.
T_{H2}	Exit hub blade thickness, in.
t_t	Tip thickness, in.
T_{T1}	Inlet tip blade thickness, in.
T_{T2}	Exit tip blade thickness, in.
TSH	Thermodynamic suppression head, ft
T_1	Inlet temp., °R
U_{1T}	Inlet blade tip speed, fps
U_{2m}	Exit mean blade speed, fps
\dot{W}	Flow rate, lb/sec
\dot{W}_c	Cooling flow rate, lb/sec
X	Number of diffusers
Z	Number of blades
α	Surface tension
α_2	Absolute fluid angle, deg
β_{1h}	Inlet hub blade angle, degrees
β_{2h}	Exit hub blade angle, degrees
β_{1M}	Inlet mean blade angle, degrees
β_{2M}	Exit mean blade angle, degrees
β_{1T}	Inlet tip blade angle, degrees
β_{2T}	Exit tip blade angle, degrees
β_3	Volute width, in.
ΔH_{TP}	Total head rise overall, ft
ψ_{TP}	Total head coefficient

ABBREVIATIONS AND SYMBOLS (Continued)

Symbols

ΔP_{TP}	Total pressure rise, overall, psi
ΔH_{SP}	Static head rise overall, ft
ψ_{SP}	Static head coefficient
ΔP_{SP}	Static pressure rise overall, psi
ΔH_{TI}	Static head rise rotor, ft
ψ_{SI}	Rotor head coefficient
ΔP_{TI}	Total pressure rise rotor, psi
ΔH_{SI}	Static head rise rotor, ft
ΔP_{SI}	Static pressure rise rotor, psi
δ	Specific gravity
ϵ	Nozzle area ratio
η	Efficiency, % overall
η_c^*	(Average temperature/ideal temperature) ^{0.5} x 100
η_{IO}	Engine impulse efficiency, percent
θ	Camber, deg
2θ	Diffuser included angle, deg
λ_1	Inlet hub-tip diameter ratio
λ_2	Exit hub-tip diameter ratio
μ	Viscosity, lb-sec/ft ²
ρ	Density, slug/ft ³ , lb-sec/ft ⁴
ρ_1	Inlet/exit density, lb/ft ³
σ	Solidity
ϕ_{it}	Inlet tip flow coefficient
ϕ_{2M}	Flow coefficient at mean exit diameter

ABBREVIATIONS AND SYMBOLS (Continued)

Symbols

ϕ_{1T}	Flow coefficient at inlet tip diameter
ψ	Head coefficient

Abbreviations

AFRPL	Air Force Rocket Propulsion Laboratory
Ag	Silver
AISI	American Iron and Steel Institute
AMS	Aerospace Material Specification
cps	Cycles per second
EDM	Electric discharge machining
FRDC	Florida Research and Development Center
FS	Flow split
GHe	Gaseous helium
gpm	Gallons per minute
GN ₂	Gaseous nitrogen
Hz	Hertz
ID	Inside diameter
K	One-thousand
LCF	Low cycle fatigue
L/D	Length-to-diameter ratio
LH ₂	Liquid hydrogen
LO ₂	Liquid oxygen
LN ₂	Liquid nitrogen
LSI	Low speed inducer
MCOV	Main chamber oxidizer valve

ABBREVIATIONS AND SYMBOLS (Continued)

Abbreviations

NPSH	Net positive suction head
OD	Outside diameter
psia	Pounds per square inch absolute
psid	Pounds per square inch differential
psig	Pounds per square inch gage
PWA	Pratt & Whitney Aircraft
°R	Degrees Rankine
r	Mixture ratio
scfm	Standard cubic feet per minute
SDA	Supporting Data and Analysis
S/N	Serial number
SSME	Space Shuttle Main Engine
TIG	Tungsten inert gas
TSH	Total suction head
v	Volt
vs	Versus
W/D	Width-to-diameter ratio

SECTION I INTRODUCTION

A. GENERAL

The Air Force XLR129-P-1 Reusable Rocket Engine Program was an advanced development program originally contracted to cover a 54 month period starting 6 November 1967 and ending 6 May 1972. The overall objective of the original program was to demonstrate the performance and mechanical integrity of a 250,000 lb thrust, oxygen-hydrogen, reusable rocket engine having the characteristics outlined in table I. However, the program was redirected to a demonstration of critical components and completed on 15 August 1970 after the last hot turbine test was conducted. The redirection was accomplished to avoid duplicating work performed on the NASA Phase B Space Shuttle Main Engine (SSME) studies.

Table I. Demonstrator Engine Characteristics

Nominal Thrust	250,000 lb vacuum thrust with area ratio of 166:1 244,000 lb vacuum thrust with area ratio of 75:1 209,000 lb sea level thrust with area ratio of 35:1
Minimum Delivered Specific Impulse Efficiency	96% of theoretical shifting I_s at nominal thrust; 94% of theoretical shifting I_s during throttling
Throttling Range	Continuous from 100 to 20% of nominal thrust over the mixture ratio range
Overall Mixture Ratio Range	Engine operation from 5:1 to 7:1
Rated Chamber Pressure	2740 psia
Engine Weight (with 75:1 nozzle)	3520 lb with flight-type actuators and engine command unit 3380 lb without flight-type actuators and engine command unit
Expansion Ratio	Two-position booster-type nozzle with area ratios of 35:1 and 75:1
Durability	10 hours time between overhauls, 100 reuses, 300 starts, 300 thermal cycles, 10,000 valve cycles
Single Continuous Run Duration	Capability from 10 seconds to 600 seconds
Engine Starts	Multiple restart at sea level or altitude
Thrust Vector Control	Amplitude: ± 7 deg Rate: 30 deg/sec Acceleration: 30 rad/sec ²

Table I. Demonstrator Engine Characteristics (Continued)

Control Capability	±3% accuracy in thrust and mixture ratio at nominal thrust. Excursions from extreme to extreme in thrust and mixture ratio within 5 seconds
Propellant Conditions	LO ₂ : 16 ft NPSH from 1 atmosphere boiling temperature to 180°R LH ₂ : 60 ft NPSH from 1 atmosphere boiling temperature to 45°R
Environmental Conditions	Sea level to vacuum conditions combined acceleration: 10 g axial with 2 g transverse, 6.5 g axial with 3 g transverse, 3 g axial with 6 g transverse
Engine/Vehicle	The engine will receive no external power, with the exception of normal electrical power and 1500-psia helium from the vehicle

The XLR129-P-1 demonstrator engine program schedule is shown in figure 1. The program was divided into five tasks. Task 1, Supporting Data and Analysis, generated test and analytical data to complete the necessary technology to design the engine and components. During task 2, all components and the demonstrator engine were designed. Task 3, Component Development, was the phase during which the program was terminated, and this task was to fabricate and test the components to qualify them for engine use. Task 3 was redirected, as noted, to limit fabrication and testing to critical components only. Task 4 was to have been integration of the components into the demonstrator engine and testing of the demonstrator engine. A flight engine was to have been defined in task 5.

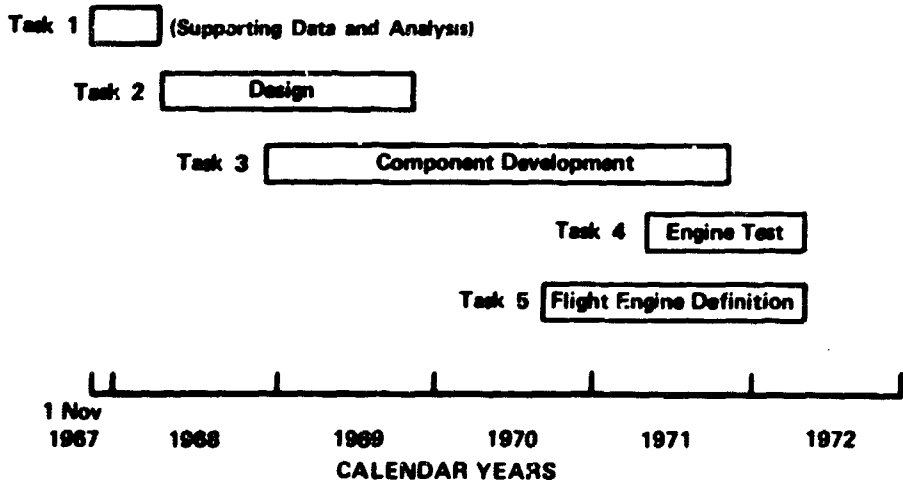


Figure 1. XLR129-P-1 Demonstrator Engine Program Schedule

FD 27857C

B. PROGRAM TASKS

The entire program was to have consisted of five tasks and specific subtasks as follows:

Task 1 - Supporting Data and Analysis

Subtasks

- 1.1 - Fixed Fuel Area Preburner Injector Evaluation**
- 1.2 - Roller Bearing Durability Tests**
- 1.3 - Pump Inlet Evaluation**
- 1.4 - Nozzle Fabrication Investigation**
- 1.5 - Controls Component Test**

Task 2 - Design

Subtasks

- 2.1 - Preburner Injector**
- 2.2 - Main Burner Injector**
- 2.3 - Nozzles**
- 2.4 - Main Burner Chamber**
- 2.5 - Transition Case**
- 2.6 - Fuel Turbopump**
- 2.7 - Oxidizer Turbopump**
- 2.8 - Fuel Low-Speed Inducer**
- 2.9 - Oxidizer Low-Speed Inducer**
- 2.10 - Control System**

Task 3 - Component Development

Subtask

- 3.1 - Preburner Injector**
- 3.2 - Main Burner Injector**
- 3.3 - Nozzles**
- 3.4 - Main Burner Chamber**
- 3.5 - Transition Case**
- 3.6 - Fuel Turbopump**
- 3.7 - Oxidizer Turbopump**
- 3.8 - Fuel Low-Speed Inducer**
- 3.9 - Oxidizer Low-Speed Inducer**
- 3.10 - Control System**

Task 4 - Engine Integration and Demonstration

Task 5 - Flight Engine Definition

SECTION II
SUMMARY, CONCLUSIONS, AND RECOMMENDATIONS

A. DEMONSTRATOR ENGINE

The design of the 250K demonstrator engine and its major components, including plumbing was completed during the second task of the contract. The XLR129 demonstrator engine design is shown in figure 2. Design of the engine and major components was based on proven test technology; namely, all major components such as combustion devices and turbomachinery were tested at either 250K or 350K thrust level, demonstrating their feasibility. Design studies were also conducted on the demonstrator engine in the areas of engine mockup and plumbing. A full-scale mockup of the demonstrator engine was used as a working tool during design. Numerous design iterations were conducted on the mockup for component arrangement and plumbing. A satisfactory component arrangement for the engine mockup was established. In the area of engine plumbing, satisfactory designs and arrangement were established for the major plumbing lines and associated components. Layout designs of major plumbing lines along with detail designs of the preburner fuel line, fuel pump discharge lines, and small line connectors were completed. A static seal rig was built to evaluate 23 different seal configurations. Thirty-five builds of the rig were used. The 0.025 in. thick heat treated toroidal segment seal configuration met the required leakage of less than 10^{-4} standard cubic centimeters per second (sccs) leakage per inch of seal circumference after the 500 pressure cycle endurance test was completed. It is recommended that the toroidal segment seal be incorporated in the XLR129 engine design where coupling seals larger than 1 inch are required. Engine system analyses were also conducted during the program to define component system requirements, estimate capabilities of the integrated engine system, and to include the results of component and engine tests. These analyses include steady-state analysis, transient analysis, shutdown analysis, special design cycle studies, and generation of performance data.

B. PREBURNER INJECTOR

The preburner is an oxygen/hydrogen combustor supplying hot gases to drive the oxidizer and the fuel pump turbines. Because preburner gases are used to drive the fuel and oxidizer pump turbines, the design goal temperature profile is 150°R peak-to-average to permit operating the turbines at the maximum allowable average temperature. The design of the preburner injector consists of 253 dual-orifice, tangential swirler oxidizer elements with concentric fuel annuli positioned around each oxidizer element. All are arranged in a hexagonal pattern as shown in figure 3. Under the Supporting Data and Analysis task the preburner injector was tested and developed to produce a stable slot swirler dual orifice injector element. A model test water flow program was conducted during the supporting data analysis task to develop a stable oxidizer injection element, which had a 0.124 in. inside diameter. Fourteen full-scale preburner combustion tests were conducted with the fixed fuel area preburner during the Supporting Data and Analysis task. Peak-to-average combustion temperature profile of 76°R in a radial plane was demonstrated at an average temperature of 2388°R. This fixed area, fuel-injection design concept is feasible because of density changes occurring in gaseous fuel allowing throttling while simultaneously

maintaining a suitable injection velocity. However, because liquid oxygen is essentially incompressible, the dual-orifice principle is applied to a slot-swirler element to provide suitable injection velocity over the throttling range. The preburner injector housing has 28 slots to allow gaseous hydrogen to flow from the outer field manifold to the manifold behind the faceplates. Preliminary oxidizer flow enters the primary oxidizer manifold through six equally spaced ports in the preburner injector housing. Secondary oxidizer flow arrives at the secondary oxidizer manifold directly from the preburner oxidizer valve. The porous injector faceplate is fabricated from Rigimesh. Ignition systems will be integral spark igniter-exciter units that are mounted on both the preburner and the main chamber. Two systems will be provided for the preburner and two for the main chamber to provide total spark redundancy. During the component development task the fabrication and calibration of an engine type preburner injector was completed. Fourteen firings were made with an engine type preburner injector. The six initial tests produced unacceptable temperature profiles and the uncooled combustion liner sustained damage. The next eight tests demonstrated acceptable temperature profiles and damage to the combustion liner was not evident. As a result of these hot firings, hardware modifications were made to improve both the life and performance of the preburner injector. Eight firings were then made with the modified preburner injector. This modified injector performed satisfactorily, and no further modifications were necessary. The general conclusions that can be made from the preburner tests are:

1. The temperature profile is acceptable for driving the fuel pump turbine
2. A transpiration cooled liner is necessary in the high energy release zone of the preburner chamber
3. The addition of the transpiration cooled section of the preburner liner will allow operation of the preburner above 20% thrust.

C. TRANSITION CASE

The transition case consists of one main sphere and four small spherical segments that intersect the main sphere. The centerlines of three of the small spherical segments lie in a plane that is perpendicular to the engine thrust axis. The smaller spheres act as the attachment points for three major components; the preburner injector, the oxidizer turbopump, and the fuel turbopump. The centerline of the fourth spherical segment coincides with the engine thrust axis. The fourth segment provides the attachment point for the main burner. The entire assembly is a pressure vessel. The transition case contains internal ducting that routes preburner discharge gases through the fuel and oxidizer pump turbines and to the preburner injector as well. The goal of the transition case subtask was to demonstrate the structural adequacy of the inner ducts of the transition case when operating at an internal pressure of 4856 psia and with the internal gas temperature as high as 2325°R. The transition case with the centerbody installed is shown in figure 4. With incorporation of the preburner injector, fuel turbopump and oxidizer turbopump, the transition case is a self-contained powerhead supplying the main burner thrust chamber with high-pressure propellants necessary to produce the design thrust. Moreover, it serves as the primary combustor stage for the staged combustion cycle. Internal ducting of

the transition case divides the hot fuel-rich gases from the preburner to provide adequate proportionate gas flow to each turbine. The fuel turbine requires about twice the mass flow required to drive the oxidizer turbine. Cooling liners, positioned between the outer case and the hot gas flow path, are not included so the outer gas temperature is retained below 540°R.

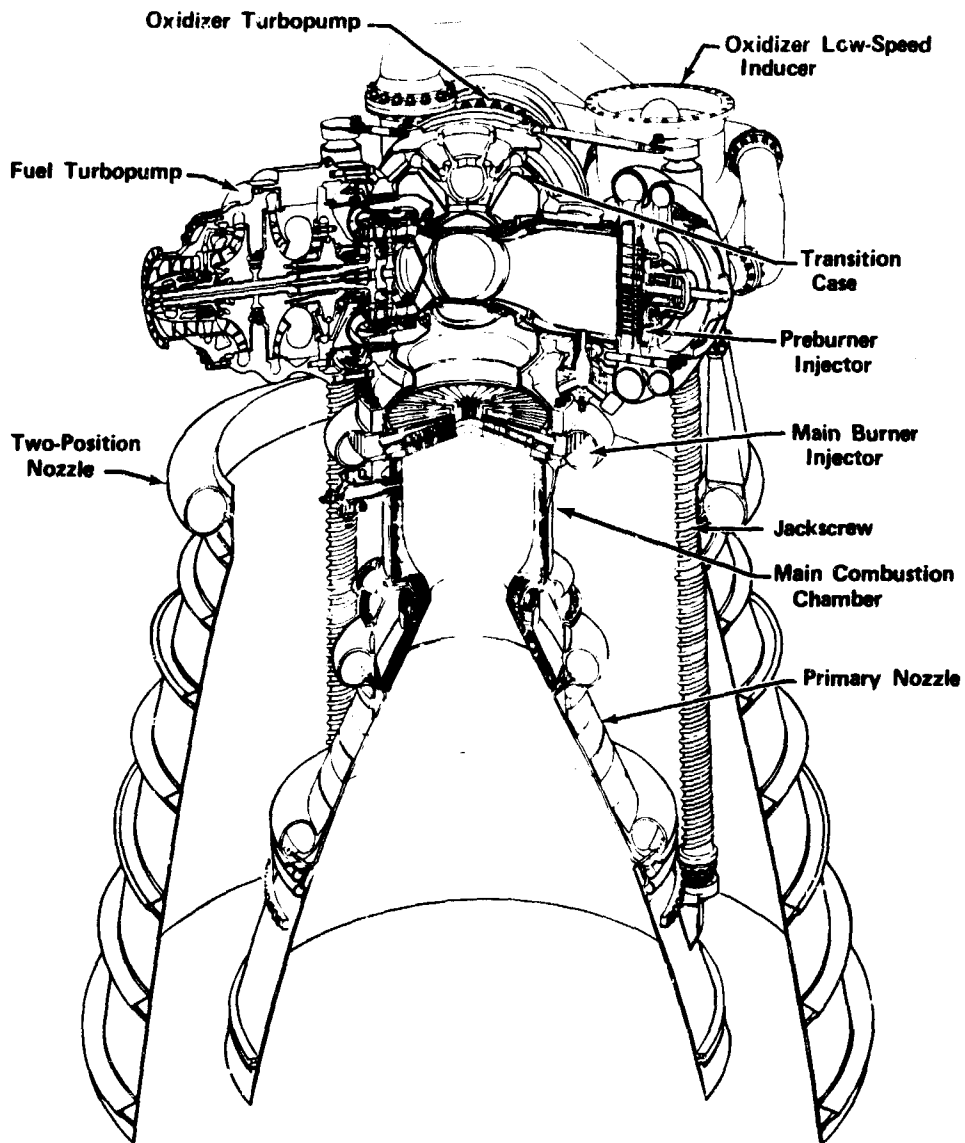


Figure 2. XLR129 Demonstrator Engine

FD 27533E

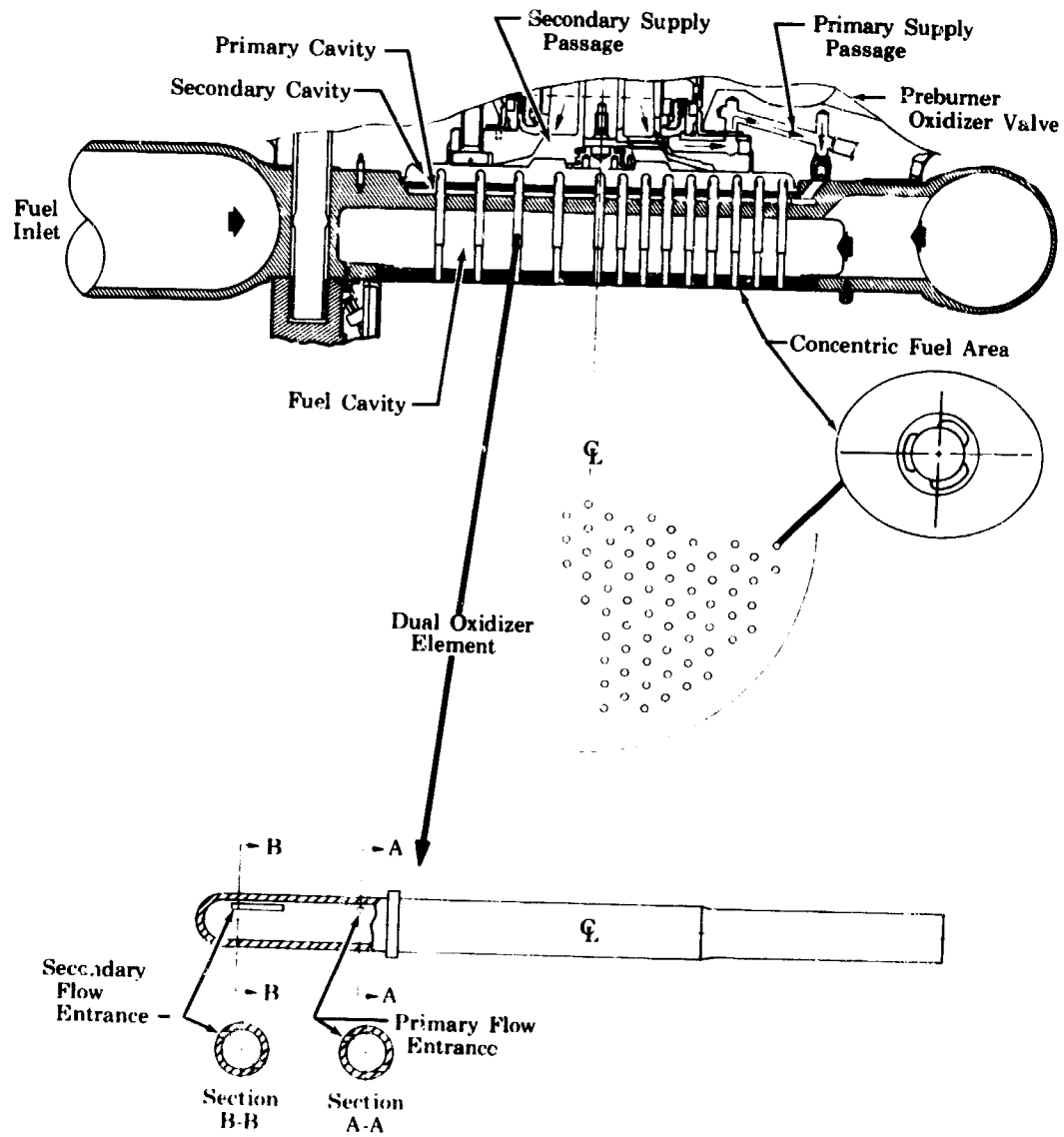


Figure 3. XLR129 Demonstrator Engine
Preburner Injector

FD 25970B

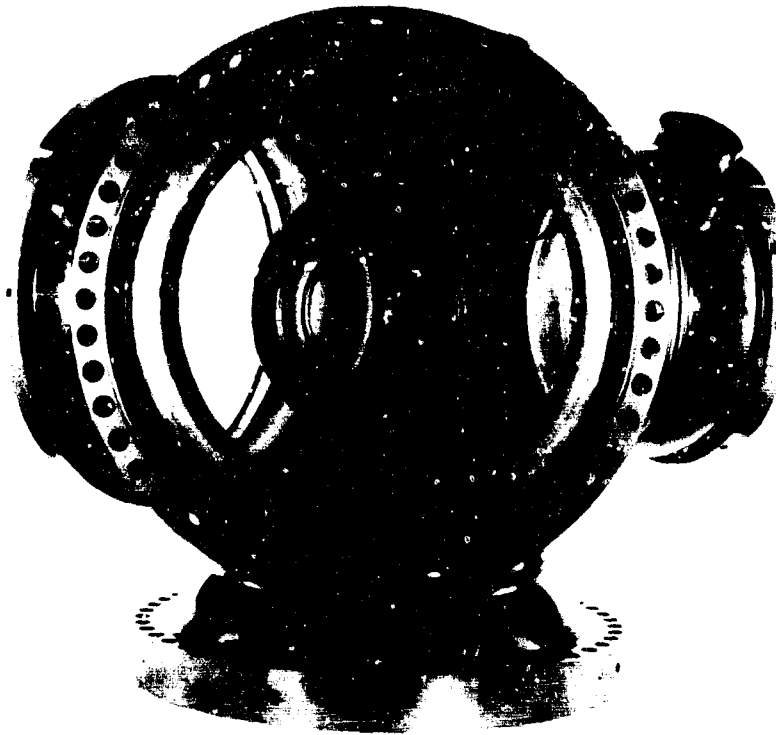


Figure 4. Transition Case With Centerbody Installed

FE 97596

Hand welding methods were used in the fabrication of the transition case. A study of welded specimens was conducted showing that hand welding was superior to machine welding when cost, quality and consistency were considered. The porous cooling liner that routes the coolant to the outer case was installed in subassembly sections in the outer case. The liners were fabricated by a vendor and were formed to the case contour. Because the coolant flowrates, after forming, proved from tests to be unpredictable, the flow was tailored by a flame spraying process. The transition was hot gas tested during the latter phase of the program. For the initial preburner/transition case testing, turnaround caps, closely simulating the fuel and oxidizer turbines, were planned. Where possible, actual turbine parts were designed into the cap assemblies. These tests demonstrated that a satisfactory transition case had been evolved, and that the basic requirements had been fulfilled. It is recommended that these design concepts be applied to future high pressure rocket engines.

D. MAIN BURNER INJECTOR

The main burner injector introduces, atomizes, and mixes liquid oxygen with the hot, fuel-rich turbine discharge (preburner combustion products) so efficiency and stable combustion is achieved over the full operating range of thrust and mixture ratios. The design of the main burner injector was completed during task 2 of this contract.

The main burner injector design consists of the oxidizer manifold and housing, spraybar type internal manifolds, oxidizer-injection elements, and the porous faceplate shown in figure 5. The main injector housing consists of an oxidizer inlet horn, the oxidizer manifold, and crossover passages to the spraybars. The spraybar injector body consists of 48 individually machined spraybars brazed into the oxidizer-manifold ring. The spraybars are individually supported at the outside diameter only, thus permitting free thermal growth. This approach simplifies manufacturing and provides a lightweight design. Forty-eight radial spraybars are divided into three groups; 12 long spraybars equally spaced around the circumference, 12 medium spraybars equally spaced between the long spraybars, and 24 short spraybars equally spaced between the medium and long spraybars. This arrangement yields the maximum number of spraybars consistent with mechanical considerations, and results in good oxidizer-element density and uniform radial flow distribution. Self-atomizing injection elements are spaced along the spraybars to obtain good atomization and distribution. The fuel faceplate is made of Rigimesh, which forms the support structure as well as the porous face. The faceplate directs approximately 92% of the hot, fuel-rich, preburner combustion gases through slots surrounding the oxidizer-injector elements. The remainder of the gas passes through the porous faceplate. Major components are assembled by brazing and welding techniques that simplify manufacturing the components. This main burner injector configuration represents a minimum overall length and weight design that satisfies the demonstrator engine cycle requirements.

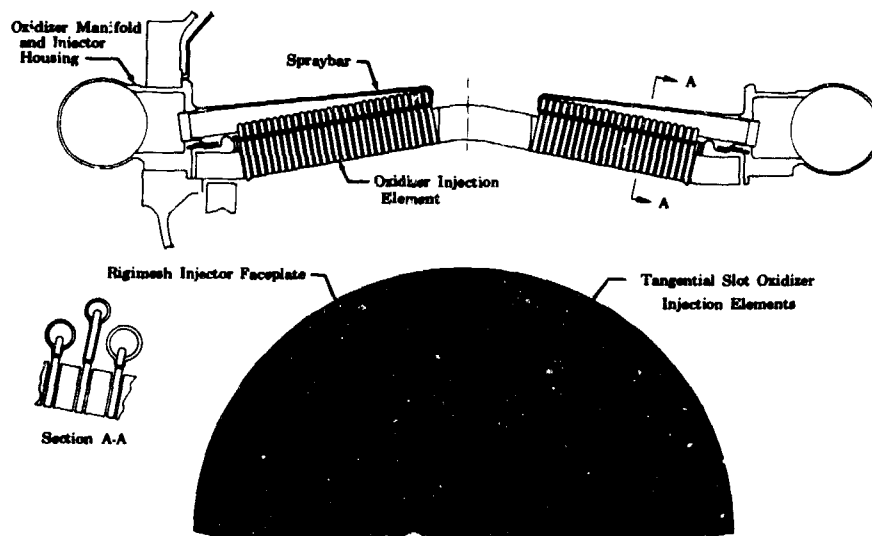


Figure 5. Main Burner Injector

FD 25641A

During task 3, the Component Development Task, two finished, machined spraybars were fabricated, but the final fabrication of the main burner injector was terminated because of program redirection. Design of the main burner igniter was also completed. The concepts of individual tapered tube spraybars and a one-piece, self-supporting, porous metal faceplate are recommended to develop a durable, lightweight and easily fabricated injector.

E. MAIN BURNER CHAMBER

The main burner chamber contains the pressure resulting from propellant combustion, serves as the structural member supporting the primary and two-position nozzles, transmits thrust, and absorbs gimbal actuator loads. The overall goals of the main burner chamber subtask were to design, build, and demonstrate through full-scale testing, performance and operational capability of a lightweight, durable, thrust chamber for use in the demonstrator engine program over the specified throttling and mixture ratio ranges. The design of the main burner chamber was completed during task 2 of this contract. The main burner chamber design consists of two main components; an outer pressure shell and a transpiration cooled, copper wafer, chamber liner shown in figure 6. The outer pressure shell also provides the coolant manifold and serves as a mount for attaching the chamber liner in two sections. Copper cylindrical wafers forming the chamber are divided into 28 zones. Each wafer consists of front and back plates. A zone is a collection of composite wafers fed by interconnected zone coolant manifolds. The chamber liner consists of a stackup of 512 0.040 in. thick copper wafer halves brazed together. Spiral groove patterns photoetched into one side of each wafer half provide the path from the zone coolant manifold to the inside diameter of the chamber where they open into the main burner chamber. Composite wafers are constructed of two half plates brazed at the unetched center plane with an axial thermal relief slot in the front wafer half. By locating the slot in this plane, the heat exchanger spiral grooves on the opposite face are not affected. The addition of axial thermal strain relief slots minimizes the wafer thermal strain level by allowing free axial growth at the hot wall of the chamber, thus producing an acceptable low cycle-fatigue life. Coolant is distributed to the cylindrical copper combustion chamber cooling liner of the main burner chamber by internal cooling manifolds. Use of internal cooling manifolds eliminates radial pressure loads, and thereby allows the wall thickness to be greatly reduced resulting in considerable weight savings. The throat and the rear sections of the chamber use basically the same coolant distribution concept. Material was purchased to fabricate an outer case and coolant liner before the program was redirected.

F. NOZZLES

The function of the primary nozzle is to contain the combustion gases and allow their shock-free expansion from an area ratio of 5.3:1 to 35:1. High-pressure hydrogen from the fuel pump is supplied as coolant to two regeneratively cooled portions of the primary nozzle. During task 2, the design of the primary nozzle was completed. The primary nozzle design consists of two tubular, regeneratively cooled heat exchangers shown in figure 7. The downstream heat exchanger is a double pass type, and supplies hydrogen to the hydrogen inducer turbine and transpiration cooled main burner chamber. The upstream heat exchanger is a single pass type, and cools the nozzle from an area ratio of 5.3 to 18 using approximately 85% of the pump discharge hydrogen flow prior to delivery to the preburner injector. Both heat exchangers are shaped from tubes forming the desired nozzle contour.

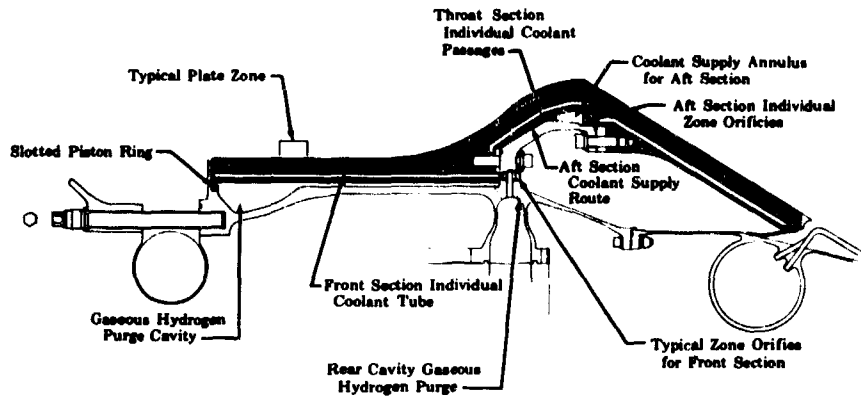


Figure 6. Main Burner Chamber Wafer Assembly FD 31972

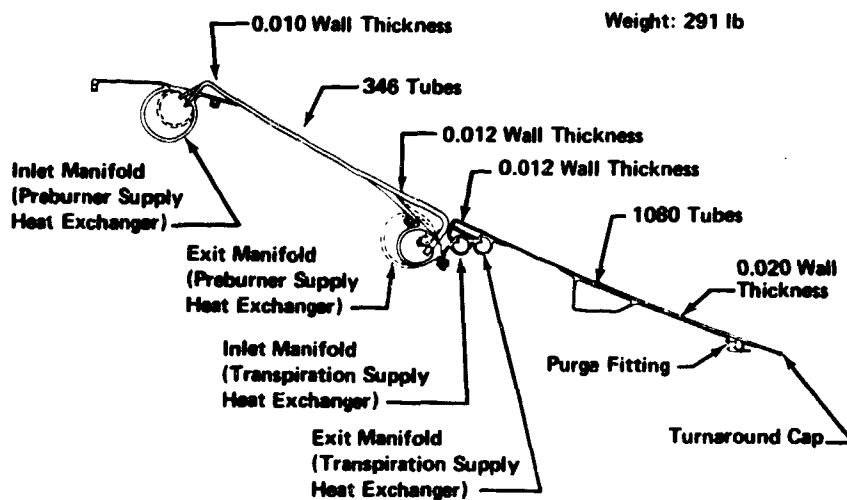


Figure 7. Primary Nozzle Design FD 37255

The function of the two-position nozzle in the extended position is to contain the combustion gases and allow additional shock-free expansion from an area ratio of 35:1 to 75:1. The two-position nozzle translates to provide a compact engine package in the retracted position. The translating mechanism is designed to provide positive extending and retracting of the two-position nozzle during engine operation. During task 2, the design of the two-position nozzle was also completed. The two-position nozzle design consists of a circumferential coolant distribution manifold, a smooth nozzle outer skin with circumferential stiffening bands, and a corrugated inner nozzle skin shown in figure 8. The corrugated inner skin forms longitudinal coolant passages. This nozzle is designed to be dump cooled with low pressure hydrogen taken from the fuel pump interstage. The translating mechanism was designed to extend and retract the two-position nozzle during engine operation and to provide precision positioning in the extended and retracted positions. Positive locking devices

maintain the nozzle position when the engine is not operating. During task 3, raw materials necessary to fabricate both the primary nozzle and the two-position nozzle were purchased and received. The long lead time bearings and forgings required to fabricate two translating mechanism assemblies were purchased and received.

Material	Inconel 625
Outer Sheet	Smooth
Outer Sheet Thickness	0.016
Inner Sheet	Corrugated
Inner Sheet Thickness	0.010 in.
Number Corrugations	360
Inlet Dia	46 in.
Exit Dia	66 in.
Length	50 in.
Weight (Sea Level)	227 lb
Weight (Altitude)	186 lb

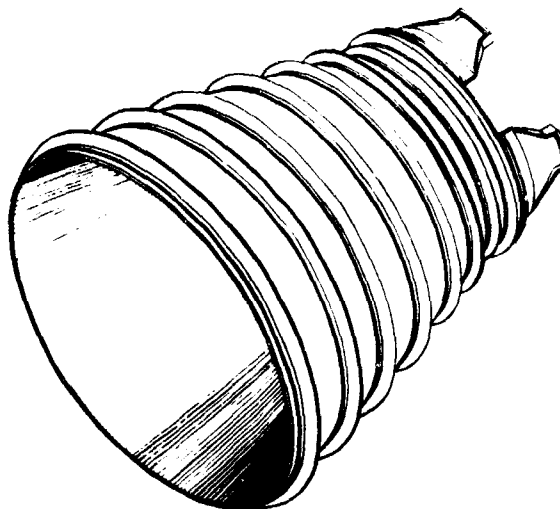


Figure 8. Design of Two-Position Nozzle

GS 12309

G. FUEL TURBOPUMP

The fuel turbopump supplies liquid hydrogen to the primary nozzle, the two-position nozzle, and to the preburner injector at sufficient pressure and flowrates for engine operation from 20% to 100% maximum thrust and at mixture ratios from 5 to 7. The overall goal of the fuel turbopump subtask was to demonstrate an operational capability for use in the demonstrator engine program. The demonstrator engine requires the fuel turbopump to deliver liquid hydrogen at a flowrate of 91.3 lb/sec at a pressure of 5654 psia at its design point of 100% thrust and a mixture ratio of 5. The design of the fuel turbopump is shown in figure 9. Major components of the fuel turbopump are the pump, turbine, rotor assembly, and housings. The two-stage turbine delivers approximately 49,900 horsepower to the pump at 100% thrust and a mixture ratio of 5. The turbine operates at a maximum inlet temperature of 2325°R at 100% thrust and a mixture ratio of 7. Life is based on 10 hours between overhaul and 300 starts. The fuel pump must also demonstrate satisfactory starting capability and stable operation over the engine operating range. During task 3, the following were accomplished:

1. The fuel turbopump design was completed and fabrication drawings were released to manufacturing.
2. Two complete turbopumps and one spare rotor were fabricated.

3. Subcomponent tests were conducted in the following areas:
 - a. Rotor spin tests
 - b. Blade vibration tests
 - c. Main housing proof pressure tests
 - d. Liftoff seal tests
 - e. Turbine stator calibration tests
 - f. Critical speed evaluation tests
4. The subcomponent tests indicated that design objectives were achieved or exceeded in all except the liftoff seal subcomponent area. This unit failed after 2525 cycles during an endurance test to demonstrate 10,000 cycle life durability.
5. Three fuel turbopump rig builds were completed and 13 pump test series were conducted to evaluate the pump performance axial thrust balance and mechanical integrity.
6. The pump performance test series indicated that pump performance is approximately 2 to 3 percentage points better than predicted in overall efficiency, 8% better than predicted in overall head rise, and the turbopump is capable of stable operation over the wide flow range required for the demonstrator engine cycle.

H. OXIDIZER TURBOPUMP

The oxidizer turbopump supplies liquid oxygen to the preburner injector and main burner injector at sufficient pressure and flowrates for engine operation from 20 to 100% of maximum thrust and at a mixture ratio range from 5 to 7. The overall goal of the oxidizer turbopump subtask was to demonstrate performance and operational capability for use in the demonstrator engine program. The demonstrator engine requires the oxidizer turbopump to deliver liquid oxygen at a flowrate of 481 lb/sec at a pressure of 4800 psia at 100% thrust and mixture ratio of 7. During task 2, the design of the oxidizer turbopump was completed. The design of the oxidizer turbopump assembly is shown in figure 10. The oxidizer turbopump consists of a pump, turbine, and housings. The oxidizer turbopump is a single-shaft unit with a single-stage, shrouded, centrifugal impeller driven by a two-stage, pressure compounded turbine. The two-stage turbine delivers a maximum of 18,000 horsepower to the pump and operates at a maximum inlet temperature of 2325°R at 100% and a mixture ratio of 7. Life is based on 10 hours between overhaul and 300 starts. During task 3, all design layouts and detail parts prints were completed. Raw material and most of the detail parts were placed on order; however, many of these were not completed because of program redirection. Some major parts such as bearings, turbine blade casting, the first impeller detail, partial orders of the stators and exit guide vane castings were received. Fabrication of the oxidizer turbopump hardware was approximately 45% complete when terminated.

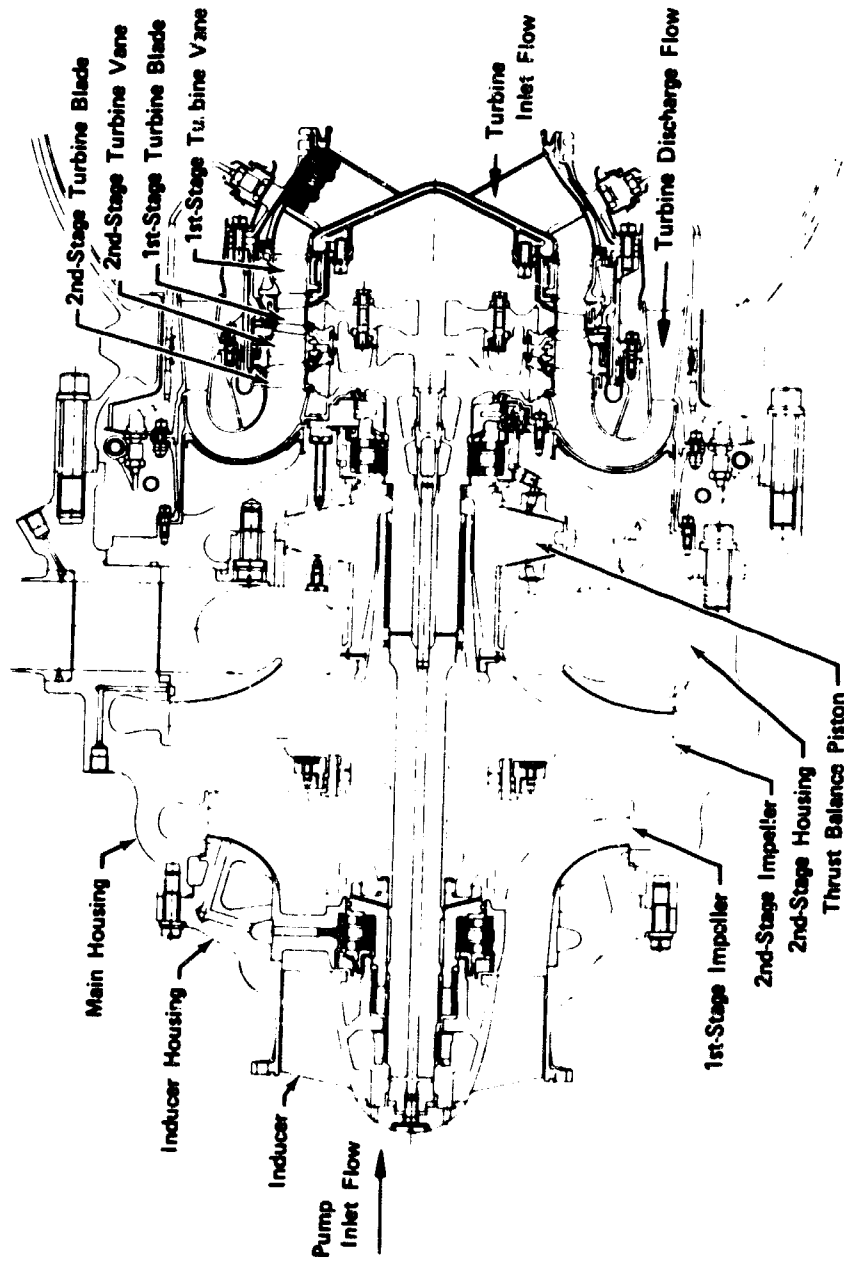


Figure 9. Fuel Turbopump Assembly

FD 29206E

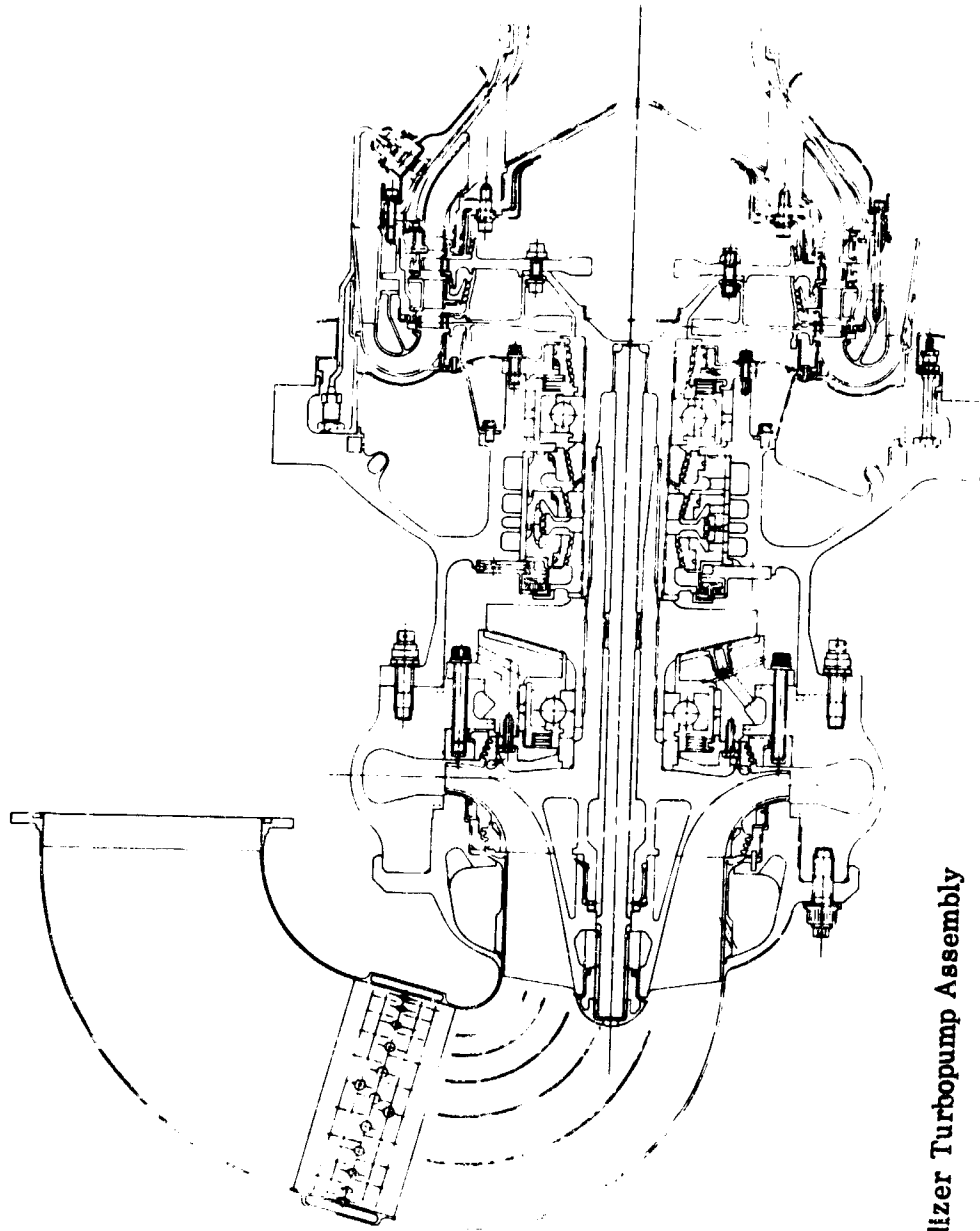


Figure 10. Oxidizer Turbopump Assembly

GS 12366A

I. LOW-SPEED INDUCERS

The function of the fuel and oxidizer low-speed inducers is to supply propellants to the main turbopumps at a pressure (NPSH) sufficient to prevent cavitation. This permits the vehicle propellant tanks to be maintained at a lower pressure thus saving tank and vehicle weight. The overall goal of the fuel and oxidizer low-speed inducer subtasks was to demonstrate performance and operational capability for use in the demonstrator engine. The fuel and oxidizer low-speed inducer layouts were completed. The three-bladed fuel inducer is driven by a single-stage, partial-admission turbine. The fuel operates independently of the main turbopump and at a speed lower than the main turbopump. This permits the fuel inducer to operate with a low inlet NPSH without cavitation. The fuel inducer is capable of operating with an NPSH as low as 60 feet, over a hydrogen inlet temperature range, from 36°R to 45°R. This inducer is designed for a suction specific speed of 48,400 rpm gpm $1/2$ ft- $3/4$ and a maximum pressure rise of 90 psid. The fuel low-speed inducer consists of bearings, shaft and thrust piston, turbine, and housings and is shown in figure 11. The oxidizer low-speed inducer is a single-shaft axial flow unit with high suction specific speed. It is driven by a variable admission, single-stage, radial inflow, hydraulic turbine. The turbine is driven by fluid supplied from the discharge of the main oxidizer turbopump. The oxidizer inducer is of helical design with three blades, and is attached to the drive shaft and turbine assembly as shown in figure 12. The shaft axial thrust imbalance is absorbed by a single acting thrust balance piston. The oxidizer inducer was designed to operate at a minimum NPSH of 16 ft over an oxygen inlet temperature range from 162°R to 180°R with a suction speed of 44,000 rpm gpm $1/2$ ft- $3/4$ and a maximum pressure rise of 197 psid. Both inducers were designed for 300 starts and a 10 hour life span between overhaul. After the design layouts were completed, work on both the fuel and oxidizer low-speed inducers was terminated.

J. CONTROL SYSTEM

A closed loop control system is required to ensure safe, precise, and responsive performance of the engine throughout its operating range. The planned system will accept vehicle or man-in-the-loop command signals at any rate or sequence, and provide rapid response within the functional and structural limits of the engine. The system will be stable at any setting and will respond smoothly to command.

Four discrete electric current signals from the vehicle will accomplish engine starting, shutdown, and modulation of thrust and mixture ratio. The control signals may originate either in the vehicle guidance control or from a pilot command console in a manned vehicle. Response of the engine to these signals will be governed by an electronic Engine Command Unit (ECU). The demonstrator engine ECU will be a solid state electronic component incorporating all flight engine control logic. The control valves, actuators, igniters, and plumbing will be lightweight, flight-type parts contained within the engine envelope. The closed loop control system will use flowmeters in both propellant lines to generate signals proportional to actual thrust and mixture ratio. These flowmeter signals will be compared to the vehicle input signals in the ECU and will automatically correct any difference between actual and desired values by modulating the engine propellant valves. An analysis of the XLR129 rocket engine cycle established the following four control points are

required for satisfactory steady-state operation: (1) preburner oxidizer valve, (2) preburner fuel valve, (3) main-chamber oxidizer valve, and (4) oxidizer low-speed inducer, variable turbine, actuator. Several on-off sequenced valves are also used in the control system as follows: (1) nozzle-skirt coolant valve, (2) propellant vent valves, and (3) helium system valves. The control system consists of a basic control computer that includes scheduled valve and oxidizer low-speed inducer turbine areas, with limited authority trim based on measured engine parameters. Various engine operating limits will be protected by override authority. Control capability protecting the engine is critical to a manned system. Within the demonstrator engine operating envelope, the propellant schedule in the control will prohibit operation beyond component limits. Requirements for the engine command unit actuator, sensor, and control system computer were defined. The Bendix Corporation was selected as the control system vendor. Control circuit logic was designed and an engine computer simulation effort was subsequently conducted by Bendix. During tasks 2 and 3, the principal control valves and subsystems were designed. The preburner oxidizer valve, preburner fuel valve, main burner oxidizer valve and the vent valve were all designed and detailed prints for each were released. Both the preburner oxidizer valve and the preburner fuel valve were water flow calibrated and cryogenic endurance tested. The preburner oxidizer valve was used for hot tests of the preburner and the integrated component test rigs. Parts for two main burner oxidizer valves were procured, and assembly and testing of this valve is recommended. One vent valve was assembled and it is recommended that tests be conducted on this valve. The electrical ignition system purchase specification was written and the request for proposal published. The Benton Corporation agreed to supply, at no cost, two units for this program for evaluation and development testing, and this is recommended.

K. INTEGRATED COMPONENTS

During task 3, the preburner and transition case were integrated with other essential components and tested as a hot gas system rig. The fuel turbo-pump was then added to the rig and it was tested as a hot turbine rig.

The hot gas system rig consisted of a preburner oxidizer valve, a preburner injector and transition case assembly with rig hardware to simulate the fuel and oxidizer turbopumps. This hot gas system rig allowed the preburner injector to be check fired into the hot gas flow path used in the engine system before driving the fuel turbopump turbine with the preburner. Six firings were made with the hot gas system, which demonstrated that the preburner injector and transition case with the fuel and oxidizer turbopump simulator could be operated satisfactorily under hot gas conditions. The hot gas system rig mounted in the test stand is shown in figure 13.

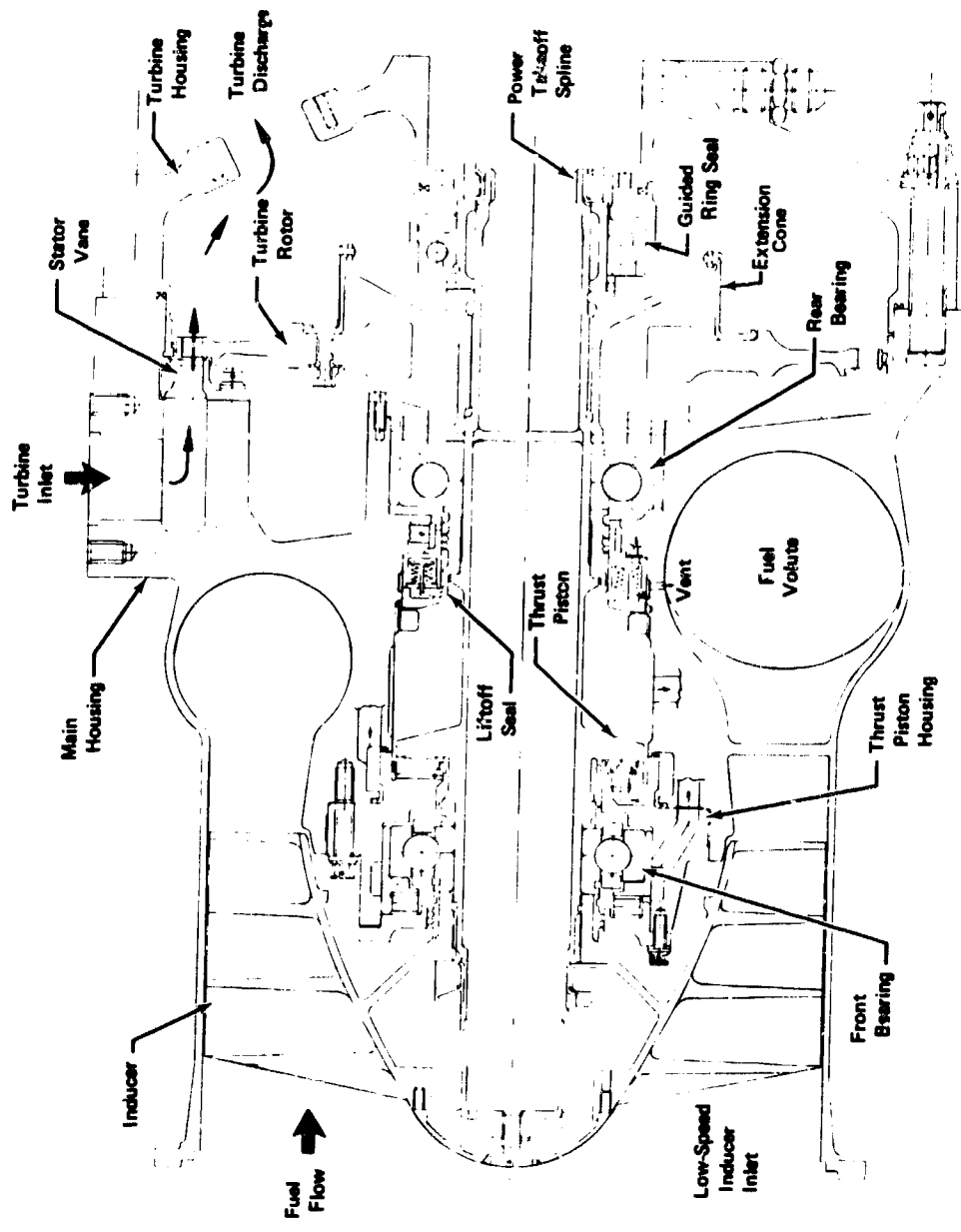


Figure 11. Fuel Low Speed Inducer

FD 33411

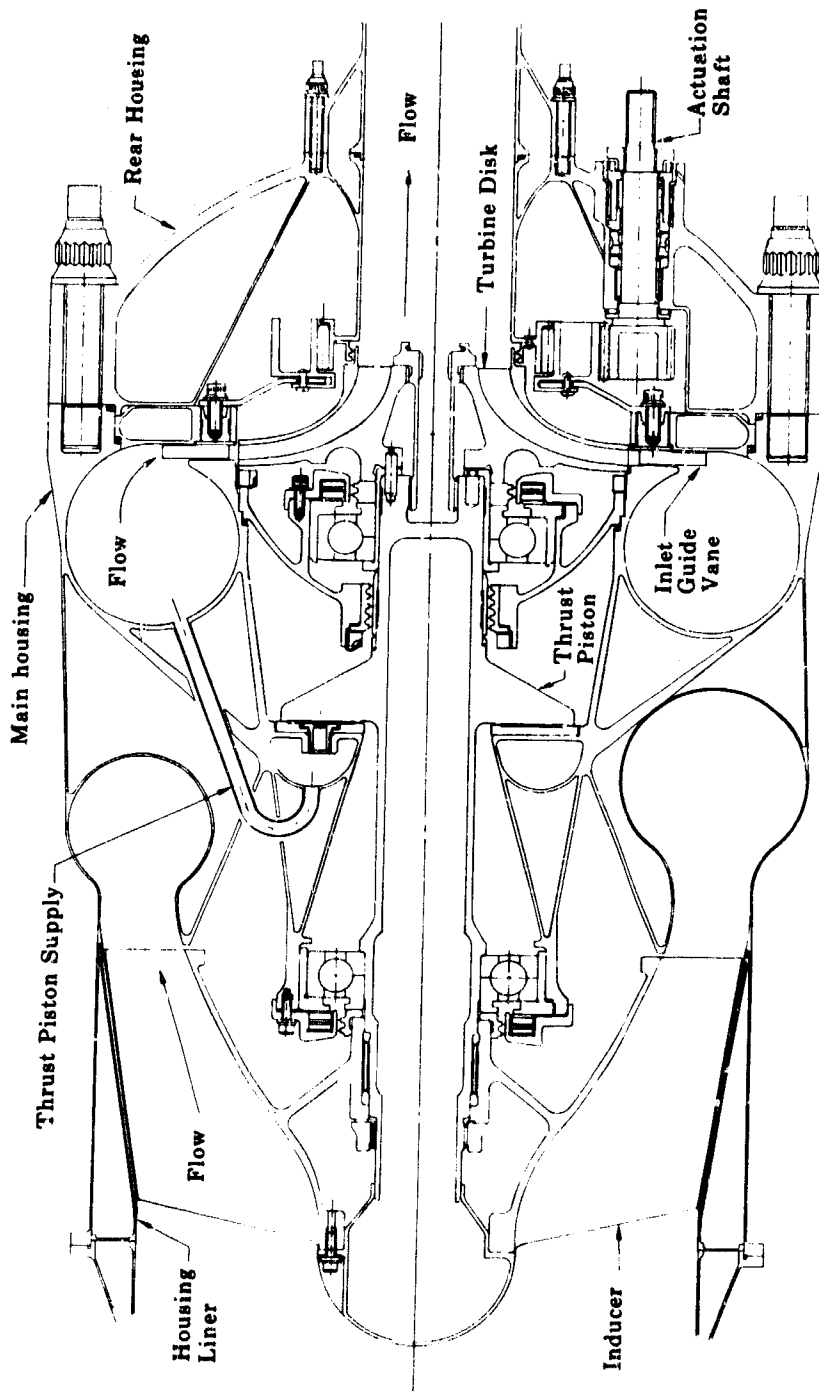


Figure 12. Oxidizer Low Speed inducer

FD 33343A

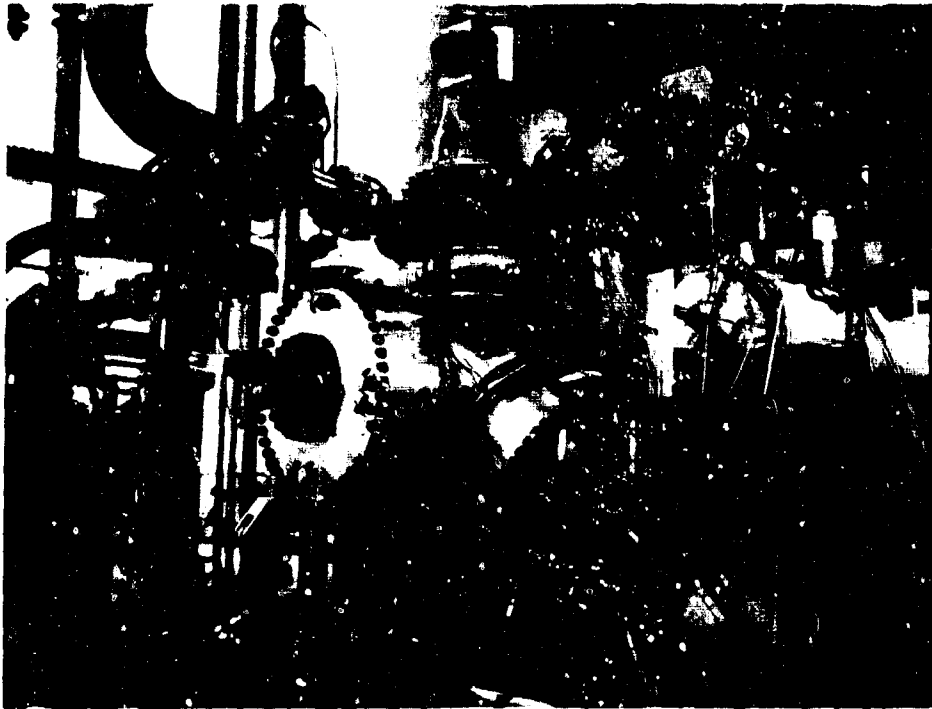


Figure 13. Hot Gas System Rig Mounted In
Test Stand

FE 97733



Figure 13a. Hot Turbine Rig

FE 99486

The hot turbine rig was similar to the hot gas system except that the fuel turbopump was mounted on the rig. The hot turbine rig is shown in figure 13a. Six tests were conducted with the hot turbine rig. During these tests, a preburner chamber pressure of 4200 psia was achieved and the fuel turbine operated at temperature levels 86°R in excess of the maximum engine cycle requirement of 2325°R. The peak turbopump flow and discharge pressure achieved was 9956 gpm and 5554 psia, respectively. These six turbine rig tests totalled 95.8 sec and demonstrated the capability of the integrated fuel turbopump, transition case, preburner injector and preburner oxidizer valve to operate at conditions equivalent to 50, 75, and 100% thrust and mixture ratios of 5, 6, and 7. From these tests it was concluded:

1. The integrated components are capable of operation over a range of thrust and mixture ratios that satisfy operational requirements.
2. The feasibility of the spherical transition case concept and cooling scheme was demonstrated.
3. The adequacy of the mixed cooling scheme used in the turbine static structure was demonstrated.
4. A suitable preburner temperature profile for operation with the turbopump turbine was demonstrated.

It is recommended that these integrated component concepts be used in the design of future high-pressure staged combustion rocket engines.

SECTION III
ENGINE SYSTEM DESCRIPTION AND PERFORMANCE

A. DESCRIPTION

The staged combustion, high-pressure demonstrator engine with a two-position bell nozzle is a 250,000 lb thrust (class), throttleable, high-performance propulsion system. The operating envelope of thrust and mixture ratio is shown in figure 14. Nozzle interchangeability and the two-position nozzle concept permit operation of the same engine system with optimum nozzle area ratios for improving the performance of the lower or upper stages. This interchangeability is achieved by using the same turbomachinery power package and attaching the desired nozzle skirt for the various application requirements. A cutaway view of the engine is presented in figure 15. A propellant flow schematic illustrating the principal flowpaths is presented in figure 16.

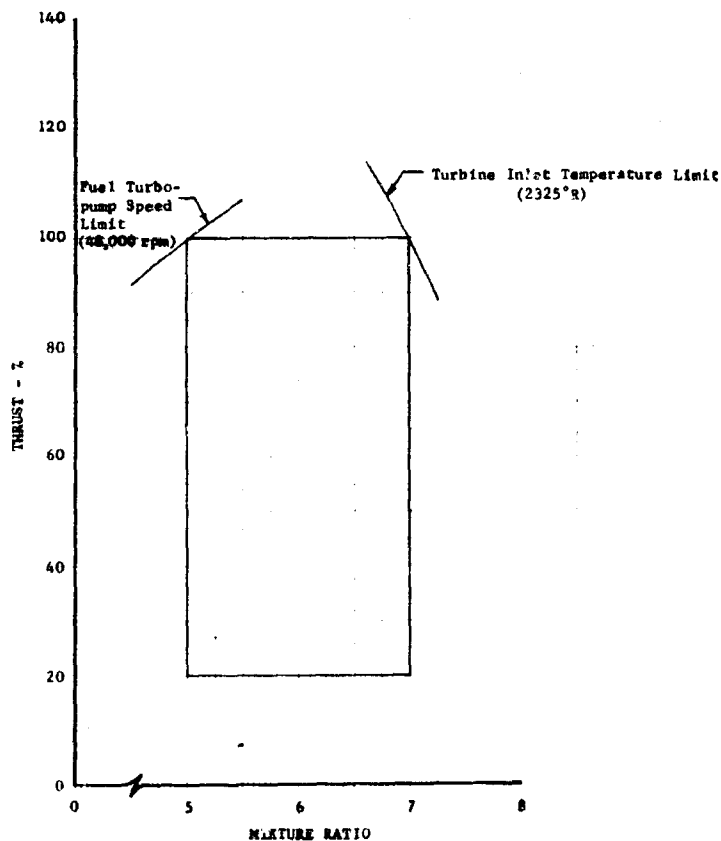


Figure 14. Operating Range for Demonstrator Engine

DF 70704

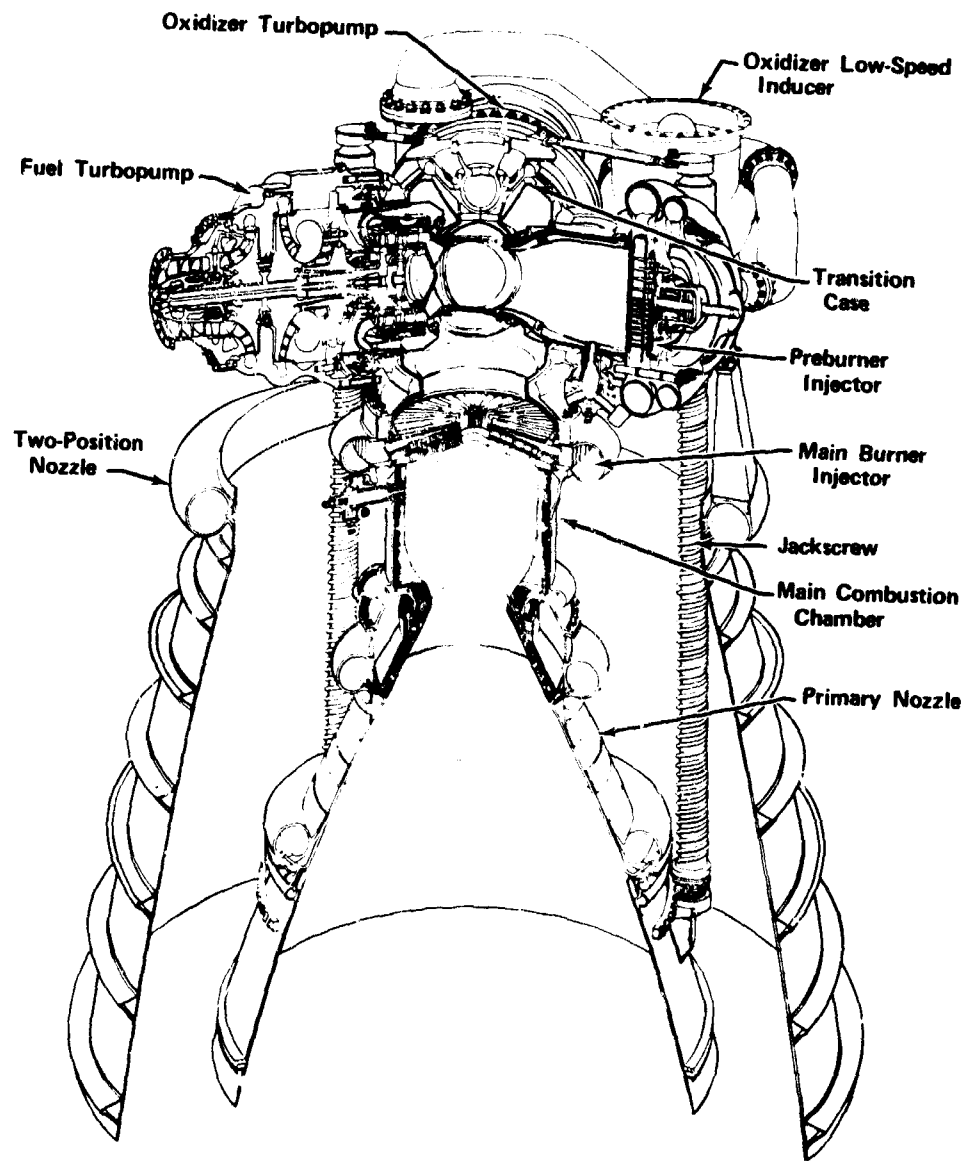


Figure 15. XLR129 Demonstrator Engine

FD 27533E

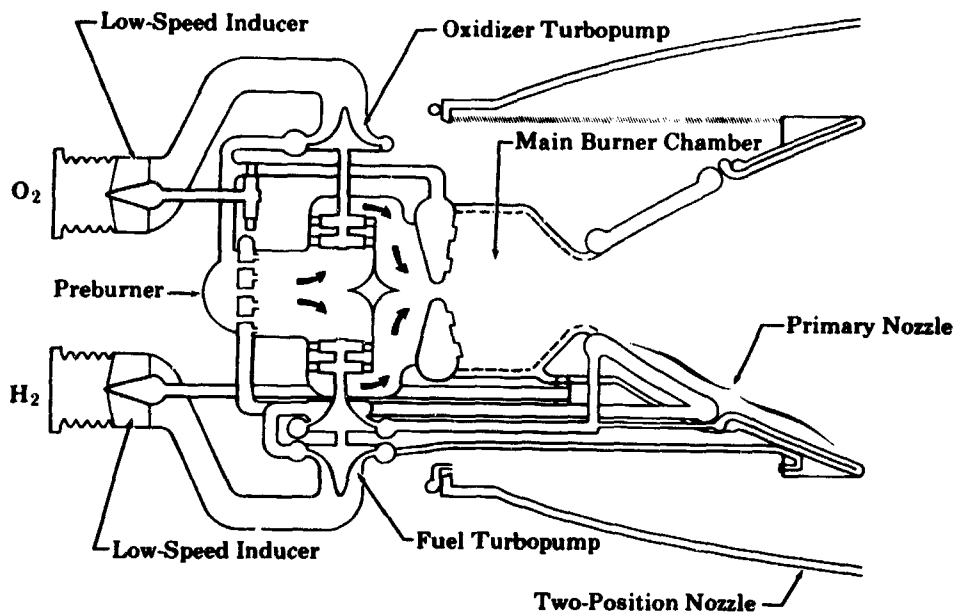


Figure 16. Demonstrator Engine Propellant Flow Schematic FD 25389

Hydrogen and oxygen enter at the engine driven low-speed inducers. The low-speed inducers minimize vehicle tank pressure requirements while allowing high-speed main propellant pumps to obtain high turbopump efficiencies. The fuel low-speed inducer is a single shaft unit with a high specific speed, axial-flow inducer driven by a partial admission, single-stage, hydrogen turbine. The oxidizer low-speed inducer is also a single shaft unit with a high specific speed, axial-flow inducer driven by a variable admission, radial inflow single-stage liquid oxygen turbine.

The main fuel turbopump is a single shaft unit with two back-to-back centrifugal pump stages driven by a two-stage, pressure compounded turbine. A double-acting thrust balance piston is provided between the pump and turbine.

The oxidizer turbopump is a single shaft unit with a single, centrifugal pump stage driven by a two-stage, pressure compounded turbine. A single-acting thrust balance piston is provided between the pump and turbine.

The preburner injector consists of dual orifice, tangential-swirler oxidizer injection elements with concentric fixed area fuel injection. A translating sleeve valve is incorporated at the rear of the injector assembly to vary the total oxidizer flowrate to adjust engine power level and to adjust the relative flow of the primary and secondary elements. The preburner combustion chamber is an integral part of the transition case, which contains the turbine drive gas ducts and a cooled outershell. The main turbopumps are mounted to the transition case with a plug-in arrangement of the turbines to provide maintainability.

The main burner injector consists of a tangential-swirler oxidizer injection elements arranged in radial spraybars. The fuel side directs fuel-rich

gas flow (preburner combustion products after expansion through the turbine) through slots in a porous faceplate. The combustion chamber wall is composed of a hydrogen cooled liner extending from the injector face to an area ratio of 5.3. The liner is composed of porous plates providing transpiration cooling.

The nozzle, which attaches at the end of the transpiration cooled section, is composed of two fixed regeneratively cooled sections and a retractable, low-pressure, dump cooled section.

The main fuel flow is pumped to system operating pressure levels by the main fuel pump and is ducted to cool the regeneratively cooled sections of the nozzle. The forward section is cooled with the majority of the fuel flow from the pump in a single pass heat exchanger. This flow exits from the nozzle and is ducted to the preburner. The regeneratively cooled rear section of the fixed nozzle is cooled with the remainder of the fuel flow in a two-pass heat exchanger. This flow is subsequently used as the working fluid to power the fuel low-speed inducer drive turbine and is then used to cool the porous main chamber walls.

A small amount of fuel is ducted from the fuel pump interstage to cool the retractable nozzle skirt. This fuel is heated to high temperature in the skirt and expelled overboard through small nozzles at the ends of the coolant passages. A valve is provided to shut off the flow when the secondary nozzle is retracted.

After being pumped to system operating pressure, the oxidizer is divided between the preburner and the main chamber. The smaller portion of the flow is supplied to the preburner and is burned with the fuel. The resulting combustion products provide the working fluid for the main turbines, which are arranged in parallel. The turbine exhaust gases are collected and directed to the main burner injector.

The main burner oxidizer flow provides the oxidizer low-speed inducer turbine working fluid and uses the available pressure drop between the main oxidizer pump discharge pressure and the main chamber pressure for the turbine power. The oxidizer flow is then injected into the main burner chamber and is mixed and burned with the fuel-rich turbine exhaust gases. The resulting combustion gas is then expanded through the bell nozzle.

The primary engine control valves are located in the liquid oxygen supply lines to the preburner and the main chamber and in the liquid hydrogen supply line to the preburner.

B. OPERATING CHARACTERISTICS

1. Steady-State Operating Parameters

The component and engine system steady-state operating parameters are given in table II, for mixture ratios of 5, 6, and 7 at 100%, 75, 50, and 20% thrust. (These operating parameters result from an iterative optimization process described in Section III, paragraph F.)

Table II. Demonstrator Engine Operating Characteristics, Booster

	50% Thrust F = 5.0	50% Thrust F = 6.0	50% Thrust F = 7.0	20% Thrust F = 5.0	20% Thrust F = 6.0	20% Thrust F = 7.0
Two-Position Nozzle						
Coolant Flow, lb/sec	1.77	1.75	1.70	1.42	1.35	1.27
Thrust, lb	625	640	640	406	408	402
Fuel Turbopump						
Pump:						
Number of Pump Stages	2	2	2	2	2	2
Speed, rpm	31,195	32,474	33,591	20,843	22,262	23,357
Pressure Rise, psi	2450	2630.6	2736	1092	1183	1233
Overall Efficiency, %	61.8	58.2	55.3	49	44.9	42.0
Impeller Tip Velocity, 1st Stage, ft/sec	1445	1505	1556	966	1032	1082
Impeller Tip Velocity, 2nd Stage, ft/sec	1715	1785	1847	1146	1224	1284
Temperature Rise, °R	47.4	58.2	68.1	28.6	37.1	44.3
Inlet Flow, lb/sec	45.2	39.1	34.8	18.8	16.4	14.7
Turbine:						
Number of Stages	2	2	2	2	2	2
Pressure Ratio	1.37	1.37	1.37	1.27	1.28	1.29
Inlet Temperature, °R	1534	1881	2197	1442	1850	2211
Inlet Pressure, psia	2004	1949	1905	734	721	712
Temperature Drop, °R	92.2	108.5	123	60.2	76.3	89.9
Mean Wheel Velocity, ft/sec	966	1006	1041	646	690	724
Efficiency, %	74.0	73.6	73.6	66.4	65.7	65.6
Inlet Flow, lb/sec	47.2	43.6	41.1	16.8	15.7	15.0
Oxidizer Turbopump						
Pump:						
Number of Stages	1	1	1	1	1	1
Speed, rpm	16,376	16,476	16,365	10,431	10,650	10,712
Pressure Rise, psi	2921	2862	2796	1229	1279	1291
Efficiency, %	58.5	39.4	60.3	44.9	45.5	46.5
Impeller Tip Velocity, ft/sec	613	610	605	385	394	396
Temperature Rise, °R	20.1	19.3	18.5	11.0	11.3	11.2
Inlet Flow, lb/sec	287.7	285.7	304.1	132.5	137.0	141.5
Turbine:						
Number of Stages	2	2	2	2	2	2
Pressure Ratio	1.37	1.36	1.37	1.27	1.28	1.28
Inlet Flow, lb/sec	20.7	19.2	18.2	7.4	6.9	6.66
Inlet Temperature, °R	1534	1881	2197	1442	1850	2211
Inlet Pressure, psia	2008	1952	1908	735	722	713
Temperature Drop, °R	79.8	91.8	102	49.4	61.1	70.0
Mean Wheel Velocity, ft/sec	723	714	714	455	465	467
Efficiency, %	64.6	62.8	61.6	53.3	53.5	52.1

Table II. Demonstrator Engine Operating Characteristics, Booster (Continued)

	100% Thrust r = 5.0	100% Thrust r = 6.0	100% Thrust r = 7.0	75% Thrust r = 3.0	75% Thrust r = 6.0	75% Thrust r = 7.0
Thrust Position Nozzle						
Coolant Flow, lb/sec	2.33	2.24	2.24	2.02	2.02	1.99
Thrust, lb	901	905	922	760	783	792
Fuel Turbopump						
Pump:						
Number of Pump Stages	2	2	2	2	2	2
Speed, rpm	48,043	44,548	44,490	34,783	38,724	39,404
Pressure Rise, psi	5493	4845	4915	3086	3723	3841
Overall Efficiency, %	65.9	65.3	63.7	650	63.1	60.6
Impeller Tip Velocity, 1st Stage, ft/sec	2226	2064	2061	1797	1794	1826
Impeller Tip Velocity, 2nd Stage, ft/sec	2641	2449	2446	2132	2129	2166
Temperature Rise, °R	91.3	83.1	89.6	66.1	71.9	80.5
Inlet Flow, lb/sec	91.3	78.5	69.7	67.7	58.4	51.8
Turbine:						
Number of Stages	2	2	2	2	2	2
Pressure Ratio	1.59	1.49	1.47	1.46	1.43	1.42
Inlet Temperature, °R	2011	2079	2326	1702	1967	2252
Inlet Pressure, psia	4721	4283	4106	3220	3066	2971
Temperature Drop, °R	177	157.0	163	124	131.7	144
Mean Wheel Velocity, ft/sec	1488	1380	1378	1201	1200	1221
Efficiency, %	78.1	77.9	77.8	76.5	76.3	76.2
Inlet Flow, lb/sec	110.6	96.6	89.5	76.1	68.9	64.5
Oxidizer Turbopump						
Pump:						
Number of Stages	1	1	1	1	1	1
Speed, rpm	25,727	23,399	22,612	20,839	19,972	19,555
Pressure Rise, psi	5732	5139	4628	4397	3952	3726
Efficiency, %	55.6	63.5	66	61.8	63.0	63.8
Impeller Tip Velocity, ft/sec	952	806	837	771	739	725
Temperature Rise, °R	40.1	31.7	28.1	29.2	25.3	23.4
Inlet Flow, lb/sec	619.4	545.9	558.2	413.0	421.2	432.1
Turbine:						
Number of Stages	2	2	2	2	2	2
Pressure Ratio	1.59	1.49	1.46	1.45	1.42	1.42
Inlet Flow, lb/sec	48.1	42.3	39.4	33.2	30.3	28.5
Inlet Temperature, °R	2011	2079	2326	1702	1967	2252
Inlet Pressure, psia	4730	4280	4113	3226	3071	2875
Temperature Drop, °R	156.1	137	142.0	109	114	122
Mean Wheel Velocity, ft/sec	1123	1021	987	912	871	855
Efficiency, %	69.4	68.5	67.6	67.5	66.3	65.2

Table II. Demonstrator Engine Operating Characteristics, Booster (Continued)

	50% Thrust r = 5.0	50% Thrust r = 6.0	50% Thrust r = 7.0	20% Thrust r = 5.0	20% Thrust r = 6.0	20% Thrust r = 7.0
Low-Speed Inducer						
Fuel Inducer:						
Flowrate, lb/sec	45.2	39.1	34.8	18.3	15.9	14.2
Speed, rpm	12,473	12,630	12,663	7748	7978	8043
Pressure Rise, psi	58.0	70.3	77.5	32.3	37.2	39.5
NPSH, ft	60.2	60.2	60.2	60.2	60.2	60.2
Efficiency, %	54.6	47.8	42.9	35	30.2	28.9
Oxidizer Inducer:						
Flowrate, lb/sec	226.2	234.7	243.7	91.5	95.3	99.6
Speed, rpm	3745	3906	4115	1971	2077	2163
Pressure Rise, psi	176	192	213	54	60	65
NPSH, ft	16.0	16.0	16.0	16.0	16.0	16.0
xy, %	48.9	48.8	48.2	36.0	36.1	36.4
Fuel Low-Speed Inducer Turbine						
Pressure Ratio						
Flowrate, lb/sec	1.44	1.49	1.52	1.51	1.55	1.57
Speed, rpm	2.51	2.75	2.96	1.20	1.30	1.35
Efficiency, %	12,473	12,630	12,663	7748	7978	8043
	50.3	48.7	47.5	34.5	34.4	33.9
Oxidizer Low-Speed Inducer Turbine						
Pressure Drop, psi						
Flowrate, lb/sec	835	923.2	1062	573	650.1	695.4
Speed, rpm	195	202	210	80.6	83.5	87.1
Efficiency, %	3745	3906	4115	1971	2077	2163
	48.6	48.2	47.3	28.8	28.3	28.5
Preburner Fuel Valve						
Flow, lb/sec						
Pressure Drop, psi	38.5	32.0	27.5	14	12	10
Effective Area, in ²	348	628	808	380	500	570
	1.55	0.98	0.76	0.56	0.43	0.35
Preburner Oxidizer Valve						
Flow, lb/sec						
Pressure Drop, psi	23	24	25	5	5.5	6
Effective Area, in ²	1020	1040	1040	580	640	680
	0.150	0.140	0.140	0.04	0.04	0.04
Main Chamber Oxidizer Valve						
Flow, lb/sec						
Pressure Drop, psi	194	202	210	80	85	90
Effective Area, in ²	360	530	640	120	140	150
	1.42	1.60	2.02	1.22	1.29	1.46

Table II. Demonstrator Engine Operating Characteristics, Booster (Continued)

	100% Thrust r = 5.0	100% Thrust r = 6.0	100% Thrust r = 7.0	75% Thrust r = 5.0	75% Thrust r = 6.0	75% Thrust r = 7.0
Low-Speed Inducer						
Fuel Inducer:						
Flowrate, lb/sec	90.31	77.5	68.8	67.67	58.4	51.8
Speed, rpm	19,923	18,146	17,699	16,150	15,742	15,618
Pressure Rise, psi	90.0	88.7	100.1	74.5	86.7	97.5
NPSH, ft	60.2	60.2	60.2	60.2	60.2	60.2
Efficiency, %	61.6	60.1	56.7	60.0	55.2	50.7
Oxidizer Inducer:						
Flowrate, lb/sec	451.5	465.2	481	338.4	377.0	362.8
Speed, rpm	5417	4935	4904	4857	4659	4989
Pressure Rise, psi	238	197	186	254	224.2	257
NPSH, ft	16.0	16.0	16.0	16.0	16.0	16.0
Efficiency, %	57.2	60.7	61.4	52.9	55.8	54.1
Fuel Low-Speed Inducer Turbine						
Pressure Ratio	1.48	1.43	1.46	1.42	1.45	1.49
Flowrate, lb/sec	5.55	4.62	4.73	3.64	3.72	3.87
Speed, rpm	19,823	18,146	17,699	16,150	15,742	15,618
Efficiency, %	63.1	60.3	58.8	57.4	55.1	53.7
Oxidizer Low-Speed Inducer Turbine						
Pressure Drop, psi	772	523.0	478	940	727.6	875
Flowrate, lb/sec	568	391	408	256	298	310
Speed, rpm	5417	4935	4904	4857	4659	4989
Efficiency, %	68.5	72.7	73.8	52.9	63.7	62.5
Preburner Fuel Valve						
Flow, lb/sec	77	66	57	58.0	49.0	42.5
Pressure Drop, psi	270	200	550	162	473	745
Effective Area, in ²	3.48	3.48	1.83	3.43	1.69	1.20
Preburner Oxidizer Valve						
Flow, lb/sec	75	66	68	43	43	44
Pressure Drop, psi	670	380	230	1220	900	795
Effective Area, in ²	0.54	0.49	0.82	0.215	0.260	0.286
Main Chamber Oxidizer Valve						
Flow, lb/sec	370	380	410	283	300	310
Pressure Drop, psi	630	1120	1520	520	547	1100
Effective Area, in ²	1.74	2.13	2.96	1.58	1.56	2.49

Table II. Demonstrator Engine Operating Characteristics, Booster (Continued)

Configuration	50% Thrust r = 5.0	50% Thrust r = 6.0	50% Thrust r = 7.0	20% Thrust r = 5.0	20% Thrust r = 6.0	20% Thrust r = 7.0
Thrust, lb	122,000	122,000	122,360	48,800	48,800	48,800
Vacuum Specific Impulse, sec $\epsilon = 75$	449	446	438	444	439	429
Sea Level Specific Impulse, sec $\epsilon = 35$	344	339	334	269	264	262
Envelope:						
Diameter, in.	69.25	69.25	69.25	69.25	69.25	69.25
Length: Nozzle Extended/Retracted, in.	131.7/80.0	131.7/80.0	131.7/80.0	131.7/80.0	131.7/80.0	131.7/80.0
Nozzle Area Ratio: Extended/Retracted	75/35	75/35	75/35	75/35	75/35	75/35
Fuel Flow, lb/sec	45.2	39.1	34.8	18.3	15.9	14.2
Oxidizer Flow, lb/sec	226.2	243.7	243.7	91.5	95.3	99.6
Total Propellant Flow, lb/sec	261.4	273.8	278.5	109.8	111.2	113.8
Main Burner Chamber						
Throat Total Pressure, psia	1360	1360	1329	552	537	526
Mixture Ratio (injector)	5.61	6.92	8.25	5.99	7.45	8.93
Specific Impulse Efficiency, %	96.8	96.6	96.4	96.3	96	95.9
Fuel Injector Pressure Loss, psi	543	53.5	52.8	17.4	18.0	18.3
Oxidizer Injector Pressure Loss, psi	230	246	265	13.1	42	45.6
Momentum Pressure Loss, psi	15.2	11.6	9.5	9.0	7.6	7.1
Transpiration Coolant Flow, lb/sec	2.95	3.23	3.36	1.45	1.57	1.62
Throat Diameter, in.	7.68	7.68	7.68	7.68	7.68	7.68
Preburner						
Total Injector Pressure, psia	2026	1970	1926	741	728	719
Mixture Ratio (preburner injector)	0.90	1.01	1.21	0.76	1.00	1.24
Temperature, °R	1548	1901	2223	1464	1883	2255
Fuel Injector Pressure Loss, psi	106	86	74	30.687	27.810	22.382
Oxidizer Injector and Control Valve Pressure Loss, psi	1093	1105	1102	583	652	677
Total Injector Propellant Flow, lb/sec	67.3	62.2	58.8	23.8	22.24	21.3
Combustion Efficiency, %	100	100	100	100	100	100
Primary Nozzle						
Transpiration Supply Section:						
Coolant Flow, lb/sec	3.43	3.81	3.95	1.66	1.80	1.86
Coolant Inlet Pressure, psia	2474	2668	2779	1156	1251	1302
Coolant Inlet Temperature, °R	93.8	105	116	75.6	84.8	92.6
Coolant Pressure Loss, psi	60.7	67.9	71.9	28.7	31.5	33.2
Coolant Temperature Rise, °R	375	365	365	392	387	392
Preburner Supply Section:						
Coolant Flow, lb/sec	37.7	31.3	26.9	13.7	11.2	9.6
Coolant Inlet Pressure, psia	2195	2100	2035	785	768	750
Coolant Inlet Temperature, °R	95.4	107	117	75.0	82.0	87.6
Coolant Pressure Loss, psi	44.8	35.8	30.0	10.9	9.6	7.8
Coolant Temperature Rise, °R	45.9	55.8	60.8	53.0	52.0	50.9

Table II. Demonstrator Engine Operating Characteristics, Booster (Concluded)

Configuration	100% Thrust r = 5.0	100% Thrust r = 6.0	100% Thrust r = 7.0	75% Thrust r = 5.0	75% Thrust r = 6.0	75% Thrust r = 7.0
Thrust, lb	244,000	244,000	244,000	183,000	183,000	183,000
Vacuum Specific Impulse, sec ϵ 75	450	450	444	451	448	441
Sea Level Specific Impulse, sec ϵ 35	387	386	380	370	367	364
Envelope:						
Diameter, in.	69.25	69.25	69.25	69.25	69.25	69.25
Length: Nozzle Extended/Retracted, in.	131.7/80.0	131.7/80.0	131.7/80.0	131.7/80.0	131.7/80.0	131.7/80.0
Nozzle Area Ratio: Extended/Retracted	75/35	75/35	75/35	75/35	75/35	75/35
Fuel Flow, lb/sec	90.3	77.5	68.8	67.7	58.4	51.8
Oxidizer Flow, lb/sec	431.5	465.2	481.4	338.4	350.1	362.8
Total Propellant Flow, lb/sec	541.9	542.8	550.1	406.1	408.5	414.6
Main Burner Chamber						
Throat Total Pressure, psia	2806	2740	2676	2101	2059	2002
Mixture Ratio (injector)	5.56	6.68	7.94	5.53	6.77	8.06
Specific Impulse Efficiency, %	96.7	97.0	96.9	96.9	96.8	96.7
Fuel Injector Pressure Loss, psi	164	134	125	97.7	89.7	86.3
Oxidizer Injector Pressure Loss, psi	851	910	979	496	532	572
Momentum Pressure Loss, psi	-1.6	0.8	-0.4	13.2	9.7	6.4
Transpiration Coolant Flow, lb/sec	6.42	5.36	5.49	4.24	4.34	4.50
Throat Diameter, in.	7.68	7.68	7.68	7.68	7.68	7.68
Preburner						
Total Pressure, psia	4778	4332	4152	3256	3100	3003
Mixture Ratio (preburner injector)	1.08	1.12	1.28	0.98	1.06	1.23
Temperature, °R	2026	2085	2345	1715	1984	2274
Fuel Injector Pressure Loss, psi	320.5	248.0	200.5	201.9	158	129
Oxidizer Injector and Control Valve Pressure Loss, psi	1141	944	599	1385	1065	966
Total Injector Propellant Flow, lb/sec	157.8	138.1	128.2	108.6	98.6	92.4
Combustion Efficiency, %	100	100	100	100	100	100
Primary Nozzle						
Transpiration Supply Section:						
Coolant Flow, lb/sec	7.75	6.44	6.59	5.06	5.17	5.36
Coolant Inlet Pressure, psia	5279	4723	4830	3595	3701	3836
Coolant Inlet Temperature, °R	142	133	139	114	120	129
Coolant Pressure Loss, psi	142	120	126	89	94	100
Coolant Temperature Rise, °R	266	338	341	336	350	349
Preburner Supply Section:						
Coolant Flow, lb/sec	76.5	65.5	56.7	57.7	48.4	41.7
Coolant Inlet Pressure, psia	5271	4712	4455	3561	3341	3199
Coolant Inlet Temperature, °R	142	133	142	114	121	131
Coolant Pressure Loss, psi	147	112	90.1	90	69	56.4
Coolant Temperature Rise, °R	35.7	44.2	48.5	40.7	48.8	53.4

2. Start, Shutdown, and Throttle Transients

Estimated start, shutdown, and throttle transient data are presented in figure 17.

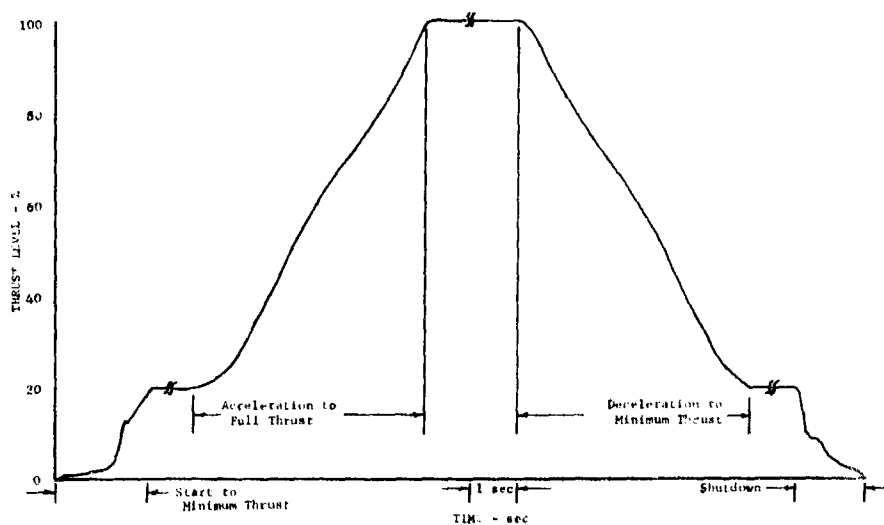


Figure 17. Demonstrator Engine Estimated Start, Shutdown, and Throttle Transient Data DF 75785

C. LAYOUT AND SCHEMATIC

The engine layout is illustrated in figure 18. The complete engine system schematic shown in figure 19 illustrates the helium supply system and the primary propellant flowpaths and the interrelationship of all of the major components.

D. WEIGHT

The calculated demonstrator engine weight based on lightweight rather than flightweight component designs is presented in table III. The targeted demonstrator engine weight is 3380 lb. Component weights are discussed in more detail in the component sections of this report.

E. INTERFACES

The ranges of temperature, pressure, and NPSH conditions required at the inlet to the fuel and oxidizer low-speed inducers are shown in figures 20 and 21.

17

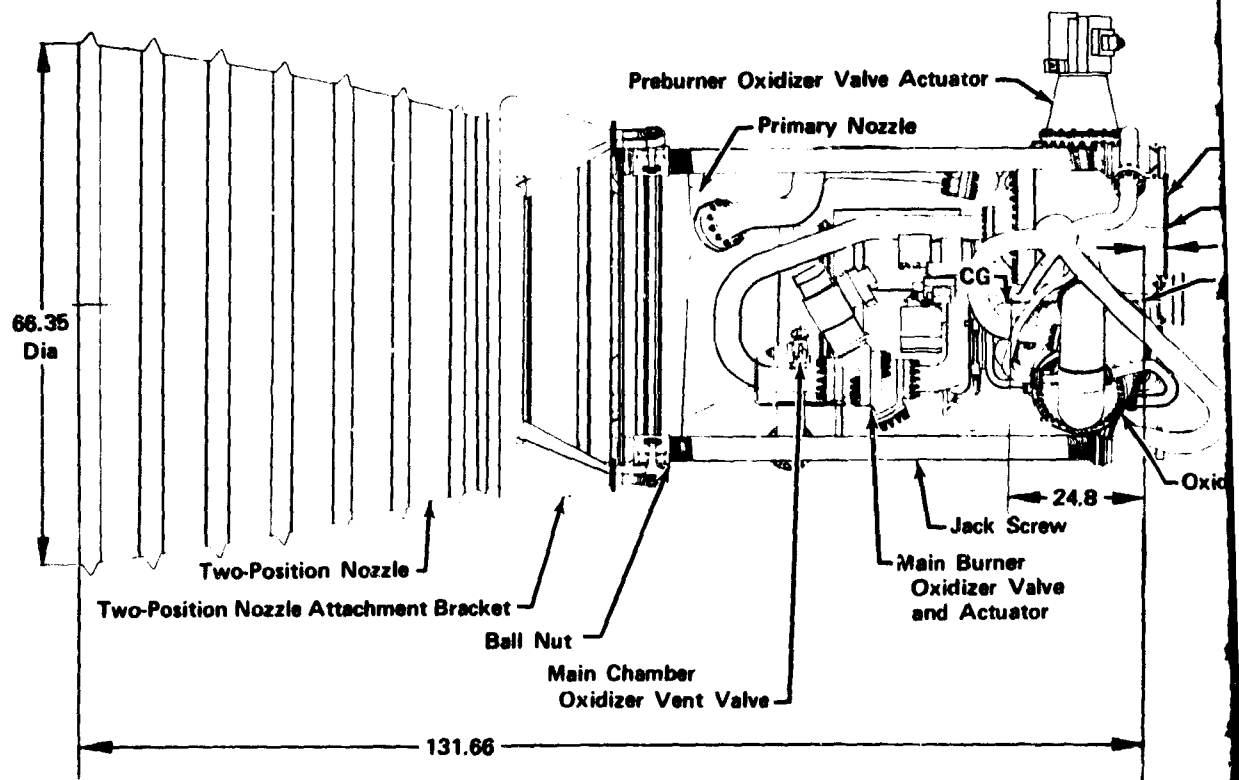
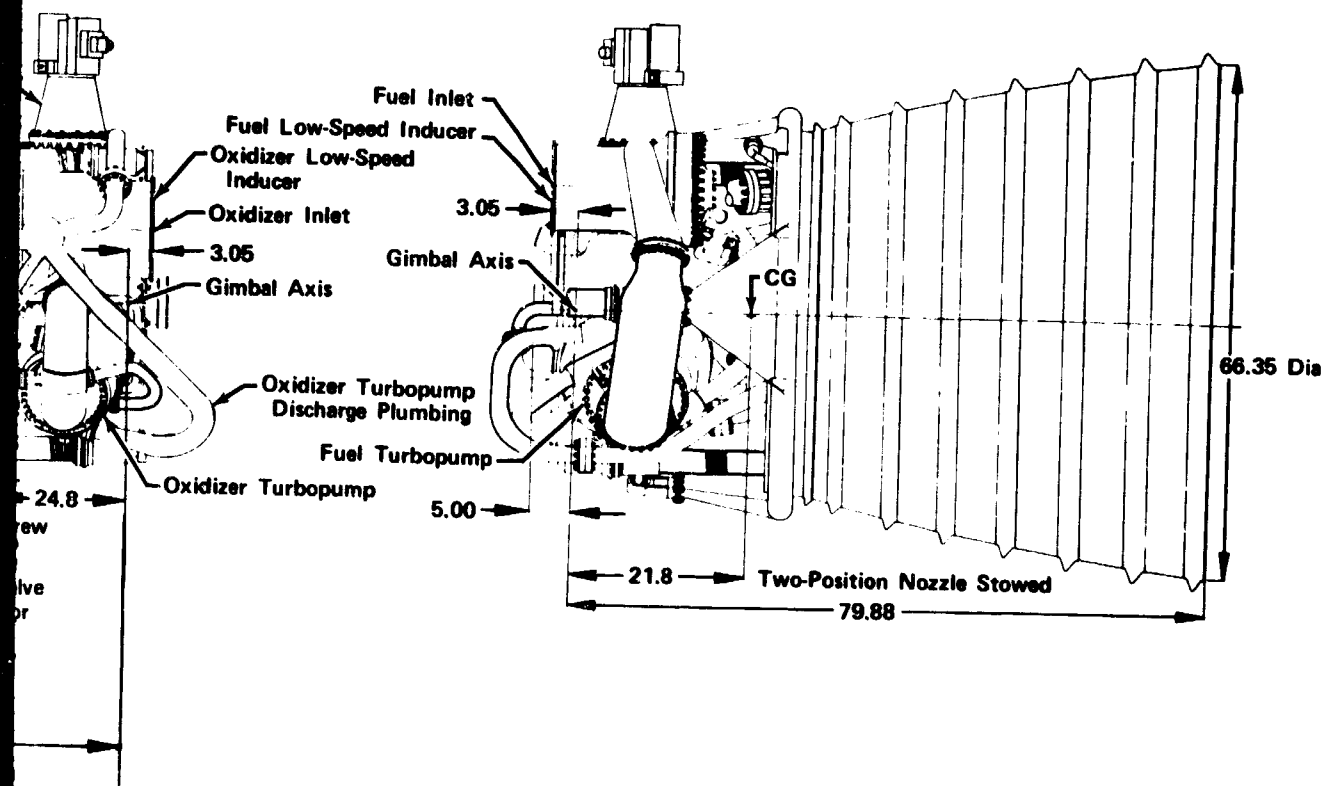


Figure 18. Demonstrator Engine Layout

11



FD 27725C

43/44

Table III. Demonstrator Engine Calculated Weight

Item	Calculated Weight, lb	Targeted Weight, lb
Preburner and Hardware	92	90
Transition Case and Gimbal	324	370
Main Burner Injector and Hardware	99	115
Main Burner Chamber	410	425
Nozzle and Actuation	652	640
Fuel Turbopump	554	480
Oxidizer Turbopump	383	335
Low-Speed Inducers	348	235
Controls	230	305
Plumbing	290	310
Miscellaneous	50	75
Total	3432	3380

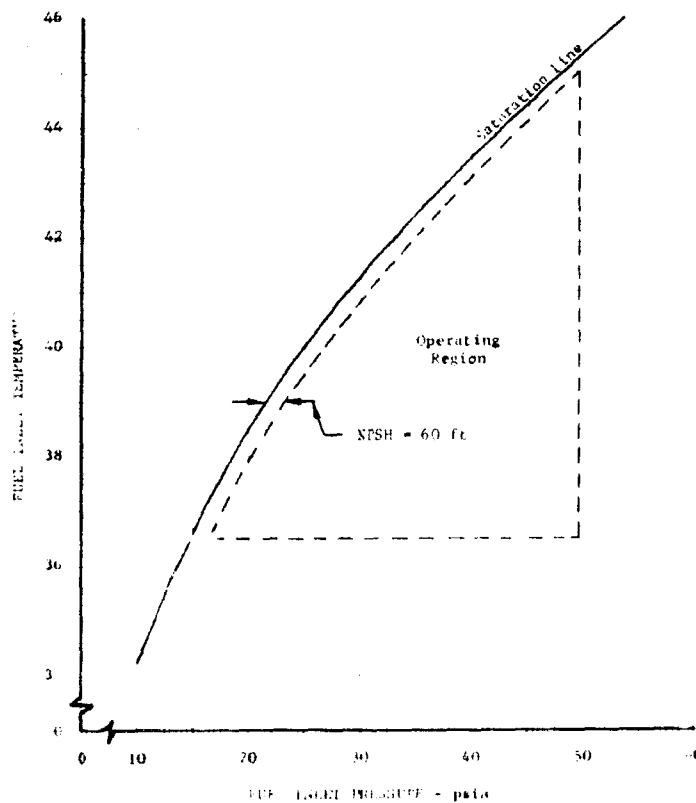


Figure 20. Fuel Inlet Operating Region

DF 69932

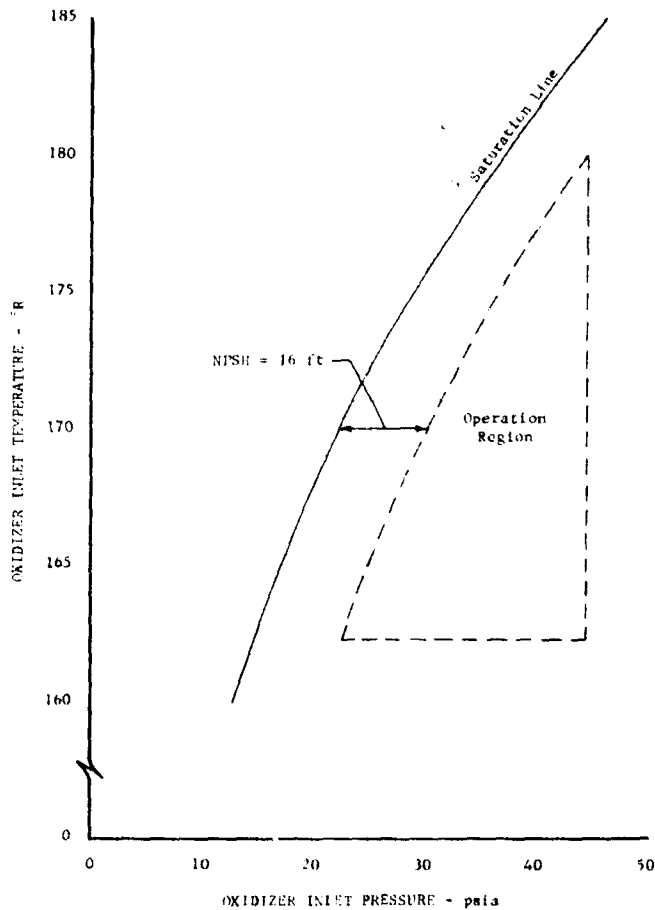


Figure 21. Oxidizer Inlet Operating Region

DF 69933

A study selected the inlet propellant temperatures used for the design cycle analysis of the engine. Engine power requirements were found to vary significantly with engine inlet temperature. The required turbine inlet temperature varied approximately 96°R, and the fuel pump speed varied approximately 3000 rpm over the full range of inlet temperature specified for the demonstrator engine.

The highest proposed inlet conditions were selected for component design to assure the engine power requirements can be met under the most severe operating conditions.

The relationship required between fuel temperature and oxidizer temperature, so that the maximum turbine inlet temperature (2325°R) will not be exceeded at 100% thrust is shown on figure 22.

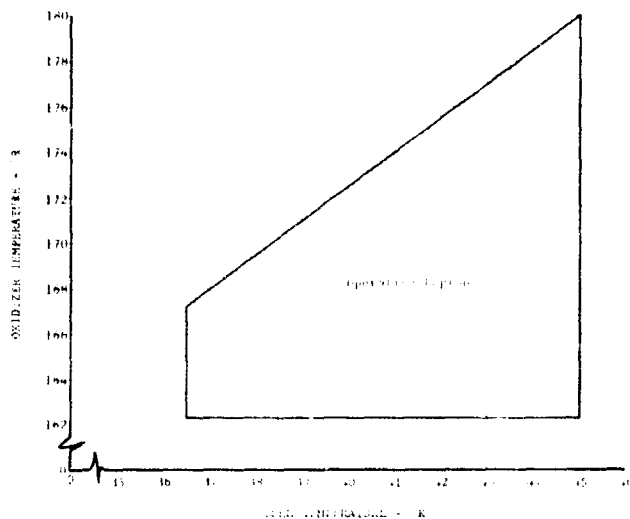


Figure 22. Propellant Temperature Limits for Fuel Trim Capability DF 70473

The engine/vehicle main structural interface is a ring flange on the thrust ball cone with a 6-in. diameter bolt circle. Eighteen equally spaced 0.2493-in. diameter holes are provided for bolt attachment of the engine to the vehicle. (Refer to Section IV, paragraph B for a description of the gimbal thrust ball.)

Gimbal actuators for control of pitch and yaw rate are attached by 0.5625 in. thread, UNF-3A, 12-point shoulder bolts to two gimbal actuator brackets on the main burner chamber pressure shell.

F. SYSTEMS ANALYSIS

1. General

System analyses of the demonstrator engine were conducted throughout the program to define component design requirements, to estimate the capabilities of the integrated engine system, and to incorporate the results of component and engine tests.

An initial analytical study was conducted to define those component design criteria that meet the design requirements of engine performance (as shown in table II) within the integrated engine system. These design data were derived by steady-state and transient analyses over the complete engine operating range using digital computer mathematical models. The steady-state analysis consists of studies that establish a cycle balance between design limitations and component performance. The transient studies define the engine design requirements based on dynamic requirements and operating sequences for engine start, throttling, propellant utilization, and shutdown.

As component and engine test data became available, the steady-state and transient analyses have been updated as required to provide the design data necessary to improve the component and module designs.

The system design resulted from an iterative optimization process between mechanical and analytical studies, and component and engine test data. Using a digital computer, a cycle balance program defines component design point data and determines engine performance for the design and off-design point operating conditions. These design data are used in the completion of design layouts. Specific component limitations defined in the process of designing the individual components are again input into the cycle balance and the iteration is continued until an optimum design is established.

2. Initial System Analysis

a. Analysis Method

A balance was established between component thermodynamic performance, mechanical design requirements, and engine operating requirements. This balance was established by using an optimization procedure in which component geometry and performance are varied to maximize mechanical design margin while meeting the engine operational goals. Table IV summarizes the various inputs, engineering considerations, and results of this process.

b. Analysis Criteria

The engine characteristics presented in table II were used for the systems analysis of the demonstrator engine. They represent the targets toward which the demonstrator engine program is being directed. Technology limits used for the system analysis were set at the state-of-the-art level per data obtained in subscale and full-scale combustion testing under Air Force Contract AF04(611)-11401 and turbopump testing under NASA Contracts NAS8-20540 and NAS8-11714. Because an accurate estimate of the anticipated component performance was known prior to the design analysis, the engine was designed with confidence that the structural margins and performance levels will be sufficient to allow maximum flexibility of engine operation.

c. Steady-State Cycle Optimization

The cycle balance program used for steady-state cycle optimization is configured to afford flexibility in the integration of component requirements over the thrust and mixture ratio ranges. Features include: (1) a means of selecting the optimum component design points, (2) a procedure for optimizing the turbine area match for required engine operating range, and (3) a method of evaluating component off-design performance effects on overall cycle performance.

The initial step of the cycle balance program defines the chamber and nozzle geometry necessary to provide the required thrust at the nominal mixture ratio within the allowable design limitations. The main chamber combustion and nozzle efficiencies were maintained at a level consistent with the goals of the demonstrator engine program. The chamber pressure was fixed at the maximum level consistent with turbopump design limitations.

Table IV. Cycle Definition Procedures

Component	Inputs or Specifications	Engineering Considerations	Results
Combustion chamber and nozzles	Nominal vacuum thrust	Component performance available	Structural dimensions - chamber size, tube diameters, injector areas, etc.
	Chamber pressure (target value)	Mechanical design limits	
	Limiting engine dimensions	Weight tradeoffs	Nozzle expansion ratio
	Minimum specific impulse efficiency	Cooling requirements	Operating performance - thrust, specific impulse, propellant flowrates, cooling flows, etc.
	Nominal mixture ratio	Component integration	Operating limits
	Durability requirements		Weight
	Environmental conditions		
Turbopump power package	Pressure requirements	Component performance available	Structural dimensions - pump and turbine diameters, injector areas, bearing sizes, etc.
	Propellant flowrates	Mechanical design limits	
	Thrust and mixture ratio range	Weight tradeoffs	Operating performance - preburner temperature, pump pressures, speeds, efficiencies, coolant flowrates, NPSH, etc.
	Environmental and interface conditions	Design and off-design characteristics of engine cycle	Operating limits
		Component integration	Weight

Table IV. Cycle Definition Procedures (Concluded)

Component	Inputs or Specifications	Engineering Considerations	Remarks
Control system	Engine operating modes	Design and off-design characteristics of engine cycle	Control point locations
	Operating limits		Structural dimensions
	Engine thrust and mixture ratio accuracy	System pressure drops	Valve functions
	Environmental and interface conditions	Mechanical design limits - area turndown, valve accuracy, response, etc.	Valve sequences
			Valve area schedules
			Weight

The chamber geometry is established to provide 244,000-lb thrust for a booster stage vehicle application with an area ratio of 75:1.

The nozzle coolant flowrates and passage sizes were varied until a balance was achieved between coolant pressure loss, nozzle weight, and coolant flowrate. The coolant pressure loss in the regenerative nozzles is important because it adds directly to fuel pump pressure. The nozzle skirt and transpiration coolant flowrates are important because these flows are not available for providing turbopump power. These flows also bypass the main injector, which increases the chamber mixture ratio and tends to decrease the overall specific impulse efficiency.

The engine flowrates and pressures defined in the nozzle/chamber design calculations provide the basic data used to design the turbopump power package.

The design approach taken in the cycle studies to obtain the required mixture ratio operating range was to use the extreme of the mixture ratio range as the power package design points.

The fuel pressure requirement controls the power balance at the lowest mixture ratio, and the oxidizer pressure requirement controls the balance at the highest mixture ratio. In addition, the minimum available turbine power occurs at the highest mixture ratio where the fuel flow is at a minimum. At the extremes in mixture ratio, where one pump controls the power match, the other pump is in an overspeed condition. Overspeed means that the pressure provided exceeds the pressure required to satisfy the flow conditions.

A reduction in efficiency results when a centrifugal pump is operated at flowrates and rotor speeds other than the pump design point. By selecting the design point of the main pumps at their respective maximum flow conditions, two advantages are obtained. First, the best efficiency point of the pump coincides with the engine operating point where the respective pump is controlling the power balance; second, the reduced efficiency at the low flow condition (i. e., the other extreme mixture ratio point) tends to minimize overspeed and to minimize the control system corrections required. Thus, the fuel pump is designed for a mixture ratio of 5.0 and rated thrust, and the oxidizer pump is designed for a mixture ratio of 2.0 and rated thrust. Use of this cycle optimization technique results in appreciably reduced pump pressure and speed requirements.

The basic turbopump design variables other than efficiency, namely turbine areas, pump impeller diameters, speed, and turbine inlet temperature, are optimized through an iterative procedure. Turbine areas and pump diameters are varied to meet the cycle pressure requirements within rotor speed and turbine temperature limitations.

The maximum turbine inlet temperature occurs at the maximum mixture ratio point, where the preburner fuel flow is at a minimum. The maximum allowable temperature is approximately 2325° R and is determined by the turbine stresses, which vary as functions of the turbine diameter, speed, and fluid bending forces.

Variation in the total turbine area (fuel turbine area plus the oxidizer turbine area) affects the total power through pressure ratio, whereas the ratio of turbine areas (fuel turbine area/oxidizer turbine area) affects the division of turbine power. As these areas are changed, the pump head requirements vary, and the pump impeller diameters are then sized to provide the required pump pressures within allowable design limitations.

At a particular value of total turbine area, the ratio of oxidizer turbine area to fuel turbine area is established to balance the turbopump power at the maximum allowable turbine inlet temperature (high mixture ratio). With this area ratio fixed, the cycle is rebalanced at the low mixture ratio extreme. Because of the turbopump power trends, the fuel and oxidizer turbopump speeds increase at the low mixture ratio. If the speeds are greater than allowable, the pump diameters are changed to hold the speed within the mechanical limitations defined by critical speed, turbine wheel speed, and bearing DN.

Because a modification to either the fuel or oxidizer pump at low mixture ratio will affect its operating requirements at high mixture ratio, the turbine area ratio at high mixture ratio may need to be changed. This process (changing components at one mixture ratio and checking the effects at the other mixture ratio) was continued until an optimized cycle balance was obtained.

In balancing the engine cycle, the components that maximized chamber pressures within the restraints of pump speed and pressure and turbine maximum temperature were selected.

Combustion performance and injector characteristics are considered in conjunction with control pressure loss scheduling. In the preburner and main burner injector designs, the major performance considerations are the fluid velocities, the momentum exchange between the fuel and oxidizer, and the injector

pressure potentials for combustion stability. In the control system designs, the major considerations are pressure drop for flow control potential and valve turn-down ratio. Off-design performance characteristics are used to obtain basic injector and control design data to ensure that sufficient pressure drop to satisfy both the stability and control system pressure requirements is provided. At each balanced operating point the required injector and control pressure drop is maintained or exceeded.

Design characteristics of the low-speed inducers were also determined within the cycle balancing effort. The inducer design discharge pressure must satisfy the main turbopump NPSH requirements and the estimated line losses between the low-speed inducers and pump.

The low-speed inducer diameter and drive turbine speed were selected to provide the necessary inducer discharge pressure and turbine efficiency while remaining consistent with the available low-speed inducer inlet NPSH and inducer suction characteristics. The turbine areas were sized to provide sufficient energy to drive the inducers without increasing the maximum pressure of the main pumps.

d. Transient Analysis

The transient characteristics of the XLR129 engine were investigated to identify any component design limits and to define the optimum control sequences to provide rapid, safe, and repeatable start throttling and shutdown transients. Variations in environmental conditions, such as inlet and ambient temperatures and pressures, were considered. Evaluation of the effects of engine component performance and control system on the system transients are an integral part of the design process.

The basis for the control system used in the system analysis was a detailed controls study performed under Contract NAS8-11427. This study evaluated several control systems and 17 control points for an advanced high pressure rocket engine system using a preburner cycle.

(1) Throttle Transient Analysis

Transient analyses of the engine system within the extremes of main stage thrust and mixture ratio define the engine and control system dynamics, and define engine transient response and component protection required during rapid transients.

Engine throttle transients were simulated using representative control systems that use engine parameters as input and/or feedback to the control areas. The preburner oxidizer valve was selected to provide closed-loop thrust control by using oxidizer and fuel flowmeter flows (summed) as a thrust indication. The ratio of the flowmeter flows was fed back to the main chamber oxidizer valve to provide closed-loop mixture ratio control. Accelerations and decelerations between idle and rated thrust in 2 seconds were simulated at engine mixture ratios of 5 and 7. Three-second mixture ratio excursions between 5 and 7 were simulated at 100% thrust. Throttling transient analysis revealed no limitations that would require hardware or control mode changes from that established during steady-state analysis.

(2) Start and Shutdown Transient Analysis

Similar mathematical models were used to simulate the start, throttling and shutdown modes of operation. Additional calculations in the start and shutdown simulations include: (1) the propellant filling processes, (2) fluid properties for phase transitions from gas to two-phase to liquid flow, (3) preburner and main chamber ignition, and (4) low-speed performance of the main turbopumps and low-speed inducers. Similar models have been used extensively during Phase I, Contract AF04(611)-11401, Module Design task and also in conjunction with the preburner and stage combustion test programs. A summary of the conclusions of these studies is presented below:

(a) Start Transient

1. The engine can be safely started to 20% thrust in approximately 2 seconds using a time sequenced control method.
2. The orifice restriction in the primary flowpath of the preburner oxidizer valve must be made smaller than that established during steady-state cycle analysis to reduce the preburner temperature spike when the primary cavity fills.
3. The use of helium purges in the secondary cavity of the preburner oxidizer injector and the main oxidizer injector is recommended to prevent back flow of the combustion product predicted to occur during the start transients.

(b) Shutdown Transient

1. A shutdown analysis showed that the engine can be shut down safely from 20% thrust at all mixture ratios by using a single time-based propellant valve sequence that schedules all shutoff valves to their fully closed position in a maximum of 1.5 sec.
2. The valve sequence can be modified to adjust the rate of preburner temperature decay during shutdown, if necessary for turbine stress and cycle life considerations.
3. The shutdown transient analysis revealed no limitations that would require hardware or control mode changes from that established during steady-state cycle analysis.

3. Special Design Cycle Studies

a. Design Point Trade Studies

Trade studies were made to establish the sensitivity of engine characteristics to component performance levels to identify the critical component characteristics and minimize any undesirable effects. The trade factors presented in table V were determined by varying each parameter separately and rematching engine components to provide maximum chamber pressure within component limitations and cycle ground rules. The change in preburner temperature required to maintain a constant chamber pressure with variations in component performance was also calculated by using the trade factor for chamber pressure and turbine temperature defined in table V.

The turbine area changes required to reoptimize (rematch) the cycle for full mixture ratio range at the indicated changes in chamber pressure were also established. For example, if main fuel turbine efficiency were increased 1 point, chamber pressure could be increased 12.6 psi over the full mixture ratio range provided the fuel turbine area was reduced by 0.25% and the main oxidizer turbine area was increased by 0.87%. The trade factors presented in table V may be assumed to be linear for small component variations.

b. Maximum Oxidizer Pump Discharge Pressure

An analytical study was made to determine the optimum method of obtaining a maximum chamber pressure. Engine design cycles were established with components matched for maximum allowable oxidizer pump discharge pressures of 6500, 7000, and 7250 psia.

The following major factors were noted:

1. The maximum excess thrust capability is available for an engine designed for a peak oxidizer pump discharge pressure of 7050 psia.
2. The maximum design chamber pressure increases with increasing maximum oxidizer pump discharge pressure.
3. As the peak oxidizer pump discharge pressure is decreased, the assumed fuel pump speed limit of 48,000 rpm is approached at 100%, $r = 7$.
4. With increasing oxidizer pump discharge pressure, the assumed preburner temperature limit of 2325°R is approached at 100%, $r = 5$.
5. Overall specific impulse at a mixture ratio of 5 decreases with increasing maximum oxidizer pump discharge pressure as a result of increased transpiration cooling flow.

Table V. XLR129-P-1 Design Trades

Design Change	Magnitude of Change	Chamber Pressure (psia)	Preburner Temperature - °R P _c = Constant	Main Fuel Turbine Area, (%)	Main Oxidizer Turbine Area, (%)
1. Preburner Temperature	+10°R at r = Max	+ 6.9		+ 0.48	- 0.50
2. 1st-Stage Fuel Pump Efficiency	+ 1 point	+18.0	- 26.0	- 0.37	- 1.13
3. 2nd-Stage Fuel Pump Efficiency	+ 1 point	+ 8.1	- 12.0	- 0.08	- 0.76
4. Main Fuel Turbine Efficiency	+ 1 point	+12.6	- 18.0	- 0.24	- 0.87
5. Fuel Side Pressure Loss (Pump Discharge Through Preburner Injector)	+10 psi at r = Min	- 3.3	+ 4.7	- 0.36	- 0.48
6. Fuel Turbine Upstream Housing Loss	+10 psi at r = Min	- 3.0	+ 4.3	+ 0.08	- 0.19
7. Fuel Turbine Downstream Housing Loss	+10 psi at r = Min	- 5.9	+ 8.5	+ 0.13	- 0.37
8. Main Oxidizer Pump Efficiency	+ 1 point	+ 8.3	- 12.0	+ 0.49	- 1.24
9. Main Oxidizer Turbine Efficiency	+ 1 point	+ 9.1	- 13.0	+ 0.57	- 1.00
10. Oxidizer Side Pressure Loss (Pump Discharge Through Preburner Injector)	+10 psi	- 3.0	+ 4.3	- 0.17	- 0.21

Table V. XLR129 Design Trades (Concluded)

Design Change	Magnitude of Change	Chamber Pressure (psia)	Preburner Temperature - °R $P_c = \text{Constant}$	Main Fuel Turbine Area, (%)	Main Oxidizer Turbine Area, (%)
11. Maximum Oxidizer Pump Discharge Pressure	+ 100 psi at $r = \text{Min}$	+ 13.8	- 20.0	+ 0.76	+ 2.60
12. Maximum Fuel Pump Pressure Rise	+ 100 psi at $r = \text{Min}$	+ 21.0	- 30.0	- 3.0	- 5.3
13. Preburner Pressure Loss (Upstream of Turbine)	+ 10 psi	- 6.0	+ 8.6	Not Available	Not Available
14. Main Burner Hot Gas Duct Loss (Downstream of Turbine)	+ 10 psi	- 10.0	+ 14.0	Not Available	Not Available
15. Preburner/Turbine Bypass Flow	- 1.0 lb/sec	+ 22.0	- 32.0	+ 1.6	+ 1.6

Consideration of all the above factors indicates that an engine designed for a maximum oxidizer pump discharge pressure of 7050 psia would provide the optimum design. Although a slight loss in specific impulse would result at a mixture ratio of 5, no significant loss will be encountered at a mixture ratio of 6 and above, and the chamber pressure level attainable would be consistent with present design goals. An engine designed for higher oxidizer pump pressures could operate at slightly higher chamber pressure, but the specific impulse at mixture ratios of both 5 and 6 and excess thrust capability would be reduced.

c. Transition Case Coolant Flow Source

A design analysis of the transition case cooling passage indicated that structural problems may exist during the shutdown transient if the cooling is obtained from the preburner fuel valve discharge. This cycle analysis confirmed the acceptability of the alternative supply source located at the transpiration supply heat exchanger discharge.

For the analysis, the transpiration supply heat exchanger configuration was maintained and its cooling flowrate was increased by the level of transition case cooling flow. The increased cooling flow at 100% thrust, mixture ratio of 7, did the following: (1) reduced the transpiration wafer inlet temperature 63°R , (2) reduced required wafer cooling flow 0.25 lb/sec, (3) increased specific impulse 0.3 sec, and (4) decreased required preburner temperature 18.2°R .

Rerouting of the flow reduced the maximum available fuel low-speed inducer turbine power 16% because of the increased turbine inlet line loss (higher flow) and decreased turbine temperature.

d. Two-Position Nozzle Flow Source

This study investigated three engine locations for supplying the two-position nozzle coolant flow with and without a control valve. The locations investigated were: (1) the fuel pump interstage, (2) the fuel low-speed inducer discharge, and (3) the fuel preburner supply. For operation with the control valve in the system, the minimum coolant flow was scheduled into the nozzle. For operations without a control valve, an orifice was sized to provide the minimum coolant requirements at a critical engine operating point and allowed overcooling at all other operating conditions.

The fuel pump interstage was chosen to supply cooling flow for the two-position nozzle because (1) acceptable nozzle cooling was provided without requiring a control valve, (2) the source was insensitive to variations in engine inlet conditions (the LSI tapoff was very sensitive to them), and (3) the slight penalty in chamber pressure and overall impulse efficiency caused by the overcooling characteristic inherent in the orifice configuration was acceptable.

The engine characteristics with the three candidate locations are presented in figures 23 through 28.

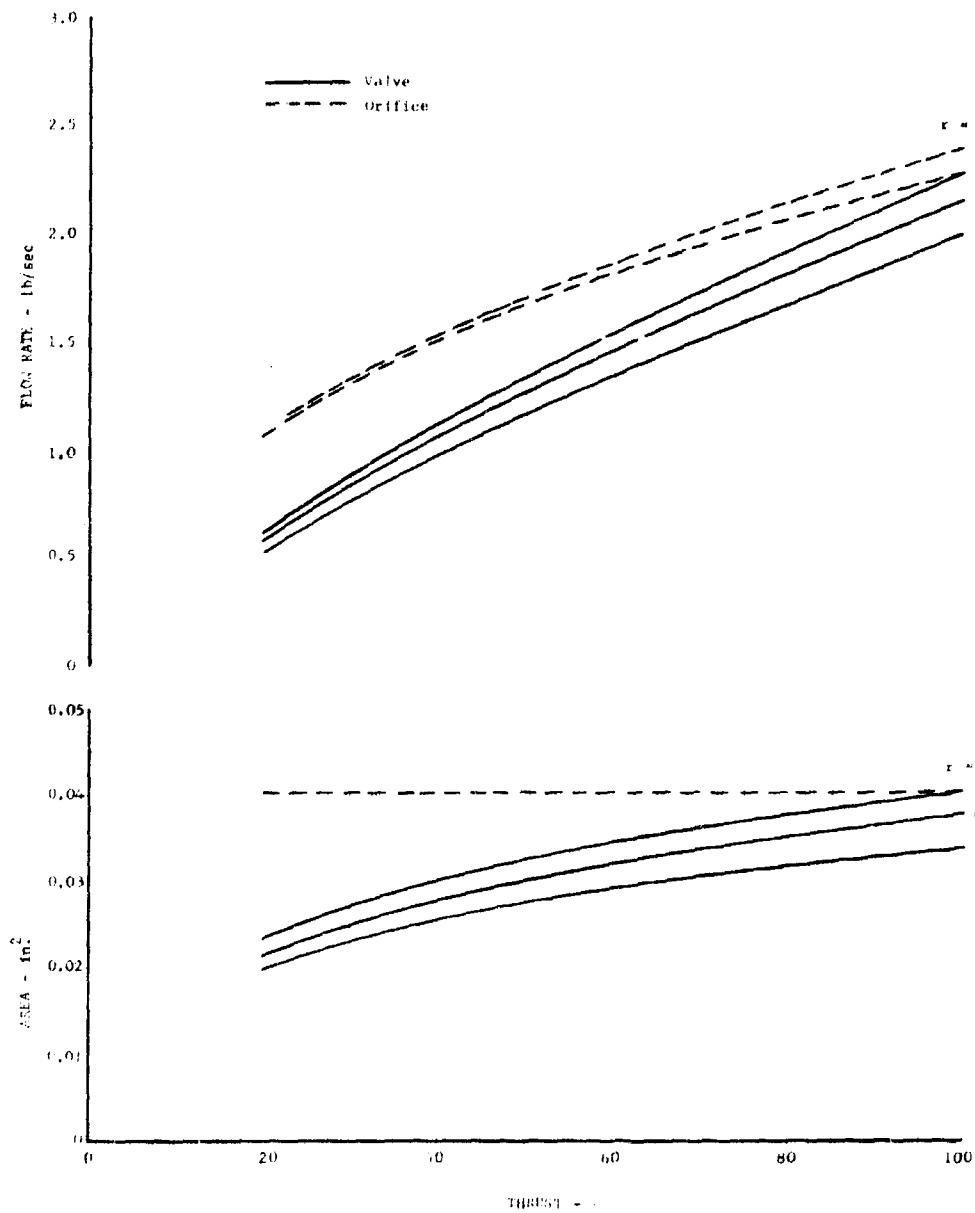


Figure 23. Effect of Pump Interstage Tapoff Location on Light-weight Heat Exchanger Coolant Valve DF 65466

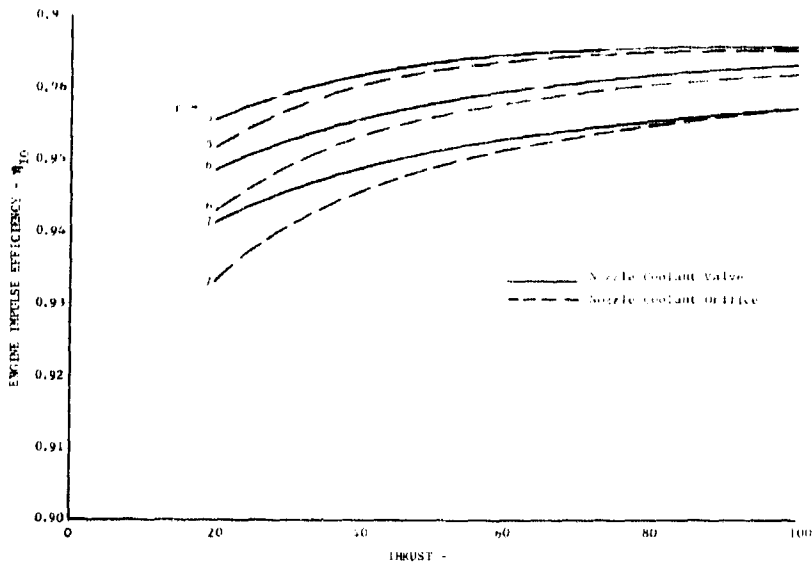


Figure 24. Effect of Pump Interstage Tapoff Location DF 76002 on Engine Impulse Efficiency

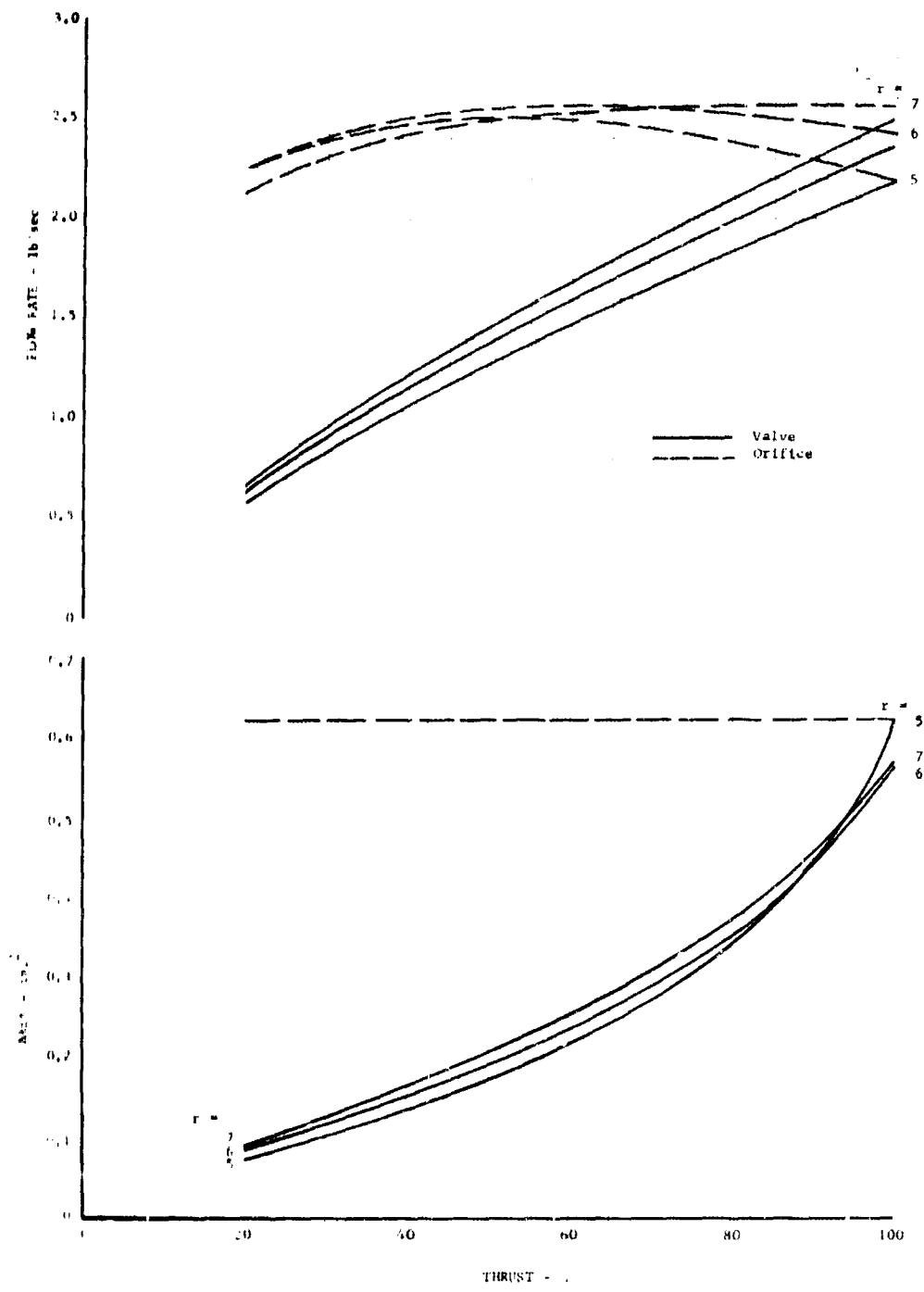


Figure 25. Effect of Low Speed Inducer Tapoff Location on Light-weight Heat Exchanger Coolant Valve DF 76004

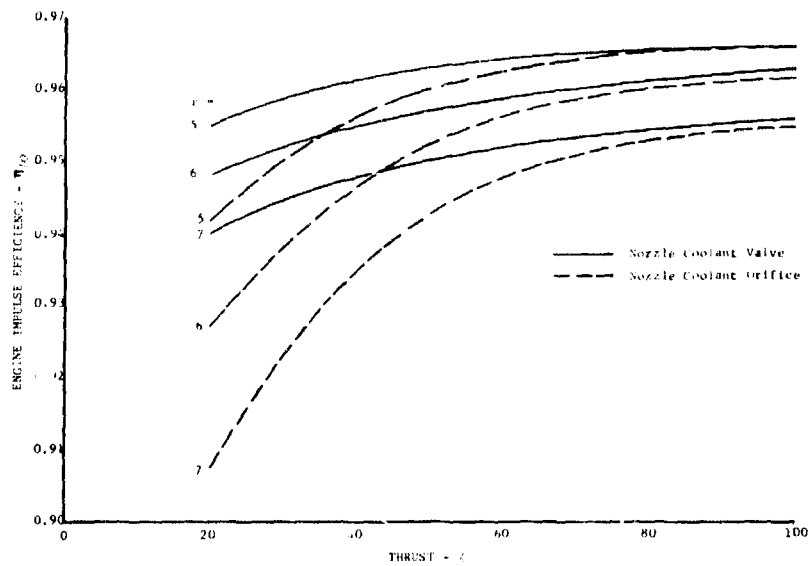


Figure 26. Effect of Low Speed Inducer Tapoff Location on Engine Impulse Efficiency DF 65467

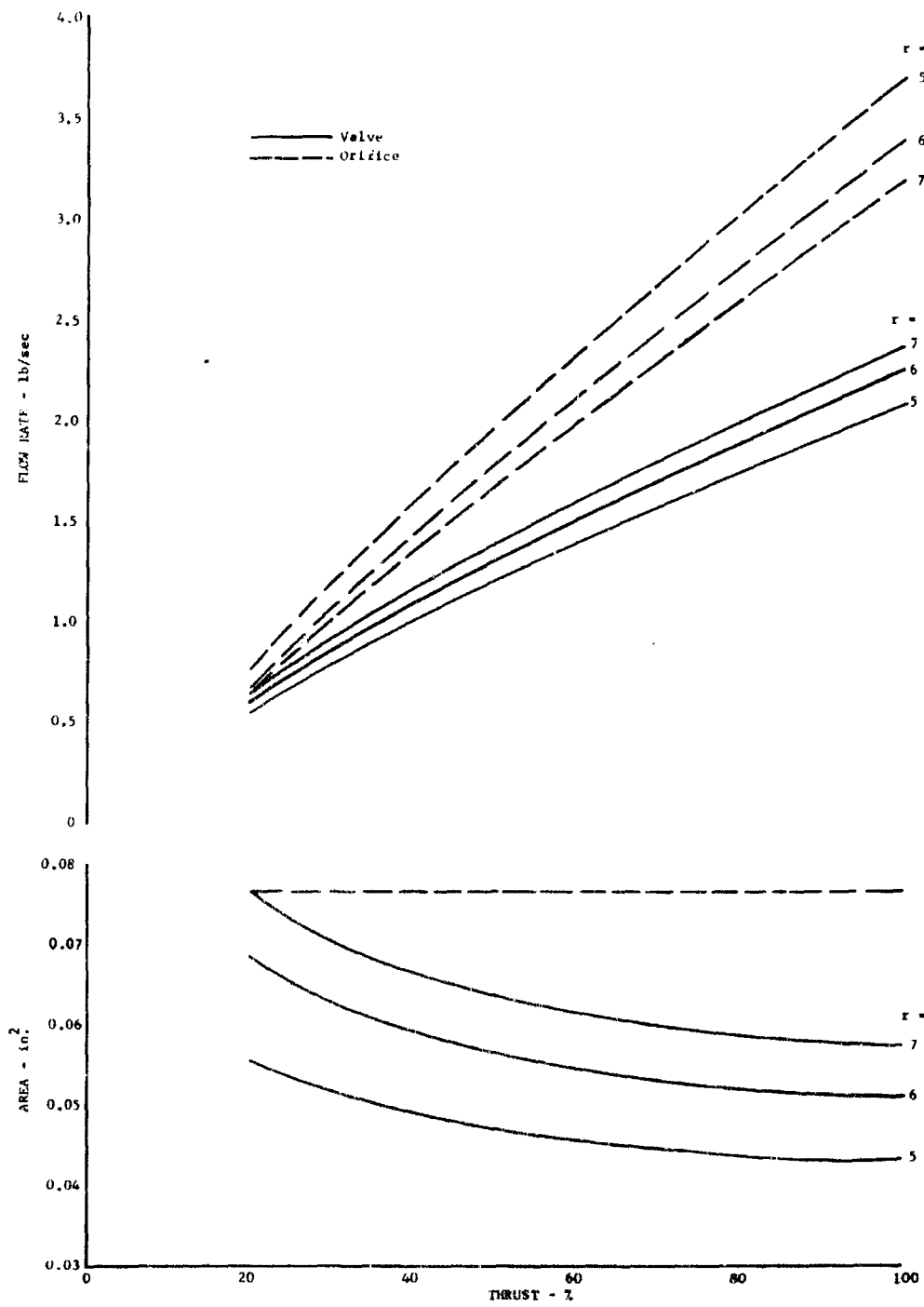


Figure 27. Effect of Fuel Preburner Supply Tapoff Location on Lightweight Heat Exchanger Coolant Valve DF 65468

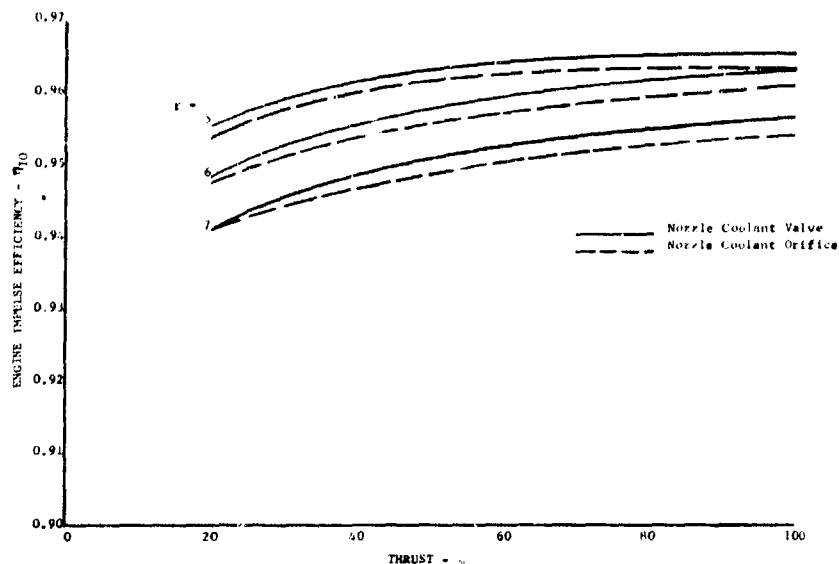


Figure 28. Effect of Fuel Preburner Supply Tapoff Location on Engine Impulse Efficiency DF 76003

G. PERFORMANCE DATA

The booster configuration operating at sea level, utilized the nozzle in the retracted position resulting in an expansion ratio of 35, which improves the thrust and specific impulse. At an altitude of 20,000 ft the two-position nozzle is translated to the extended position to provide an area ratio of 75 for improved altitude engine specific impulse. Use of the two-position nozzle provides nearly optimum performance for each operating regime. Altitude performance, i. e., thrust and specific impulse, for the booster configuration is presented in figure 29. The variation in sea level specific impulse with mixture ratio is shown in figure 30. The vacuum specific impulse variation with thrust and mixture ratio is given in figure 31.

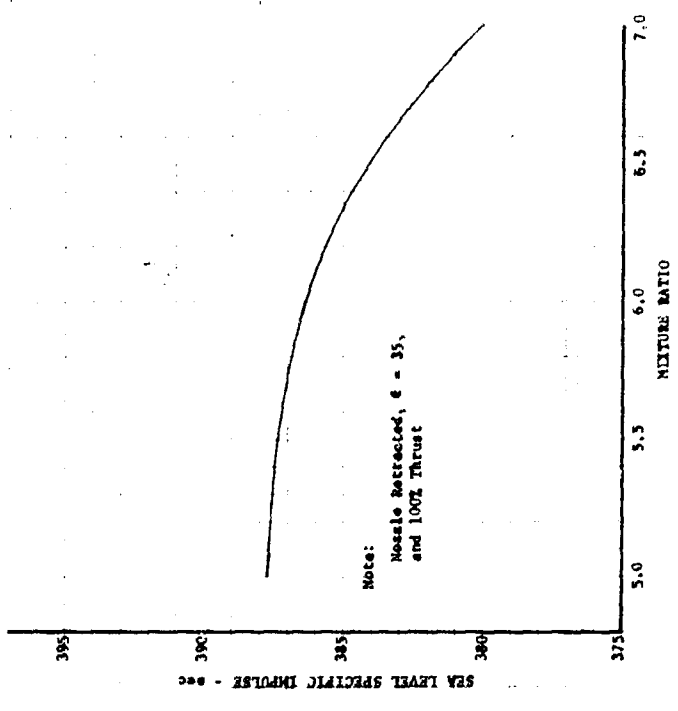
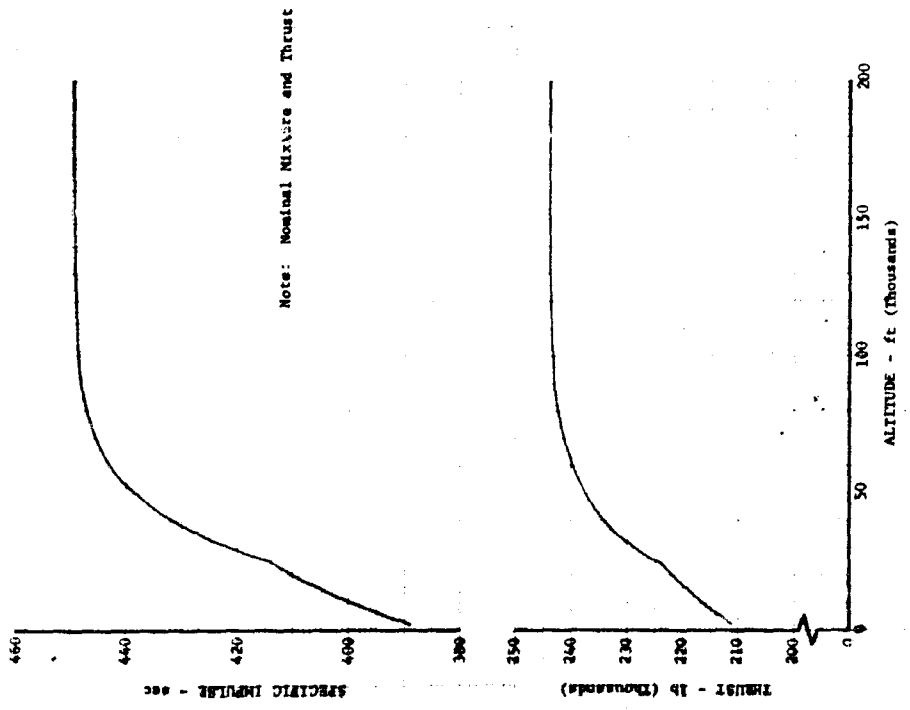


Figure 29. Altitude Performance for Demonstrator Engine (Booster Application) DF 70090 Figure 30. Sea Level Specific Impulse vs Mixture Ratio (Booster Application) DF 70699

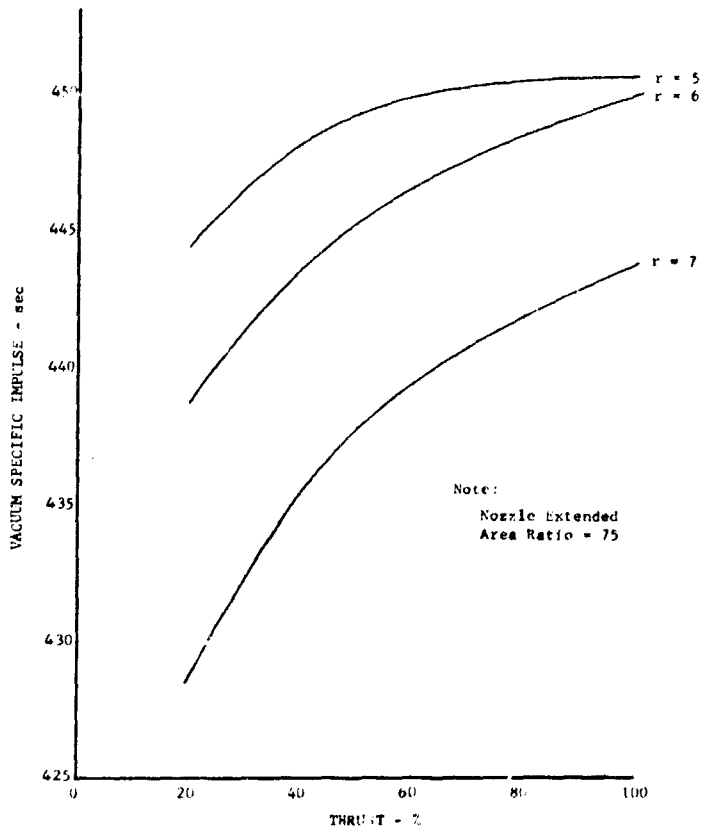


Figure 31. Vacuum Specific Impulse vs Thrust
(Booster Application)

DF 70091

SECTION IV DESIGN SUPPORT TESTING

A. FIXED FUEL AREA PREBURNER INJECTOR

1. Introduction

The objective of the fixed fuel area preburner injector subtask was to design, fabricate, and test a fixed fuel area preburner injector that would provide a temperature profile of less than 150°R peak-to-average at an average temperature of 2325°R. The injector tested had 252 dual orifice, tangential-swirl oxidizer and fixed concentric fuel area elements.

2. Summary, Conclusions, and Recommendations

The fixed area preburner injector must operate on cold gaseous hydrogen and liquid oxygen. The gaseous fuel allows throttling the fuel while still maintaining a suitable injection velocity due to the compressible fuel density change. On the liquid oxygen side, a dual orifice principle was applied to a slot swirler element to provide suitable injection velocity over the throttle range for the essentially incompressible liquid oxygen. The slot swirler element was selected because of its excellent very fine atomization and mechanical simplicity.

Initial water flow tests of the liquid oxygen injection element were conducted to determine the element discharge coefficients, cone angle, and stability during pulse testing. The originally selected element (0.095 in. inside diameter) had undesirable vortex instability characteristics at several flow levels. Similar tests of an alternative element (0.124 in. inside diameter) showed none of the undesirable features encountered with the 0.095 in. inside diameter tube. A series of water flow tests were conducted to determine the significant injection element geometry for vortex stability. These tests showed that there is a required relation of slot area to tube area for vortex stability in the injection element ($A_S/A_T < 0.5$) as well as that required for the element to meet the required ΔP of the cycle.

The 0.124 in. inside diameter element was selected for the fixed area preburner injector with slot areas to provide the required engine cycle injection ΔP 's.

Fourteen full scale preburner combustion tests were conducted with the fixed fuel area preburner. The preburner temperature profile was significantly improved over the results obtained with the variable area preburner injector tested during Phase I (Contract AF04(611)-11401). A peak-to-average combustion temperature profile of 76°R in a radial plane was demonstrated at an average temperature of 2388°R. Damaged oxidizer elements in a section of the injector in line with the temperature rake in a second radial plane (thermocouples No. 31 to 39) distorted the temperature profile causing a reduction in average temperature to 2325°R and subsequent increase in measured peak-to-average temperature of 215°R.

Four ignition tests were conducted to determine if the preburner would ignite with a secondary helium purge flowrate and the low engine starting tank head flowrate. Successful ignition and sustained combustion occurred during all four tests. Four additional tests were programmed to simulate the engine start transients from the ignition flowrates to the 20% flowrate level. Purge timing during shutdowns was adjusted to study the best engine shutdown sequence.

During testing of the preburner injector, low frequency combustion instability was encountered at thrust levels below 25% and several tests were programed to obtain data on influential parameters. An analog model of the preburner injector, combustion chamber, and a portion of the test stand was constructed to determine the influence of various parameters on stability. Water flow tests of the injector assembly and single element test rigs were also made.

It was concluded from the test data where high-pressure drop orifices had been installed in the facility lines that the test facility line volumes were not the cause of the chugging. The analog model that duplicated the test results of frequency and amplitude fairly well indicated that the low secondary pressure drop and large secondary volume contributed significantly to the instability and that reducing the liquid oxygen injector secondary volume would detune this cavity eliminating the instability.

3. Oxidizer Element Testing

Tangential slot swirler elements are mechanically simple, durable and provide excellent atomization. They can be easily manufactured from drawn tubing and the tangential slots accurately electric discharge machined into the tube. To meet the throttling requirements of the preburner, a second set of small "primary" tangential slots were added. At the low end of the throttling range a reasonably high injection pressure drop can still be maintained across these small "primary slots." The larger secondary tangential slots provide flow area and prevent the injection pressure drop requirement at full thrust level from being excessive for the engine cycle.

Oxidizer injector element inside diameters from 0.085 in. and larger with the proper slot sizes will satisfy the cycle injection ΔP requirements. Test elements were manufactured with 0.085, 0.095, and 0.124 in. inside diameters, and the flow passages were sized to fit the pressure drop of the engine cycle. It appeared that the smaller tube diameters would keep the hollow vortex gas core small inside the element. Larger tubes produce larger injection cone angles and better atomization. The dimensional characteristics of these elements to meet the engine cycle ΔP are presented in table VI.

Table VI. Element Dimensional Characteristics

Tube P/N	ID (in.)	A_S (in ²)	A_O (in ²)	A_S/A_O	Number of Slots	Primary Diameter (in.)	Primary Holes	Length (in.)
AKS-5360	0.085	0.017	0.00567	3.0	3	0.0145	2	3.090
AKS-5361	0.095	0.0103	0.00709	1.45	3	0.0145	2	3.090
AKS-5362	0.124	0.0101	0.0121	0.84	3	0.0145	2	3.090

The sizing of tangential slots was based on water flow element discharge coefficient data shown plotted in figure 32. With the element inside diameter and total secondary effective area required by the preliminary engine cycle, the total secondary physical area for an element can be obtained from the curve. Earlier experience showed that slot widths of less than 0.015 in. were difficult to manufacture with any degree of repeatability, while slot width-to-diameter

ratios (W/D) of more than 0.20 were undesirable with the required length-to-diameter ratio (L/D) because of deterioration of the element spray cone angle. With the total element secondary physical area slot width limits known, it was possible to choose the number and length of the secondary flow passages. Because of their small size, the major portion of the primary pressure drop occurs across the primary slots making the primary flow insensitive to any small changes in static pressure inside the element. Therefore, the primary passages were sized by the engine effective area requirements combined with the primary discharge coefficient experience from earlier testing.

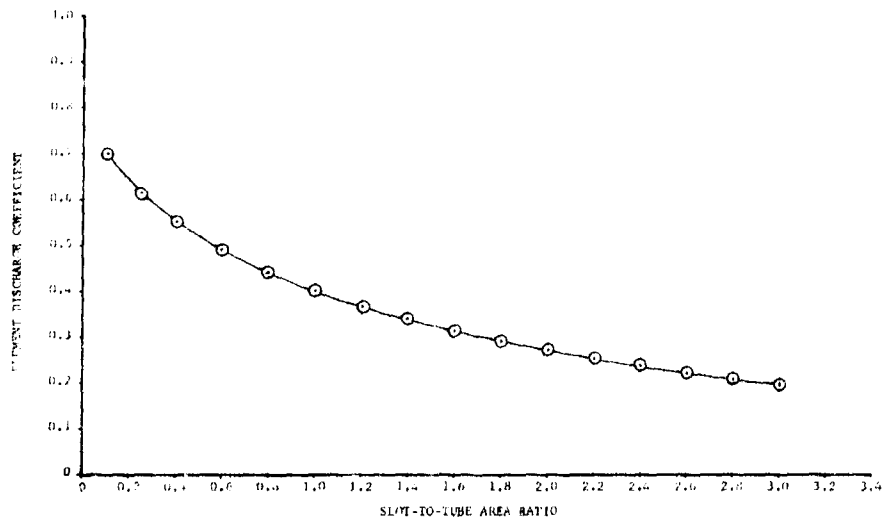


Figure 32. Data from Prior Tangential Entry Oxidizer Element Testing

DF 65430

The individual oxidizer elements were water flowed to determine individual effective flow area and cone angles. The flow testing required a test piece that (1) contained the individual oxygen injection element, (2) separated the primary and secondary cavities, and (3) provided manifolding in the slot areas.

The first flow blocks used were welded units containing a single oxygen injection element with the primary-to-secondary cavities sealed with braze material as shown in figure 33. The primary and secondary manifold heights were the same as the Bill-of-Material injector to simulate the pressure distribution. Pressure taps were provided inside the manifold flow cavities to ensure accurate static pressure data. For tests requiring gas core observation, the element tip was removed and replaced with an optically clear lucite adapter as shown in figure 34. The adapter length (1.9 in.) was sufficient to enable observations of the gas core behavior. This type of flow block was used for all liquid nitrogen testing because of its positive braze seal between the primary and secondary passages, thus eliminating a static seal problem at cryogenic temperatures.

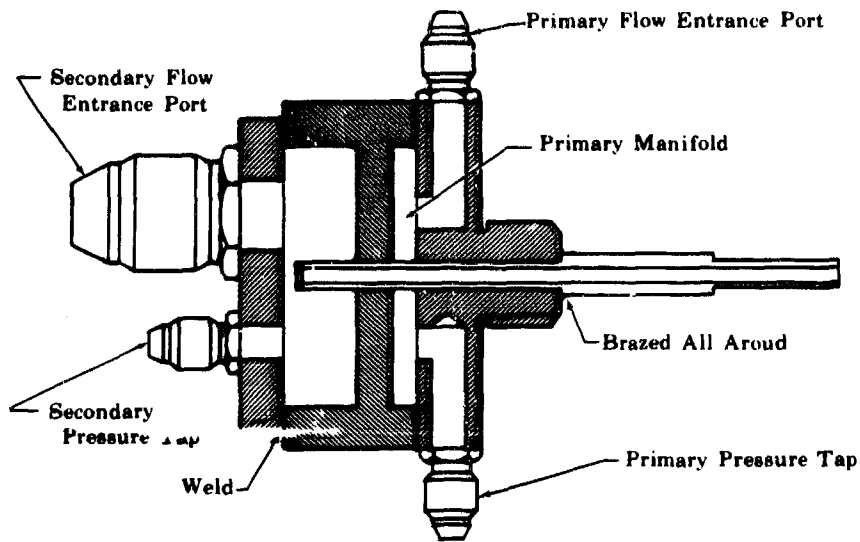


Figure 33. Integral Flow Block

FD 25207

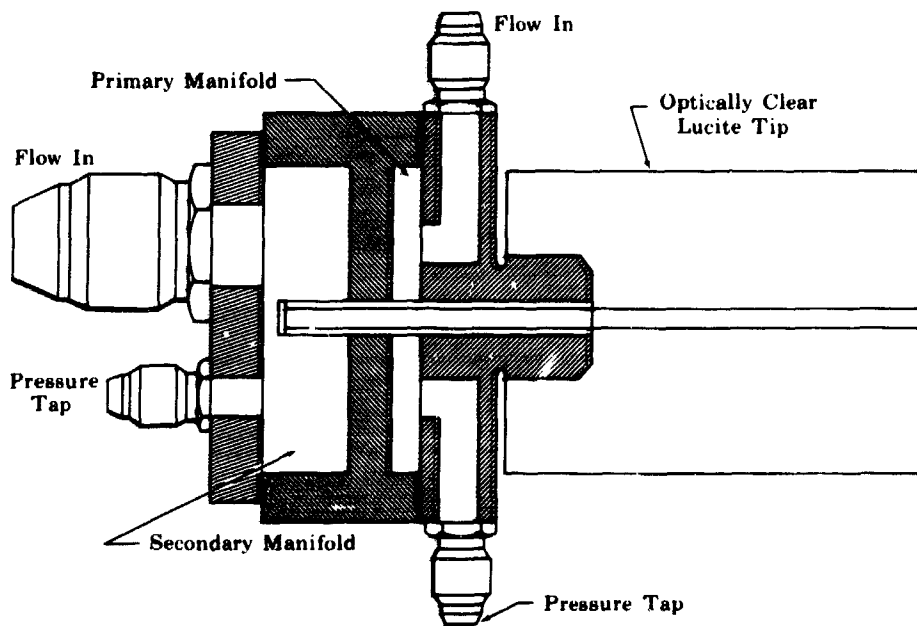


Figure 34. Integral Flow Block With Optically Clear Lucite Adapter

FD 25208

For repetitive flow testing, a quick change flow block, which is shown in figure 35, was used. The individual primary and secondary manifolds were formed by separate steel details bolted together. Rubber O-rings were used to seal the primary from the secondary cavities. Injector primary and secondary manifolds were simulated, and pressure taps intersecting the manifolds were

supplied. Injection elements to be tested were inserted into the flow block and held in place with the locking screw. Tubes tested for gas core behavior were shorter than the Bill-of-Material tubes. Optically clear lucite adapters were bolted to the flow block to provide the additional tube length and means of gas vortex core observation.

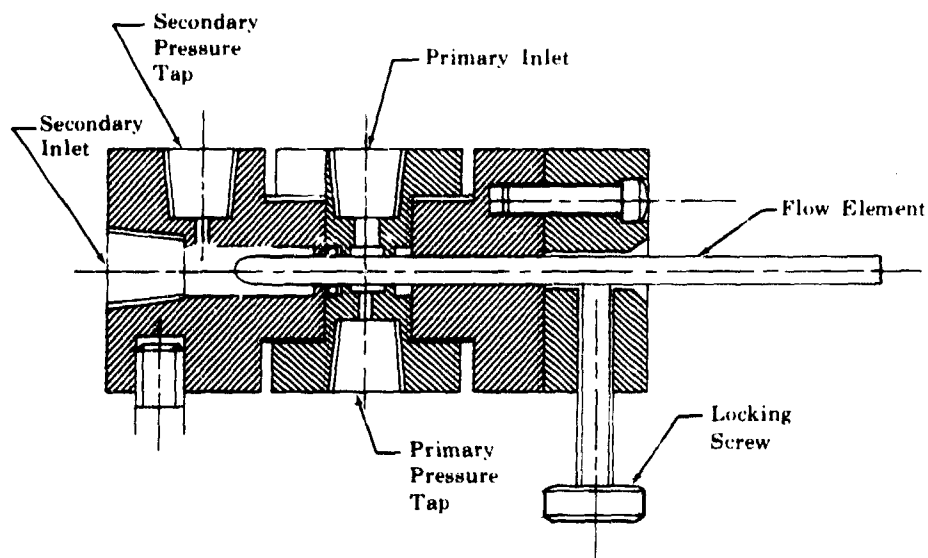


Figure 35. Quick Change Flow Block

FD 25209A

Pulse chambers were made for water and liquid nitrogen pulsing tests. The pulse chambers were constructed so that the element flow discharged into a closed volume, which allowed pressure disturbances to be created at the element discharge. The pulse chamber used in the water flow test series was fabricated from optically clear lucite and bonded with epoxy resin. This design allowed observation of the spray cone and the gas core.

The pressure disturbance, or pulse, was created inside the pulse chamber by a burst of gaseous nitrogen supplied through an electrical solenoid valve. The magnitude and time of the pulse was regulated by trial and experience adjustment of the valve cycle time and upstream nitrogen pressure. Figure 36a shows a typical water pulse test setup.

The liquid nitrogen pulse tests were conducted at a chamber back pressure of 100 psig created with gaseous helium. The back pressure requirement, plus possible thermal stresses from the liquid nitrogen bath, required that the liquid nitrogen pulse chamber be fabricated from stainless steel. Pulsing of the chamber was accomplished by a burst of gaseous helium supplied through an electrical solenoid valve. The magnitude and time of the pulse was regulated by trial and experience adjustment of the valve cycle time and upstream helium pressure. Figure 36b shows a typical liquid nitrogen pulse test setup.

The discharge coefficient data of the primary and secondary on the selected elements were obtained by varying the element pressure drops from 25 to 300 psi in 25 psi increments. The dual flow discharge coefficients were obtained by setting the primary-to-total mass flowrate ratios (\dot{w}_p/\dot{w}_t) between 0 and 100%. The single and dual flow calibrations for the 0.095 and 0.124 in. inside diameter elements are shown in figures 37 and 38, respectively.

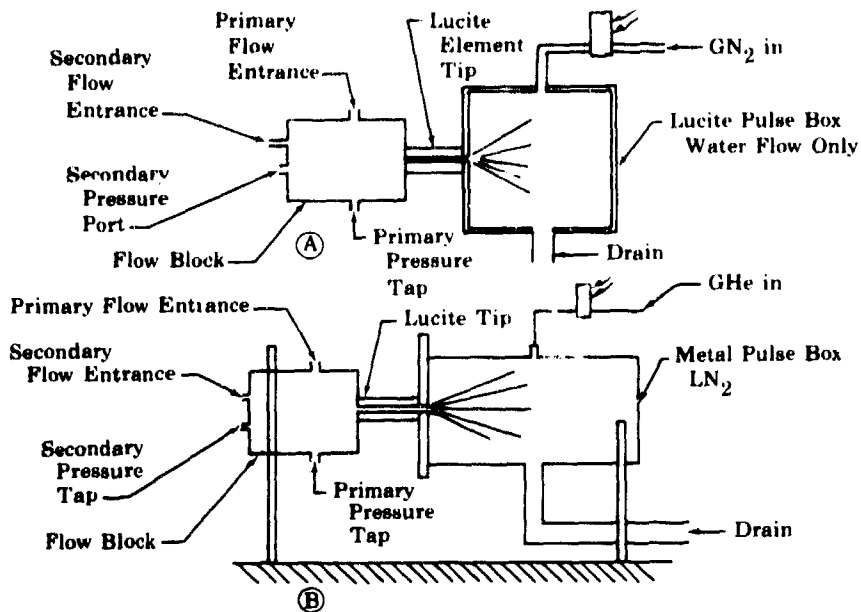


Figure 36. Pulse Chambers

FD 25210A

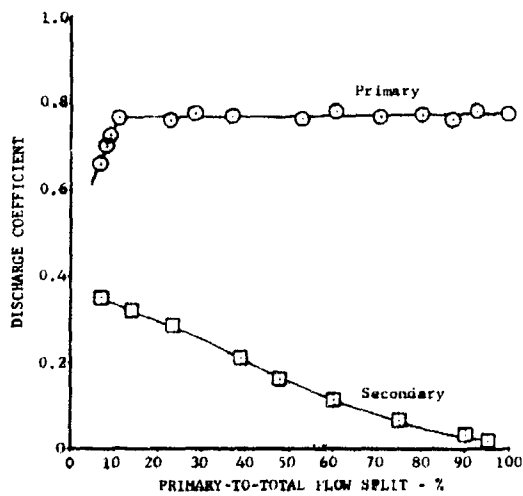


Figure 37. Flow Calibrations for 0.095-Inch Tube

DF 65431

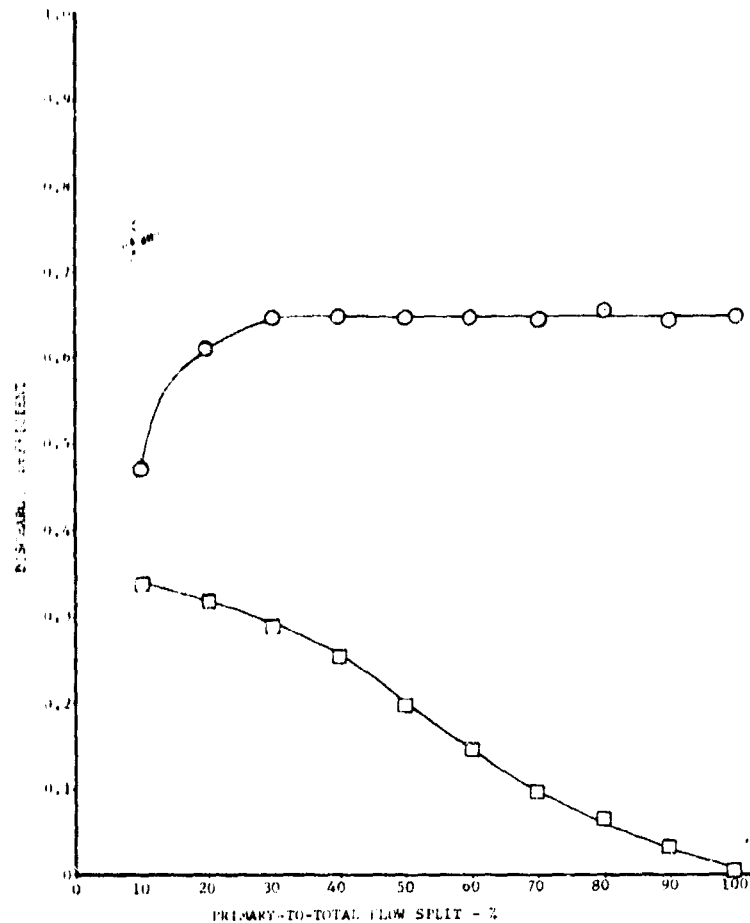


Figure 38. Flow Calibrations for 0.124-Inch Tube DF 65432

To verify that the sizing of the 0.095, 0.124, and 0.085 in. inside diameter flow passages were in accordance with figure 32, which was based on earlier dual tangential entry data, test data from these elements were plotted as shown in figure 38.

Generally, the larger the spray cone angle of oxidizer elements the smaller the drop size of the spray. Small drop size promotes more rapid vaporization and better mixing between the oxidizer and fuel, and provides more efficient and uniform combustion. It is also desirable to have the spray cones impinge slightly prior to the establishment of the flame front. It is possible to predict analytically the maximum and minimum spray cone angle and where impingement will occur for a given thrust condition. For the fixed fuel area injector at 100% thrust, 60 deg was the maximum cone angle, and 39 deg the minimum. The predicted impingement was 0.680 in. from the injector face at 100% thrust, and a mixture ratio of 7.

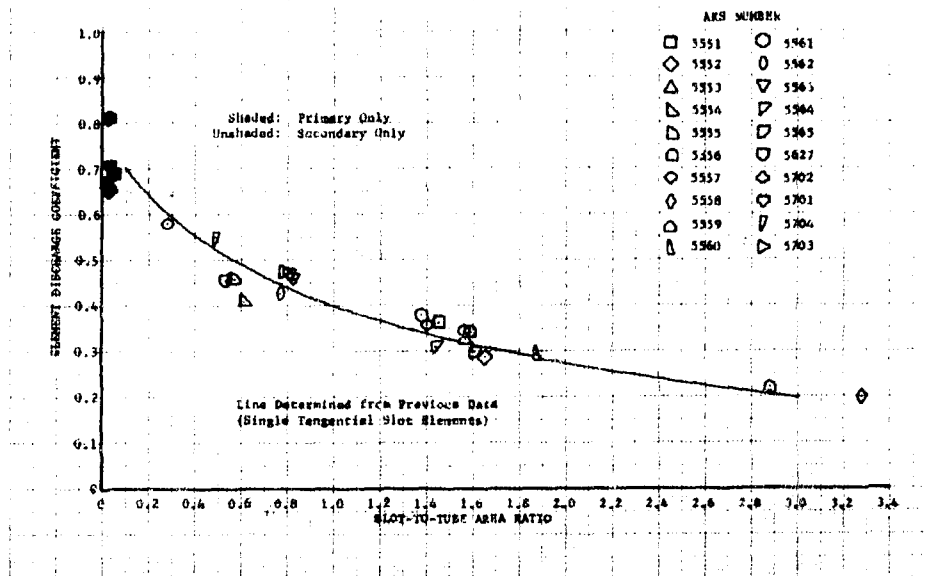


Figure 39. Element Discharge Coefficient

DF 65433

To verify that the predicted spray cone angles were valid, the 0.085, 0.095, and 0.124 in. inside diameter elements were flowed at the 20, 40, and 60% simulated thrust levels, and the angles recorded by direct observation of the spray above a graduated template. The spray cone angles of the 0.124 in. inside diameter elements are shown in figure 40. The cone angles for this element with water were within the predicted limits at 100% simulated thrust. The spray cone angles of the 0.085 and 0.095 in. inside diameter elements were of no value because of a fluctuating gas core and cone angle.

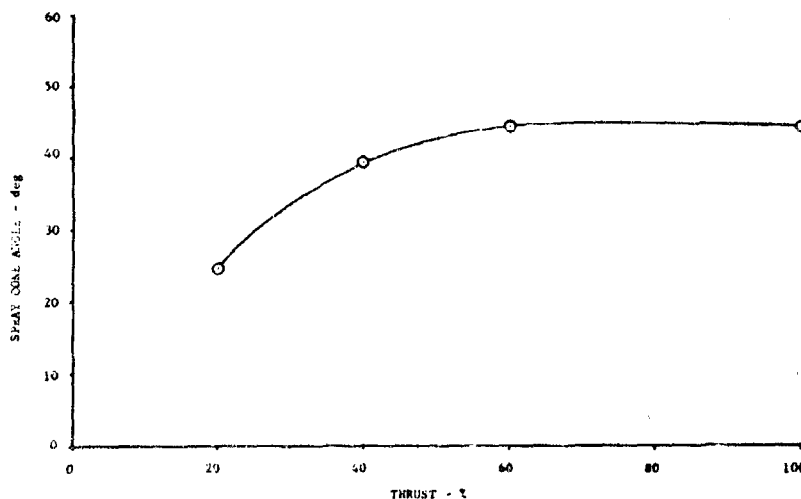


Figure 40. Cone Angle vs Thrust for 0.124-Inch Element

DF 65434

To observe the size and movement of the gas core during testing, a plexiglass tip was installed on the element. For downstream pulse testing, this tip discharged into a plexiglass box where the static pressure could be forced to rise and decay 10 psi above ambient very rapidly (250 milliseconds) by a gas pulse. High-speed movies at 300 frames per second film speed were taken to record the activity of the gas core during the pulse. The relative change of the gas core diameter gives a qualitative rating of the flow stability inside the test element.

The 0.095 in. inside diameter element was the first element to be flowed with the plexiglass tip and pulse box. With secondary flow alone and dual flows, the spray cone angle was observed to vary from the nominal of approximately 45 deg by as much as 30 deg of the included angle. The secondary manifold pressure fluctuated by as much as 5 to 10 psi during large cone angle variations. It was also observed that the size and formation of the gas core were unpredictable when the primary alone was flowing at less than 250 psid, or when the secondary alone was flowing at less than 72 psid.

When the 0.095 in. inside diameter element was pulse tested at 20% simulated thrust, a primary pressure drop of 320 psi and a flow ratio (\dot{w}_p/\dot{w}_t) of 55%, a large gas core was observed in the downstream portion of the plexiglass tip with no visible gas core in the upstream portion. The visible gas core was moving axially rapidly and erratically and appeared to be trying to form completely through the element from the discharge. When the pulse occurred, the gas core was driven upstream approximately 95% of the length of the plexiglass portion of the element. Immediately, the core moved downstream and was discharged completely before recovering.

At 40% of simulated thrust on the 0.095 in. inside diameter element and at a primary pressure drop of 460 psid and flow ratio (\dot{w}_p/\dot{w}_t) of 27%, the same behavior observed at 20% was noted, before, during, and after the pulse, except that a very small diameter gas core was observed in the upper portion of the element.

At 60% simulated thrust and at a primary pressure drop of 570 psid and flow ratio (\dot{w}_p/\dot{w}_t) of 17%, a large diameter, well defined gas core was observed completely through the plexiglass portion of the element. The pulse did not visibly affect the gas core and, therefore, there was no recovery of the core.

Preliminary testing on the 0.124 in. inside diameter element revealed steady, well defined spray cones and gas cores at steady-state conditions corresponding to 20, 40, and 60% simulated thrust on the pump-fed test facility. Pressure fluctuations of 1 to 1.5 psi maximum were noted in the secondary manifold. To determine if the fluctuations in secondary cavity pressure were inherent in the element or if the fluctuations were caused by the pump-fed facility, the test rig was moved to a pressure-fed test stand. The steady-state conditions and pulse testing were then repeated with no differences in the observed or recorded data.

At 20% simulated thrust on the 0.124 in. inside diameter element, and at an element pressure drop of 320 psid and flow ratio (\dot{w}_p/\dot{w}_t) of 55%, as mentioned, the gas core was complete and well defined at steady-state. When the pulse occurred, the gas core was deformed and then recovered.

At 40% simulated thrust and at an element pressure drop of 460 psid and flow ratio (\dot{w}_p/\dot{w}_t) of 27%, the steady-state gas core of the 0.124 in. element was well defined. The pulse had no visible effect on the gas core.

At 60% simulated thrust and at an element pressure drop of 570 psid and flow ratio (\dot{w}_p/\dot{w}_t) of 17%, again the 0.124 in. inside element exhibited a steady, well-defined gas core at steady-state. The pulse had no visible effect on this gas core.

Preliminary testing of the 0.085 in. inside diameter element exhibited poorly defined or unpredictable gas cores, with rapid axial movement at all conditions. This element also exhibited 1 to 1.5 psi fluctuations in the secondary manifold. The spray cone angle varied as much as 30 deg from the nominal of approximately 45 deg. This element was dropped from consideration and no pulse testing was conducted.

Because the water flow testing of the originally selected element design (0.095 in. ID) revealed a rapidly changing cone angle and visually unstable gas core, an effort was made to correct this element instability through modifications. This testing was qualitative in nature because a fix for the instability was sought, and not necessarily the causes of the instability. The following modifications to the original element design were tested and were unsuccessful at stabilizing the element flow:

1. Length reductions of 3, 5, 8, 11, 15, 19, 23, and 35%
2. Area reductions at the element discharge ranging from 14 to 27%
3. An area reduction of 27% at the element discharge with a reduction in length of 0.125 in.
4. An inside diameter of 0.120 in. producing an A_S/A_0 ratio of 0.965
5. An inside diameter of 0.12- in. and a 37% area reduction for the last 0.800 in. of the element
6. A 33% secondary slot area reduction by eliminating one of three secondary slots leaving two slots spaced unequally
7. A 33% secondary slot area reduction by closing one-third of each slot
8. A 33% secondary slot area reduction by having two equally spaced slots
9. The element with the 37% area reduction opened for the last 0.800 in. and one-third of each secondary slot closed
10. Top and bottom edges at the entrance to the secondary slots machined to provide a radius and a curved lead into the slots
11. All entrance edges to the secondary slots machined to provide a radius

12. Reduce wall thickness in the region of the primary and secondary slots by 9, 29, 54, and 68%
13. Inside diameter roughened 0.002 in. deep
14. A tube inserted to eliminate the gas core
15. Interchanged location of the primary holes and secondary slots
16. Replaced secondary slots with thirty-two 0.020 in. diameter holes.

To further investigate the effect of the secondary flow area to the element area ratio (A_S/A_O), the secondary slots were modified on two different 0.095 in. inside diameter elements to yield A_S/A_O ratios of 0.300 and 0.542 as opposed to the A_S/A_O ratio of 1.5 on the original 0.95 in. diameter element design. Flow from these elements were stable when tested indicating that lowering the A_S/A_O ratio yields a stable element.

To judge the stability effects of primary slot geometry, a 0.124 in. ID tube was made and tested with one primary hole of equivalent area to the two-hole original design. The element flow was stable and the cone angle was constant but the cone angle axis revolved in a circular pattern. This configuration was considered unsatisfactory because of the spray cone axis shift observed during tests.

Another modification considered was a typical 0.124 in. ID tube, except for a 0.095 in. inside diameter the last 0.300 in. of tube length. This configuration proved to be essentially stable during initial tests. Pulse testing, however, showed that the gas core was momentarily eliminated at the 20% and 40% simulated thrust flow points. The core was not affected at the 60% thrust flow point. The configuration was considered unsatisfactory because of gas core behavior during pulsing.

Because all the modifications attempted were unsuccessful at stabilizing the element flow, and only one alternative design (0.124 in. ID) indicated stable flow on water, a more comprehensive program was initiated to determine both the cause of element instability, and possible corrective action to the fundamental design.

The first section of this program approached the cause of element instability in terms of element geometry. Past performance and analytical data had shown the influential parameters to be: slot width, slot length, element inside diameter, slot area to element area ratio (A_S/A_O), and length of element to element inside diameter ratio (L/D). Sixteen elements were fabricated to form a matrix covering these parameters at inside diameters ranging from 0.075 in. to 0.124 in. The test matrix is provided in table VII and the dimensional characteristics of the elements investigated are provided in table VIII.

Each element of the matrix was water flowed on the B-21 pressure fed test facility. Two individual tests were conducted on each element. The first test consisted of visual observations of the spray cone angle, spray cone and gas core stability, pressure fluctuations in the primary and secondary manifolds,

and flowrate fluctuations while flowing the element in the as-designed length configuration. This test was then repeated with the length of each element reduced by approximately 35%. Because of geometry of the test rig, examination of the gas core could not be performed during investigation of elements in the reduced length configuration.

Table VII. Test Matrix

Slot Area		Element Length										Element Letter	
		Nominal ID (in.)	Short Length Configuration					Long Length Configuration					
			0.075	0.085	0.095	0.110	0.124	0.075	0.085	0.095	0.110		0.124
Constant Area Ratio $A_3/A_0 = 1.5$ Nominal	0.245 Constant W/D, Slot Width to Tube Diameter	P	H	B	L	D	P	H	B	L	D	Element Letter	
	0.010 Inch Min Nominal Slot Width	O	G	A	K	C	J	G	A	K	C	Element Letter	
Constant Equivalent Cycle A_{cd}	0.245 Constant W/D, Slot Width to Tube Diameter	X	J	B	N	F	X	J	B	N	F	Element Letter	
	0.010 Inch Min Nominal Slot Width	X	I	A	M	E	X	I	A	N	I	Element Letter	

Typical test conditions during the first test on the matrix elements included flowing at primary ΔP 's corresponding to the 20%, 40%, and 60% thrust levels with secondary ΔP 's varying between zero and 250 psid. Visual observations were recorded at steady-state points within this range.

The second test on each of the matrix elements consisted of water flow calibration, oscillograph recording of primary and secondary manifold pressures, and high-speed movies of the spray cone and gas core while flowing the element in the Bill-of-Material length configuration. Flow calibration was performed at flow splits (primary flow rate to total flow rate, \dot{w}_p/\dot{w}_t) of 8.75% to 80% and high-speed movies were taken at the 20%, 40%, and 60% thrust levels while at the corresponding flow splits. Movies were also taken at steady-state points ranging above and below the fore-mentioned thrust levels.

Table VIII. Dimensional Characteristics of Elements Tested

Element No.	Number of Secondary Slots ^a	Length of Slot (in.)	Width of Slot (in.)	ID of Element (in.)	Area of Slot A_s (in ²)	Area of Tube A_0 (in ²)	Area Ratio A_s/A_0	L/D Short Configuration	L/D Long Configuration
A	3	0.361	0.0102	0.0950	0.01110	0.00710	1.563	20.31	33.80
B	3	0.150	0.023	0.0950	0.01035	0.00710	1.458	18.10	31.60
C	4	0.455	0.0110	0.1240	0.0200	0.01206	1.658	18.45	30.00
D	3	0.1997	0.0315	0.1235	0.01887	0.01198	1.575	14.31	24.70
E	2	0.328	0.0106	0.1205	0.00696	0.01138	0.612	15.75	26.35
F	2	0.108	0.032	0.1240	0.00690	0.01206	0.572	13.51	23.80
G	3	0.2734	0.0411	0.0855	0.00909	0.00571	1.592	21.58	36.60
H	3	0.085	0.0320	0.0860	0.00816	0.00580	1.407	19.25	34.10
I	4	0.4248	0.0111	0.0858	0.01884	0.00575	3.276	23.30	38.20
J	3	0.1780	0.0320	0.0870	0.01797	0.00592	2.883	20.01	34.80
K	3	0.4592	0.0129	0.1096	0.01776	0.00947	1.875	18.45	30.01
L	3	0.1676	0.0270	0.1120	0.01356	0.00983	1.379	15.50	26.90
M	3	0.2533	0.0096	0.1091	0.00729	0.00940	0.776	16.71	28.50
N	3	0.0948	0.0027	0.1095	0.00078	0.00945	0.082	15.20	26.90
O	3	0.2140	0.0102	0.0763	0.00654	0.00453	1.444	23.40	40.20
P	3	0.1420	0.0190	0.0800	0.00807	0.00500	1.614	21.40	37.40

^aAll elements incorporated two primary slots (0.015-inch diameter nominal) upstream of the secondary.

Table IX tabulates the results obtained from the test matrix section of the stability program. Figure 41 illustrates the test results tabulated in table IX. The following conclusions were made on the basis of these results:

1. Slot width is not significant to stability when the slot area to tube area ratio (A_s/A_0) is 1.5
2. Slot width is significant in creating stability in a 0.110 in. diameter tube with an A_s/A_0 ratio of 0.80
3. Slot widths between 0.010 and 0.030 in. are stable with a 0.124 in. diameter tube at an A_s/A_0 ratio of 0.542
4. Tube diameter variation between 0.075 and 0.124 in. is not significant to stability at an A_s/A_0 ratio of 1.5
5. All tubes of 0.095 in. diameter and smaller are unstable when their A_s/A_0 ratio is greater than 0.80
6. Reduced tube length decreases the magnitude of instability.

The stability investigations showed that certain elements were more stable than others. To confirm these results, it was decided to flow selected elements with liquid nitrogen. The vapor pressure, surface tension, and temperature of liquid nitrogen are similar to the corresponding properties of liquid oxygen.

The liquid nitrogen flow splits and differential pressures set for the various test points were the same as the corresponding water flow tests. The element discharged into a chamber pressurized to 100 psig.

Table IX. Test Matrix Results

SHORE LENGTH CONFIGURATION

LUBE LENGTH

0.0075 0.0093 0.0110 0.0127 0.0175 0.0193 0.0275 0.0393 0.0997 0.1117 0.1227

Normal ID (in.)	0.075	0.083	0.093	0.110	0.127	0.075	0.083	0.0997	0.1117	0.1227	
Nominal ID (in.)	Element Letter	Unstable	Unstable	Unstable	Unstable	Unstable	Unstable	Unstable	Unstable	Unstable	
	Spray Cone	Unstable	Unstable	Unstable	Unstable	Unstable	Unstable	Unstable	Unstable	Unstable	
	Gas Core	Unstable	Unstable	Unstable	Unstable	Unstable	Unstable	Unstable	Unstable	Unstable	
	Secondary Gas Fluctuation	3 psi max	3 psi max	2 psi max	3 psi max	2 psi max	3 psi max	2 psi max	3 psi max	2.5 psi max	
	Oscilloscope	6 psi max	8 psi max	Not Recorded	1.0 psi max at 50 cps	Not Recorded	6 psi max	8 psi max	Not Recorded	1.7 psi max	1.7 psi max
	Secondary Frequency & Amplitude	600 cps max	Frequency not Recorded	30 to 30 deg Fine Drop Size	55 to 65 deg Fine at All Times	12 to 25 deg Fine Drop Size	20 to 40 deg Heavy to Medium	15 to 40 deg Very Heavy to Fine	20 to 50 deg Heavy to Fine	15 to 35 deg Medium to Fine	2.5 to 30 deg Heavy to Fine
	Spray Cone Angle & Drop Size	45 to 60 deg Fine to Medium	35 to 45 deg Medium to Fine	A	K	C	G	G	A		
	Element Letter	0	G	A	K	C	G	G	A		
	Spray Cone	Unstable	Unstable	Unstable	Unstable	Unstable	Unstable	Unstable	Unstable	Unstable	Unstable
	Gas Core	Unstable	Unstable	Unstable	Unstable	Unstable	Unstable	Unstable	Unstable	Unstable	Unstable
Constant Area Ratio $A_2/A_1 = 1.5$ Nominal	Secondary Gas Fluctuation	3 psi max	3 psi max	3 psi max	1.0 psi max	0.5 psi max	6 psi max	2 psi max	3 psi max	2 psi max	
	Oscilloscope	2 psi max	3.6 psi max	Not Recorded	5 psi max	2 psi max	2 psi max	2 psi max	3 psi max	3 psi max	
	Secondary Frequency & Amplitude	Frequency not Recorded	Frequency not Recorded	15 to 30 deg Medium to Fine	25 to 45 deg Heavy to Fine	40 to 65 deg Medium to Fine	20 to 30 deg Heavy to Fine	30 to 50 deg Heavy to Fine	15 to 45 deg Very Heavy to Medium	15 to 45 deg Heavy to Fine	
	Spray Cone Angle & Drop Size	25 to 45 deg Heavy to Fine	45 to 55 deg Heavy to Fine	B	N	F			B		
	Element Letter		2	B	N	F			B		
	Spray Cone	Unstable	Unstable	Unstable	Unstable	Stable	Unstable	Unstable	Unstable	Unstable	
	Gas Core	Unstable	Unstable	Unstable	Unstable	Stable	Unstable	Unstable	Unstable	Unstable	
	Secondary Gas Fluctuation	8 psi max	8 psi max	Same as Element "B" Above	6 psi max	5 psi max	6 psi max	8 psi max	Same as Element "B" Above	5 psi max	
	Oscilloscope	9.6 psi max at 100 cps	9.6 psi max at 100 cps	1 psi max	1 psi max	6 psi max	6 psi max	9 psi max at 200 cps	1 psi max	1 psi max	
	Secondary Frequency & Amplitude	30 to 65 deg Medium to Fine	30 to 65 deg Medium to Fine	30 to 45 deg Heavy to Fine	30 to 45 deg Heavy to Fine	55 to 70 deg Heavy to Fine	20 to 30 deg Heavy to Fine	25 to 45 deg Heavy to Medium	15 to 50 deg Heavy to Fine	15 to 45 deg Heavy to Fine	
Spray Cone Angle & Drop Size	30 to 65 deg Medium to Fine	30 to 65 deg Medium to Fine	N	N	E			A			
Element Letter	1	1	A	N	E			A			
Spray Cone	Unstable	Unstable	Unstable	Stable	Stable	Unstable	Unstable	Stable	Stable		
Gas Core	Unstable	Unstable	Unstable	Stable	Stable	Unstable	Unstable	Stable	Stable		
Secondary Gas Fluctuation	1 psi max	1 psi max	Same as Element "A" Above	1.5 psi max	2 psi max	2 psi max	2 psi max	Same as Element "A" Above	1 psi max		
Oscilloscope	4.2 psi max at 200 cps	4.2 psi max at 200 cps	3 psi max at 100 cps	3 psi max at 100 cps	1 psi max	1 psi max	3 psi max at 200 cps	0.2 psi max at 100 cps	0.2 psi max		
Secondary Frequency & Amplitude	60 to 65 deg Medium to Fine	60 to 65 deg Medium to Fine	55 to 65 deg Fine Drops at All Times	55 to 65 deg Fine Drops at All Times	35 to 65 deg Medium to Fine	35 to 65 deg Medium to Fine	40 to 60 deg Heavy to Fine	40 to 55 deg Medium to Fine	25 to 50 deg Medium to Fine		
Spray Cone Angle & Drop Size	60 to 65 deg Medium to Fine	60 to 65 deg Medium to Fine	55 to 65 deg Fine Drops at All Times	55 to 65 deg Fine Drops at All Times	35 to 65 deg Medium to Fine	35 to 65 deg Medium to Fine	40 to 60 deg Heavy to Fine	40 to 55 deg Medium to Fine	25 to 50 deg Medium to Fine		
Element Letter	1	1	A	N	E			A			

STRET AREA

Constant Equivalent Cycle $A_2/A_1 = 1.5$

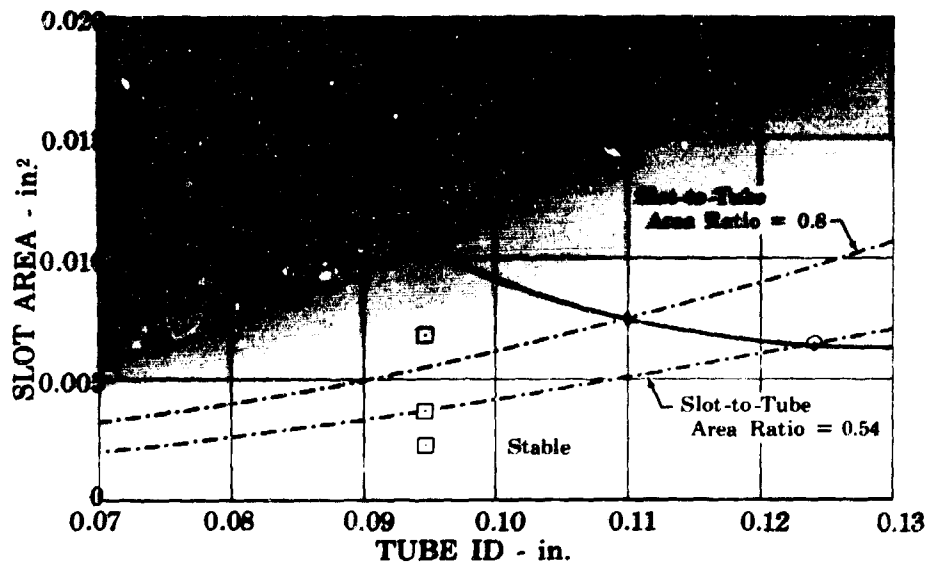


Figure 41. Element Test Matrix Test Results

FD 23225B

After the desired liquid nitrogen flows were set, movie and oscillograph data were taken. During the data point, a 10 to 15 psig pulse of helium was flowed into the chamber.

The first configuration that was flowed with liquid nitrogen was the original design 0.095 in. diameter element. These were conducted at the engine cycle primary injection pressure (primary upstream pressure to element back pressure) and secondary mass flowrate set to give the cycle primary to total mass flowrate ratio corresponding to 20%, 40%, and 60% thrust levels at an engine mixture ratio of seven. Chamber pulses of approximately 10 psi above steady-state back pressure were used.

The movies revealed the following facts:

1. Gas cores exist on liquid nitrogen flows
2. Cores were unstable at 20% and 40% thrust level at steady-state conditions
3. Cores were eliminated by the pulse at the 20% and 40% thrust level
4. The core was stable at 60% thrust level
5. The core was distorted but not eliminated at 60% thrust level by the pulse.

The oscillograph data showed fluctuations in secondary cavity pressure of 0.5 psi at 20%, 1.0 psi at 40%, and 1.5 psi at 60% thrust level points.

The second configuration tested was the alternative design; 0.124 in. inside diameter element. Tests were conducted at flowrates corresponding to 20%, 40%, and 60% thrust levels. Each thrust level was pulsed. Two other tests conducted were a 60% thrust volumetric flow and a 60% secondary sweep. The 60% thrust volumetric point consists of setting primary and secondary flows corresponding to the liquid oxygen volumetric flowrate according to the engine cycle. The 60% thrust secondary sweep consists of setting 60% thrust cycle primary injection pressure (secondary upstream pressure to element back pressure) from zero to 400 psi.

The movies revealed the following facts:

1. Gas cores were large, varying from 55% of the diameter at 20% thrust points to 60% at 60% thrust volumetric point
2. Pulsing at 20% caused an enlargement of the core by 5% of the diameter
3. Pulsing at 40% and 60% thrust points had no effect on the cores
4. Cores at all points were stable.

The oscillograph data showed fluctuations in secondary cavity pressure of 0 psi at 20%, 0.1 psi at 40%, and 0.1 psi at 60% thrust level points.

The third configuration tested was a modification to the 0.124 in. inside diameter tube. The modifications were as follows: (1) an area reduction was incorporated in the tube 0.250 in. from the exit to an inside diameter of 0.095 in., (2) the slot areas were increased in size by 24% to accommodate the 0.095 in. diameter at the tip while keeping the overall element pressure drop as required by the engine cycle.

Tests were conducted at flows corresponding to 20%, 40%, and 60% thrust levels plus secondary sweeps at 40% and 60% levels.

The movies revealed the following facts:

1. Gas cores could exist upstream of the tube tip restriction
2. The gas core at 20% was relatively small (22% of tube diameter) and slightly unstable. Pulsing momentarily eliminated the gas core.
3. The gas core at 40% was still small (28% of the tube diameter) and relatively stable. Pulsing again momentarily eliminated the gas core.
4. The gas core at 60% was small but stable. Pulsing had no visible effect on the gas core.

4. Preburner Rig Testing

a. Hardware Description

An existing preburner test rig fabricated during Phase I (Contract AF04(611)-11401) was modified for use in testing the fixed fuel area preburner injector. Figure 42 shows the major details of the test rig including the oxidizer dome, preburner oxidizer valve, combustion chamber, back pressure simulator, injector assembly, and temperature rakes.

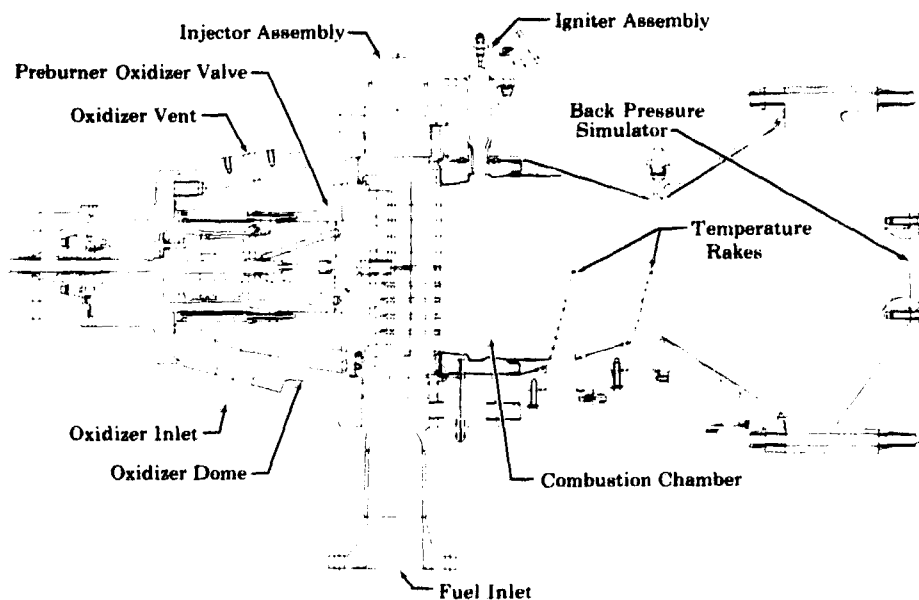


Figure 42. Preburner Rig Configuration

FD 23248B

The oxidizer dome was modified to eliminate flange leakage and thus permit higher rig operating pressures than were possible during Phase I (Contract AF04(611)-11401) tests. Figure 43 shows the oxidizer dome used in these previous tests and the modified dome used in the current tests. The modifications included a thicker flange, larger seal vent area, a relief cut on the flange mating surface to move the bolt reaction more directly in line with the pressure source, and tensitized stretch studs for higher loads.

The preburner oxidizer valve, which controls the primary-to-secondary flow split, was basically unchanged from the configuration used during Phase I (Contract AF04(611)-11401) testing, except that the upper and lower piston rings were replaced with balanced piston rings.

The combustion chamber liner was modified by reducing the distance from the outermost injection element to the chamber wall to 0.5 in.

The back pressure simulator was modified to accept inserts of various inside diameters, thus allowing a wide range of simulated chamber pressures.

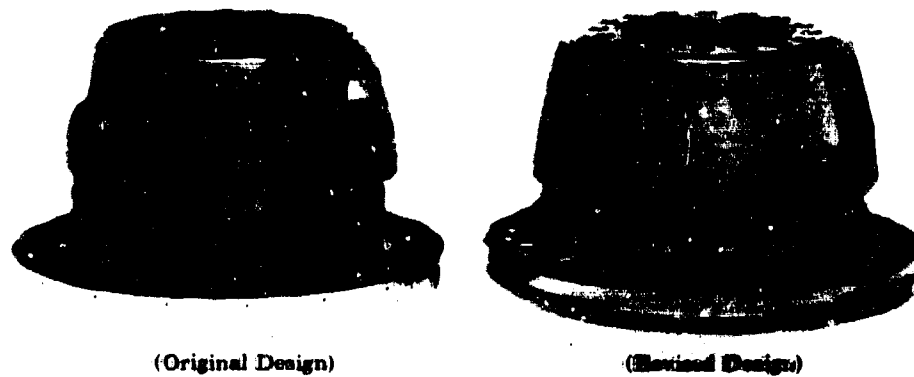


Figure 43. Original and Revised Oxidizer Domes FD 23472

The injector assembly was an existing variable fuel area housing that was bored and threaded to accept the fixed fuel area injector block assembly. The injector block assembly, which is shown in figure 44, was a brazement composed of the oxidizer elements, divider plate, oxidizer block, and the Rigimesh faceplate.

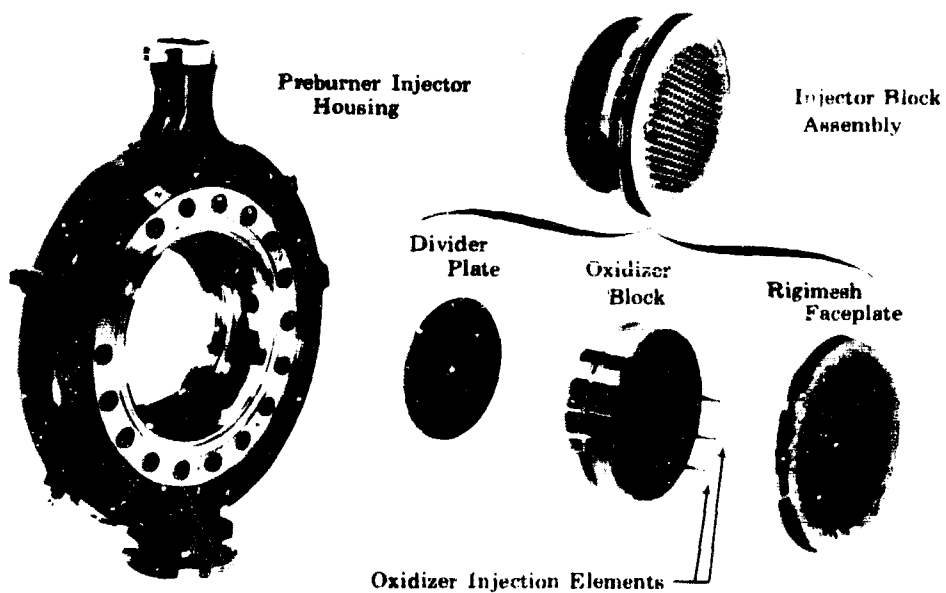


Figure 44. Preburner Injector Block Assembly FD 23221C

Temperature rakes were installed in two circumferential locations at axial distances of 7 and 11 in. from the injector face.

Figure 45 is a cross section of the fixed fuel area preburner injector and the following paragraph is keyed to this figure.

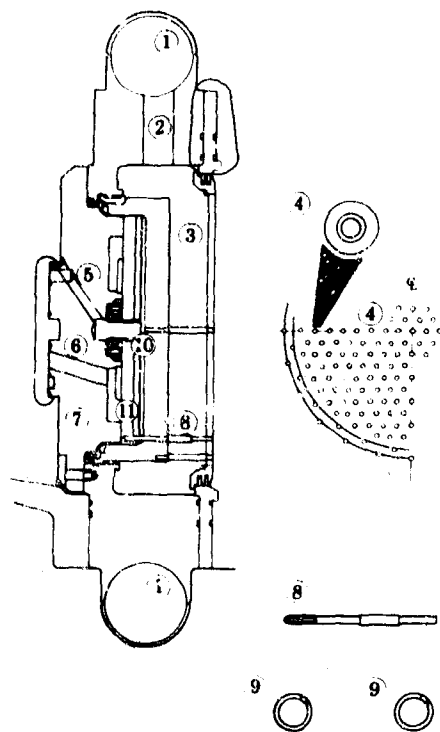


Figure 45. Cross Section of Fixed Fuel Area Preburner Injector

FD 24990

Fuel is supplied to the circular fuel manifold (1) by the fuel system. The fuel then flows through the feed holes (2) into the manifold (3) behind the face-plate rigimesh and is metered into the combustion chamber through annuli (4) around each oxidizer element (252 places). Liquid oxygen is supplied to the injector from the preburner oxidizer valve, which controls and meters the total oxidizer flow to primary (5) and secondary (6) flow passages in the injector oxidizer plate (7). The two oxidizer flows, primary and secondary, are used to maintain safe injection differential pressures at all engine cycle points. The series of flow passages (5 and 6) delivers oxidizer to the primary (10) and secondary (11) supply manifolds. Oxidizer flow is transferred to the combustion chamber through individual oxidizer elements (8). Each element has flow orifices machined tangentially to the tube ID (9): rectangular slots for the secondary flow and circular holes for the primary flow. Element length is determined by the manifold heights of the fuel (3), primary oxidizer (10), and secondary oxidizer (11), and heights of each are kept to a minimum, consistent with low distribution losses.

The concentric fuel annuli of this design act as fixed orifices as opposed to the variable fuel metering area design. Two injector assemblies were fabricated

for this test program, each having a different fuel annulus area. The initial testing (tests No. 1.01 and 2.01) was made with a fuel annulus designed for 200 psi pressure drop at the design point of 100% thrust mixture ratio of 7. The remaining tests were made with a fuel annulus designed for 400 psi pressure drop at design point.

b. Test Facilities and Procedures

The fixed fuel area preburner injector rig was tested in the E-8 test facility. A plan view of this facility is shown in figure 46. The E-8 test facility permits preburner testing to chamber pressures of 5000 psia. The preburner control configuration is shown in figure 47.

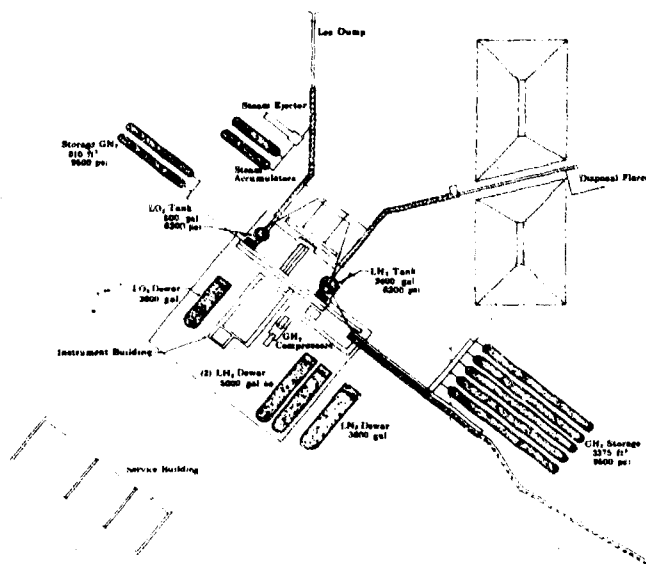


Figure 46. Plan View of E-8 Test Facility

FD 21139A

The preburner starting sequence was initiated by diverting the required fuel and oxidizer flows from a preset overboard condition to the injector. The diverted fuel and oxidizer were then allowed to stabilize. The combustion chamber pressure at this point was less than 1% for tank head ignition tests and 7% for other tests.

After the fuel and oxidizer valves were in position and were stabilized at the 7% level, they were switched to flow control. The run tanks were then pressurized to the operating levels, and the preburner flows were ramped to the desired equivalent thrust level and combustion temperature.

The fuel mixture temperature control section modulated the valves that regulated the GH_2 flow into the mixing section and provided the desired injector fuel temperature. The total fuel flow was determined by measuring both the gaseous and liquid flowrates; however, only liquid flow was controlled by the system.

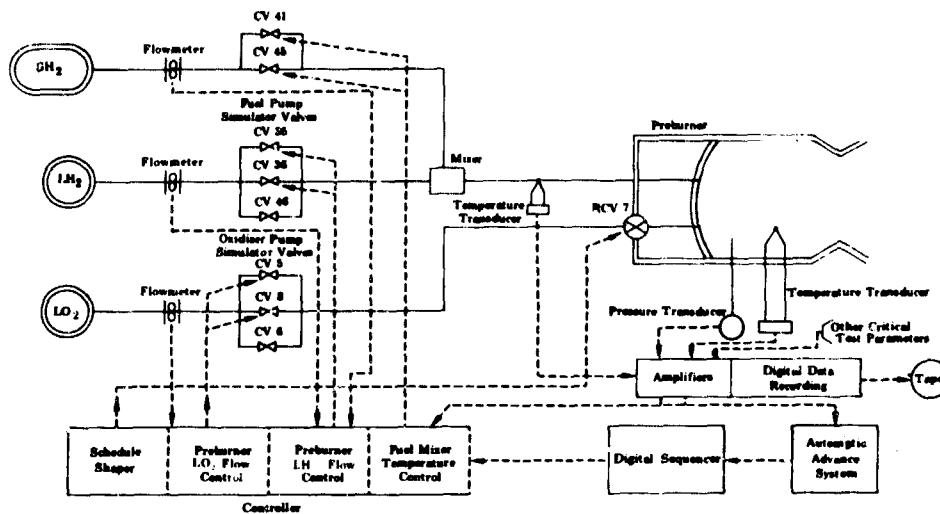


Figure 47. Preburner Rig Control System

FD 21136C

The oxidizer flow was also closed loop controlled through the computer with the necessary timing to maintain the required mixture ratio during the transient.

Starting flows, automatic changes of flow levels, and test conditions other than those scheduled by power lever, were programmed in and out of the control by the digital sequencer.

c. Test Results

The test objectives were to evaluate: (1) temperature profile, (2) tank head ignition and start transient, and (3) combustion stability pulsing with 80 grain charges. Both the 200 psid and 400 psid injector assemblies were tested. A low frequency chugging instability was present at thrust levels below 25% for all engine mixture ratio conditions.

Pulse guns, as shown in figure 48, were used to introduce the pressure upsets in the preburner test rig. In the combustion chamber, pressure upsets were caused by the dissipation of the high pressure gases from the gun barrel. The intensity of these gases may be regulated by charge size and burst disk rupture level.

Each test is described in the following paragraphs. The measured parameters are summarized in table X and the calculated results are summarized in table XI.

Figure 49 shows the injector face prior to test 1.01, which was conducted on 31 May 1968. Data at five of the six planned engine cycle data points were obtained. The test was advanced before the last data point condition was reached because of excessive combustion temperature resulting from a facility oxidizer valve oscillation. Data were taken at 20% and an equivalent engine cycle condition for mixture ratios of 5, 6, and 7 and at 60% for mixture ratios of 5 and 6. The chamber was pulsed with 80 grain charges at 20% for mixture ratios of 5 and 7 and at 60% for a mixture ratio of 5.

Analysis of the data from test 1.01 showed that although combustion stability was essentially insensitive to the pulse gun discharges, a low frequency (approximately 100 cps) system instability occurred on the ramp from 7% to 20% flow levels and persisted through all three mixture ratios at 20% thrust levels. The instability in chamber pressure was limited to 150 psi peak-to-peak. On ramping from 20% to 60% the instability stopped and did not recur at higher thrust levels. The maximum peak-to-average combustion temperature profile at the 20% level was 124° R at a mixture ratio of 7 as shown in figure 50. At the 60% level and a mixture ratio of 6, one of the oxidizer pump simulator valves (CV8) was required to operate on a portion of its stroke where large effective area changes are made by small valve stroke changes. The oxidizer flow control system became unstable causing combustion overtemperature. The test sequence was automatically advanced by the overtemperature prior to attaining the 60% thrust level and mixture ratio of 7 steady-state data point. The peak-to-average combustion profile at 60% level was 119° R at an average temperature of 1848° R and a mixture ratio of 6 as shown in figure 51.

Pulse guns with 80-grain charges were fired at the 20% and 60% thrust levels on test 1.01. The pulses at the 20% and mixture ratio of 5 and 7 levels caused a chamber pressure rise of 292 and 302 psi and combustion recovered to normal levels in 10 and 6 milliseconds, respectively. The pulse at the 60% and mixture ratio of 5 level caused a chamber pressure rise of 364 psi that dissipated within 10 msec. The firing of the pulse guns damaged the combustion liner in four places; however, the damaged combustion liner was suitable for use on test 2.01.

Test 2.01 was conducted on 4 June 1968. The run was programmed for data points at a mixture ratio of 5 at 20% thrust and mixture ratios of 6 and 7 at 100% thrust. The run was automatically advanced during the flow ramps from the mixture ratio of 6 data point by an overtemperature.

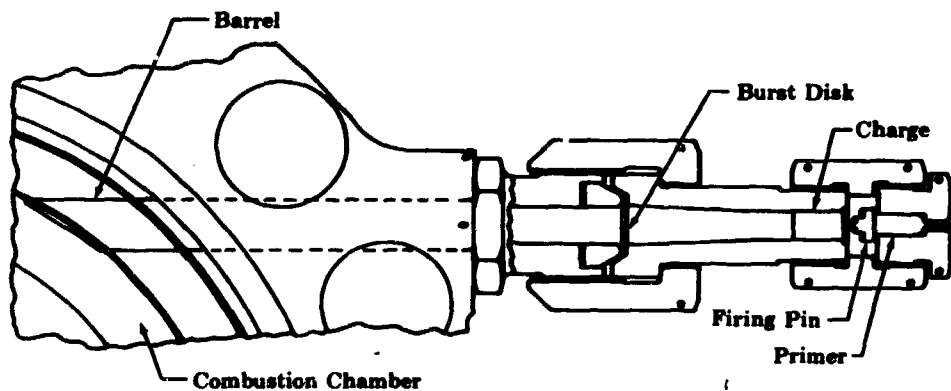


Figure 48. Preburner Rig Pulse Gun

FD 25307

A

Table X. Summary of Measured Parameters Dur

Test No.	Thrust (%) (1)	Date	Rig No. Build No.	Test Duration (sec)	Ambient Pressure (psia)	Oxidizer Inlet Temperature (°R)	Fuel Inlet Temperature (°R)	Liner Coolant Inlet Temperature (°R)	Oxidizer Inlet Pressure (psia)
1.01	20	31 May 1968	35117-1	35.9	14.71	191.9	129.5	129	9
1.01	20	31 May 1968	35117-1		14.71	192.1	144.4	144	9
1.01	20	31 May 1968	35117-1		14.71	192.7	150.2	150	9
1.01	60	31 May 1968	35117-1		14.71	189.3	154.7	155	34
1.01	60	31 May 1968	35117-1		14.71	189.1	164.2	164	31
2.01	20	4 Jun 1968	35117-1	29.4	14.49	196.0	303.2	303	9
2.01	100	4 Jun 1968	35117-1		14.49	181.6	188.5	188	51
3.01	20	14 Jun 1968	35117-2	62.1	14.73	195.8	134.6	135	10
3.01	20	14 Jun 1968	35117-2		14.73	196.8	133.1	133	9
3.01	20	14 Jun 1968	35117-2		14.73	198.5	131.3	131	7
3.01	60	14 Jun 1968	35117-2		14.73	191.2	148.9	149	27
3.01	100	14 Jun 1968	35117-2		14.73	186.4	184.8	185	432
4.02	97	19 Jun 1968	35117-2	23.1	14.69	185.3	149.9	150	506
12.01	20	27 Jun 1968	35117-2	31.1	14.71	170.5	446.7	447	89
14.02	20	28 Jun 1968	35117-2	45.2	14.74	173.4	95.4	95	83

(1) Data point at percent equivalent engine thrust

Parameters During Preburner Injector Testing

Liner Inlet Temperature (°R)	Oxidizer Injector Primary Inlet Pressure (psia)	Oxidizer Injector Secondary Inlet Pressure (psia)	Fuel Injector Inlet Pressure (psia)	Liner Coolant Inlet Pressure (psia)	Chamber Static Pressure (psia)	Fuel Injector ΔP (psid)	Oxidizer Injector Primary ΔP (psid)	Oxidizer Injector Secondary ΔP (psid)
129	986	713	745	745	691	32.2	278	7.6
144	971	699	729	729	685	34.4	285	10.8
150	934	667	694	694	652	30.0	284	10.2
155	3401	2806	2868	2868	2653	106	692	87.4
164	3125	2660	2682	2682	2534	85.4	585	90.4
303	901	670	753	753	644	73.4	246	7.2
188	5171	4801	4618	4618	4285	168.7	929	403
135	1053	619	663	663	608	80.3	447	8.4
133	904	614	665	665	611	80.0	307	6.6
131	700	596	666	666	611	76.1	111	3.9
149	2783	2349	2485	2485	2210	217.8	549	76.1
185	4322	4270	4397	4397	3911	388	424	283
150	5062	4854	5092	5092	4406	526	587	317
447	891	650	892	892	639	237	242	4.0
95	830	598	626	626	589	35.1	220	6.8

A

Table XI. Summary of Calculated Parameters

Test No.	Date	Rig No. Build No.	Total Combined Flowrate (lb _m /sec)	Total Fuel Flowrate (lb _m /sec)	Total Oxidizer Flowrate (lb _m /sec)	Upper Liner Fuel Coolant Flowrate (lb _m /sec)	Lower Liner Fuel Coolant Flowrate (lb _m /sec)	Total Liner Flowrate (lb _m /sec)	Overall Mixture Ratio
1.01	31 May 1968	35117-1	23.72	14.46	9.26	0.21	0.21	0.42	0.64
1.01	31 May 1968	35117-1	21.65	12.35	9.30	0.17	0.18	0.35	0.75
1.01	31 May 1968	35117-1	19.84	10.57	9.27	0.15	0.16	0.32	0.88
1.01	31 May 1968	35117-1	85.04	46.63	38.41	0.73	0.54	1.27	0.82
1.01	31 May 1968	35117-1	77.95	39.63	38.32	0.55	0.48	1.02	0.97
2.01	4 Jun 1968	35117-1	23.04	14.43	8.61	0.21	0.19	0.40	0.60
2.01	4 Jun 1968	35117-1	142.81	65.32	77.49	0.99	0.69	1.68	1.19
3.01	14 Jun 1968	35117-2	23.58	14.40	9.18	0.19	0.28	0.47	0.64
3.01	14 Jun 1968	35117-2	23.74	14.56	9.18	0.19	0.28	0.47	0.63
3.01	14 Jun 1968	35117-2	23.88	14.62	9.26	0.20	0.29	0.48	0.63
3.01	14 Jun 1968	35117-2	77.77	39.85	37.92	0.80	0.71	1.51	0.95
3.01	14 Jun 1968	35117-2	128.57	57.52	71.05	1.22	0.94	2.16	1.24
4.02	19 Jun 1968	35117-2	152.08	75.98	76.10	1.66	1.13	2.79	1.00
12.01	27 Jun 1968	35117-2	24.76	15.51	9.25	0.29	0.26	0.55	0.60
14.02	28 Jun 1968	35117-2	23.96	14.77	9.19	0.17	0.26	0.43	0.62

(1) Injector fuel flowrate = total fuel flowrate - total liner coolant flowrate

(2) Based on injector mixture ratio

(3) ΔT = maximum temperature - average temperature at 11-inch location

(4) $\eta_c^* = (\text{average temperature/ideal temperature})^{0.5} \times 100$

(5) Measured temperature based on r

(6) Throat Effective Area = 6.620 in²

(7) Throat Effective Area = 7.573 in²

(8) Throat Effective Area = 8.00 in²

B

Parameters During Preburner Injector Testing

Overall Mixture Ratio	Injector Mixture Ratio ⁽¹⁾	Ideal Temperature ⁽²⁾ °R	Average Combustion Temperature (°R)	ΔT Profile at 11 in. ⁽³⁾ (°R)	$\eta_{c^* 1}$	η_{c^*} at 11 in. ⁽⁴⁾ (%)	Fuel Injection Velocity (ft/sec)	Oxidizer Injection Velocity (ft/sec)	Fuel/Oxidizer Momentum Ratio
0.64	0.66	1285	1268	72	98.0 ⁽⁶⁾	99.3	495	131	5.8
0.75	0.78	1504	1716	94	101.6 ⁽⁶⁾	103.9	555	133	5.4
0.88	0.90	1728	1823	124	101.6 ⁽⁶⁾	102.8	545	132	4.6
0.82	0.85	1628	1589	107	98.0 ⁽⁶⁾	98.8	579	145	4.7
0.97	0.99	1881	1849	119	98.2 ⁽⁶⁾	99.1	547	137	4.0
0.60	0.61	1390	1552 ⁽⁵⁾	25 ⁽⁵⁾	102.0 ⁽⁷⁾	105.4 ⁽⁵⁾	1163	132	14.4
1.19	1.22	2272	2388 ⁽⁵⁾	76 ⁽⁵⁾	99.0 ⁽⁷⁾	102.5 ⁽⁵⁾	690	246	2.8
0.64	0.66	1290	1322	310	99.3 ⁽⁷⁾	101.3	813	221	5.6
0.63	0.65	1276	1326	260	99.4 ⁽⁷⁾	102.0	805	160	7.7
0.63	0.65	1281	1266	144	98.7 ⁽⁷⁾	99.4	780	70	17.0
0.95	0.99	1861	1793	211	99.0 ⁽⁷⁾	98.2	828	136	6.2
1.24	1.28	2369	2325	215	99.7 ⁽⁷⁾	99.0	1022	198	4.0
1.00	1.04	1950	1920	115	99.0 ⁽⁷⁾	99.2	1074	213	4.9
0.60	0.62	1552	1676	58	94.3 ⁽⁸⁾	103.9	2088	119	28.3
0.62	0.64	1216	1140	255	96.9 ⁽⁷⁾	96.9	437	113	6.0

Area based on rake No. 3
 Area = 6.620 in²
 Area = 7.573 in²
 Area = 8.00 in²

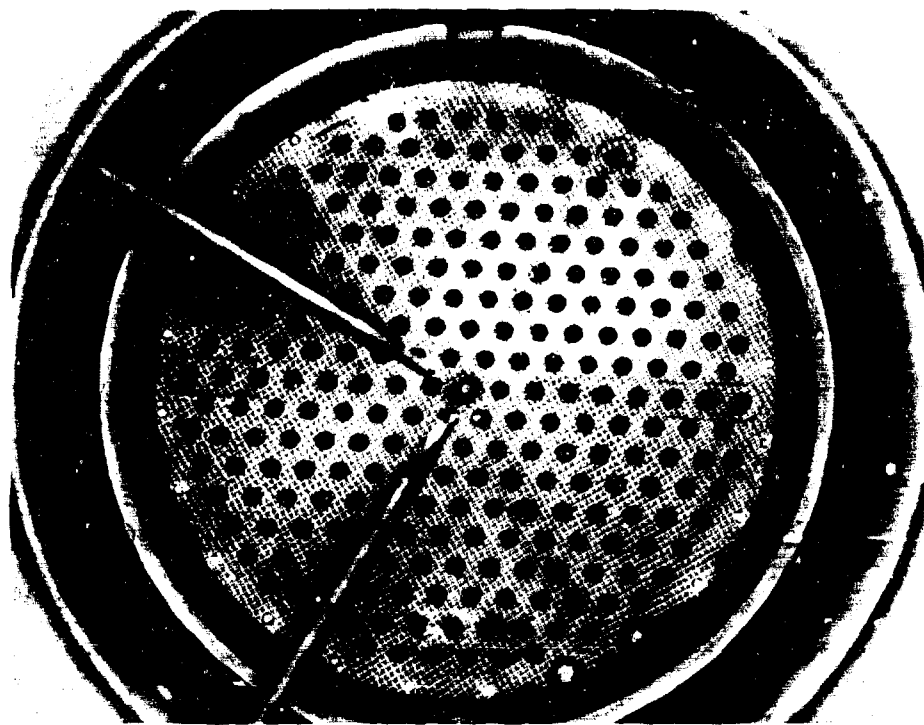


Figure 49. Injector Face Prior to Test 1.01

FE 77800

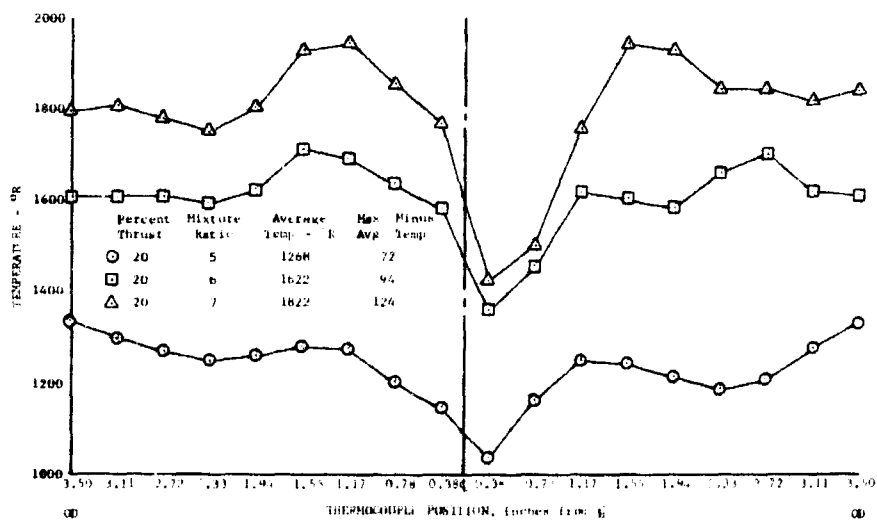


Figure 50. Preburner Temperature Profile, Rig 35117-1, Test 1.01, 11-In. Rake

DF 65190

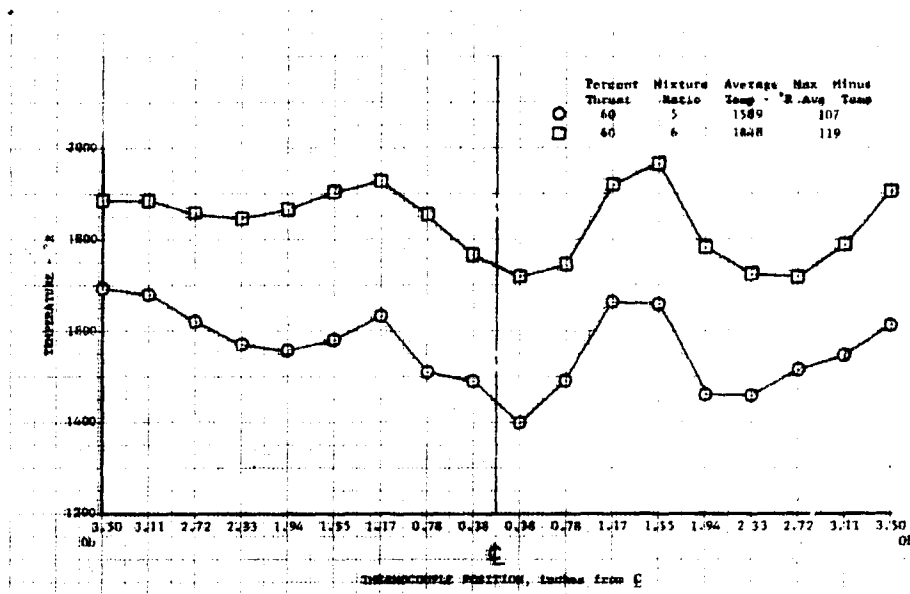


Figure 51. Preburner Temperature Profile, Rig DF 65191
35117-1, Test 1.01, 11-In. Rake

The acceleration to mixture ratio of 5 and 20% thrust level was made with the fuel inlet temperature held constant at 300°R instead of being ramped to 127°R as in test 1.01. This was an attempt to determine the effect of fuel temperature on the system instability. During the ramp from 7% to 20%, system instability was encountered. The instability persisted through the 20% data point and disappeared on the ramp to 100%. The peak-to-average temperature on the acceptable temperature rake (thermocouples No. 21 to 29) at a mixture ratio of 5 and 20% level was 25°R, and at a mixture ratio of 6 and 100% it was 75°R as shown in figure 52. During the ramp to the mixture ratio of 7 at 100%, the run was automatically advanced because of high combustion temperature. This was caused by the large oxidizer valve (CV5) being at a portion of the stroke where little or no effective area change was made with stroke changes. As a result, even though the oxidizer valve was closing as scheduled, the oxidizer flow was not reducing as required to match the reducing fuel flow for the mixture ratio of 7 set point at 100% level.

On test 2.01, two of the combustion temperature rakes in the same radial plane at 7 and 11 in. axial planes (thermocouples No. 31 to 39 on 11 in. rake shown in figure 52) indicated a reduction in temperature toward the chamber outside diameter. These rakes had not shown a temperature reduction during test 1.01, which indicated that the injector had been damaged on the first test.

The teardown inspection revealed approximately 35 oxidizer elements burned in the secondary area. Figure 53 shows the injector face after test 2.01, and figure 54 shows the secondary burning. The burned elements in most instances reduced the secondary flow area. The burned elements were concentrated in an area directly in line with the temperature rakes that showed a reduction in temperature at the chamber outside diameter. Consequently, these temperature rakes are not representative of the actual injector profile. The burning of the oxidizer elements was attributed to aspirating fuel into the cavity during the ex-

tended fuel lag shutdown. To prevent this from recurring, the shutdown fuel lag was reduced and increased oxidizer cavity purges were provided.

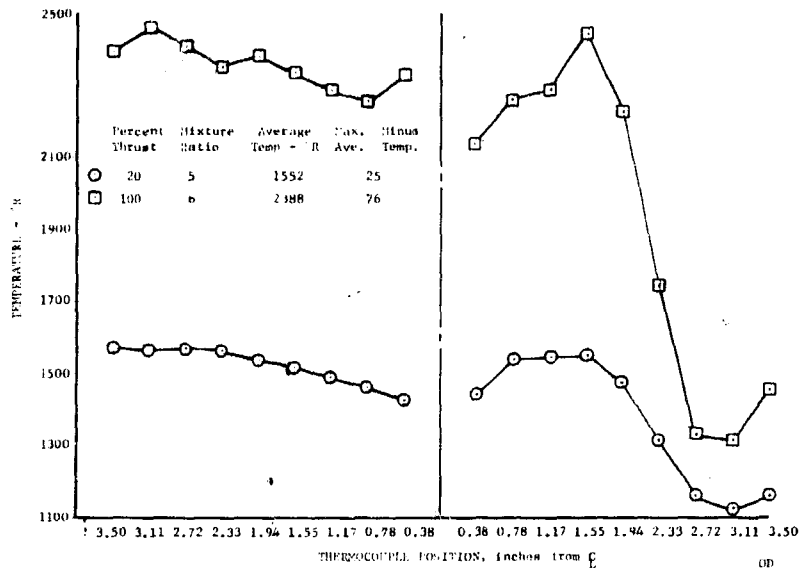


Figure 52. Preburner Temperature Profile, Rig 35117-1, Test 2.01, 11-In. Rake DF 65192

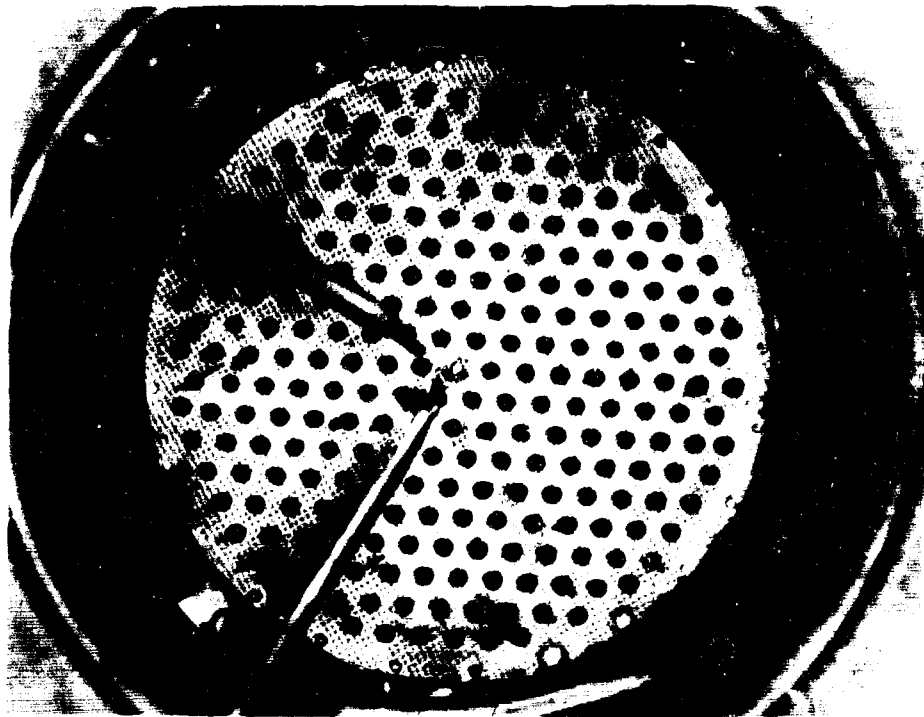


Figure 53. Injector Face After Test 2.01 FE 77966

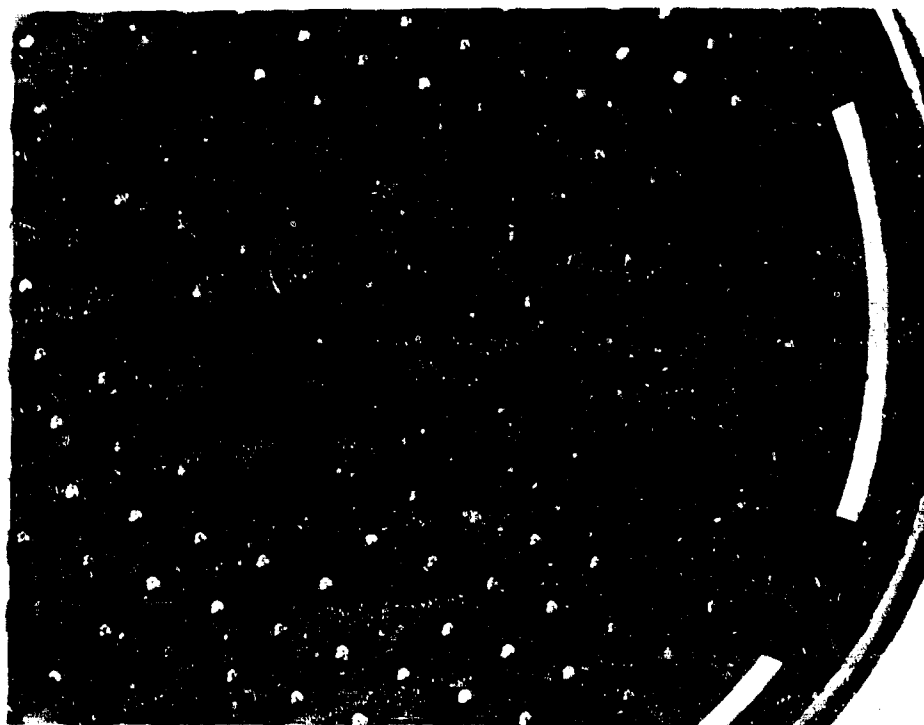


Figure 54. Injector Secondary Burned Area After
Test 2.01

FE 77098

The preburner rig was rebuilt using the backup injector, which was the same as the original injector, except that the fuel size was designed for a pressure drop of 400 psid at mixture ratio of 7 and 100% thrust level, instead of 200 psid. Figure 55 shows the face of the backup injector prior to test 3.01.

Test 3.01 was conducted on 14 June 1968. This test was programed for data points at a mixture ratio of 5 at 20% thrust level, a mixture ratio of 6 at 60% thrust level, and a mixture ratio of 7 at 100% thrust level.

Low frequency (approximately 100 cps) system instability developed after the 20% level flowrates had been attained while the fuel temperature was being lowered to cycle set point. While at the steady-state 20% thrust levels, the preburner oxidizer valve was moved to give primary-to-total oxidizer flow splits of 86% to 45% at a constant cycle point fuel temperature. The system instability persisted during this preburner oxidizer valve excursion. The instability ceased after ramping away from the 20% thrust level flow rates toward 60% set point.

The maximum-to-average temperature at a mixture ratio of 5 and 20% thrust level was 144°R at an average temperature of 1266°R; however, the temperature profile deteriorated with an increasing flow split as shown in figure 56. This effect of flow split on the temperature profile is attributed to the result of built-in injector distribution, which is a function of the match of individual oxidizer primary flow area to the corresponding fixed fuel annulus area. This is substantiated by the fact that the profile was not symmetrical. The injector was assembled by matching the oxidizer total element area with the fuel annuli based on the water

calibration of the individual elements prior to assembly. Oxidizer element primary area variation was 17% total span with 76% of the elements falling in a 6% band. No attempt was made to match the primary area to its respective fuel annulus thus explaining the deterioration in profile with increasing flow split.

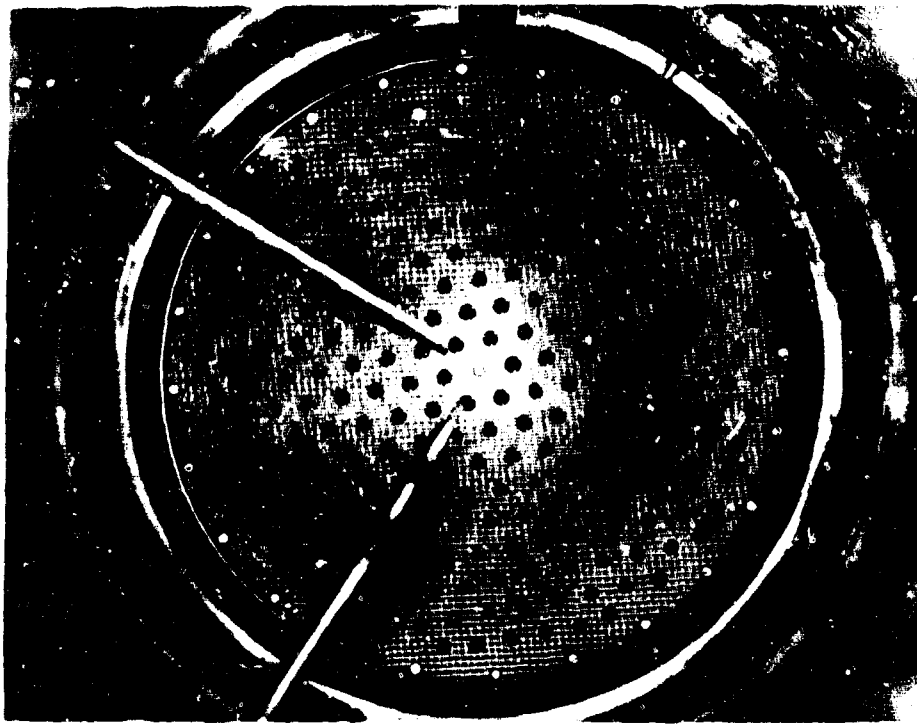


Figure 55. Face of Backup Injector Prior to Test 3.01

FE 78185

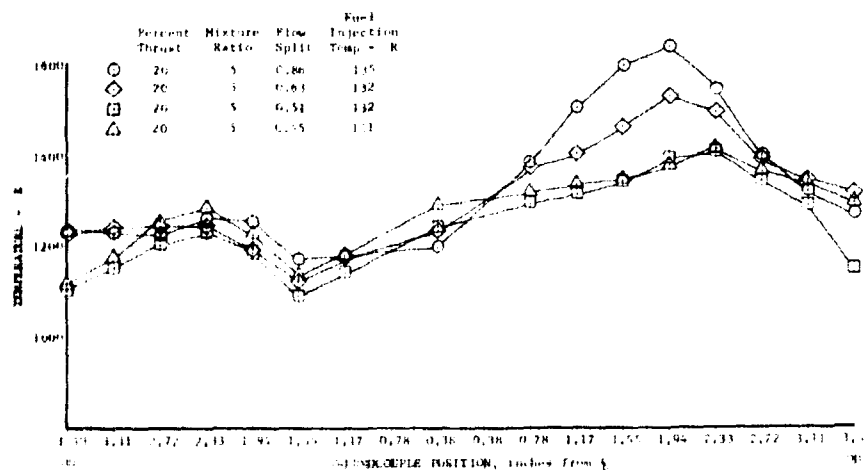


Figure 56. Preburner Temperature Profile With Primary-to-Total Oxidizer Flow Split Variation, Rig 35117-2, Test 3.01, 11-in. Rake

DF 66774

The maximum-to-average temperature at a mixture ratio of 6 and 60% thrust level was 211°R at an average temperature of 1793°R. The maximum-to-average temperature at a mixture ratio of 7 and 100% thrust level was 215°R at an average temperature of 2325°R. (See figure 57.)

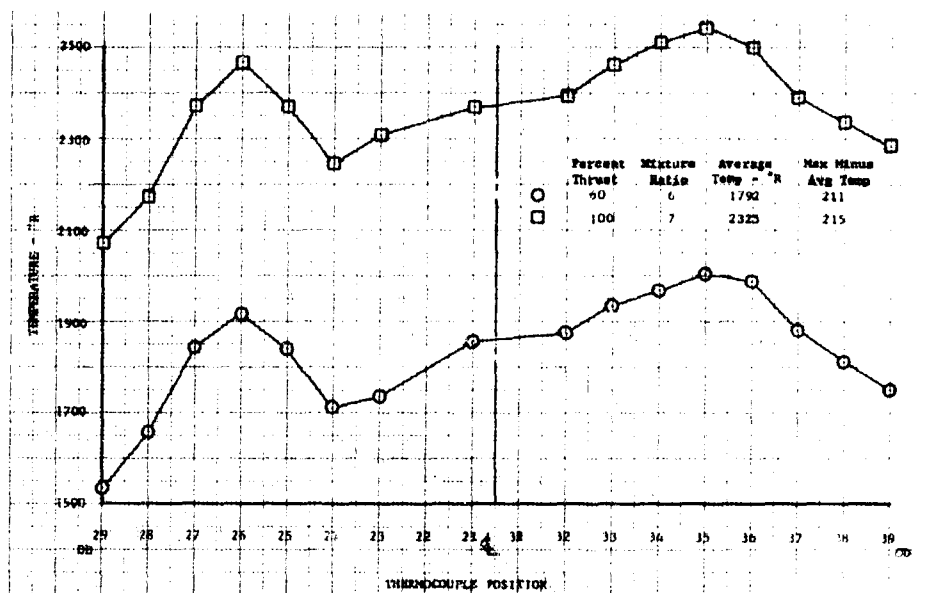


Figure 57. Preburner Temperature Profile, DF 65193
Rig 35117-2, Test 3.01, 11-in. Rake

The magnitude of the peak-to-average temperature may be attributed to fuel leakage around the faceplate piston rings causing low combustion temperature at the outside on one of the rakes. The modified shutdown and purge procedure worked properly with no indication of hardware damage. The procedure used was to bring on a 2 lb/sec GH₂ supply and a 0.6 lb/sec GHe supply to the fuel side at shutdown. A small GN₂ supply was opened to the primary and secondary oxidizer injector cavities at shutdown. One and a half seconds after shutdown, the small GN₂ purge was calculated to have cleared the majority of oxidizer out of the injector, and at this time, a 0.25 lb/sec GHe purge was opened to the primary and secondary cavities to create approximately 10 psid across the elements without causing excessive overtemperature. A 2 sec after shutdown, the 2.0 lb/sec GH₂ purge was turned off to clear the rig of any fuel.

Test 4.02 was programed for 100% thrust at a mixture ratio of 5 including the firing of a pulse charge. The test was automatically advanced by a high combustion temperature just after the top of the propellant ramps to the set point. The pulse charge was not fired. The test was advanced because the liquid hydrogen run tank was depleted, which caused the fuel temperature to rise. The gaseous hydrogen control valves, which are on fuel temperature control, started closing in an attempt to reduce fuel temperature. This combination of events delivered low fuel flow to the rig causing a high combustion temperature advance. The cause of liquid hydrogen depletion was insufficient topping off of the liquid hydrogen tank.

The maximum-to-average temperature on test 4.02 was 115°R with an average temperature of 1920°R, at 97% thrust and a mixture ratio of 5. See figure 58.

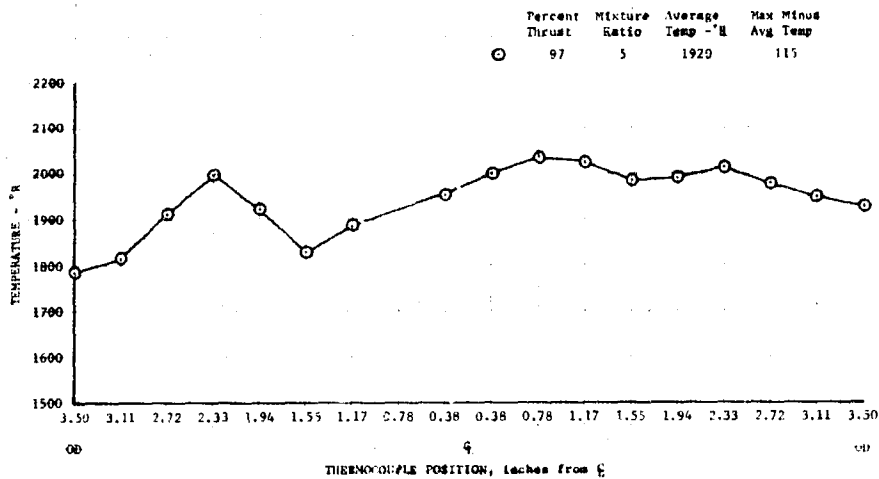


Figure 58. Preburner Temperature Profile, DF 66720
Rig 35117-2, Test 4.02, 11-in. Rake

Tests 5.12, 6.01, 7.01, and 8.01 were ignition checks to determine if the preburner would ignite with a secondary helium purge flowrate (0.20 lb/sec) and the low engine tank head flowrate. The ignition fuel and oxygen flowrates were both below 1.0 lb/sec. All four ignition tests successfully ignited and sustained combustion. In tests 5.12 and 6.01 the oxygen was programed to lead the fuel by 2 sec. Test 7.01 was a repeat of test 6.01 with the oxygen and fuel flows opened to the rig simultaneously. These two tests showed that the oxygen to fuel timing did not influence ignition within this time span. Tests 7.01 and 8.01 were run at essentially constant total propellant flowrate and constant helium flowrate with mixture ratio variations from 1.0 during test 7.01 to 0.5 during test 8.01. The flowrates for tests 7.01 and 8.01 are provided in table XII.

Table XII. Flowrates for Tests 7.01 and 8.01

Test No.	He (lb/sec)	O ₂ (lb/sec)	H ₂ (lb/sec)
7.01	0.205	0.56	0.56
8.01	0.202	0.35	0.71

Tests 9.01, 9.02, and 9.03 were liquid oxygen cold flows to determine the response of oxidizer flow to the rig with a programed 420 msec ramp of the oxidizer pump simulator valves and the oxidizer tank pressurized to 1700 psia. The delivered flowrate from these cold flows was matched with the fuel flow-

rate for the simulated engine start transient from ignition flowrates to the 20% flowrates.

Tests 9.04, 10.01, 11.01, and 12.01 were programed to simulate the engine start transients from ignition flowrates to the 20% flowrate level, plus a fuel temperature excursion from ambient temperature to cycle temperature of 127°R and back to ambient temperature. The rig shutdowns for these tests omitted the initial low flowrate nitrogen purges to the primary and secondary cavities, but instead used the 0.20 lb/sec helium supply to purge the liquid oxygen. The shutoff valve for the primary and secondary helium supply, which previously had been approximately 40 feet away, was close coupled to the rig on tests 9.04, 10.01, and 11.01.

Test 9.04 was automatically advanced by high combustion temperature after 2.75 sec. Test 10.01 was automatically advanced by a low combustion temperature after 2.0 sec. The rig ignited, but failed to sustain combustion. Test 11.01 was manually advanced by a low combustion temperature after 3.60 sec. Again, the rig ignited but failed to sustain combustion. These tests showed that helium was being delivered much earlier to the injector with the helium valve close coupled to the rig. The early arrival of helium influences the ignition process causing unsustained combustion.

Test 12.01 was made with the helium valve that opens the helium start purge located in its original position, approximately 40 feet from the rig. Because of the large volume between the helium valve and the rig, the helium flowrate arrives at the rig after ignition has taken place and thus does not affect the ignition process. Test 12.01 ran successfully through to the programed shutdown. The required rapid chamber pressure rise that simulates an engine start was attained. The chamber pressure rise rate was approximately 4400 psi/sec. System instability was encountered at the 20% flowrates as the fuel temperature was lowered from the ambient to cycle set point. The instability began at approximately 290°R fuel temperature. The instability disappeared at 230°R as the fuel temperature was ramped up from 126°R to ambient. The effect of fuel injection temperature on the temperature profile is shown in figure 59, which shows a reduction in profile with increasing fuel temperature. The valve that opens the helium shutdown purge to the primary and secondary cavities was close coupled to the rig as in tests 9.04, 10.01, and 11.01. The close coupled valve delivered the full helium purge flowrate to the rig rapidly, which caused a high temperature spike just after shutdown on test 12.01.

Tests 13.01, 13.02, 13.04, 14.01, and 14.02 were programed for fuel temperature excursions from 300°R to 85°R and flow divider valve excursions from 90% to 40% primary-to-total oxidizer flow splits while at the 20% flowrates. For these tests, orifices were installed in the fuel and oxidizer stand run lines just upstream of the rig. The orifices create a high-pressure drop in an effort to isolate the volumes in the stand run lines from the injector cavities. In an attempt to correct the high temperature spikes encountered during shutdown purge of test 12.01, these tests were made with the close-coupled helium valve opening the primary and secondary purges after approximately 0.1 sec delay. The delay was to allow more time for chamber pressure to decline and the fuel line to bleed in an attempt to drive the mixture ratio above stoichiometric and thus reduce the shutdown temperature spike.

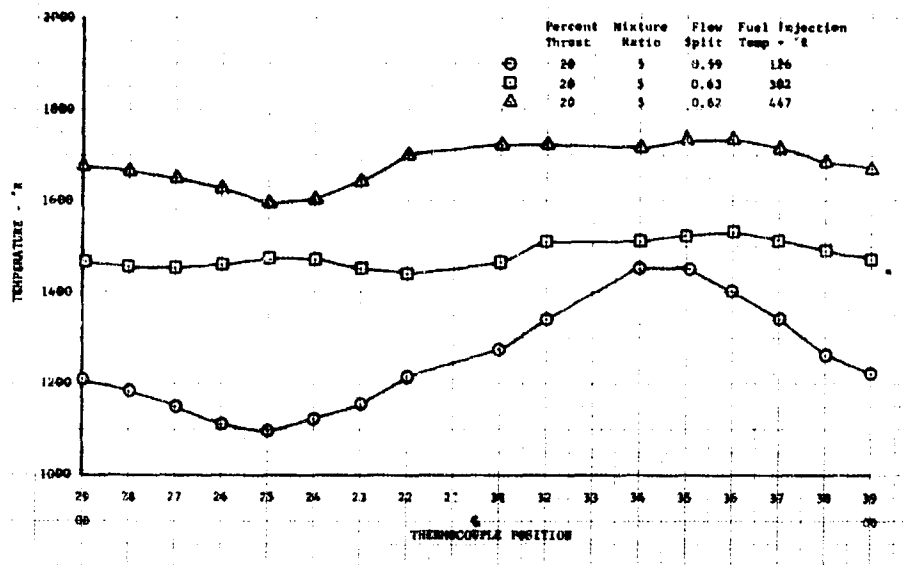


Figure 59. Preburner Temperature Profile, DF 66721
Rig 35117-2, Test 12.01, 11-in. Rake

Tests 13.01 through 14.01 were unsuccessful attempts because of various control and operational problems. Test 14.02 was a successful test to the programmed shutdown. System instability was encountered at the 20% level as fuel temperature was ramped down past 290°R to the cycle set point of 127°R. The preburner oxidizer valve excursions at cycle temperature did not correct the system instability. The instability remained as the fuel temperature was ramped from 127°R to 290°R. The shutdown on test 14.02 had a high temperature spike even with the delayed opening of the shutdown helium purge. Figure 60 shows the injector face at the conclusion of test 14.02.

d. Performance Calculations

The characteristic velocity efficiency computed from rig pressures and flowrates had an average value of approximately 99.5% as shown in figure 61. Figures 62 and 63 show the characteristic velocity efficiency based on the average combustion temperature at the 7 in. and 11 in. locations, respectively. The results of both indicate an average η_c^* of approximately 100% with a scatter band of $\pm 4\%$. The agreement of η_c^* calculated from measured combustion temperatures and that calculated from rig pressure and flowrates tends to verify the validity of combustion temperatures and the method used to calculate average combustion temperature.

The oxidizer injector secondary effective area compared well with the predicted levels determined from water flow tests of the individual elements and showed the same effect of flow split on effective area. A comparison between preburner rig results and the levels predicted from water flows of individual tubes are shown in figure 64. Combustion rig data and water bench calibrations indicate that the injector used on Build 1 had a secondary effective area about 7% smaller than the injector used on Build 2.

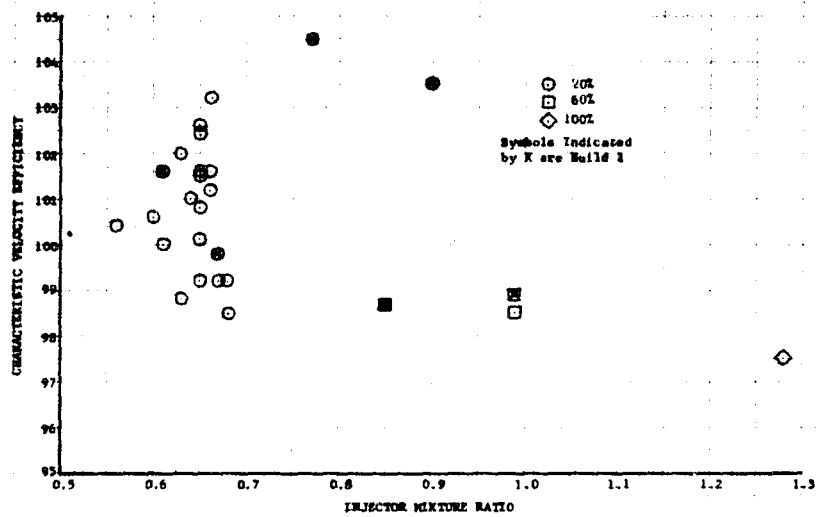


Figure 62. Characteristic Velocity Efficiency
Based on Combustion Temperatures
at the 7-in. Rake

DF 66723

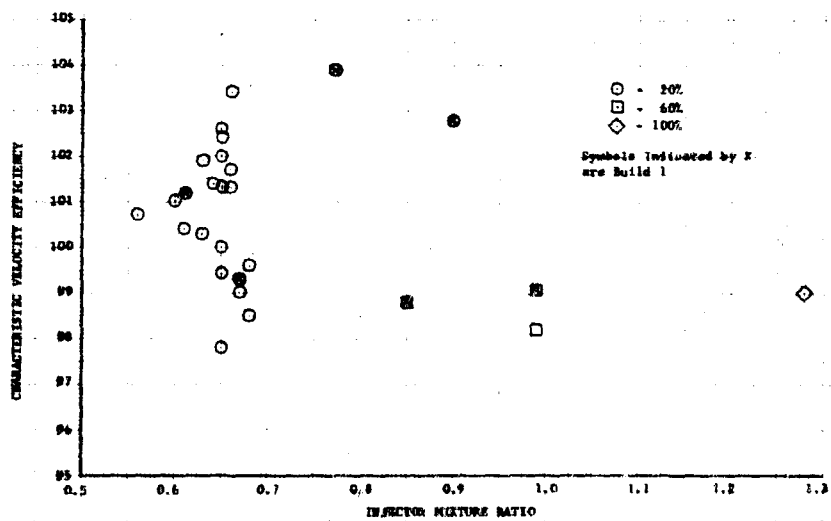


Figure 63. Characteristic Velocity Efficiency
Based on Combustion Temperatures
at the 11-in. Rake

DF 66768

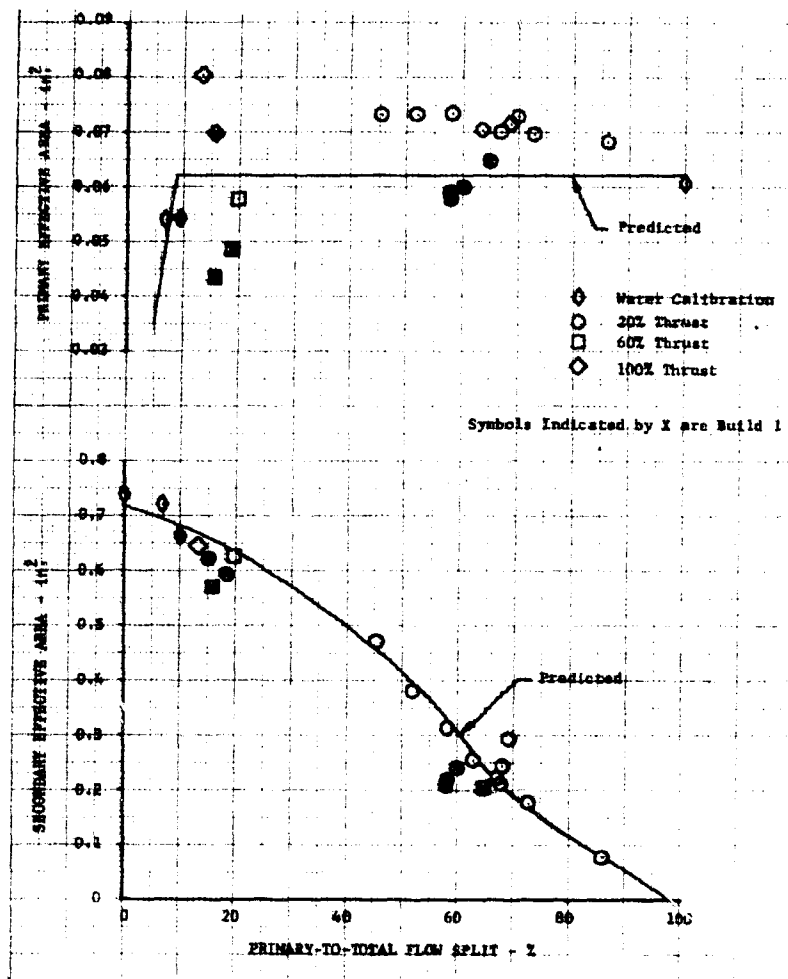


Figure 64. Oxidizer Injector Calibration

DF 66769

The calculated primary effective area had a large amount of scatter, particularly at low flow splits. This would be expected because slight errors in the estimated flow split will result in proportionately larger errors in the primary flow and primary effective area. The flow split for the preburner rig tests was estimated from the measured preburner oxidizer valve pressure drop and the water calibration of the preburner oxidizer valve. The agreement between the preburner rig test data and the predicted shape of the secondary effective area versus flow split curve indicated that the flow divider valve calibration provided an acceptable method of determining secondary flowrate.

The oxidizer secondary effective area increased slightly with an increasing fuel to oxidizer momentum ratio as shown in figure 65. Data from tests 3.01, 12.01, and 14.02 were used with data points corresponding to 20% thrust and a mixture ratio of 5. All points were obtained with a constant preburner oxidizer valve position to minimize the effect of flow split on effective area. A slight increase in flow split did result, however, when momentum ratio was increased as shown in figure 66. This makes the increase in secondary effective area with momentum ratio slightly larger than is indicated. The increase in oxidizer

effective area with increasing momentum ratio was contrary to the trend expected and that experienced during Phase I (Contract AF 04(611)-11401) testing. No change in the primary effective area with changing momentum ratio was observed as shown in figure 67.

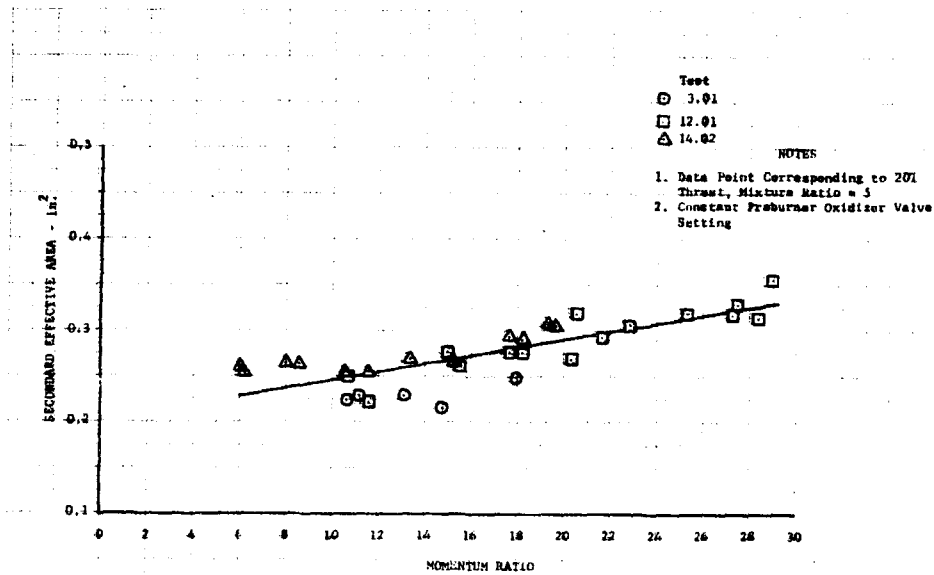


Figure 65. Secondary Effective Area vs Momentum Ratio

DF 66770

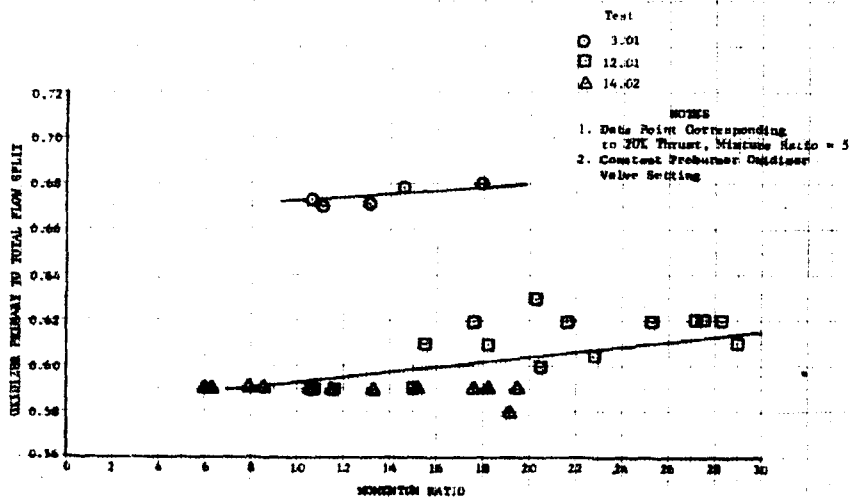


Figure 66. Primary-to-Total Flow Split vs Momentum Ratio

DF 66771

5. Stability Investigation

During testing of the preburner injector, low frequency combustion instability was encountered while operating at the 20% thrust level. To evaluate the cause of the combustion instability, several tests were programed to obtain data on the suspected influential parameters. An analog model of the preburner injector, combustion chamber, and a portion of the test stand was constructed to determine the influence of various parameters on stability. Also water flows of the injector assembly and single element test rigs were made in an attempt to relate hot firings to water flow tests.

a. Special Preburner Rig Tests

Of the possible causes of combustion instability, three of the conditions could be controlled to some extent in a typical preburner test without compromising the basic test objective. The three conditions were (1) liquid oxygen flow split between the primary and secondary, (2) fuel temperature, and (3) separation of the test stand propellant volumes from the preburner rig. Portions of preburner rig tests were scheduled to vary these parameters.

(1) Flow Split Evaluation

At the 20% thrust cycle conditions during tests 3.01 and 14.02, the oxidizer primary-to-total flow split was varied from approximately 30% to 90% as shown in figure 69. This change had no significant effect on the combustion instability even though the percent effective oxidizer pressure drop varied from 4% to 57% of preburner pressure as shown in figure 70. In the injector designed during Phase I (Contract AF04(611)-11401), it was possible to eliminate combustion instability by increasing the percent effective oxidizer pressure drop above 4%. Because this was not true with the current injector, it was concluded that this fully tangential dual orifice element does not achieve the momentum addition at the secondary slot. Therefore, with the vapor core in the center of the element, the oscillations in the preburner pressure bypass the high pressure drop primary stream and come into direct contact with the low pressure drop secondary.

The range of primary and secondary pressure drop is shown as a percent of chamber pressure in figures 71 and 72, respectively. The primary pressure drop is across a large range, but the secondary pressure drop varies only between 0.6 and 1.7% of chamber pressure. The primary pressure drop is always well above the range where instability occurs when compared to past experience. The secondary pressure drop, however, is always lower than that required for stable operation. It was concluded that the low secondary pressure drop contributes significantly to the instability and the high primary pressure drop does not influence the instability.

Some oscillations in the oxidizer injector almost always exist either because of inherent instabilities in the injector cavities or the possible interaction between the oxidizer spray cone and the surrounding fuel flow. The repeatable effect on the frequency by changing the oxidizer primary-to-total flow split shown in figure 69 indicates the oxidizer injector affects the instability to some extent.

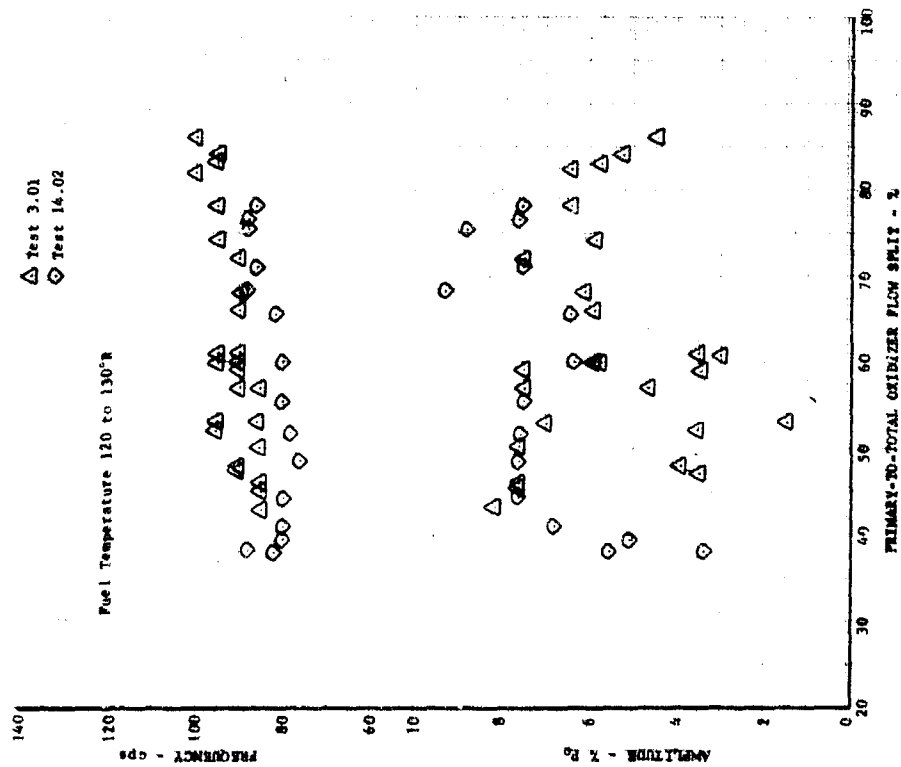


Figure 89. Flow Split Variation

DF 66711

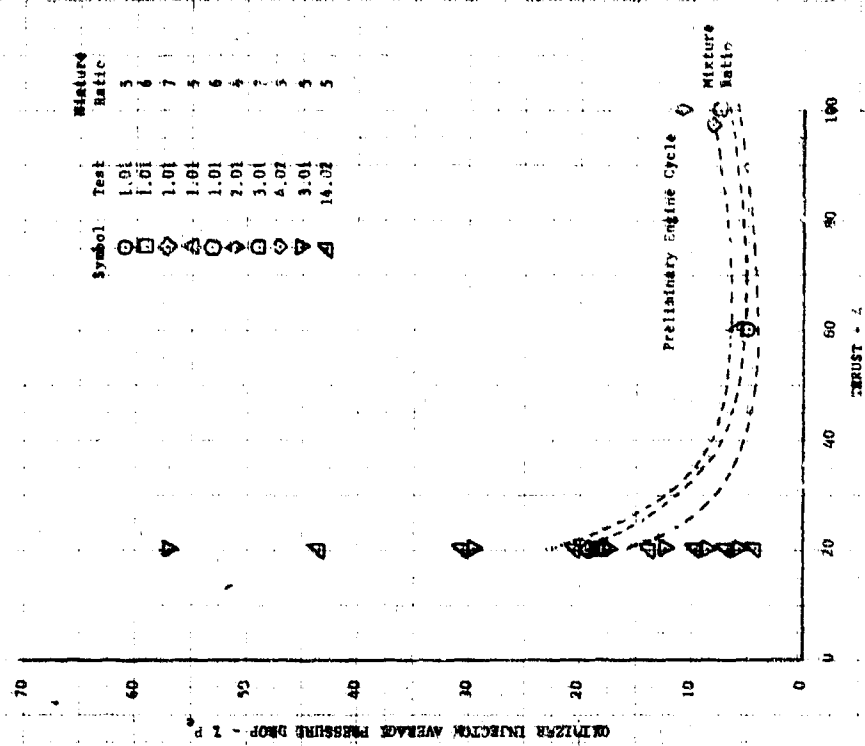


Figure 90. Oxidizer Injector Percent Pressure Drop vs Percent Thrust

DF 66710

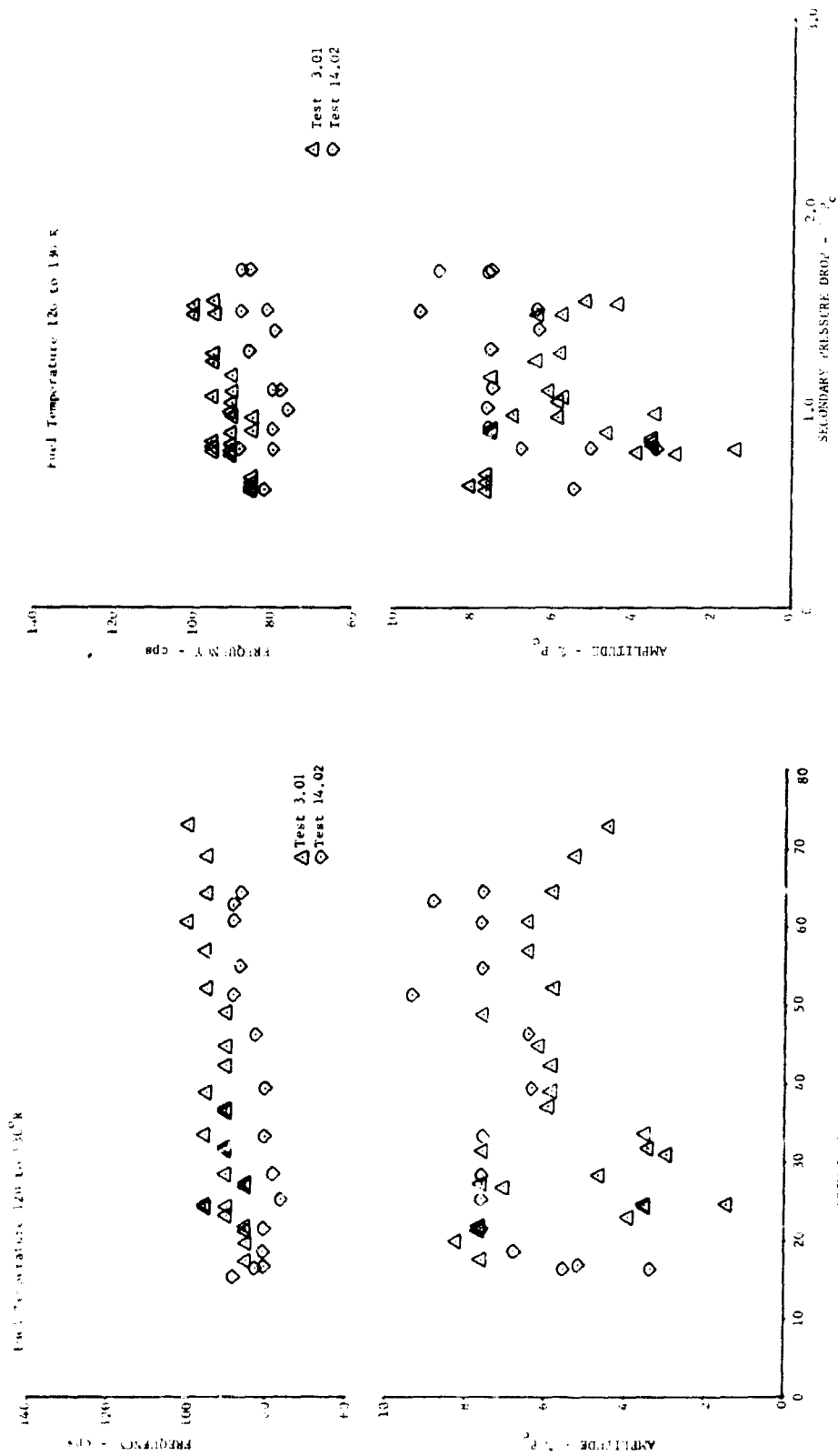


Figure 71. Primary Pressure Drop as a Percent of Chamber Pressure

Figure 72. Secondary Pressure Drop as a Percent of Chamber Pressure

(2) Fuel Temperature Evaluation

Increasing the fuel injection temperature consistently eliminated the combustion instability as shown in figure 73. Changing the fuel injector effective area at constant temperature by changing from the low pressure drop to the high pressure drop fuel plate did not affect the combustion instability as shown in figure 74. Therefore, it was concluded that the fuel temperature, and not the fuel pressure drop or velocity, eliminates the combustion instability.

The most probable theory on how the fuel temperature affects the combustion instability is that the increase in fuel temperature decreases the combustion delay enough to uncouple the preburner combustion from the oxidizer injector.

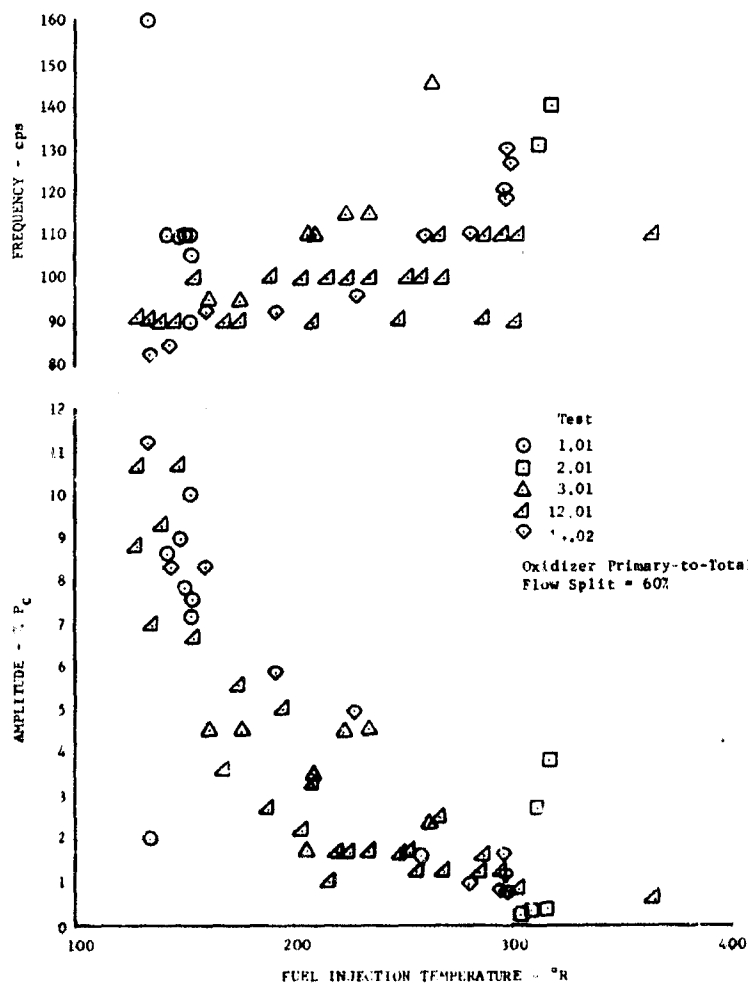


Figure 73. Effect of Fuel Injection Temperature

DF 66714

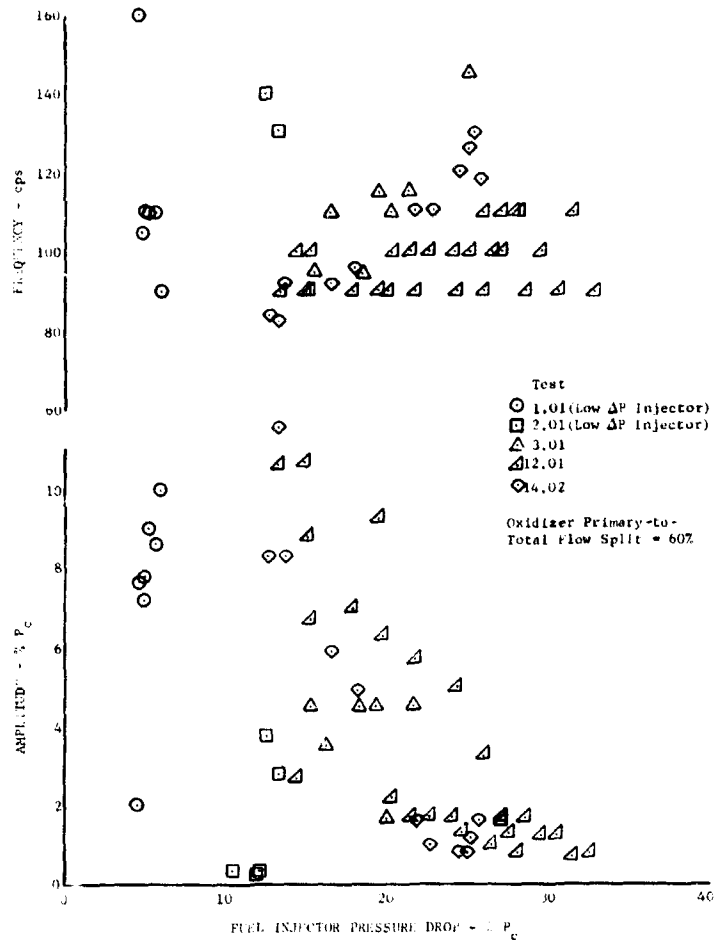


Figure 74. Effect of Fuel Injector Pressure Drop DF 66715

During test 12.01, the fuel injector temperature at 20% thrust was varied extensively. Figures 75, 76, and 77 are traces that show the path and the effects of fuel temperature on the amplitude and frequency of the combustion instability. The phase relationships are also indicated in figures 75, 76, and 77. The only two consistent phase relationships observed were that the secondary oxidizer cavity is in phase with the chamber oscillations and the fuel manifold is 180 deg out of phase with the combustion chamber. It is not understood what bearing this particular phase relationship has on the stability problem. However, the frequency of the parameters was not always equal at a particular fuel temperature. When frequencies are not equal, the phase relationship between the parameters is constantly changing, which lessens the significance of phase relationships. Another significant item is the large reduction in combustion chamber amplitude at fuel temperatures above 180°R.

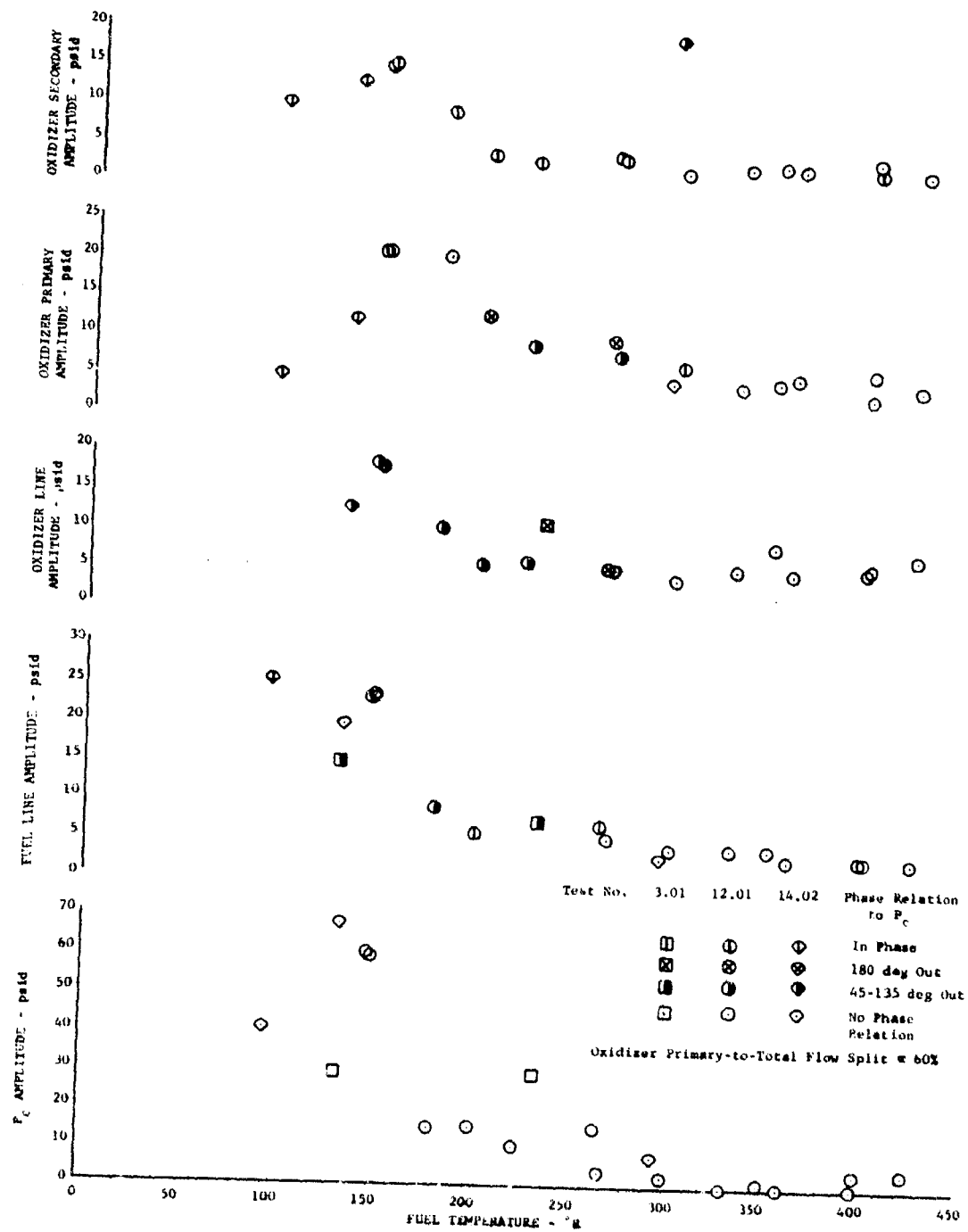


Figure 75. Fuel Temperature Effect on Amplitude

DF 66716

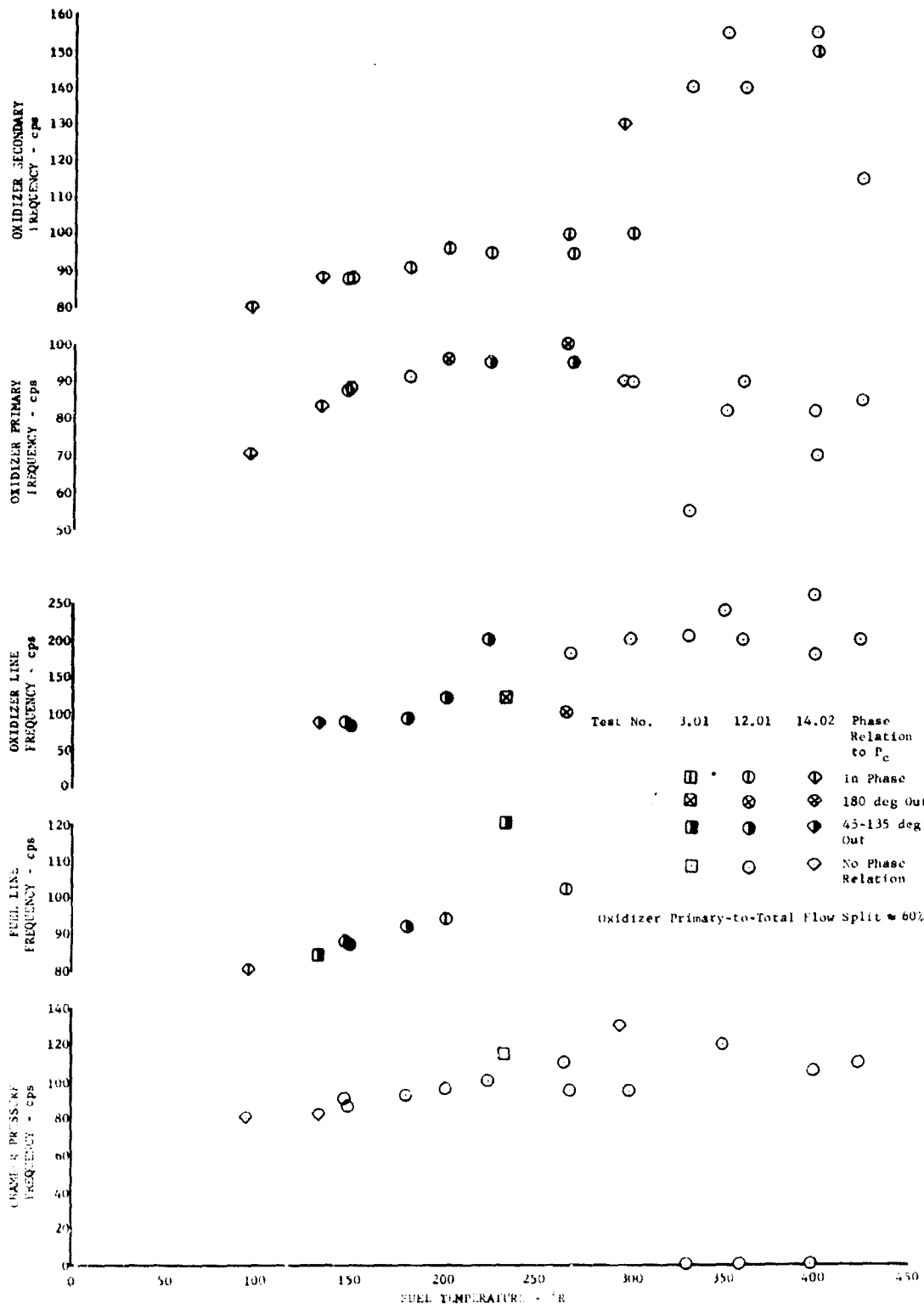


Figure 76. Fuel Temperature Effect on Frequency

DF 66717

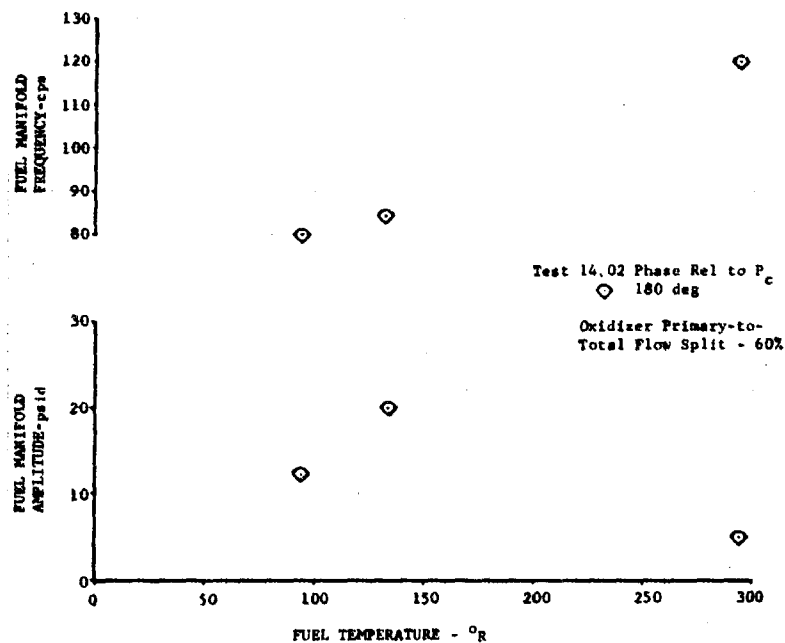


Figure 77. Fuel Temperature Effect on Fuel Manifold Amplitude and Frequency

DF 66709

(3) Evaluation of Test Stand Volumes

During test 14.02, high pressure drop orifices ($\Delta P/P > 0.6$) were installed in the stand lines just upstream of the rig in an attempt to isolate the test facility from the rig. There was no significant change in either the amplitude or the frequency of the combustion instability.

Preburner injector testing during Phase I (Contract AF04(611)-11401) showed stable combustion at approximately the same flow rates, pressures, and temperatures with the identical test facility. Table XIII compares a previous test with cold fuel temperatures with a recent test.

Table XIII. Preburner Test Comparison

Item	Phase I (Contract AF04(611)-11401) Testing	Current Testing
Rig	33447-5	35117-2
Test No.	49.01	12.01
Primary Oxidizer Pressure Drop (psid)	50.7	235
Secondary Oxidizer Pressure Drop (psid)	15.0	9.3
Fuel Injector Pressure Drop (psid)	73.3	83.0
Fuel Temperature ($^{\circ}$ R)	118	147
Fuel Flow (lb_m/sec)	11.9	14.1
Oxidizer Flow (lb_m/sec)	8.7	9.1
Oxidizer Primary-to-Total Flow Split	0.22	0.59
Preburner Chamber Pressure (psia)	474	560
Chamber Pressure Amplitude (psid)	0	± 60
Chamber Pressure Frequency (cps)	-	90

Based on these observations it was concluded that the combustion instability was not caused by the test facility.

b. Analog Model of Preburner Test Rig

Many variables that could strongly influence the combustion instability could not be readily controlled in a special test or changed in the existing hardware. An analog model was therefore constructed in which the suspected variables were investigated to show the relative influence of each variable.

(1) Model Formulation

A mathematical representation of dual-orifice oxidizer, fixed fuel area preburner rig was formulated and programed on the analog computer. The formulated system is illustrated in figure 78. The simulation included the preburner injector, preburner oxidizer valve, combustion chamber, and a segment of the stand propellant lines feeding the injector. The propellant feed lines having a large L/D (fuel = 65, oxidizer = 70) were formulated as a distributed system. The injectors with their concentrated volumes and low L/D were represented as a lumped parameter system. The combustion chamber dynamics were represented by a gas residence time constant and an oxidizer vaporization delay.

(2) Program Verification

The program was set up at idle thrust ($T_{\text{fuel}} = 125^{\circ}\text{R}$) to attempt to match with the instability of tests 12.01 and 14.02. The input contained the oxidizer injector effective area vs flow split variation in figure 64 and the oxidizer vaporization delays shown in figure 79. The injector effective area characteristic was obtained from test data and the vaporization delay was derived from a relationship from NASA TN D-851 and modified as influenced by oxidizer velocity.

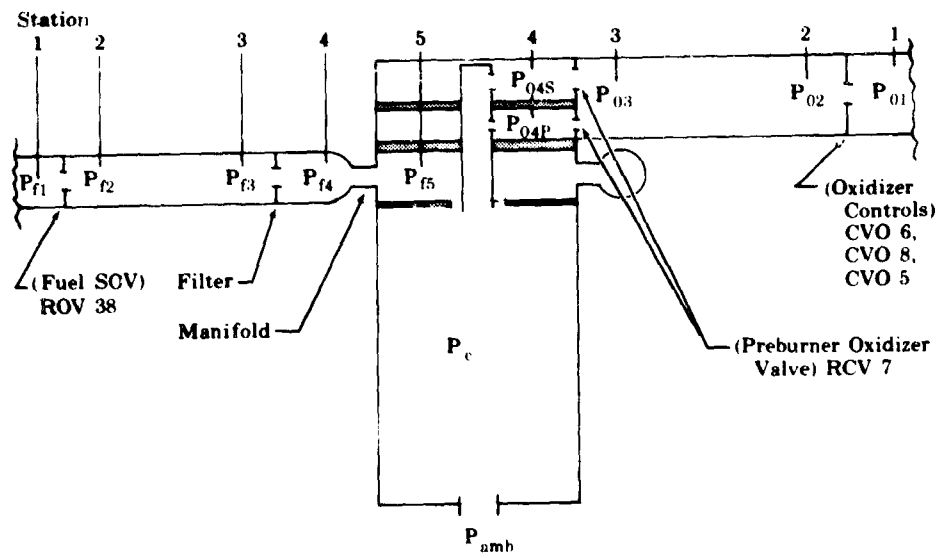


Figure 78. Preburner Injector Analog Stability Model FD 25235

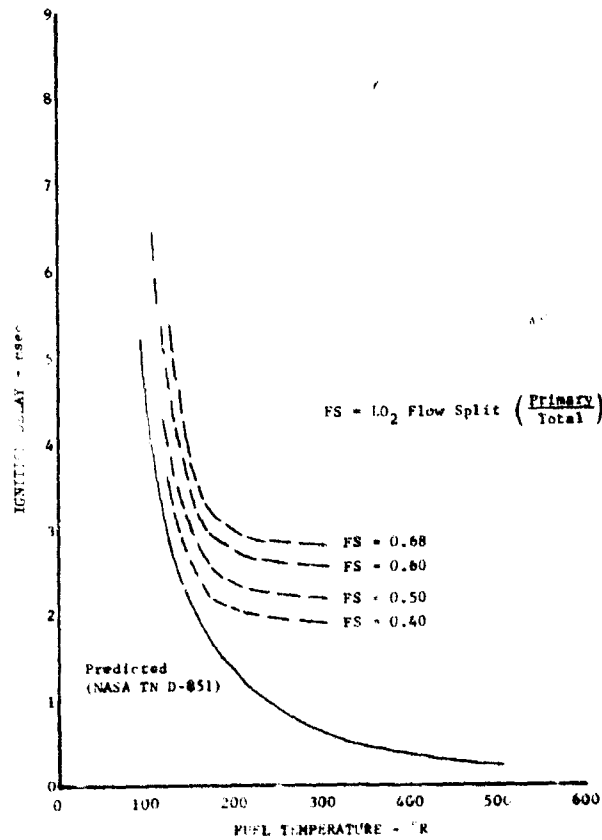


Figure 79. Oxidizer Vaporization Delay

DF 66779

A flow split and fuel temperature excursion was run on the analog simulation with the results presented in figures 80 and 81. The analog frequency trend as a function of flow split agreed with the test data with a slight increase with increasing flow split. No correlation of amplitude with the test data could be made; however, the analog showed an increasing then decreasing amplitude with flow split. As previously discussed, no conclusions were drawn from phase relationships. The analog results as a function of fuel temperature agreed with the test data as shown in figure 81.

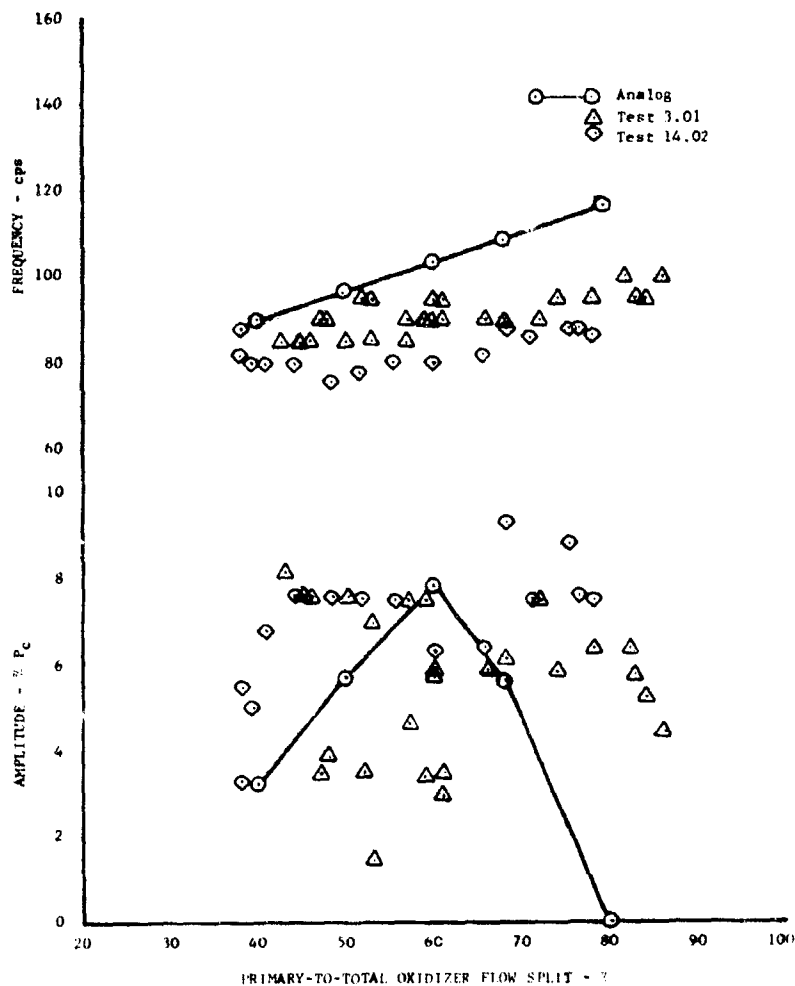


Figure 80. Analog Simulation of Flow Split Variation

DF 66780

Phase angles (relative to chamber pressure) differed somewhat between the test and the analog. The test data showed that the oxidizer secondary was always in phase with chamber pressure. The analog showed the oxidizer secondary was in phase at low fuel temperature (high combustion delay), but the phase angle increases with fuel temperature, reaching 100 deg at 300°R fuel. The oxidizer primary phase angle varied from 0 to 180 deg during test with no apparent correlation. The analog showed the oxidizer primary varied 50 to 160 deg as fuel temperature is increased and combustion delay decreased. During test, the fuel manifold was consistently 180 deg out of phase with chamber

pressure. The analog fuel manifold had a phase lag of 60 deg. A comparison of phase angles is presented in table XIV.

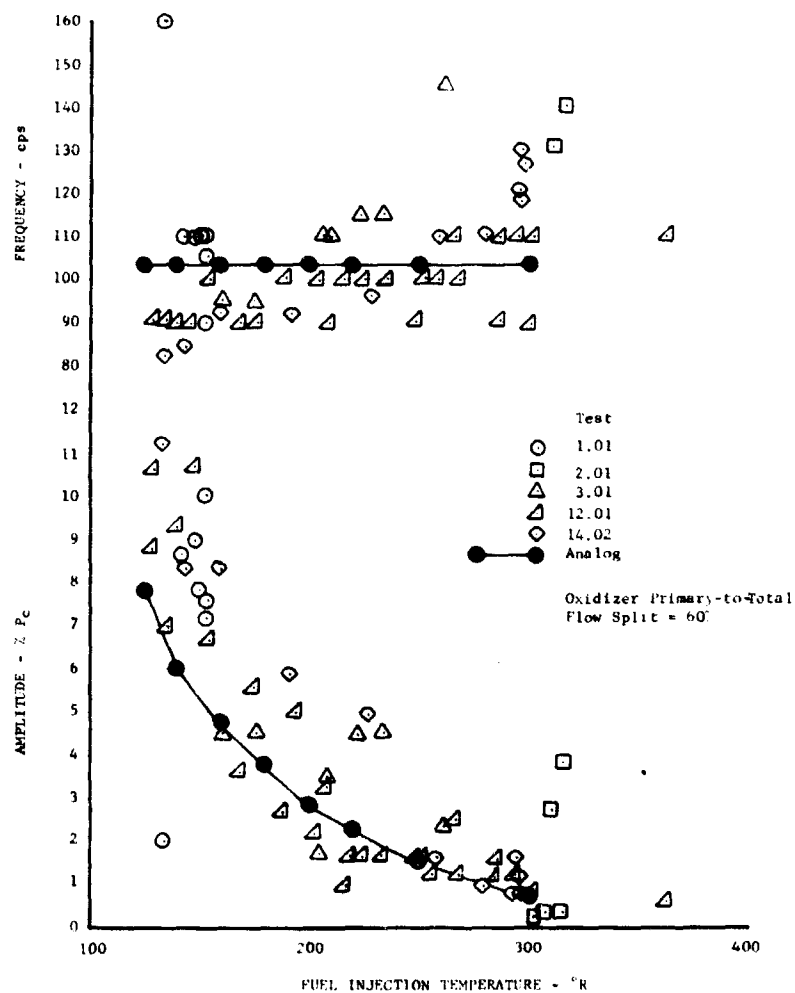


Figure 81. Analog Simulation of Fuel Temperature Variation DF 66781

Table XIV. Phase Angle Comparison

	Test	Analog
Fuel Injector (deg)	180	60
Fuel Line (deg)	0 to 180	75
Primary (deg)	0 to 180	50 to 160
Secondary (deg)	0	25 to 100
Oxidizer Line (deg)	0 to 180	70 to 180

The inability to obtain a closer match of phase angles could be influenced by the fact that the high response instrumentation was not flush-mounted in the injector cavities. Instrumentation passages were drilled through the injector housing, which created volumes and could affect the indicated pressure recording.

(3) Injector Cavity Volumes

(U) The primary, secondary, and fuel injector volumes were varied in the analog to determine the effects on the instability. The results show that a 20% reduction in secondary volume will stabilize the process as shown in figure 82. Variations in the primary and fuel volumes had only minor effects on the instability.

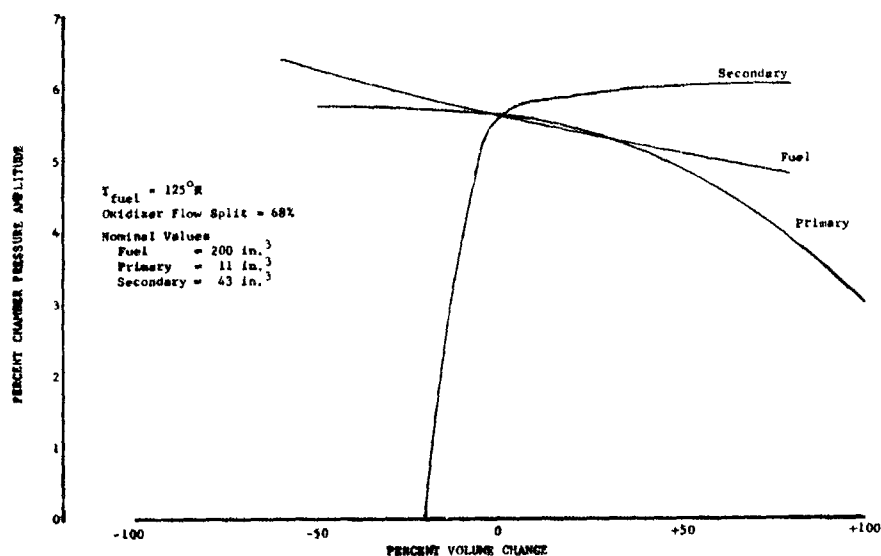


Figure 82. Predicted Volume Influence on Preburner Stability DF 66766

(4) Injector Effective Areas

The secondary and fuel effective areas were varied to determine the effect on instability. (See figure 83.) A reduction in secondary area did influence the instability; however, a reasonable change in area (for cycle considerations) will not eliminate the instability. A reduction in fuel area has no significant influence on the instability, while an increase of approximately 60% causes the analog to stabilize.

(5) Effect of Instability on Engine Operations

A mathematical simulation of the 250K engine, which was programed on the analog computer during Phase I (Contract AF04(611)-11401), was used to determine what effects preburner injector instability would have on engine operation. This engine simulation was developed to study control systems, therefore it contains the necessary system dynamics (turbopump acceleration, heat exchanger dynamics, etc.) that affect starting, throttling, and shutdown. The simulation is complete in that it contains all the turbopumps, heat exchangers, propellant lines, combustors, etc.

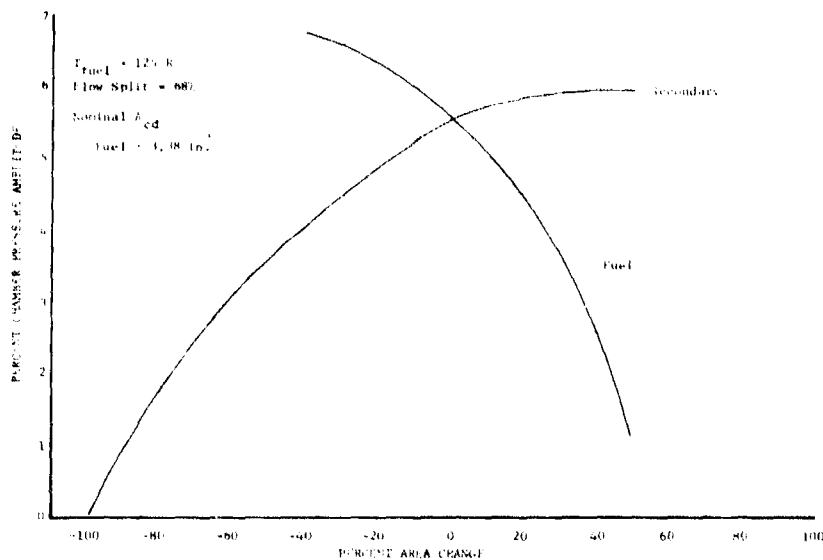


Figure 83. Influence of Effective Areas on Preburner Stability DF 66767

The engine was trimmed at idle thrust and nominal mixture ratio. A sine wave was superimposed on preburner combustion pressure of such magnitude to produce an instability of ± 70 psi ($\pm 9\%$) amplitude. The frequency of this sine wave was varied from 1 to 200 cps to investigate the effects on the engine. The external forcing sine wave applied to the preburner chamber pressure was used to obtain the preburner instability and was present in the system throughout the investigation. Engine feedback to the preburner reduced the instability such that the forcing function always had to be greater than the resulting instability.

The results of this investigation are shown as amplitude-frequency plots of some of the major engine parameters. These plots are included as figures 84 and 85. Frequencies of 75 to 150 cps were experienced during tests of the preburner. At this frequency level, most of the engine variables have attenuated to an amplitude of approximately 1%. The exception to this are those variables directly associated with the preburner injector flows, mixture ratio, combustion products, etc.

c. Water Flow Correlation

Water flow tests were conducted on the injector assembly and single element flow blocks in attempt to correlate water flow with hot firing instability through pressure fluctuations. The following paragraphs describe these tests.

(1) Injector Assembly

After the preburner test series, the entire preburner injector was water flowed with high response instrumentation. High frequency and high amplitude oscillations existed in all fuel and oxidizer cavities. Further investigation showed that these instabilities were present in the stand system (B-21) even when the injector was removed. The injector effective area was simulated by hand valves in the stand supply lines. Water was flowed through the test stand just

as had been done previously with the injector in place. Pressure oscillations with high frequencies and amplitudes were recorded. Table XV presents these data. It is concluded that no direct correlation could be made between preburner hot firing instability and preburner injector water flows.

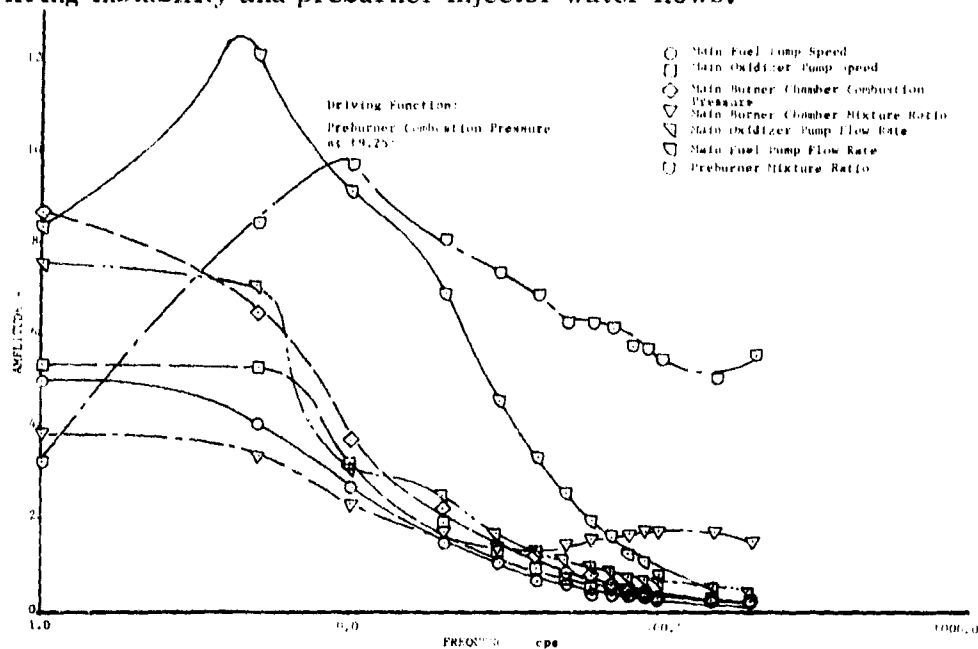


Figure 84. Predicted Frequency Response

DF 66718

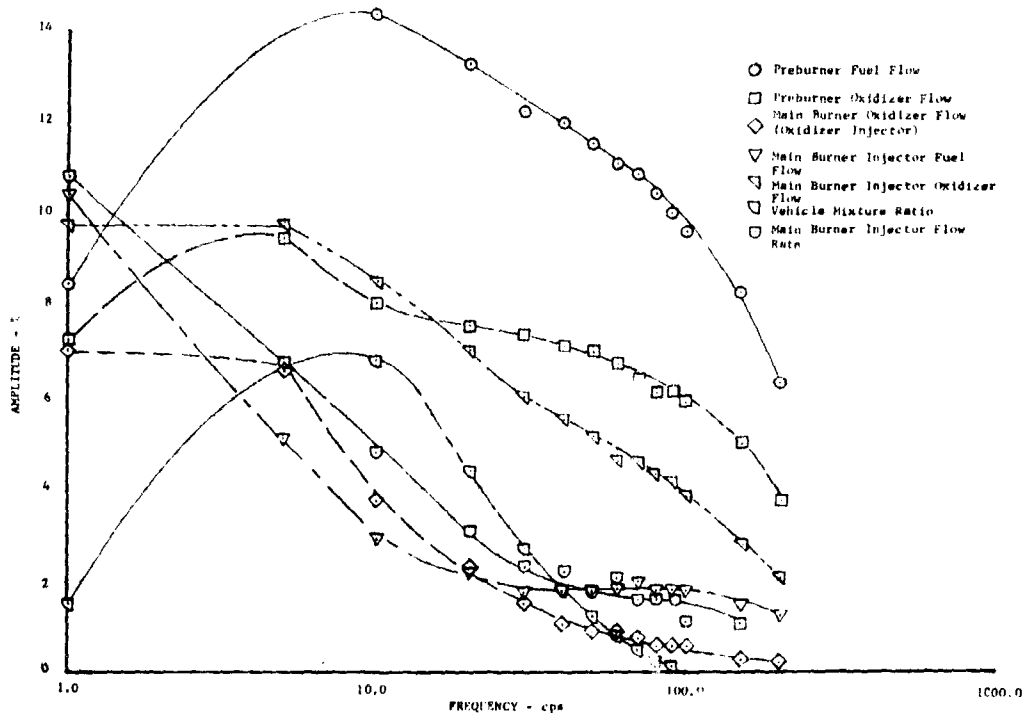


Figure 85. Predicted Frequency Response

DF 66719

Table XV. Injector Water Flow Test Results

OXIDIZER INJECTOR ONLY									
Level (psi)	Primary Pressure Transducer		Secondary Pressure Transducer		Primary Kistler		Secondary Kistler		
	Amplitude (psi)	Frequency (cps)	Level (psi)	Amplitude (psi)	Frequency (cps)	Amplitude (psi)	Frequency (cps)	Amplitude (psi)	Frequency (cps)
72	3.6	50	0	-	-	19.3	150	0	-
253	9.6	135	0	-	-	-	-	0	-
420	6.0	230	0	-	-	-	-	0	-
460	4.8	270	0	-	-	17.2	830	0	-
447	6.2	200	0	-	-	21.0	630	0	-
460	6.7	240	39	0.82	135	26.0	530	7	480
420	4.8	240	38	0.60	140	29.7	730	7	500

FUEL INJECTOR ONLY				
Fuel Pressure Transducer		Fuel Kistler		
Level (psi)	Amplitude (psi)	Frequency (cps)	Amplitude (psi)	Frequency (cps)
16	0	-	1.0	60
26	0.6	-	1.5	56
49	1.5	22	1.9	510
67	1.8	40	2.57	370
75	4.0	32	2.97	610
97	5.0	35	2.28	720
92	6.0	40	2.67	760
94	5.0	38	2.48	850
95	5.0	38	2.57	900
94	5.0	38	2.18	900
95	5.0	40	2.38	920

FEED LINE ONLY									
Level (psi)	Primary Feed Line Pressure Transducer		Secondary and Fuel Feed Line Pressure Transducer		Primary Feed Line Kistler		Secondary and Fuel Feed Line Kistler		
	Amplitude (psi)	Frequency (cps)	Level (psi)	Amplitude (psi)	Frequency (cps)	Amplitude (psi)	Frequency (cps)	Amplitude (psi)	Frequency (cps)
15	4.0	200	0	0	-	5.0	730	0	-
200	12.0	645	0	0	-	45.0	2300	0	-
375	17.3	670	0	0	-	40.0	3600	0	-
440	20.0	730	40	4.1	5	56.0	5100	2.5	130
440	14.6	670	210	13.3	190	63.0	5600	32.0	465
440	20.0	750	235	16.6	230	63.0	5500	48.0	445
440	14.6	730	230	12.5	230	50.0	5300	25.5	520

(2) Individual Elements

Even though a direct correlation between water flow frequencies and amplitudes did not exist, the possibility remained that a shift in pressure oscillations away from a base line water flow would indicate a combustion stability shift. With this in mind, individual element water flow tests were designed to determine if the 'vena contracta' at the secondary tangential slot could be shifting and thus causing the pressure oscillations. To change the vena contracta characteristics, the secondary slot entrances were rounded in steps as shown in figure 86. The element was water flowed in condition 1 (Bill-of-Material) to establish a baseline frequency and amplitude of secondary cavity pressure fluctuation. The secondary cavity pressure oscillated at 150 cps and an amplitude of 3 psid. The element slot was reoperated to the shape of condition 2. Water flow revealed a secondary pressure fluctuation of 2.5 psid at 150 cps. With the slot revised as shown in condition 3 the cavity pressure was 2 psid at 150 cps. The final configuration, shown as configuration 4, gave cavity pressure oscillations of 2 psid at 150 cps.

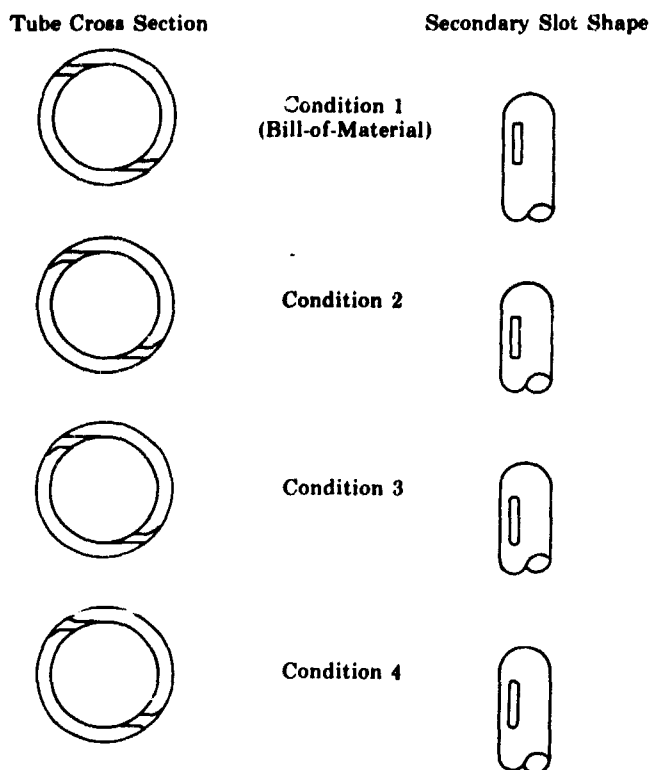


Figure 86. Oxidizer Element Slot Modifications for Water Flow Testing

FD 25236

An individual element GN_2 water flow rig that discharged into a pressurized chamber was fabricated. The pressurized chamber allows the adjustment of the density of the GN_2 to approach that of hydrogen in the preburner. Fuel-to-oxidizer momentum ratios could be equated with GN_2 -to-water momentum ratios with the GN_2 flow remaining unchoked. Flow conditions were varied to produce a range of momentum ratio from 0 to 20% and a primary-to-total flow split range from 0 to 100% about the nominal conditions. The conditions provided in table XVI were established as nominal test conditions.

Table XVI. Nominal Test Conditions

	E-8 Combination Tests	B-21 Flow Tests
Primary pressure drop (psid)	235.0	235.0
Secondary pressure drop (psid)	9.3	9.3
Fuel side pressure drop (psid)	83.0	83.0
Fuel temperature (°R)	147.0	540.0
Fuel flow (lb/sec/element)	14.1/252*	14.1/252*
Oxidizer flow (lb/sec/element)	9.1/252*	9.1/252*
Primary-to-total oxidizer flow split	0.59	0.59
Chamber pressure (psia)	560.0	145.0
Momentum ratio (fuel/oxidizer)	12.7	12.7

*Total injector flow/no. injector elements

A base primary and secondary effective area was established by calibrating the element with no GN₂ flowing through the fuel injector. The calibration was made over a primary-to-total flow split range of 0 to 100%. This calibration is presented in figure 87. The momentum ratio was varied by varying the primary, secondary, and fuel side pressure drops. This effect of momentum ratio on primary and secondary effective area is shown in figure 88. The primary area change at nominal momentum ratio (12.7) is a 1.0% area change for an 8.0% momentum ratio change. For the primary alone to produce an instability in chamber pressure of 10% amplitude, it was calculated that the primary flow must change 26.5%. This results in a momentum ratio change of 19.8%. This slope is also presented in figure 88. Comparison of these two slopes indicate that it was not possible for the momentum influence alone to have caused the observed combustion instability. The momentum ratio has the effect of increasing the primary area over the base area. This could be caused by a lowering of the static pressure at oxidizer discharge by the fuel velocity. Data from the combustion tests show that the primary injector, operating under nominal conditions, also had an area increase of approximately 15% above base calibrated area. Increasing the momentum ratio has the effect of decreasing the secondary area. At nominal momentum ratio (12.7) the secondary area is being reduced at the rate of 1% area change for 16% momentum ratio increases. For the secondary alone to produce 10% amplitude in chamber pressure, secondary flow must change 40%. This requires a momentum ratio change of 4.3%. This slope is also presented in figure 88. Comparison of these slopes shows that it would not be possible for this interaction of the secondary alone to cause the instability.

The fuel injector was calibrated with GN₂ with no flow through the oxidizer element. Momentum ratio was varied by varying primary, secondary, and fuel pressure drops. The chamber pressure was maintained as necessary to prevent the fuel pressure ratio from exceeding critical pressure ratio. The momentum was found to have no influence on fuel effective area as seen in figure 89; therefore changes in fuel area could not cause injector instability. Upon introduction of oxidizer element flow, the fuel area reduces 5% and remains at this level throughout the momentum ratio range. This phenomenon is unexplained but is not considered to have any bearing on the instability.

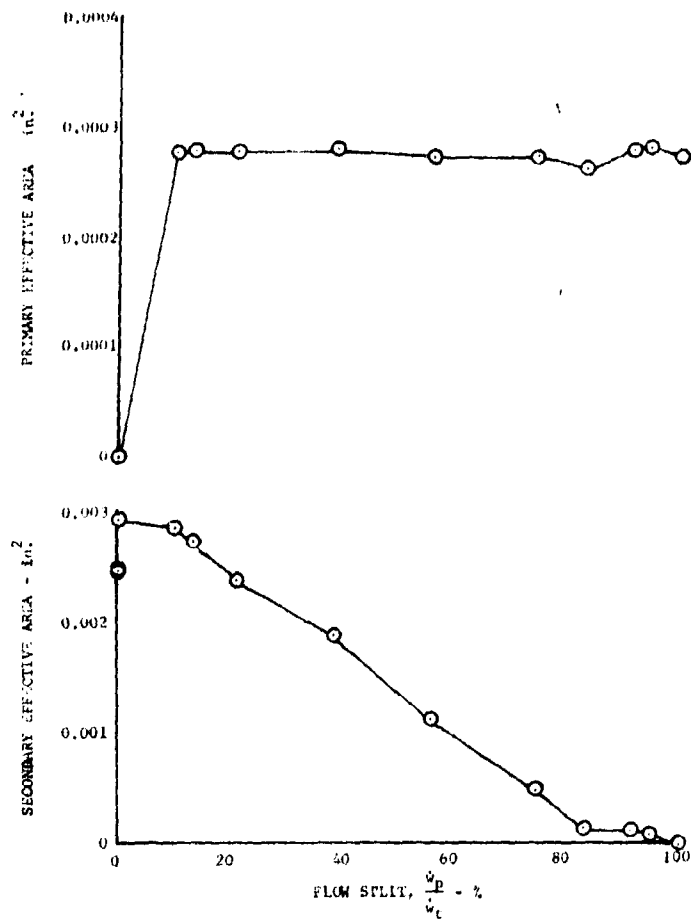


Figure 87. Oxidizer Element Calibration for
Injector Flow Tests

DF 68229

Dynamic pressure instrumentation was installed in the water and GN₂ flow rig (primary, secondary, fuel, and chamber) to measure any instability that might occur. This instrumentation indicated that instabilities of the frequency and amplitude observed during hot firings were not present.

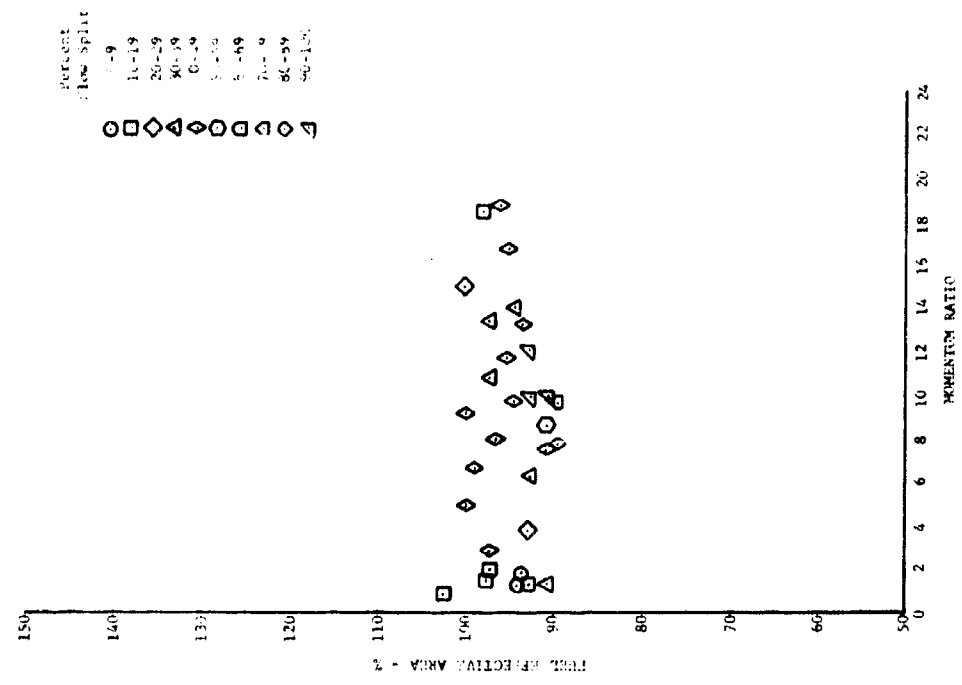


Figure 88. Effect of Momentum Ratio on Primary and Secondary Effective Area

DF 68230

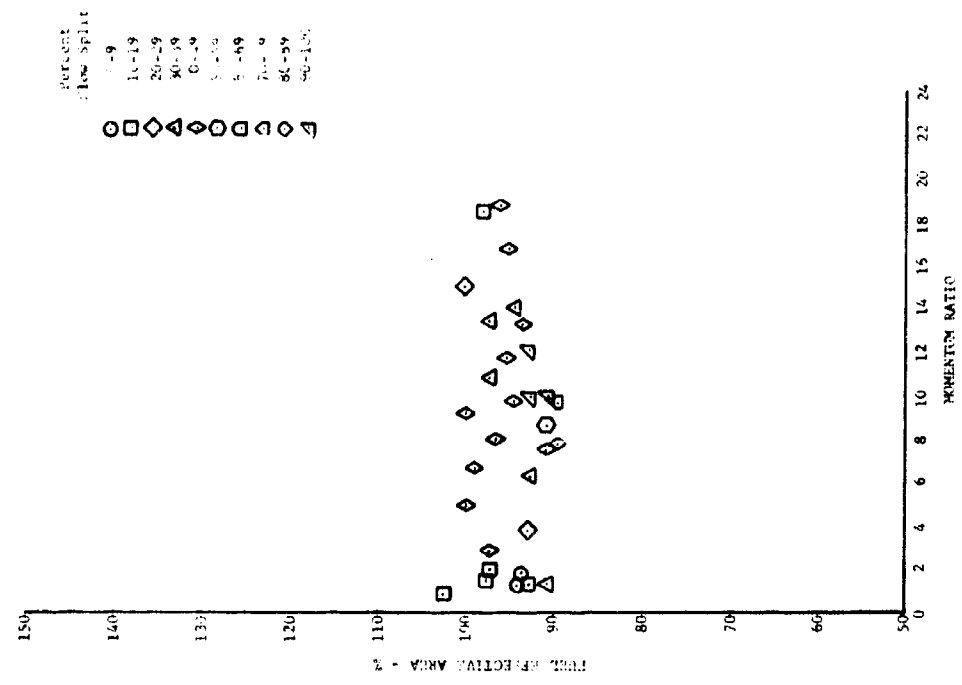


Figure 89. Effect of Momentum Ratio on Fuel Effective Area

DF 68231

Table XVII presents the test results of the injector area change per momentum ratio change as well as the required change to give 10% chamber pressure amplitude.

Table XVII. Injector Area Change Per Momentum Ratio Change

	Test Results (%/%)	Required for 10% Chamber Pressure Change (%/%)
Primary	1.0/-8.0	26.5/-19.8
Secondary	1.0/-16.0	40.0/-4.3
Fuel	None	--

The following conclusions were made from the flow tests:

1. The secondary oxidizer injector effective area is affected by fuel flow but the simulated effect was not large enough to produce the observed instability.
2. The primary injector effective area is also affected by fuel flow, but the effect is not predicted to be large enough to cause the instability.
3. The fuel effective area is not significantly influenced by oxidizer flow and does not cause the instability.

B. ROLLER BEARING DURABILITY TESTS

1. Introduction

The objective of the roller bearing durability program was to evaluate 55 x 96.5mm roller-bearings for use in the 250K fuel turbopump. Testing was conducted with liquid hydrogen cooling at a shaft speed of 48,000 rpm and with a 1700 lb radial load. The radial load requirement resulted from design studies of bearing loads based on hydraulic and vehicle maneuver loading, and the pump speed was established by the engine cycle studies. Preliminary bearing tests, during Phase I (Contract AF04(611)-11401), indicated that it was feasible to operate a roller bearing at these conditions, but that roller end wear and skewing could affect bearing repeatability and durability. The current program investigated the effects of roller length-to-diameter ratio, roller crowning, internal clearance, and roller-to-side rail clearance on roller end wear and bearing durability. The ultimate objective of the program is to conduct 10 hour endurance tests on ten sets of bearings.

2. Summary, Conclusions, and Recommendations

During the current program, which accumulated 58.1 hours of test time at 48,000 rpm, tests were conducted to evaluate the effects of roller length-to-diameter ratio, roller end-to-side rail clearance, internal clearance, and roller crowning on roller end wear and bearing durability. The test matrix, shown in figure 90, graphically shows the four variables and the bearing configurations evaluated. Table XVIII is a summary of the bearing tests conducted to date on this program. During all the tests, a 1700 lb radial load was applied to the load bearing resulting in an approximate 1445 lb radial load on the reaction bearing. Five bearing configurations (matrix points 3, 22, 23', 27', and 43') surpassed the 10 hour goal test duration at the design operating conditions.

Because of the limited scope of the bearing program and the many variables being evaluated, conclusions were necessarily made based on a single test of a particular bearing configuration unless abnormal test conditions indicated that a repeat test on a configuration was required. This technique was used to indicate the direction on the test matrix for subsequent tests in an effort to reduce the investigation to the most promising area.

Based on the roller bearing tests, it appears that both roller end wear and skewing can be minimized or eliminated by increasing the negative diametral internal clearance and increasing the side rail clearance over the normally used values. The 0.005 in. tight fit of the outer race on the rollers is the negative diametral clearance required to maintain a load on the rollers on the unloaded side of the bearing, when the bearing is operating at design conditions and fabricated from stainless steel alloy (AMS 5630). Roller skewing, which accounted for most of the bearing failures during the current program, was not found to be related to roller end wear or roller end-to-side rail clearance if sufficient negative internal clearance was incorporated in the bearing.

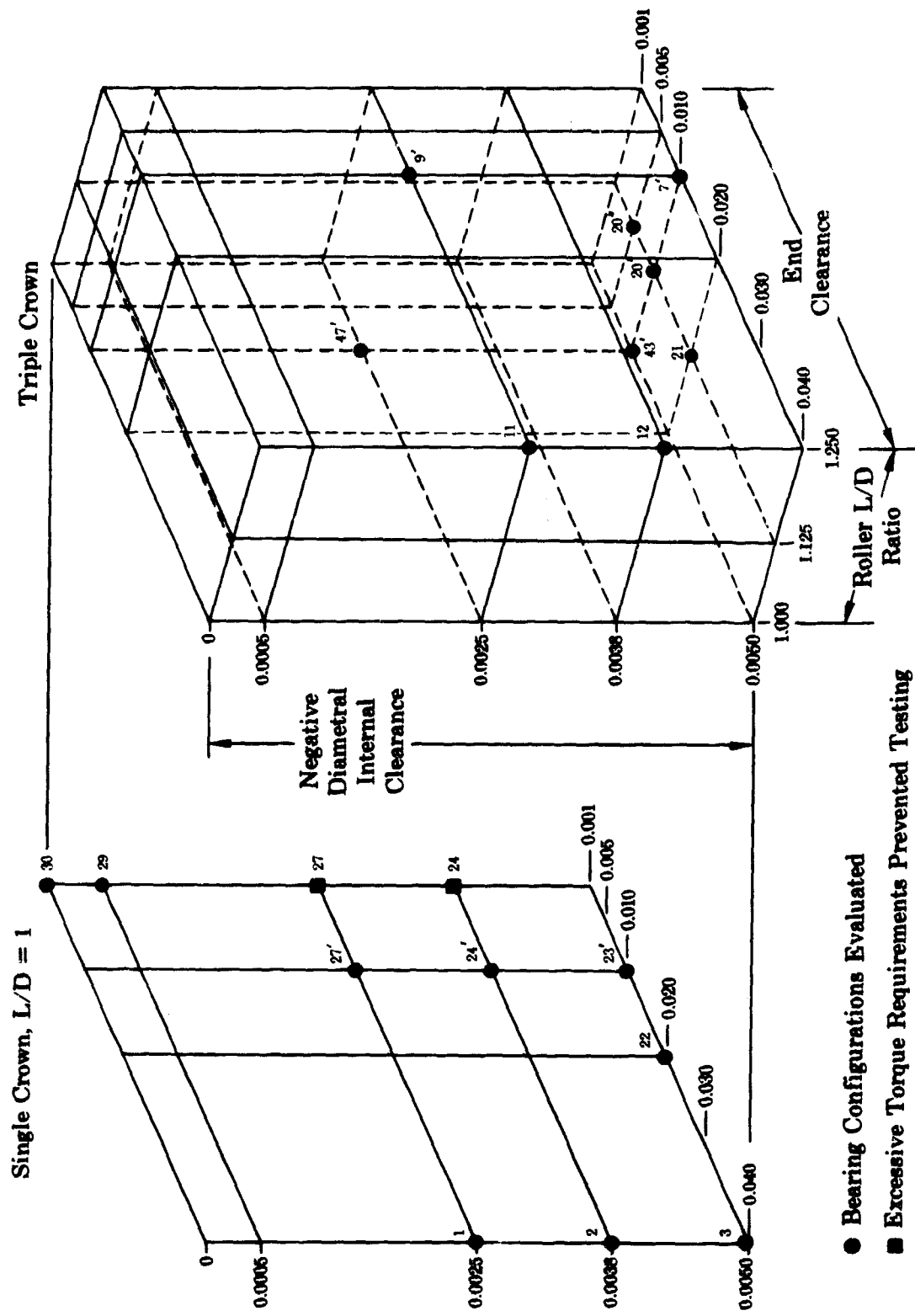


Figure 90. Roller Bearing Test Matrix

Table XVIII. Summary of Roll

Build No.	Date of Testing ⁽¹⁾	Identification S. N.	Matrix Point	Internal Clearance	Configuration End Clearance	L/D	Roller Crown	Accumulated Time at Speed (hr. cycle)	Total Accumulated Time (hr. cycle)
17	15-3-68	V-1	1	-0.0027	0.0395	1.000	Single	1.1/1	1.0/1
	18-3-68	V-2	2	-0.0038	0.0402	1.000	Single	1.1/1	1.0/1
18	26-3-68	V-1	1	-0.0027	0.0395	1.000	Single	1.2/3	1.1/1
		V-2	2	-0.0038	0.0402	1.000	Single	1.2/3	1.1/1
19	10-4-68	V-1	1	-0.0027	0.0395	1.000	Single	1.2/3	1.1/1
		V-2	2	-0.0038	0.0402	1.000	Single	1.2/3	1.1/1
20	8-5-68	V-1	1	-0.0027	0.0395	1.000	Single	1.3/4	2.0/6
		V-2	2	-0.0038	0.0402	1.000	Single	1.3/4	2.0/6
21	20-5-68	V-1	1	-0.0027	0.0395	1.000	Single	1.3/4	2.0/6
		V-2	2	-0.0038	0.0402	1.000	Single	1.3/4	2.0/6
22	27-5-68	V-1	1	-0.0027	0.0395	1.000	Single	2.2/7	4.3/11
	28-5-68	V-2	2	-0.0038	0.0402	1.000	Single	2.2/7	4.3/11
23	6-6-68	W-1	30	+0.0001	0.0007	1.000	Single	2.0/4	2.8/5
	7-6-68	W-2	29	-0.0006	0.0007	1.000	Single	2.0/4	2.8/5
24	27-6-68	W-1	30	+0.0001	0.0007	1.000	Single	2.0/7	4.2/11
		W-2	29	-0.0006	0.0007	1.000	Single	2.0/7	4.2/11
25A	12-7-68	X-1	27	-0.0026	0.0090	1.000	Single	9.7/17	10.0/17
	18-7-68	X-2	24	-0.0037	0.0097	1.000	Single	9.7/17	10.0/17

NOTE: Number 1 bearing is reaction bearing. Number 2 bearing is at load position.

(1) All test speeds were run at 48,000 rpm except Build No. 19, which was at 20,000 rpm.

(2) No. 15 roller had begun skewing and turbine end of roller had worn a 0.007 in. bevel at corner radius.

I. Summary of Roller Bearing Tests

Accumulated Time at Speed (hr/cycles)	Total Accumulated Time (hr/cycles)	Radial Load (lb)	Cooling Flow (gpm)	Roller End Wear (in.)		Remarks
				Total Average	Maximum	
1.1/2	2.0/3	1445	30	None-Scuffing On Turbine End	-	Bearing condition excellent. Rig rebuilt because of moisture.
1.1/2	2.0/3	1700	30	None-Scuffing On Rear End	-	
1.2/3	2.4/4	1445	28	Same as Build 17	-	Bearing condition excellent. Rig rebuilt because of failed slave bearing.
1.2/3	2.4/4	1700	32	Same as Build 17	-	
1.2/3	2.4/5	1445	15	None-Scuffing On Both Ends	-	Testing terminated during acceleration to test speed because of unequal cooling flow through test bearings. Flow split was balanced by adjusting valve in load bearing discharge line but rig would not rotate. Rig rebuilt because of jammed rollers and to change shaft thrust loading.
1.2/3	2.4/5	1700	48	None-Scuffing On Both Ends	-	
1.3/4	2.6/6	1170	16	None-Scuffing On Both Ends	-	Test terminated because of rising slave-bearing outer race temperature and high vibration on turbine end.
1.3/4	2.6/6	1375	29	None-Scuffing On Both Ends	-	Rig rebuilt to increase tie bolt load by incorporating new design tie bolt.
1.3/4	2.6/6	N/A	N/A	None-Scuffing On Both Ends	-	Rig would not rotate when cold after two rotations during cooldown.
1.3/4	2.6/6	N/A	N/A	None-Scuffing On Both Ends	-	Locked up at ambient. Freed. Tried cooldown again without rotation, then tried again. Locked up cold and at ambient. Rebuilt with slave bearing not loaded at ambient.
2.2/7	4.3/11	1445	25	0.0004	0.0008	Completed three accelerations to speed. Test terminated by rising outer race temperature on reaction bearing. One roller in reaction bearing failed after 2.2 hours at design speed.
2.2/7	4.3/11	1700	25	0.0009	0.0011	
2.0/4	2.8/5	1480	32	0.0004	0.0121	Completed four accelerations to rated speed. Test terminated because of rise in slave bearing outer race temperature and turbine vibration. Slave bearing, turbine, and shaft replaced and balance procedure revised to incorporate a final assembly balance of the rotor assembly on the test bearings.
2.0/4	2.8/5	1740	26	0.0031	0.0062	
2.9/7	4.2/11	1445	29	0.0091	0.0113	Completed three accelerations to speed. Test was terminated by rise in load bearing outer race temperature. One roller and inner race side rails in load bearing failed after 2.9 hours at design speed.
2.9/7	4.2/11	1700	27	0.0082	0.0123	
9.7/17	10.0/17	1445	30	0.0010	0.0013	Completed 17 accelerations to speed. Testing was terminated because of rapid increase in vibration level. Both races of the load bearing were broken but no rollers had skewed. Reaction bearing was in good condition.
9.7/17	10.0/17	1700	30	0.0003 (Heavy Impact Damage)	0.0017	

er radius.

Table XVIII. Summary of Roller Bearing Tests (Continued)

Build No.	Date of Testing ⁽¹⁾	Identification S N	Matrix Point	Internal Clearance	Configuration End Clearance	L/D	Roller Crown	Accumulated Time at Speed (hr/cycles)	Total Accumulated Time (hr/cycles)	Radial Load (lb)	Cooling Flow (gpm)
26	23-7-68	Y-1	11	-0.0025	0.0388	1.250	Triple	0.2/1	0.2/1	1440	15
		Y-2	12	-0.0038	0.0414	1.250	Triple	0.2/1	0.2/1	1700	15
27	29-7-68	Y-1A	11	-0.0023	0.0388	1.250	Triple	0.3/2	0.3/2	1440	15.5
		Y-2	12	-0.0038	0.0414	1.250	Triple	0.5/3	0.5/3	1700	15.5
28	2-8-68	Z-1	47'	-0.0026	0.0098	1.000	Triple	6.4/14	6.7/14	1440	30
	6-8-68	Z-2	43'	-0.0051	0.0097	1.000	Triple	6.4/14	6.7/14	1700	30
29	12-8-68	AA-1	9'	-0.0027	0.0097	1.250	Triple	3.1/6	3.2/6	1440	31
	14-8-68	AA-2	7'	-0.0049	0.0095	1.250	Triple	3.1/6	3.2/6	1700	31
30	16-8-68	X-1	27'	-0.0028	0.0090	1.000	Single	16.0/27	16.5/27	1445	31
	20-8-68	Z-2	43'	-0.0049	0.0097	1.000	Triple	12.8/24	13.2/24	1700	31
31	23-8-68	BB-1	20'	-0.0051	0.0098	1.125	Triple	1.0/1	1.0/1	1440	29
	26-8-68	BB-2	20"	-0.0050	0.0048	1.125	Triple	1.0/1	1.0/1	1700	29
32	29-8-68	CC-1	23'	-0.0049	0.0099	1.000	Single	(4)2.3/6	(4)2.4/6	1445	29
	30-8-68	CC-2	22	-0.0052	0.0199	1.000	Single	(4)2.3/6	(4)2.4/6	1700	29

(3) Severe scoring on both ends of rollers prevented any meaningful end wear measurements.

(4) Conglomerate bearings. CC-1 high time roller had 1.5 hours, 3 cycles before Build 32 tests. CC-1 cage had 0.3 hour, 1 cycle. CC-1 races were unused. CC-2 rollers had 2.2 hours, 7 cycles before Build 32 tests. CC-2 cage had 0.3 hour, 1 cycle. CC-2 races were unused.

Summary of Roller Bearing Tests (Continued)

Accumulated Time at Speed (hr/cycles)	Total Accumulated Time (hr/cycle)	Radial Load (lb)	Cooling Flow (gpm)	Roller End Wear (in.) Total Average	Maximum	Remarks
0.2/1	0.2/1	1440	15	None(2)	0.007	Testing terminated after 0.2 hours at design speed of first cycle because of increase in reaction bearing outer race temperature and vibration levels. One roller of reaction bearing was beginning to skew and was wedged in side rails. Inner race of reaction bearing was not properly seated on shaft. Load bearing in good condition.
0.2/1	0.2/1	1700	15	None	N A	
0.3/2	0.3/2	1440	15.5	0.0004	0.0005	Reaction bearing incorporated new rollers and cage load bearing same as previous test. Testing was terminated early in second cycle because of rise in reaction bearing outer race temperature and erratic speed. One roller in reaction bearing had skewed and rubbed against adjacent roller. Load bearing in good condition.
0.5/3	0.5/3	1700	15.5	0.0001	0.0003	
5.4/14	6.7/14	1440	30	0.0039	0.0075	Testing terminated after 1 minute at design speed of cycle 14 because of increase in reaction bearing outer race temperature and vibration levels. One roller in reaction bearing had skewed. Load bearing in good condition.
5.4/14	6.7/14	1700	30	0.0026	0.0070	
3.1/6	3.2/6	1440	31	0.0037	0.0220	Testing terminated after 0.1 hour at design speed of 6th cycle because of increase in reaction bearing outer race temperature and vibration levels. The rollers in reaction bearing were beginning to skew. Load bearing in good condition.
3.1/6	3.2/6	1700	31	0.0004	0.0010	
6.0/27	16.5/27	1445	31	0.0021	0.0029	Testing terminated after 6.3 hours at design speed when load bearing had accumulated 12.8 hours; reaction bearing accumulated 16 hours. Both bearings in excellent condition.
2.8/24	13.2/24	1700	31	0.0032	0.0095	
1.0/1	1.0/1	1440	29	0.0002	0.0005	Testing terminated after first cycle. Shaft locked when attempted to start second cycle and after six attempts to free shaft and start rig. Shaft locked tight. Teardown revealed the load bearing rollers were wedged between the side rails and the rollers were heavily scored on both ends. Pitting was evident on roller OD and on roller tracks on inner and outer races. Reaction bearing in good condition except for cracked outer race.
1.0/1	1.0/1	1700	29	(3)	(3)	
2.3/6	(4)2.4/6	1445	29	0.0016	0.0021	Testing terminated after 0.1 hour on 6th cycle because of increase in vibrations, increase in slave bearing temperature, and decay in speed. Teardown inspection showed turbine end of shaft had cracked and bent causing heavy rub of turbine on housing. Test bearings in good condition except for cracked outer race on reaction bearing.
2.3/6	(4)2.4/6	1700	29	0.0013	0.0020	

CC-1 cage had 0.3 hour, 1 cycle.
 CC-2 cage had 0.3 hour, 1 cycle.

A

Table XVIII. Summary of Roller Bearing T

Build No.	Date of Testing ⁽¹⁾	Identification		Internal Clearance	Configuration		Roller Crown	Accumulated Time at Speed (hr/cycles)	Total Accumulated Time (hr/cycles)
		S/N	Matrix Point		End Clearance	L/D			
33	10-9-68	DD-1	20'	-0.0050	0.0098	1.125	Triple	1.3/5	1.4/5
	11-9-68	DD-2	21	-0.0051	0.0198	1.125	Triple	1.3/5	1.4/5
34	20-8-68	EE-1	23'	(A)-0.0039	0.0105	1.000	Single	(5)2.3/6	(5)2.4/6
		EE-2	22	(B)-0.0042	0.0204	1.000	Single	(5)2.3/6	(5)2.4/6
35	25-9-68	EE-1	23'	(A)-0.0039	0.0105	1.000	Single	(5)6.4/15	(5)6.8/16
	26-9-68	EE-2	22	(B)-0.0042	0.0204	1.000	Single	(5)6.4/15	(5)6.8/16
36	3-10-68	EE-1	23'	(A)-0.0039	0.0105	1.000	Single	(6)14.9/31	(6)15.5/32
	8-10-68	EE-2	22	(B)-0.0042	0.0204	1.000	Single	(6)14.9/31	(6)15.5/32
37	18-10-68	FF-1	3	(C)-0.0040	0.0392	1.000	Single	3.9/3	4.3/7
	21-10-68	FF-2	22	(D)-0.0041	0.0196	1.000	Single	3.9/3	4.3/7

(5) Conglomerate bearings from Build 32. EE-1 high time rolling had 3.8 hours, 9 cycles after Build 32 tests. EE-1 cage had 2.5 hours, 7 cycles. EE-1 and EE-2 inner race have 2.3 hours, 6 cycles. EE-1 and EE-2 outer races are new parts of steel alloy (AMS 626). EE-2 rollers had 4.5 hours, 13 cycles after Build 32 tests. EE-2 cage had 2.5 hours, 7 cycles.

(6) Conglomerate bearings from Build 35. EE-1 high time rollers had 16.4 hours, 34 cycles after Build 36 tests. EE-1 and EE-2 inner races had 14.9 hours, 31 cycles. EE-1 and EE-2 outer races had 12.6 hours, 25 cycles. EE-2 rollers had 17.0 hours, 38 cycles, EE-1 and EE-2 cages had 15.1 hours, 32 cycles.

(7) Load bearing load ring coolant seal failed causing coolant leak around load bearing negating flow split determination. Total test bearing coolant supply flow was 60 gpm and bearing outer race temperatures were normal.

(8) Higher than normal cooling flow was used to maintain slave ball bearing outer race temperature within operating limits.

(A) Equivalent to -0.0049 fit of stainless steel (AMS 5630) outer race

(B) Equivalent to -0.0052 fit of stainless steel (AMS 5630) outer race

(C) Equivalent to -0.0050 fit of stainless steel (AMS 5630) outer race

(D) Equivalent to -0.0051 fit of stainless steel (AMS 5630) outer race

Summary of Roller Bearing Tests (Continued)

Roller Crown	Accumulated Time at Speed (hr/cycles)	Total Accumulated Time (hr/cycles)	Radial Load (lb)	Cooling Flow (gpm)	Roller End Wear (in.)		Remarks
					Total Average	Maximum	
Triple	1.3/5	1.4/5	1440	30	None-Scuffing On Turbine Ends	0.0002	Testing terminated after 1 minute on 5th cycle because of a decay in coolant flows, and an increase in vibrations and slave bearing outer race temperature. Teardown inspection showed the bellows seal had failed, the slave bearing inner race was spalled, and there was light rub on the turbine and turbine lab seal. Test bearings in good condition except for cracked outer race on reaction bearing.
Triple	1.3/5	1.4/5	1700	30	None-Scuffing On Turbine Ends	0.0001	
Single Single	(5)2.3/6 (5)2.3/6	(5)2.4/6 (5)2.4/6	N A N A	N A N A	N A N A	N A N A	Test bearings identical to CC-1 and CC-2 except for new outer races which are made from steel alloy (AMS 6260) carburized on the ID. Testing terminated during initial turbine pressurization because of failure of turbine housing. No data had been accumulated at time of failure. Turbine and turbine housing replaced on next build.
Single Single	(5)6.4/15 (5)6.4/15	(5)6.8/16 (5)6.8/16	1445 1700	36 24	0.0017 0.0027	0.0045 0.0047	
Single Single	(6)14.9/31 (6)14.9/31	(6)15.5/32 (6)15.5/32	1445 1700	(7) (7)	0.0020 0.0044	0.0072 0.0068	Same test bearings as previous build. Testing terminated after 8.4 hours at design speed when outer races had accumulated 12.6 hours. Both test bearings in good condition.
Single Single	3.9/3 3.9/3	4.3/7 4.3/7	1440 1700	33 33	0.0011 0.0002	0.0022 0.0004	

9 cycles after Build 32 tests. EE-1 cage had 2.5 hours. E-2 outer races are new parts of steel alloy (AMS 6260). 2.5 hours, 7 cycles.

8, 34 cycles after Build 36 tests. E-2 outer races had 12.6 hours, 25 cycles. 8, 32 cycles.

bearing negating flow split determination. Total test were normal.

race temperature within operating limits.

Table XVIII. Summary of Roller Bearing Test

Build No.	Date of Testing	Identification S/N Matrix Point	Internal Clearance	End Clearance	L/D	Roller Crown	Accumulated Time At Speed (hr/cycles)	Total Accumulated Time (hr/cycles)	Ra I.o (11)
38	25-10-68	FF-1 3	(C)-0.0040	0.0392	1.000	Single	6.2/4	6.7/8	144
		FF-2 22	(D)-0.0041	0.0196	1.000	Single	6.2/4	6.7/3	170
39	30-10-68	FF-1 3	(C)-0.0040	0.0392	1.000	Single	9.9/6	10.6/12	144
	31-10-68	FF-2 22	(D)-0.0041	0.0196	1.000	Single	9.9/6	10.6/12	170
40	6-11-68	GG-1 3	(A)-0.0028	0.0411	1.000	Single	1.6/1	1.6/1	144
		GG-2 3	(B)-0.0031	0.0396	1.000	Single	1.6/1	1.6/1	170
41	18-11-68	HH-1 3	(C)-0.0036	0.0391	1.000	Single	10.0/6	10.0/6	144
	19-11-68	HH-2 3	(D)-0.0040	0.0393	1.000	Single	10.0/6	10.0/6	170
42	2-12-68	JJ-1 22	(E)-0.0044	0.0202	1.000	Single	15.3/305	15.4/305	1440
	5-12-68	JJ-2 22	(F)-0.0043	0.0202	1.000	Single	15.3/305	15.4/305	1700

(A) Equivalent to -0.0048 fit of stainless steel (AMS 5630) outer race
 (B) Equivalent to -0.0051 fit of stainless steel (AMS 5630) outer race
 (*) Heavy impact damage of rollers prevented any meaningful end wear measurements
 (C) Equivalent to -0.0046 fit of stainless steel (AMS 5630) outer race
 (D) Equivalent to -0.0050 fit of stainless steel (AMS 5630) outer race
 (E) Equivalent to -0.0054 fit of stainless steel (AMS 5630) outer race
 (F) Equivalent to -0.0053 fit of stainless steel (AMS 5630) outer race

Summary of Roller Bearing Tests (Concluded)

g Test	Accumulated Time At Speed (hr/cycles)	Total Accumulated Time (hr/cycles)	Radial Load (lb)	Cooling Flow (gpm)	Roller End Wear (In.)		Remarks
					Total Average	Maximum	
144 170	6.2/4 6.2/4	6.7/8 6.7/8	1440 1700	(8) (8) 45 45	0.0010 0.0003	0.0021 0.0005	Testing terminated after 2.3 hours of 1st cycle because of increase in reaction and slave bearing outer race temperatures. The slave bearing cage was beginning to fall. The test bearing outer races showed some increase in thermal cracks but were reused in next build.
144 170	9.9/6 9.9/6	10.6/12 10.6/12	1440 1700	33 33	0.0011 0.0003	0.0019 0.0004	Test rig modified to provide slave bearing inner race cooling. Testing terminated after 2 hours of the 2nd cycle because of increase in vibrations and load bearing outer race temperature and speed shift. The load bearing outer race cracked directly under the point of radial loading. The reaction bearing was in good condition except for increased thermal cracking on outer race. Slave bearing and turbine end of rig in good condition.
144 170	1.6/1 1.6/1	1.6/1 1.6/1	1440 1700	36 36	0.0001 (*)	0.0005 (*)	Test bearings incorporated Inconel 718 (AMS 5663) outer races. Testing terminated after 1.5 hours of the 1st cycle because of increase in load bearing outer race temperature and vibrations. Teardown revealed that the load bearing outer race had failed and the rollers and inner race were heavily damaged. The reaction bearing was in good condition except for material spalling in the roller track of the outer race.
144 170	10.0/6 10.0/6	10.0/6 10.0/6	1440 1700	31 31	0.0082 0.0021	0.0120 0.0048	Test bearings incorporated steel alloy (AMS 6265) outer races. Testing terminated after 1 minute of the 6th cycle when a speed shift was detected and the reaction bearing outer race temperature increased. Teardown revealed a skewed roller in the reaction bearing. Slight inner race side rail chipping and moderate thermal cracks in the outer race were noted. The load bearing was in good condition and can be reused.
144 170	15.3/305 15.3/305	15.4/305 15.4/305	1440 1700	31 31	0.0070 0.0005	0.0098 0.0014	Test bearings similar to previous build except for increased fits and decreased end clearance. After completion of 125 of the goal duration a coolant reduction survey was performed. This indicated that the bearing outer race temperature was not affected when coolant flow was reduced to approximately 10 gpm. Cooling flow was returned to normal operating level and 295 additional acceleration cycles were completed to conclude the program. Teardown inspection revealed all parts in excellent condition except for surface thermal cracks on the outer races in the cage contact areas.

The increased length-to-diameter ratio, triple crown rollers did not demonstrate the anticipated improvement in resistance to roller skewing over $L/D = 1.000$ single crown rollers. The longer L/D rollers demonstrated more skewing tendency than the $L/D = 1.0$ rollers with the same internal clearance and side rail clearance as indicated by a comparison of matrix points 1 and 11. Comparing matrix points 9', 47', and 27' as well as 7', 43', and 23' confirms this trend. Refer to table XVIII.

The durability of a bearing configuration with a 0.005 in. negative diametral fit (matrix point 43') was initially demonstrated on Build 30. The three subsequent tests on bearings with the 0.005 in. negative diametral fit were terminated prematurely because of cracking of the reaction bearing outer race. An analysis of the cracked races indicated that the failures were the result of flexing stress cycles. The solution to the outer race cracking problem appears to be adjusting the ring design to keep the inside diameter in compression or to use a material with more elongation and fracture toughness than the stainless steel (AMS 5630). An outer race design fabricated from steel alloy (AMS 6260) with the inner diameter carburized and hardened has demonstrated 12.6 hours on two bearings without failure, and 9.9 hours on two other bearings before the outer race of the load bearing failed. The most promising bearing configuration tested used stainless steel (AMS 5630) inner race and rollers; an outer race guided Armalon cage; a steel alloy (AMS 6265) outer race, single crown, $L/D = 1.0$ rollers with 0.020 in. roller end-to-inner race side rail clearance and 0.0043 in. negative diametral internal clearance. It is recommended that bearings of this configuration be used in the fuel turbopump.

3. Analysis

Based upon experience gained during the fuel pump technology program under Contract NAS8-11714, a roller bearing configuration was selected for the 250K fuel turbopump. The spring rate and capacity requirements of the pump design necessitated a roller bearing to provide high radial stiffness to minimize instabilities associated with rotor bouncing or rocking modes. The design speed of 48,000 rpm and a shaft diameter of 55mm selected for the fuel turbopump resulted in a bearing DN requirement of 2.64×10^6 . A preliminary calculation of the radial bearing loads indicated that the maximum loading occurs on the front fuel turbopump bearing and is approximately 1700 lb. Analytical studies indicated that 55 x 96.5mm roller bearings should have a life in excess of the 10 hour life requirement at this value of load as shown in figure 91. The 55 x 96.5mm bearing is the same as bearing B in figure 91 except that the outer race has been thinned to 96.5mm outside diameter.

After conducting screening tests on several roller bearing and cage configurations during the Phase I (Contract AF04(611)-11401) program, the bearing configuration selected for test evaluation was a 55 x 96.5mm bearing with races and rollers of stainless steel (AMS 5630) and a cage fabricated from Armalon. The roller bearing is an inner race flanged configuration and the cage is outer race piloted. The outer race is a thin ring design that was sized to permit an outside diameter clearance in the housing at operating conditions and is retained by a lateral load across the end faces. This feature provided a stiff spring shaft supporting arrangement. The flexible outer race permitted the incorporation of a negative internal fit on the rollers, which is desirable to permit more load sharing among the rollers, thereby reducing the roller

loads and ensuring that the rollers are never completely unloaded. This negative internal clearance also provides more rotor restraint and reduces the hydraulic-mechanical vibrator interchange on the turbopump.

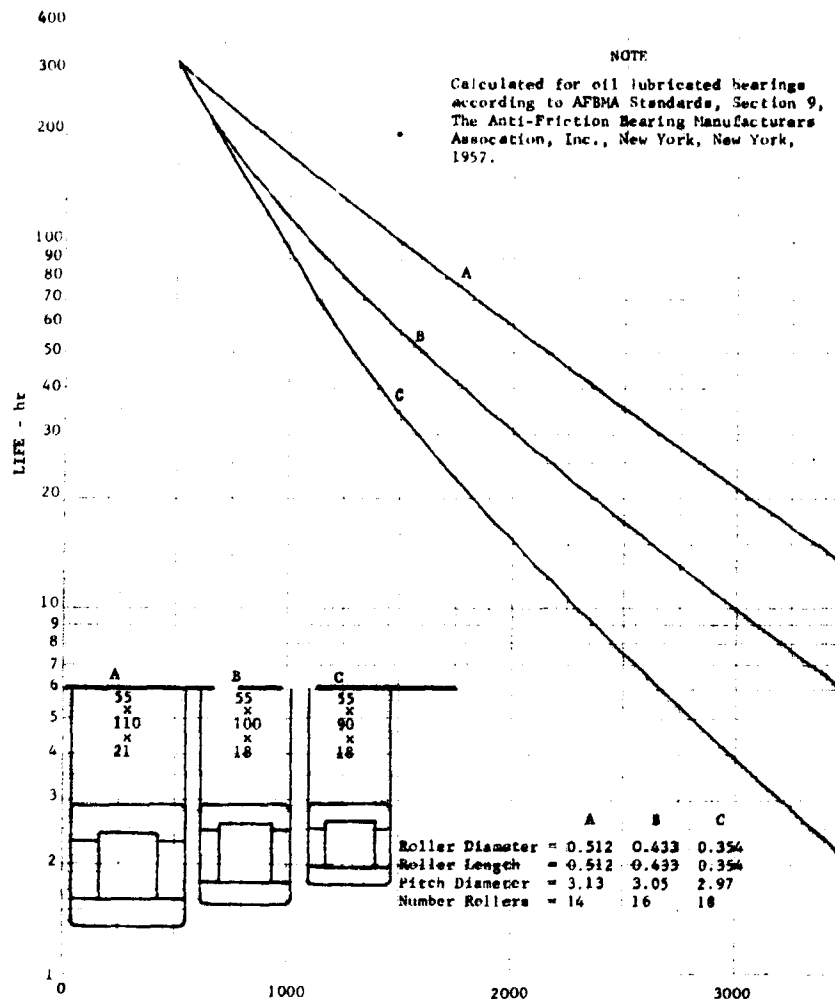


Figure 91. Roller Bearing Fatigue Life vs Radial Load DF 52756 (50,000 rpm)

The initial testing with roller bearings operating at these high shaft speeds and radial loads indicated that roller end wear was most probably the failure mode that would prevent obtaining the goal duration. Subsequent testing showed that roller end wear could be significantly reduced if the inner race side rail-to-roller end clearance was increased from the normally used 0.001 in. to 0.040 in.; however, roller skewing resulted.

It was theorized that if the outer race could be used as the guiding mechanism by using its deflection to conform to the roller crown, and if the rollers were always in contact with both the inner and outer races that skewing could be eliminated. Because the existing bearing analysis programs were not applicable to this unique bearing configuration, a computer program was formulated to aid in the understanding of the bearing elements.

This new computer program indicated that a radial internal fit of approximately 0.005 in. at ambient assembly conditions with stainless steel, rollers and races was required to maintain sufficient contact between the rollers and both races in the unloaded zone when the 1700 lb radial load was applied. This ambient assembly fit is adjusted when other race materials are used to provide an equivalent operating condition. Testing with this internal fit has eliminated roller skewing, and roller end wear values of approximately 0.001 in. have been obtained after 10 hours of testing. This tight internal fit has caused failure of some outer races and it is believed that these failures can be eliminated by using material with improved fracture toughness and elongation such as carburized steel alloy (AMS 6260 or AMS 6265) or an outer race that is maintained with a compressive surface by shrinking a ring over the outside diameter of the hardened roller track material. The first of these approaches was investigated, and six bearings surpassed the goal duration with excellent results. Two others completed 9.9 hours before one outer race failed in the area of thermal checks caused by the cage contact.

The effect of surface hardness on calculated radial roller bearing life is based on the following equation:

$$L = \left(\frac{C'}{F_e}\right)^{10/3}$$

when hardness is less than 58

$$C' = C \left(\frac{Rc}{58}\right)^{3.6}$$

when hardness is over 58

$$C' = C$$

where:

Rc = Rockwell Hardness
 C = Basic Dynamic Capacity
 Fe = Equivalent Radial Load
 L = Revolutions x 10⁶

This equation is from T. A. Harris, Rolling Bearing Analysis, John Wiley & Sons, 1966, and indicates that as the bearing contact surface hardness is decreased from a Rockwell Hardness of 58 that the calculated bearing life is also decreased. Because the carburized surface hardness of the steel alloy (AMS 6260) outer races is in the Rc 59 to 61 range it is anticipated that the life of these races should be approximately the same as the stainless steel (AMS 5630) races, which have a hardness in the Rc 56 to 62 range.

4. Hardware Description
 - a. Bearing Test Rig

The rig that was used for these tests was the same rig that was used in the tests during Phase I (Contract AF04(611)-11401) except that modifications

were made to the load bearing mounting and to the drive turbine labyrinth seal areas. These modifications were made to improve the alignment of the load bearing and to improve control of the thrust load on the turbine ball bearing.

As shown in figure 92, the test rig consists of four housings that enclose a shaft driven by a radial inflow gaseous nitrogen turbine. The shaft is supported by a 35mm ball bearing (slave bearing) at the turbine drive end and a 55mm roller bearing (reaction bearing) at the opposite end. The test load is applied through another 55mm test bearing (load bearing) that is located adjacent to the reaction bearing. This bearing test rig has the versatility required to test roller bearings with length-to-diameter ratios of 1.000, 1.125, and 1.250.

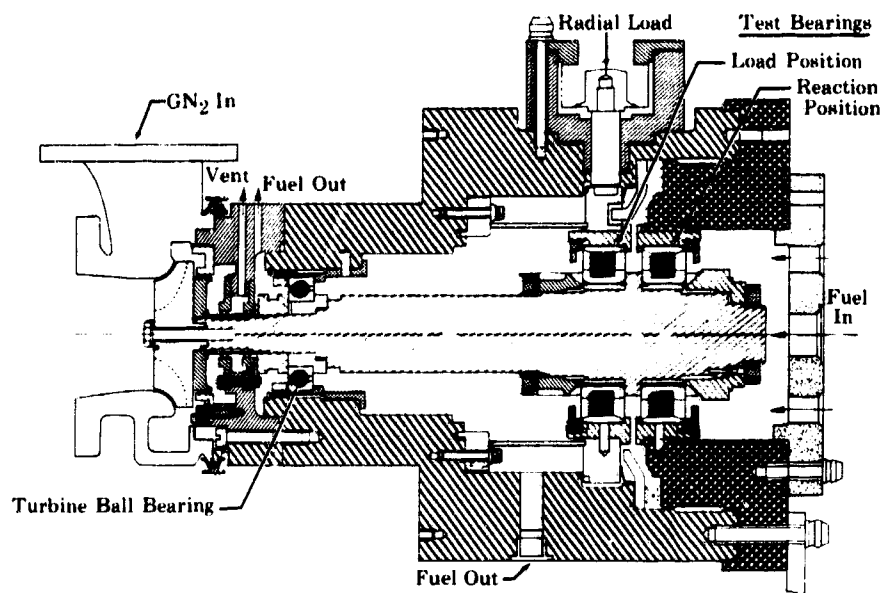


Figure 92. Roller Bearing Test Rig Cutaway

FD 19278H

The test rig is operated at a shaft speed of 48,000 rpm with a 1700 lb radial load applied to the shaft through the load bearing. The load bearing is mounted in a flexure unit that provides axial stiffness and bearing alignment while offering radial flexibility when subjected to actuator loads. The radial load is applied by a pneumatic actuator through the load bearing. The reaction test bearing, which is just aft of the load bearing, absorbs 85% of the applied radial load and the turbine ball bearing supports the balance of the load (15%).

b. Bearing Configuration

Figure 93 shows the basic bearing configuration used during these tests. A common width was used on the inner and outer races to minimize the changes required to the test rig rotor when different L/D ratio rollers were tested. The roller track width on the inner races was adjusted by grinding the side rails to establish the desired roller-to-side rail clearance with each of the different roller configurations. Some tests were conducted with inner and outer races that were 0.8268 in. wide instead of 0.935 in. wide because these races were available from the Phase I (Contract AF04(611)-11401) program. These narrow races were used on the following bearings: S/N V-1, V-2, W-1, W-2, X-1, X-2, CC-1, CC-2, EE-1, and EE-2.

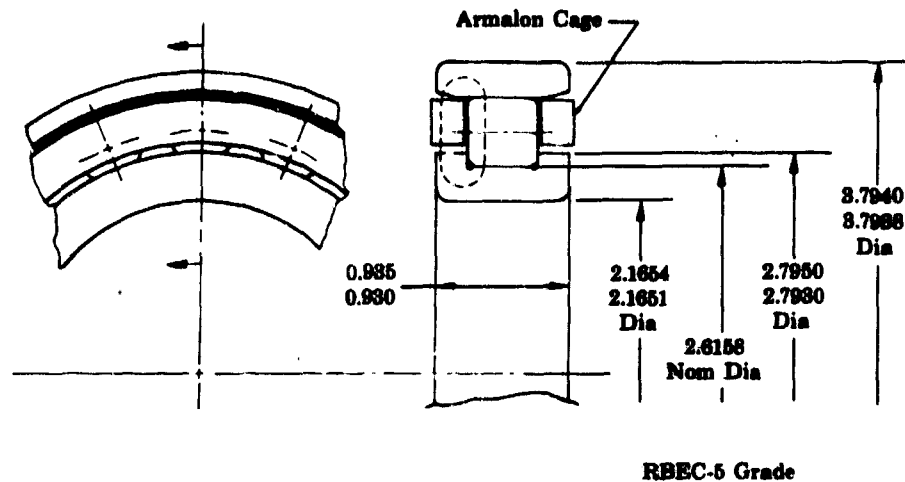


Figure 93. 250K Roller Bearing Configuration FD 25522

Four types of stainless steel (AMS 5630) rollers were used in the bearing program. Single crown rollers with a length-to-diameter ratio of 1.000, and triple crown roller with length-to-diameter ratio of 1.000, 1.125, and 1.250 have been tested. These roller configurations are shown in figure 94.

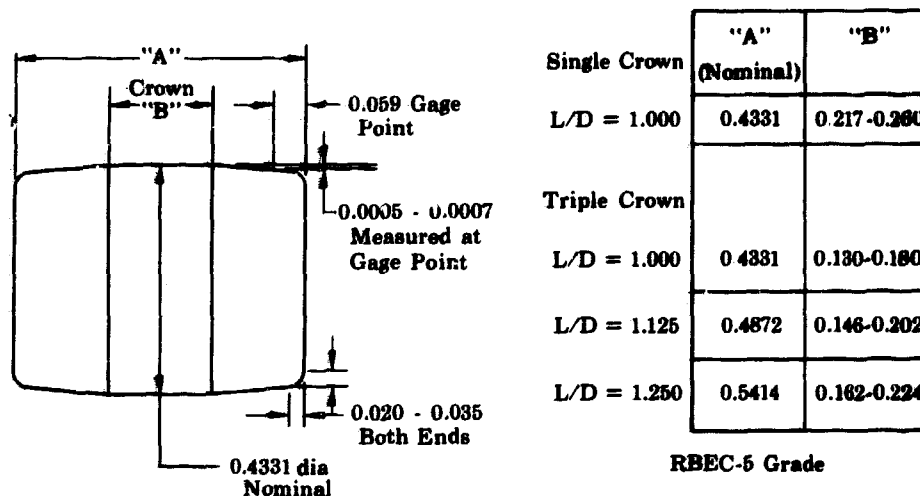


Figure 94. Roller Configuration FD 25523A

Roller length-to-diameter ratio, the roller end-to-side rail clearance, the amount of negative diametral internal clearance, and the amount of roller crowning were the variables to be evaluated during the current program testing before the final bearing design could be selected. The negative diametral clearance of 0.005 in. was found to minimize the roller end wear and to effectively control roller skewing. By maintaining a load on all of the rollers, the beam structure of the outer race deformed around the elements providing roller alignment and skewing restraint. However, the negative diametral fit did adversely affect the outer race durability because of the sensitivity of this hard material to particle ingestion and irregularities in the microstructure. Substitute outer race material of steel alloy (AMS 6260 and AMS 6265) was selected. The

inside diameter of the outer race was carburized to a depth of approximately 0.043 in. and hardened to a value of Rc 60. The core of the outer race was maintained at a hardness value of Rc 40. This outer race configuration was selected because it could be carburized and hardened, which offered a hard-wear resistant roller track, and it put the inside diameter in compression to minimize the effects of bearing loads. The notch sensitivity and impact resistance of the outer race was improved significantly with this material.

c. Test Facility

Testing of the roller bearing test rig is being conducted on the B-13 test stand shown schematically in figure 95. Gaseous nitrogen is supplied for rig purging, for turbine drive, and for actuating the pneumatic load piston. Gaseous hydrogen is used as the final prerun rig purge and liquid hydrogen is used as the bearing coolant. Test parameters such as being outer race temperature, speed, vibration levels, coolant flowrate, coolant supply and discharge conditions, and load are monitored and recorded.

d. Test Procedures

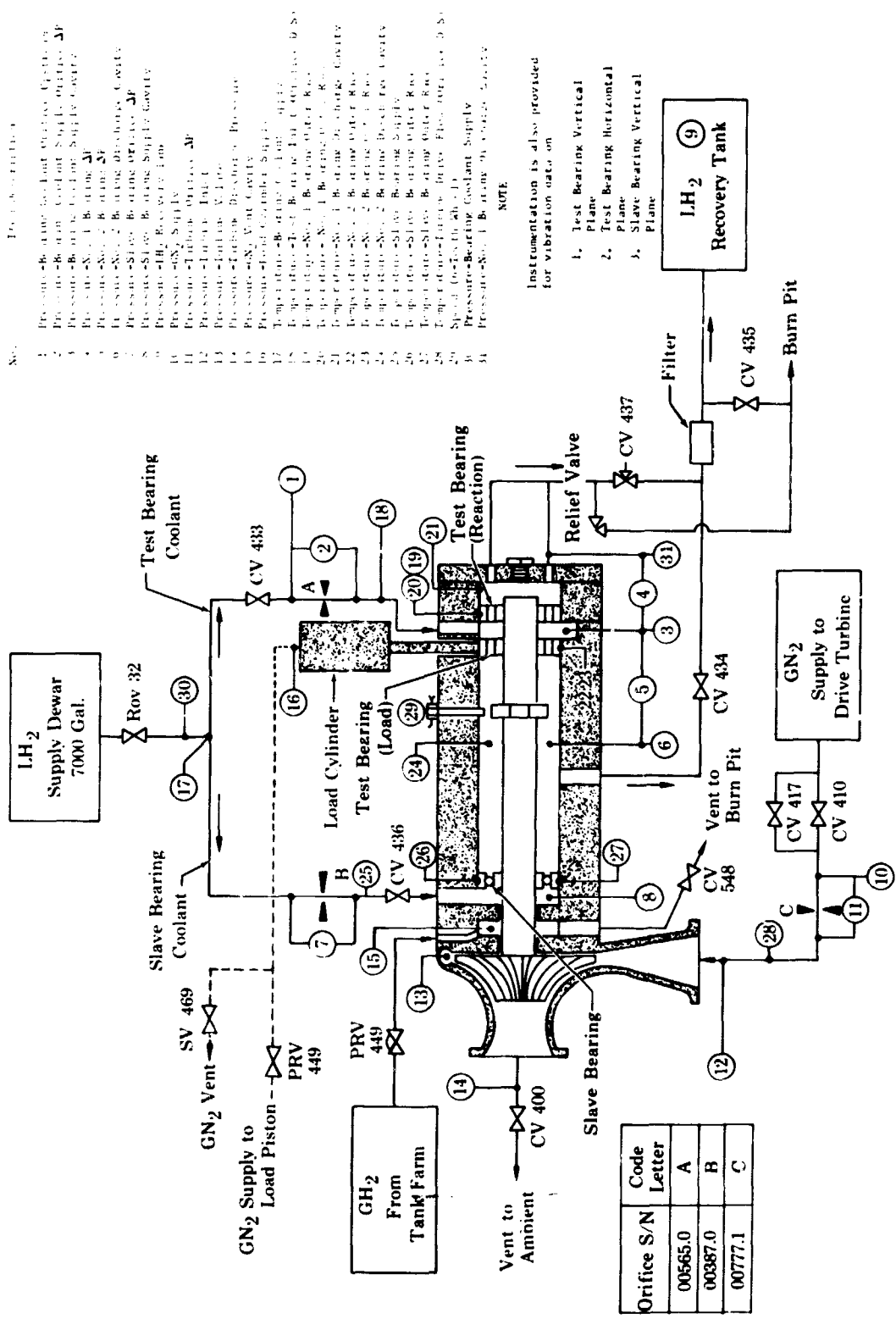
The general test procedures that were used on this test program were as follows:

1. The test rig was purged and temperature conditioned to a liquid hydrogen environment.
2. The radial load was applied in increments as the rig was accelerated to 48,000 rpm.
3. The abort parameters of vibrations and outer race temperatures are monitored to ensure that vibration levels remained below 15g and to detect sudden rises in bearing outer race temperature, either of which could indicate a bearing failure.

5. Test Results

During this program, tests were conducted on the roller bearing test rig to evaluate the bearing configurations listed in table XVIII. Eight test bearings surpassed the goal test duration of 10 hours at design conditions, and four other bearings completed 9.0 hours or more.

The same test bearings were incorporated during Builds 17 to 21 and accumulated 1.2 hours and 4 cycles. These builds were used primarily to evolve build procedures on the modified test rig, to optimize the facility, and to develop test procedures. The initial roller bearing testing of the current program was with Build 17 of the bearing test rig. The configuration of the test bearings was the same as that used on the last Phase I (Contract AF04(611)-11401) endurance test, i. e., test matrix points 1 and 2. This configuration was selected to establish a new baseline following the rig modifications that changed the load bearing mount arrangement and the thrust load on the ball bearing. Both test bearings incorporated single crown stainless steel (AMS 5630) rollers with an L/D of 1.000 stainless steel (AMS 5630) races, 0.040-in. roller end-to-side rail clearance and outer-land-guided Armalon cages. Negative internal clearance was incorporated between the rollers and races; namely, 0.0038 in. on the load bearing and 0.0027 in. on the reaction bearing at ambient conditions.



1. Pressure-Bearing Load Chamber Pressure
 2. Pressure-Bearing Load Chamber Supply Orifice ΔP
 3. Pressure-Bearing Load Chamber Supply Orifice
 4. Pressure-Slave Bearing Orifice ΔP
 5. Pressure-Slave Bearing Orifice
 6. Pressure-Slave Bearing Orifice ΔP
 7. Pressure-Slave Bearing Orifice
 8. Pressure-Slave Bearing Orifice ΔP
 9. Pressure-Slave Bearing Orifice
 10. Pressure-Slave Bearing Orifice ΔP
 11. Pressure-Slave Bearing Orifice
 12. Pressure-Slave Bearing Orifice ΔP
 13. Pressure-Slave Bearing Orifice
 14. Pressure-Slave Bearing Orifice ΔP
 15. Pressure-Slave Bearing Orifice
 16. Pressure-Slave Bearing Orifice ΔP
 17. Temperature-Bearing Load Chamber Supply
 18. Temperature-Bearing Load Chamber Supply
 19. Temperature-Slave Bearing Orifice Row
 20. Temperature-Slave Bearing Orifice Row
 21. Temperature-Slave Bearing Orifice Row
 22. Temperature-Slave Bearing Orifice Row
 23. Temperature-Slave Bearing Orifice Row
 24. Temperature-Slave Bearing Orifice Row
 25. Temperature-Slave Bearing Orifice Row
 26. Temperature-Slave Bearing Orifice Row
 27. Temperature-Slave Bearing Orifice Row
 28. Temperature-Slave Bearing Orifice Row
 29. Slave Bearing Orifice Row
 30. Slave Bearing Orifice Row
 31. Slave Bearing Orifice Row

Figure 95. B-13 Test Stand Schematic

The initial test of the current roller bearing program, Build 17, began on 15 March 1968 and was terminated on 18 March 1968 when the shaft locked on the third cycle after cooldown to liquid hydrogen temperature. The teardown inspection revealed moisture contamination of the rig. The test rig was cleaned and reassembled as Build 18, and testing was initiated on 26 March 1968. The facility and rig purge procedures were modified to prevent moisture contamination between tests and during cooldown. Testing of Build 18 was terminated after 0.1 hour at design speed on the first test cycle because of high vibrations at the turbine end of the rig. The teardown inspection showed that the slave bearing had failed.

The test rig was reassembled with the same test bearings used in Builds 17 and 18 and with a new slave bearing. Testing of Build 19 began on 10 April 1968. After the rig was accelerated to 20,000 rpm, to permit final flow settings prior to accelerating to design speed, it was determined that the flow split to the test bearings was unequal and the test was terminated. Before resuming, test facility modifications were made to the bearing coolant vent systems to permit better control of the coolant flow split. Attempts to resume testing were unsuccessful because of a locked shaft. The teardown inspection did not reveal any reason for this malfunction, except for the possibility that the roller ends were jammed against the inner race side rails. There was some fretting on the outside diameter of the outer race of both test bearings and some scuffing of the roller ends, but no measurable roller end wear. A series of assembly and inspection checks on the test rig was completed in an attempt to isolate the reason for this malfunction. The tests indicated that roller bearings with tight internal fits tend to track with the rollers in the center of the races if they are assembled in that position. If a thrust load is applied to the shaft, the shaft will shift axially by an amount equal to the internal clearance of the turbine slave bearing and lock up with the rollers of the reaction bearing against the side rail. When this thrust load is released, and shaft rotation is continued, the shaft returns to the original position with the rollers and races centered. If the bearings are assembled with the rollers against the side rails, there is a tendency for the rig to lock up before the rollers become aligned in the center of the races. The assembly procedure for the test rig was changed so that the rig was assembled with the rollers of both bearings aligned in the center of the races and with the turbine slave bearing in its rearward position to maintain the shaft in this aligned condition.

During all tests conducted prior to this time, the turbine discharge had been throttled to provide a backpressure on the turbine and a thrust load on the shaft in a direction away from the turbine end. Because this backpressure on the turbine was maintained by manual adjustment of the test stand valves by the test operator, this procedure was not repeatable, and there were periods of operation when the shaft thrust loading was not in the desired direction or of the desired magnitude. The slave bearings from Builds 17 to 19 showed tracks on both sides of the inner race indicating a change in thrust load on the shaft. It was determined that if the rig was operated without throttling the turbine discharge, the thrust loading on the shaft would be in the direction toward the turbine as a result of the pressure from the bearing cooling flow and the shaft areas. If additional thrust in this direction was desired, it could be obtained by applying pressure in the bellows seal vent compartment.

As a result of these findings, Build 20 was assembled with the rollers and races centered and the turbine slave bearing positioned with the thrust

load toward the turbine. The direction of shaft thrust loading was reversed from that previously used to allow better control of the shaft thrust loading by regulating the pressure in the seal cavity. The outside diameter of the outer races of the roller bearings were silver flashed in an effort to reduce the fretting at these locations.

Testing of Build 20 was initiated on 8 May 1968. The bearing rig was accelerated to design speed but was shut down after recording a set of data because there were high turbine vibrations and the turbine slave bearing outer race temperature was rising. A teardown inspection indicated fretting of the shaft spacers on the turbine end of the rig and one area of rub on the turbine labyrinth seal. The vibration data showed that the synchronous vibration (one per revolution) increased with the rig speed. The evidence indicated that the turbine tie bolt did not have sufficient stretch to keep the stackup tight at operational conditions. The turbine tie bolt torque was within the blueprint limits on teardown; therefore, it appears that thermal and/or centrifugal effects cause the tie bolt to loosen during rig operation.

On Build 21, the rig was rebuilt with the same test bearings that were used on the previous tests, a new slave bearing, and a new design turbine tie bolt. A titanium (AMS 4928) stretch-type tie bolt was incorporated to replace the Inconel 718 (AMS 5663) bolt. Testing on Build 21 was attempted on 20 May 1968. During the cooldown of the rig, two rotational checks were completed successfully and free rotation was verified. After the cooldown was complete the rig would not rotate and it remained locked even when warmed to ambient temperature. The shaft was freed by rotating it backward. Another attempt was made to test the rig, but without the rotational checks during the cooldown, and the same results were experienced. A series of ambient tests was then made that revealed that if the shaft was in the rearward position on shutdown that the turbine did not have sufficient breakaway torque to start the rig. If the shaft was in the forward or normal operating position on shutdown, the rig would start up easily with the turbine drive. The rig was returned to assembly for a teardown inspection, which revealed no change from the previous build.

On Build 22, the rig was reassembled with the test bearings centered and the slave bearing 0.007 in. from the front loaded position to compensate for the thermal differences between the shaft and housings when the rig was cooled down for operation. Thus, both the slave bearing and the test bearings would be in their normal operating position after rig cooldown. Testing of Build 22 was initiated on 27 May 1968 and terminated on the third test cycle to design speed when a temperature rise on the reaction bearing outer race was detected. A total of 0.9 hour test time at design speed was accumulated during Build 22 with a total of 7 cycles and 2.2 hours accumulated on the test bearings.

The teardown inspection revealed one skewed roller in the reaction bearing as shown in figure 96. All of the other rollers were in good condition, as shown in figure 97, with an average roller end wear of 0.0004 in. and 0.0008 in. on the roller with the maximum wear. The load bearing was in good condition, as shown in figure 98, with an average roller end wear of 0.0009 in. and 0.0011 in. on the roller with the maximum wear.

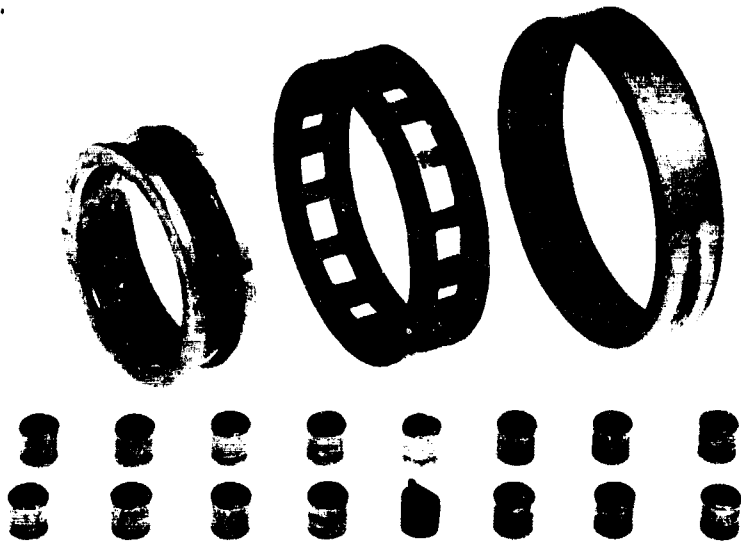


Figure 96. Disassembly Condition of Reaction Bearing (S/N V-1) With Turbine End of Rollers Up (Build 22)

FE 77884

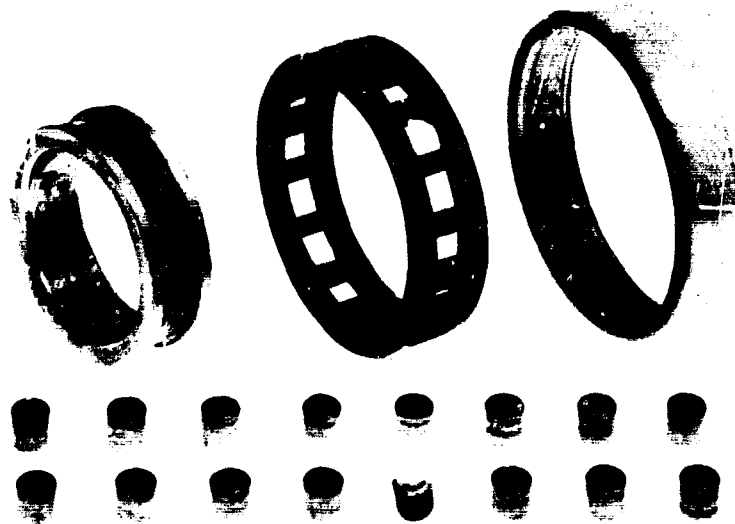


Figure 97. Disassembly Condition of Reaction Bearing (S/N V-1) With Rear End of Rollers Up (Build 22)

FE 77883

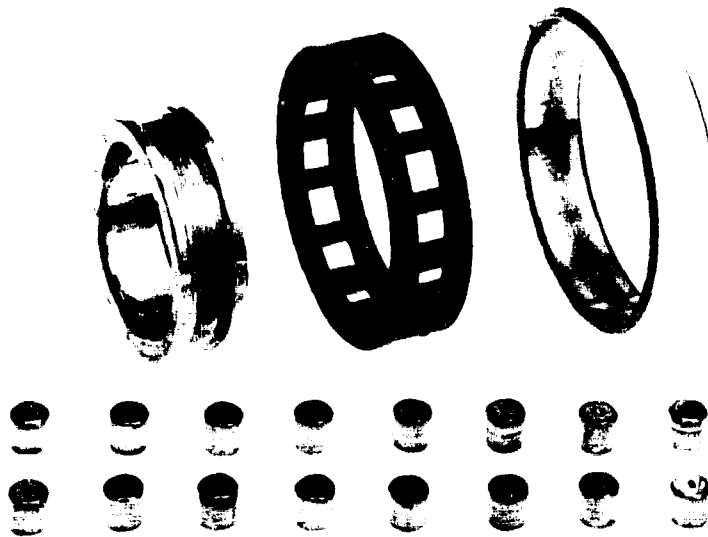


Figure 98. Disassembly Condition of Load Bearing (S/N V-2) With Turbine End of Rollers Up (Build 22) FE 77891

Because the reaction bearing from Build 22, which was identical in configuration to the only Phase I (Contract AF04(611)-11401) bearing to surpass the 10 hour goal duration, did not repeat the durability evaluation, the subsequent testing through Build 30 was used primarily to determine a configuration that would prevent roller skewing. This series of tests ended with Build 30 when both test bearings surpassed 12.8 hours at design operating conditions.

Build 23 of the bearing test rig incorporated test bearings with stainless steel (AMS 5630) rollers and races, Armalon outer-race-guided cages, and the standard roller end-to-side rail clearance (0.0007 in.). The load bearing internal clearance was 0.0006 in. tight and the reaction bearing internal clearance was 0.0001 in. loose, (matrix points 29 and 30, respectively). Build 23 was tested on 6 and 7 June 1968 and testing was terminated after accumulating four cycles and 2.0 hours at design speed when the outer race temperature on the turbine slave bearing and the vibration level on the turbine end increased. The teardown inspection revealed that the slave bearing had failed. The roller bearings were in good condition, although there was high roller end wear. The average roller end wear was 0.0031 in. on the load bearing with 0.0062 in. on the roller with maximum end wear. The average roller end wear on the reaction bearing was 0.0064 in. with 0.0121 in. on the roller with maximum end wear.

Build 24 of the roller bearing test rig included the test bearings from Build 23 and a new slave bearing. Build 24 testing was conducted on 27 June 1968 and was terminated after accumulating three cycles and 0.9 hour at design speed when the outer race temperature on the load bearing increased. The teardown inspection revealed that one roller in the load bearing had failed (skewed), as shown in figure 99, and that the inner race side rails had heavy spalling as shown in figure 100. Spalling was also found on four rollers, and

two additional rollers showed heavy end scuffing. The average load bearing roller end wear was determined to be 0.0082 in. (not including the failed roller) with 0.0123 in. on the roller with maximum end wear. The reaction bearing had two rollers with moderate spalling and the average end wear was 0.0091 in. The roller in the reaction bearing exhibiting the greatest end wear had 0.0143 in. wear and was one of the two rollers spalled as shown in figure 101. The roller end wear was on the turbine end of the load bearing rollers and on the rear end of the reaction bearing rollers. The high end wear is attributed to the coolant flow pressure drop across the bearings. The accumulated total cycles and time for the bearings used during Builds 23 and 24 (matrix points 29 and 30) are 7 cycles and 2.9 hours at design speed.

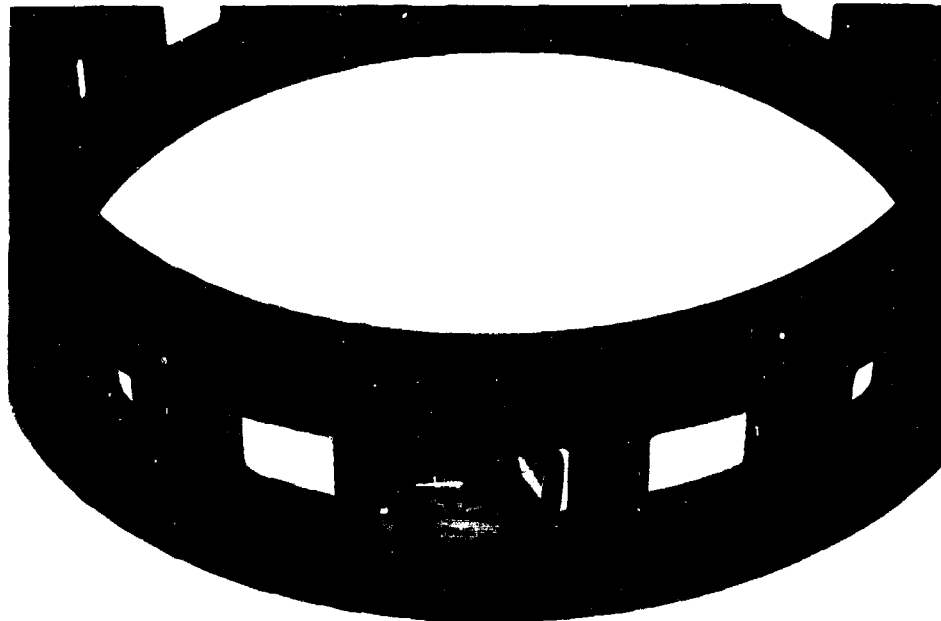


Figure 99. Teardown Condition of Failed Roller (No. 4) and Cage From Load Bearing S/N W-2 FE 78430

Build 25 of the roller bearing test rig contained stainless steel (AMS 5630) rollers and races, Armalon outer-race-guided cages, and 0.0016 in. roller end-to-side rail clearances. The load bearing internal clearance was 0.0037 in. tight and the reaction bearing internal clearance was 0.0026 in. tight (matrix points 24 and 27, respectively). During final torque checks of the rotor prior to final balancing, it was determined that excessive torque was required to rotate the shaft and the required torque exceeded the drive turbine capability. The rig was disassembled and roller drag on the inner race side rails was confirmed to have been the cause of the high drive torque requirement.

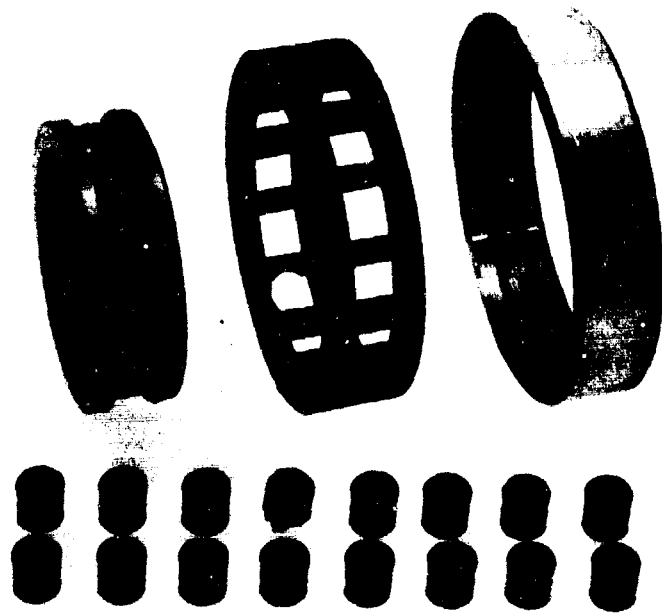


Figure 100. Disassembly Condition of Load Bearing FE 78433
(S/N W-2) With Turbine End of Rollers
Up (Build 24)

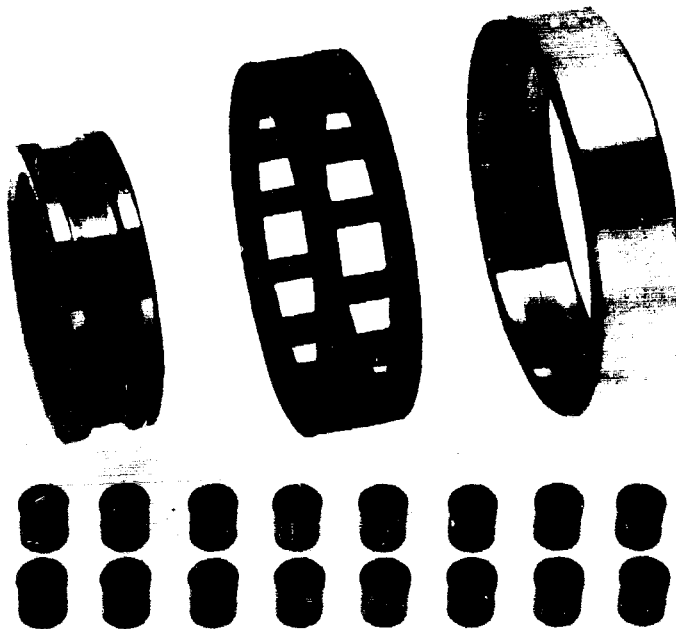


Figure 101. Disassembly Condition of Reaction Bearing FE 78431
(S/N W-1) With Rear End of Rollers Up
(Build 24)

The configuration of Build 25A was identical to Build 25, except the roller end-to-side rail clearances were increased to 0.0097 in. on the load bearing and 0.0090 in. on the reaction bearing (matrix points 24' and 27', respectively). Build 25A testing began 12 July 1968. The first test cycle of 0.8 hour duration at rated speed was successfully completed. On the next two acceleration attempts of the rig, the shaft would not rotate. The shaft was freed by rotation in the reverse direction and required a break-away torque of 80 lb-in. After being freed, the rotating torque was determined to be 5 to 7 lb-in. in the direction of normal rotation. Testing was continued and no further torque problems were encountered during the subsequent 16 cycles. Testing was concluded on 18 July 1968, after accumulated 17 cycles and 9.7 hours. During the final test cycle, all three vibration readouts increased suddenly and the load bearing outer race temperature increased. The teardown inspection revealed that the load bearing inner and outer races had failed, as shown in figures 102 and 103. The load bearing rollers were severely impact damaged, as shown in figure 104, and one roller and its cage pocket exhibited some of the characteristics noted on rollers that had skewed during previous tests. Sufficient roller end surface remained on 12 of the load bearing rollers to permit end wear measurements and an average of 0.00034 in. and a maximum of 0.0017 in. were recorded on these rollers. The reaction bearing was in excellent condition, as shown in figure 105, and was reusable. The average roller end wear of the reaction bearing was 0.00095 in. with 0.0013 in. on the roller with maximum end wear. A metallurgical analysis of the inner and outer races did not reveal any microstructure void or inclusions, nor could any evidence of fatigue failure be determined. From the appearance of the inner race side rail chipping, it appears that this damage was caused by roller impacts on the side rails. Displaced side rail material could then have been ingested through the bearing, causing the inner and outer races to crack because of the increased loading and possible stress concentration resulting from these chips.

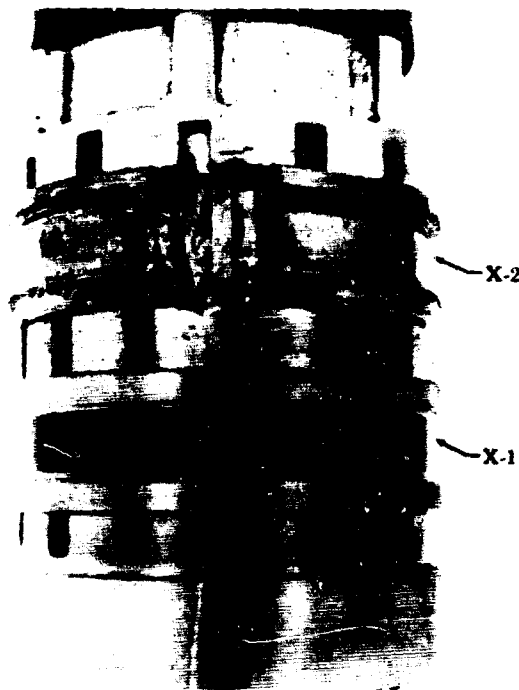


Figure 102. Inner Races of Bearings (S/N X-1 and X-2) Following Test of Build 25A FD 24458

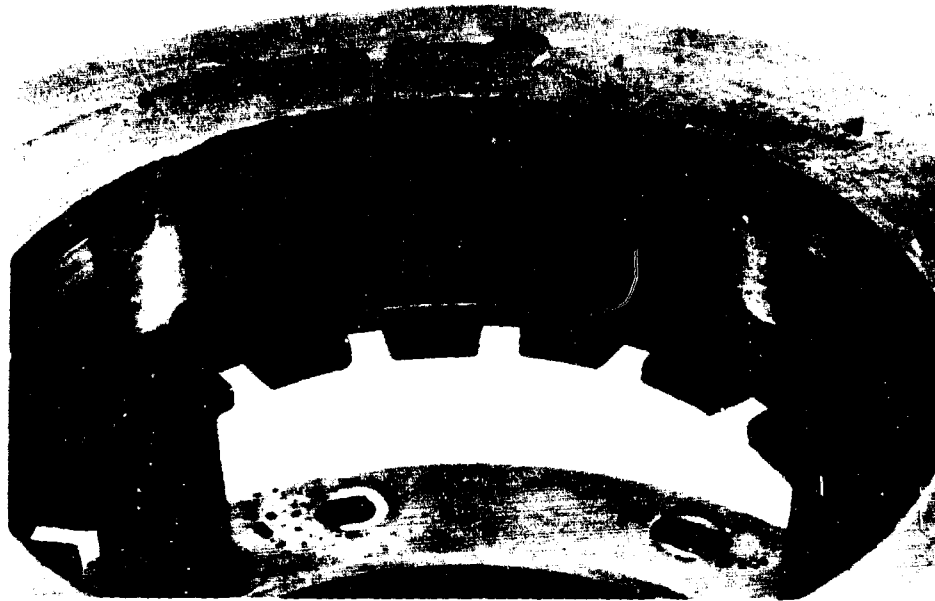


Figure 103. Outer Race Failure in the Unloaded Zone of Load Bearing (S/N X-2) FE 78744
Following Test of Build 25A

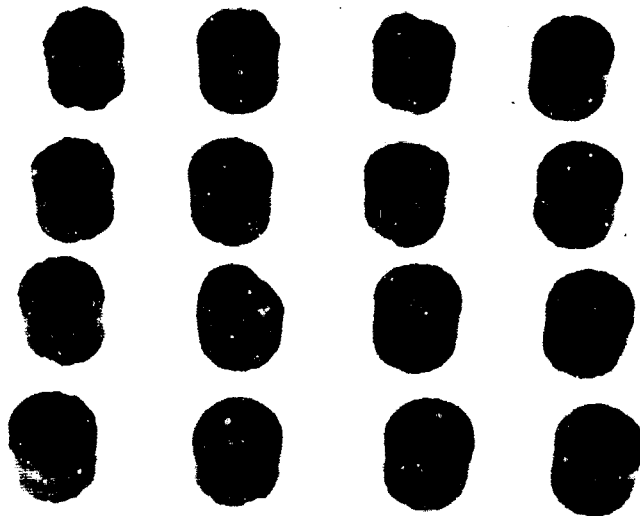


Figure 104. Rollers from Load Bearing (S/N X-2) FE 78748
Showing Impact Damage to Turbine End of Rollers (Build 25A)

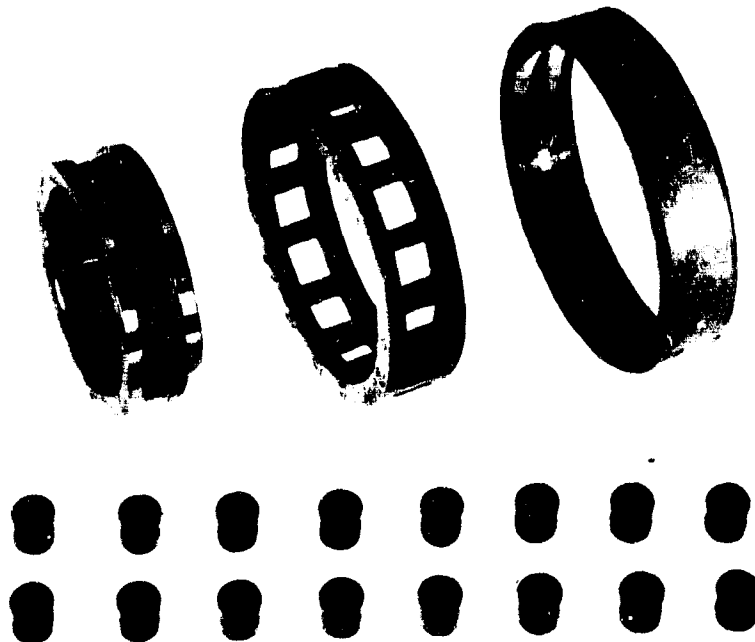


Figure 105. Disassembly Condition of Reaction Bearing (S/N X-1) With Turbine End of Rollers Up (Build 25A) FE 78782

Build 26 of the roller bearing test rig incorporated the new triple-crown rollers. This build configuration also included stainless steel (AMS 5630) rollers and races, L/D of 1.250 rollers, Armalon outer-race-guided cages, and roller end-to-side rail clearances of 0.040 in. The load bearing internal clearance was 0.0038 in. tight and the reaction bearing internal clearance was 0.0025 in. tight (matrix points 12 and 11, respectively). Testing of Build 26 was conducted on 23 July 1968. After 11 minutes operation at design speed of the first test cycle, the reaction bearing outer race temperature and the vibration readouts increased suddenly. The teardown inspection revealed that one roller in the reaction bearing had begun to skew as shown in figure 106 and was wedging between the side rails. The probable cause of this failure was found to be the result of the reaction bearing inner race not being fully seated, resulting in approximately 0.025 in. misalignment between the inner and outer races. No measurable roller end wear was detected on either bearing except for the wedged roller, which exhibited approximately 0.0007 in. wear.

The configuration of Build 27 of the roller bearing test rig was the same as Build 26, except the reaction bearing rollers and cage were replaced with new parts of the same configuration. Testing of Build 27 was completed on 29 July 1968 when, after 2 minutes operation at design speed on the second cycle, erratic speed indications and excessive reaction bearing outer race temperature were detected. The teardown inspection showed that one roller in the reaction bearing had skewed and had worn through the cage rib and was in contact with the adjacent roller as shown in figure 107. Except for the damaged roller and cage described above, the remaining parts were in good condition. The average

reaction bearing roller end wear was 0.00035 in. with 0.0005 in. on the roller with the maximum wear. The average load bearing roller end wear was 0.0001 in. with 0.0003 in. wear on the roller with the maximum wear. Figures 108 and 109 show the teardown condition of the reaction bearing and load bearing.

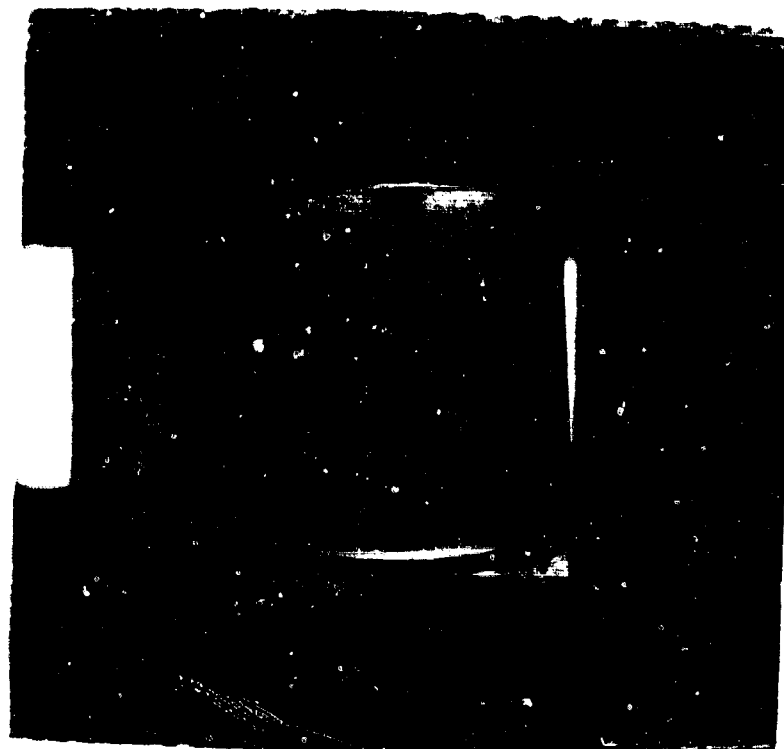


Figure 106. Disassembly Condition of Reaction Bearing (S/N Y-1) Showing Skewed Position of Roller (Build 26)

FE 79085



Figure 107. Disassembly Condition of Reaction Bearing (S N Y-1A) Showing Skewed Position of Roller (Build 27)

FE 78915

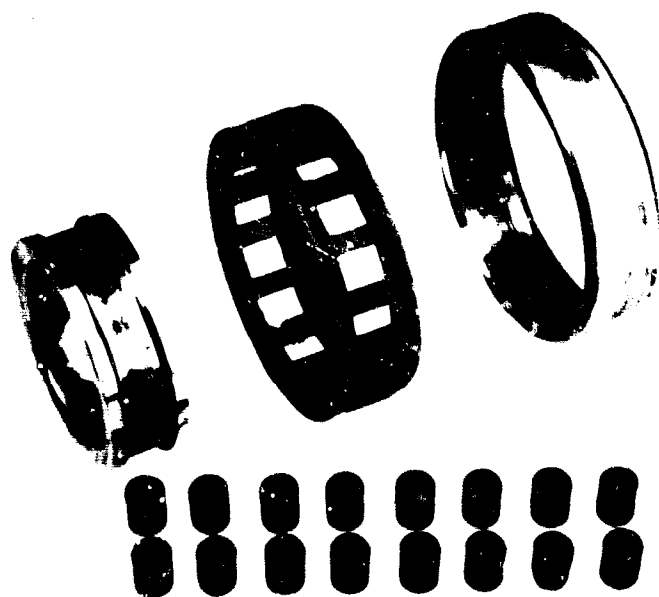


Figure 108. Disassembly Condition of Reaction Bearing (S N Y-1A) With Turbine End of Rollers Up (Build 27)

FE 78959

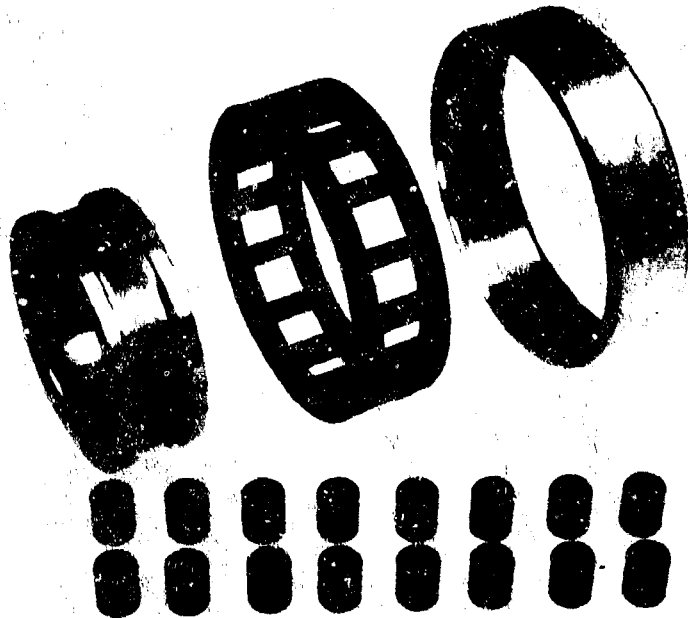


Figure 109. Disassembly Condition of Load Bearing (S/N Y-2) With Turbine End of Rollers Up (Build 27)

FE 78907

The test bearings incorporated in Build 28 were triple-crown, L/D of 1.0 rollers, stainless steel (AMS 5630) rollers and races, Armalon outer-race-guided cages, and 0.010 in. roller end-to-side rail clearance. The load bearing internal clearance was 0.0051 in. tight and the reaction bearing internal clearance was 0.0026 in. tight (matrix points 43' and 47', respectively). Testing of Build 28 was completed on 6 August 1968. After 1 minute of design speed operation on the 14th cycle, the reaction bearing outer race temperature and the vibration levels increased suddenly, and the test was terminated. Approximately 6.5 hours had been accumulated at this time. The teardown inspection of Build 28 revealed that one roller in the reaction bearing had skewed as shown in figure 110. Except for the skewed roller and related cage pocket damage, the remaining parts of the reaction bearing end wear was 0.00385 in. with 0.0075 in. on the roller with maximum wear. All the wear was on the turbine end of the rollers. The load bearing was in good condition and was reused in Build 30. Figure 111 shows the condition of the reaction bearing after disassembly. Figure 112 shows the post-test condition of the load bearing. The average load bearing end wear was 0.00257 in. with 0.007 in. on the roller with the maximum wear. All the wear was on the turbine end of the rollers.

Build 29 of the roller bearing test rig incorporated test bearings with stainless steel (AMS 5630) races and triple-crown L/D of 1.250 rollers. A roller end-to-side rail clearance of 0.010 in. was used in both bearings. The load bearing internal clearance was 0.0049 in. tight, and the reaction bearing internal clearance was 0.0027 in. tight (matrix points 7' and 9', respectively). Armalon outer-race-guided cages were used in both bearings. Testing of Build 29 was started on 12 August 1968 and completed on 14 August 1968. Test-

ing was terminated after 0.1 hour at design speed on the sixth cycle because of an increase in the reaction bearing outer race temperature and vibration levels. At the time that testing was suspended, approximately 3.1 hours had been accumulated. The teardown inspection of Build 29 showed that two rollers in the reaction bearing had begun to skew and had high end wear because of wedging with the inner race side rails. The primary wear on the reaction bearing was on the rear end of the rollers with an average wear of 0.0037 in. The maximum end wear was 0.022 in. on one of the skewed rollers and the other skewed roller had 0.018 in. end wear. The post-test condition of the reaction bearing is shown in figure 113. The load bearing was in good condition with only light wear on the turbine end of the rollers. The average load bearing roller end wear was 0.00037 in. with 0.0098 in. on the roller with maximum wear. Figure 114 shows the condition of the load bearing.

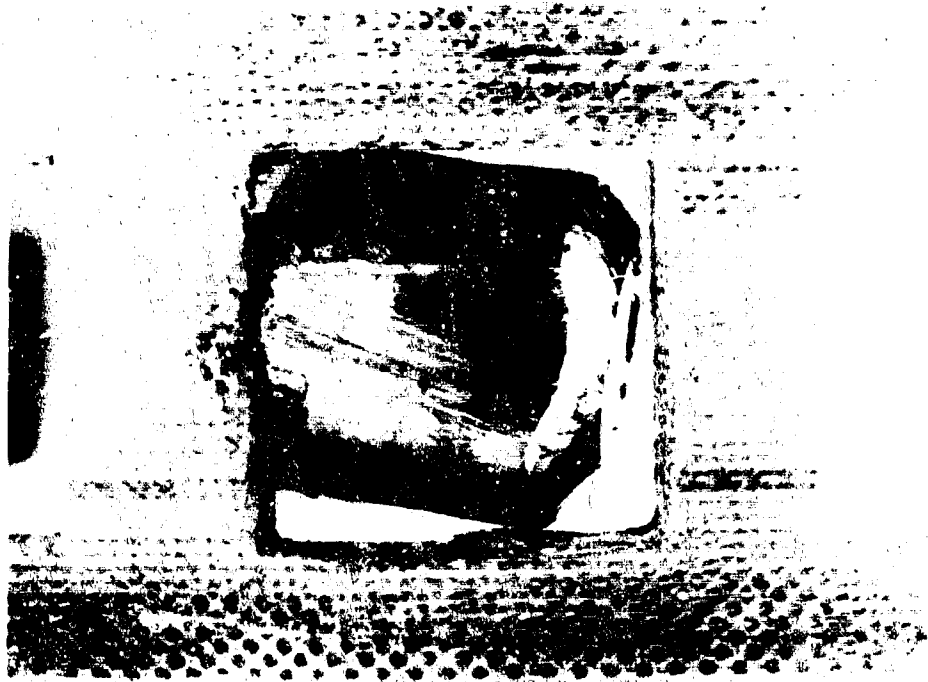


Figure 110. Disassembly Condition of Reaction
Bearing (S/N Z-1) Roller No. 5
(Build 28)

FE 79271

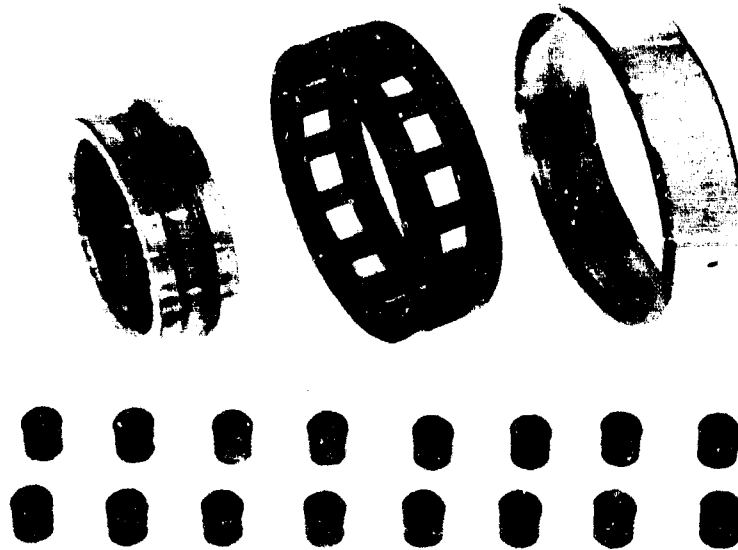


Figure 111. Disassembly Condition of Reaction Bearing (S/N Z-1) With Turbine End of Rollers Up (Build 28) FE 79269



Figure 112. Disassembly Condition of Load Bearing (S/N Z-2) With Turbine End of Rollers Up (Build 28) FE 79267

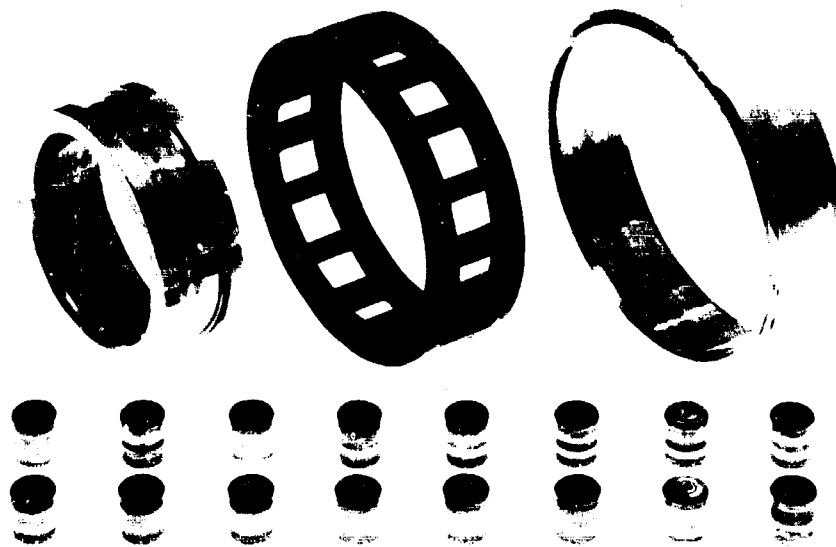


Figure 113. Disassembly Condition of Reaction Bearing (S/N AA-1) With Turbine End of Rollers Up (Build 29)

FE 79334

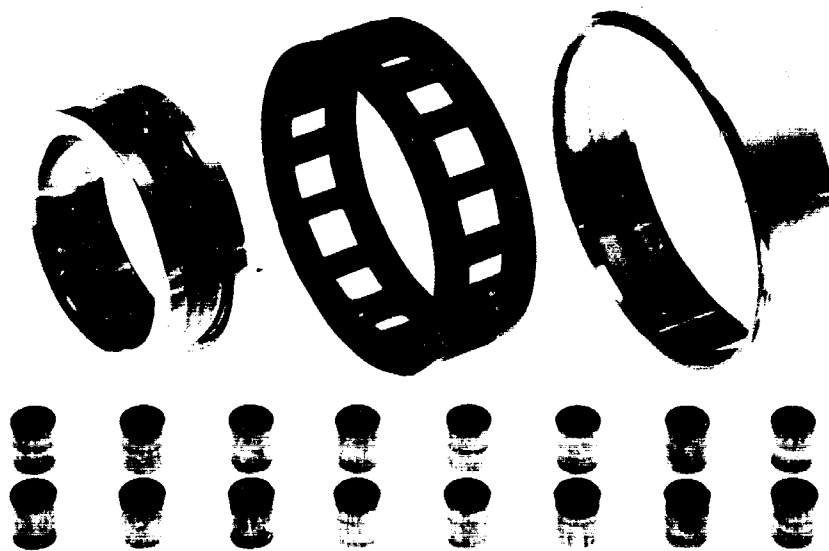


Figure 114. Disassembly Condition of Load Bearing (S/N AA-2) With Turbine End of Rollers Up (Build 29)

FE 79336

Build 30 of the roller bearing rig incorporated test bearings used in previous testing. The reaction bearing (matrix point 27') was from Build 25A and had accumulated approximately 9.7 hours. The load bearing (matrix point 43') was from Build 28 and had accumulated approximately 6.5 hours. The reaction bearing incorporated in Build 30 consisted of single-crown rollers with an L/D ratio of 1.0, 0.009 in. roller end-to-side rail clearance, and a 0.0028 in. tight internal clearance. The primary end wear was on the turbine side of the reaction bearing rollers with an average wear of 0.00095 in. before testing on Build 30. The load bearing consisted of triple-crown rollers with an L/D ratio of 1.0, 0.0097 in. roller end-to-side rail clearance, and a 0.0049 in. tight internal clearance. The average load bearing roller end wear was 0.00257 in. nearly evenly distributed on both ends of the rollers before Build 30 testing. Build 30 testing began on 16 August and was concluded on 20 August 1968 after 12.8 hours had been accumulated on the lower time, load bearing. During Build 30, ten test cycles were completed with 6.3 hours test time at design conditions. The load bearing had accumulated a total of 24 cycles with 12.8 hours of operation at design conditions, and the reaction bearing had a total of 27 cycles with 16.0 hours. The teardown inspection revealed that both test bearings were in good condition and could be used for additional testing. The average reaction bearing end wear was 0.00213 in. with 0.0029 in. on the roller with maximum wear. Both ends of the reaction bearing rollers were worn nearly evenly. Figures 115 and 116 show the post-test condition of the reaction bearing. The average load bearing end wear was 0.00318 in. that had 0.007 in. end wear before testing on this build. All load bearing wear was on the turbine end of the rollers. Figures 117 and 118 show the post-test condition of the load bearing.

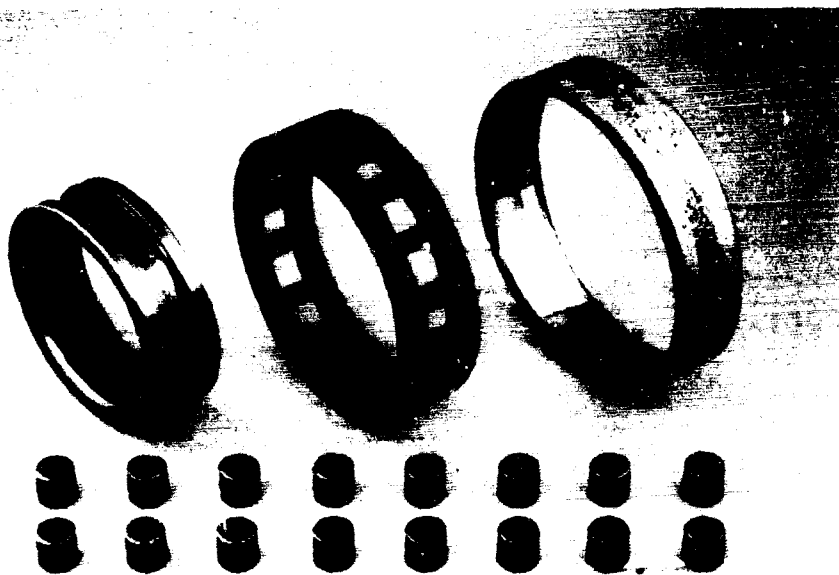


Figure 115. Disassembly Condition of Reaction Bearing (S/N X-1) With Rear End of Rollers Up (Build 30)

FE 79420

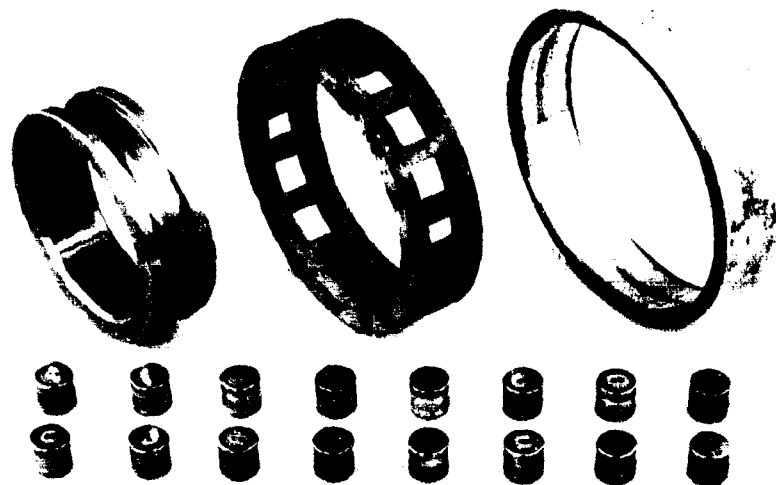


Figure 116. Disassembly Condition of Reaction Bearing (S/N X-1) With Turbine End of Rollers Up (Build 30)

FE 79421

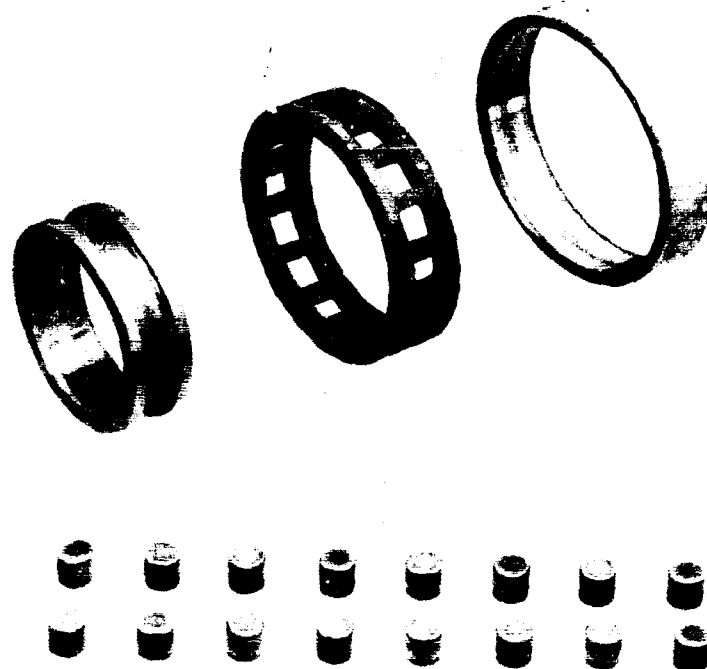


Figure 117. Disassembly Condition of Load Bearing (S/N Z-2) With Rear End of Rollers Up (Build 30)

FE 79491

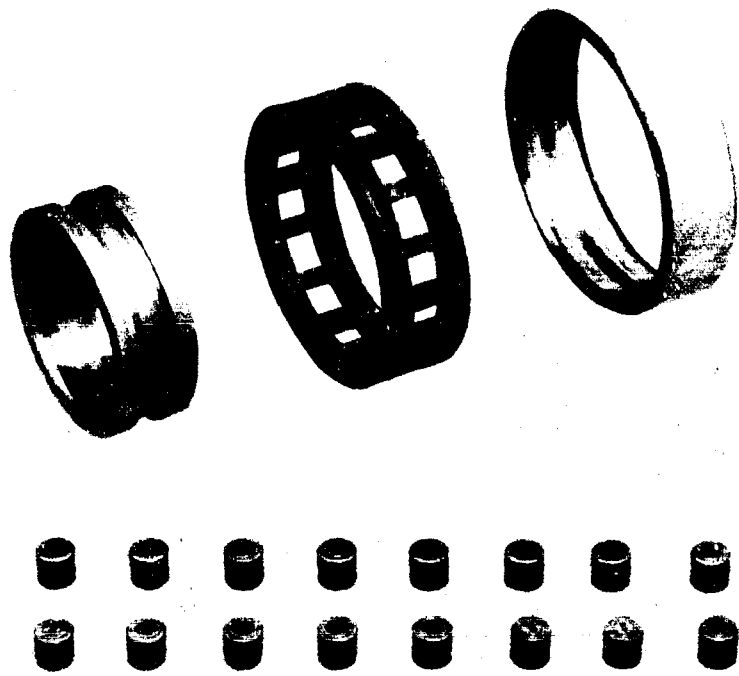


Figure 118. Disassembly Condition of Load Bearing (S/N Z-2) With Turbine End of Rollers Up (Build 30) FE 79492

Both roller bearings incorporated in Build 31 consisted of triple-crown, L/D of 1.125, stainless steel (AMS 5630) rollers and races. The reaction bearing (matrix point 201) had a 0.0051 in. tight internal clearance and a roller end-to-side rail clearance of 0.0098 in. The load bearing (matrix point 20'') had a 0.005 in. tight internal clearance and a roller end-to-side rail clearance of 0.0048 in. Testing of Build 31 began on 23 August 1968. A high turbine drive pressure was required to start rotation, however, operational parameters were normal during the first cycle as soon as the design speed level was obtained. One hour at design speed was accumulated during the first cycle. The second test cycle was started on 26 August 1968, but the rig failed to rotate. Six attempts were made to accelerate the rig with the drive turbine after the shaft had been freed by rotation in the reverse direction, but on each attempt the shaft locked. On the seventh attempt, the shaft locked tight and could not be freed by turning in either direction.

During disassembly of the test rig, it was determined that the locked shaft was caused by the load bearing rollers wedging into the inner race side rails. Scoring on both ends of the load bearing rollers was very heavy, as shown in figures 119 and 120, and prevented the measurement of end wear. Figure 121 shows a comparison of typical rollers from the reaction bearing (matrix point 20') and the load bearing (matrix point 20''), which were configured identically, except that the load bearing roller end-to-side rail clearance was half that of the reaction bearing. The inner race side rails of the load bearing also showed heavy scoring. The reaction bearing was in good condition, except for an axial crack in the outer race, which is shown in figure 122. The primary end wear of the reaction bearing was on the rear side of the rollers with an

average wear of 0.00018 in. and 0.0005 in. on the roller with maximum wear. Figure 123 shows the overall condition of the load bearing (matrix point 20') and figure 124 shows the condition of the reaction bearing (matrix point 20').

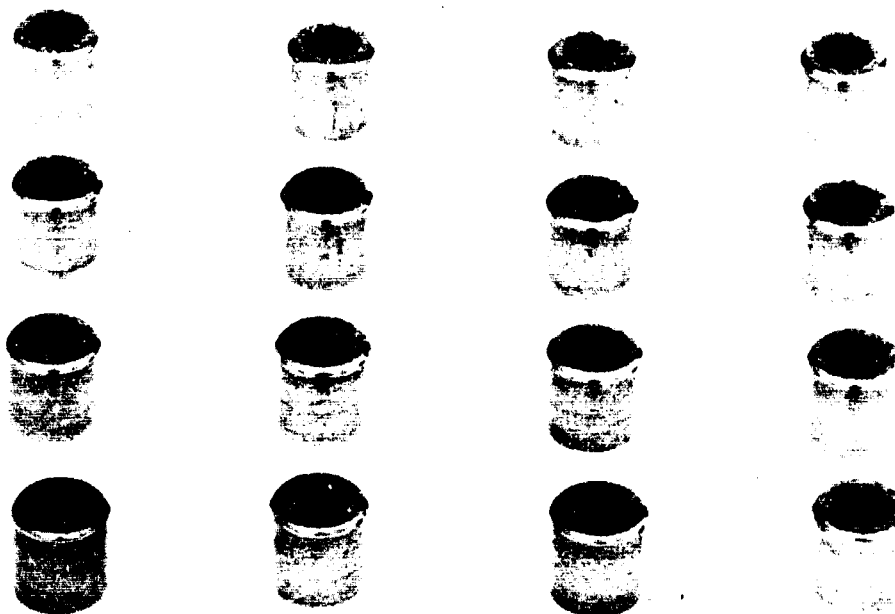


Figure 119. Rollers from Load Bearing (S/N BB-2) FE 79574
Showing Heavy Scoring on Turbine
End of Rollers (Build 31)

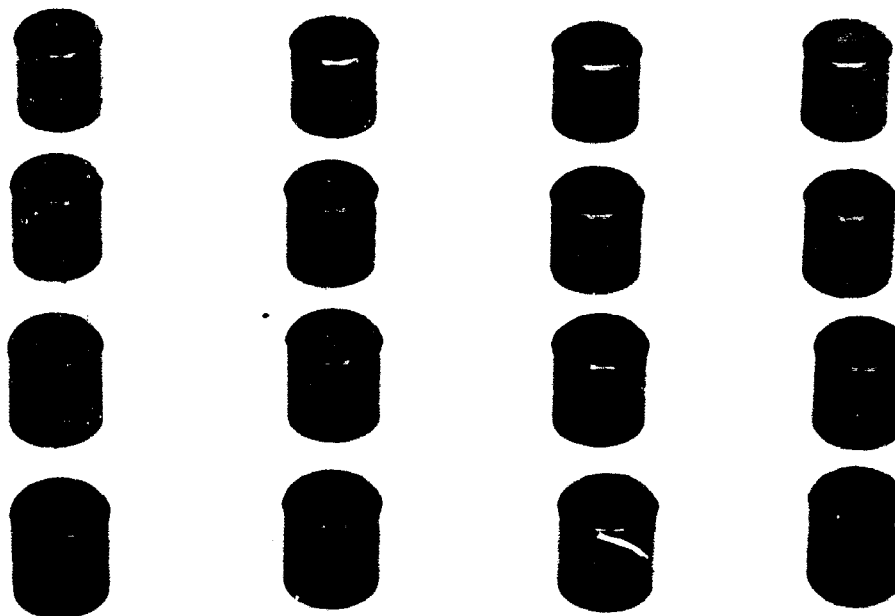


Figure 120. Rollers from Load Bearing (S/N BB-2) FE 79575
Showing Heavy Scoring on Rear End of
Rollers (Build 31)



BB-1



BB-2

Figure 121. Comparison of Post-Test Condition of a Typical Roller from Reaction Bearing (S/N BB-1) and Load Bearing (S/N BB-2) of Build 31 FD 24500

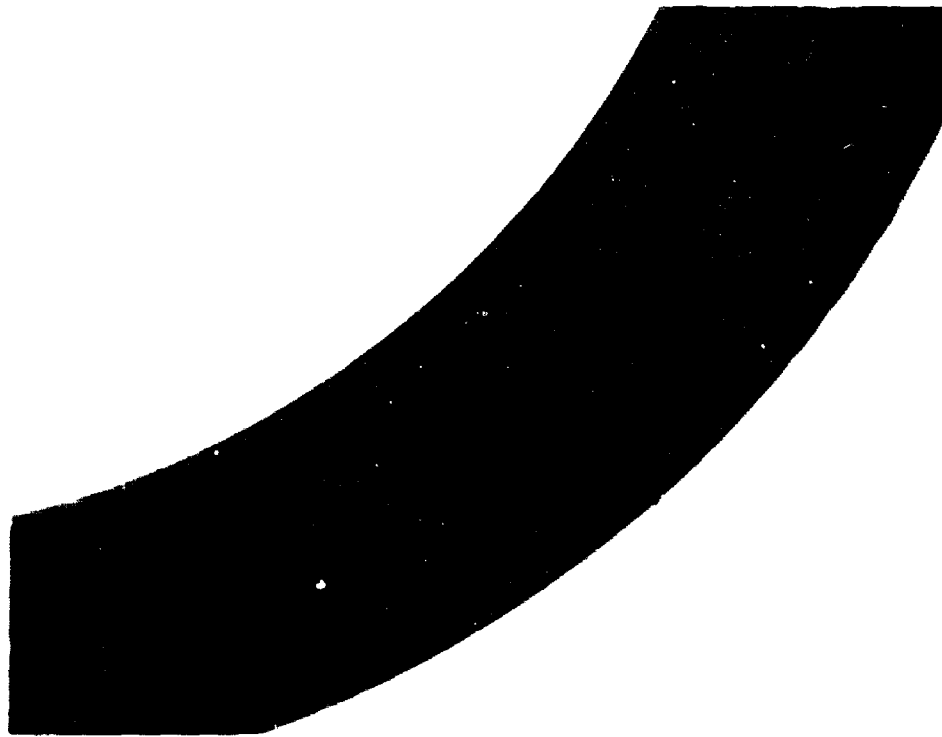


Figure 122. Cracked Outer Race from Reaction Bearing (S/N BB-1) of Build 31

FE 79499

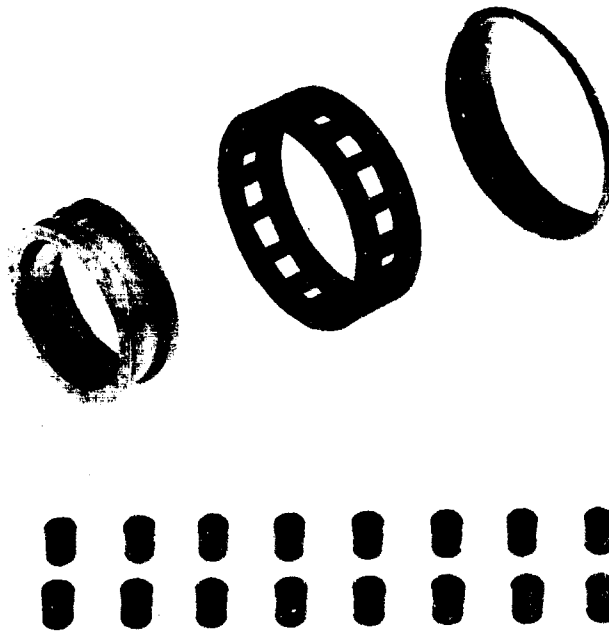


Figure 123. Disassembly Condition of Load Bearing (S/N BB-2) With Turbine End of Rollers Up (Build 31)

FE 79496

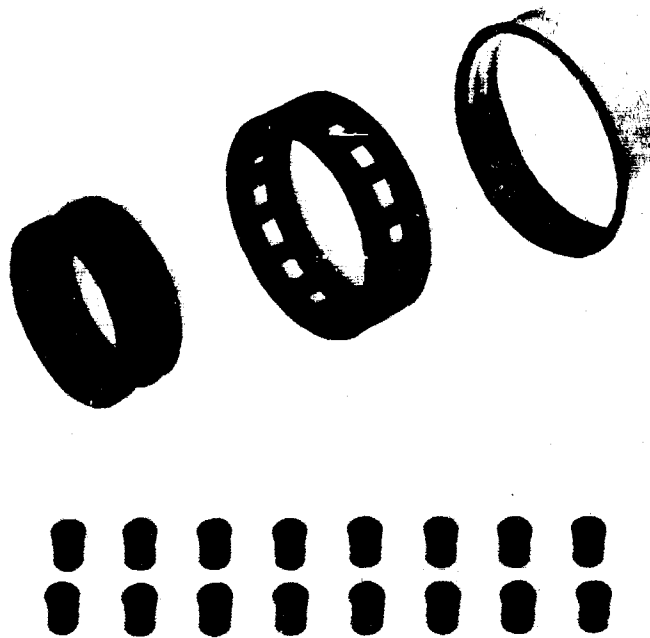


Figure 124. Disassembly Condition of Reaction Bearing (S/N BB-1) With Turbine End of Rollers Up (Build 31)

FE 79494

Build 32 of the roller bearing test rig incorporated bearing elements used in the previous tests. The load bearing incorporated rollers from Build 22 that had accumulated 2.2 hours, and the cage was from Build 6 (Phase I (Contract AF04(611)-11401) program) that had 0.3 hour of test time. Both inner and outer races were new. The reaction bearing had rollers selected from Phase I (Contract AF04(611)-11401) test bearings (Builds 12 and 15) with 1.5 hours on the maximum time rollers; the cage was from Build 6 and had 0.3 hour of test time. The inner race was from Build 5 with no test time at rated conditions, and the outer race was new. Both test bearings incorporated single-crown, L/D of 1.0 rollers, stainless steel (AMS 5630) rollers and races with outer-race-guided Armalon cages. The load bearing (matrix point 22) had a 0.0052 in. tight internal clearance and a roller end-to-side rail clearance of 0.0199 in. The reaction bearing (matrix point 23') had a 0.0049 in. tight internal clearance and a roller end-to-side rail clearance of 0.0099 in. Build 32 testing began on 29 August and ended on 30 August 1968. Testing was terminated after 0.1 hour at design speed on the sixth cycle when the vibration levels and the slave bearing outer race temperature increased, and the operating speed dropped off significantly. At the time of shutdown, 6 cycles and 137 minutes of testing at design speed had been accumulated. The teardown inspection revealed that the shaft had cracked halfway through in the necked-down section on the turbine end. The crack allowed the turbine end of the shaft to deflect during operation allowing the turbine to rub heavily on the turbine housing. The labyrinth seals and the turbine spacer were also damaged by rubbing. The test bearings were in good condition except for the reaction bearing outer race, which was cracked in the same location as the preview test (Build 31), as shown in figure 125. The greatest wear was on the rear end of the rollers in the reaction bearing, while the load bearing rollers wore on both ends in nearly equal amounts in a random manner. The roller end wear measurements are shown in table XIX. Except for the outer races, both roller bearings were reused in Builds 35 and 36 of the test rig. Figure 126 shows the overall condition of the reaction bearing (matrix point 23') and figure 127 shows the condition of the load bearing (matrix point 22).

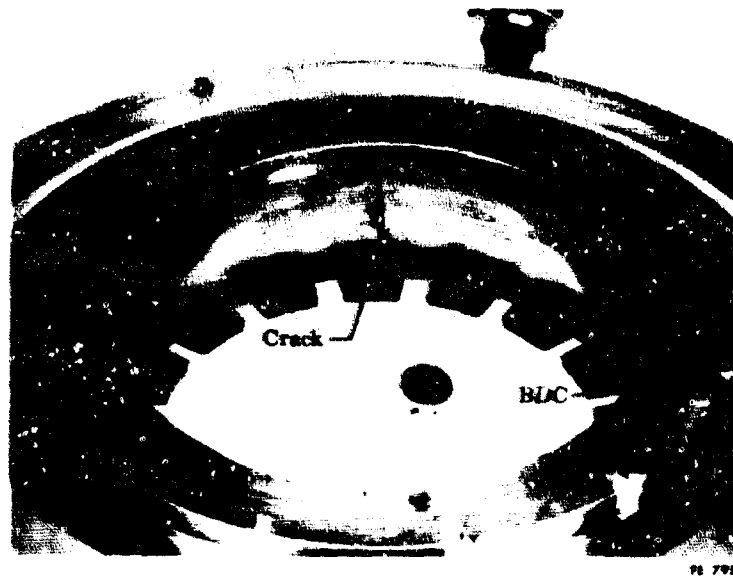


Figure 125. View Showing Crack in Outer Race of Reaction Bearing (S/N CC-1) (Build 32)

FD 25098

Table XIX. End Wear Summary (Matrix Points 22 and 23')

	Before Build 32 Testing	After Build 32 Testing	After Build 35 Testing	After Build 36 Testing
Reaction Bearing Rollers (23')				
Accumulated time and cycles at design speed	1.5 hours 3 cycles	3.8 hours 9 cycles	7.9 hours 18 cycles	16.4 hours 34 cycles
Average end wear (in.)	0.0006	0.0016	0.0017	0.0020
Maximum end wear (in.)	0.0012	0.0021	0.0045	0.0072
Load Bearing Rollers (22)				
Accumulated time and cycles at design speed	2.2 hours 7 cycles	4.5 hours 13 cycles	8.6 hours 22 cycles	17.0 hours 38 cycles
Average end wear (in.)	0.0009	0.0013	0.0027	0.0044
Maximum end wear (in.)	0.0011	0.0020	0.0047	0.0068



Figure 126. Disassembly Condition of Reaction Bearing (S/N CC-1) With Rear End of Rollers Up (Build 32)

FE 79593

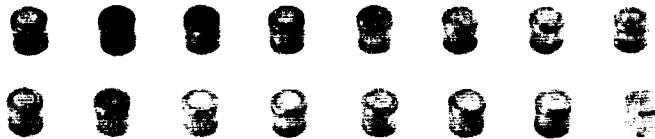
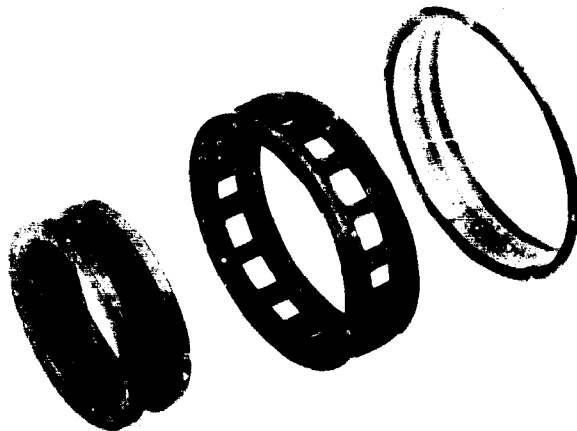


Figure 127. Disassembly Condition of Load Bearing (S/N CC-2) With Rear End of Rollers Up (Build 32)

FE 79598

In the investigation to determine the cause of the reaction bearing outer race failures on Builds 31 and 32, a metallurgical examination of the fracture faces indicated that the point of origin was a small surface depression on the inside diameter of the race on Build 31 and was a small crack, approximately 0.0025 in. deep, on the outside diameter surface on Build 32. Metallurgical analysis also indicated that the failures resulted from flexing stress cycles and they were not associated with fatigue spalling. With bearing operation at 48,000 rpm, a given point on the race is subjected to 400,000 roller passing cycles per minute. After consultation with the bearing vendor and with the P&WA bearing group at East Hartford, it was decided that the thin outer ring inside diameter should be in compression to withstand the cycling stresses induced with the tight internal fit and high shaft speed. The compressive stresses could be induced by means of a microstructure change such as carburizing the inside diameter of the ring; by shot peening the inside surface, or by outside diameter restraint.

The similarity of the angular orientation of the cracked outer races on Builds 31 and 32, coupled with the fact that the surface depressions found at the origin of the fatigue failures were less severe than observed on previously successful bearing outer races, indicated that stresses in excess of the normal operating levels were involved in these failures. The bearing test rig housings were reassembled for a bearing support alignment check. This inspection showed that the reaction bearing outer race carrier was misaligned by approximately 0.006 in. in the plane of the outer race failure, and was loose from the rear housing restraining pins. The damaged reaction bearing carrier was replaced and it was both pinned and weld attached to the rear housing. In addition, a stress relief heat treat cycle was instituted after the final grind operation, which established the desired internal clearance on the bearing, to minimize residual stresses that may be present.

Build 33 of the roller bearing test rig incorporated test bearings with triple-crown, L/D 1.125, stainless steel (AMS 5630) rollers and races. The reaction bearing (matrix point 20') had a 0.005 in. tight internal clearance and a roller end-to-side rail clearance of 0.0098 in. The load bearing (matrix point 21) had a 0.0051 in. tight internal clearance and a roller end-to-side rail clearance of 0.0198 in. Testing of Build 33 began on 10 September 1968 and ended the next day. Testing was terminated after 1 minute at design speed on the fifth cycle when a decay in coolant flows and an increase in vibrations and in slave bearing outer race temperature was observed. At the time of failure, 5 cycles and 1.3 hours of testing at design speed had been accumulated. The teardown inspection of Build 33 revealed that the liquid hydrogen bellows seal had failed. The test bearings were in good condition except for a crack in the reaction bearing outer race. The crack was located approximately 180 degrees from the two previous failures as shown in figure 128. The rollers from both test bearings were in excellent condition with negligible end wear, but did exhibit moderate scuffing on the turbine end as shown in figures 129 and 130. Failure analysis of the reaction bearing outer race fracture faces again showed a brittle-failure originating in a small depression in the roller track.

Build 34 of the roller bearing test rig incorporated the inner races, single-crown, L/D of 1.000 rollers, and Armalon outer-race guided cages from Build 32. New outer races were fabricated from steel alloy (AMS 6260) with the inside diameter carburized to a depth of approximately 0.043 in. and heat treated to provide a hard surface in the roller contact area. The reaction bearing (matrix

point 23') internal clearance was 0.0039 in. tight and the roller end-to-side rail clearance was 0.0105 in. The load bearing (matrix point 22) internal clearance was 0.0042 in. tight and the roller end-to-side rail clearance was 0.0204 in. These internal clearances correspond to values of 0.0049 and 0.0051 in., respectively, for the stainless steel (AMS 5630) races when adjusted for the difference in coefficient of expansion between steel alloy (AMS 6260) and stainless steel (AMS 5630). Build 34 of the bearing test rig was mounted and ready for test on 20 September 1968. During the initial start sequence the turbine housing failed as the turbine pressure was applied to start rotation of the test rig. The housing failed in the thin section below the Marmon clamp flange and caused damage to the turbine wheel and tie bolt. A detailed inspection revealed that the outer parts were in good condition.



Figure 128. View Showing Crack in Outer Race of Reaction Bearing (Build 33)

FE 79648

FD 25268

Build 35 of the bearing test rig incorporated the same test bearings that were used in Build 34. A new tie bolt, turbine, and turbine housing were used on this build. Testing of Build 35 of the roller bearing test rig began on 25 September 1968 and was ended on the next day. Testing was terminated on the ninth test cycle at design speed when, after 0.2 hour of operation, a speed shift was detected and the slave bearing outer race temperature increased. Build 35 testing accumulated 4.1 hours and nine cycles at design speed. The teardown inspection revealed that the slave ball bearing had failed. The test bearings were in good condition and were incorporated in the next build to continue testing of this configuration. End wear measurements summarizing the condition of the bearings after Builds 32 and 35 are previously listed in table XIX.

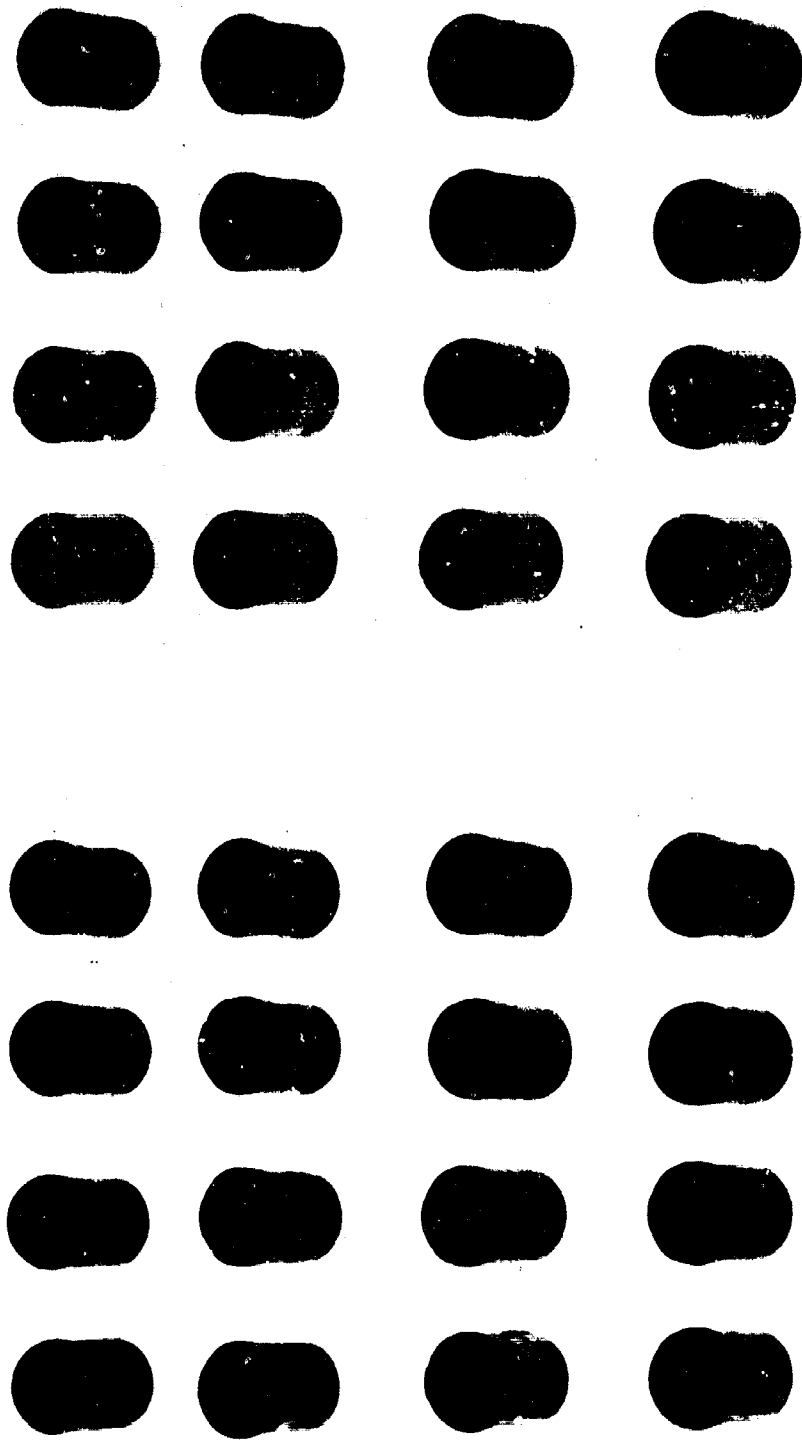


Figure 129. View Showing Moderate Scuffing on Turbine End of Rollers from Reaction Bearing (Build 33)

FE 79866

Figure 130. View Showing Moderate Scuffing on Turbine End of Rollers from Load Bearing (Build 33)

FE 79870

Build 36 of the roller bearing test rig incorporated test bearings from Build 35. Testing of Build 36 began on 3 October 1968 and ended 8 October 1968. Testing was terminated after 8.4 hours at design speed when outer races had accumulated 12.6 hours. The teardown inspection of Build 36 revealed that both test bearings were in good condition and could have been used for additional testing. Figure 131 and 132 show the post-test condition of the reaction bearing, (matrix point 23'). Figures 133 and 134 show the post-test condition of the load bearing, (matrix point 22). Table XIX summarizes the roller end wear on both test bearings after testing on Builds 32, 35, and 36.

Build 37 of the bearing test rig was configured similar to Build 36 to provide a repeatability test on the load bearing (matrix point 22) and to evaluate the effects of increased roller end clearance on the reaction bearing by doubling the largest Build 36 end clearance. Increased end clearance is desirable for the 250K fuel pump to accommodate the hydrostatic thrust piston travel and the difference in thermal contraction between the housings and the rotor assembly. Build 37 also used wider races and the reaction bearing roller-end-to-side rail clearance was increased to 0.040 in. The test bearings had single crown L/D of 1.000 rollers, stainless steel (AMS 5630) rollers and inner races, and steel alloy (AMS 6260) outer races carburized and hardened similar to the outer rings in Build 36. The races were 0.108 in. wider than the races in the previous build and the cage width was increased accordingly. The reaction bearing (matrix point 3) had a 0.0040 in. tight internal fit and the load bearing (matrix point 22) had a 0.0041 in. tight internal fit. The load bearing roller end-to-side rail clearance was 0.020 in. Revisions were made to the test rig in this build to provide a double labyrinth seal with a vent cavity to replace the carbon bellows seal, thereby increasing rig durability.

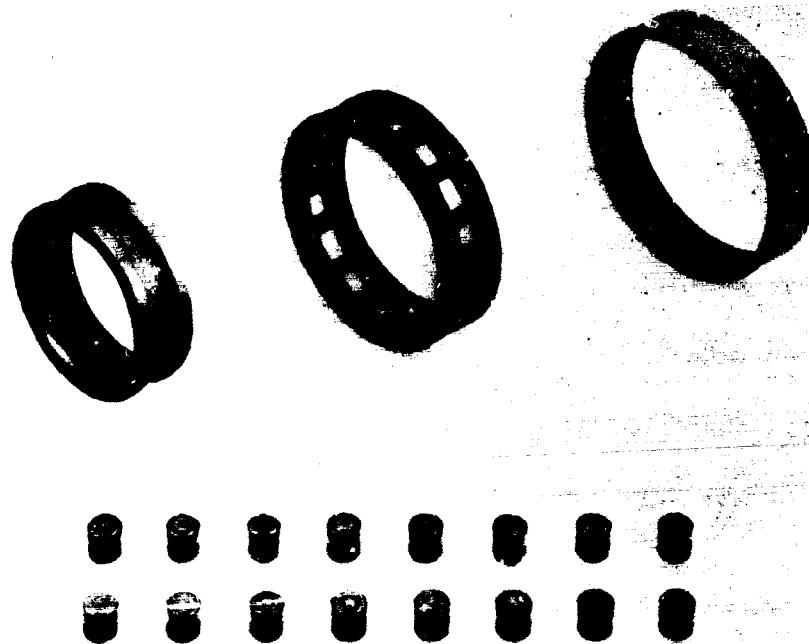


Figure 131. Disassembly Condition of Reaction Bearing (S/N EE-1) With Rear End of Rollers Up (Build 36)

FE 80637

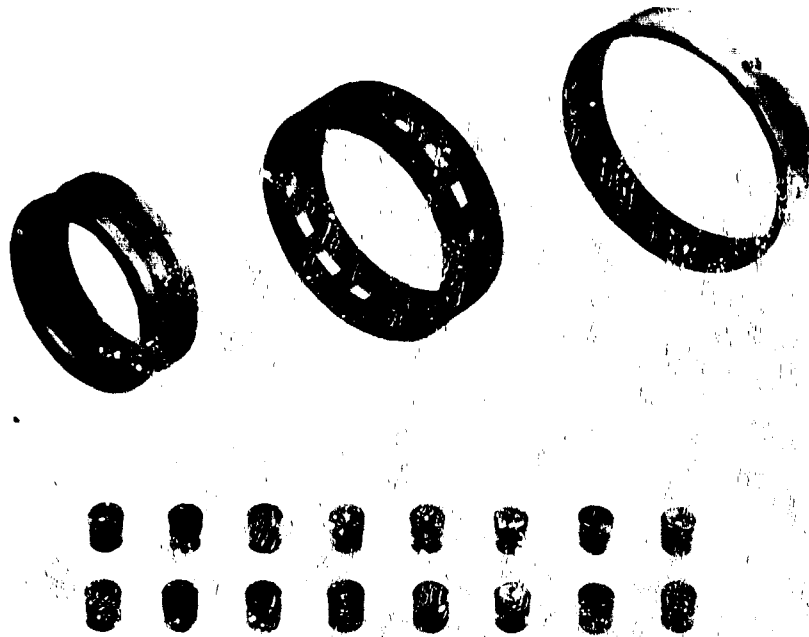


Figure 132. Disassembly Condition of Reaction Bearing (S/N EE-1) With Turbine End of Rollers Up (Build 36)

FE 80638

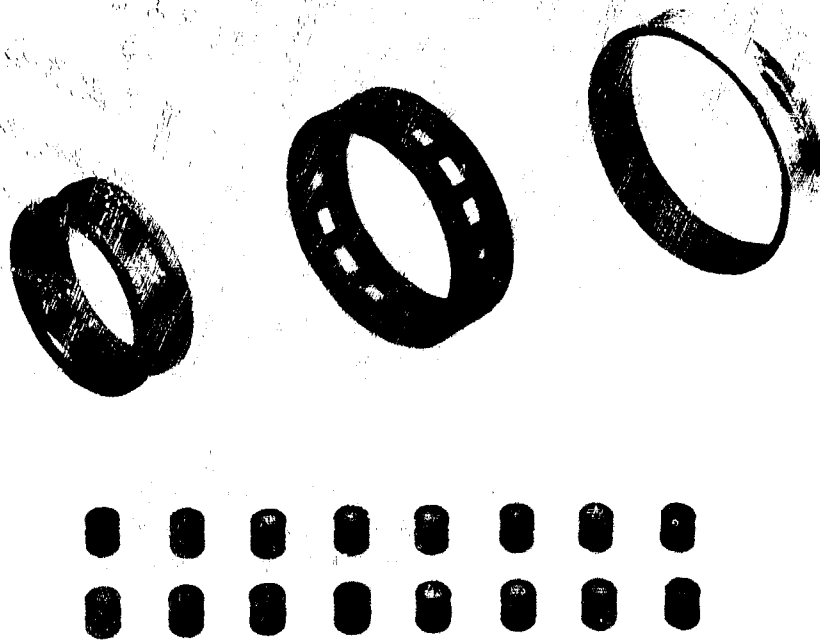


Figure 133. Disassembly Condition of Load Bearing (S/N EE-2) With Rear End of Rollers Up (Build 36)

FE 80639

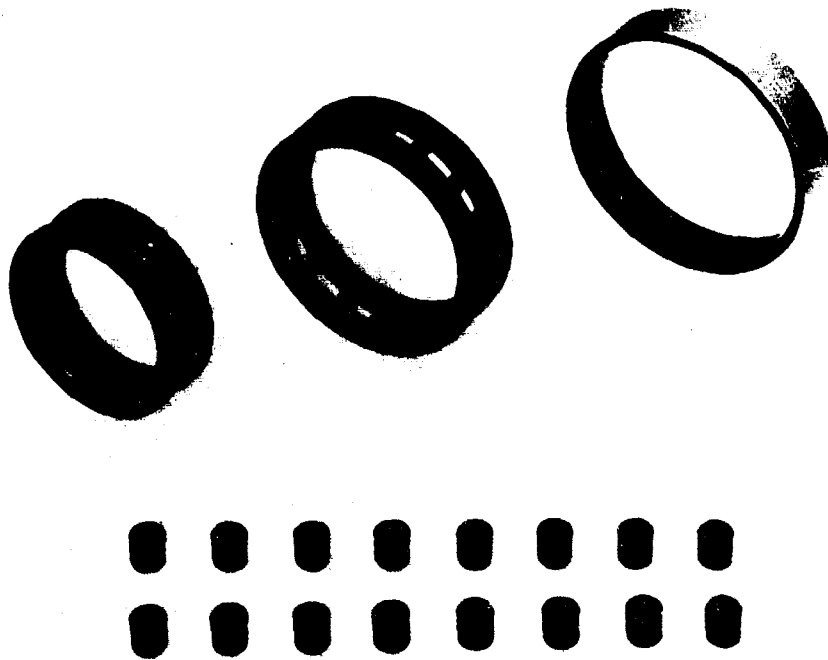


Figure 134. Disassembly Condition of Load
Bearing (S/N EE-2) With Turbine
End Rollers Up (Build 36)

FE 80640

Prior to testing Build 37 of the bearing test rig, the bearing coolant system was revised to provide a series coolant flow arrangement to reduce the coolant consumption. The coolant was supplied to the reaction bearing, and after cooling the two test bearings, it was split to provide flow control through the slave bearing. Testing of Build 37 began on 18 October 1968 and ended on 21 October. Testing was terminated after 2 minutes on the third cycle to rated speed because of high slave bearing outer race temperatures and increased vibrations. Build 37 testing had accumulated 3.9 hours of operation at design conditions. The teardown inspection revealed that the slave bearing had failed but that the test bearings were in good condition. Slight thermal cracking was seen on both outer races outside the roller track in the area of cage contact. The average reaction bearing end wear was 0.0011 in. with 0.0022 in. on the roller with maximum wear. The average load bearing end wear was 0.0002 in. with 0.0004 in. on the roller with maximum wear. The wear was on the turbine end of the rollers for both bearings with moderate scoring on the rear end of both

Build 38 of the roller bearing test rig included the same test bearings as Build 37 and a new slave bearing. Testing of Build 38 was performed on 25 October and the test was terminated after 2.3 hours of the first cycle because of an increase in the reaction bearing and the slave bearing outer race temperature that could not be reduced by increasing the coolant flow rate. The teardown inspection revealed no appreciable damage to the test bearings other than increased thermal cracking on the outer races as shown in figures 135 and 136. One crack had extended into the roller track but it was considered acceptable for continued

testing. No measurable change was noted in the roller end wear for either test bearing. The slave bearing cage ball pockets showed wear from the differential pressure across the cage and from ball excursion.



Figure 135. Reaction Bearing
(S/N FF-1) Outer Race ID
Showing Thermal Cracks
(Build 38)

FE 80934

Build 39 of the roller bearing test rig included the same test bearings as Build 38 and a new ball bearing with a Salox cage instead of Rulon as used previously. Revisions were incorporated in the rig build to provide bearing coolant flow under the inner race of the slave bearing in addition to the normal flow path through the bearing cage. Testing of Build 39 began on 30 October and ended on 31 October. Testing was terminated after 2 hours of the second cycle to rated speed because of increase in vibrations, decrease in speed, and increase in the load bearing outer race temperature. The test bearings had accumulated a total time of 9.9 hours. The teardown inspection revealed that the outer race of the load bearing had cracked at the loaded side with the fracture faces coincident with the thermal cracks as shown in figure 137. Except for the thermal cracks on the outer races, both test bearings were in good condition and the roller end wear was found to be nearly identical with the

previous build measurements. The average roller end wear on the reaction bearing was 0.0011 in. with 0.0019 in. on the roller with maximum wear. The average load bearing end wear was 0.0003 in. with 0.0004 in. on the roller with maximum wear. Figures 138 and 139 show the post-test condition of the reaction bearing (matrix point 3) and load bearing (matrix point 22).



Figure 136. Load Bearing (S/N FF-2)
Outer Race ID Showing
Thermal Cracks (Build 38)

FE 80935

Build 40 of the roller bearing test rig incorporated single crown $L/D = 1.000$, stainless steel (AMS 5630) rollers and stainless steel (AMS 5630) inner races with outer race guided Armalon cages. The load bearing cage had lateral cooling slots 0.055 in. wide (circular diameter) and 0.035-in. deep machined between the pockets. The outer races were fabricated from Inconel 718 (AMS 5663). The reaction bearing (matrix point 3) had a 0.0028 in. tight internal clearance and a roller end-to-side rail clearance of 0.0411 in. The load bearing (matrix point 3) had a 0.0031 in. tight internal clearance and a roller end-to-side rail clearance of 0.0386 in. These diametral fits are equivalent to the 0.005 in. tight fit used with the stainless steel (AMS 5630) outer races when adjusted for the difference in thermal expansion coefficients of the two materials.

Testing of Build 40 was completed on 6 November 1968. The test was terminated after 1.5 hours of the first cycle when there was a speed shift and an increase in the load bearing outer race temperature and vibration level.

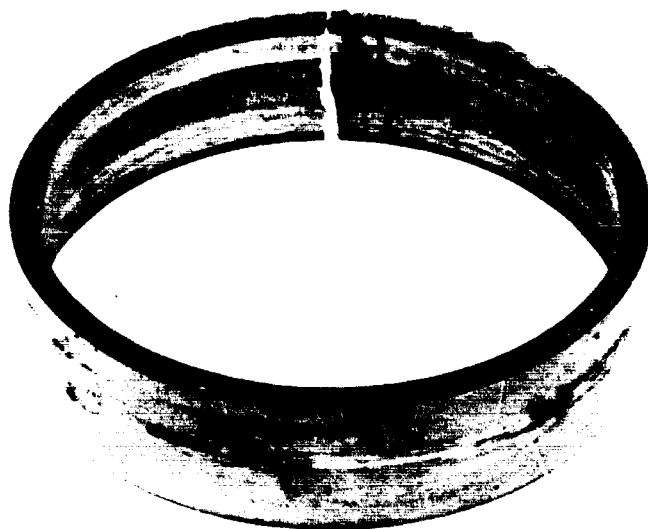


Figure 137. Condition of Load Bearing
(S/N FF-2) Outer Race (Build 39)

FE 81074

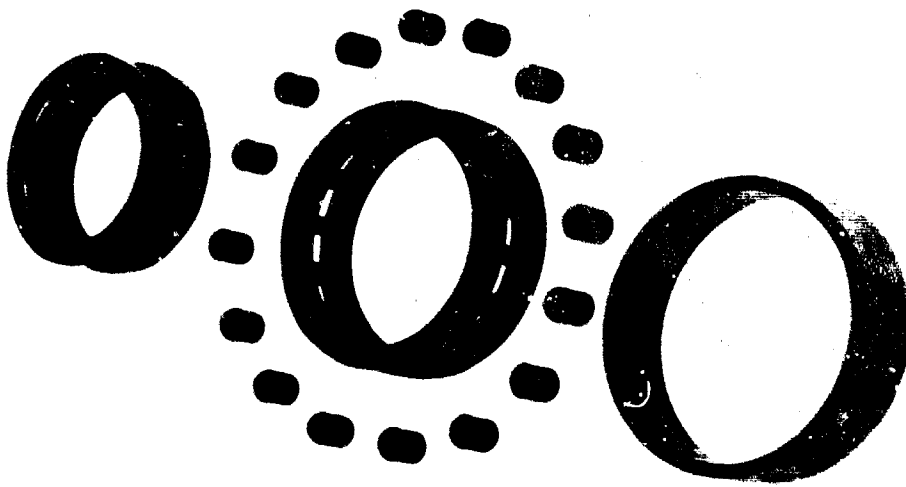


Figure 138. Disassembly Condition of Reaction Bearing (S/N FF-1) With Turbine End of Rollers Up (Build 39)

FE 81183

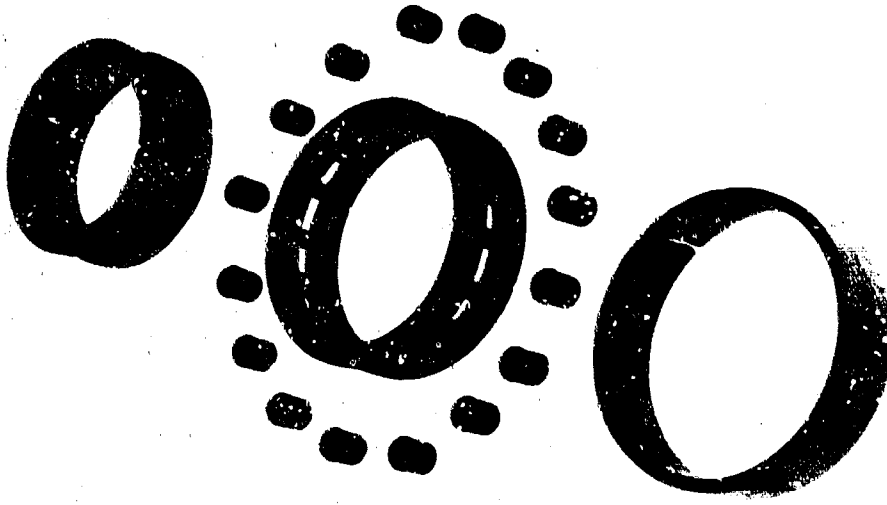


Figure 139. Disassembly Condition of Load Bearing (S/N FF-2) With Turbine End of Rollers Up (Build 33)

FE 81058

A teardown inspection revealed that the load bearing outer race had cracked in two places in the loaded zone and the roller path was severely spalled and deformed as shown in figure 140. The rollers suffered severe impact damage particularly on the rear end as shown in figures 141 and 142. The inner race side rails were heavily spalled as a result of the rollers impacting with the rear rail, this condition is shown in figure 143. The cage sustained severe abrasive damage as a result of particle ingestion from the rollers and races as shown in figure 144. The overall condition of the load bearing (matrix point 3) is shown in figures 145 and 146. The heavy damage on the load bearing rollers prevented measurement of roller end wear. The reaction bearing was in good condition except for some spalling on the outer race roller path in the loaded area as shown in figure 147. The rollers exhibited an average end wear of 0.0001 in. with 0.0005 in. on the roller with maximum wear. All wear was on the turbine end of the rollers. The overall condition of the reaction bearing (matrix point 3) is shown in figure 148.



Figure 140. View Showing Condition of Load Bearing Outer Race (S/N GG-2) After Test of Build 40

FE 81239

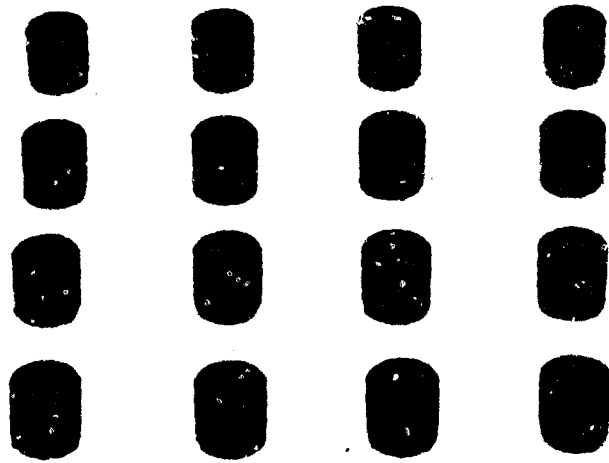


Figure 141. View Showing Condition of Load Bearing Rollers (S/N GG-2), Turbine End Up (Build 40)

FE 81245

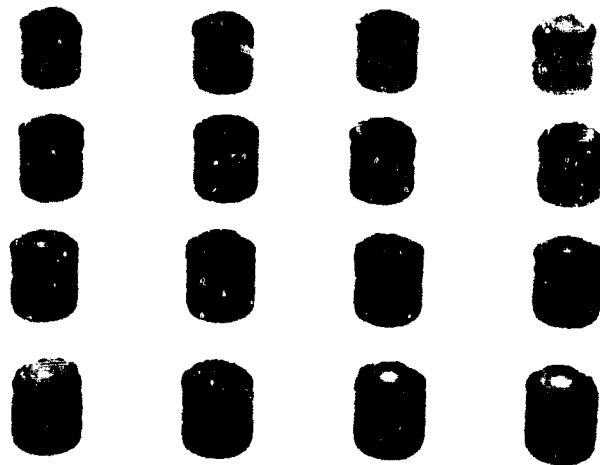


Figure 142. View Showing Condition of Load Bearing Rollers (S/N GG-2), Rear End Up (Build 40)

FE 81244

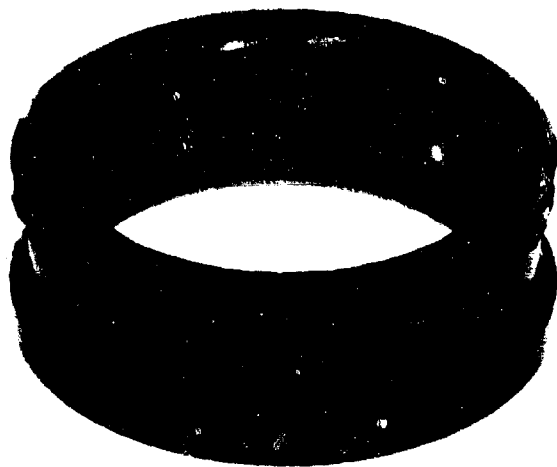


Figure 143. View Showing Condition of Load Bearing Inner Race (S/N GG-2) After Test of Build 40

FE 81241

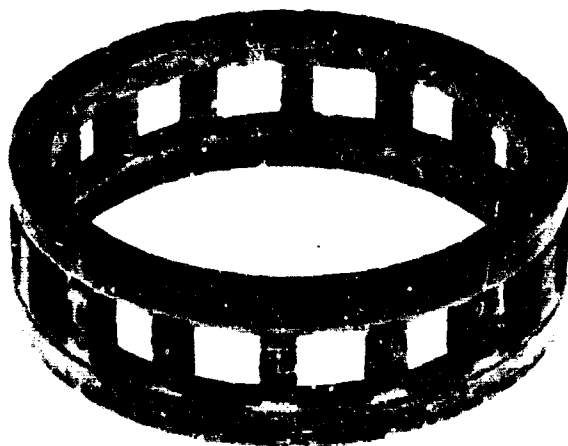


Figure 144. View Showing Condition of Load Bearing Cage (S/N GG-2) After Test of Build 40

FE 81247

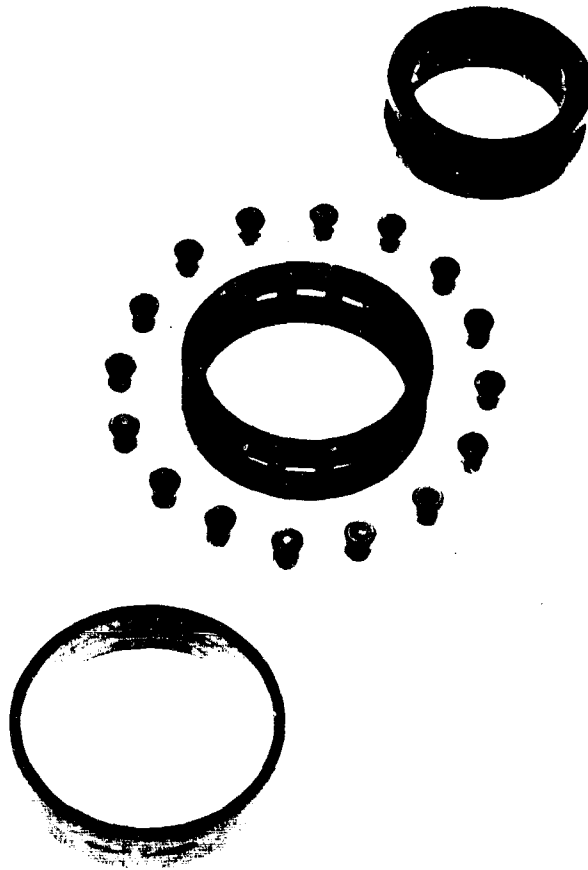


Figure 145. View Showing Overall Condition
of Load Bearing (S/N GG-2),
Rear End Up (Build 40)

FE 81234

Metallurgical analysis of the failed outer race from the Build 40 load bearing indicates that the Inconel 718 (AMS 5663) race was severely overloaded, which can be attributed to the mechanical deformation in the roller track. Heat generation from the deformed roller track appears to have permitted further plastic deformation until the failure was completed with the lateral cracks seen in the plastically deformed area. Metallurgical examination revealed that the microstructure in the failed zone had transformed to a cast structure. The less heavily loaded reaction bearing had begun spalling in the loaded zone and it is viewed as preliminary to the failure encountered with the load bearing. It appears that the hardness of Rc 44 on these races is not sufficient for the loads and life required in this bearing application.

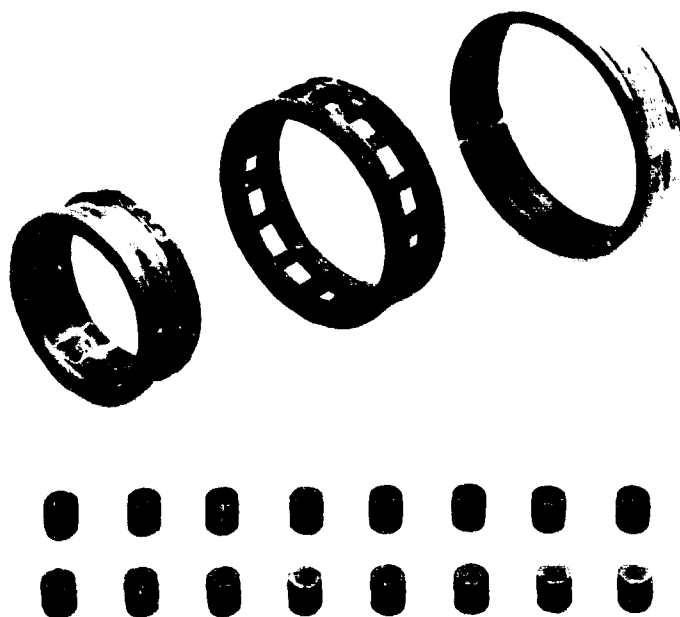


Figure 146. View Showing Overall Condition of Load Bearing (S/N GG-2), Turbine End Up (Build 40)

FE 81233

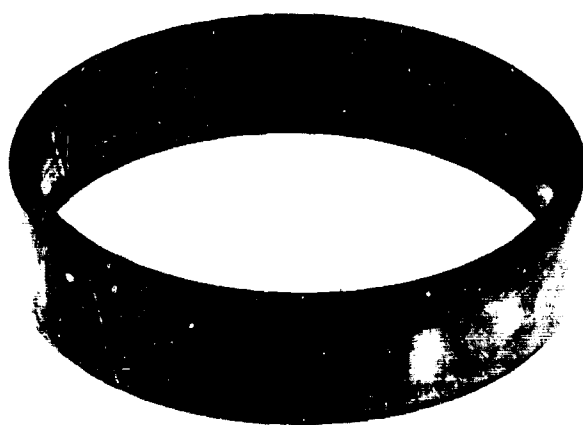


Figure 147. View Showing Condition of Reaction Bearing Outer Race (S/N GG-1) After Test of Build 40

FE 80830

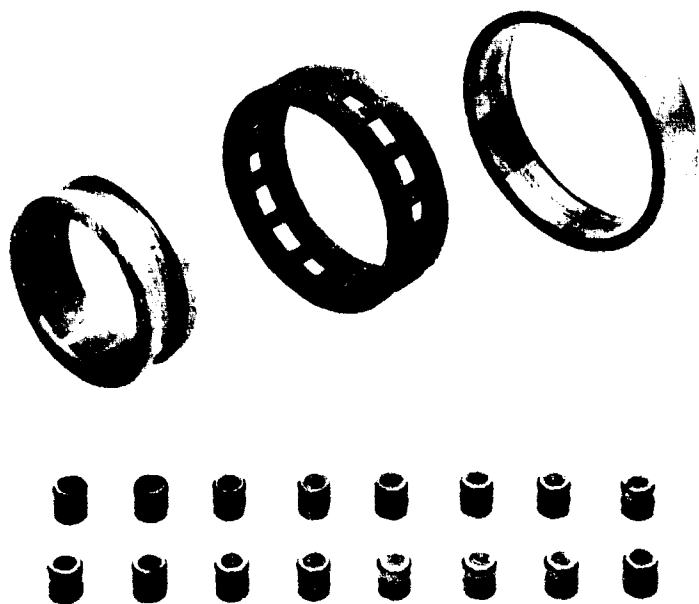


Figure 148. View Showing Overall Condition
of Reaction Bearing (S/N GG-1),
Turbine End Up (Build 40)

FE 81231

Build 41 of the bearing test rig consisted of test bearings with single crown L/D = 1.000 stainless steel (AMS 5630) rollers, stainless steel (AMS 5630) inner races, Armalon outer race guided cages with lateral coolant slots, and steel alloy (AMS 6265) outer races. The reaction bearing (matrix point 3) had a 0.0036 in. tight internal clearance and a roller end-to-side rail clearance of 0.0391 in. The load bearing (matrix point 3) had a 0.0040 in. tight internal clearance and a roller end-to-side rail clearance of 0.0393 in. These diametral fits are equivalent to a 0.0046 and 0.0050 in. tight fit, with stainless steel (AMS 5630) outer races respectively, when adjusted for the difference in coefficient of expansion.

Build 41 testing, was begun on 18 November 1968 and was ended the next day after accumulating 10.01 hours. Testing was terminated after 1 minute of the sixth test cycle when a speed shift and an increase in the reaction bearing outer race temperature were observed.

A teardown inspection revealed that one roller in the reaction bearing had skewed as shown in figure 149. The cage packet from another roller showed the characteristic dog-bone wear pattern associated with insufficient roller preload. The equivalent negative internal clearance on this bearing, 0.0046 in., was the lowest value tested recently. The inner race showed light chipping on both side rails with the turbine end more heavily damaged. Moderate thermal cracking of the outer race was detected in the cage contact areas on each side of the roller tract. The average roller end wear was 0.0082 in. with 0.012 in. on the roller with the maximum wear. The turbine end of the rollers exhibited the heaviest wear. The post-test condition of the reaction bearing is shown in figure 150 with detail views of the rollers, inner race and outer race shown in figures 151, 152, and 153, respectively. The load bearing was in excellent condition as shown in figure 154 and could be used for further testing. The average load bearing roller

end wear was 0.021 in. with 0.0048 in. on the roller with the maximum wear. Both ends of the rollers exhibited some wear with the maximum wear on the rear end.

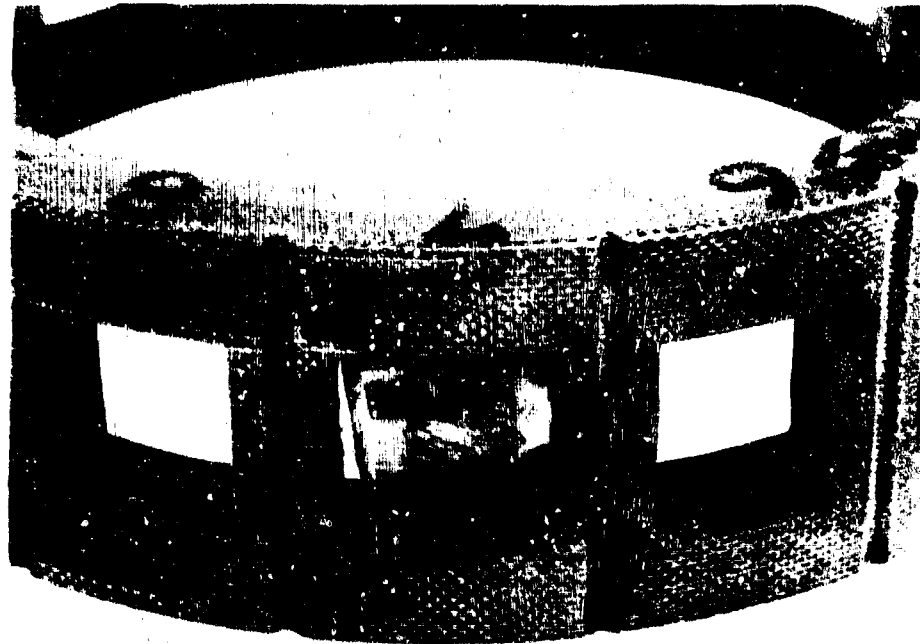


Figure 149. View Showing Skewed Position of Roller No. 7 in Reaction Bearing Cage (S/N HH-1) After Test of Build 41

FE 81483

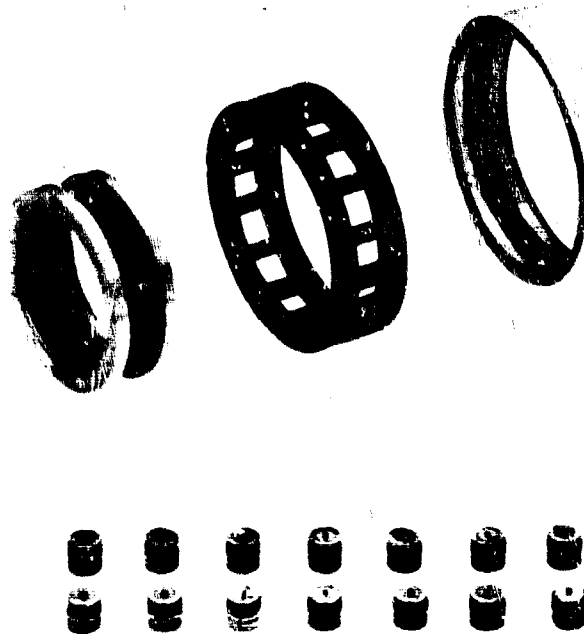


Figure 150. View Showing Overall Condition of Reaction Bearing (S/N HH-1), Turbine End Up (Build 41)

FE 81214

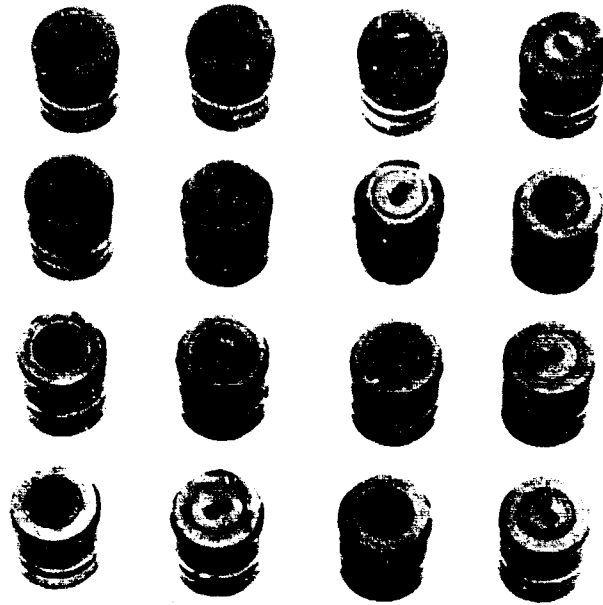


Figure 151. View Showing Condition of Reaction Bearing Rollers (S/N HH-1), Turbine End Up (Build 41)

FE 81478

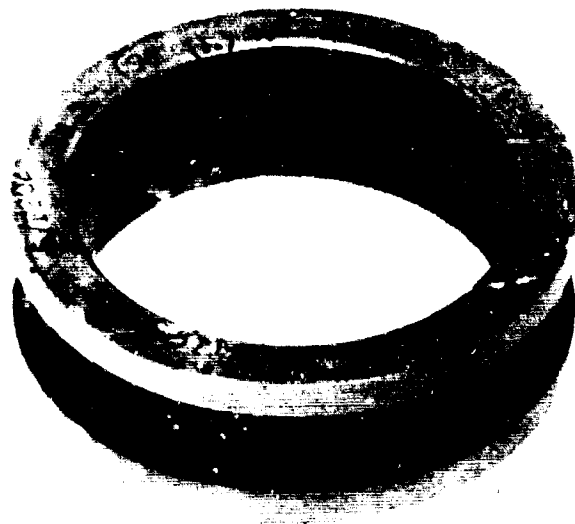


Figure 152. View Showing Condition of Reaction Bearing Inner Race (S/N HH-1) After Test of Build 41

FE 81475

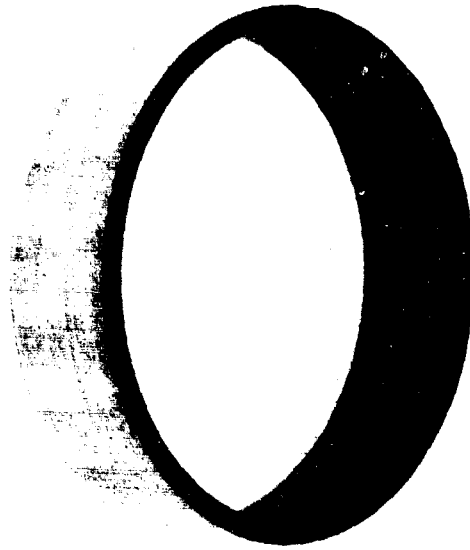


Figure 153. View Showing Condition of
Reaction Bearing Outer Race
(S/N HH-1) After Test of Build 41

FE 81473



Figure 154. View Showing Overall Condition
of Load Bearing (S/N HII-2),
Turbine End Up (Build 41)

FE 81216

Build 42 of the roller bearing test rig incorporated single crown L/D = 1.000 stainless steel (AMS 5630) rollers, stainless steel (AMS 5630) inner races, Armalon outer-race-guided cages with lateral cooling slots, and outer races fabricated from steel alloy (AMS 6265) with the inside diameter carburized. Both test bearings had a roller end-to-side rail clearance of 0.0202 in. and a negative diametral internal clearance of 0.0043 in. This fit corresponds to a 0.0053 in. internal clearance with a stainless steel (AMS 5630) outer race.

Testing of Build 42 began on 2 December and was concluded on 5 December 1968. During the test program, 15.3 hours of bearing operation at maximum load and speed condition, and 305 acceleration cycles were accumulated. A bearing coolant reduction survey was also conducted. No increase in outer race temperature was observed when the coolant flow was reduced from 31 gpm to 10 gpm in increments of approximately 5 gpm. Below 10 gpm coolant flow, a rapid increase in bearing outer race temperature was observed and the coolant flow was increased back to 31 gpm where the outer race temperature again stabilized. After completing all program objectives the test rig was pulled from the test stand to permit teardown inspection of the bearings.

Post-test inspection of the roller bearings revealed that both bearings were in good condition and could have undergone further testing. The only discrepancy noted was thermal cracking of the outer races in the areas of cage contact as shown in figure 155. End wear measurements showed moderate wear on the reaction bearing and extremely light wear on the load bearing. The wear on the reaction bearing was on the turbine end with an average wear of 0.0070 in. and 0.0098 in. on the roller with the maximum wear. Figures 156 and 157 show the condition of the reaction bearing rollers. The wear on the load bearing was on the rear end with an average wear of 0.0005 in. and 0.0014 in. on the roller with the maximum wear. Figures 158 and 159 show the condition of the load bearing rollers. The overall condition of the reaction bearing is shown in figures 160 and 161, and the load bearing is shown in figures 162 and 163. The roller bearing qualification test program was concluded with the completion of the Build 42 test.



Figure 155. Enlarged View of ID of Outer Race Showing Numerous Thermal Cracks

FAL 14328

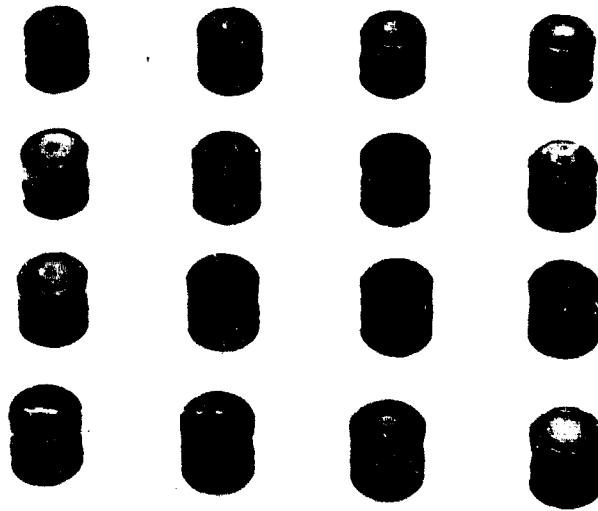


Figure 156. View Showing Condition of Reaction Bearing Rollers (S/N JJ-1) With Rear End Up (Build 42)

FE 81801

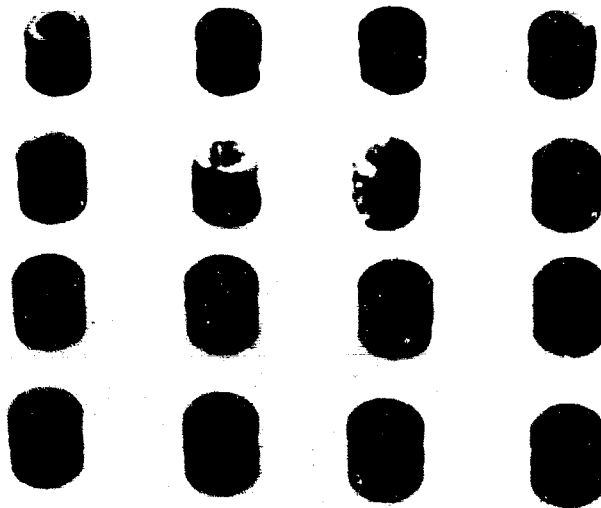


Figure 157. View Showing Condition of Reaction Bearing Rollers (S/N JJ-1) With Turbine End Up (Build 42)

FE 81802

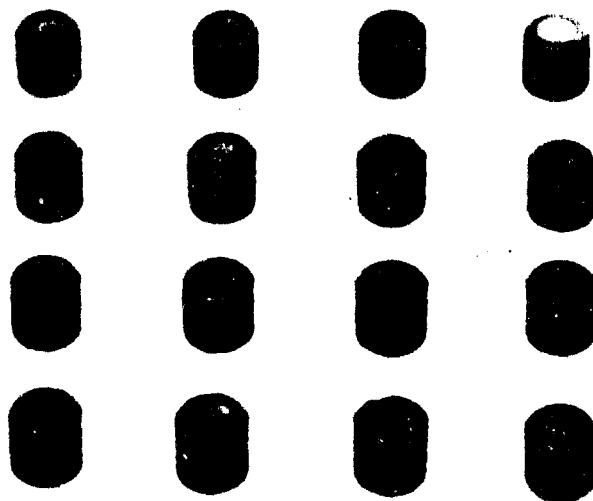


Figure 158. View Showing Condition of Load Bearing Rollers (S/N JJ-2) With Rear End Up (Build 42)

FE 81803

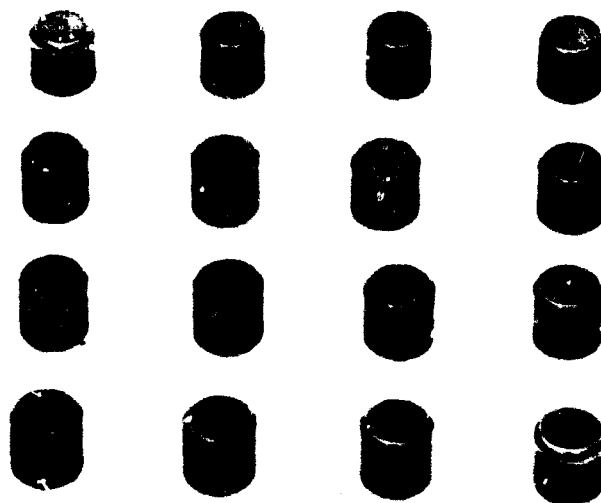


Figure 159. View Showing Condition of Load Bearing Rollers (S/N JJ-2) With Turbine End Up (Build 42)

FE 81804



Figure 160. View Showing Overall Condition of Reaction Bearing (S/N JJ-1) Turbine End Up (Build 42)

FE 81794

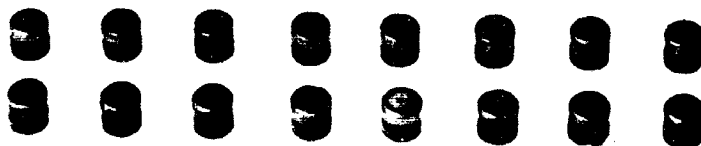
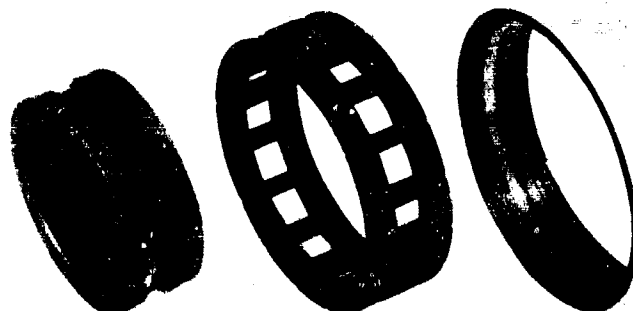


Figure 161. View Showing Overall Condition of Reaction Bearing (S/N JJ-1) Rear End Up (Build 42)

FE 81793

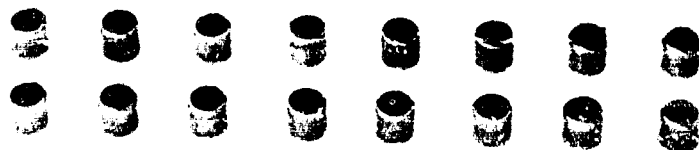
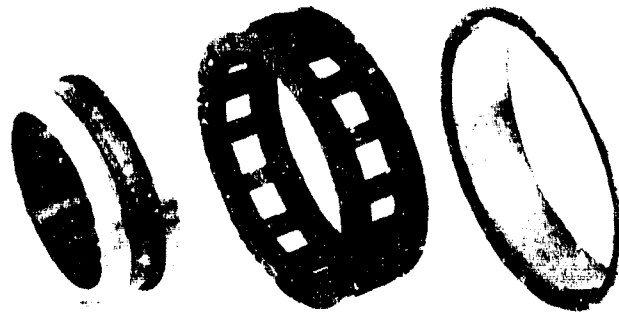


Figure 162. View Showing Overall Con-
dition of Load Bearing (S/N
JJ-2) Turbine End Up (Build 42)

FE 81796

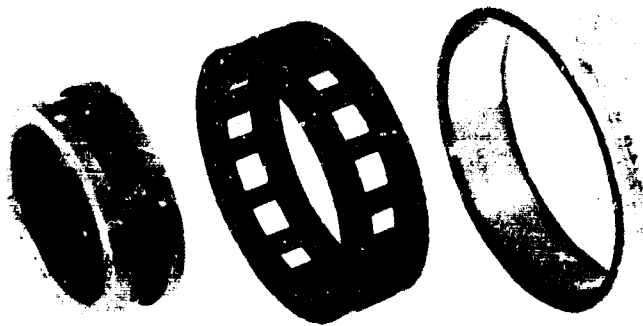


Figure 163. View Showing Overall Condition
of Load Bearing (S/N JJ-2)
Rear End Up (Build 42)

FE 81795

C. PUMP INLET EVALUATION

1. Introduction

The objective of this test program was to obtain supporting data for the design of the inlet configuration to be used on the liquid hydrogen and liquid oxygen turbopumps. Because of engine packaging considerations, the proposed demonstrator engine has a flow distributor at the inlet to each main turbopump as shown in figure 164. The effect of an inlet flow distributor on the head-flow and suction characteristics of the inducer was investigated using water as the test fluid. These data are being used to design a suitable pump inlet configuration within the demonstrator engine envelope.

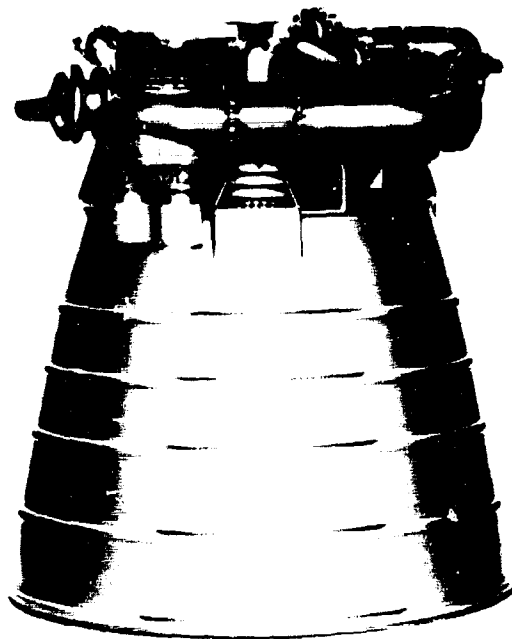


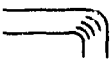
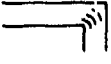
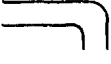
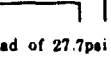
Figure 164. Demonstrator Engine Showing Inlet Flow Distributors at the Fuel and Oxidizer Inlets (Circled Areas)

FF 70835

GS 7466A

2. Summary, Conclusions, and Recommendations

Nine inlet configurations were evaluated during the preliminary study as shown in figure 165. Electrical analog studies of these candidate configurations were performed and the head loss coefficients shown in figure 165 resulted from this study.

NO.	INLET DESCRIPTION	INLET CONFIGURATION	HEAD LOSS COEFFICIENT	HEAD LOSS * psi
1	90 Deg Elbow With Guide Vanes and R/D = 0.76		0.06	1.5
2	90 Deg Miter With Guide Vanes		0.20	5.6
3	90 Deg Elbow Without Guide Vanes and R/D = 0.75		0.26	7.2
4	Double Inlet Without Line Branch Loss (Double Discharge Boost Pump)		0.40	11.1
5	Single Inlet Without Guide Vanes		0.50	13.9
6	Single Inlet With Guide Vanes		0.46	12.5
7	Stepanoff		0.70	19.4
8	Scroll		0.75	20.8
9	90 Deg Miter Without Guide Vanes		1.20	33.1

*Assuming an Inlet Velocity Head of 27.7psi

Figure 165. Candidate Inlets and Predicted Pressure Loss

FD 23194A

Two configurations were selected as a result of this electrical analog study for evaluation on the water test loop. These were a short radius elbow with turning vanes and a single inlet without guide vanes similar to configurations No. 1 and 5 of figure 165. Although an elbow inlet with guide vanes was the best design analyzed from a head loss and velocity distribution standpoint, it was less suitable for the fuel pump because of the severe space limitations. The single inlet without guide vanes was a more flattened design that would satisfy the envelope requirements of the fuel pump and was selected as the second candidate for evaluation on the water test loop.

Three inlet configurations were tested on the water loop using an existing 350K oxidizer pump inducer fabricated under Contract NAS8-20540. These were: (1) a straight inlet to establish baseline inducer performance, (2) a 112 deg elbow inlet with turning vanes, and (3) a 112 deg flattened pancake inlet.

Suction characteristics of the 350K inducer with the straight inlet compared favorably with predicted levels. Peak suction specific speed was near 25,000 rpm (gpm)^{1/2}/ft^{3/4}.

Suction performance with the elbow inlet compared favorably with that of the straight inlet and with predicted suction performance levels. Maximum demonstrated suction specific speed was 24,000 rpm (gpm)^{1/2}/ft^{3/4}.

Suction performance with the pancake inlet also compared favorably with that of the straight inlet and with predicted levels of suction performance. Maximum demonstrated suction specific speed was $23,500 \text{ rpm (gpm)}^{1/2}/\text{ft}^{3/4}$.

Indicated noncavitated performance with the straight inlet was about 15% lower than determined during oxidizer pump tests under Contract NAS8-20540 using LO_2 and LN_2 as the pumped fluids.

The noncavitated head coefficient versus flow coefficient slope was steeper with the elbow inlet and the head coefficients were higher at low flow coefficients than obtained with the straight inlet. The head coefficient flow coefficient characteristic with the pancake inlet was approximately the same level as with the straight inlet, but had a discontinuity between flow-to-speed ratios of 0.16 and 0.18.

Higher noise levels emanate from the pancake inlet at low flow-to-speed ratios and also at high speeds indicating a possible structural problem.

Large static pressure losses occur in the inlet section of both the elbow and pancake housings at low flow-to-speed ratios. These losses appear to be pump related and are accompanied by severe inlet pressure oscillations.

The various inlet configurations were tested over the range of flow-to-speed ratios expected in the engine throttling range; however, maximum speed and flow rates were restricted by test stand limitations to about 40% of design. It is believed, however, that the test results can be extrapolated to design conditions.

The elbow inlet appears to be superior to the pancake inlet and is recommended for both the fuel and liquid oxygen pumps although some slight modification to the inlet may be required to fit this configuration into the engine envelope on the fuel pump inlet.

3. Testing

The pump inlet evaluation test program was conducted using the existing closed loop water test facility in test stand D-34, which is shown in figure 166. This facility includes a 250 hp dc motor gearbox unit capable of closely controlled speeds up to 9000 rpm. The test stand has one 5 in. and two 8 in. parallel loops with flow measurement capability from zero to 4000 gpm. A schematic of the D-34 test stand is shown in figure 167. The test rig incorporated an existing 350K liquid oxygen turbopump inducer, which demonstrated a suction specific speed capability of $23,000 \text{ rpm (gpm)}^{1/2}/\text{ft}^{3/4}$ in liquid oxygen during the 350K Liquid Oxygen Program, Contract NAS8-20540.

Water testing of a straight inlet section, shown in figure 168, was conducted to establish a baseline. Testing was then conducted on a short radius elbow with turning vanes (figure 169) and a pancake inlet (figure 170). Each of these configurations was constructed with transparent windows to permit taking photographs of the flow patterns at the inducer inlet. However, the lucite material was easily damaged by inducer tip cavitation as shown in figure 171 and little useful information was obtained. In each configuration, damage to the viewing section necessitated replacing the window with a steel insert or fibreglassing over the window.

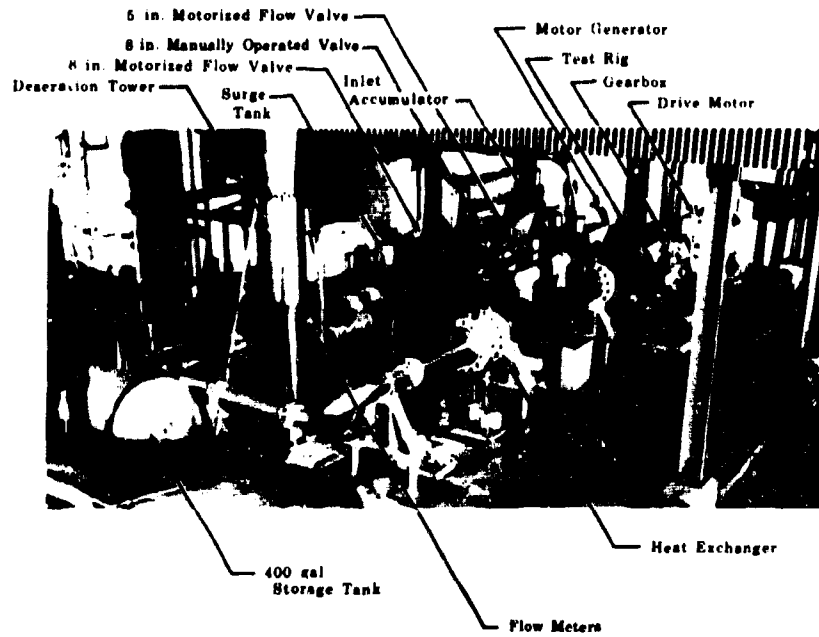


Figure 166. Closed Loop Water Test Facility

FD 19643A

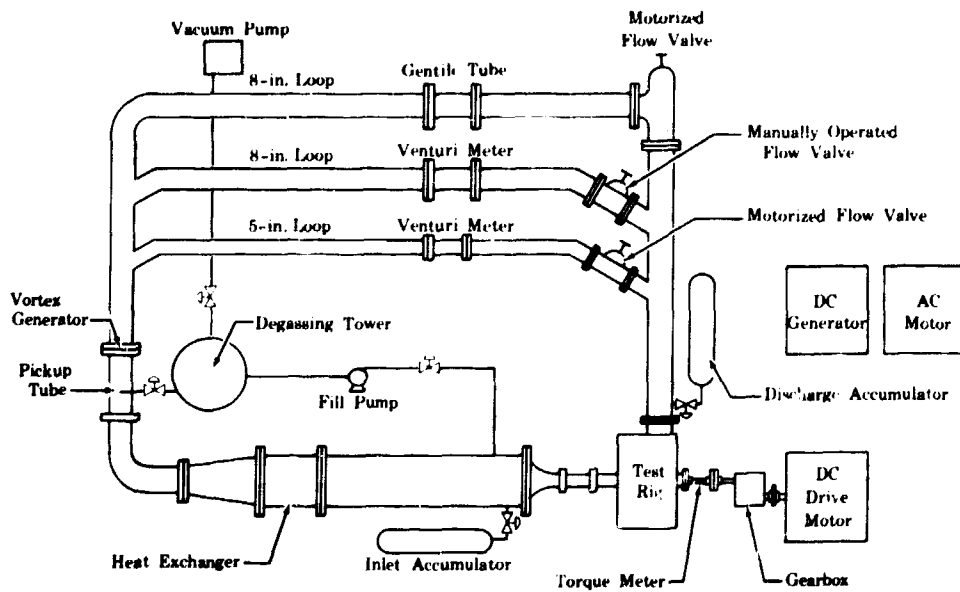


Figure 167. Water Test Stand Schematic

FD 19703

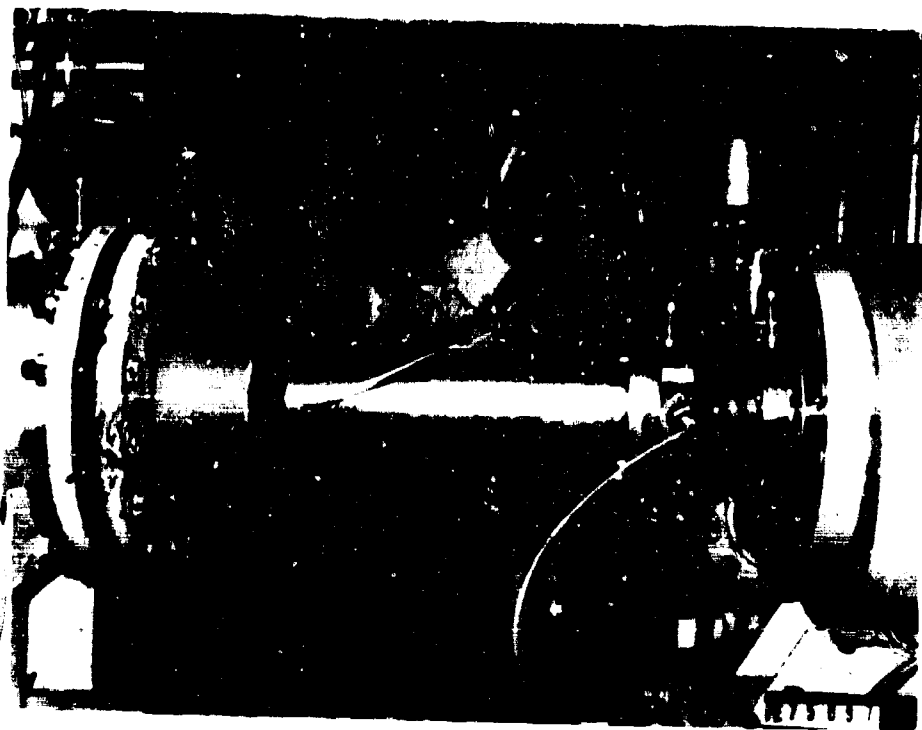


Figure 168. Straight Inlet Test Installation

FE 75097

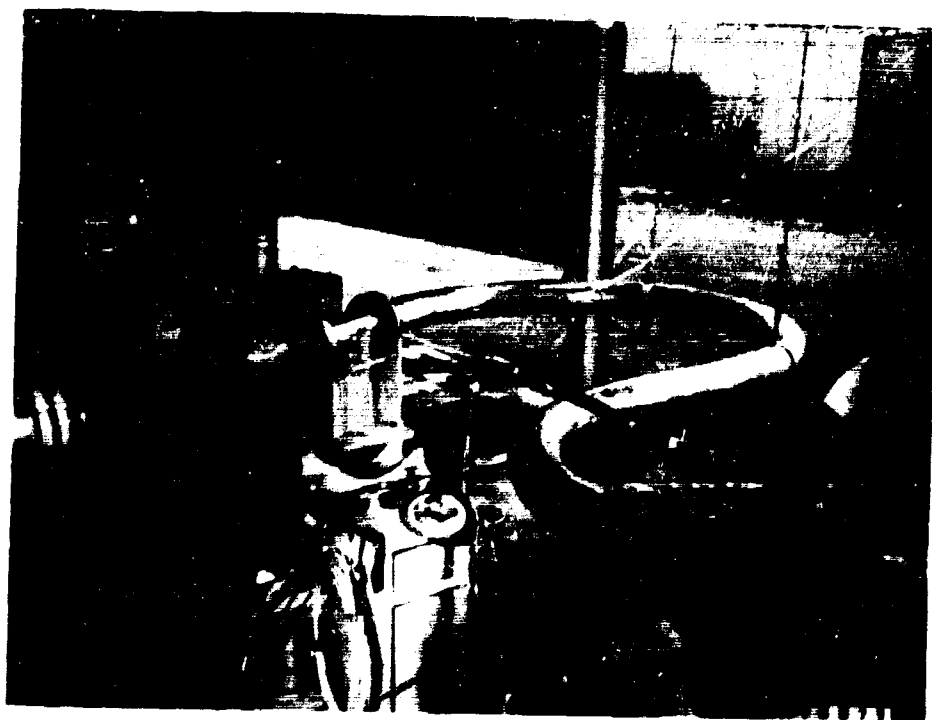


Figure 169. Short Radius Elbow With Turning Vanes
Inlet Test Installation

FC 16029



Figure 170. Pancake Inlet Test Installation

FE 76743

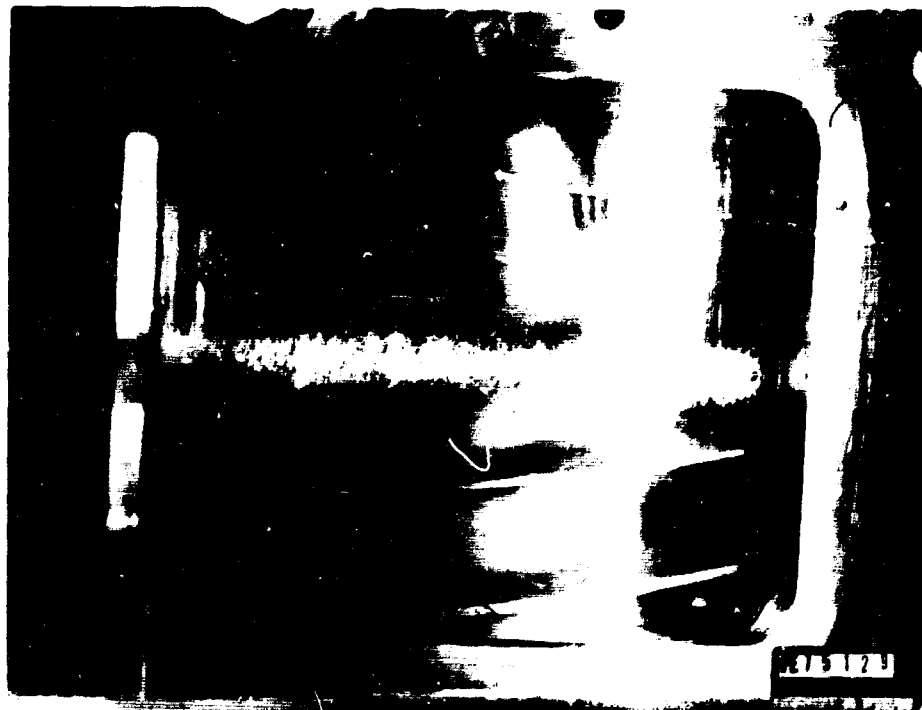


Figure 171. Cavitation Damage on Lucite Viewing Section

FE 75129

Testing was conducted by setting a positive inlet pressure at the rig and then accelerating to the desired speed. Flowrate was varied to determine the head-flow characteristics, and inlet pressure was reduced until cavitation occurred to determine suction performance. The test results are summarized in table XX.

Table XX. Cavitation Test Data

Flow (gpm)	Speed (rpm)	Q/N (gpm/rpm)	Inlet Pressure at 3% Cavitation (psia)	Suction Specific Speed $\left(\frac{(\text{rpm})(\text{gpm})^{1/2}}{\text{ft}^{3/4}}\right)$	Net Positive Suction Head (ft)
Straight Inlet					
1450	7000	0.21	12.5	22,600	27.0
1540	8500	0.18	17.8	20,900	40.0
1260	7000	0.18	13.0	19,900	29.0
1670	7000	0.24	13.9	21,900	31.0
2025	8500	0.24	19.2	22,600	43.3
1750	8500	0.21	17.4	22,800	39.0
1035	7000	0.15	15.4	15,300	35.0
1030	7000	0.15	14.6	16,700	32.5
1260	8500	0.15	20.0	17,400	45.0
420	7000	0.06	22.0	7,800	49.0
500	6000	0.08	14.6	9,900	32.5
Elbow With Turning Vanes					
1910	8500	0.23	18.2	22,500	42.0
1750	8500	0.21	16.4	23,250	38.0
1455	7000	0.21	11.3	23,060	26.3
1545	7500	0.21	12.3	23,900	28.5
2015	8500	0.24	17.4	23,700	40.5
1670	7000	0.24	12.1	23,450	28.1
1565	7000	0.22	11.7	23,100	27.5
1495	8500	0.18	17.9	20,200	41.5
Banjo Inlet					
1250	8500	0.15	20.7	17,370	44.7
1550	8500	0.18	16.3	22,830	36.0
1830	8500	0.22	16.9	23,450	38.5
2050	8500	0.24	21.3	21,400	47.2
1770	8000	0.22	17.2	22,500	37.0
600	7000	0.086	17.3	11,330	37.5
1010	7000	0.14	14.0	17,100	30.5
1220	7000	0.17	11.0	22,950	23.5
1575	7000	0.23	13.2	22,200	29.0
1695	7000	0.24	15.1	21,100	32.8

4. Analysis

a. Cavitation Performance

Suction performance was based on an inlet pressure in a straight section of line upstream of each of the inlet housings. The approximate locations of the inlet pressure taps are shown in figures 172, 173, and 174. The suction specific speed versus unit flow for the straight, elbow, and pancake inlets is presented in figures 175, 176, and 177, respectively. These curves are based on 3% inducer noncavitating head fall off. The percent predicted head coefficients versus net positive suction head for all cavitation points is provided in figures 178 through 183. In some instances, the 3% head fall off point was not reached; however, it was visually apparent, and from increased noise, that the inducer was cavitating. Percent predicted head coefficient versus suction specific speed is shown in figures 184 through 189.

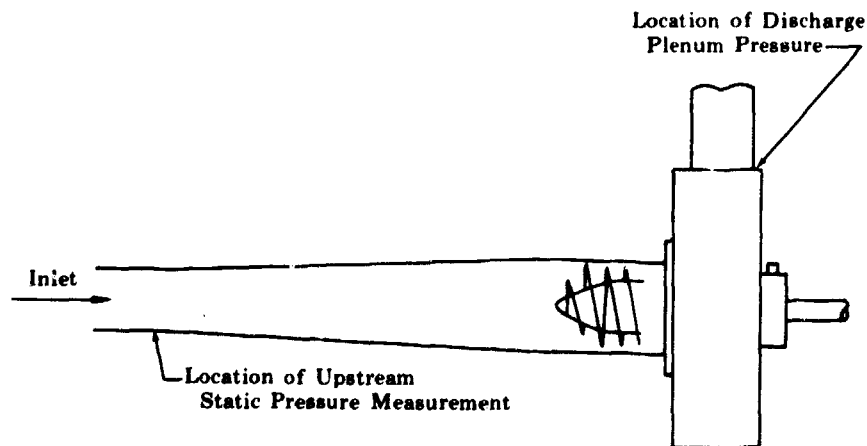


Figure 172. Straight Inlet Test Section Pressure Tap Locations FD 25424

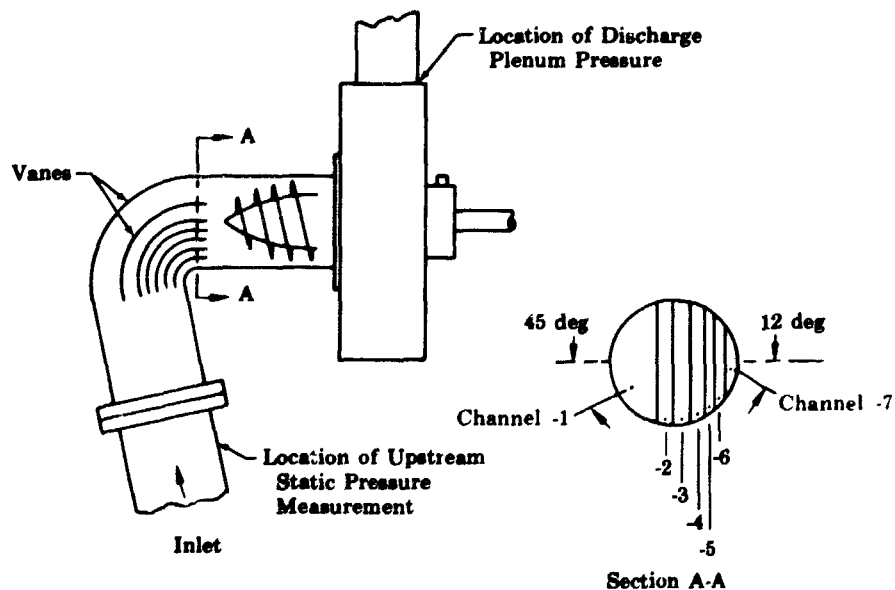


Figure 173. Elbow Test Section Pressure Tap Locations FD 25425

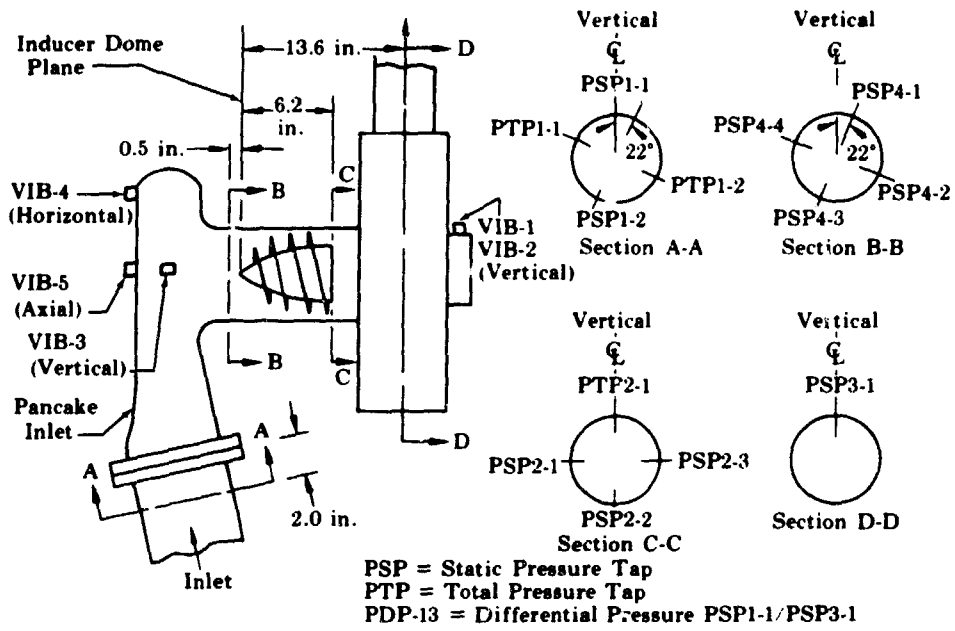


Figure 174. Pancake Test Section Pressure Tap Locations FD 25426

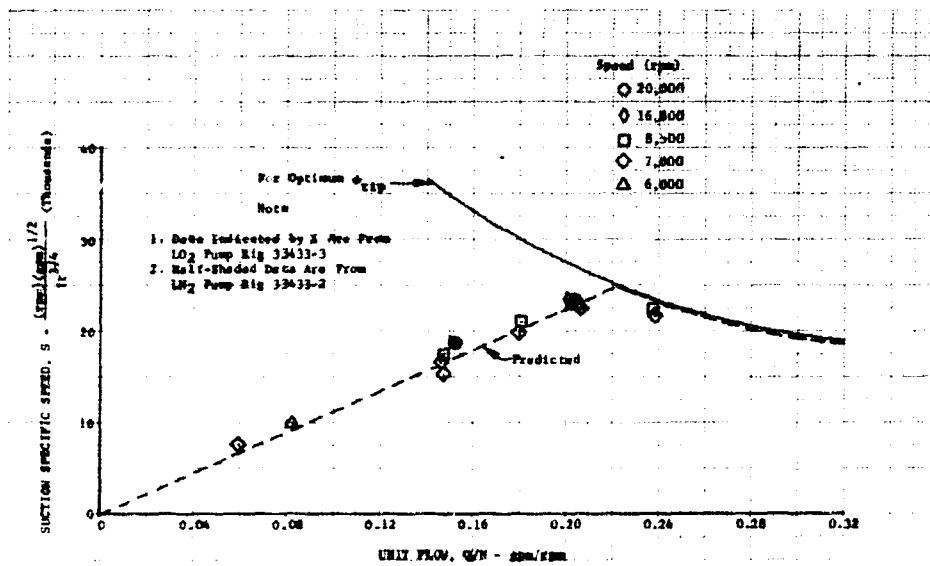


Figure 175. Suction Specific Speed vs Unit Flow for Straight Inlet DF 66833

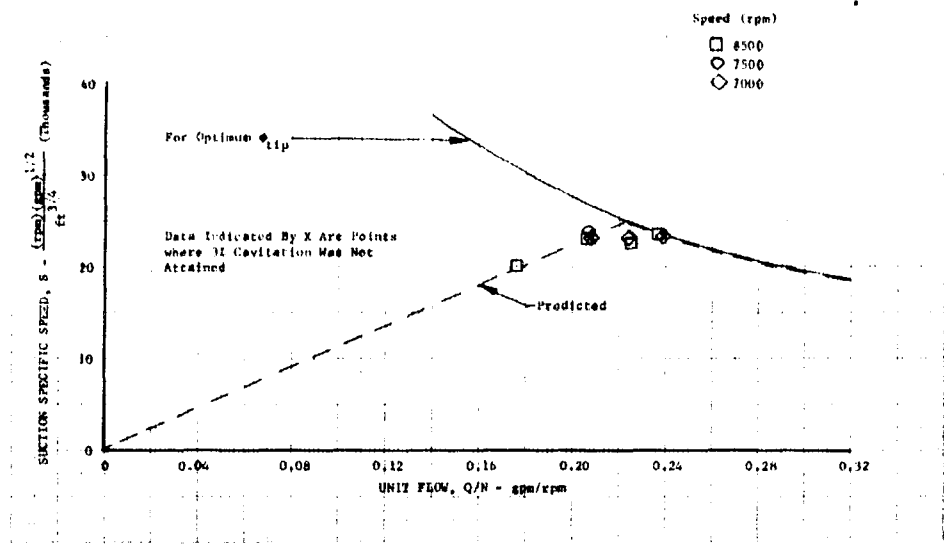


Figure 176. Suction Specific Speed vs Unit Flow for Elbow Inlet DF 66834

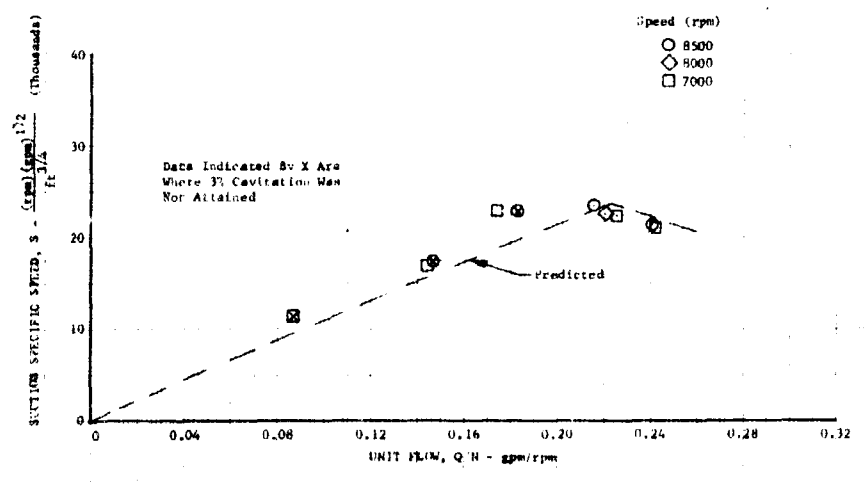


Figure 177. Suction Specific Speed vs Unit Flow for Pancake Inlet DF 66835

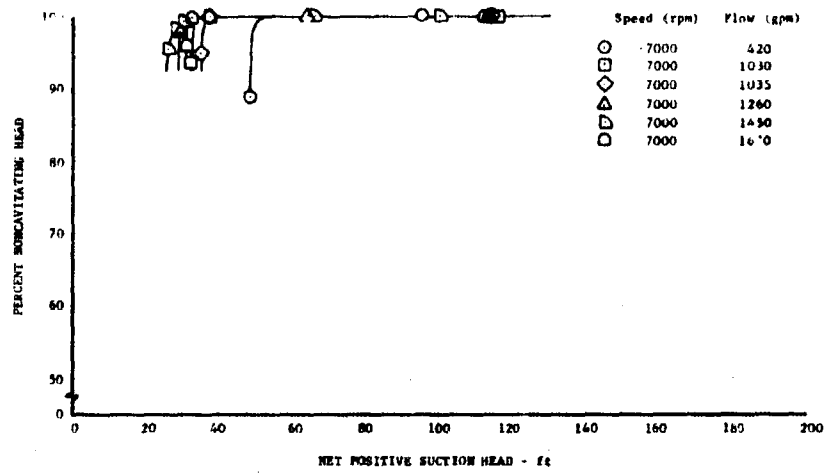


Figure 178. Percent Noncavitating Head vs Net Positive Suction Head (Straight Inlet) DF 66836

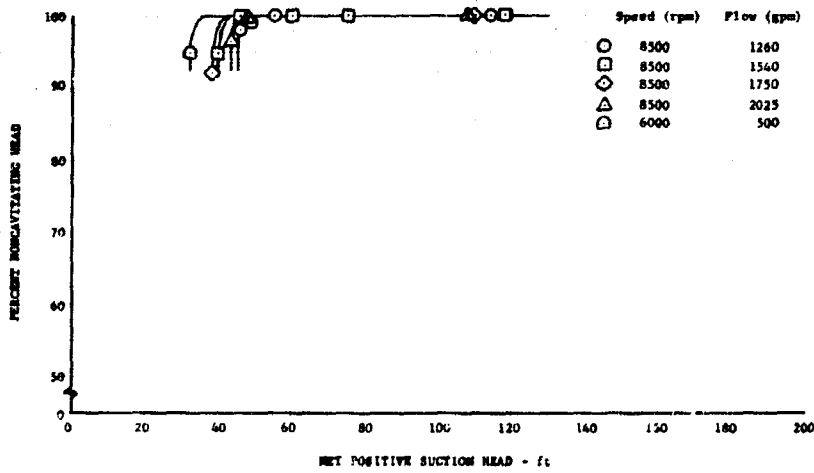


Figure 179. Percent Noncavitating Head vs Net Positive Suction Head (Straight Inlet) DF 66837

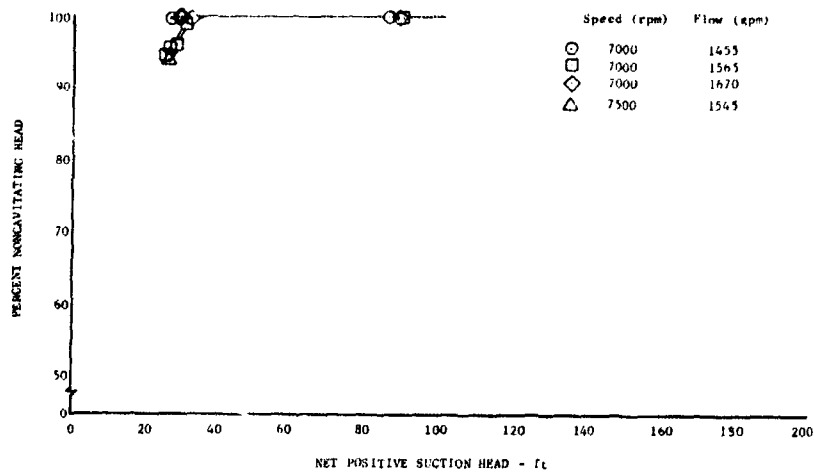


Figure 180. Percent Noncavitating Head vs Net Positive Suction Head (Elbow Inlet)

DF 66838

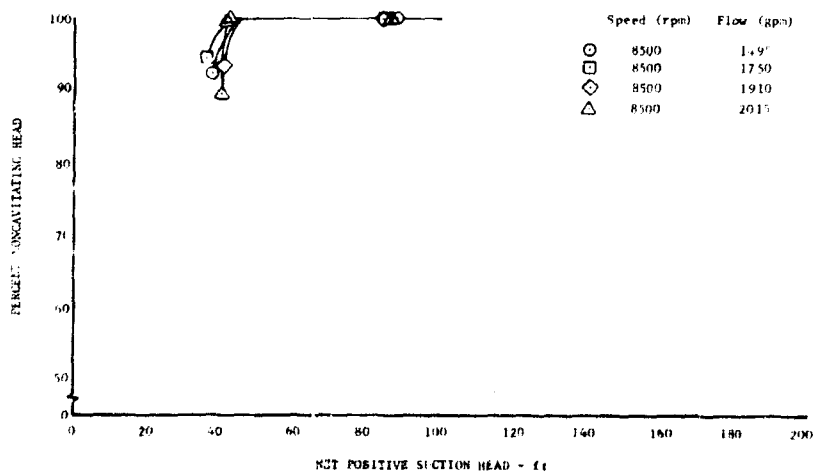


Figure 181. Percent Noncavitating Head vs Net Positive Suction Head (Elbow Inlet)

DF 66839

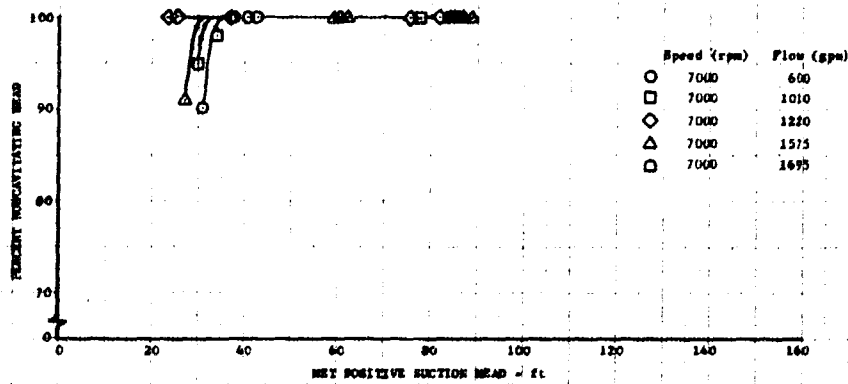


Figure 182. Percent Noncavitating Head vs Net Positive Suction Head (Pancake Inlet) DF 66840

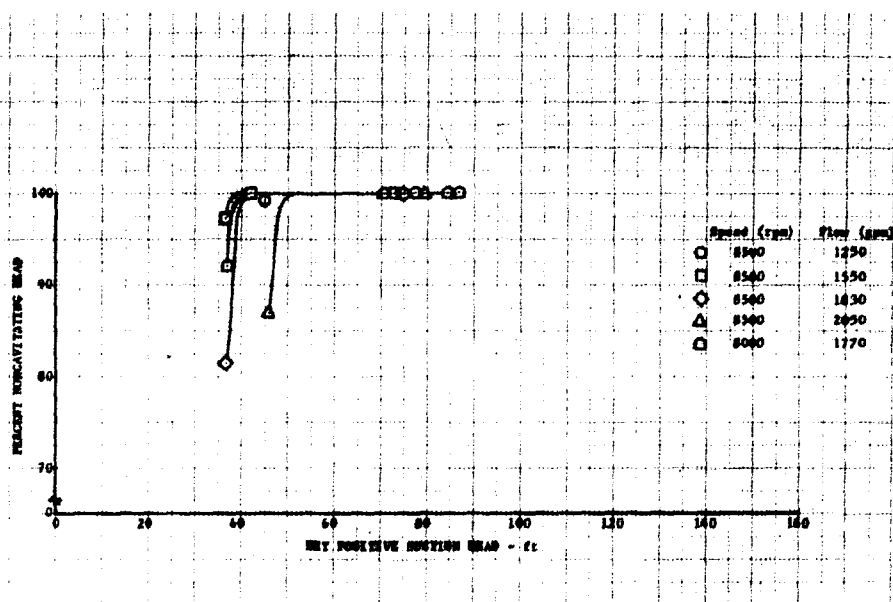


Figure 183. Percent Noncavitating Head vs Net Positive Suction Head (Pancake Inlet) DF 66841

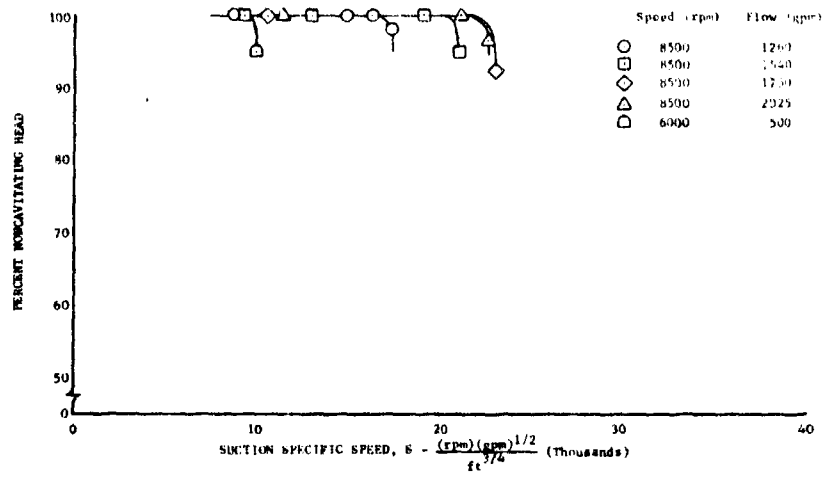


Figure 184. Percent Noncavitating Head vs Suction Specific Speed (Straight Inlet) DF 66842

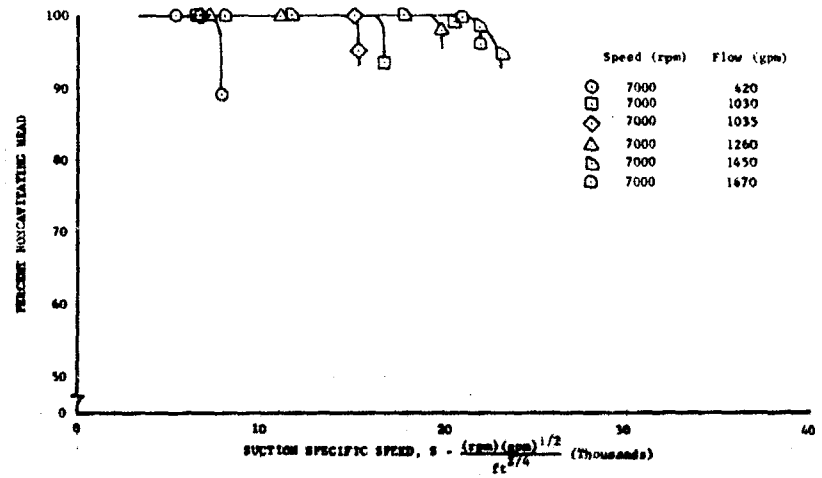


Figure 185. Percent Noncavitating Head vs Suction Specific Speed (Straight Inlet) DF 66843

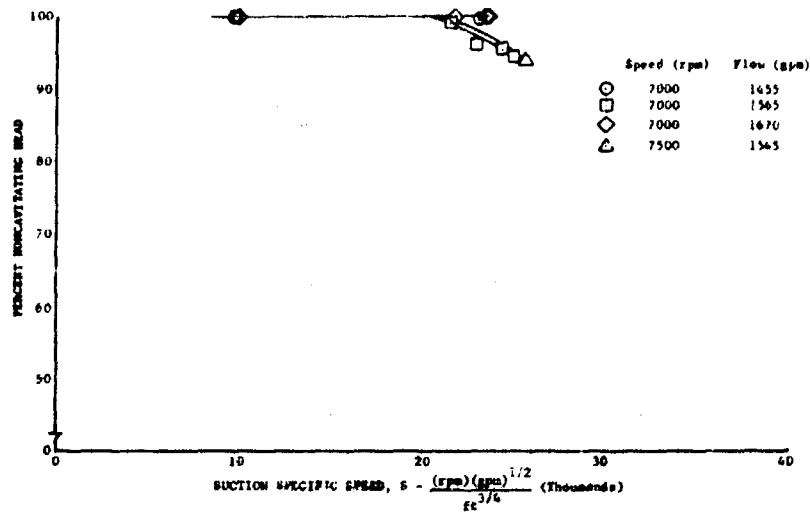


Figure 186. Percent Noncavitating Head vs Suction Specific Speed (Elbow Inlet) DF 66844

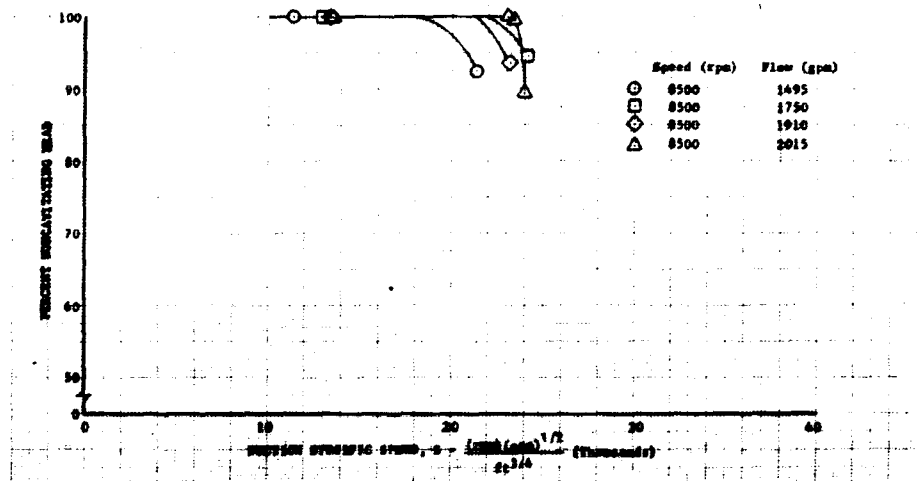


Figure 187. Percent Noncavitating Head vs Suction Specific Speed (Elbow Inlet) DF 66845

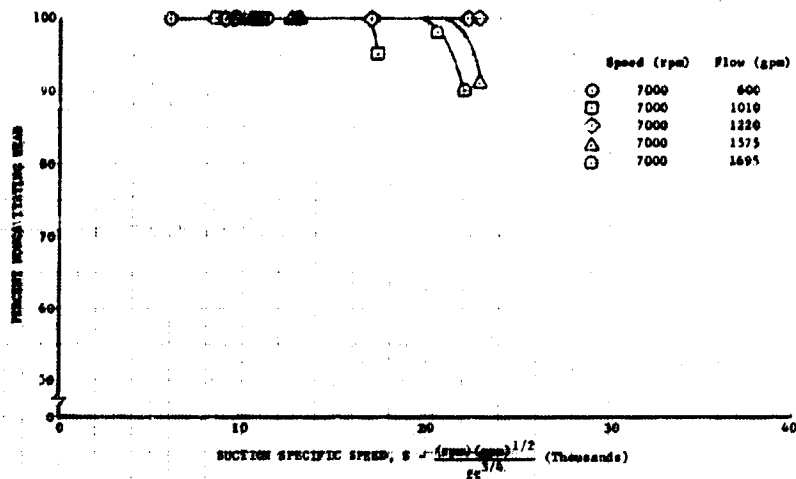


Figure 188. Percent Noncavitating Head vs Suction Specific Speed (Pancake Inlet) DF 66846

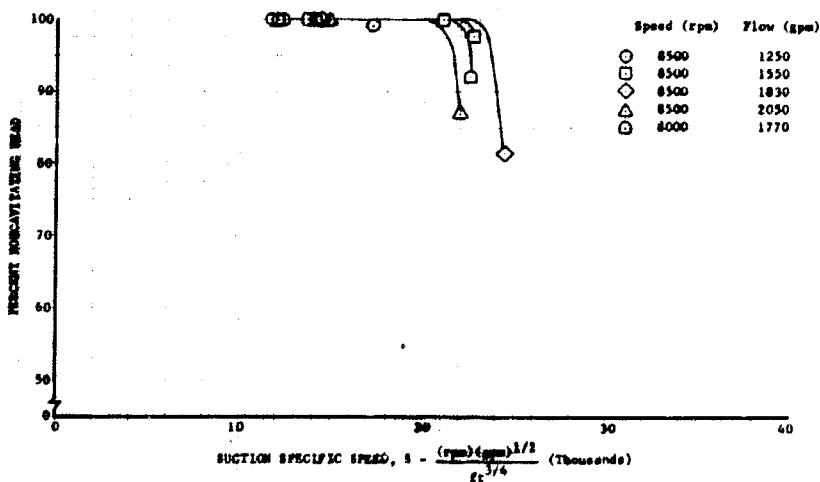


Figure 189. Percent Noncavitating Head vs Suction Specific Speed (Pancake Inlet) DF 66847

Suction performance of the 350K inducer for all three inlet configurations was as predicted. The predicted levels for the elbow and pancake inlets used the baseline level for the straight inlet, corrected for the expected total pressure losses in the elbow and pancake, respectively, using the loss factors predicted by the electrical analog study previously shown in figure 165. The predicted total pressure loss through the elbow inlet was small, thereby providing a suction specific speed curve that is essentially the same as the baseline straight inlet. Predicted peak suction specific speed for the pancake was 23,700 rpm $(\text{gpm})^{1/2}/\text{ft}^{3/4}$, which represents a loss of 1300 rpm $(\text{gpm})^{1/2}/\text{ft}^{3/4}$ from the straight inlet baseline.

Data from the 350K pump rig using both LO_2 and LN_2 obtained under Contract NAS8-2540 are previously shown in figure 175. Suction specific speed values for LO_2 and LN_2 data were corrected for recirculation flow and thermodynamic suppression head and are also based on 3% inducer head fall off. Although the water tests were limited to flowrates and speed of about 40% of design because of test stand limitations, the excellent agreement between the water data and the high-speed (20,000 rpm) LO_2 tests indicate that the water test results can be used to predict engine requirements.

At low flow-to-speed ratios, noise and vibration levels were considerably higher than at flow-to-speed ratios near design. Large static pressure losses in the inlet section of both the elbow and pancake configurations accompanied by severe inlet pressure oscillations were also noted. During throttling operation the pump would operate in the flow-to-speed ratio range of these inlet disturbances. Several cavitation points were taken with the pancake inlet at these conditions and suction performance was as predicted. No cavitation data were obtained at low flow-to-speed ratios with the elbow inlet, however, the results of the pancake inlet did not indicate that cavitation performance was adversely affected.

b. Noncavitated Performance

Noncavitated performance, which is shown in figures 190, 191, and 192, was based on a static discharge pressure measured in the discharge plenum. Although this does not represent the true inducer characteristics because of the additional housing losses, it was used for comparison because it was believed that the plenum pressure measurement was the most repeatable.

Noncavitated head rise based on the static pressure tap at the impeller discharge was approximately 15% lower than observed with liquid oxygen during previous testing with the discharge pressure tap in a similar location. The reduced head rise may be attributed to; (1) leakage past labyrinth seals that could affect the static inducer discharge measurement (the pressure tap location was directly upstream of the impeller front labyrinth seals and the water test rig had no seals or impeller); (2) the running blade clearance was greater for the water tests than on the liquid oxygen tests. Although both pumps had the same assembled tip clearances they operated at significantly different temperatures and the difference in thermal contraction of the inducer and housing reduced running clearance at liquid oxygen temperatures. The increased recirculation flow during the water tests with increased tip clearances would be expected to reduce head rise.

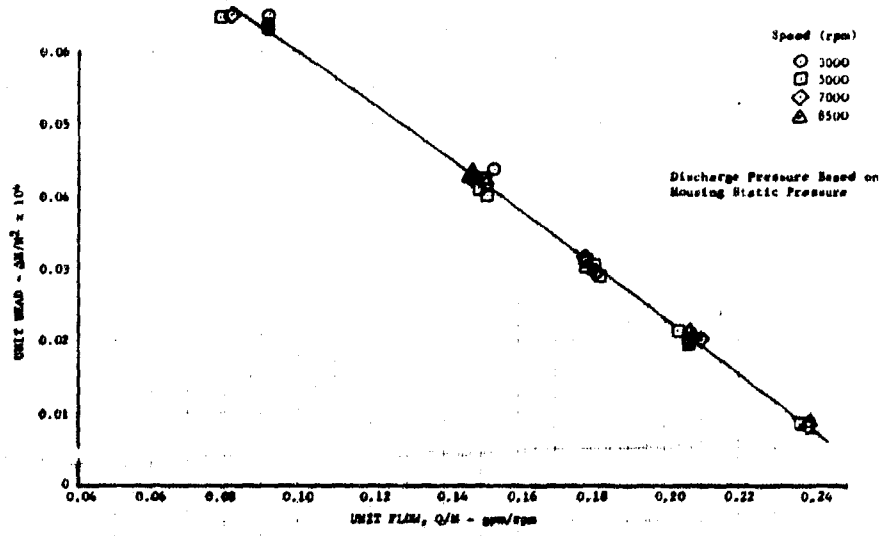


Figure 190. Unit Head vs Unit Flow (Straight Inlet)

DF 66848

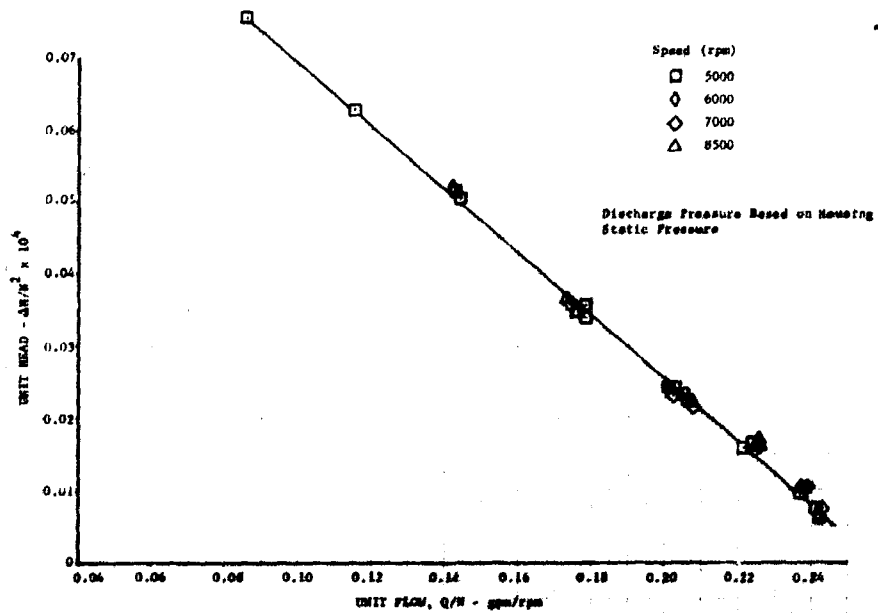


Figure 191. Unit Head vs Unit Flow (Elbow Inlet)

DF 66849

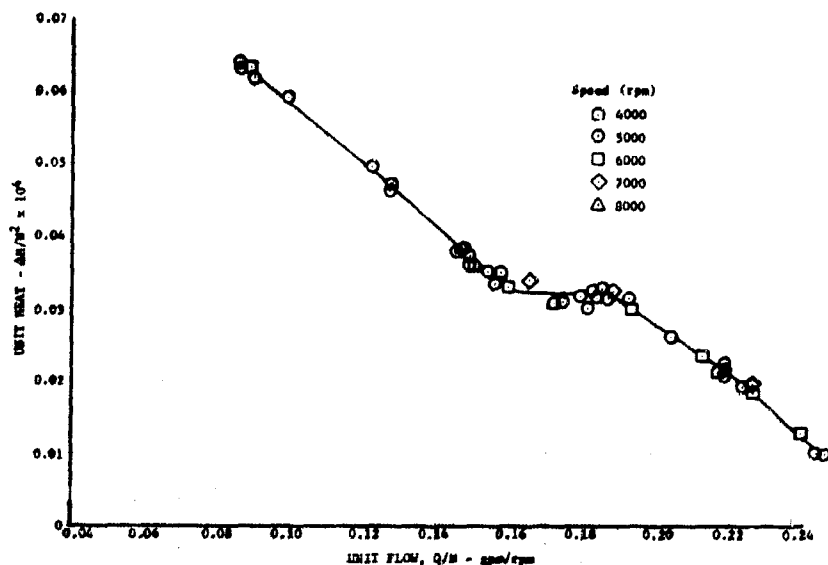


Figure 192. Unit Head vs Unit Flow (Pancake Inlet) DF 66850

The noncavitated head coefficient for the elbow inlet was higher and had a steeper slope than the straight inlet. This effect is because of the reduction of prerotation with the elbow inlet. At capacities less than design, prerotation with a straight inlet is in the direction of impeller rotation, which results in a reduction of head. It can be seen from Euler's equation for ideal head rise,

$$H_1 = \frac{U_2 C_{u_2} - U_1 C_{u_1}}{g}$$

that with the tangential component of inlet fluid velocity (C_{u_1}) positive (i. e., in the direction of impeller rotation) a reduction of head results. Prerotation with the straight inlet was investigated and is shown in figure 193, presented as an inlet line wall static pressure rise. It can be seen that the pressure rise reached a minimum (no prerotation) at the design flow-to-speed ratio of 0.22.

The head coefficient, flow coefficient characteristic with the pancake inlet was approximately the same level as with the straight inlet but had a discontinuity between flow-to-speed ratios of 0.16 and 0.18.

A comparison of the head coefficient, flow coefficient characteristics for all inlets tested is provided in figure 194. The velocity profile obtained from a traversing total pressure probe located just upstream of the inlet is provided in figure 195. The curve indicates the effect of the upstream bend. The magnitude of the variation about a mean velocity is small and should not be a major factor in the inlet pressure disturbances.

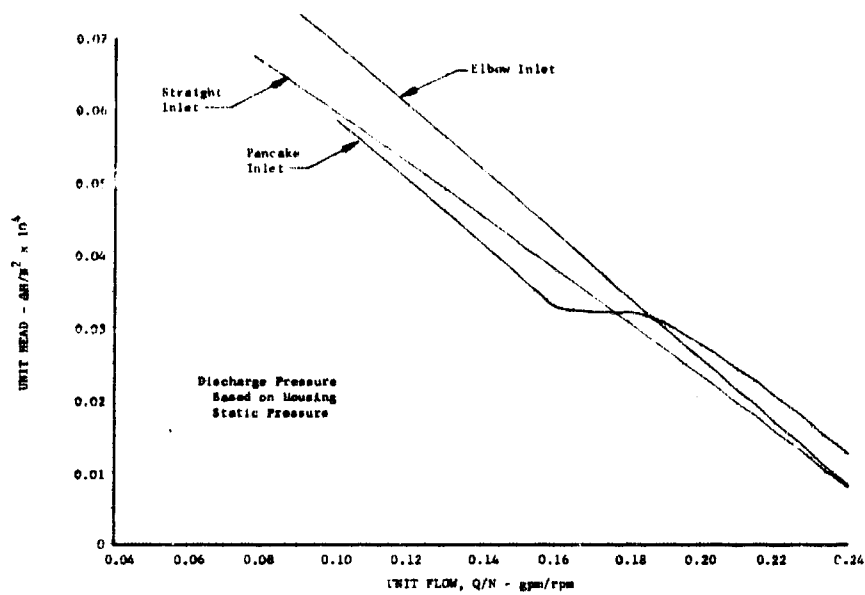


Figure 193. Comparison of Unit Head vs Unit Flow for All Inlets Tested DF 66851

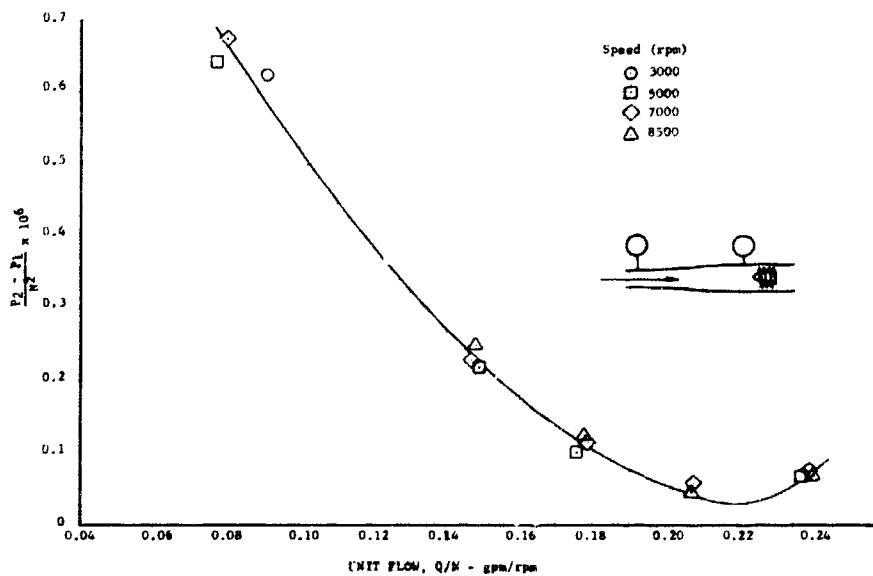


Figure 194. Inlet Line Wall Static Pressure Rise Because of Prerotation (Straight Inlet) DF 68530

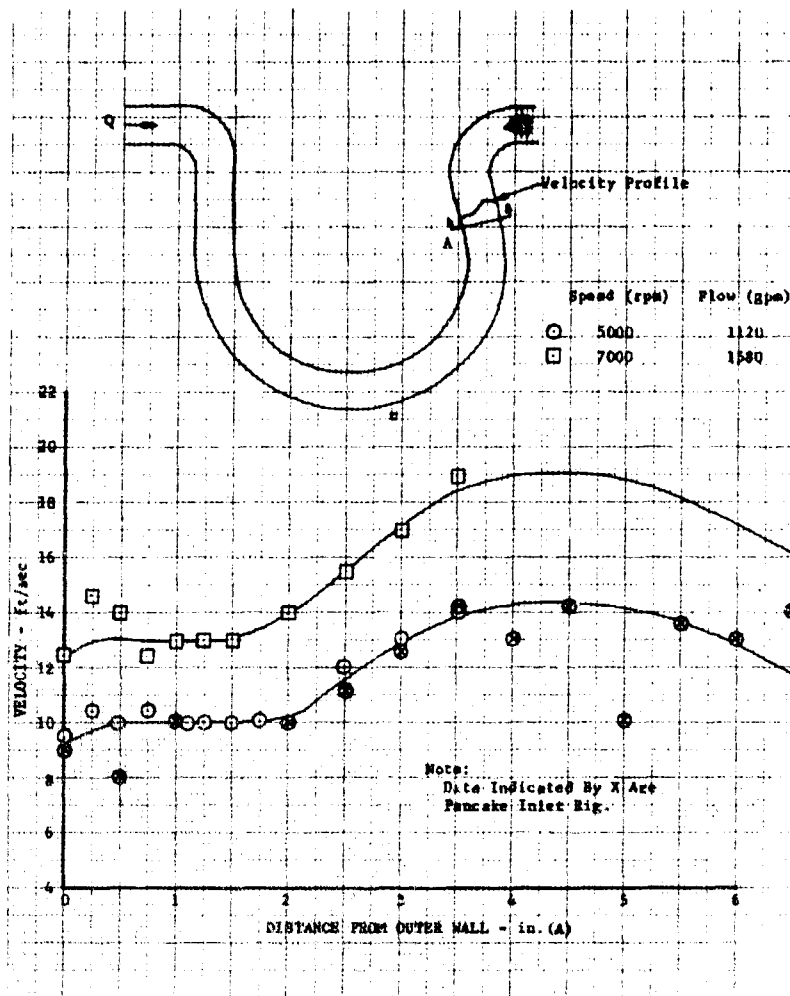


Figure 195. Velocity Profile at Inlet Housing Flange DF 66852

D. NOZZLE FABRICATION INVESTIGATION

1. Introduction

An investigation of nozzle fabrication techniques was conducted to provide additional data and information to support the subsequent design of the two-position nozzle. Sample nozzle panels were fabricated to evaluate manufacturing techniques, and successful panels were subjected to hydraulic stress and thermal cycling tests to determine structural capability.

2. Summary, Conclusions, and Recommendations

Nozzle design and fabrication optimization studies were conducted and completed. It was concluded that the material most suitable for constructing this two-position nozzle application was Inconel 625 (AMS 5599) and that the internal corrugated design was the most feasible to fabricate. An important factor in this selection was that the design allowed the use of standard stiffener bands on the smooth outer surface.

It was also concluded that stiffener bands of the "dunce hat" design would be used for the optimum lightweight configuration. The progressive die forming process produced good corrugation detail with minimum elongation and was selected for final fabrication. Resistance seam welding the assembly provided the easiest and most reliable construction method and produced high quality stiffener bands, as substantiated by the samples fabricated and the hydrostatic tests performed.

Twenty-one thermal fatigue tests were conducted on segments of the sample panels. The proposed panel (0.005 in. thick corrugated inner sheet with 0.010 in. thick outer sheet) could not complete the required minimum of 300 thermal cycles at the predicted nozzle temperatures; in fact, the average was 33 cycles. The nozzle hot wall temperature had to be decreased to 1760°R, which is 400°R below that desired, before 300 cycle fatigue life could be achieved. Increasing the thickness of the corrugated sheet to 0.010 in. allowed the hot wall temperature to be increased to 2010°R for 300 cycles of fatigue life, while causing only a 10% increase in the total nozzle weight. Therefore, this 0.010/0.010 in. thick nozzle configuration using the internal corrugation design is recommended for the subsequent two-position nozzle design.

3. Analysis

a. Design Study

To optimize the performance of an engine using a lightweight, two-position nozzle, it was necessary to design the nozzle to maintain the inner wall temperature as hot as possible. This level of temperature was controlled mainly by the material selection, material thickness, coolant flow rate, coolant velocity, and configuration geometry.

It is desirable to exit the cooling gases at as high a temperature as possible, which would be as shown in figure 196. To do this, the inner hot wall must be run at as high a temperature as physically possible for the entire length of the nozzle (i. e., constant hot wall temperature).

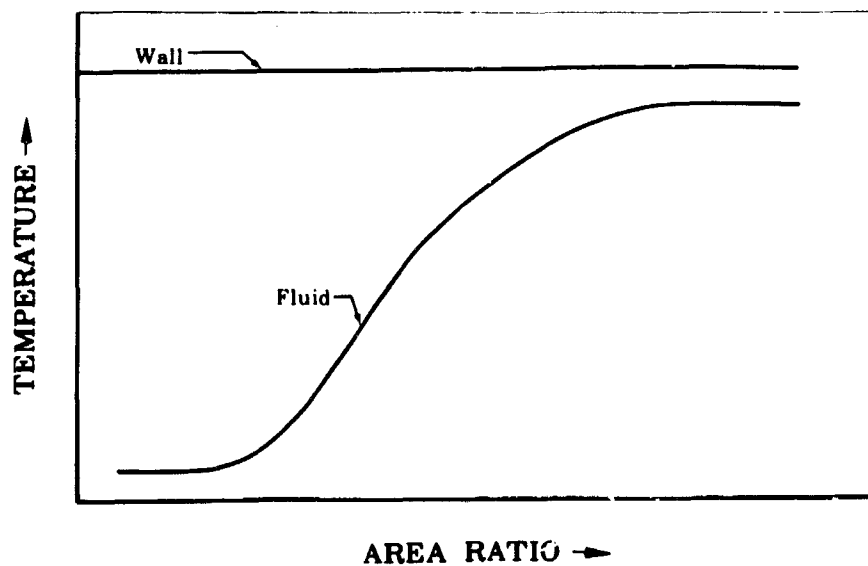


Figure 196. Fluid Temperature vs Area Ratio FD 25317

Because the heat flux (Q/A) decreases along the nozzle length, as shown in figure 197, and film coefficient, h , is equal to $(Q/A)\Delta T$, the inside film coefficient plotted against area ratio is as shown in figure 198. Because $h \cong (1/A)$, the coolant passageway flow area required along the nozzle is shaped as shown in figure 199.

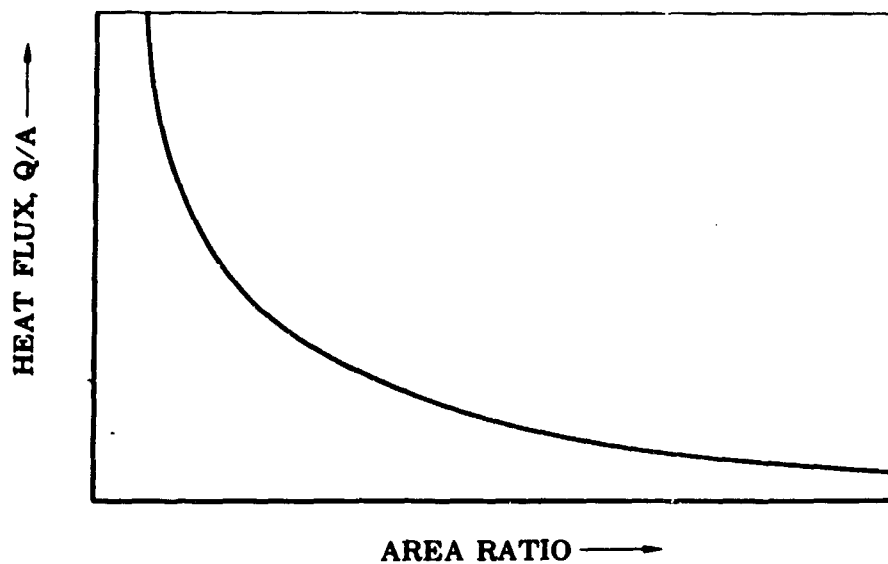


Figure 197. Heat Flux vs Area Ratio

FD 25318

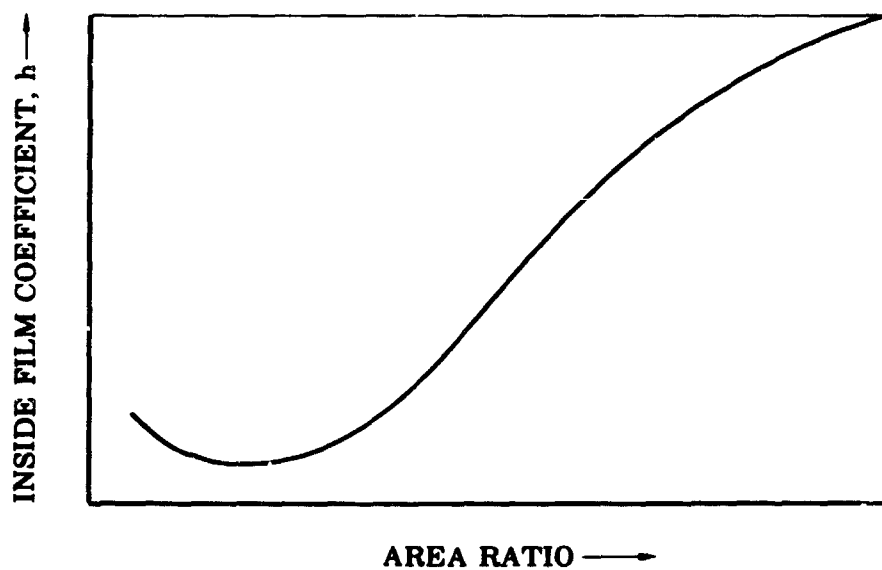


Figure 198. Inside Film Coefficient vs Area Ratio

FD 25319

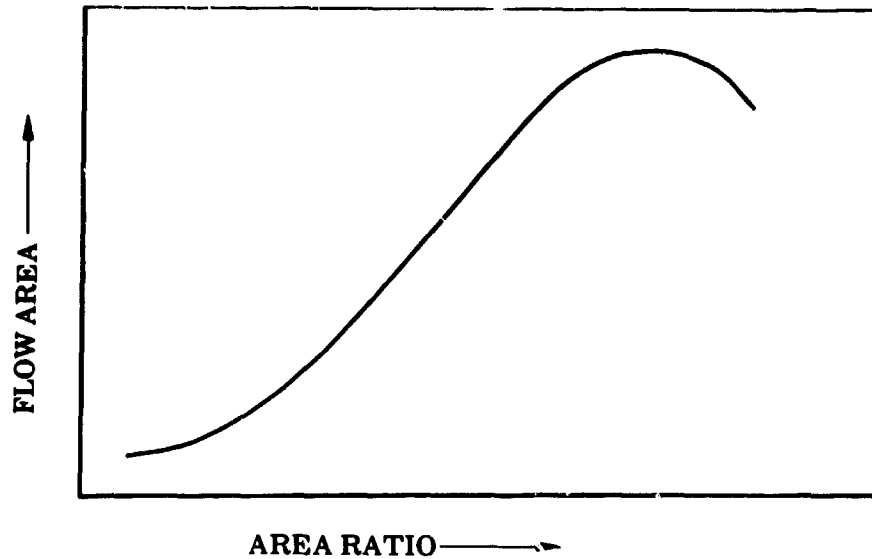


Figure 199. Coolant Passageway Area vs Area Ratio FD 25320

b. Material Selection

All available material candidates were studied for use in this nozzle application, comparing physical properties, mechanical properties, and ease of fabrication. The material had to have high strength at elevated temperatures and good ductility at both room temperature and elevated temperatures so it could be formed easily and would exhibit high thermal cycle fatigue strength. Table XXI provides a comparison between the final material candidates. Inconel 625 (AMS 5599) proved to be the most suitable for this application. Table XXII lists the pertinent material properties.

Table XXI. Comparison of Material Candidates

	Elongation, %		0.2% Yield Strength at 2000°R (psi)	Weldability
	Room Temperature	2000°R		
Inconel 625 (AMS 5599)	50	*105	40,000	Good
Hastelloy X (AMS 5536)	37	20	22,000	Fair
Hastelloy N (PWA 1036)	45	12	22,000	Fair
Ni 200 (AMS 5553)	50	*110	3,600	Good
TD Nickel (PWA 1035)	12	2	20,000	Poor
Stainless Steel (AMS 5646)	50	35	10,000	Good

*International Nickel Data

Table XXII. Properties of Inconel 625 (AMS 5599)

Property	Parameter/Characteristic
Density	0.305 lb/in ³
Ultimate Tensile Strength at Room Temperature	147,000 psi
0.2% Yield Strength at Room Temperature	72,300 psi
0.2% Yield Strength at 1460°R	53,000 psi
0.2% Yield Strength at 2160°R	32,000 psi
Elongation	50% at Room Temperature
Brazability and Formability	Good
Corrosion Resistance	Excellent
Weldability	Good

c. Configuration Study

A study of different heat exchanger configurations was conducted. Table XXIII summarizes the advantages and disadvantages of each configuration studied. Several configurations were eliminated during this study, with only two candidates selected for further investigation. These were the corrugated inside and outside diameter configurations.

Table XXIII. Configuration Study

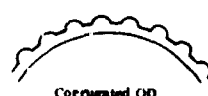
	Advantages	Disadvantages
<p>1.</p>  <p>Annular</p>	<ol style="list-style-type: none"> 1. Simplicity of construction. 2. More uniform inner sheet temperature gradient. 	<ol style="list-style-type: none"> 1. Area required would dictate a 0.020 in. high gap at the inlet that would present a tolerance control problem. 2. Hot inner sheet would expand approximately 0.230 in. on the radius at the inlet during operation and would close off 0.020 in. gap due to cold (not expanding) outer sheet. 3. Both sheets will see entire coolant pressure as hoop pressure at the 33 in. fl station, stress = 240,000 psi. 4. No vibration control of inner liner. 5. Excessive axial growth which is only restrained at inlet and exit.
<p>2.</p>  <p>Corrugated OD</p>	<ol style="list-style-type: none"> 1. Smooth inner sheet might result in better nozzle performance. 2. Lower coolant flow than corrugated ID. 3. Can be gather formed and spot welded (small die required). 	<ol style="list-style-type: none"> 1. Nozzle requires stiffener bands which are cold and the inner sheet (being stronger of two sheets) expands approximately 0.230 in. on the radius and cuts off coolant passageway or buckles the inner sheet. 2. Difficult to attach stiffeners to thin material. 3. High bending stress because coolant is on hot low strength side - 90,000 psi bending.

Table XXIII. Configuration Study (Concluded)

	Advantages	Disadvantages
<p>3.</p>  <p>Corrugated ID</p>	<ol style="list-style-type: none"> 1. Hot inner sheet removes radial thermal growth in corrugation and has no tendency to close off passageways (even with stiffener bands). 2. Can be gather formed and spot welded (small die required). 3. Easier stiffener attachment. 4. Might allow axial growth with folded integral bands on flat sheet, thereby increasing LCF life. 3. Because flat sheet is always thicker than corrugation, this configuration has an enhanced "fin" effect at the welds. 	<ol style="list-style-type: none"> 1. 25% higher coolant flow than outside corr. because of larger surface area to be cooled. 2. Exit rocket nozzle fabrication difficult in order to keep discontinuities out of hot gas stream.
<p>4.</p>  <p>Tubular</p>	<ol style="list-style-type: none"> 1. Has rigid construction. 2. Allows installation of stiffener bands directly to tubes without closing off passageway. 3. Experience and test data are available from RL10. 4. Less exposed surface area than configuration 3. Somewhat less flow requirement. 	<ol style="list-style-type: none"> 1. Heavy because of 15 lb brace material and double wall thickness between passageways. 2. Taper of the tubes would be complicated to maintain required area and circumference. 3. Expensive to fabricate (tubes, mandrels, retort). 4. Difficult to attach stiffener rings to thin wall tube. 5. Great number of tubes at inlet (2330 round tubes). 6. High temperature pushing braze limit. 7. Deviations from area schedule to smooth out contour would require more coolant flow. 8. More pressure drop for same coolant flow as in configuration 3.
<p>5.</p>  <p>Waffle Plate</p>	<ol style="list-style-type: none"> 1. Rigid structure in all planes. 2. Adaptable to bonding in the flat, then hydroforming. 	<ol style="list-style-type: none"> 1. Depends on elongation to form. 2. Tolerance control to match weld flats would be difficult. 3. Full size (entire nozzle) dies would be necessary to form contour if passageways were formed first or full size dies would be necessary. 4. LCF possibility in radial as well as axial. 5. Difficult to predict inside film coefficient due to uncontrolled flowpath. 6. Poor flow area control axially. 7. Should stagger local area reductions to increase heat transfer. 8. High pressure drop.
<p>6.</p>  <p>Double Corrugations</p>	<ol style="list-style-type: none"> 1. If radial growth is not allowed by attachment to the flats, thermal radial growth is taken in corrugations with little effect on area. 2. Might allow hydroforming in an inside-outside die. 3. Low stress from coolant pressure. 	<ol style="list-style-type: none"> 1. Corrugation angles would have to be smaller to obtain a given area schedule since the area would be cut approximately in half for each corrugation. Shallow corner angles give poor heat transfer. 2. Difficult to attach stiffeners and prevent buckling. 3. All hoop loads must be transmitted to the stiffener bands, because corrugations cannot take loads.
<p>7.</p>  <p>Sandwich Design</p>	<ol style="list-style-type: none"> 1. Rigid construction for buckling and noise. 2. Coolant flow requirement similar to 2 above because of minimum surface area. 3. Radial growth would be tolerated as flat sheet deforms between supports. 4. Simplified support bands. 5. Minimum surface area exposed to hot gas - thus low flow requirements relative to configurations 3, 4, 5, and 6. 6. Webs are easier to cool than welds of configurations 2, 3, 5, and 6. 	<ol style="list-style-type: none"> 1. High bending stress on inside sheet hot side from coolant pressure - 90,000 psi. 2. Struts may buckle because of thermal growth. 3. Difficult to fabricate. 4. Exit rocket nozzle fabrication problem similar to inside corrugations. 5. Gap height very small at inlet section, therefore, heavy - relatively thick webs will be required to keep the gap height to reasonable values at the inlet region. 6. Probably more pressure drop than configuration 2.

Two additional sandwich type configurations were investigated (rectangular and triangular coolant passages) in response to an Air Force request for alternative designs and for geometries suitable for diffusion bonding. These configurations were not fabricated because of the limited time allowable for this initial investigation and the nonavailability of equipment for diffusion bonding.

d. Heat Transfer Analysis

All work performed during the heat transfer analysis assumed a low-speed inducer tapoff coolant supply condition.

(1) Corrugated Geometry

The design point weight flows were set using a one-dimensional "idealized" analysis. However, a two-dimensional procedure was used to set the flow area and included-angle schedules and to investigate the effects of geometry variations from the design point. The external corrugation design was evaluated first. To prevent hoop failure, it was necessary to attach a system of external bands to the nozzle outer diameter. Corrugations on the external surface made the band attachment extremely difficult; therefore, the internal corrugation design was chosen. Because this configuration increased the exposed surface area to the hot gases, a 22% coolant flow increase was required.

(2) Alternative Configuration Analysis

The rectangular coolant passage configuration was investigated first. Parametric curves were developed that defined the coolant passage geometry at locations of primary interest. Using these geometries, the cross-sectional temperature distribution was established, and coolant pressure drop and temperature rise trend information was obtained. Results indicate that this scheme offers a reduction in coolant flow relative to the internal corrugation configuration with little change in weight.

In analyzing the triangular coolant passage, the coolant flow requirements were assumed to be identical to the rectangular configuration. Parametric curves were developed that defined the coolant passage geometry. This configuration weighed more than the basic corrugated and rectangular passage configurations. Figure 200 illustrates the three basic designs with a weight and flow comparison.

e. Structural Band Study

Several configurations of the sheet metal support bands for the ring-stiffened translating nozzle under hoop compression were studied. Of all the configurations, the integral "rib," the "hat band," and the "dunce-hat" designs seemed more promising, and these were studied in detail. The "rib" band was found to have serious adverse pressure drop effects as compared to the "hat band" or "dunce hat" configurations. Of the two remaining configurations, the "dunce hat" stiffener had the best characteristics (ease of fabrication, moment of inertia, buckling, etc.) and showed a 33% weight savings in comparison to the "hat band" design. Figure 201 shows that the "dunce hat" design has the largest moment of inertia for a given material cross section of the several configurations studied. A comparison of the band weights for different applications is previously shown in figure 200.

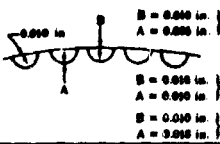
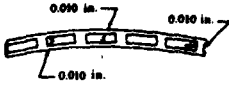
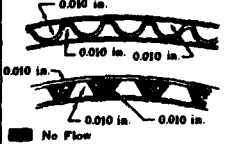
Configuration	Nozzle Weight Parameter	Nozzle Basic Weight (lb)	Support Band Weight (Sea Level) (lb)	Support Band Weight (Altitude) (lb)	Total Weight (Sea Level) (lb)	Total Weight (Altitude) (lb)	Coolant Flow Rate (lb/sec)
	$R_T = 6.75$	50	80	40	130	90	2.35
	$R_T = 11.6$	66	70	35	136	101	
	$R_T = 16.3$	80	70	35	150	124	
	$R_T = 13.1$	75	60	30	135	105	1.88
	$R_T = 23.1$	130	60	30	190	160	1.88
	$R_T = 13.4$	75	60	30	135	105	

Figure 200. Nozzle Configuration Comparison

FD 25321A

4. Fabrication Investigation

a. Method Selection

The first step in this fabrication study was to select a method to form the corrugated section of the assembly. Several techniques were considered, including explosive forming, hydrostatic forming, and die forming. The explosive forming method was used previously on a small dump-cooled nozzle extension of an RL10 nozzle, but material thinning and difficulty in holding tolerances eliminated this method. From the two remaining methods, die forming was selected because it offered the highest degree of success. Figure 202 illustrates the type of gather forming die selected to form the sample panel and low cycle thermal fatigue test samples. The corrugated sheets were joined to the flat sheets by resistance welding (as was successfully demonstrated in the RL10 dump-cooled nozzle program).

A die was fabricated to form corrugated panels, but with a panel size reduced to 18 in. long and 16 corrugations wide. The corrugation height was varied from 0.293 to 0.350 in. over the 18 in. sample. The samples represented the nozzle inlet configuration where maximum thermal stresses occur.

b. Fabrication

The first corrugated sheet formed with the die set was measured and found to have corrugation heights 16.5% below the blueprint requirements. The material spring-back after forming had caused this. The final die set for the actual nozzle will be designed to compensate for this material spring-back to obtain the blueprint limits. It was impractical to rework this die set because it was for sample panels only. To eliminate some of the spring-back, all the corrugated panels were placed in a retort, annealed at $1875^\circ\text{F} \pm 25^\circ\text{F}$ for 30 minutes in hydrogen, cooled in the retort, and then restruck with the forming die. This increased the corrugation height to within 5% of the blueprint requirements.

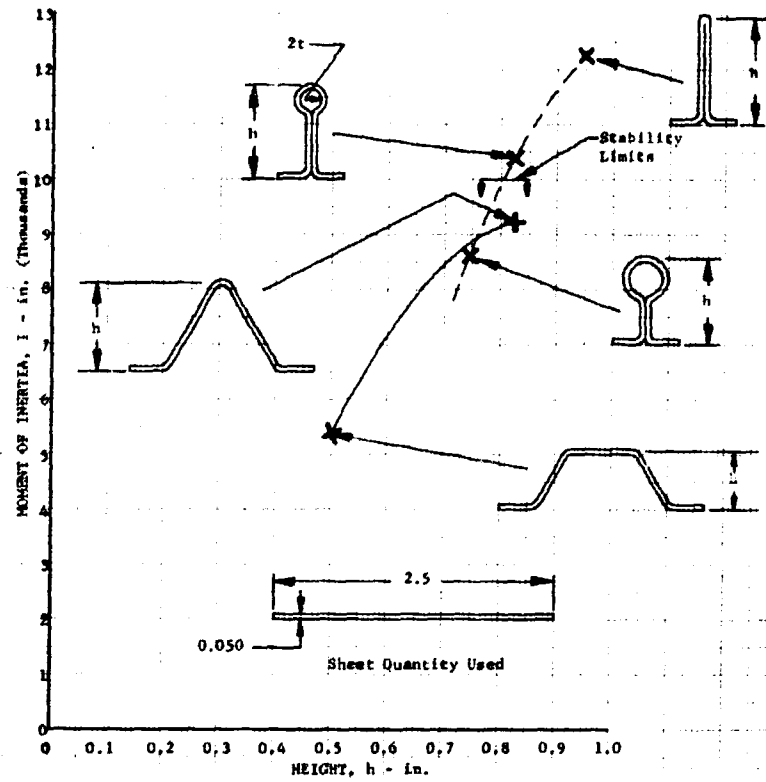


Figure 201. Band Height vs Moment of Inertia for Several Configurations

DF 77225

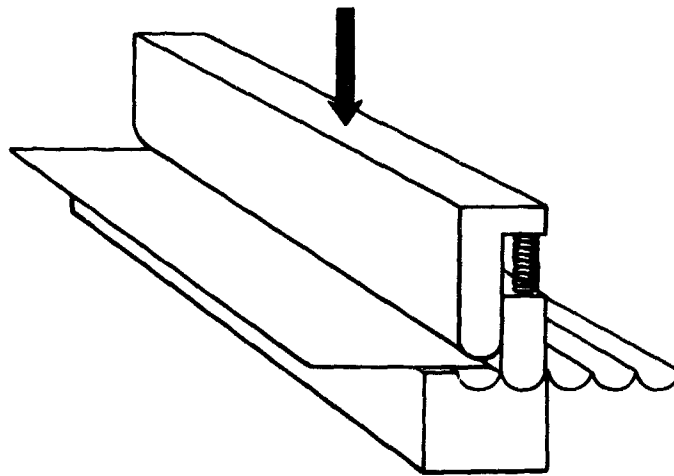


Figure 202. Gather Forming Die

FD 23215

The corrugated sheets were then resistance seam welded to flat sheet stock to make sample assemblies, as shown in figure 203.

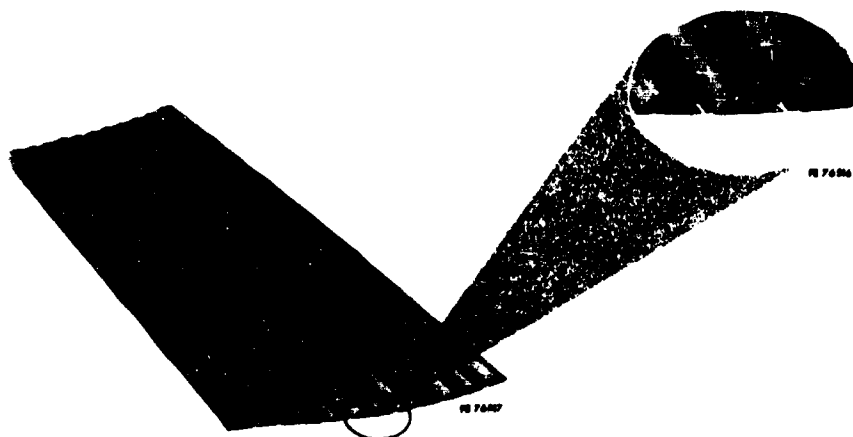


Figure 203. Corrugation Sample Panel

FD 23227

Altitude and sea level configuration supporting bands of the "hat band" style were spun. These rings were cut into segments and tacked in place on the flat side of the sample assemblies to maintain their position during the braze cycle. Silver braze wire was then tacked in place at the joints of the stiffeners and the assembly run through the furnace braze cycle. The stiffeners would not need to be tack welded to the full-scale nozzle, as was done in the case of these small segments, but would be fixtured and held in position.

Three assemblies were made that demonstrated the integral band design. The corrugated sheets were resistance welded to stacked segments of a spun ring. The ribs of the rings were then welded to form the assembly, as shown in figure 204. The corrugated sheets were also cut into smaller segments and seam welded to special shaped flat sheets for thermal fatigue subassembly samples. The sample panels were cut into segments and used as hydrostatic pressure test specimens.

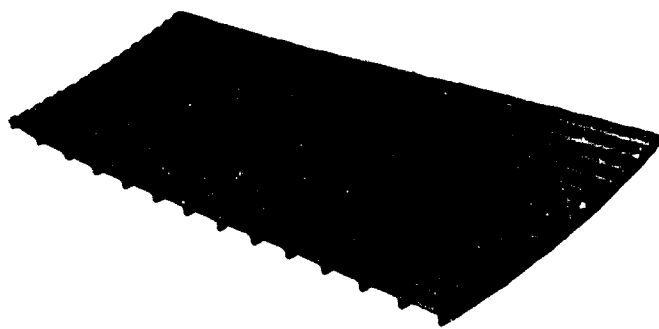
5. Test

a. Hydrostatic Pressure Test

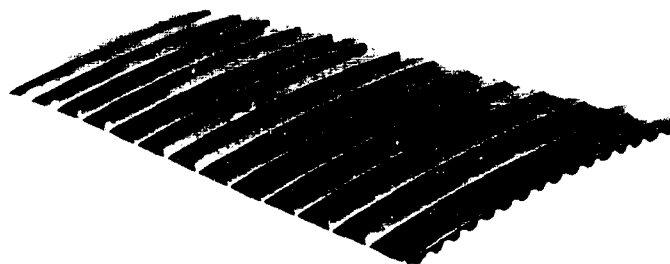
(1) Unrestricted Specimens

Three 2-corrugation, pressure-test specimens were made per figure 205. These specimens are sections of the sample 12-corrugation panel assemblies.

The first specimen pressurized failed at 225 psig. Examination revealed that the specimen failed at a spot tack weld that was outside the resistance weld width. The failure is depicted in figure 206a. The corrugated sheets were spot tack welded to the flat back sheet prior to resistance welding of the assemblies. The resistance welds were supposed to cover the spot tacks. The test specimen failed at one tack weld that was not centered and the resistance weld had not covered it.



FE 76719



FE 76718

Figure 204. Integral Band Design Sample Panel

FD 25322

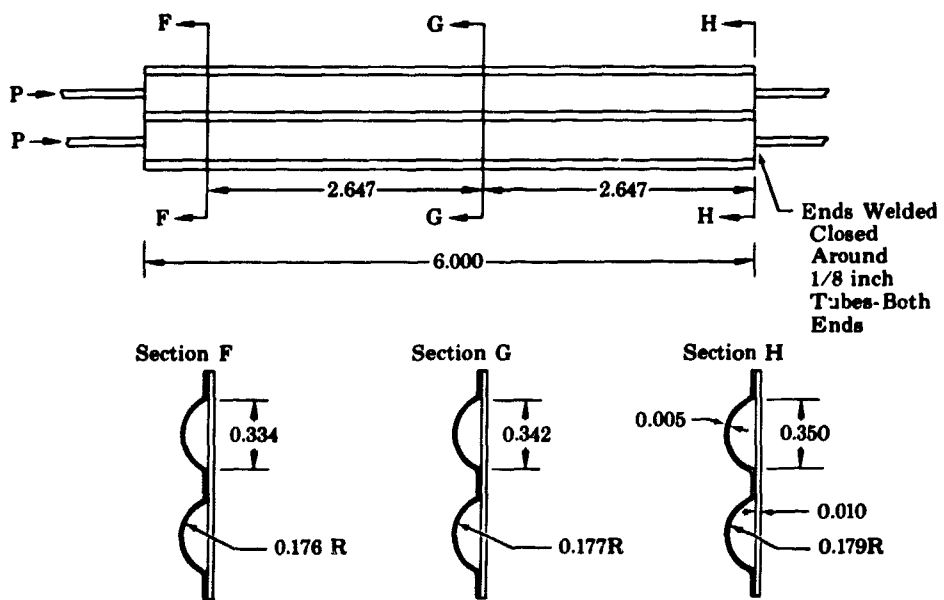


Figure 205. Hydrostatic Test Samples

FD 24993

The next two specimens were pressurized and failed at 275 psig and 400 psig, respectively. Both specimens started to roll up as shown in figure 206b, and both failed at the edge of the resistance weld, but at random points along the specimen.

(2) Restricted Specimen

All of the unrestricted specimens tended to roll up. To assure that this rolling did not cause early failures, a specimen was tack welded along the edges (four places both sides) to a 1/8-in. steel sheet. This specimen was pressurized to 380 psig, at which point one of the tack welds tore loose and caused a leak in the corrugation, as shown in figure 206c. The other tack welds on the No. 1 corrugation side still held, so the No. 2 corrugation was pressurized. This corrugation held until the other tack welds on the No. 1 side broke loose; when the No. 1 corrugation folded up, the No. 2 corrugation failed next to the resistance weld. This again indicated that the rolling up caused premature failures.

The second specimen was seam welded on both sides to the 1/8 in. thick plate, as shown in figure 206d. This specimen had both corrugations pressurized to 1300 psig. At this pressure, one corrugation failed next to the seam weld. The other corrugation held 1300 psig with no failure.

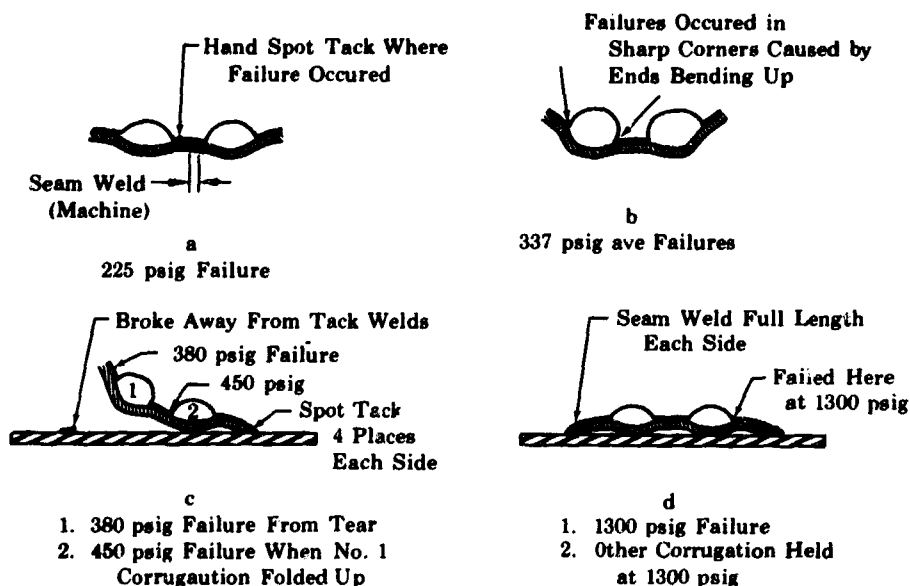


Figure 206. Failed Hydrostatic Test Samples FD 24994

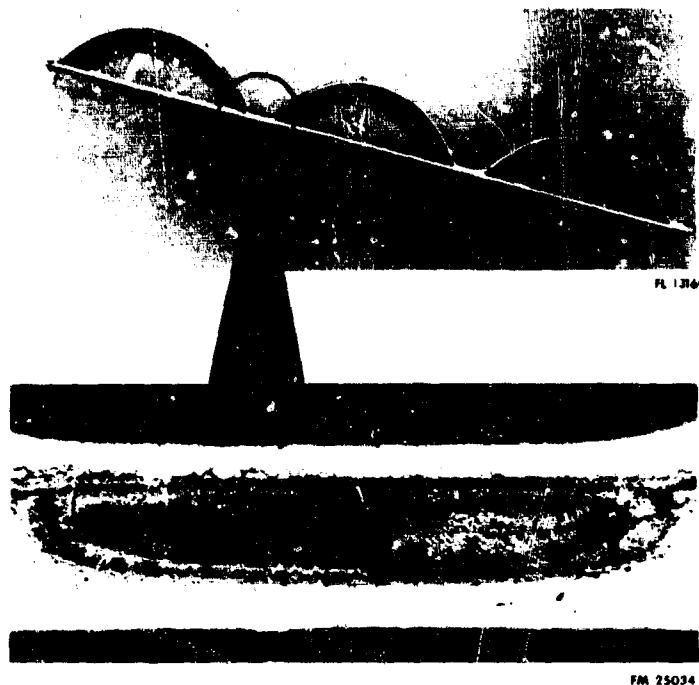
b. Resistance Weld Quality Tests

(1) Micro-Examination of Joints

A section of a sample corrugated panel was taken to the Materials Development Laboratory (MDL), mounted in plastic, and examined to determine the quality of the resistance weld. The mounted specimen and a closeup of the joint are shown in figure 207. Table XXIV shows the results of this examination.

Surface burning and expulsion were present in the seam welds. These conditions can cause rejection and must be eliminated on the final assembly.

Mounted Nozzle Sample Panel Specimen



Closeup of Joint of Specimen

Figure 207. Resistance Weld Examination Specimen

FD 25323

Table XXIV. Resistance Weld Measurements

	No. 1 (in.)	No. 2 (in.)	No. 3 (in.)
Penetration into 0.005 in. thick material	0.001	0.001	0.001
Penetration into 0.010 in. thick material	0.005	0.004	0.003
Weld nugget width	0.045	0.044	0.040

During this examination, the thickness of the 0.005 in. thick corrugated sheet was checked to see if thinning had occurred during die forming. Microscopic and micrometer readings showed no measurable thinning had occurred.

(2) Tensile Test of Resistance Welds

The tensile test specimens were constructed by cutting the sheet into 1 in. wide strips, 12 in. long. The two thicknesses to be evaluated were stacked and resistance welded 6 in. from the end, giving a 1 in. length of weld to be tested.

The two ends of the same thickness material were folded back together and the load applied to these ends, as shown in figure 208.

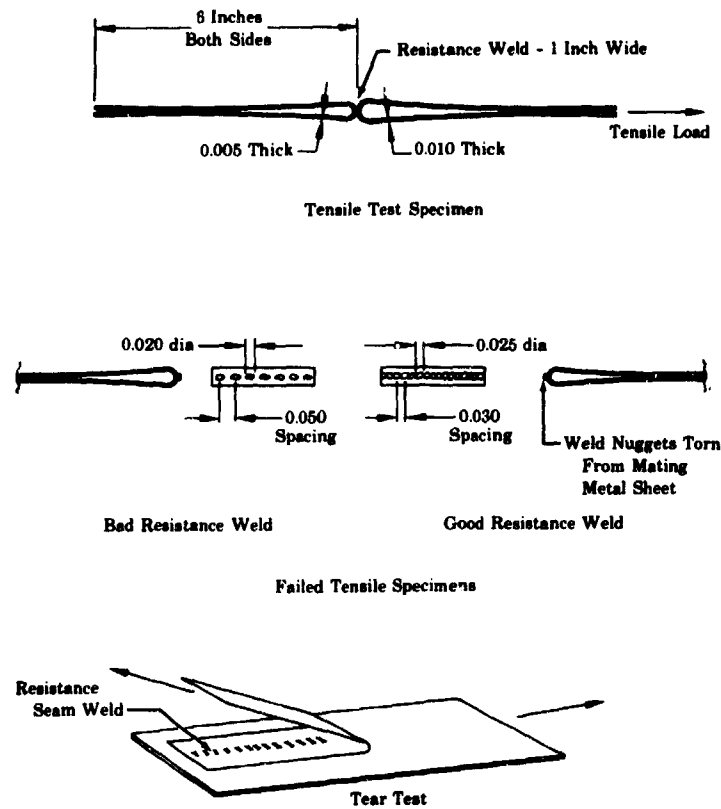


Figure 208. Resistance Weld Test Samples

FD 24995

The initial tests were conducted with 0.005 in. thick Inconel 625 (AMS 5599) welded to 0.010 in. Inconel 625 (AMS 5599) with the following results:

Maximum Load, lb

225	}	189 lb average
218		
125		

Examination of the welds after failure revealed the weld nuggets to be 0.050 in. apart (center-to-center) and the nugget diameter was 0.020 in. The nuggets should overlap as illustrated in figure 208. A second test conducted with this material combination showed the following results:

Maximum load, lb

435	}	357 lb average
302		
336		

Examination revealed the weld nugget diameter to be 0.025 in. and nuggets were overlapping with 0.030 in. center-to-center distance. Figure 209 shows the specimens from the first two tests.

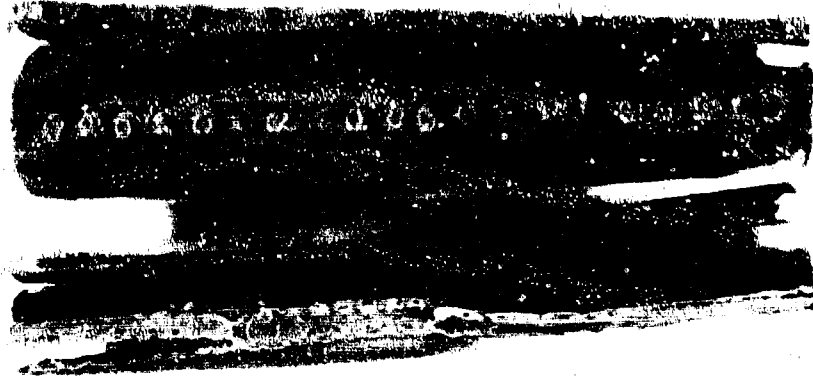


Figure 209. Specimens After First Two Tests FE 78030

The next test was conducted with 0.010 in. thick Inconel 625 (AMS 5599) welded to 0.010 in. thick Inconel 625 (AMS 5599) with the following results:

Maximum Load, lb

353	}	423 lb average
599		
343		
399		

The weld nuggets were 0.035 in. in diameter and nugget center-to-center distance was 0.030 in. resulting in a good overlapping seam weld.

(3) Tear Test of Resistance Weld

An inch wide piece of 0.005 in. thick Inconel 625 (AMS 5599) and 0.010 in. thick Inconel 625 (AMS 5599) were resistance welded along the length for 2 in. and centered 0.500 in. from the edge. The ends not welded were pulled apart, and a maximum force of 7.5 lb average was recorded, as shown in figure 208. All specimens tore evenly, with the original torn edge rounded with a 0.015 in. radius. The weld nugget was 0.020 in. in diameter.

c. Thermal Fatigue Investigation

An attempt was made to predict the LCF life for the corrugations of the two-position nozzle. The prediction system used was the S. S. Manson technique, which uses the universal slopes equation for calculating the predicted LCF life. When using this equation, it is required that, for low cycle rates and relatively high temperatures, an additional check be made to deter-

mine if the failures might be time dependent or creep limited. A check was made and the limit case for the expected operating conditions was not creep but fatigue ruptured. Therefore, the Manson equation for selected values of total strain was used to determine cycle life, as follows:

$$\Delta \epsilon_t = \frac{3.5 \sigma_u}{E} \eta_f^{-0.12} + D^{0.6} \eta_f^{-0.6}$$

where

E	=	Modulus of elasticity
σ_u	=	Ultimate tensile strength
D	=	Ductility
η_f	=	Cycle life
$\Delta \epsilon_t$	=	Total strain range

Because prediction of LCF becomes more of a definition of LCF range than an actual predicted number, it should be understood that when actual conditions are inserted in the equation, estimates of elevated temperature LCF behavior can be made as follows:

1. As an estimate of the lower range of life, use either 10% η_f or η_f' (Creep), whichever is the lower. For the two-position nozzle, the temperatures were such that the lower limit case was η_f or LCF, not η_f' creep rupture.
2. As an estimate of average life, use two times the lower range life.
3. As an estimate of upper range of life, use 10 times the lower range life.

These limits, which the LCF test data should fall within, are shown in figure 210. The actual test data from the LCF test are also shown on this figure as being within the acceptable predicted scatter of test data. It should be noted that there are no published data for reduction of area (required to determine ductility for the Manson equation) for thin sheet metal. P&WA laboratory tests indicated values around 20% to 30% and were used to establish the limits shown in figure 210.

The purpose of the thermal fatigue investigation was to develop a method to simulate in the laboratory the nozzle thermal stress that would occur during actual nozzle firings. The theoretical nozzle temperatures to be obtained with the corrugated inside diameter design were: (1) corrugation crown temperature to be 2060°R; (2) resistance weld at the valley temperature to be 1800°R to 1900°R; and (3) center of the cold side temperature to be 150°R. These conditions exist at the coolant inlet to the nozzle and produce the maximum temperature difference from cold side to crown in the nozzle.

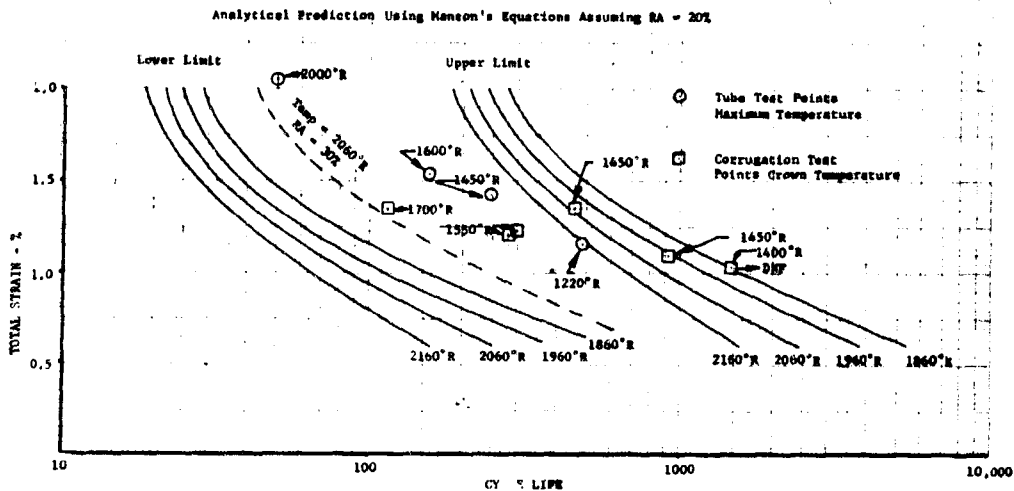


Figure 210. Strain vs Cycle Life for Inconel 625 (AMS 5599)

DF 68256

(1) Flat Sample Tests

Corrugated segments of the configuration shown in figure 211 were used for the initial investigation of heating and cooling techniques. The heat was supplied with a portable quartz lamp unit producing 75 watts per square in. The flat side of the specimen was first air cooled and then water cooled by suspending it in a water bath. One of the specimens had a 1/8 in. coating of Rockide applied to the flat side of the resistance weld area and the center of the cold side exposed.

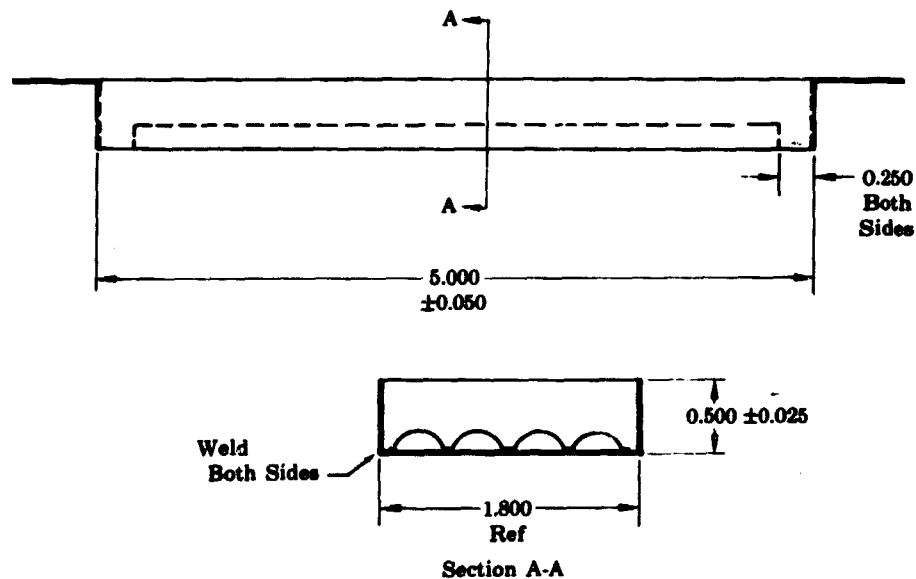


Figure 211. Initial Thermal Fatigue Sample

FD 25324

The data from these tests, shown in figures 212 through 215, showed that different heating and cooling methods were required to obtain the correct temperature difference.

(2) Finned Sample Tests

Thermal fatigue specimens of the configuration shown in figure 216 were constructed to evaluate cooling with copper fins (0.040 in. thick). Considerable time was spent developing an induction coil geometry that would give a broad heating pattern across the corrugated samples. Finally, the twin-coil configuration, which is shown in figure 217, was developed and testing begun. The first tests were run with the copper fins suspended in liquid nitrogen. Additional tests were made with prechilled helium gas flowing through the corrugations, but no liquid nitrogen on the fins. The final tests were run with prechilled helium and the cooling fins in liquid nitrogen. The best results were obtained with the cooling fins in liquid nitrogen and no helium coolant (1625°RT). The test results are shown in figure 218.

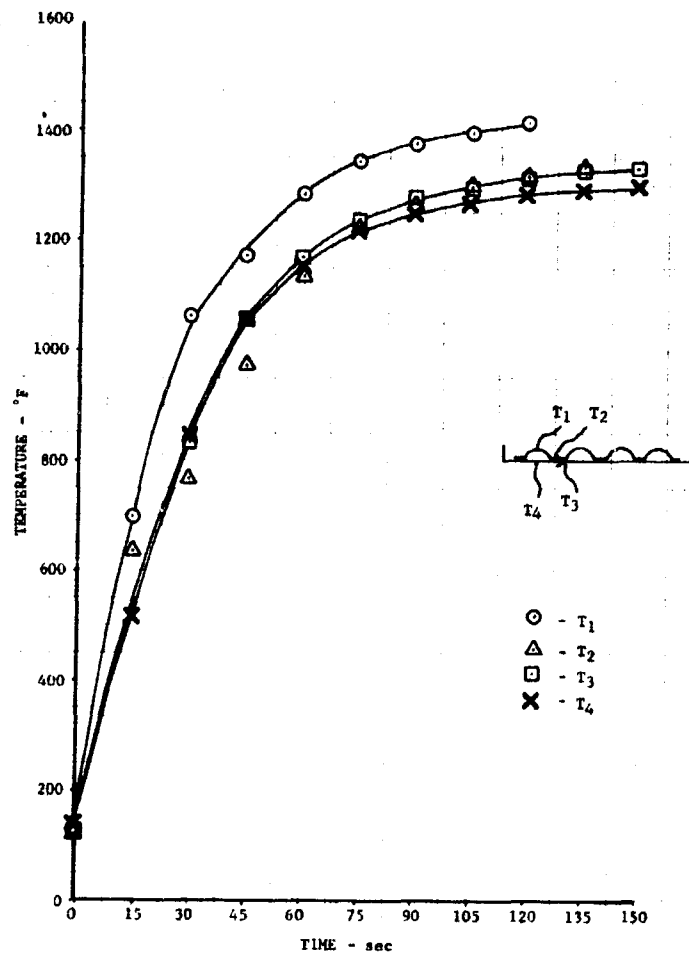


Figure 212. ΔT Investigation With Air-Cooled Back

DF 68252

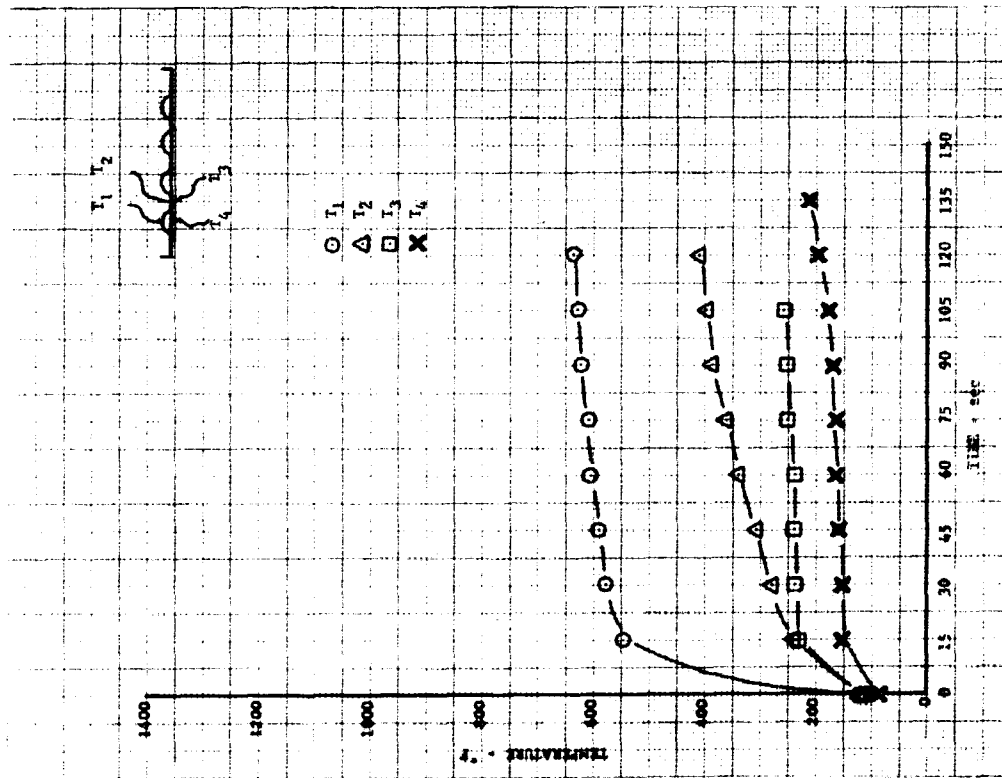


Figure 213. ΔT Investigation With Water-Cooled Back

DF 68253

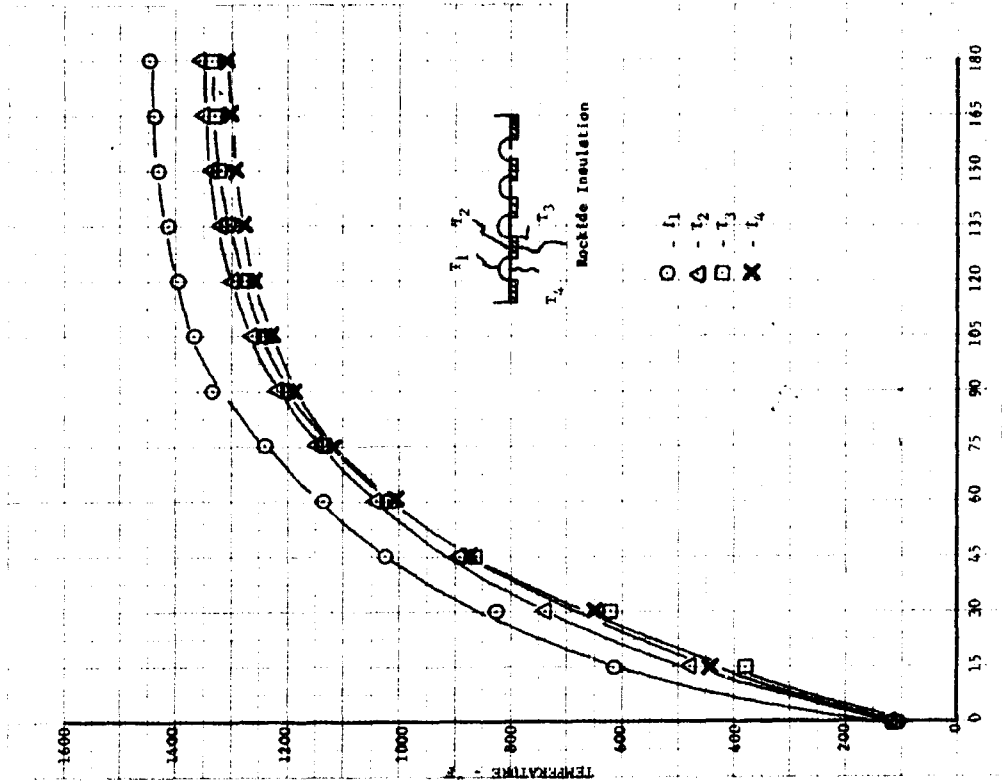


Figure 214. ΔT Investigation With Air-Cooled Back and Insulated Weld Joint

DF 68254

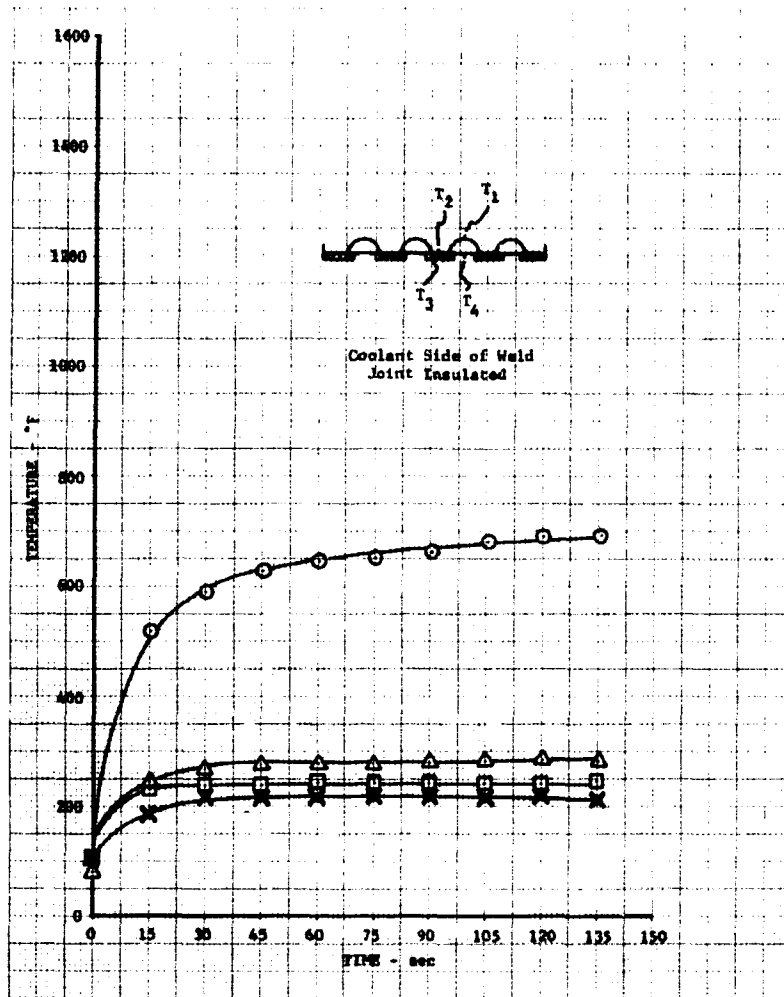


Figure 215. ΔT Investigation With Water-Cooled Back and Insulated Weld Joint

DF 68255

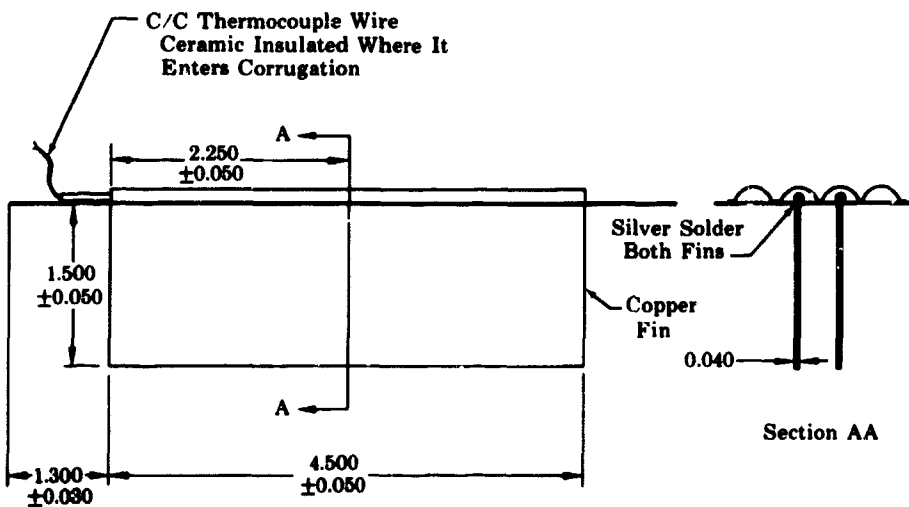


Figure 216. Thermal Fatigue Sample With Cooling Fins

FD 25325

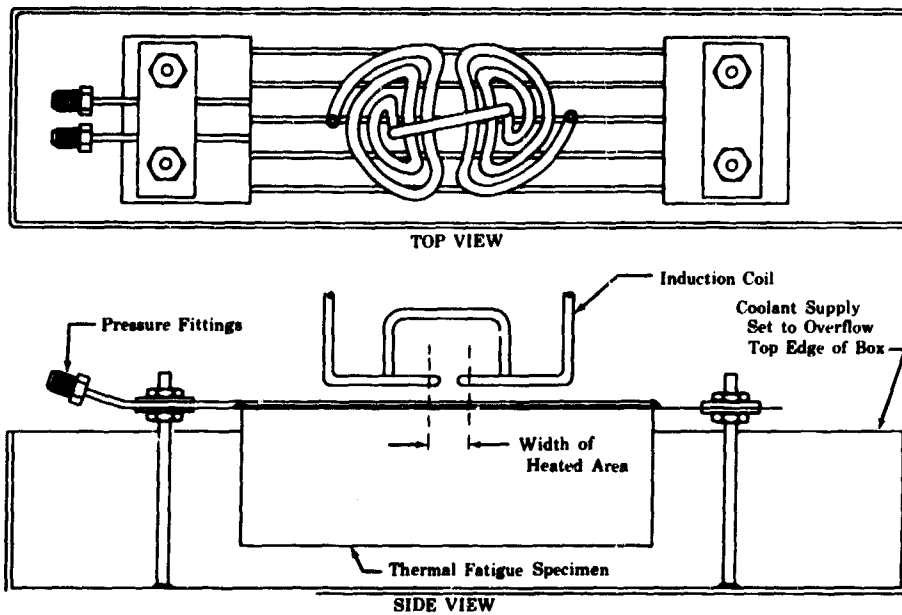


Figure 217. Thermal Fatigue Cycling Setup

FD 24996

Cooling Scheme	Induction Heater Power Settings				
	10%	30%	40%	50%	60%
LN ₂ on Fins No Helium	2135°R 77°R Steady State	2085°R 435°R Time to Peak = 3.2 sec	2080°R 435°R Time to Peak = 2.2 sec	2010°R 310°R Time to Peak = 1.7 sec	1981°R 420°R Time to Peak = 1 sec
No LN ₂ Helium Flow:		1365°R 587°R	1380°R 520°R	1160°R 400°R	1280°R 360°R
Medium		1820°R	1730°R	1680°R	1720°R
High			810°R 380°R	1470°R 1320°R	
LN ₂ on Fins Helium Flow:	640°R 280°R Steady State		2050°R 670°R	2110°R 1910°R	
Low			1730°R 570°R	2010°R 450°R	1890°R 320°R 1710°R 2220°R 2050°R
Medium			1280°R 680°R	1880°R 1880°R	1300°R 430°R
High			1280°R 680°R	1880°R 1730°R	

Figure 218. Test Results of Flat Sample With Corrugations and Copper Fins

FD 25326

(3) Evaluation of Cooling Fin Thickness

When it was determined that a corrugated sample with copper cooling fins would best simulate engine conditions, the next step was to optimize the thickness of cooling fins. Rather than waste corrugated specimens, flat sheets of 0.0165 in. thick Inconel 625 (AMS 5599) the same size as the specimen were used and different thickness copper fins were brazed on the plate. The thickness ranged from 0.040 to 0.125 in. The results of these tests are shown in figure 219.

A 0.250 in. thick cooling fin was brazed on a corrugated sample and compared to a 0.060 in. thick finned sample. These results are also shown in figure 219. The results show the optimum cooling fin thickness to be 0.065 in.

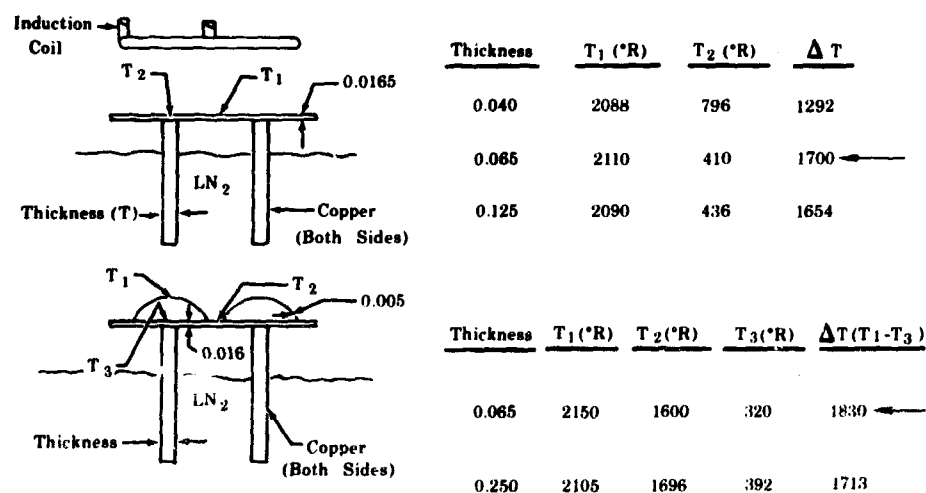


Figure 219. Cooling Fin Thickness Test Results

FD 25327

(4) Corrugated Can Configuration

A corrugated can configuration was tested in an attempt to obtain the required temperature difference. A 4 in. diameter can, with corrugations on the outside diameter and a manifold for flowing a coolant in the corrugations, was constructed. A standard circular induction coil was placed around the can and prechilled helium gas used for the coolant. The can was heated, then coolant flow was started. The results are shown in figure 220.

The third test run with the oxyacetylene torch proved that the cold side was being induction heated, and that this test method could not be used. To keep induction heating from occurring in the corrugation, and to assure heating with radiant heat, a metal shield was used on the fourth test. The cooldown time was too long (4 minutes) to make this test realistic, and good temperature gradients were not achieved.

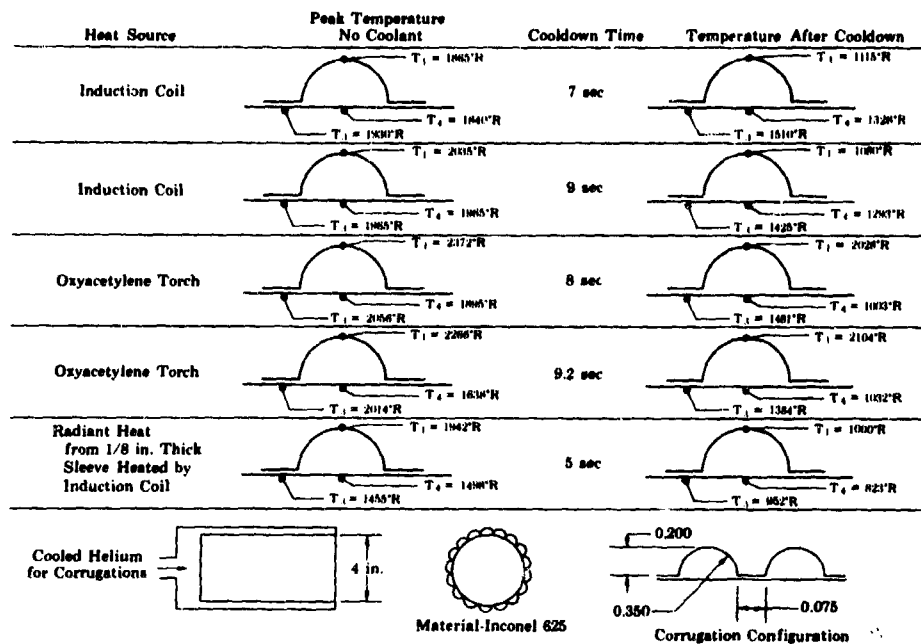


Figure 220. Test Results of 4-in. Diameter Corrugated Can FD 25328A

(5) Line Resistance Heating Using the Proximity Effect

Induction heating or flame heating in the laboratory appeared to heat the crown of the corrugation higher than the valley. For this reason, high frequency resistance heating, using the proximity effect, was investigated as a means of localizing the heat where required.

This type of heating is a form of resistance heating (where the current is passed through the material, causing the material to heat). To control the path of the current in the specimen and, therefore, control the heated areas, the proximity effect principle was used. This principle states that if the high frequency alternating current being delivered to resistance heat the piece of metal is passed through a lead that is run parallel and very close to the metal surface, the return current in the specimen will follow a path directly under the lead. The concentration of the current under the lead is dependent upon the height of the lead above the surface. This phenomenon is illustrated in figure 221.

The first test was run as illustrated in figure 221. A flat sheet 0.016 in. thick and 10 in. long was heated. The distance, d , between loops was varied to determine how close the loops could be spaced and still have effective line heating under 100% of the lead-in. At $d = 0.500$ in. the system line heated, but at $d = 0.400$ in. the current took a straight line between the inlet and discharge post.

The second test was run with another thermal fatigue specimen and the line heater set up as shown in figure 222. The copper lead-in was insulated from the specimen by coating the copper with Rockide. With the cooling fins in liquid nitrogen, the test was run and results obtained as shown in figure 223. The temperature difference between resistance weld and cooling fins

less than 1000°R, and the welds were hotter than the crown of the corrugations. In an effort to increase the temperature difference, the lead-in coil was raised by placing 1/16 in. ceramic spacers between coil and specimen. This decreased the temperature difference even more, as shown in figure 223. This type of heating was discontinued because of temperature difference limitations and also the difficulty in attaching and spacing the coil from the specimen.

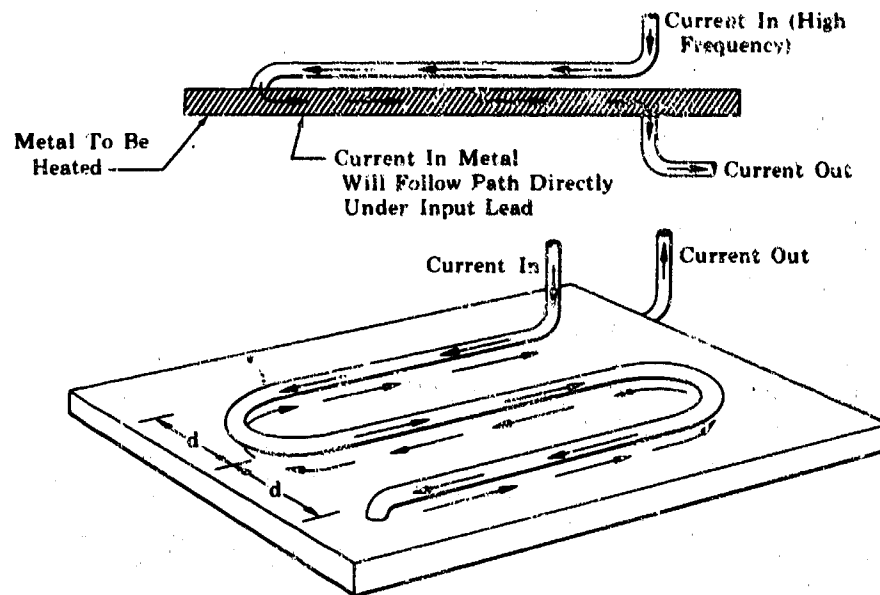


Figure 221. Line Resistance Heating Using Proximity Effect

FD 25329

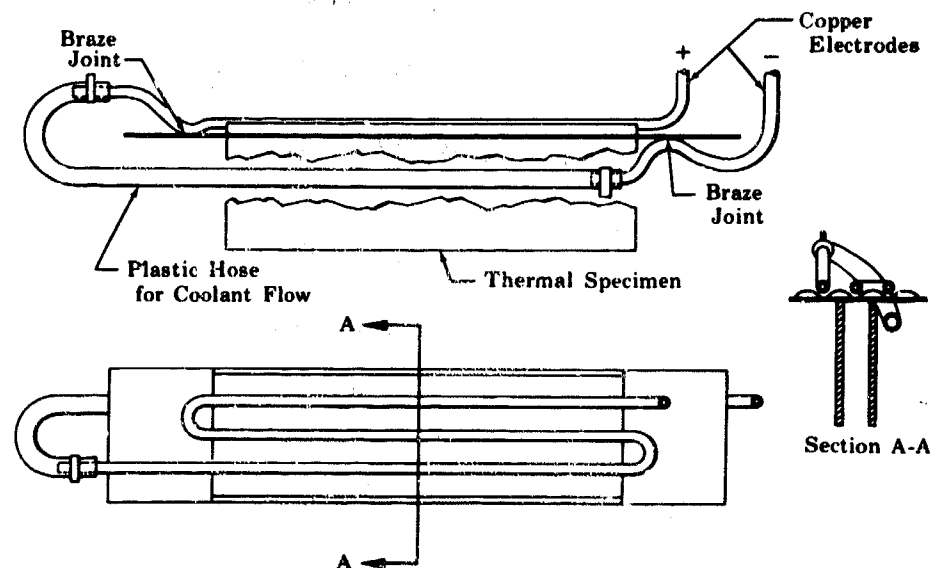


Figure 222. Line Heater Assembly

FD 25330

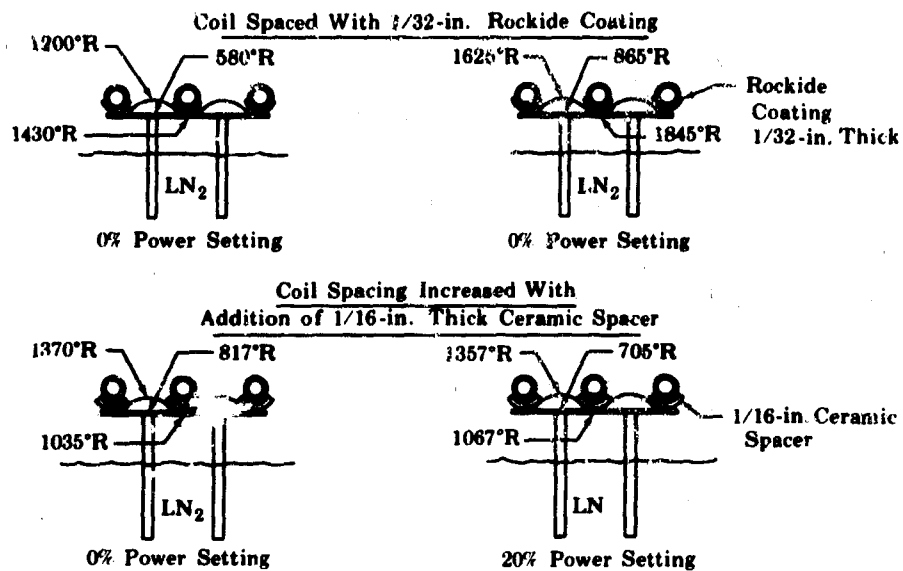


Figure 223. Line Heating Test Results

FD 25331A

d. Evaluation of Final Design Thermal Fatigue Specimen

Using the data previously obtained, five thermal fatigue specimens, as shown in figure 224, were designed and procured. These specimens were used to determine the final conditions for low cycle fatigue tests.

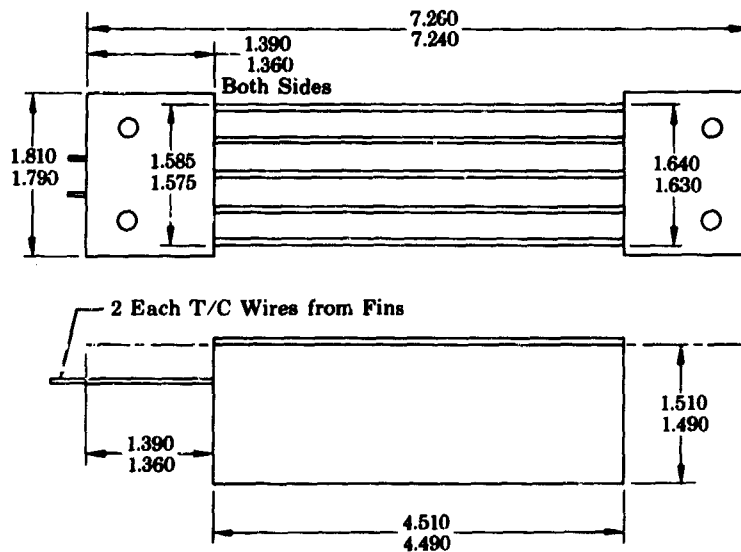
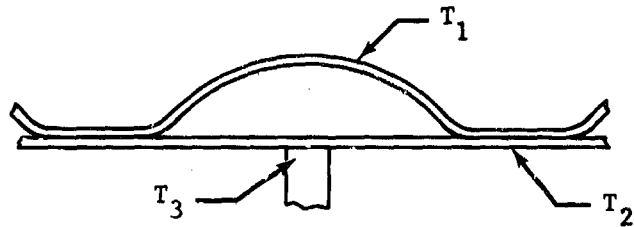


Figure 224. Thermal Fatigue Sample

FD 25332

The corrugations of the first specimen could not be pressurized. The cooling fins were immersed in liquid nitrogen and the induction heater pattern set. The induction coil was set 0.160 to 0.180 in. above the crown of the corrugation and the induction heat power setting placed at 10% to 12%. The desired temperatures and those obtained on the first test are shown in figure 225.



	T_1 ($^{\circ}\text{R}$)	T_2 ($^{\circ}\text{R}$)	T_3 ($^{\circ}\text{R}$)
Desired	2060	1800 to 1900	160
Actual	2060	1820	300

Figure 225. Initial Test Temperatures

FD 46583

The crown temperature (T_1) was read from a thermocouple attached at that point and from an optical pyrometer. The thermocouple wires were attached to the crown for these first tests so that optical pyrometer emissivity settings could be checked and calibrated.

The automatic timer was set to produce a 20 sec. heating cycle and a 21 sec. cooldown cycle. The heating cycle is shown in figure 226, which is a reproduction of the visicorder tape on these first tests. These times were sufficient to let all temperatures reach steady-state before the next cycle began.

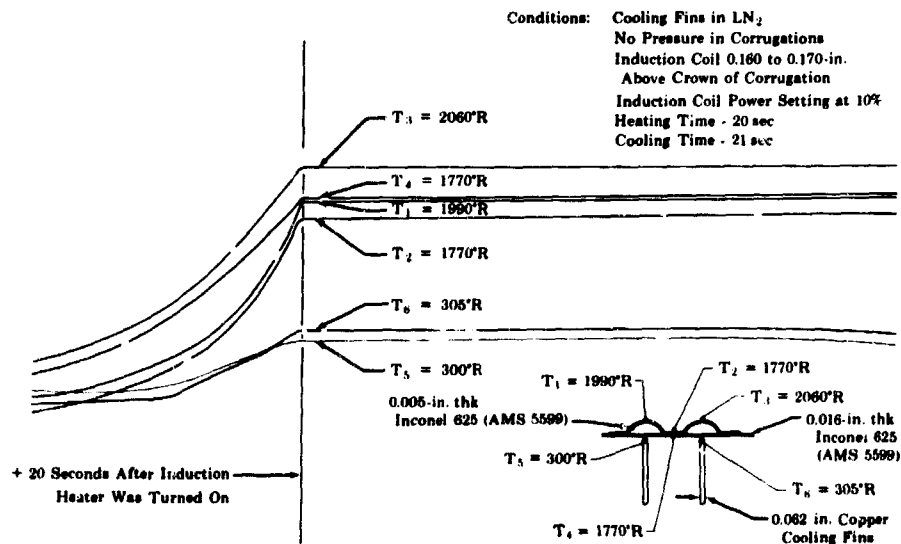


Figure 226. Visicorder Tape of Heating Cycle Tests

FD 25333A

The first specimen completed 100 cycles and was then examined. Thermal fatigue cracks were visible in all four corrugations, as shown in figure 227, and appeared to have occurred early in the 100 cycles. Because this specimen was not pressurized, the exact number of cycles at times of failure could not be determined. The failed area was sectioned and photographs were taken. Figure 228 shows one side of the crack in the 0.005 in. thick Inconel 625 (AMS 5599) prior to etching. It clearly shows the large number of fatigue cracks in the area around the failure. Figure 229 shows the same failed area after etching, with the oxide buildup on the surface and in the cracks. Contamination of the grain boundaries is also visible. The oxidation is more severe in this instance because the specimen was cycled many times after the failure had occurred.

The second specimen was assembled to allow pressurization of the passages as shown in figure 217. The 2060°R crown temperature point with the cooling fins in liquid nitrogen was repeated with this specimen with the corrugations pressurized to 80 psig. One corrugation failed after 24 cycles; another failed at 45 cycles.

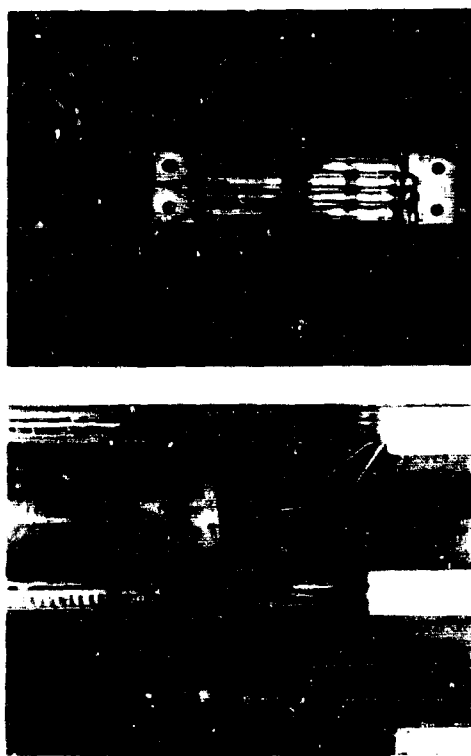


Figure 227. Initial Thermal Fatigue Specimen and Enlarged View Showing Thermal Fatigue Fractures

FM 25767

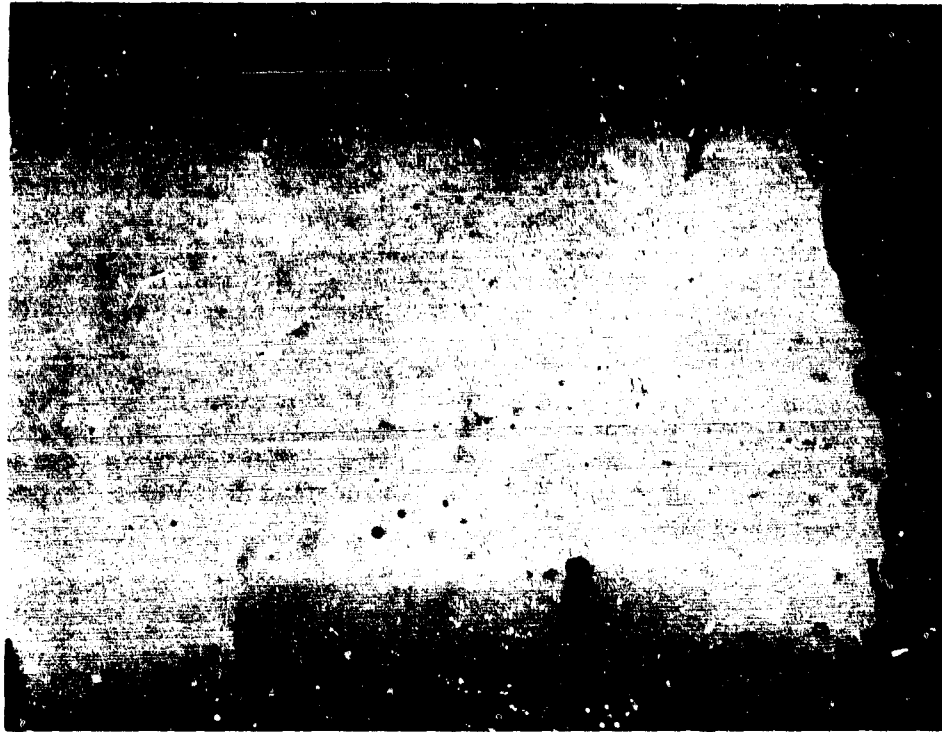


Figure 228. Crack in 0.005 in. Thick Inconel
625 (AMS 5599) Before Etching
(500X Magnification)

FM 24964

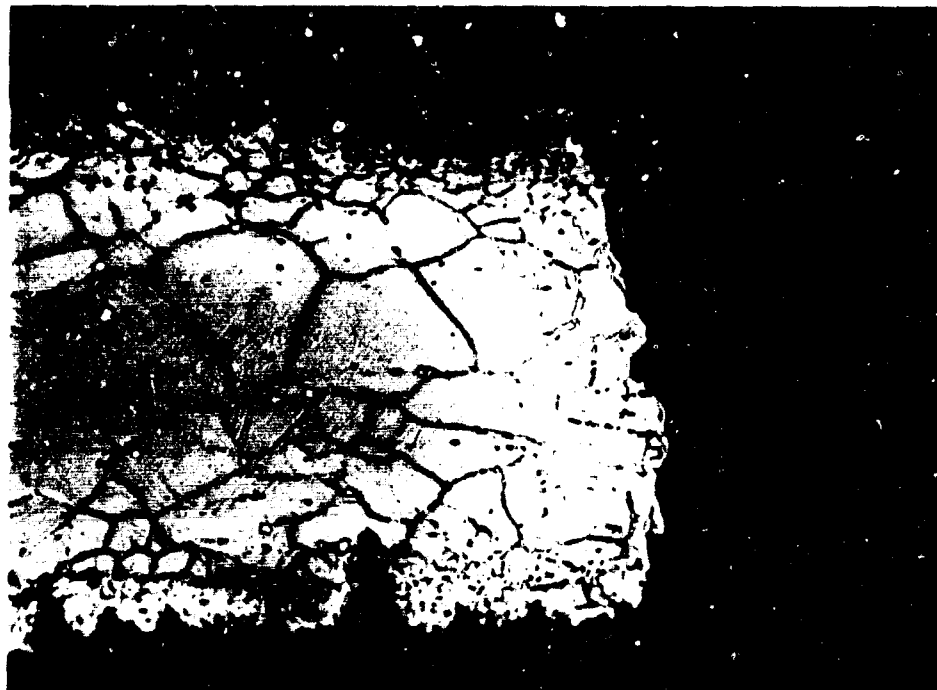


Figure 229. Crack in 0.005 in. Thick Inconel
625 (AMS 5599) After Etching
(500X Magnification)

FM 24969

Up to this point, the temperatures strived for were the predicted engine conditions. The test samples were then investigated to determine how the addition of the copper fin to the cold side affected the strain simulation. The increase in strength and stiffness from adding the large copper fin cross-sectional area allowed only a negligible strain on the cold side caused by the mismatch force. Therefore, a smaller temperature differential could be used to produce the expected hot side strain. Although the nozzle would have a 2060°R hot side and a 150°R cold side, the finned specimens only need a 2060°R hot side and 560°R cold side to produce the same hot side strain.

Three more specimens were run, setting temperatures as close to the desired level as possible. The results of these tests are shown in Table XXV. With the crown temperature 2060°R, the cold side became 100° hotter than desired. Therefore, to produce the required hot side strain, the crown temperature was raised 100°R on the final series of tests. A photograph of the specimen being run at these final conditions is shown in figure 230.

Table XXV. Preliminary Thermal Fatigue Cycling Test Results

Test No.	Crown Temperature, (°P)	Valley Temperature, (°R)	Fin Temperature (°R)	Number of Cycles Before Failure	Date		Comments
					Started	Completed	
1	2060	1820	(LN ₂) -300	approx 40 to 50	3-5-68	3-7-68	The corrugation configuration was not correctly shaped and was not pressurized; therefore, the No. of cycles is approximate.
2	2060	1720	(LN ₂) 400	24 45	3-10-68	3-10-68	Pressurized to 80 psig; one corrugation failed at 24 cycles and the other at 45 cycles.
3	2160	1960	(H ₂ O) 660	42	3-14-68	3-14-68	The specimen was highly overheated on the first heating cycle.
4	2060	2020	(H ₂ O) 649	--	3-15-68	3-15-68	Not cycled because corrugations were damaged. (Used to check heat pattern.)
5	2060	1900	(H ₂ O) 660	42	3-19-68	3-19-68	First furnace braze sample (good braze).

e. Thermal Fatigue Testing

(1) Specimen Configuration

The final specimens were assembled as shown in figure 231. The 0.005 in. thick corrugations were cut from the corrugated panels. These panels were struck on the new die set, annealed in a hydrogen atmosphere at 2335°R ± 25° for 30 minutes, and restruck to bring them to within 10% of the designed configuration. The base sheet was 0.010 in. thick. The copper fins were furnace-brazed at a temperature of 1935°R to 1960°R. This temperature was required because the copper forms an eutectic with the silver braze and lowers the melting point of the silver. The first two assemblies through the furnace braze cycle lost their fins when run in the thermal fatigue rig. The copper used for these assemblies was found to be not oxygen-free, which caused voids in the braze when the oxygen combined with the purge hydrogen to form a water vapor at the interface of the copper and the inconel 625 (AMS 5599). New Oxygen-free copper fins were made and used on later assemblies. The final assemblies are shown in figure 232, 233, and 234.

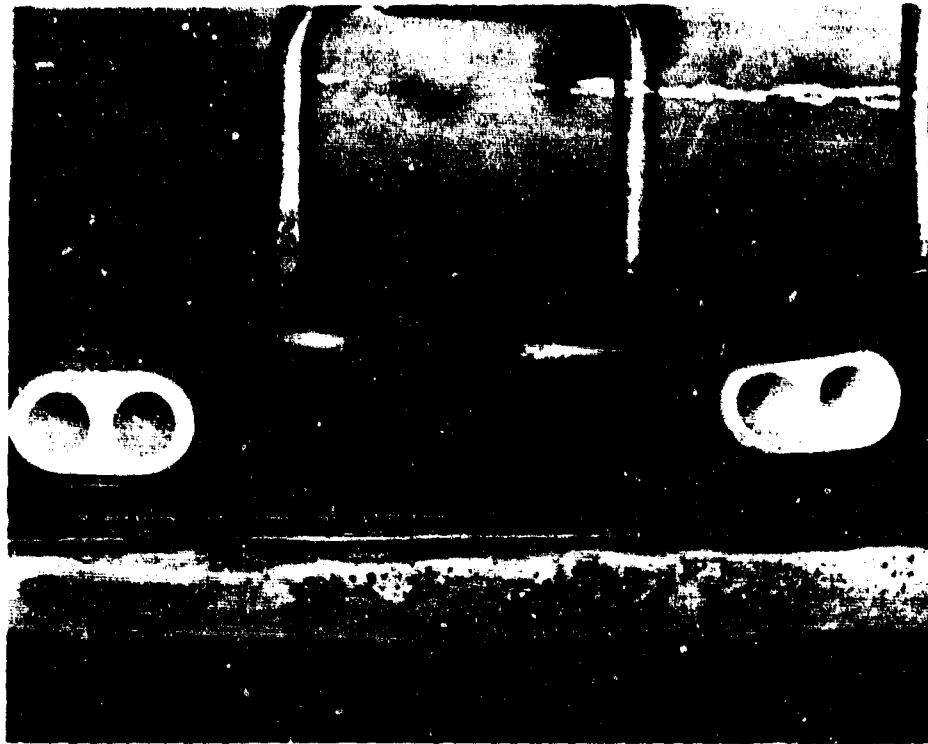


Figure 230. Specimen Being Tested at Final Conditions

FE 76618

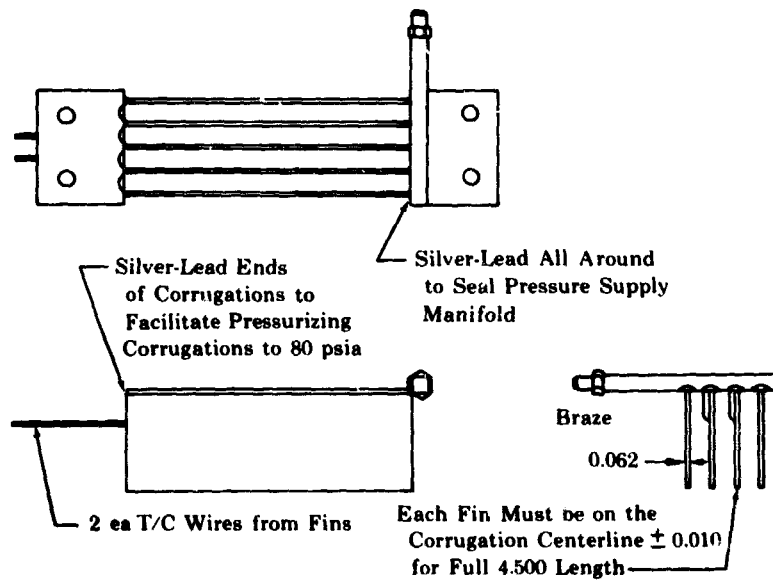


Figure 231. Final Thermal Fatigue Specimen Configuration

FD 25334

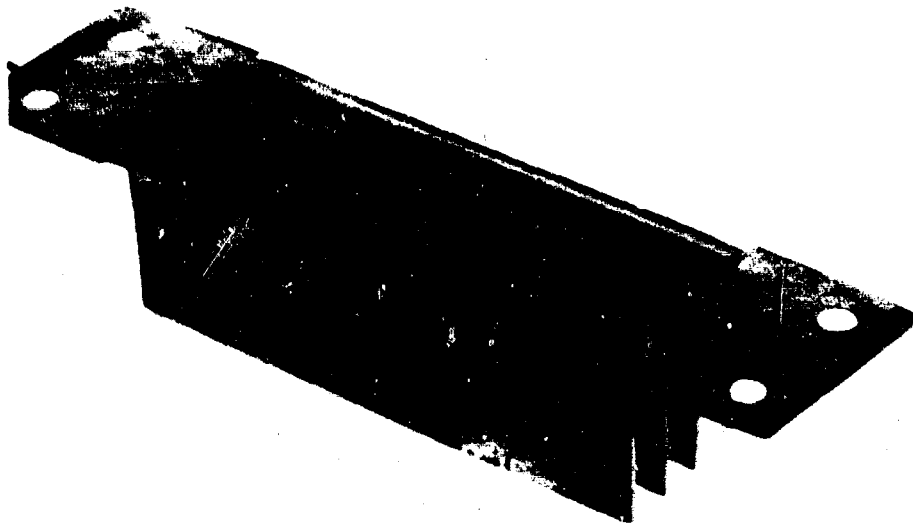


Figure 232. Thermal Fatigue Specimen
Final Assembly (Top View)

FE 76594



Figure 233. Thermal Fatigue Specimen Final
Assembly (Side View)

FE 76592

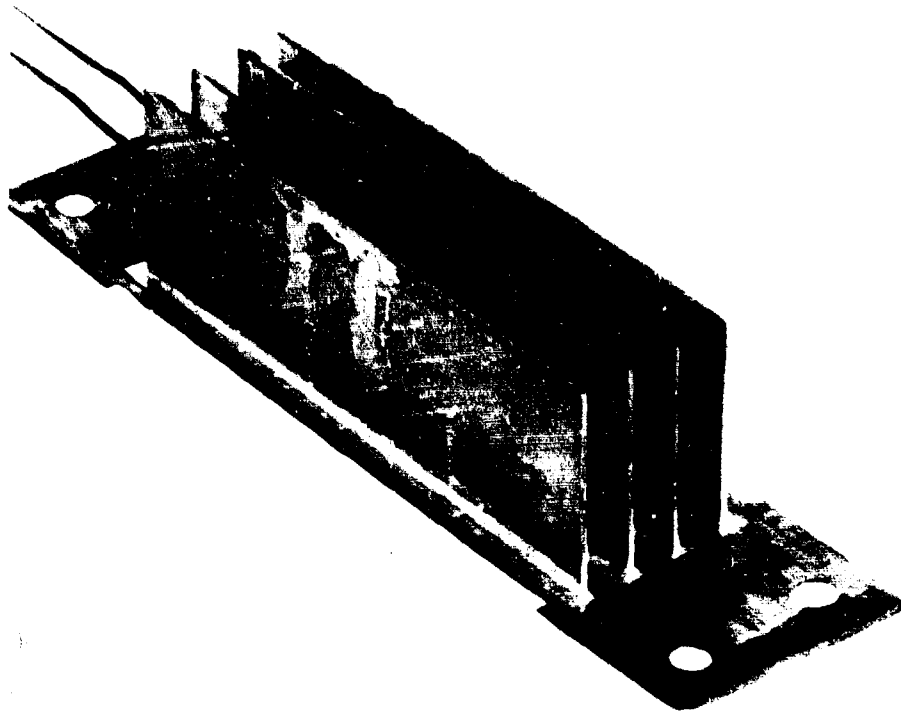


Figure 234. Thermal Fatigue Specimen Final Assembly (Bottom View)

FE 76593

(2) Instrumentation

A 1/16 in. diameter shielded copper/constantan thermocouple wire with a closed end was attached to the two center cooling fins. The tip of the wire was brazed into the silver braze joint at the same time the fin joint was being furnace-brazed. The chromel/alumel thermocouple wires for reading valley temperature were attached in the Materials Development Laboratory. The crown temperature was read using the optical pyrometer.

(3) Fatigue Testing

(a) Peak Engine Condition Tests

The following are the adjusted temperatures necessary to simulate the predicted hot side strain at peak engine conditions:

Crown temperature - 2160° R

Valley temperature - 2160° R

Fin Joint Temperature - 660° R

300 thermal cycles required

Specimens No. 1 and 2 were set to run at these temperature conditions, but voids in the braze weakened the joints so that the joints failed when a small strain was applied and the cooling fins broke off before the conditions could be set.

Specimen No. 3 had one fin break loose, but continued until the corrugation failed at 36 cycles. Number 4 ran 25 cycles at these conditions and then all the fins separated at the braze joint. Specimens No. 4 and 5 completed 30 cycles before corrugation thermal fatigue failure occurred.

(b) Determination of Crown Temperature for Required Life

The No. 6 specimen was run at 1660°R crown temperature and 650°R cold side. The specimen ran 1300 cycles without failing. The test was stopped because the specimen far exceeded the required life.

The crown temperature was raised to 1860°R, and three specimens were cycled at this level. They ran 136 cycles, 189 cycles, and 137 cycles, respectively, before failing (154 cycle average). The test was repeated at 1860°R in an argon atmosphere. This test was to determine if excessive oxidation of the surface was causing early failures. The specimen was cycled 200 times prior to failure. This increase of 11 cycles over the prior maximum was not considered sufficient to continue testing in argon.

The crown temperature was lowered to 1760°R with a cold side temperature of 660°R and three tests were performed. The first specimen completed 350 cycles and failed in the thermocouple tack weld. The tack was made too close to the corrugation and had missed the resistance weld bead. The last two tested completed 680 and 441 cycles with failures occurring in the resistance welds in both cases and a small leak occurring next to the cooling fin in the cold side of the 680 cycle specimen.

All the results of the thermal fatigue tests of the configuration shown in figure 231 are plotted in figure 235. Figure 235 indicates that for a sample with 0.005 in. thick corrugation and 0.010 in. thick flat sheet, 1580°R is the maximum ΔT for a fatigue life of 300 cycles. The cold side temperatures on all these tests stayed within the range of 660°R \pm 10°.

(4) Configurations Change and Associated Cycle Life

(a) 0.010 in. Thick Corrugation

Six specimens were fabricated with 0.010 in. thick corrugated sheet. The specimens were identical to the assembly illustrated in figure 231, except for the corrugation thickness.

The first specimen was run at 1860°R crown temperature and 660°R cold side temperature. The test was stopped at 1100 cycles without a failure. The crown temperature was increased to 2160°R on the second specimen and the cold side temperature set at 674°R. The specimen failed after 115 cycles, and a photograph of the failed corrugation is shown in figure 236. These two tests bracketed the required 300 cycles.

Two specimens were run at 2010°R crown temperature and 670°R cold side. The cycle life was 295 and 281 cycles. The temperature was dropped to 1910°R on the next specimen and cycle life increased to 960 cycles. A photograph of this failure is shown in figure 237.

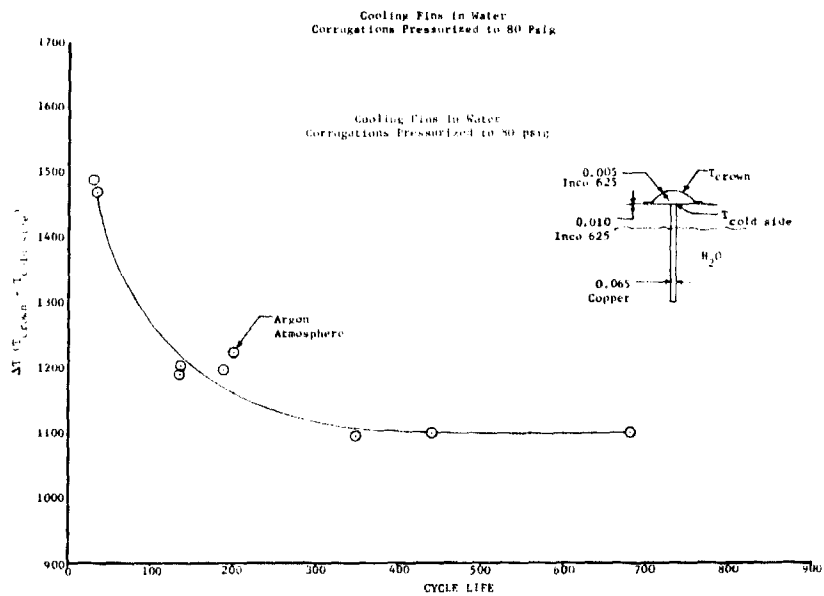


Figure 235. ΔT vs Cycle Life for 0.005 in. Thick Corrugations

DF 65303



Figure 236. Photograph of Failed Corrugation With Crown Temperature at 2160°R

FE 77547



Figure 237. Photograph of Failed Corrugation With Crown Temperature at 1910°R FE 77524

These five tests proved that by increasing the thickness of the corrugated sheet from 0.005 to 0.010 in., the maximum allowable crown temperature for a 300 cycle thermal fatigue life could be increased from 1780°R to approximately 2000°R.

The last specimen was cycled at 1910°R, but with the cooling fins in liquid nitrogen. The cold side temperature stabilized at 219°R, giving a ΔT of 1691°R. These conditions were set to determine what effect an increase in strain at a constant hot wall temperature would have on cycle life. The specimen failed at 441 cycles. Therefore, a 34% increase in strain caused a 52% loss of thermal fatigue cycle life.

It should be noted that the strain obtained with the fins in liquid nitrogen is greater than a predicted nozzle strain, and, therefore, the test was more severe than required.

(b) Inconel 625 (AMS 5599) Cooling Fins

Two thermal fatigue specimens were constructed with the cooling fins made of Inconel 625 (AMS 5599). The rest of the assembly was identical to the configuration in figure 231, with the corrugation and flat side 0.005 in. and 0.010 in. thick, respectively.

The purpose of these specimen tests was to determine if assembling and furnace-brazing corrugated sheets, flat back sheets, and cooling fins (all of the same material), would reduce the stresses built into the specimen prior to fatigue testing and, therefore, increase fatigue life.

The corrugation crown started to ripple as soon as heat was applied to the first specimen. While the crown heating pattern was being adjusted, the specimen failed. The crown had rippled so severely that it had torn the 0.005 in. material next to the resistance weld.

The second specimen was mounted and heat applied. The heating pattern was being adjusted when it was noticed that the outside cooling fin was beginning to separate from the 0.010 in. thick sheet at the braze joint. Before the heating pattern could be adjusted, all the fins had broken loose halfway across, thus relieving the crown stresses and causing the part to overheat. Eutectic braze joints were formed on these two samples. Using pure silver joints would probably eliminate joint problems. These were the only specimens available of this configuration, and production of more samples would have delayed the completion of thermal testing. Therefore, it was decided to eliminate further studies of this design.

(5) Thermal Fatigue Summary

The following data summarize the thermal fatigue testing of nozzle design specimens:

1. Fatigue life at design conditions ($T_{\text{crown}} = 2160^{\circ}\text{R}$ with 660°R cold side):
 - a. 0.005 in. thick corrugation - 30 cycles
 - b. 0.010 in. thick corrugation - 110 cycles
 - c. Required nozzle life - 300 cycles
2. Corrugation hot side temperatures that gave 300 cycles:
 - a. 0.005 in. thick corrugation - 1780°R
 - b. 0.010 in. thick corrugation - 2000°R
 - c. Designed nozzle temperature - 2160°R with 660°R cold side temperature

All the test data are summarized in table XXVI. The total strain for each of these tests has been plotted against cycle life and is shown in figure 238. The strain was calculated using the following formula:

$$\epsilon_{\text{total}} = \alpha_{\text{hot}} (T_{\text{hot}} - 70) + \alpha_{\text{cold}} (70 - T_{\text{cold}})$$

where:

$$\epsilon_{\text{total}} = \text{Total strain (in./in.)}$$

α_{hot} = Coefficient of thermal expansion in in./°R

α_{cold} = Coefficient of thermal expansion in in./°R

T_{hot} = Corrugation crown temperature in °R

T_{cold} = Cooling fin temperature in °R

These test data are compared with the total strain data from the RL10 nozzle tube fatigue tests and are also plotted on the strain vs life curve. An operating hot wall temperature of 1910°R has been selected for the design of the demonstrator engine two-position nozzle.

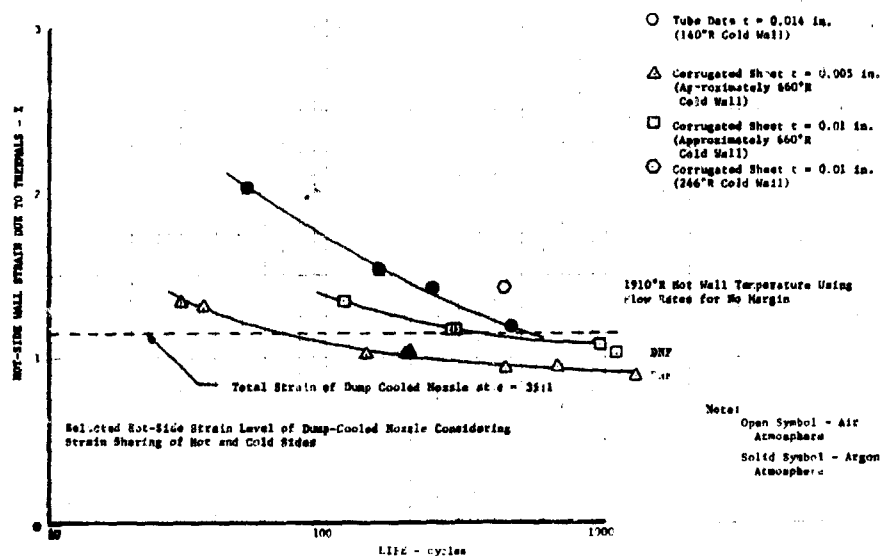


Figure 238. Thermal Fatigue of Inconel 625 (AMS 5599) Tube vs Corrugated Sheet. DF 65305

Table XXVI. Thermal Fatigue Cycling Test Results

Test No.	Crown Temperature (°R)	Valley Temperature (°R)	Fin Temperature (°R)	Number of Cycles to Failure	Date		Comments
					Started	Completed	
1					3-27-68		Cooling fins broke off due to insufficient braze coverage; not cycled.
2					3-27-68		Cooling fins broke off due to insufficient braze coverage; not cycled.
3	2130	2166	660	38	4-4-68	4-4-68	One copper fin separated from sample causing poor heat pattern - poor furnace braze.
4	2160	2157	665	No Test	4-5-68	4-5-68	Cooling fins separated from sample after 25 cycles - test was stopped.
5	2150	2140	660	30	4-5-68	4-5-68	
6	1860	1650	650	Did Not Fail	4-8-68	4-10-68	Stopped test at 1300 cycles.

Table XXVI. Thermal Fatigue Cycling Test Results (Concluded)

Test No.	Crown Temperature (°R)	Valley Temperature (°R)	Fin Temperature (°R)	Number of Cycles to Failure	Date		Comments
					Started	Completed	
7	1860	1836	670	136	4-15-68	4-15-68	
8	1760	1755	665	350	4-17-68	4-17-68	Failed in valley where thermocouple was tack welded to skin outside resistance weld.
9	1760	1718	660	680	4-18-68	4-19-68	Failed in resistance weld out of heat zone and on bottom side next to cooling fin.
10	1860	1847	663	189	4-23-68	4-23-68	
11	1860	1809	657	137	4-24-68	4-24-68	
12	1860	1801	637	200	4-29-68	4-29-68	Test run in argon atmosphere.
13	1760	1759	661	441	4-30-68	5-1-68	Failed in resistance weld.
14	1860	1759	659	Did Not Fail	5-3-68	5-7-68	(0.010 in. thick corrugation) Stopped test at 1100 cycles.
15	2160	1981	674	115	5-7-68	5-7-68	(0.010 in. thick corrugation)
16	1860	1760	700	-	5-8-68	5-8-68	(Inconel 625 fins) Corrugations rippled during heat adjustment and tore hole in material next to resistance weld.
17	1860	1760	700	-	5-9-68	5-9-68	(Inconel 625 fins) Cooling fins broke off during heat adjustment.
18	2010	1840	669	295	5-9-68	5-10-68	(0.010 in. thick corrugation)
19	2010	1840	670	281	5-13-68	5-13-68	(0.010 in. thick corrugation)
20	1910	1597	656	960	5-15-68	5-17-68	(0.010 in. thick corrugation)
21	1910	1560	(LN ₂) 219	441	5-20-68	5-23-68	(0.010 in. thick corrugation) Run to check which had most effect on life crown temperature or ΔT.

E. CONTROLS COMPONENT TESTS

1. Main Chamber Oxidizer Valve

a. Introduction

The main chamber oxidizer valve was tested during Phase I (Contract AF04(611)-11401). Eight builds of valve F-33466 and five builds of valve F-35106 were tested. This testing indicated that the disk seal required redesign to attain the 10 sccs shutoff leakage goal established for this valve. In addition, rotary shaft lip seals were developed that required valve design revisions to optimize the seal application to the valve.

b. Summary, Conclusions, and Recommendations

(1) Summary

During this report period, design, procurement, and endurance testing of four main chamber oxidizer valve shutoff seal candidate configurations were

completed. The shutoff seal candidates were; (1) the looseleaf Kapton F-FEP Teflon seal; (2) the silver-plated hoop seal; (3) the strap-actuated seal, and (4) the cam-actuated seal. All seals were tested at cryogenic conditions. None of the seals met the leakage requirements throughout the cryogenic tests; however, the silver-plated hoop seal and the cam-actuated seal test results indicated that additional development potential existed for both. Attempts to replat the hoop seal indicated a need for improved access to the inside of the seal for cleaning purposes, and improved plating procedures. The cam-actuated seal element failed during the test, indicating a need for improved support and a more flexible seal material. The shaft lip seal support housing designs were revised and two seal thicknesses were tested. A seal laminate of three layers of 0.005 in. Kapton F and one layer of 0.005 in. FEP Teflon bearing on the shaft gave satisfactory results.

(2) Conclusions

1. The silver-plated hoop seal and the cam-actuated seal designs were considered to be acceptable shutoff seals for continued development for the canted shaft butterfly valve.
2. The strap-actuated and looseleaf shutoff seals did not appear to warrant further effort.
3. Laminated Kapton-Teflon lip seals met the leakage and durability goals and were recommended for this application.

(3) Recommendations

1. Continue development of the hoop seal to improve manufacturing methods and cleaning capability.
2. Continue development of the cam actuated seal to improve durability.

c. Hardware Description

The main chamber oxidizer valve was designed and fabricated during Phase I (Contract AF04(611)-11401). It was designed to control the overall engine oxidizer-to-fuel weight ratio by regulating the flow of oxidizer to the main burner injector. The valve is positioned by a rotary servo-actuator as a function of the engine thrust level and the scheduled mixture ratio.

The main chamber oxidizer valve is located upstream of the main burner injector. The valve is a butterfly type and incorporates a shutoff seal for the oxidizer flow to the main burner injector. To accommodate this shutoff feature, a canted shaft with integral disk was selected so that an uninterrupted disk sealing surface would be provided. Incorporation of the shutoff seal in this valve eliminates the need for a separate shutoff valve between the main chamber oxidizer valve and the main burner injector.

The canted shaft arrangement requires a split main housing for assembling the valve. Widely spaced double roller bearings are incorporated to take the loads produced by the maximum valve pressure drop. Shaft thrust bearings are required to restrain the shaft against the flow-pressure thrust loads resulting from the

canted shaft. These flow loads are minimized by partially pressure balancing the shaft to oppose them. The valve configuration at the end of Phase I (Contract AF04(611)-11401) is shown in figure 239.

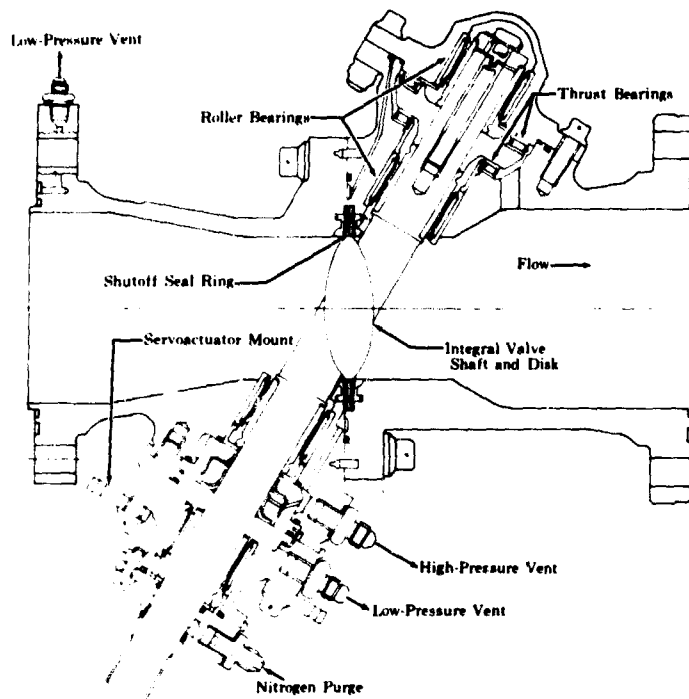


Figure 239. Main Chamber Oxidizer Valve

FD 18938A

d. Facilities

Testing was conducted in the B-22 test stand shown in figure 240. For environmental endurance tests, the valves were mounted in the stand and instrumented as shown schematically in figure 241. The tests were performed by submerging the valve in liquid nitrogen or liquid argon and pressurizing with nitrogen to internal pressures of 50 to 6000 psig. The valves were cycled at these conditions and valve seal leakages were measured periodically. For the later tests, liquid argon was selected for the cryogenic bath to ensure that all of the nitrogen leakage vaporized at the valve external ambient pressure. This allows satisfactory steady-state leakage measurement accuracy for all data points. Leakages of 0.14 to 5200 sccs were measured by a series of gaseous nitrogen flowrates. Lower leakages were measured by positive displacement leak detectors.

e. Testing

(1) Valve F-33466-Build No. 9

Main chamber oxidizer valve F-33466-9 incorporated the following sealing configurations:

1. A Looseleaf (OD bonded) Kapton F-FEP Teflon disk seal was used (0.005 in. thick sheets in alternate layers). An Inconel ring loaded each outside Kapton F layer against the housing

faces to prevent leakage around the seal. Figure 242 shows the shutoff seal configuration.



Figure 240. B-22 Cryogenic Static Cycle Test Stand

FC 13799

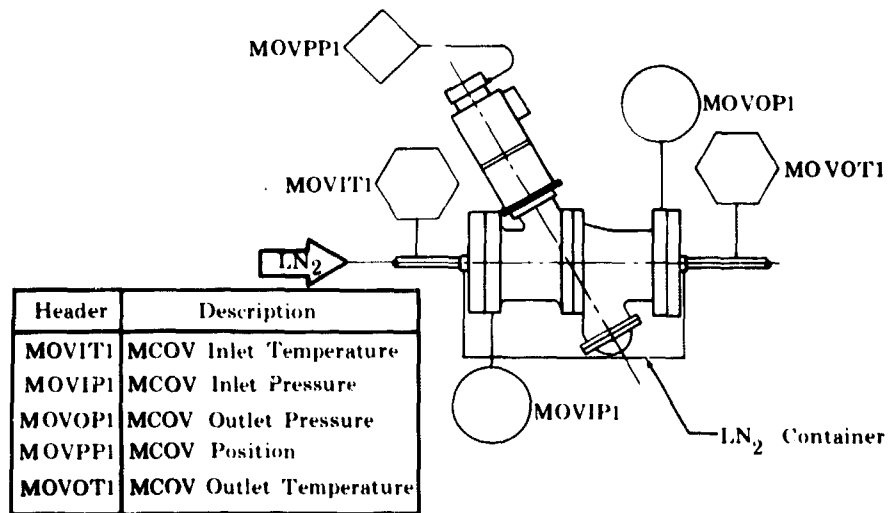


Figure 241. Main Chamber Oxidizer Valve Instrumentation Schematic (B-22 Stand)

FD 23066A

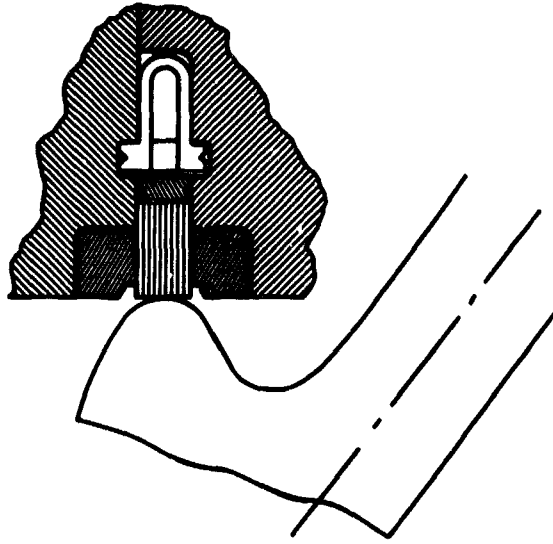


Figure 242. Laminated Kapton Shutoff Seal

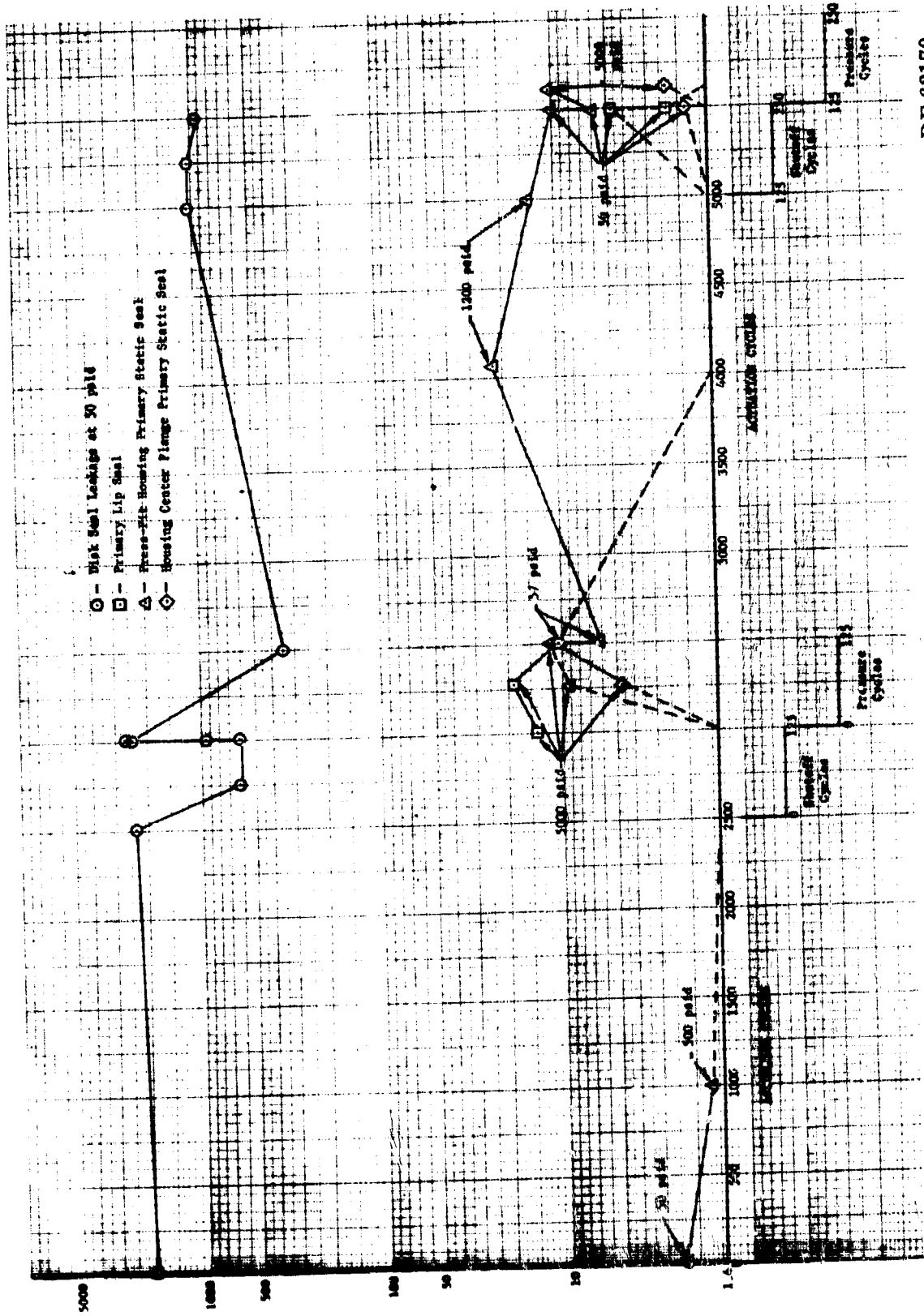
FD 25481

2. A primary lip seal of laminated Kapton F (two layers) and FEP Teflon (one layer next to shaft) of 0.015 in. total thickness was used. The lip seal retainer was modified to mate with the thinner lip seal.
3. An inverted U-ring center flange static seal assembly that loaded the 0.015 in. thick laminated Kapton F static seals was used.
4. The primary shaft seal housing was modified to isolate static seal leakage from the primary lip seal leakage. A vent passage was added to the valve inlet housing to conduct this leakage overboard.

The disk seal leakage at 50 psid was 8 sccs GN₂ with the valve ambient temperature, and the torque required to rotate the valve shaft was as follows:

Rotation out of disk seal	125 lb-in.
Clockwise and counterclockwise rotation	15 to 20 lb-in.
Rotation into disk seal	200 lb-in.

The valve was mounted in the B-22 test stand for an environmental endurance and leakage test; 5000 partial stroke actuation cycles, 250 shutoff cycles, and 153 pressure cycles were performed. Leakages from the primary lip seal, disk seal, primary shaft seal housing, and the main housing center flange primary static seal are shown in figure 243. The maximum bearing cover primary static seal leakage was 75.5 sccs and the maximum inlet flange trapped Teflon primary static seal leakage was 1.9 sccs. The outlet flange primary O-ring static seal vent was capped after 2500 actuation cycles and 125 shutoff cycles due to excessive leakage. The secondary and vent shaft seal leakages remained less than 1.4 sccs throughout the test.



DF 62170

Figure 243. Laminated Kapton F-FEP Teflon Seal Leakage vs Actuation, Shutoff, and Pressure Cycles, Rig F-33466-9

The valve was removed from the B-22 test stand when the outlet flange static seal leakage exceeded the stand limit. The torque required to rotate the valve shaft at ambient temperature was as follows:

Rotation out of disk seal	85 lb-in.
Clockwise and counterclockwise rotation	10 lb-in.
Rotation into the disk seal	90 lb-in.

Disassembly of the valve revealed the following:

1. The primary lip seal was in good condition with negligible wear.
2. A section of the disk seal had failed as shown in figure 244 and was found in the outlet housing. One disk seal axial support ring was bent as shown in figure 245.
3. The shaft disk outside diameter was scored where it contacted the bent support ring.
4. Contamination particles were embedded in the Teflon coating of the outlet flange primary O-ring static seal.

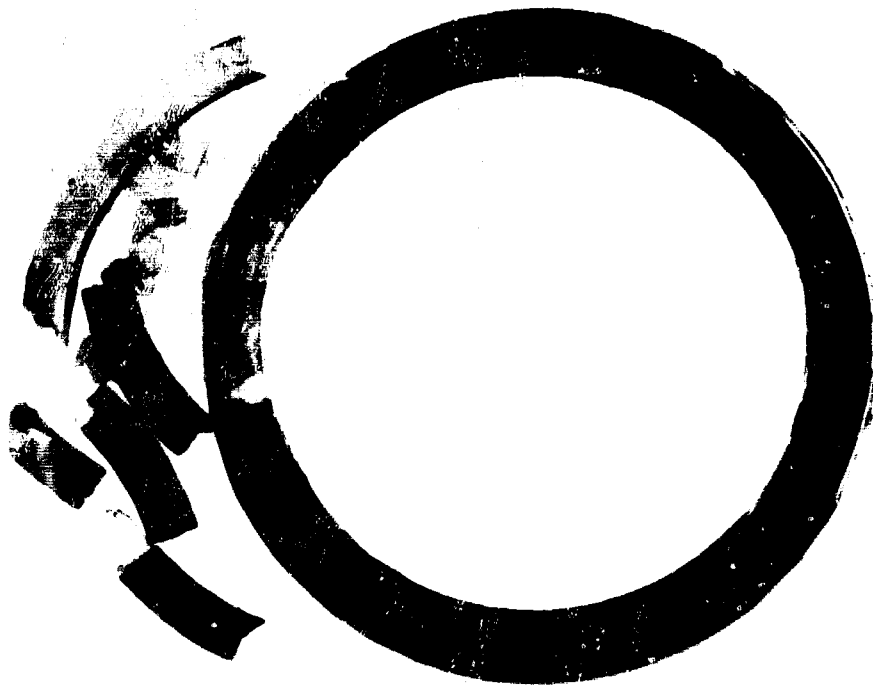


Figure 244. Failed Portion of Disk Seal After Test

FE 74152

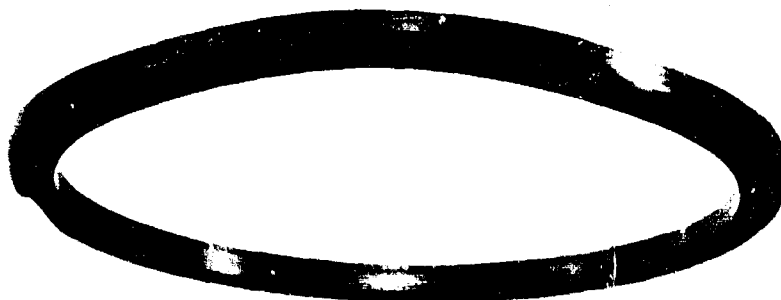


Figure 245. Disk Seal Axial Supporting Ring
After Test

FE 74153

(2) Valve F-35106-Build No. 6

Main chamber oxidizer valve F-35106-6 incorporated the following sealing configurations:

1. A silver-plated hoop disk seal with a 0.011 in. tight fit on the disk. (See figure 246.) The disk seal was installed on the shaft disk in the closed position by heating the seal to approximately 250° F and cooling the disk in liquid nitrogen.
2. The Inconel 718 (AMS 5663) disk sealing surface was 0.090 in. wide with a 5 microinch finish.
3. The revised shaft lip seal design as shown in figure 247.
4. 0.019 in. thick laminated Kapton F (3 layers) and FEP Teflon (1 layer next to shaft) primary and secondary shaft lip seals.
5. A trapped 0.010 in. thick laminated Kapton F primary inlet flange static seal.

The valve was mounted in the B-22 test stand for an environmental endurance and leakage test; 10,000 partial stroke actuation cycles, 600 shutoff cycles, and 500 pressure cycles were completed. This endurance test was conducted with the valve submerged in liquid nitrogen.

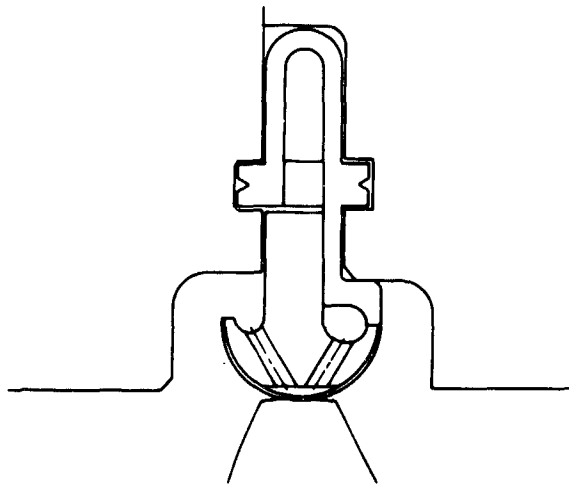


Figure 246. Hoop Shutoff Seal

FD 24949A

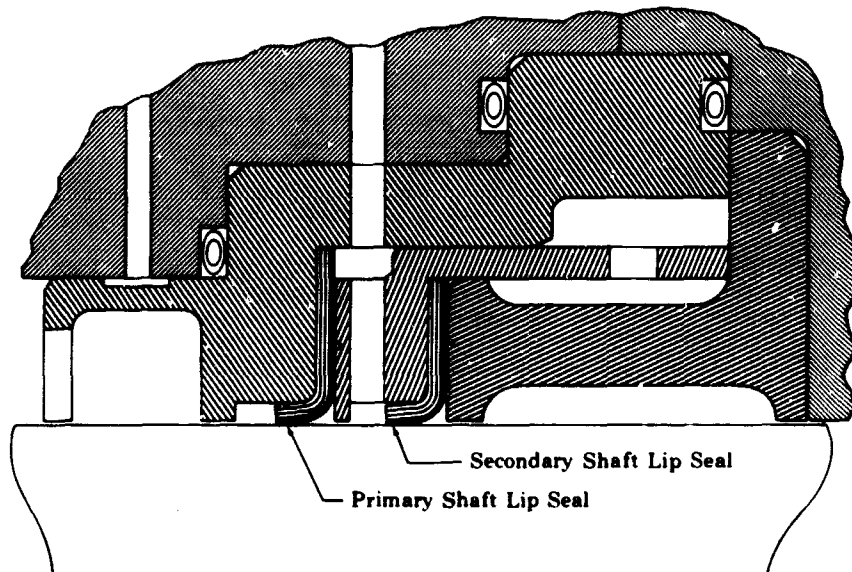


Figure 247. Lip Seal Package

FD 24852

Indicated disk seal leakage was somewhat unstable and varied with time as shown in figure 248. The measurements were apparently affected by variations in vent line vaporization rates due to both variable flowrates and cooling bath levels. The values shown on figure 249 are the final readings taken at each point. After the endurance test was completed, an additional 100 shutoff cycles were performed using helium as the pressurizing and leakage test fluid to improve stability. During these tests, the valve position for minimum leakage was found to be 3.2 deg from the full closed position. The test results using helium as the pressurizing medium and with the valve at 3.2 deg open are shown in figure 250.

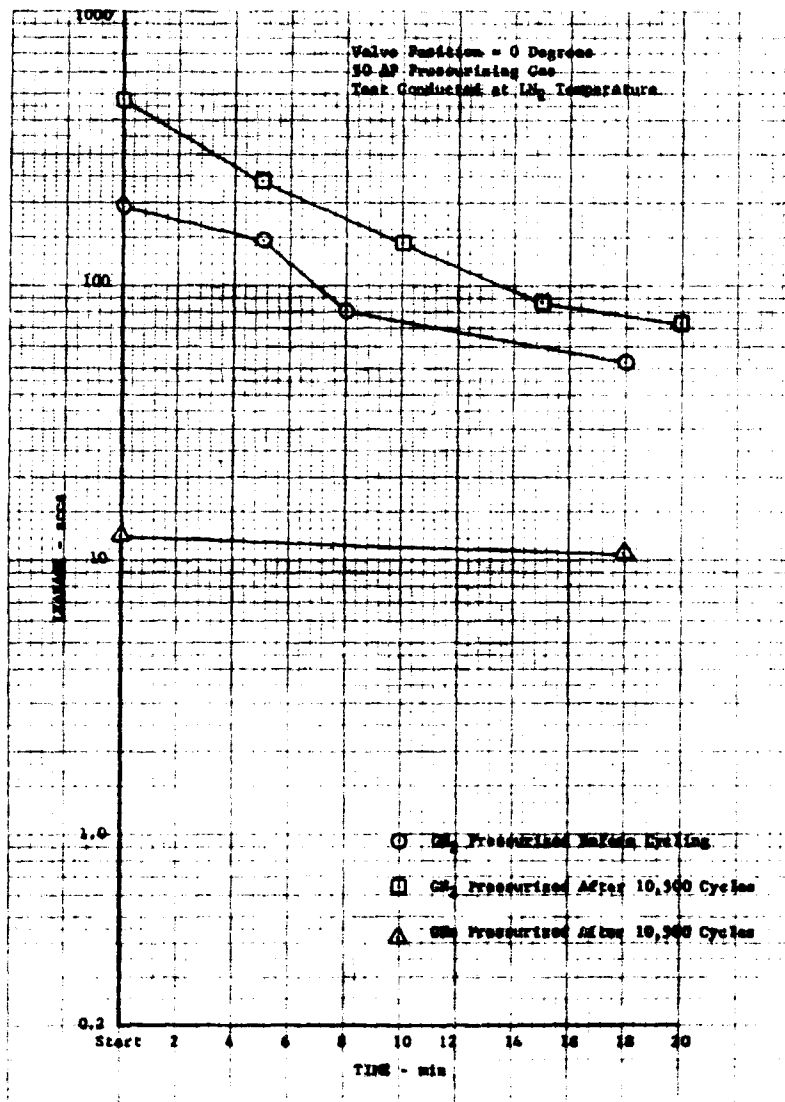


Figure 248. Hoop-Type Disk Seal Leakage vs Time, DF 65061
 Rig F-35106-6

CH₂ Pressurizing Gas - 50 ΔP
 Test Conducted at 14₂ Temperature

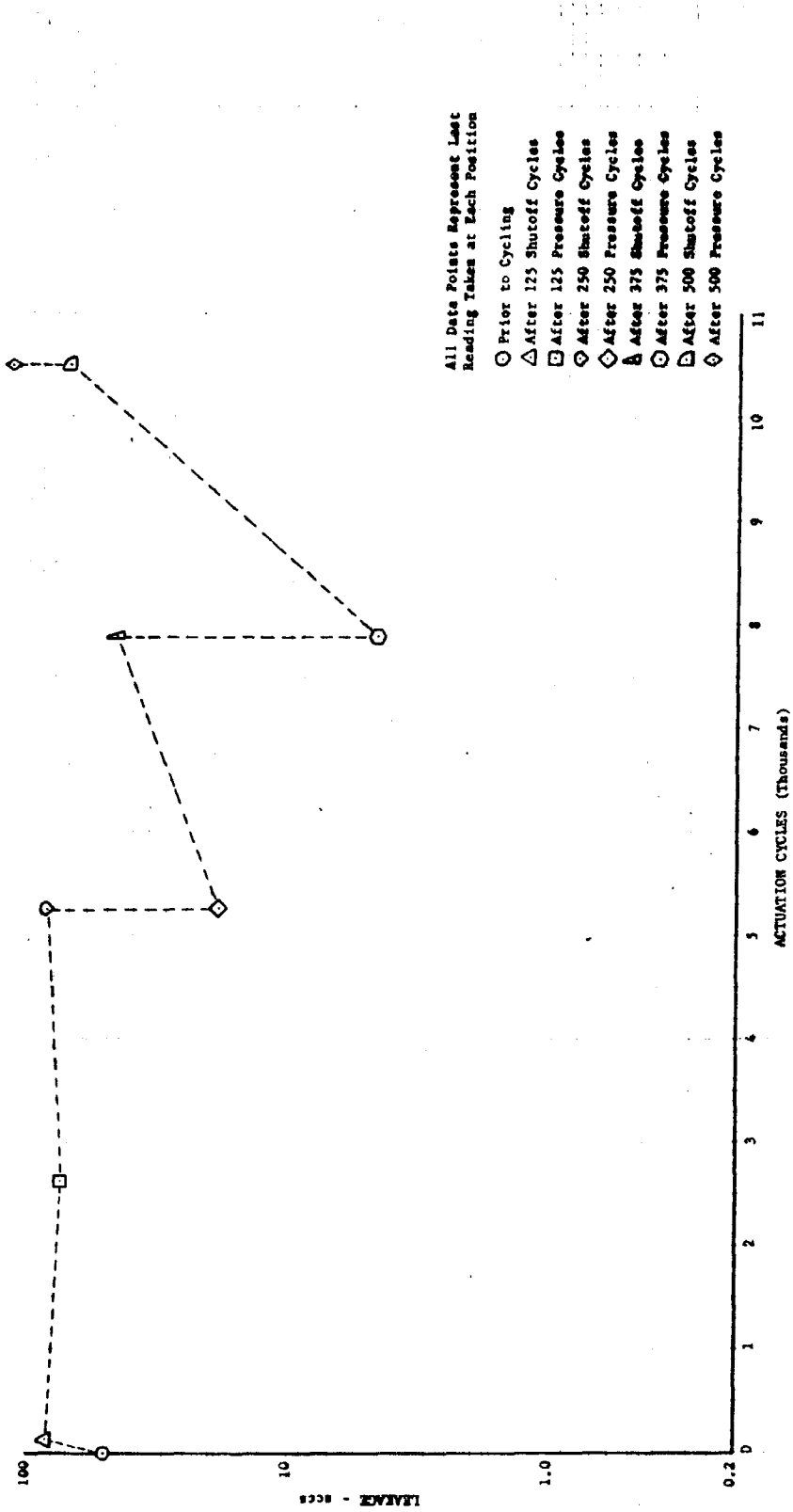


Figure 249. Hoop-Type Disk Seal Leakage vs Actuation Cycles, Rig F-35106-6

DF 65062

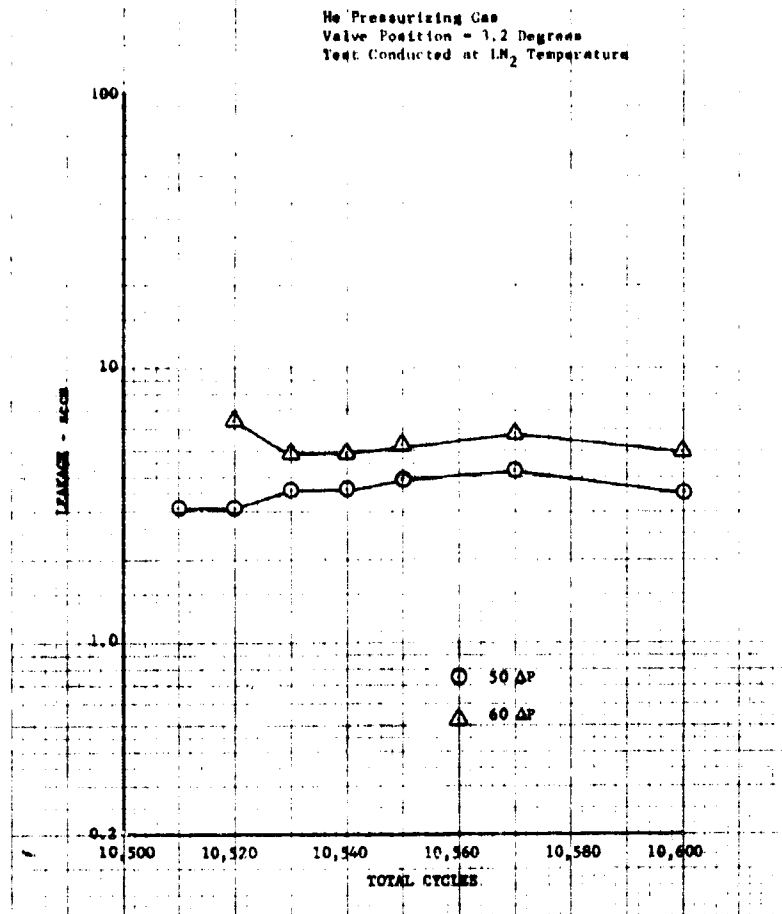


Figure 250. Hoop-Type Disk Seal Leakage vs Total Cycles, Rig F-35106-6 DF 65063

No mechanical malfunctions were observed during the test. The thrust bearing cap primary static seal leaked excessively at pressures above 2000 psig. The vent was capped after 2625 actuation cycles. The primary and secondary shaft seal and static seal leakages during the test are shown in figure 251.

Prior to disassembly, the ambient temperature disk seal leakage at 50 psid GN₂ was 1.33 cccs with the disk positioned at 3.2 deg from the closed position. At the closed position the leakage was 4.5 cccs. No other seal leakage was evident.

Disassembly of the valve revealed no significant parts deterioration. The disk seal showed some wear on the silver-plated hoop seal surface as shown in figure 252. The shaft disk sealing surface is shown in figure 253. Seal-to-disk fit was 0.0035 in. tight. All other parts were in excellent condition.

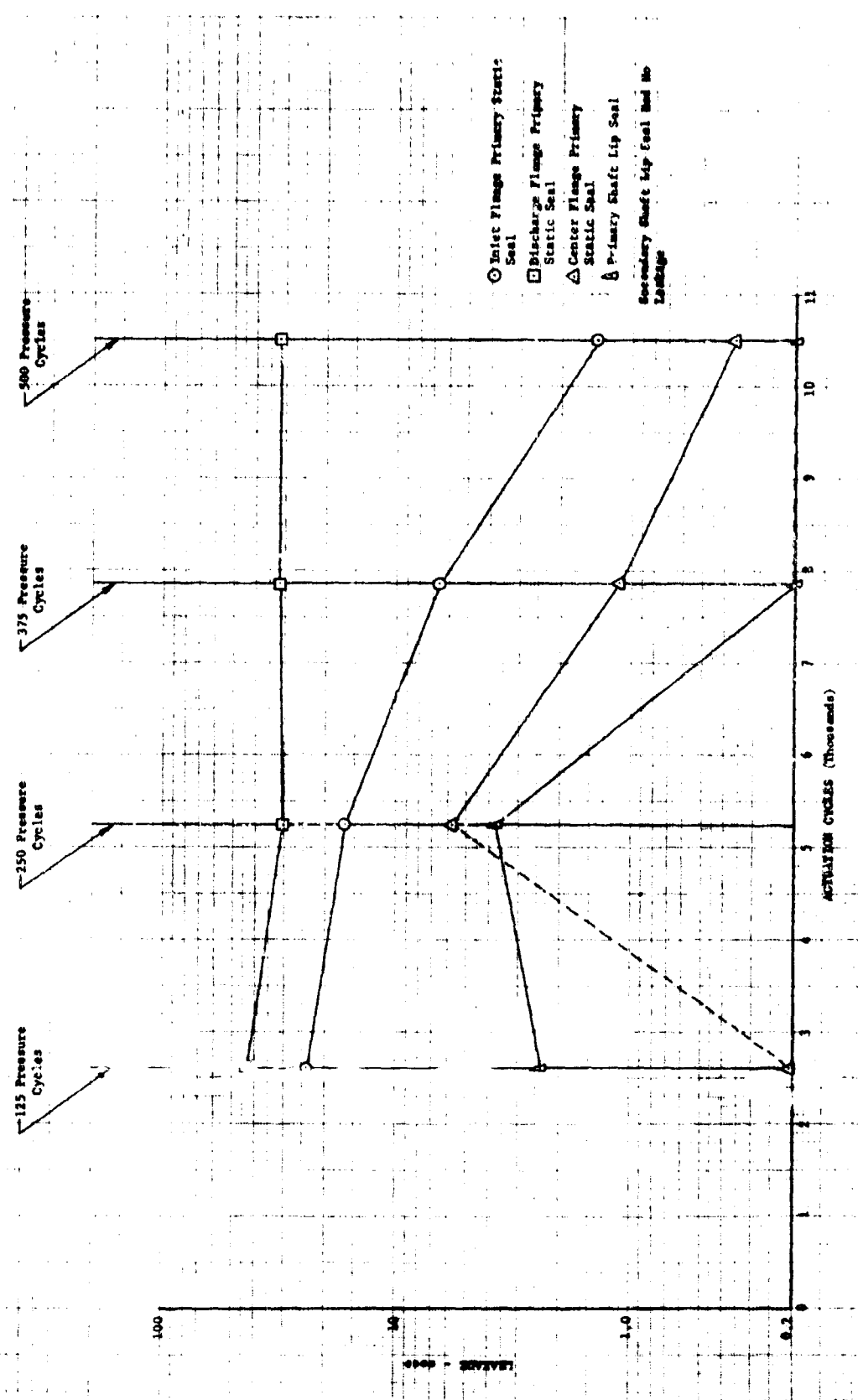


Figure 251. Primary and Secondary Shaft Lip Seals and Static Seals Leakage vs Actuation Cycles, Rig F-35106-6

DF 65064



Figure 252. Hoop Seal Surface After Test,
Rig F-35106-6

FE 77114

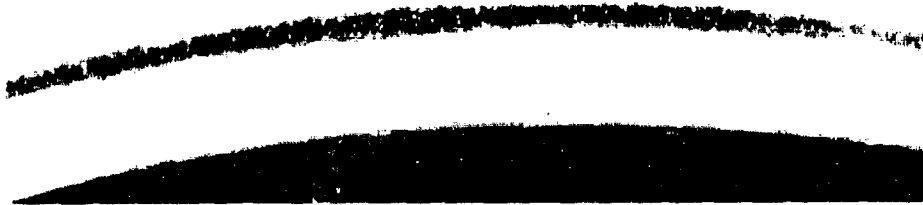


Figure 253. Shaft Disk Surface After Test,
Rig F-35106-6

FE 77111

(3) Valve F-33466-Build No. 10

Main chamber oxidizer valve F-33466-10 incorporated the following modifications from the previous build.

1. A silver-plated and Teflon primer coated 0.005 in. thick Inconel X (AMS 5598) seal element, as shown in figure 254, was used for the disk seal. The seal element was contracted against the disk surface by a shaft lug and circumferential strap. A 0.012 in. shim was used to adjust the seal load. Ambient seal leakage was 1 sccs at 50 psid of GN₂ prior to cryogenic test. Figure 255 shows the shutoff seal configuration.

2. A seal actuating lug was welded to the shaft. The disk had a flat (cylindrical) sealing surface 0.090 in. wide with an 11 microinch surface finish.
3. The revised shaft lip seal package design used is previously shown in figure 257.
4. A laminated seal of Kapton F (3 layers) and FEP Teflon (1 layer next to shaft) was used for the primary shaft lip seal. The total thickness of this lip seal was 0.019 in.
5. A trapped 0.020 in. thick laminated Kapton F seal was used for the inlet flange static seal.
6. An Inconel X (AMS 5667) inverted U-ring center flange static seal assembly was used for the center flange static seal. It loaded two 0.015 in. thick laminated Kapton F seals.
7. A Teflon coated, Omega-shape design, which incorporated an assembly preload spacer and was pressure energized to follow flange deflection during operation, was used for the discharge flange static seal.
8. A rotary hydraulic servoactuator was used.

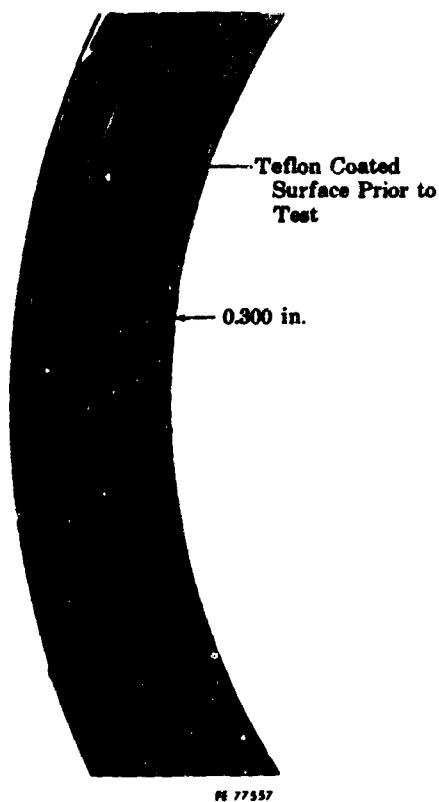


Figure 254. Shutoff Seal Prior to Test,
Rig F-33466-10

FD 24858

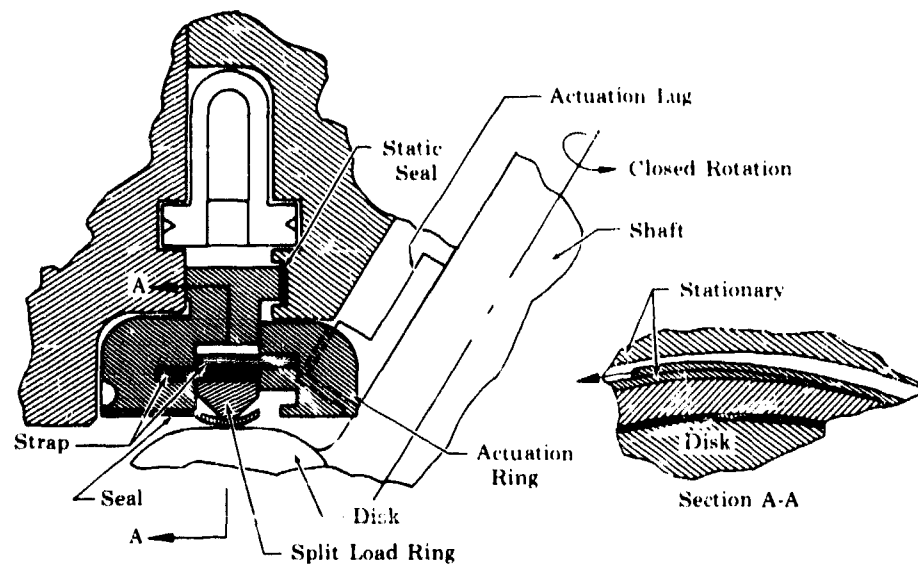


Figure 255. Strap-Actuated Shutoff Seal

FD 24851A

The valve was mounted in the B-22 test stand for an environmental leakage and endurance test; 10,000 partial stroke actuation cycles, 500 shutoff cycles and 500 pressure cycles were completed. This endurance test was conducted with the valve submerged in liquid argon.

Liquid nitrogen boiloff at the start of each measurement point resulted in indicated disk seal leakage variation with time as shown in figure 256. The values shown in figure 257 are the final readings taken at each set point. An ambient temperature GN₂ purge to the discharge housing prior to each disk seal leakage measurement point was apparently only partially effective in removing the liquid nitrogen that had accumulated in the housing.

No mechanical malfunctions were observed during the test. The thrust bearing cap and shaft seal housing static seals leaked excessively at pressures above 1200 psid. The vents were capped after 2625 actuation cycles. The primary and secondary shaft seal leakage is shown in figure 258. The static seal leakages are shown in figure 259.

Prior to disassembly, the following ambient temperature seal leakages were measured at 50 psid GN₂:

Disk Seal	0.80	sccs
Shaft Primary Static Seal	0.0059	sccs
Discharge Static Seal	0.0182	sccs

No leakage was detected at the other seals.

Disassembly of the valve revealed the following:

1. A glycol base oil was found on the inlet surface of the disk (figure 260). The same type oil was subsequently found in a line used for the valve pressure check just prior to teardown.
2. The disk seal was in good condition. The Teflon primer was worn through in two local areas of the seal surface. These conditions are shown in figures 261 and 262.
3. The shaft disk had minor seal surface scratches, and figure 263 shows a typical disk seal surface condition.
4. All other parts were in excellent condition as shown in figure 264.

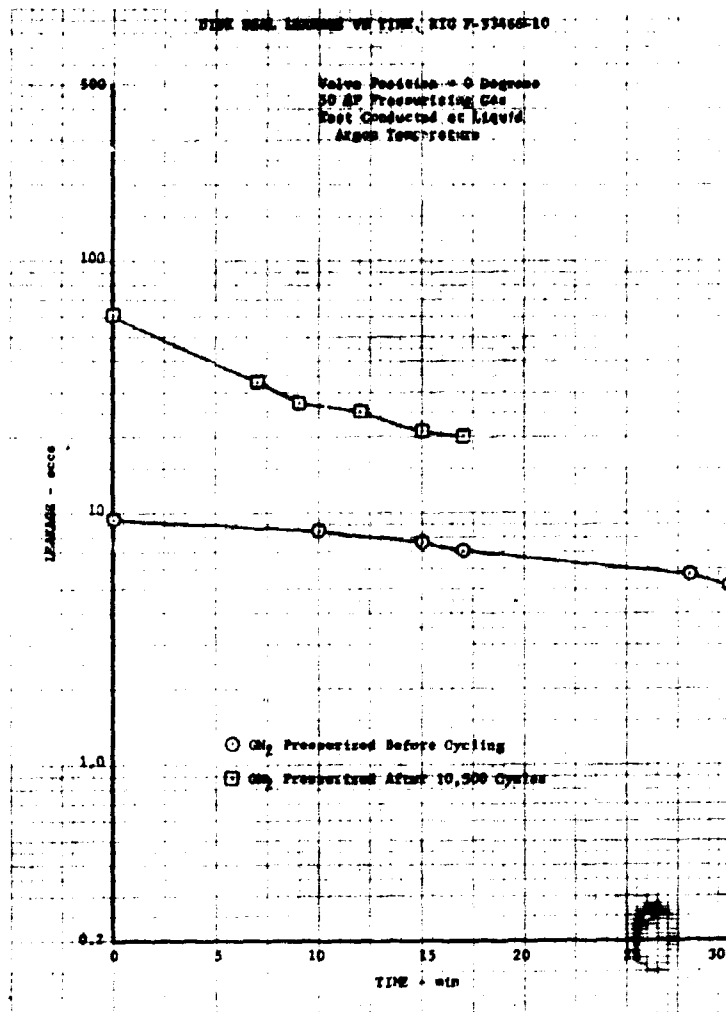


Figure 256. Strap-Actuated Disk Seal Leakage vs Time, Rig F-33466-10

DF 64959

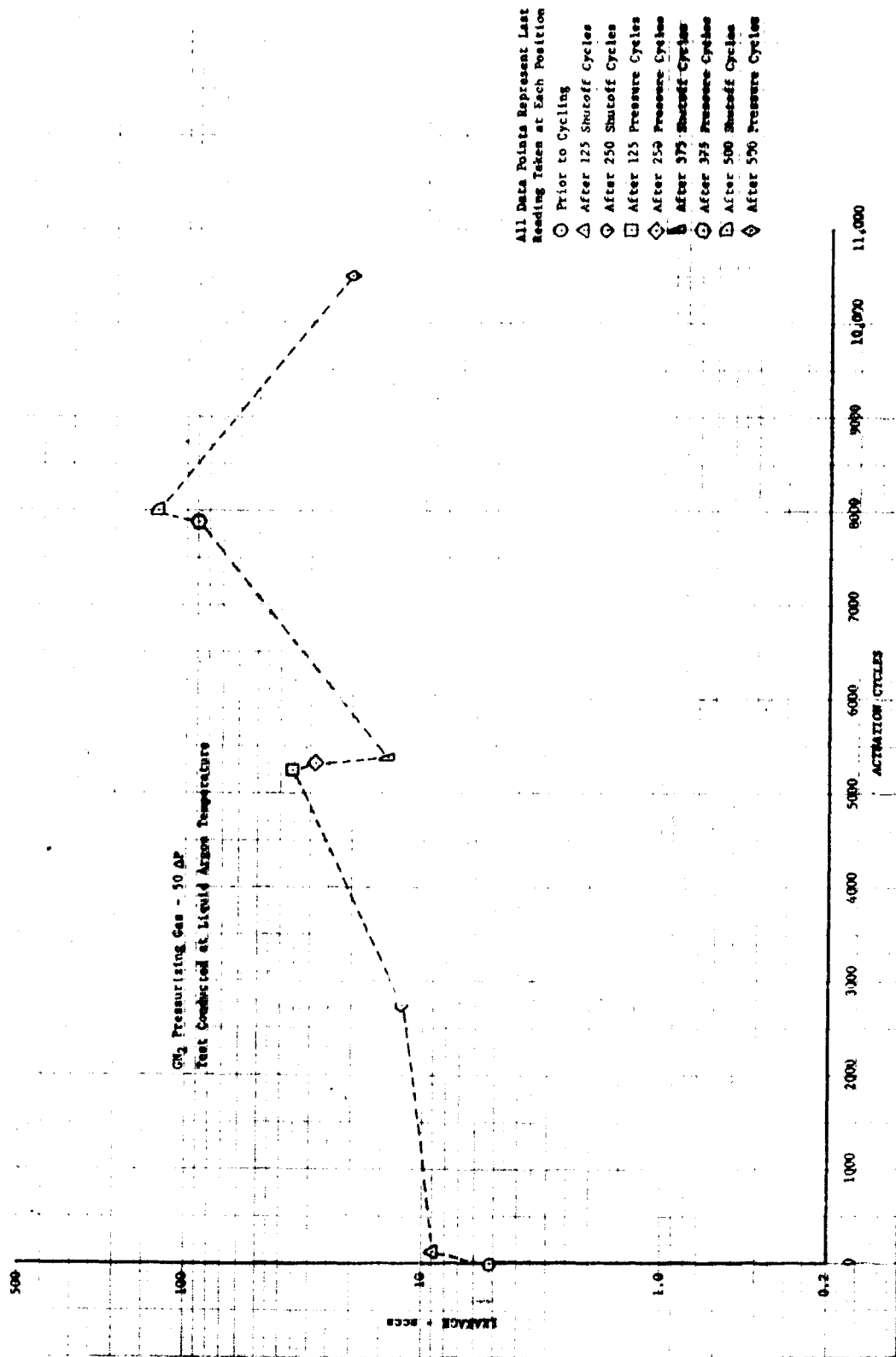


Figure 257. Strap-Actuated Disk Seal Leakage vs Actuation Cycles, Rig F-33466-20 DF 64960

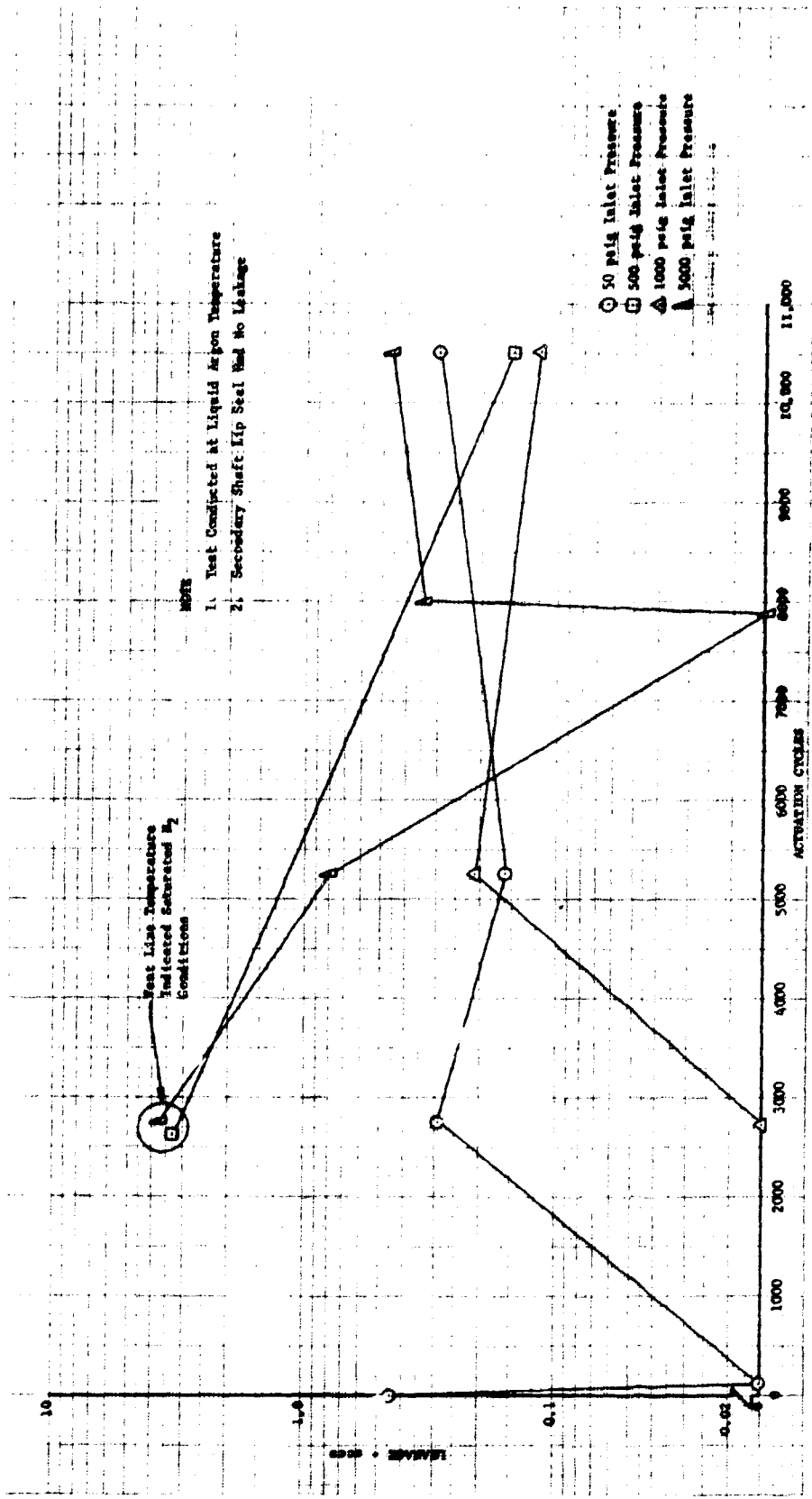
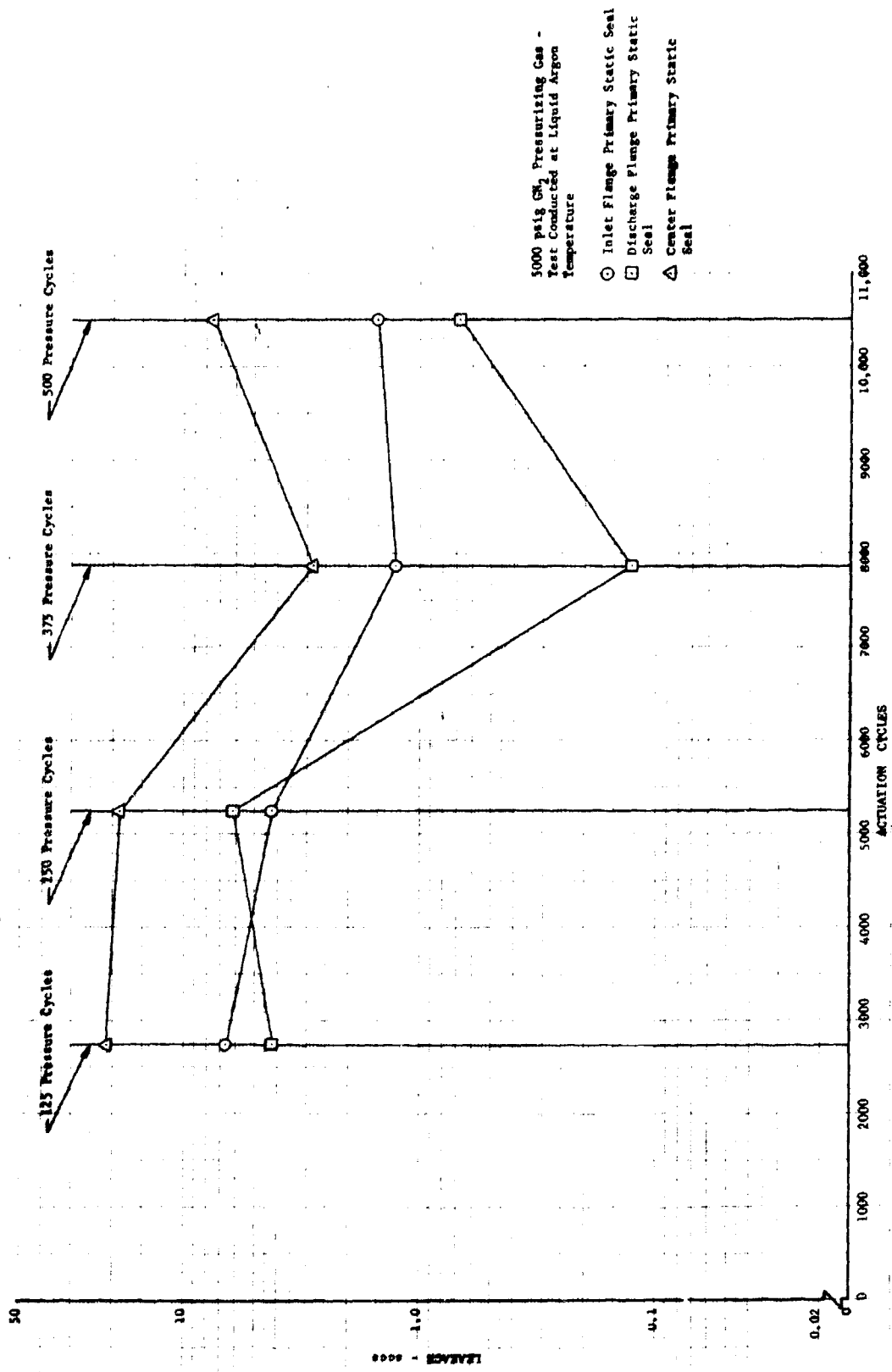


Figure 258. Primary Shaft Lip Seal Leakage vs Actuation Cycles, Rig F-33466-10 DF 64961



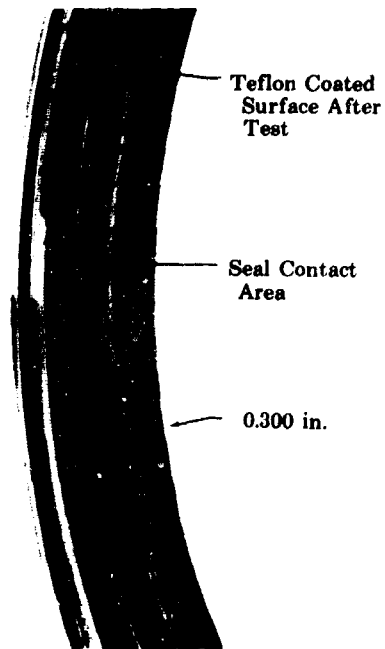
DF 64962

Figure 259. Static Seal Leakages vs Actuation Cycles, Rig F-33466-10



Figure 260. Glycol Contamination on Inlet Side of Disk, Rig F-33466-10 (Disk is 2.990 in. in Diameter)

FE 77843



FE 77845

Figure 261. Shutoff Seal After Endurance Test, Rig F-33466-10

FD 24853

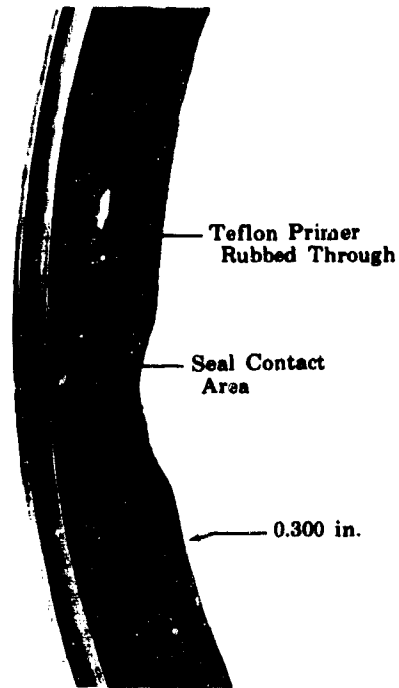


Figure 262. Shutoff Seal After Endurance Test,
Rig F-33466-10

FD 24854



Figure 263. Disk Seal Surface After Endurance Test,
Rig F-33466-10

FD 24856

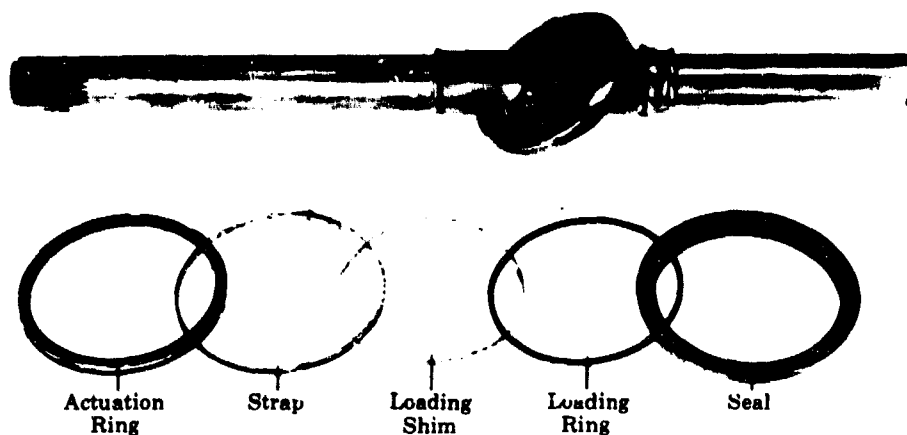


Figure 264. Strap Actuated Disk Seal, Rig F-33466-10 FD 24855

(4) Valve F-35106 - Build No. 7

Main chamber oxidizer valve F-35106-7 incorporated the following sealing configurations:

1. A Kel-F disk seal element contracted against the disk surface by a cam-actuated tapered slip ring (figure 265).
2. A spherical chrome plated Inconel 718 (AMS 5663) disk seal surface with a 9.5 microinch finish. The cam actuation lug was electron-beam welded to the shaft.
3. A trapped 0.020 in. thick laminated Kapton F primary inlet flange static seal.
4. The center flange static seal was an Inconel X (AMS 5667) inverted U-ring static seal assembly that loaded a portion of the Kel-F seal element against the inlet housing and a 0.020 in. laminated Kapton-F seal against the discharge housing.
5. The discharge flange static seal was a Teflon coated, omega-shaped design that incorporated an assembly preload spacer and is pressure energized to follow flange deflections during operation.
6. The bearing cap static seal was 0.010 in. thick laminated Kapton-F formed around the outside diameter of a ring.

The valve was mounted in the B-22 test stand for an environmental endurance and leakage test, 10,000 partial stroke actuation cycles, 500 shutoff cycles, and 260 pressure cycles were completed. The test was conducted with the valve submerged in liquid argon.

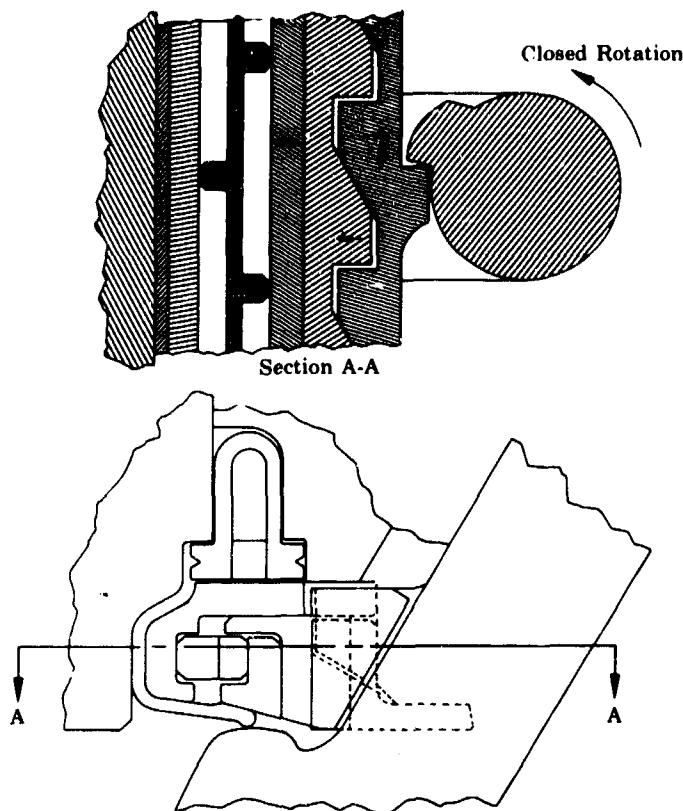


Figure 265. Cam-Actuated Shutoff Seal,
Rig F-35106-7

FD 24991

The disk seal leakage measurements varied with time as shown in figure 266. The values shown in figure 267 are the final readings taken at each set point. The disk seal leakage prior to pressure cycling was less than 0.025 sccs. The seal failed during either pressure or actuation cycling after 125 shutoff cycles and 2500 actuation cycles had been completed satisfactorily.

The test stand supply valve actuator failed after 250 pressure cycles so the remainder of the programmed 500 pressure cycles was not performed. The discharge flange primary static seal leaked excessively above 1000 psig. Primary shaft seal leakage is shown in figure 268 and static seal leakages are shown in figure 269.

Visual inspection of the disk seal prior to disassembly revealed failure of the Kel-F seal element. Pieces of the seal were found in both the inlet and the discharge housings. The seal condition after the test is shown in figure 270. Failure of the seal element at the edge of the shaft cutout, as shown in figure 271, appears to have been caused by either a reverse differential pressure across the seal or seal drag during valve opening after the pressure cycles. The possibility of excessive reverse pressurization during pressure cycling existed because of valve inlet and discharge cavity pressurizing line volume differences. The shaft disk sealing surface is shown in figure 272.

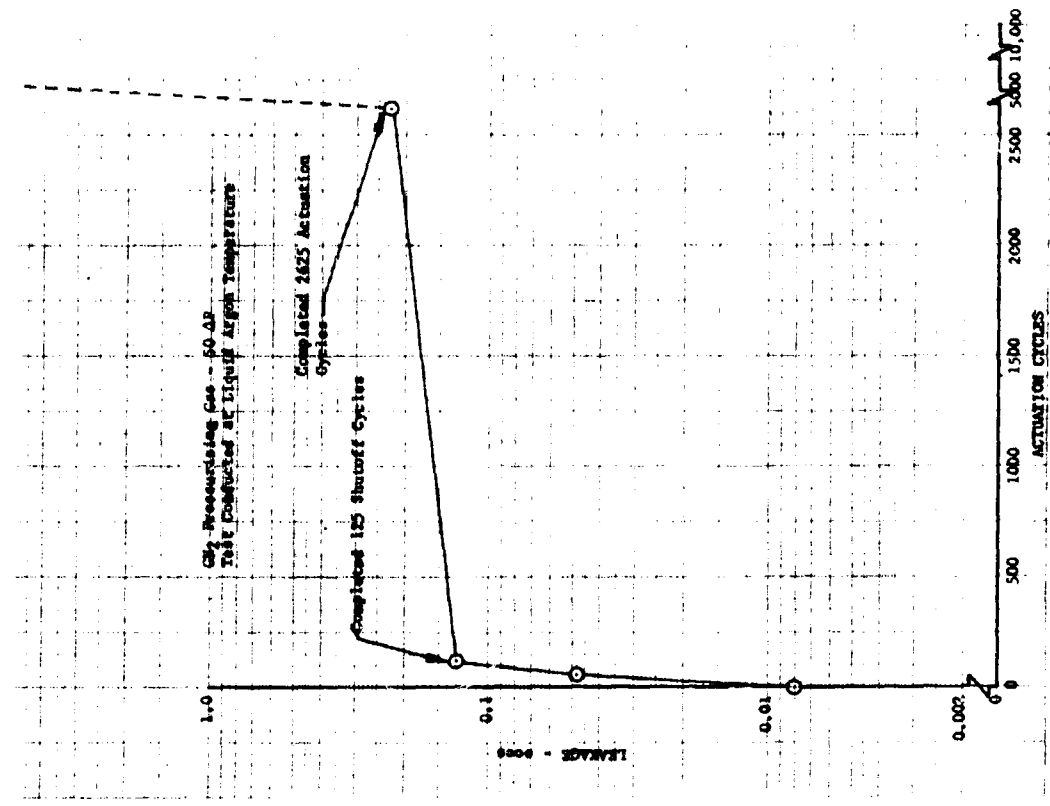


Figure 267. Cam-Actuated Disk Seal Leakage vs Time, Rig F-35106-7 DF 65227

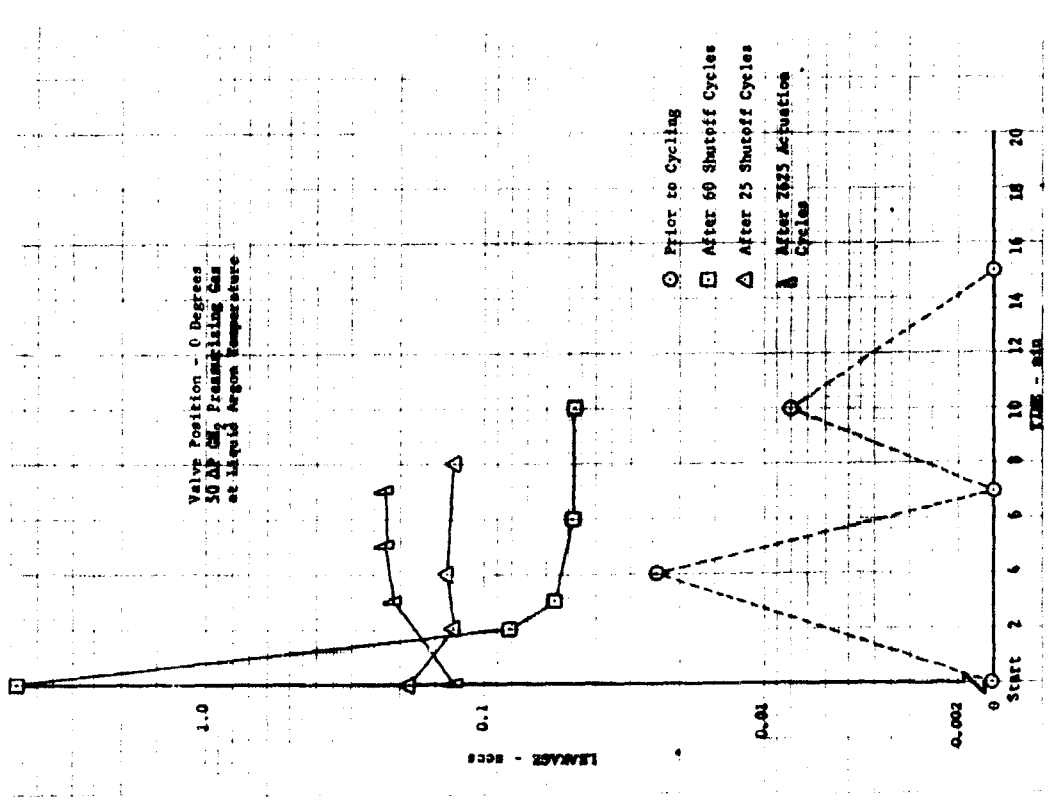


Figure 266. Cam-Actuated Disk Seal Leakage vs Time, Rig F-35106-7 DF 65226

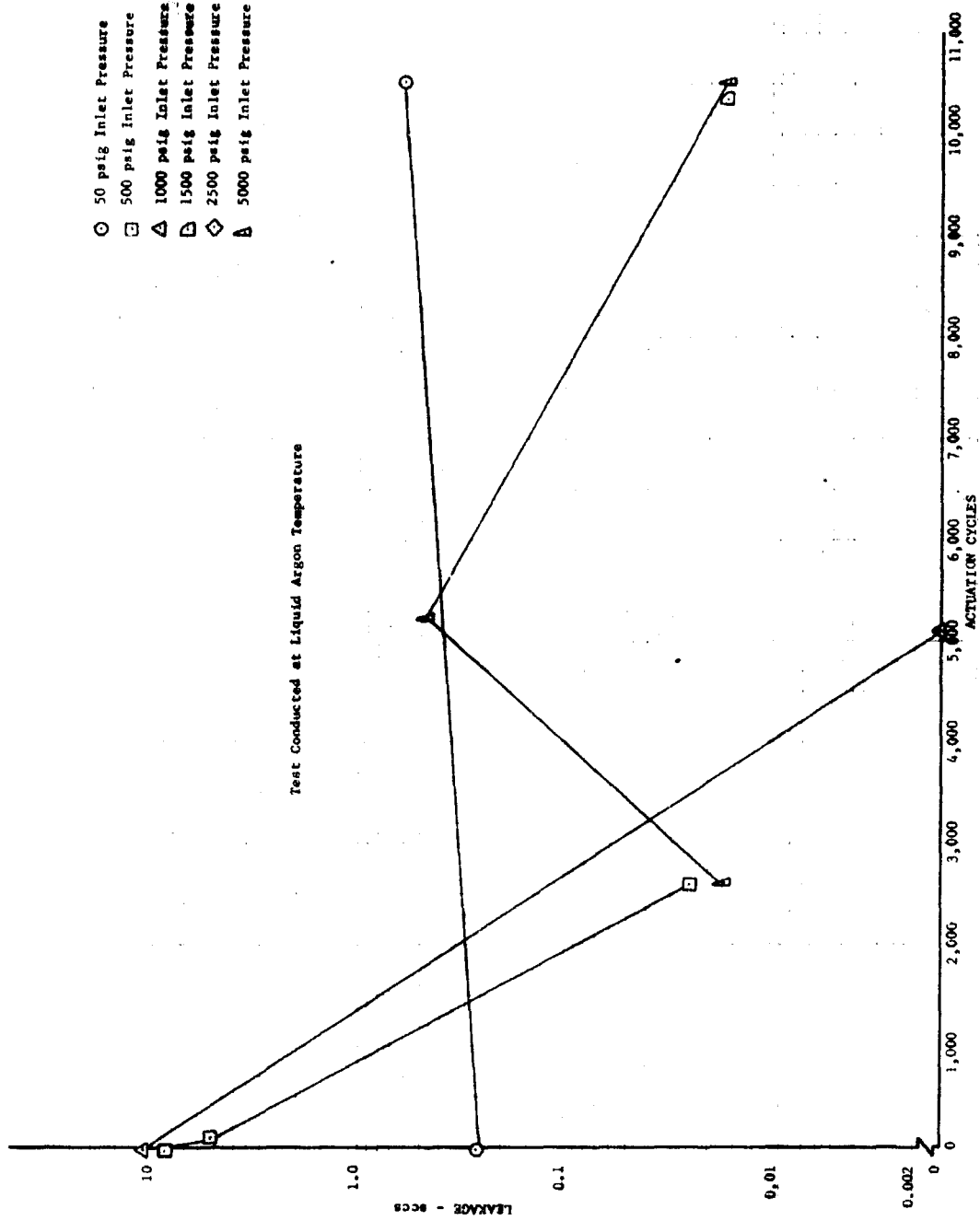


Figure 268. Primary Shaft Lip Seal Leakage vs Actuation Cycles, Rig F35106-7

DF 65228

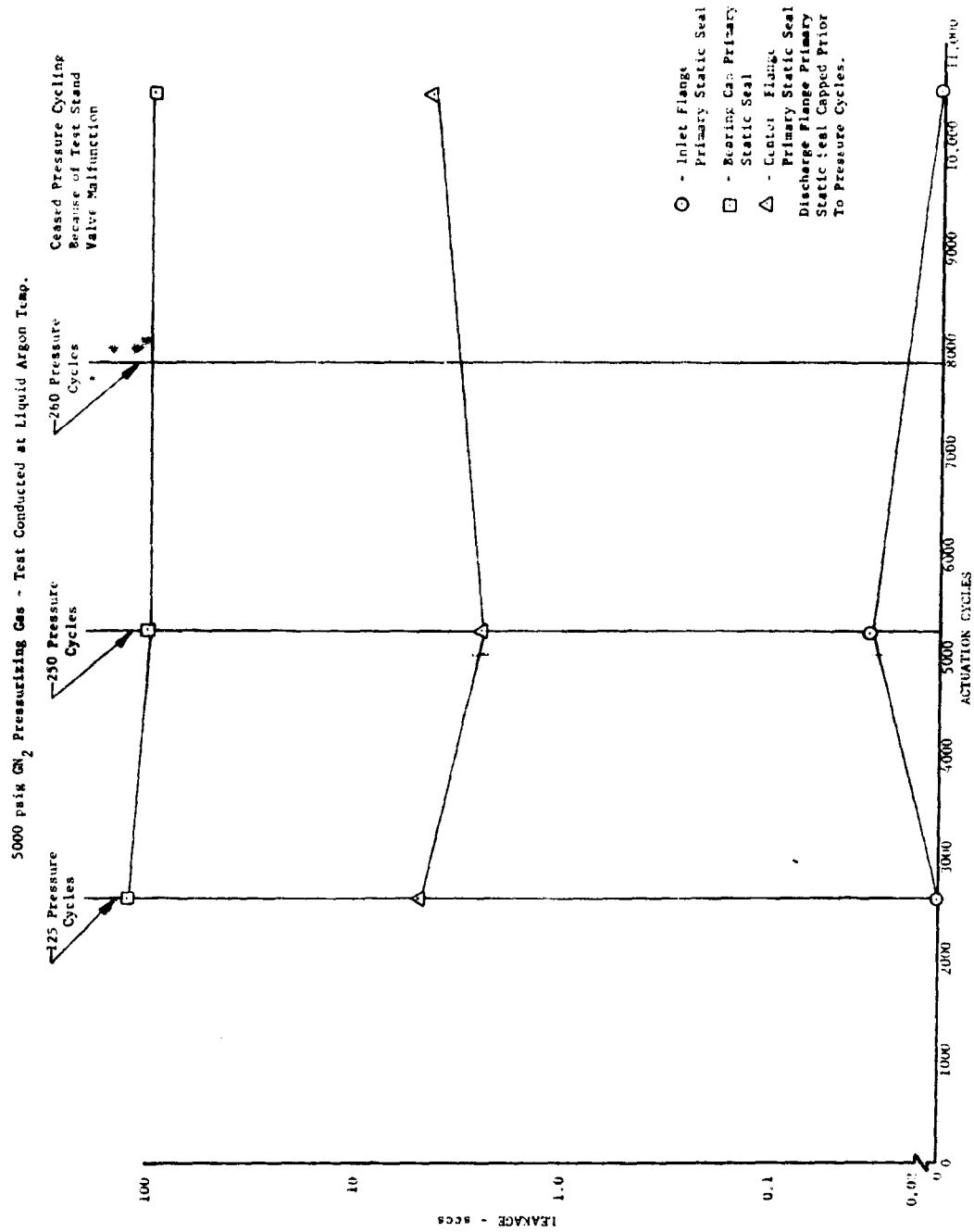


Figure 269. Static Seal Leakage vs Actuation Cycles, Rig F-35106-7

DF 65229



Figure 270. Disk Seal After Test, Rig F-35106-7

FE 78243

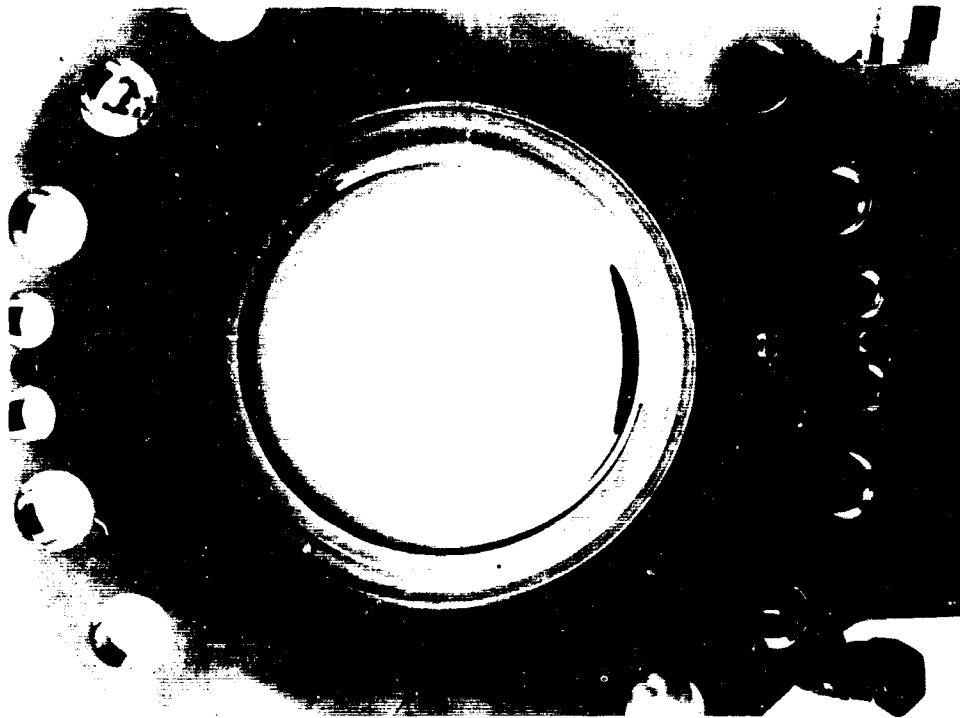


Figure 271. Area of Seal Element Failure

FE 78241



Figure 272. Shaft Disk Sealing Surface After Test, FE 78242
Rig F-35106-7

The discharge static seal, which had been used in several test series without recoating the seal surface prior to this build, had insufficient contact load. All other parts were in excellent condition.

2. Preburner Oxidizer Valve
 - a. Introduction

During testing of the sleeve-type preburner oxidizer valve during Phase I (Contract AF04(611)-11401), it was found that the wear characteristics of the BeCu piston rings on the chrome coated main housing were not acceptable. The objective, therefore, of this subtask was to investigate improved surface coatings and a pressure balanced piston ring design.

A series of tests was conducted to obtain an improved surface coating and a piston ring pressure balance study was made.

Four cyclic endurance tests were made to evaluate the design changes on the wear characteristics of the piston rings operating at high differential pressures.

b. Summary, Conclusions, and Recommendations

The wear results on all four configurations tested demonstrated acceptable wear characteristics. The piston ring leakage on all four tests was also acceptable. A variation in leakage observed between the tests was primarily because of variations in the fit between the piston ring and housing. Strain gages were installed on the secondary sleeve and actuator shaft on Rigs F-33458-7 and -8 to determine actuator loads for balanced and unbalanced piston rings.

As a result of the test program the following conclusions and recommendations have been made:

1. Precision chrome coating has been selected for the preburner oxidizer valve application because the plating techniques are sufficiently developed. The application of molybdenum-chromium will require further coordination with an outside vendor or in-house plating shop to produce consistent results. Further development of molybdenum-chromium is recommended for extremely high load applications where the wear characteristics of precision chrome are not acceptable.
2. The balanced piston rings provided acceptable wear characteristics and a reduction in actuation force as compared to the unbalanced rings; however, further force reduction is desirable to minimize actuator power requirements.

c. Electrolytic Coating Investigation

After it was discovered that the wear characteristics of the BeCu piston rings on the chrome-coated main housing were not acceptable, a program was initiated to develop and evaluate a wear resistant electrolytic coating that would be superior under high loading stress at cryogenic temperatures. A chromium-molybdenum alloy was considered the chief candidate because reports had been made that small amounts of molybdenum in chromium produce improvements in wear resistance. Several preliminary tests were conducted to compare adhesion quality, abrasive wear, surface characteristics, and corrosion resistance of normal chrome plate to a chromium-molybdenum alloy. When these tests were completed, force-wear tests were conducted on all candidates to determine the best wear resistant coating. The following paragraphs generally outline the test procedures that were followed.

(1) Preliminary Tests

Several stainless steel (ASM 5646) panels (about 3 in. x 3 in. x 0.25 in.) were plated on one side with chromium or chromium-molybdenum alloy. The chromium-molybdenum alloy was electrolytically deposited from a chromic acid bath into which about 3 oz of molybdenum per gallon of solution had been anodically dissolved. The composition of each panel was analyzed to determine the percentage of molybdenum in each deposit. It was found that the amount of molybdenum in the deposits varied with plating conditions. Plating at 1.5 amperes per square inch and 110 to 130° F yielded deposits containing about 1% molybdenum.

Adhesion tests were then made. Holes (0.27 in. diameter) were drilled from the unplated side to within 0.06 in. of the plated surface. A steel rod

(0.25 in. diameter) was then inserted in the hole and pressure was applied until the rod was forced through the plating. An examination was made of the break area to find indications of adhesion quality. Comparing the results (figure 273) revealed that the chromium-molybdenum alloy plate has the same adhesion to stainless steel (AMS 5646) as regular chrome plate. Examination of low power magnifications of the pressed out portions revealed that the crack pattern on the alloy plated surface was finer and not as severe as on the regular chromium plated surface indicating that the alloy plate was softer than the chromium plate.

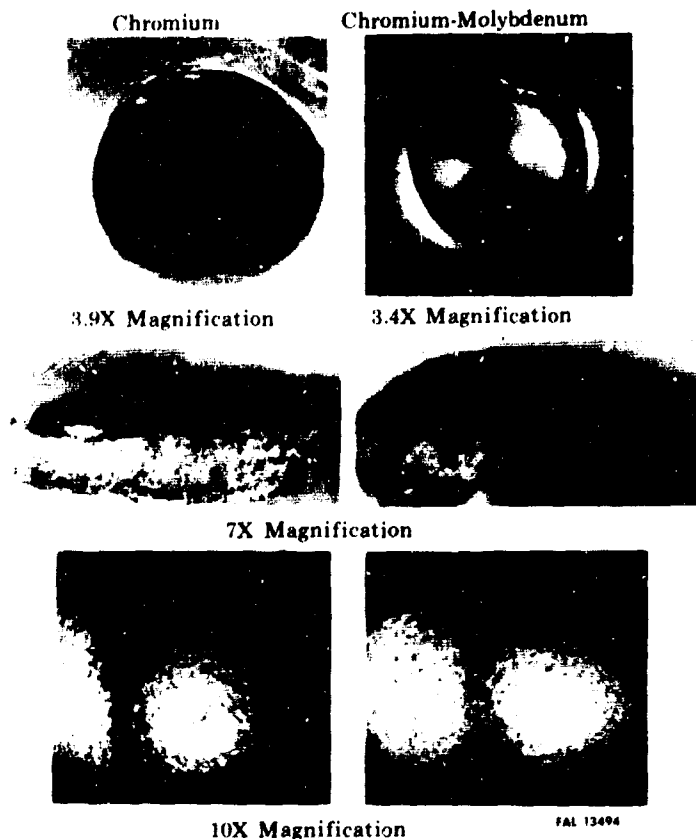


Figure 273. Adhesion Tests of Chromium and Chromium-Molybdenum Plating on Stainless Steel (AMS 5646)

FD 25271A

Abrasive wear tests were then made of chromium and chromium-molybdenum alloy deposits. A Taber Abraser Model 174 with a CS-10 Callbrase Wheel was used to make these tests. The test results, which indicate the alloy has about six times the abrasive wear resistance of chromium, are shown in table XXVII. Previous tests of the alloy in an amsler machine showed an improvement of six to eight times over chromium plate.

Table XXVII. Taber Abraser Wear Testing of Chromium and Chromium-Molybdenum Alloy Electroplate

Cycles to First Indication of Failure	
Chromium	Chromium-Molybdenum
4000	23,000
3000	19,000
4000	31,000

Surface characteristics of both the chromium plate and the chromium-molybdenum plate were then compared. Figure 274 shows magnified views of stainless steel (AMS 5646) surfaces after plating with both materials. The characteristic heavy crack pattern noted on conventional chrome is reduced substantially on the alloy.

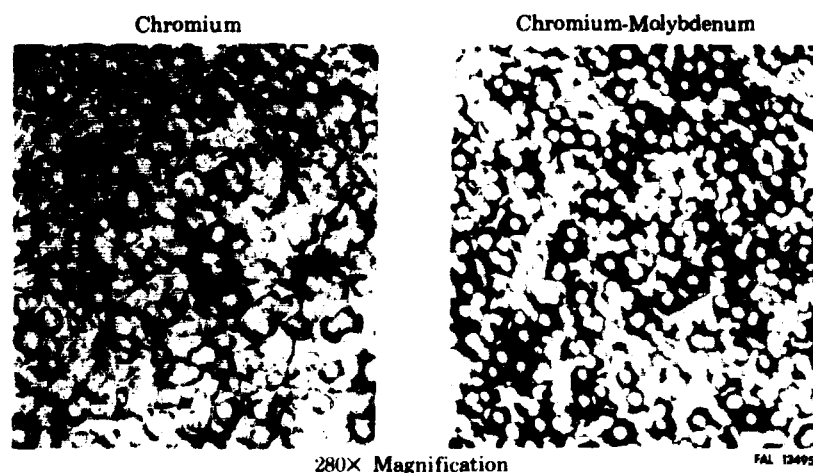


Figure 274. Surface Characteristics of Chromium and Chromium-Molybdenum Plating on Stainless Steel (AMS 5646) FD 25272A

When the plating is conducted in a bath using ultrasonic energy, the differences are more pronounced. By comparing the regular chromium and chromium-molybdenum plates shown in figure 274 with their counterparts from a bath using ultrasonic energy shown in figure 275, ultrasonic plating results in: (1) a reduction in number and size of surface cracks on the chromium plate, (2) elimination of cracks on the alloy plate, and (3) a finer texture, especially for the alloy. These results suggest that plating in a bath using ultrasonic energy will result in denser deposits with corresponding better wear and corrosion characteristics.

Corrosion resistance tests were then made with stainless steel (ASM 5646) panels plated with 0.001 in. of either chromium or chromium-molybdenum alloy. These samples were placed in a salt spray test chamber for 250 hours. As shown in figure 276, rust spots were evident on the surface of the chromium plate but no indications of corrosion were noted on the alloy.

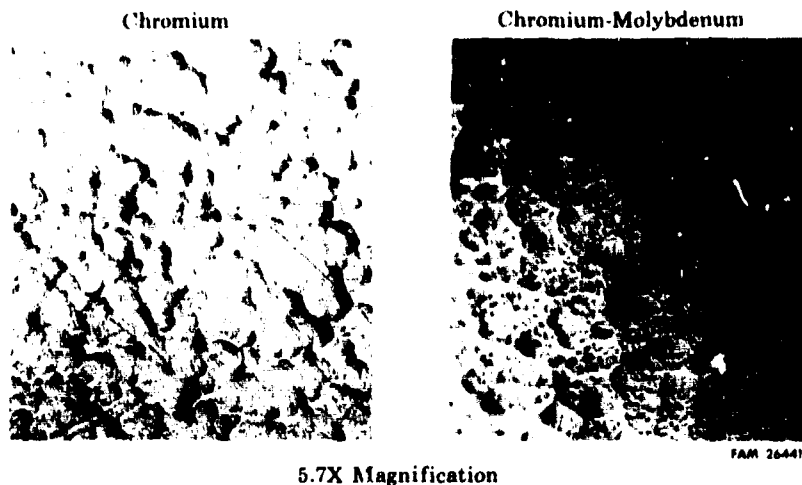


Figure 275. Surface Characteristic of Chromium and Chromium-Molybdenum Ultrasonic Plating on Stainless Steel (AMS 5646) FD 25273A

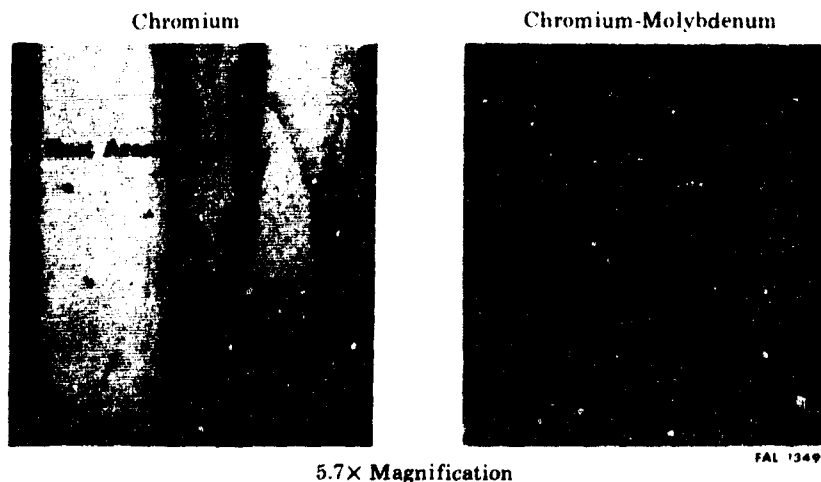
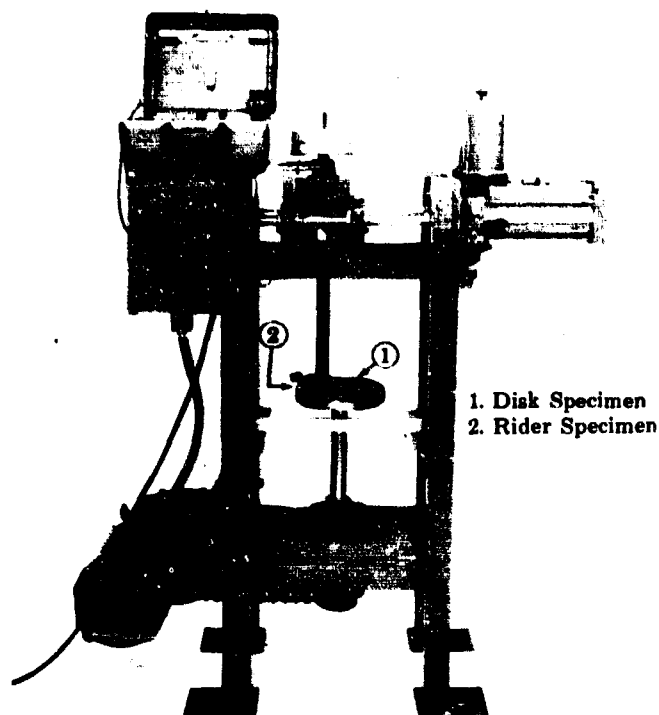


Figure 276. Chromium and Chromium-Molybdenum Plated Surfaces After 250 Hours of Salt Spray Testing FD 25274A

The results of these preliminary tests clearly indicate that a chromium-molybdenum alloy electrodeposit is generally superior to a conventional chromium electrodeposit. Ultrasonic agitation used with the chromium-molybdenum alloy plating appears to have merit in that the deposits appear to be free of cracks, denser, and more wear resistant.

(2) Force-Wear Tests

Force-wear tests were required to screen the candidates for the preburner oxidizer valve. The Materials Development Laboratory (MDL) coefficient of friction machine, shown in figure 277, was adapted to enable the disk and rider specimens to be immersed in liquid nitrogen.



FAC 9305

Figure 277. Coefficient of Friction Machine

FD 25275

The disk and rider specimens were secured to the power shaft and transfer shaft, respectively, of the friction machine and were immersed in liquid nitrogen. The start of each test was delayed until nitrogen boil-off was minimal. A normal load of 97 lb was then applied to the rider specimen and the disk was rotated at a surface speed of 6 in./sec as adjusted with the variable speed drive. Dynamic friction force curves were obtained for each rider-disk combination at various points during the 250 cycle test runs. Friction force curves were used to obtain sliding friction coefficient data. Coefficients of friction were calculated by dividing the friction force (lb) by the dead weight normal load (lb).

From the test program, summarized in table XXVIII, the following conclusions were drawn.

1. Both the chrome (0.001 in. thick) and the molychrome (0.0015 in. thick) plated disks running against uncoated Berylco 25 (AMS 4650) rider specimens produced acceptable wear characteristics.
2. The wear of the chrome plated surface was characterized by light scratches while the wear of the molychrome surface was characterized by a slight depression in the plated surface.

3. No appreciable benefit in wear characteristics or reduction in coefficient of friction was noted during testing of the various lubrication coatings. A comparison of the wear characteristics of the baseline configuration (0.0001 in. thick chrome) as compared to the 0.001 in. thick chrome and the 0.0015 in. thick molychrome surfaces is shown in figures 278, 279, and 280.

d. Piston Ring Pressure Balance Study

(1) General

During Phase I (Contract AF04(611)-11401) cryogenic endurance testing of the preburner oxidizer valve, it was found that the lower piston ring wore through the chrome coating of the main housing. An analysis of the pressure loading effects of piston rings was made to determine if a piston ring redesign to balance the loading would improve the wear characteristics. The analysis was based on a procedure outlined in Engineers Piston Ring Handbook, Koppers Co., Inc., which states that for a unit cross section of the ring, the axial force per circumferential inch (F_A) and the radial force (F_R) can be determined from the pressure distribution around the sealing surfaces. An illustration of this is shown in figure 281. The determination of F_R includes the static friction effects from the axial sealing surface. A coefficient of friction for Berylco 25 (AMS 4650) on either steel alloy (AMS 5735) or chrome plate in the presence of liquid oxygen was assumed to be 0.25. A ratio of F_A/F_R of less than 3.0 is desirable to ensure that the piston ring will not bind on the axial sealing surface.

(2) Analysis Summary

(a) As Designed Upper Piston Ring

For a given pressure differential ($P_H - P_L$), the upper seal is loaded radially at the following rate:

$$F_R = 0.065 (P_H - P_L) \text{ lb/in. circumference.}$$

At a pressure differential of 1000 psi, the radial loading of the upper seal is:

$$F_R = 0.065 (1000) \text{ lb/in. circumference,}$$

$$F_R = 65 \text{ lb/in. circumference,}$$

or, unit pressure, $UP = 620$ psi.

The upper piston ring demonstrated acceptable wear characteristics during previous testing at a pressure differential of up to 1000 psi. Therefore, a radial unit pressure of 620 psi and $F_R = 65$ lb/in. circumference, were used as design criteria. This seal to housing loading was assumed to be satisfactory providing the valve housing is chrome plated to 0.001 in. maximum thickness to approach the hardness of the valve sleeve.

Table XXVIII. Force Wear Tests

Test No.	Disk Material	Disk Plating and Thickness	Rider Material	Rider Coating	Dynamic Friction Coefficient	Wear Track Description	Material Combination Rating
1	Stainless Steel (AMS 5646)	PWA 48 chrome (0.0001 in. thick)	Berylco 25 (AMS 4650)	No coating	0.23-0.45	Scratches, light BeCu deposits	Fair
2	Stainless Steel (AMS 5646)	PWA 48 chrome (0.0010 in. thick)	Berylco 25 (AMS 4650)	No coating	0.23-0.44	Slight scratches	Good
3	Stainless Steel (AMS 5735)	PWA 48 chrome (0.0010 in. thick)	Berylco 25 (AMS 4650)	No coating	0.26-0.48	BeCu deposits	Fair
4	Stainless Steel (AMS 5646)	Molychrome (0.0015 in. thick)	Berylco 25 (AMS 4650)	No coating	0.20-0.34	Slight surface depression	Good
5	Stainless Steel (AMS 5646)	Nickel-Tin (0.0015 in. thick)	Berylco 25 (AMS 4650)	No coating	0.26-0.52	Heavy wear	Poor
6	Stainless Steel (AMS 5646)	PWA 48 chrome (0.0010 in. thick)	Berylco 25 (AMS 4650)	Microseal 100-1 Graphite	0.34-0.52	Scratches, heavy BeCu deposits	Poor
7	Stainless Steel (AMS 5646)	PWA 48 chrome (0.0010 in. thick)	Berylco 25 (AMS 4650)	Microseal 200-1 Molydi-sulphide	0.34-0.46	Light scratches, light BeCu deposits	Good
8	Stainless Steel (AMS 5646)	PWA 48 chrome (0.0010 in. thick)	Berylco 25 (AMS 4650)	PWA 566 (0.0010 in. - 0.0012 in. thick)	0.25-0.43	Scratches, light BeCu deposits	Fair
9	Stainless Steel (AMS 5646)	PWA 48 chrome (0.0010 in. thick)	Berylco 25 (AMS 4650)	Alpha Molykote Molydisulphide	0.29-0.52	Scratches, BeCu deposits	Poor
10	Stainless Steel (AMS 5646)	Molychrome (0.0015 in. thick)	Berylco 25 (AMS 4650)	Microseal 100-1 graphite	0.22-0.40	Slight depression - light BeCu deposits	Fair

Table XXVIII. Force Wear Tests (Concluded)

Test No.	Disk Material	Disk Plating and Thickness	Rider Material	Rider Coating	Dynamic Friction Coefficient	Wear Track Description	Material Combination Rating
11	Stainless Steel (AMS 5646)	Molychrome (0.0015 in. thick)	Berylco 25 (AMS 4650)	Microseal 200-1 Molydi-sulphide	0.31-0.52	Slight depression - heavy BeCu deposits	Poor
12	Stainless Steel (AMS 5646)	Molychrome (0.0015 in. thick)	Berylco 25 (AMS 4650)	PWA 566 (0.0010 in. - 0.0012 in. thick)	0.20-0.34	Slight depression	Good
13	Stainless Steel (AMS 5646)	Molychrome (0.0015 in. thick)	Berylco 25 (AMS 4650)	Alpha Molykote Molydisulphide	0.23-0.46	Slight depression - heavy BeCu deposits	Poor



Stainless Steel (AMS 5646) Disk With 0.0001-Inch Thick Chrome Plate (PWA 48) FE 75553

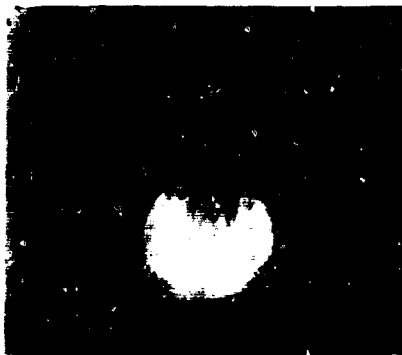


Berylco 25 (AMS 4650) Rider FE 74349

Figure 278. Wear Characteristics of 0.0001 in. Thick Chrome Plate (PWA 48) FD 25590A



AMS-5646 Disk With 0.001-Inch Thick PWA 48 Chrome Plate FE 75557



AMS-4650 Rider FE 75303

Figure 279. Wear Characteristics of 0.001 in. Thick Chrome Plate (PWA 48) FD 25591A



AMS-5646 Disk With 0.001-Inch Thick FE 75359
Chromium-Molybdenum Plate



AMS-4650 Rider FE 75395

Figure 280. Wear Characteristics of 0.001 in. Thick FD 25592A
Chromium-Molybdenum

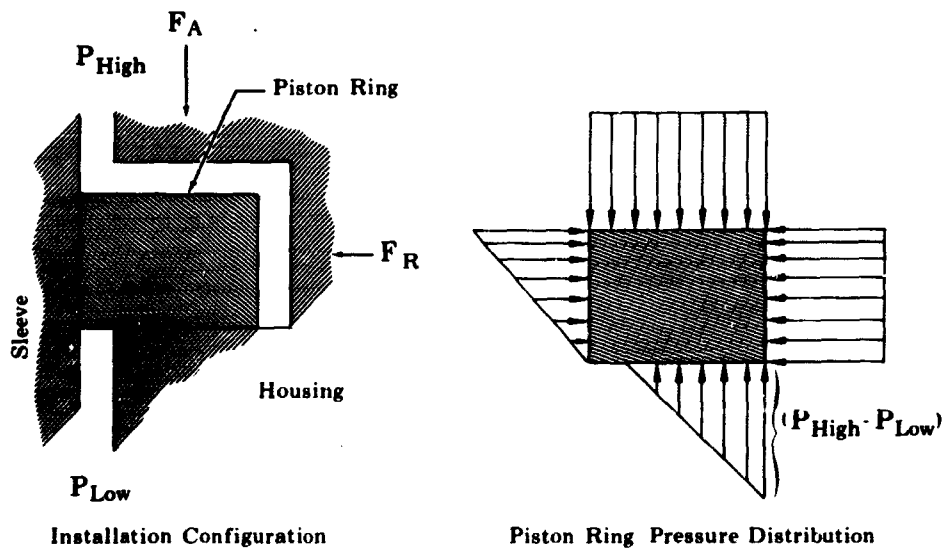


Figure 281. Piston Ring Installation Configuration FD 25267
and Pressure Distribution

(b) Reworked Upper Piston Ring

The rework configuration of the upper seal recommended for the wear rig tests at pressure differentials of up to 2000 psi is shown in figure 282. The radial and axial loading conditions of the design are:

$$F_R = 0.032 (P_H - P_L)$$
$$F_A = 0.077 (P_H - P_L)$$
$$F_A/F_R = 2.4$$
$$UP = \frac{0.32 (P_H - P_L)}{0.87}$$

Therefore, for a pressure differential of 2000 psi:

$$F_R = 64 \text{ lb/in.}$$

$$UP = 736 \text{ psi}$$

This unit pressure exceeds the maximum design criteria of 620 psi, but represents the minimum value obtainable using existing hardware, without reducing the sealing land below a minimum of 0.035 in.

(c) Reworked Lower Piston Ring

The rework configuration of the lower seal recommended for the wear rig tests at pressure differentials of up to 2000 psi is represented by figure 282. The radial and axial loading conditions of this design for complete seal to housing contact are:

$$F_R = 0.039 (P_H - P_L)$$
$$F_A = 0.090 (P_H - P_L)$$
$$F_A/F_R = 2.3$$
$$UP = \frac{0.039 (P_H - P_L)}{0.147}$$

Therefore, for a pressure differential at 2000 psi:

$$F_R = 78 \text{ lb/in.}$$

$$UP = 530 \text{ psi}$$

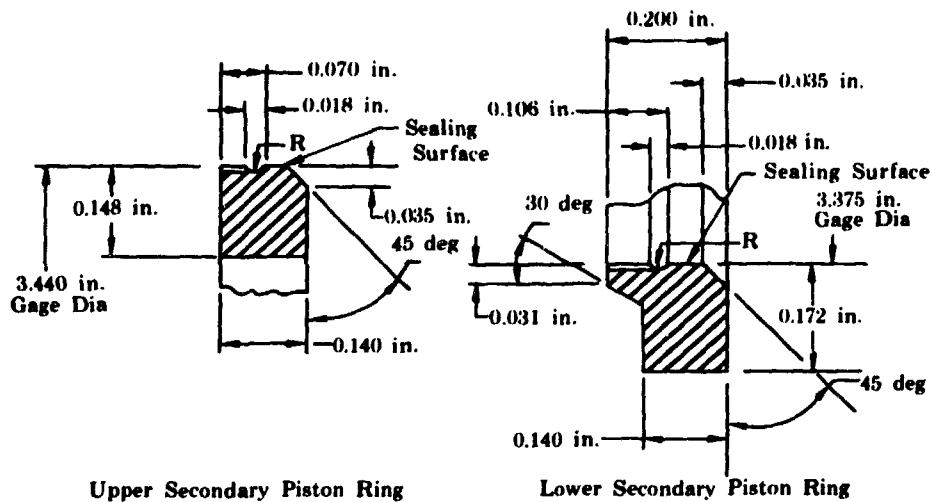


Figure 282. Pressure Balance Piston Ring

FD 24097

e. Cryogenic Testing

(1) Test Procedures

The preburner oxidizer valve rig illustrated in figure 283 was used to evaluate the housing coatings and redesigned piston rings. Tests were conducted on the B-22 test stand, which is shown in figure 284. The test procedures were similar for all four tests except that for Rigs F-33458-7 and -8 additional procedures were required to determine actuation force from the specially installed strain gages.

Piston ring leakage was measured from the secondary discharge valve through the heat exchanger with the primary discharge valve closed. The rig was cold soaked with LN₂ until the dome temperature was less than 180°R. With the rig cold, the primary discharge valve closed, and the secondary discharge valve opened, the rig was cycled with a sine wave input of 3 to 6 cps. The cooldown procedures were repeated before each cycle set. The cycles per set, stroke range, secondary differential pressure and valve position for repeating piston ring leakage were recorded as shown in table XXIX.

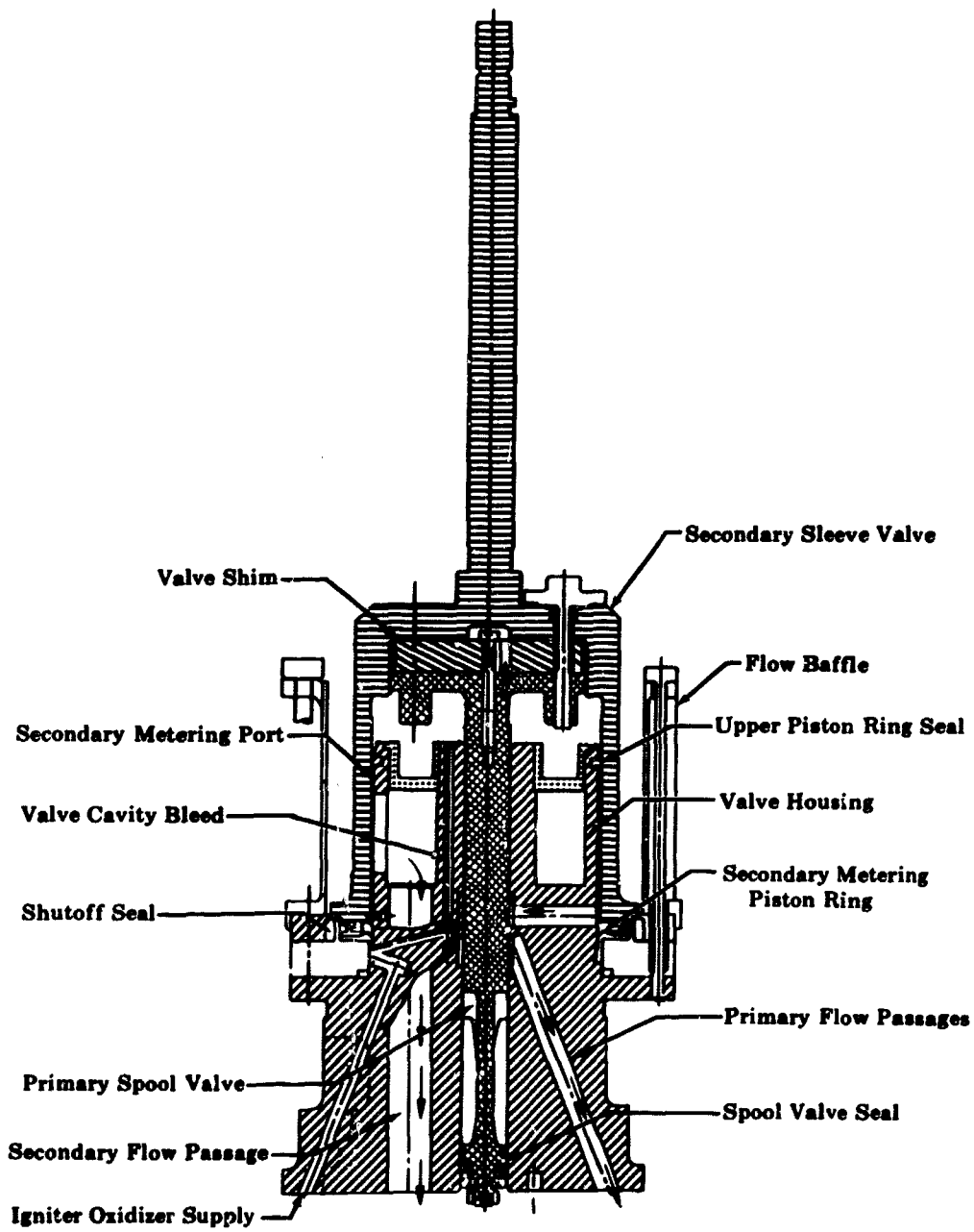


Figure 283. Preburner Oxidizer Valve Rig

FD 18909D

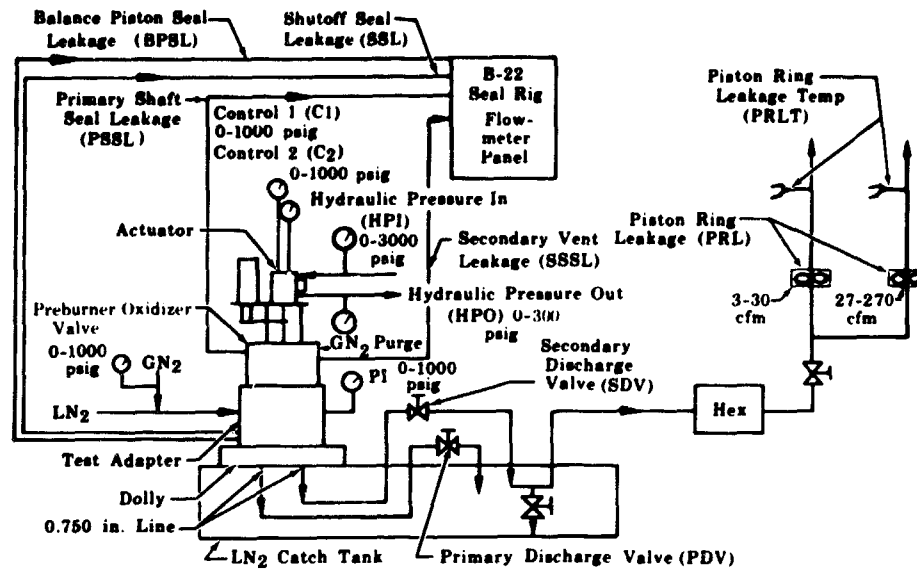


Figure 284. Schematic of Preburner Oxidizer Valve Rig Test Stand Installation

FD 22151B

Table XXIX. Data Recorded During Tests

Cycle Set	Cycles	Stroke Range (in.)	Secondary ΔP	Valve* Position
A	3334	0.470 \pm 0.050	1000	0.470
B	3334	0.580 \pm 0.050	1500	0.580
C	3334	0.690 \pm 0.050	2000	0.690

*The valve positions for Rig F-33469-7B were 0.450 with ΔP of 1000 psig, 0.600 with ΔP of 2000 psig, and 0.750 with ΔP of 1500 psig. These points were set because the primary port location did not allow a position below approximately 0.400 in. valve stroke and because the secondary port gave a maximum approximate valve position of 0.750 in. where the ports were uncovered thus providing a leakage path and the required piston ring ΔP was unattainable.

(2) Cyclic Endurance Tests

(a) Rig F-33469-7B

Rig F-33469-7B had chrome coatings applied to the valve housing and the sleeve, and had the lower and upper piston ring pressure balanced. The valve housing had a 0.001 in. thick precision chrome coating that did not require subsequent machining. The sleeve had a 0.001 to 0.0015 in. thick chrome coating (per AMS 2406) that required machining to the final dimensions. The

lower piston ring was pressure balanced to provide a unit bearing load of 500 psi at 2000 psid. The upper piston ring was pressure balanced to provide a unit bearing load of 736 psi at 2000 psid. Figure 282 shows both piston rings as they were after balancing. The valve was cycled a total of 10,000 cycles and the piston ring leakages are shown in figure 285.

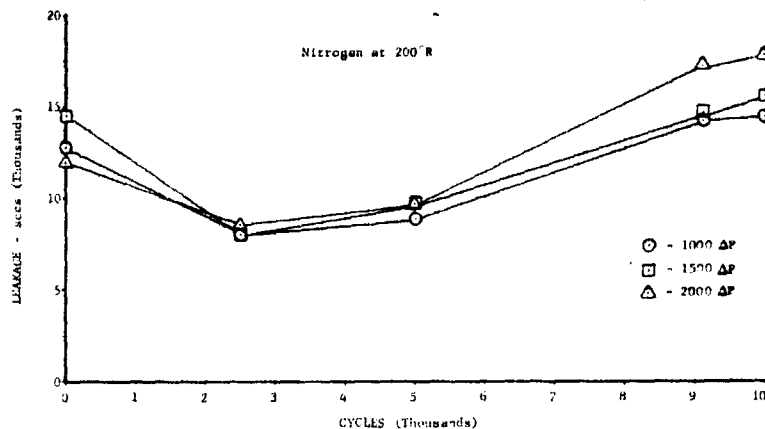


Figure 285. Piston Ring Leakage on Rig F-33469-7B

DF 62512

Pretest and post-test views of the housing are shown in figure 286. The post-test view shows a light BeCu plate as a result of the cyclic wear of the lower secondary piston rings. Figure 287 provides pretest and post-test closeup views of the housing area where piston ring wear occurred.

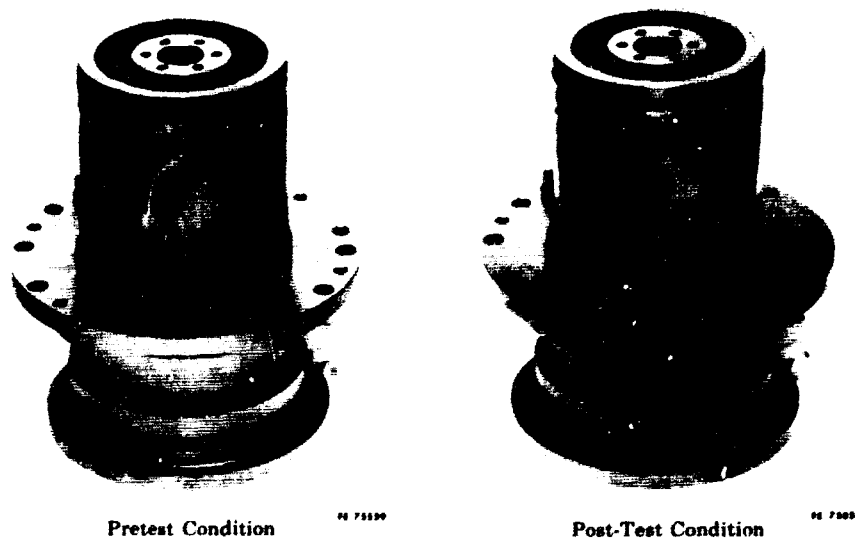


Figure 286. Pretest and Post-Test Condition of the housing

FD 24098



Pretest Condition

W 73140



Post-Test Condition

W 73054

Figure 287. Pretest and Post-Test Views
of Housing Showing Piston
Ring Wear Area

FD 24099

The upper secondary piston rings wear area is shown in figure 288. The wear pattern is characterized by a light deposit of BeCu. The wear on the upper and the lower BeCu piston rings is illustrated by comparing the pretest and post-test conditions in figures 289 and 290.



Pretest Condition

W 73746

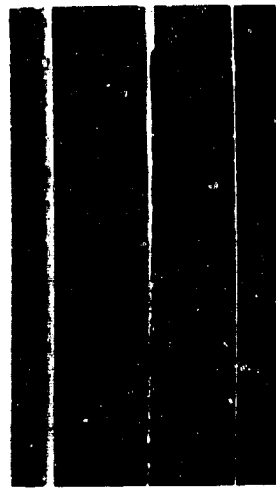


Post-Test Condition

W 73857

Figure 288. Pretest and Post-Test Condition
of Sleeve Showing Wear from
Upper Secondary Piston Ring

FD 24077



Pretest Condition



Post-Test Condition

Figure 289. Pretest and Post-Test Condition of Upper Piston Ring

FD 24100



Pretest Condition



Post-Test Condition

Figure 290. Pretest and Post-Test Condition of Lower Piston Ring

FD 24101

A comparison enlargement of the housing in the pretest condition and the three sets of wear patterns caused by the lower secondary ring are shown in figure 291. The BeCu deposits from the cyclic endurance test were removed from the valve and secondary sleeve by light polishing with aluminum oxide.



1000 psi ΔP PL 13033



1500 psi ΔP PL 13035



2000 psi ΔP PL 13034



Pretest PL 13037

Figure 291. Closeup Views of Main Housing Wear FD 24102A

(b) Rig F-33469-8

The valve housing and sleeve for Rig F-33469-8 had chrome coatings applied in the same manner as Rig F-33469-7B. The unbalanced upper and lower piston rings, shown in figure 292, provided unit bearing loads of 1240 psi and 990 psi, respectively at 2000 psid.

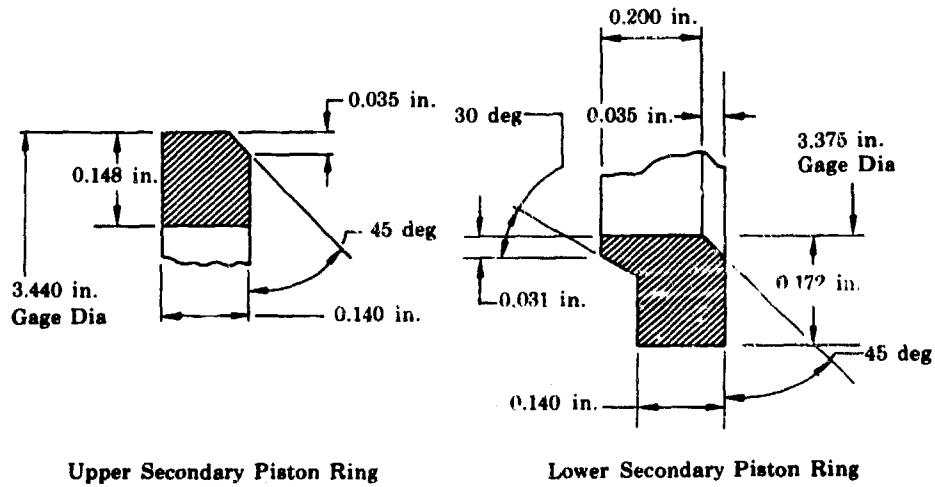


Figure 292. Unbalanced Piston Rings

FD 24973

The rig was subjected to a 6666 cycle endurance test at LN₂ temperatures. The test was terminated after 6666 cycles because of insufficient actuation force at the 2000 psi ΔP level. Piston ring leakages were measured with GN₂ at the various valve positions and are shown in figure 293.

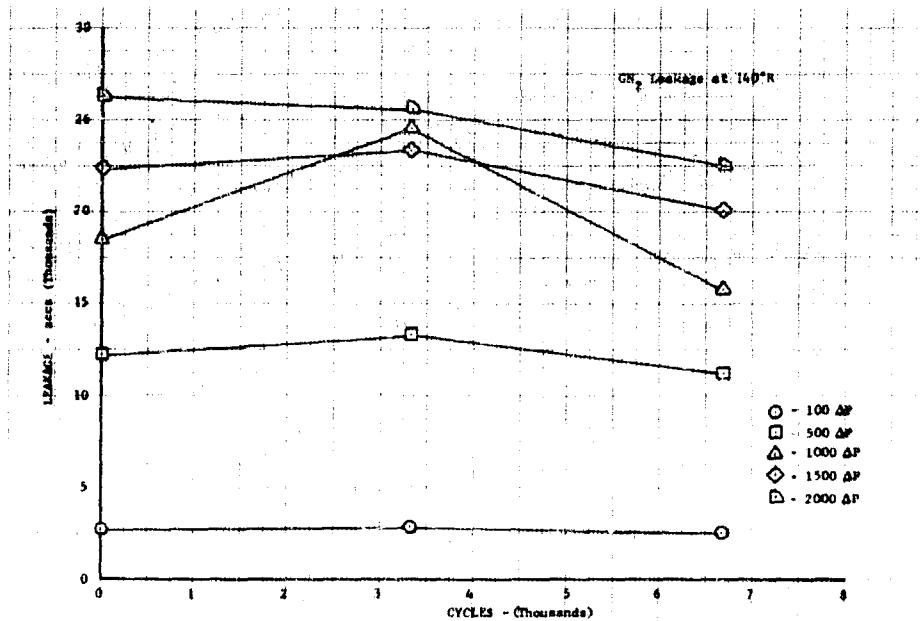
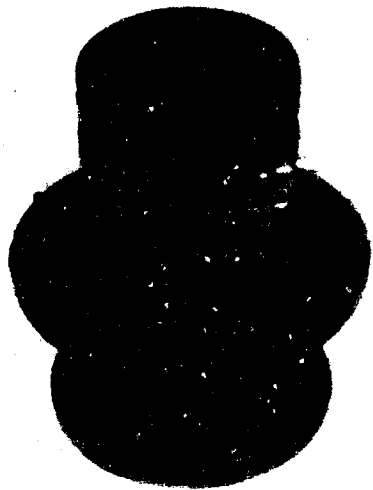


Figure 293. Piston Ring Leakage on Rig F-33469-8

DF 65289

The overall pretest and post-test views of the housing shown in figure 294 shows a light BeCu plate resulting from wear of the lower secondary piston ring. Figure 295 shows a pretest and post-test closeup of this wear area.



FE 76249

Pretest Condition



FE 74503

Post-Test Condition

Figure 294. Pretest and Post-Test Condition of Housing, Rig F-33469-8

FD 24975



FE 76250

Pretest Condition



FE 74504

Post-Test Condition

Figure 295. Pretest and Post-Test Views of Housing Showing Piston Ring Wear Area, Rig F-33469-8

FD 24976

The pretest and post-test upper secondary piston ring wear area is shown in figure 296. The wear pattern is characterized by a light deposit of BeCu. The wear on the upper and lower BeCu piston rings can be seen by comparing the pretest and post-test condition in figures 297 and 298, respectively.

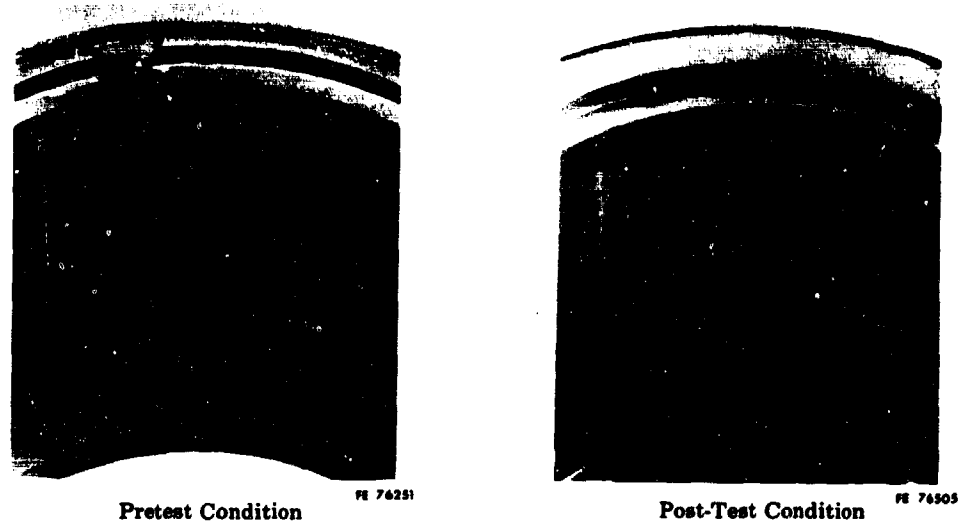


Figure 296. Pretest and Post-Test Condition of Sleeve Showing Wear from Upper Secondary Piston Ring, Rig F-33469-8

FD 24974

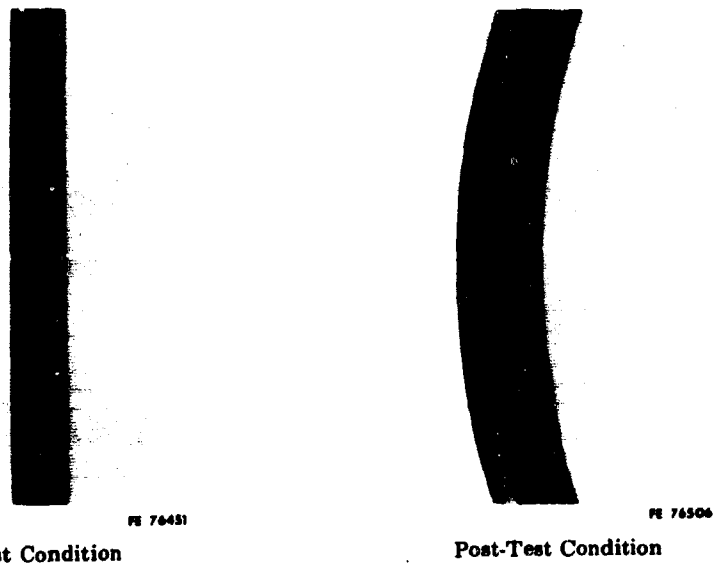


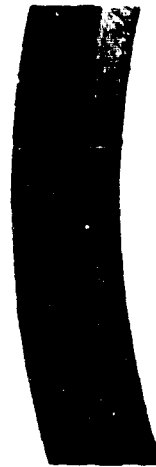
Figure 297. Pretest and Post-Test Condition of Upper Piston Ring, Rig F-33469-8

FD 24977



FE 74252

Pretest Condition



FE 74507

Post-Test Condition

Figure 298. Pretest and Post-Test Condition of Lower Piston Ring, Rig F-33469-8

FD 24978

(c) Rig F-33458-7

The Rig F-33458-7 valve housing had 0.001 in. thick molybdenum coating applied without subsequent machining. The sleeve was chrome plated 0.001 to 0.0015 in. thick (per AMS 2406) and ground to the final dimensions. The unbalanced upper and lower piston rings, shown in figure 292, provided unit bearing loads of 1240 psi, and 990 psi, respectively, at 2000 psi. The valve was cycled a total of 10,000 cycles and the piston ring leakages are shown in figure 299.

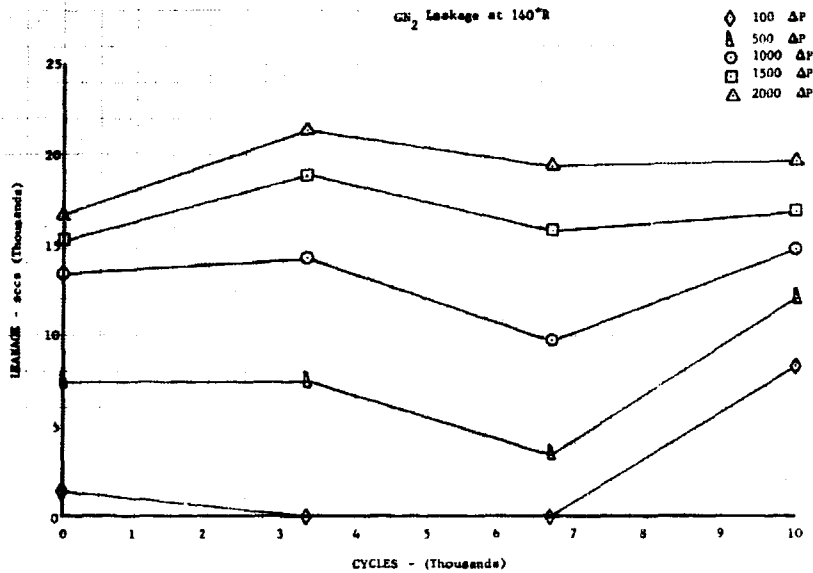


Figure 299. Piston Ring Leakages on Rig F-33458-7

DF 65291

The overall pretest and post-test views of the housing, shown in figure 300, show a light BeCu plate resulting from wear of the lower secondary piston ring. Figure 301 shows a pretest and post-test closeup of this wear area. The wear pattern of the lower piston ring on the valve housing indicates a surface waviness condition that compounded the apparent piston ring wear by increasing the unit loading.



FE 76638

Pretest Condition



FE 77728

Post-Test Condition

Figure 300. Pretest and Post-Test Condition of Housing, Rig F-33458-7 FD 24979



FE 76639

Pretest Condition



FE 77729

Post-Test Condition

Figure 301. Pretest and Post-Test Views of Housing Showing Piston Ring Wear Area, Rig F-33458-7 FD 24980

The pretest and post-test upper secondary piston ring wear area is shown in figure 302. The wear pattern is characterized by a light deposit of BeCu. The wear on the upper and lower BeCu piston rings can be seen by comparing to the pretest and post-test condition in figures 303 and 304, respectively.

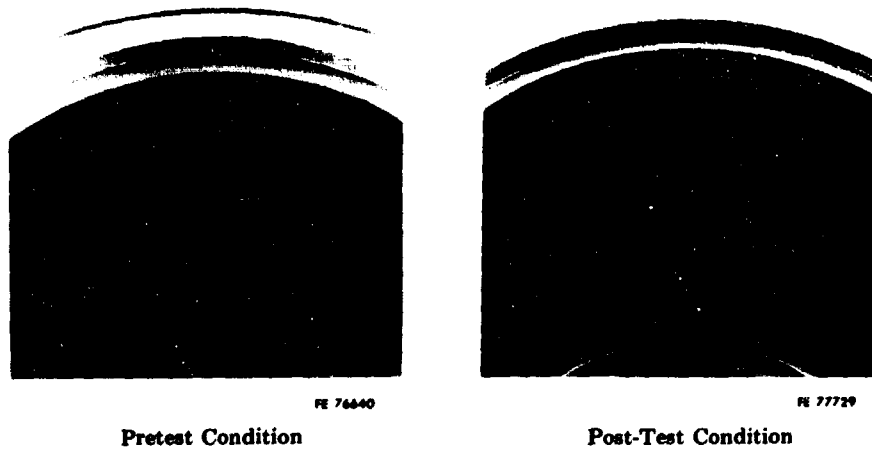


Figure 302. Pretest and Post-Test Condition of Sleeve Showing Wear from Upper Secondary Piston Ring, Rig F-33458-7 FD 24981

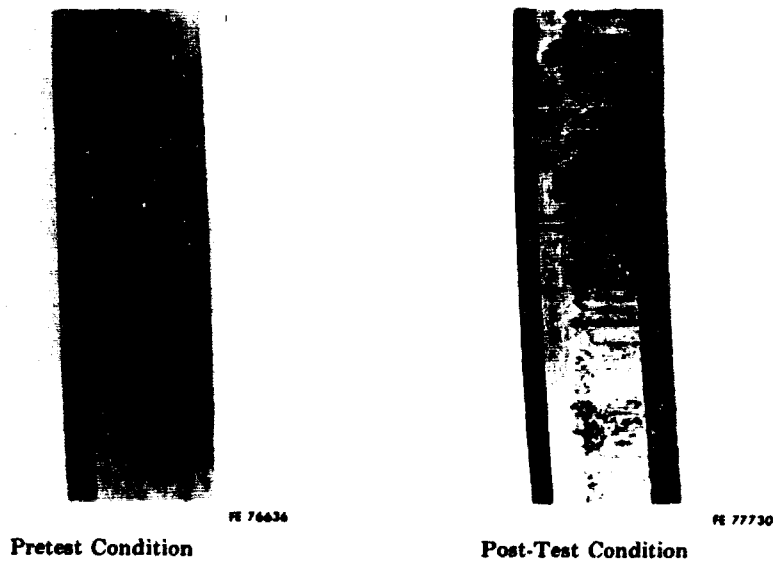


Figure 303. Pretest and Post-Test Condition of Upper Piston Ring, Rig F-33458-7 FD 24982

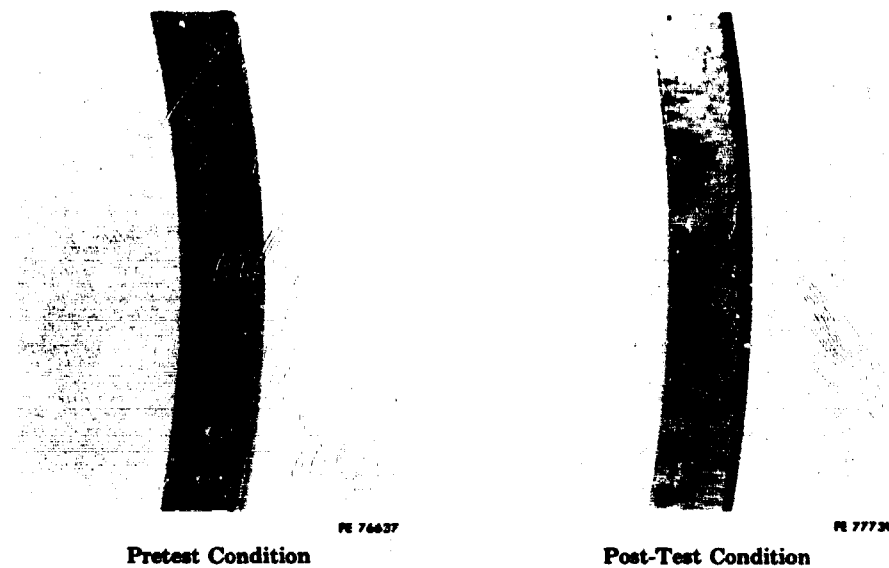


Figure 304. Pretest and Post-Test Condition of Lower Piston Ring, Rig F-33458-7 FD 24983

The actuator shaft and the secondary sleeve shaft were strain gaged by the Material Development Laboratory of FRDC to determine force requirements of the valve. The results are shown in figure 305.

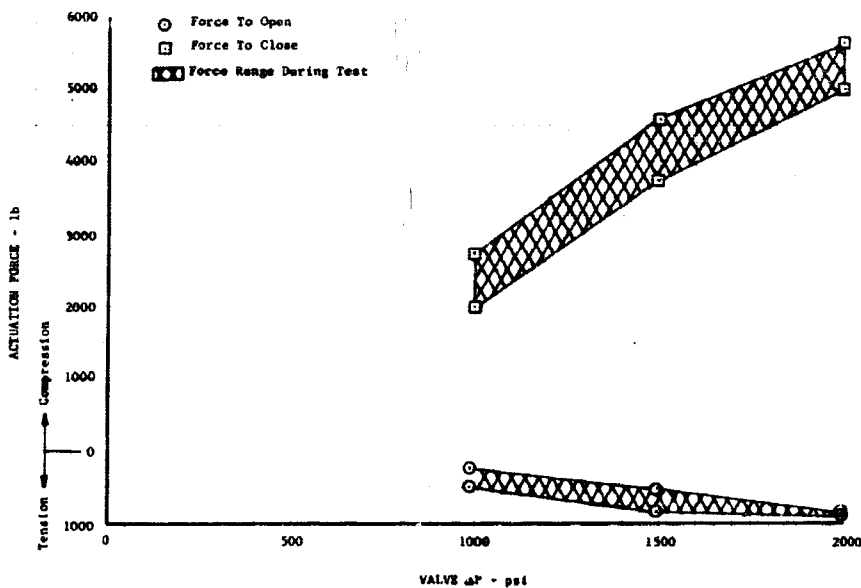


Figure 305. Rig F-33458-7 Actuation Force Requirements During Cycle Endurance DF 65290

(d) Rig F-33458-8

The valve housing and sleeve for Rig F-33458-8 had coatings applied in the same manner as Rig F-33458-7. The balanced upper and lower piston rings, previously shown in figure 282, provided unit bearing loads of 736 psi and 500 psi, respectively, at 2000 psid. The valve was cycled a total of 10,000 cycles and the piston ring leakages are shown in figure 306.

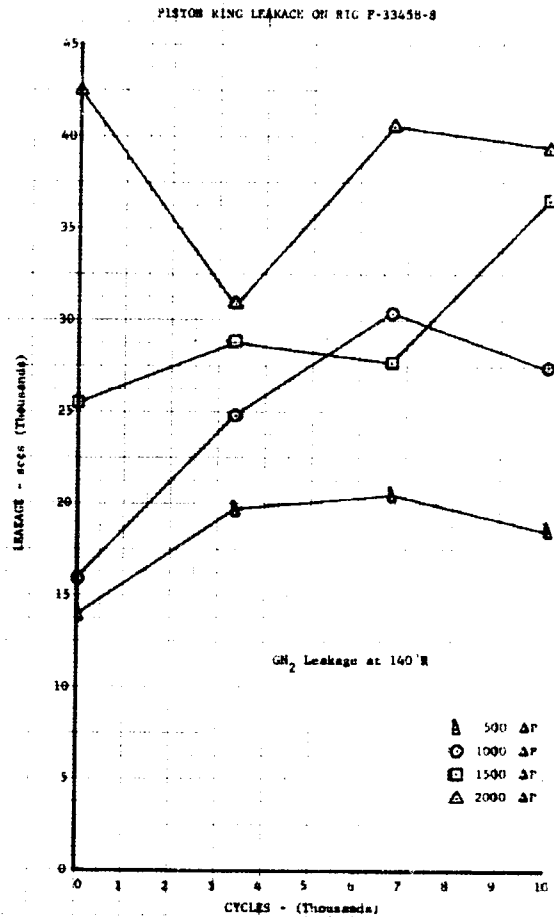
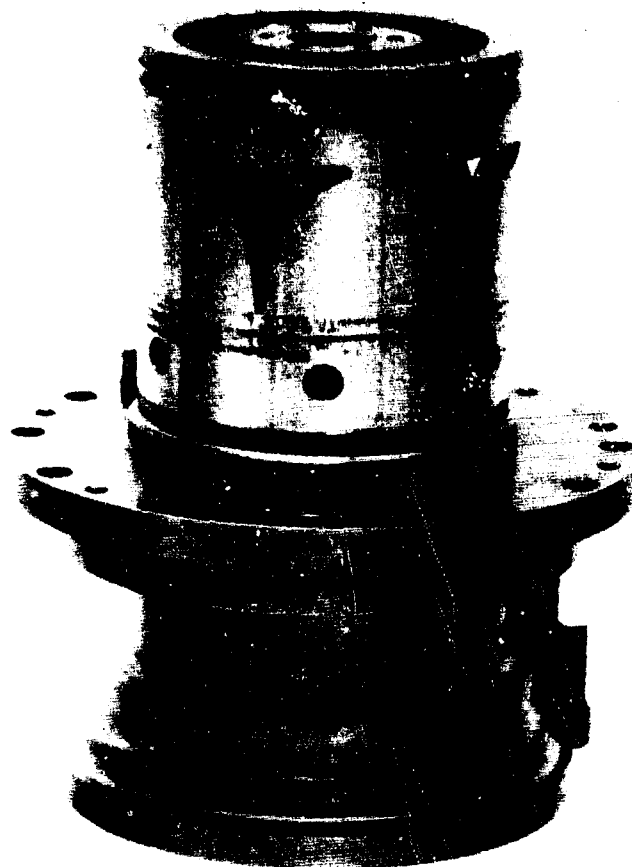


Figure 306. Piston Ring Leakage on Rig F-33458-8

DF 65292

The overall post-test view of the housing shown in figure 306 shows a light BeCu plate due to wear of the lower secondary piston ring. Figure 307 shows the post-test condition of the housing and figure 308 shows a post-test closeup of this wear area.



**Figure 307. Post-Test Condition of Housing,
Rig F-33458-8**

FE 78259

The post-test upper secondary piston ring wear area is shown in figure 309. The wear pattern is characterized by a light deposit of BeCu. The wear on the upper and lower BeCu piston rings is shown in figures 310 and 311, respectively.

The actuator shaft and the secondary sleeve shaft were strain gaged by the Materials Development Laboratory of FRDC to determine force requirements of the valve. The results are shown in figure 312.

3. Translating Seal Rig F-33435

a. Introduction

It was desired to reduce the seal package size of the preburner oxidizer valve by eliminating one shaft seal and changing the seal configuration to a Kapton-Teflon lip seal. To determine the best laminate for sealing translating shafts, five 10,000-cycle endurance tests were conducted.

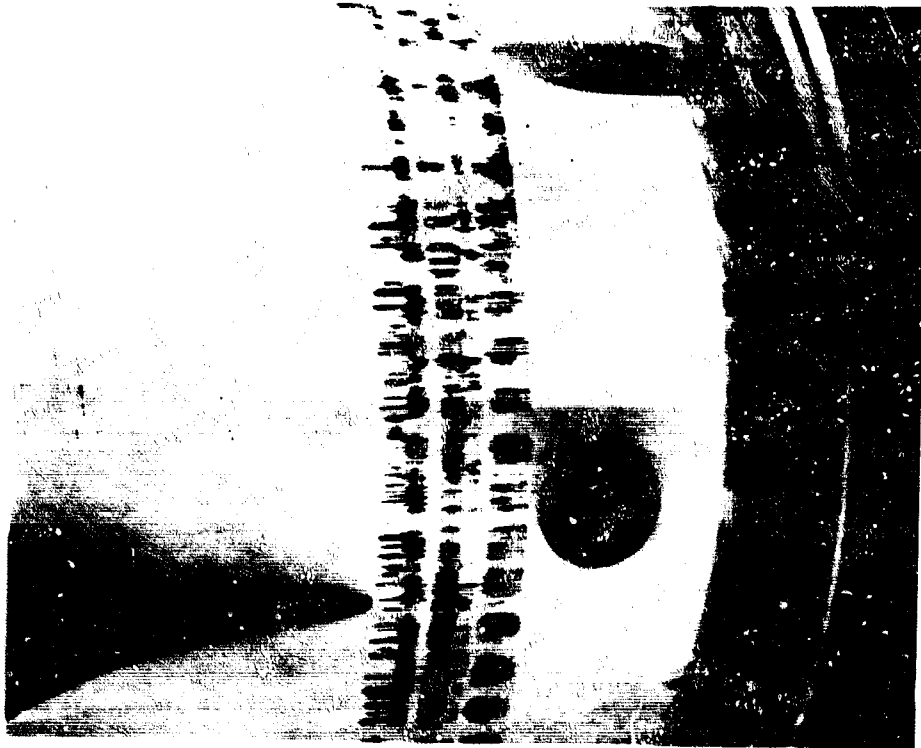


Figure 308. Post -Test View of Housing
Showing Piston Ring Wear
Area, Rig F-33458-8

FE 78256

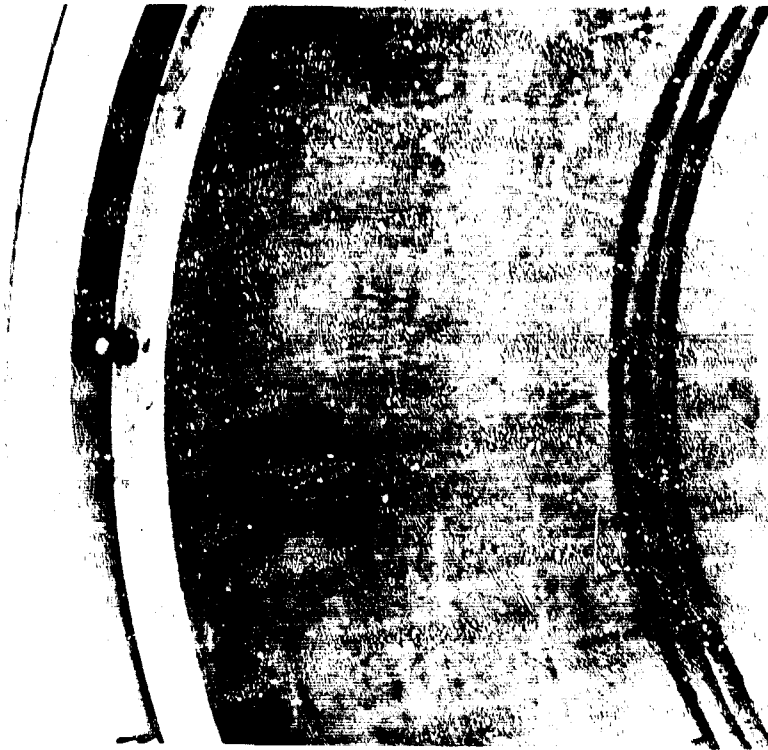


Figure 309. Post-Test Condition of Sleeve
Showing Wear from Upper
Secondary Piston Ring,
Rig F-33458-8

FE 78257



Figure 310. Post-Test Condition of Upper
Piston Ring, Rig F-33458-8



FE 78261 Figure 311. Post-Test Condition of Lower
Piston Ring, Rig F-33458-8

FE 78260

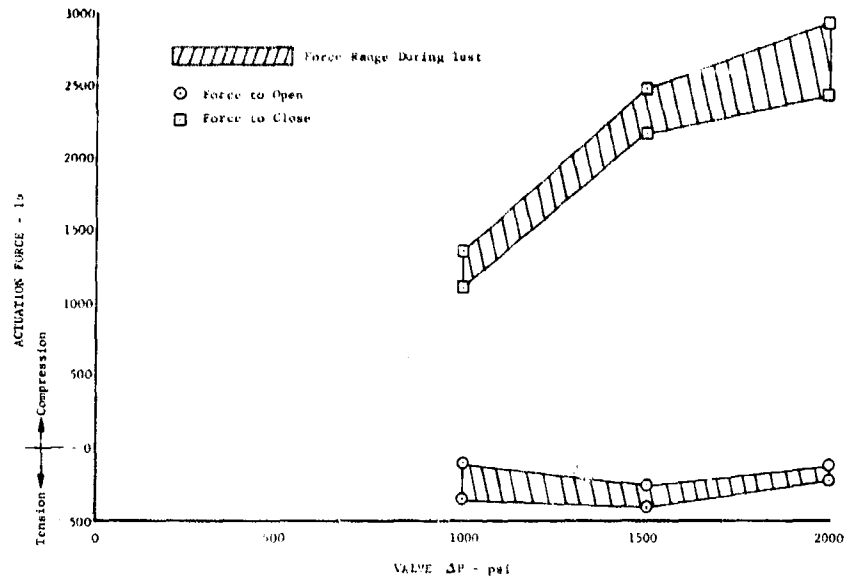


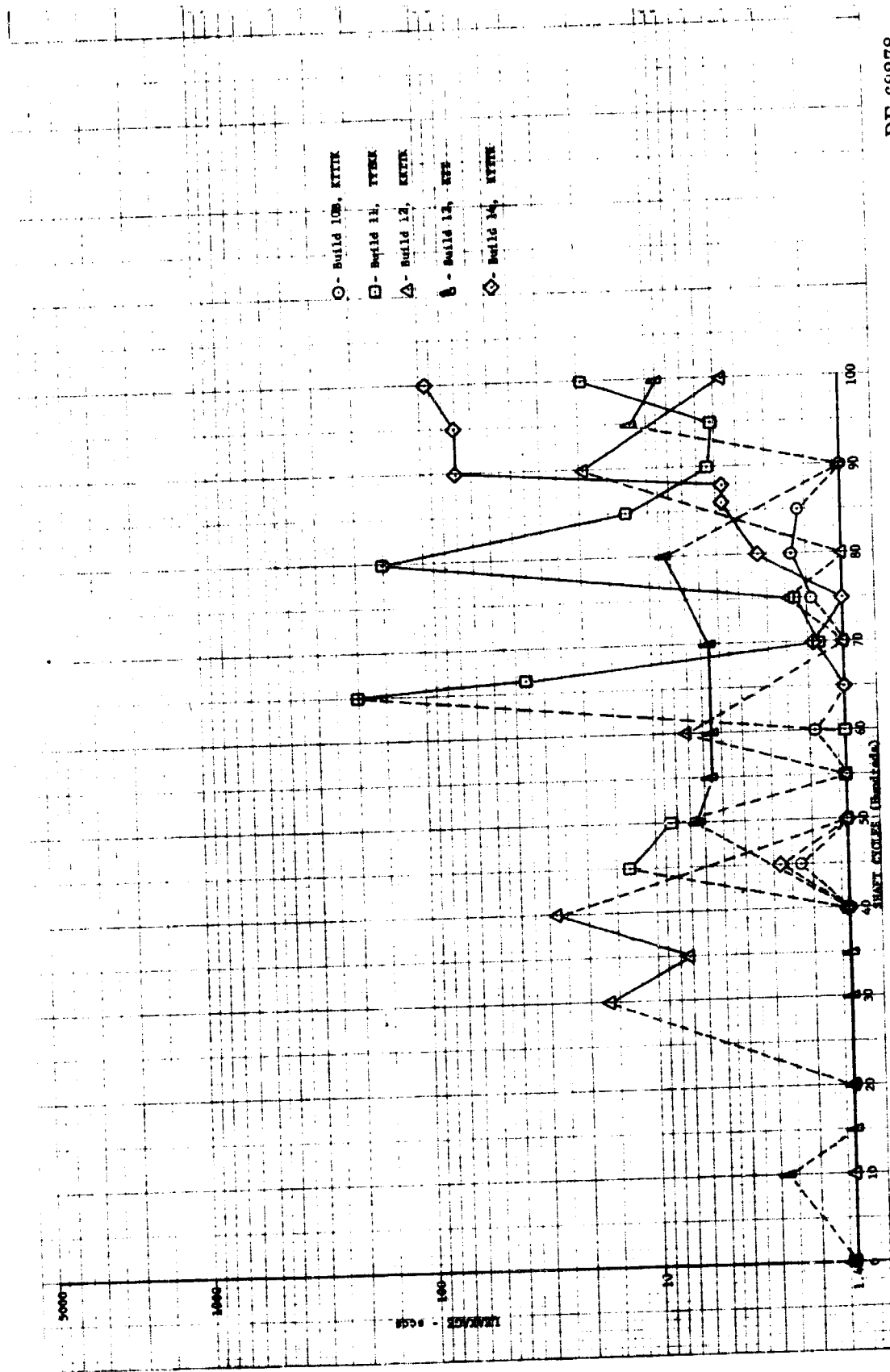
Figure 312. Rig F-33458-8 Actuation Force Requirements During Cycle Endurance DF 65294

b. Summary, Conclusions, and Recommendations

The KTTTK (a five layer laminate of Kapton and Teflon with the outer layers being Kapton) laminate used in build 10B did not exceed the vent shaft seal limit of 10 sccs as shown in figure 313; however, the same laminate tested on Build 14 had wear of the Teflon inner layer. An additional laminate of Kapton on the shaft should eliminate wear of the Teflon inner layer. The test results obtained from Build 12, which was conducted with a KKTTK laminate, were doubtful because of a one day delay that may have resulted in rig icing and a boiloff problem. A laminate configuration of KKTTK is recommended for application at the primary and vent shaft seal locations. The primary shaft seal leakages are shown in figure 314.

A secondary test was conducted as Build 13B to determine the effect of inlet pressure on leakages. As shown in figures 315 and 316 the inlet pressure effect will be negligible.

Because of the high leakage shown in figure 317, a lip seal is not recommended for the balance piston. The Omni-seal (glass-filled Teflon) tested during Phase I (Contract AF04(611)-11401) had better wear characteristics and lower leakage.



DF 68278

Figure 313. Translating Seal Test Rig Vent Shaft Seal Leakage vs Cycles

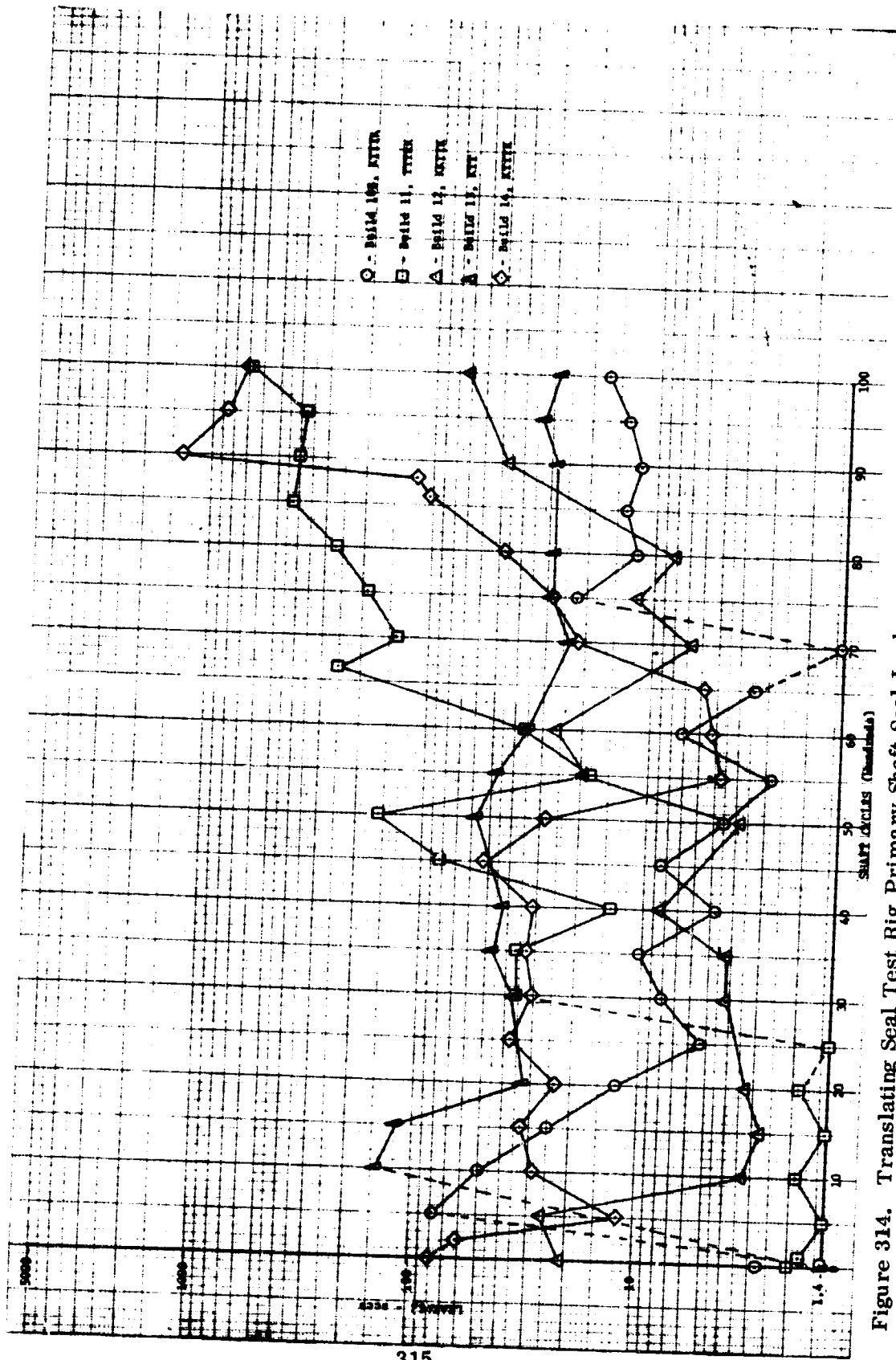


Figure 314. Translating Seal Test Rig Primary Shaft Seal Leakage vs Cycles

DF 68279

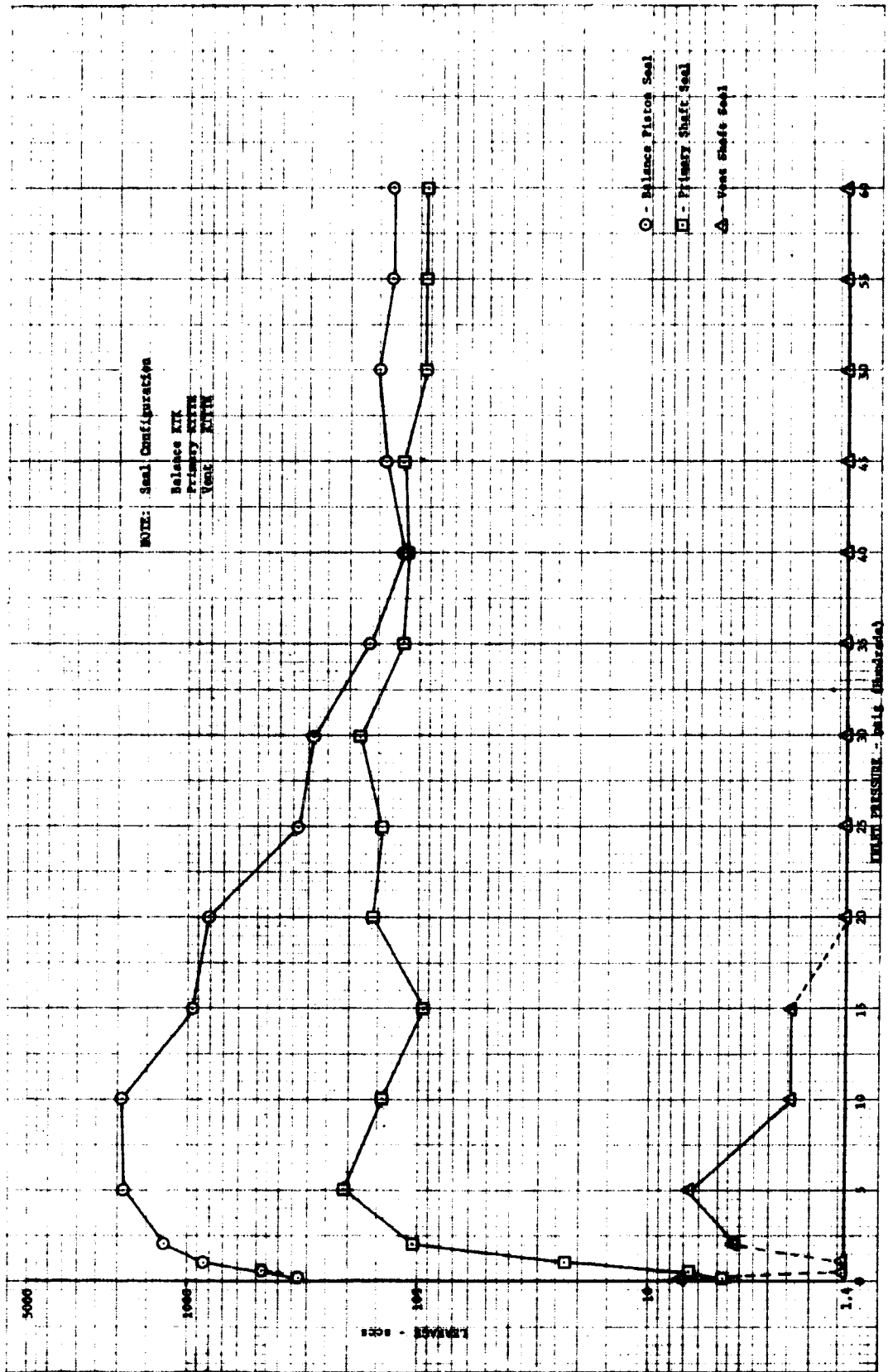
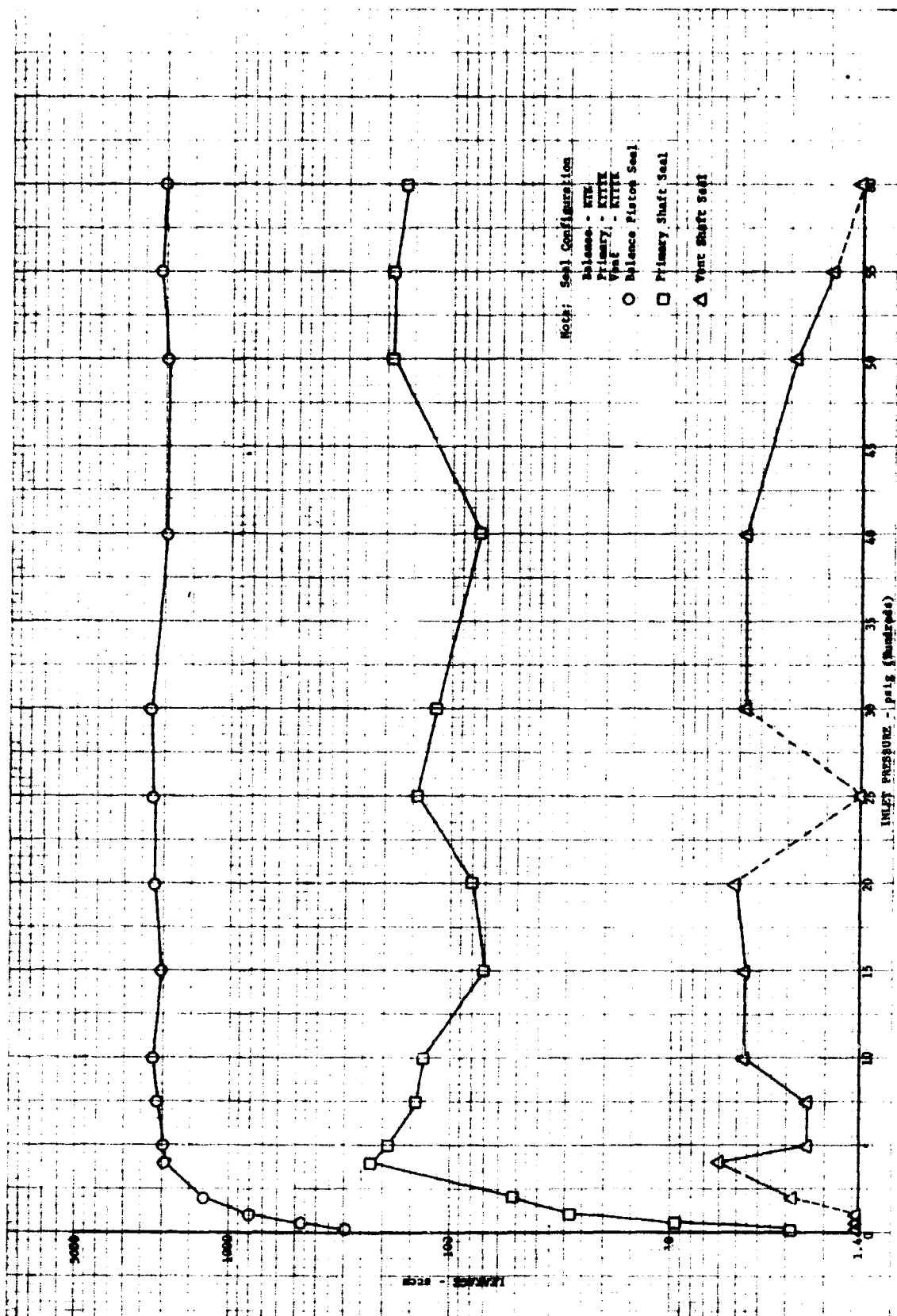
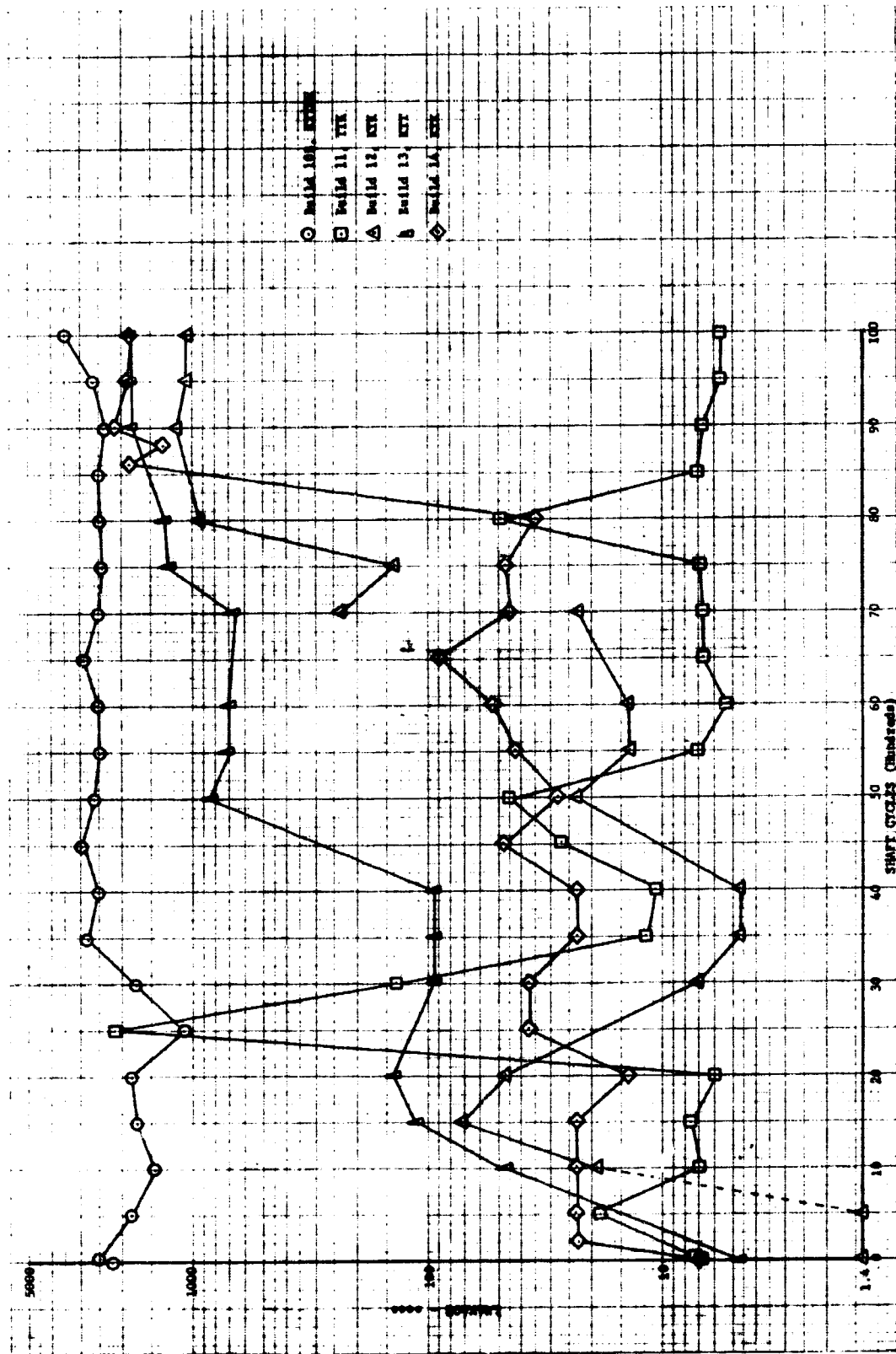


Figure 315. Translating Seal Test Rig Leakage vs Inlet Pressure (Stationary Shaft)



DF 68281

Figure 316. Translating Seal Test Rig Leakage vs Inlet Pressure (Translating Shaft)



DF 68282

Figure 317. Translating Seal Test Rig Balance Piston Seal Leakage vs Cycles

Because of the high leakage shown in figure 317, an OD sealing lip seal is not recommended for the balance piston. The ID sealing lip seal is designed so it will seal around a shaft that translates through it. This application provides a uniform radial stretch about the surface where sealing is desired. In the opposite application where the OD of a lip seal is used for the sealing surface, the seal is held by the translating shaft and sealing is obtained on the housing bore. The OD of the lip seal tends to gather and provide a scalloped sealing surface. Therefore, ID sealing lip seals should be used for the balance piston as well as the actuator shaft.

c. Hardware Description

(1) Translating Seal Rig

The translating seal rig was designed to evaluate lip seals for application to high pressure, cryogenic translating shaft and piston applications. The rig duplicates the preburner oxidizer valve shaft and housing configuration designed during Phase I (Contract AF04(611)-11401). An exploded view of the rig is shown in figure 318. The test rig is translated a total stroke of 1.375 in. at a rate of 1 cps by a pneumatically actuated piston.

(2) Shaft Lip Seals

Tests of this type seal in a rotary, 1 in. shaft seal rig at LN₂ temperature and 6000 psig GN₂ pressure during Phase I (Contract AF04(611)-11401) showed maximum primary and vent shaft (axial) leakages of 0.37 sccs and less than 0.008 sccs, respectively, after 10,000 shaft cycles. Static (radial) leakages were less than 1.4 sccs. This sealing effectiveness allows a reduction in the number of seals required for shaft sealing and eliminates separate static seals in the seal package because the lip seal seals radially as well as axially.

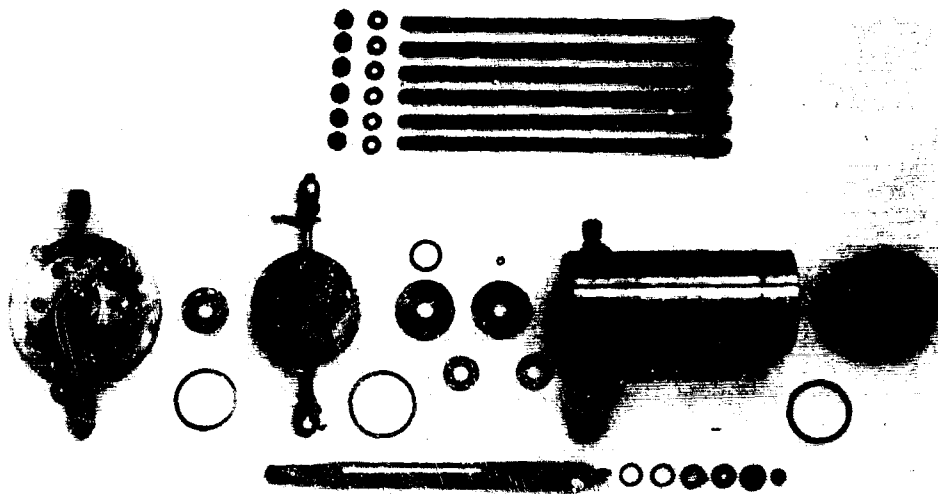


Figure 318. Translating Seal Test Rig

FE 76099

Scaling down the rotary lip seals resulted in a 1.098 in. OD, 0.600 in. ID, 0.025 in. thick seal of laminated layers of 0.005 in. FEP Teflon and 0.005 in. Kapton. The stacking of these materials was varied during testing to determine the best combination.

The shaft seal package is illustrated in figure 319. The primary seal antiextrusion backup leaves 0.001 in. clearance between the seal gland and the shaft. The secondary seal is forced against the shaft by the primary gland configuration, thus, acting as a bearing for the floating seal package. This prevents metal-to-metal contact between the primary gland and rig shaft.

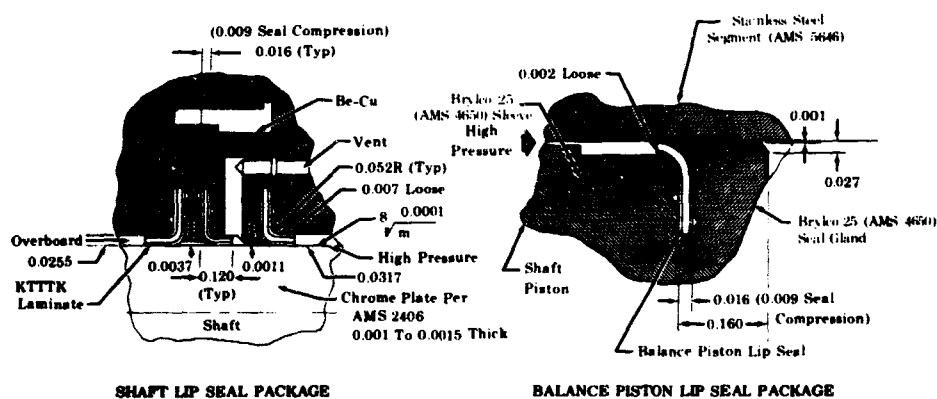


Figure 319. Shaft Seal Package

FD 24331C

(3) Piston Seal Package

The initial design dimensions of the piston lip seal were 0.715 in. OD, 0.353 in. ID, and 0.025 in. thick. Material was laminated FEP Teflon-Kapton. The piston seal package is illustrated in figure 319. The sleeve shown in figure 319 was added to give the seal a backup during forming and force the seal against the segment bore so that it acts as a bearing and prevents the seal gland and shaft piston from making metal-to-metal contact with the segment bore.

d. Seal Laminate Fabrication

The lip seals are fabricated from FEP Teflon and 500F-131 Kapton 0.005 in. thick sheet stock. The 500F-131 Kapton consists of a 0.003 in. sheet of type F Kapton with 0.001 in. thickness of FEP Teflon on each side. The following procedure outlines the fabrication process:

1. Individual seal laminates are cut with a 2.5 in. diameter cutting tool.
2. The laminates and molding tools are sonic cleaned in trichlorethylene at 630°R.
3. The desired laminate stackup is placed in a mold housing as shown in figure 320. TFE Teflon sheet stock 0.005 in. thick is placed between the individual seals and the mold housing to prevent bonding.

4. A weight is placed on the mold plunger to provide 10 psi unit loading, and the seals are baked at 985°R ± 10°R for 1 hour.
5. The seal blanks are removed and separated by peeling off the TFE Teflon separators. Individual seals are then cut by dies.

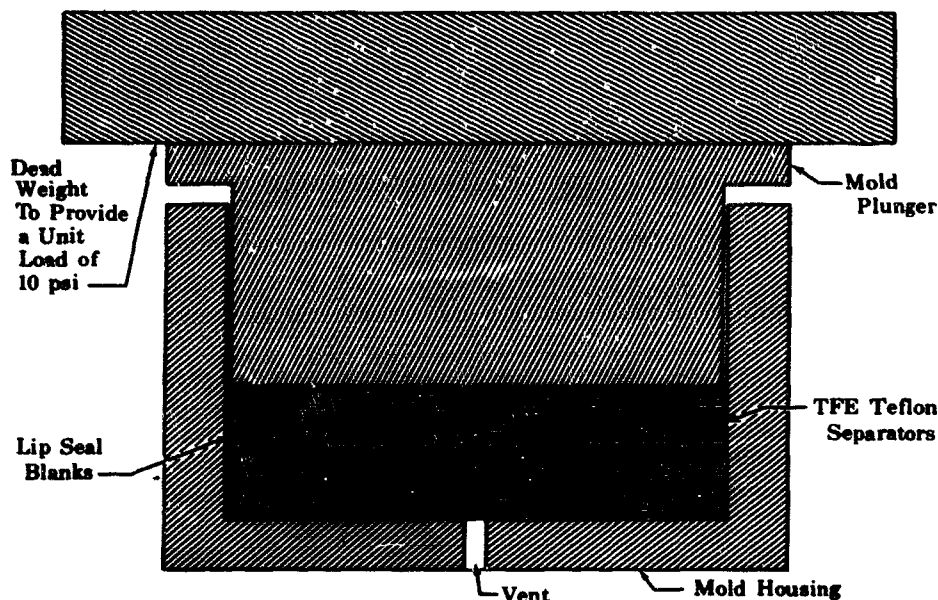


Figure 320. Lip Seal Mold

FD 24092

e. Endurance Tests

Five 10,000 cycle endurance tests were conducted to evaluate the laminated lip seals. The test results are summarized in table XXX. A coding is used to identify the seal configuration. A KTTTK laminate is two 0.005 in. thick sheets of Kapton and three 0.005 in. thick sheets of Teflon. The material next to the dynamic sealing surface is identified first.

Table XXX. Summary of Test Results

Test Number	Seal Configuration			Maximum Leakage Recorded During Test (secs)			Seal Wear After Test (grams)			Number of Cycles
	Balance	Primary	Vent	Balance	Primary	Vent	Balance	Primary	Vent	
33435-10A	KTTTK	KTTTK	KTTTK	Terminated Test			Terminated Test			
33435-10B	KTTTK	KTTTK	KTTTK	3400	78	2.4	0.00127	0.002715	0.000701	10,000
33435-11	TKK	TTTKK	TTTKK	2100	660	200	0.001648	0.00029	0.000751	10,000
33435-12	KTK	KKTKK	KKTKK	1080	70	28	0.011065	0.007348	0.000941	10,000
33435-13	KTT	KTT	KTT	1800	140	11.5	0.007721	0.001625	no wear	10,000
33435-14	KTK	KTTTK	KTTTK	2100	1350	94	0.007877	0.009078	0.002012	10,000

The maximum allowable vent seal leakage is 10 secs. Balance piston and primary seal leakages are vented to controlled areas.

(1) Build 10B

This build incorporated the same seal construction and laminate used in Build 10A; however, the balance piston seal had an increased seal lip.

A total of 10,000 shaft cycles and 500 pressure cycles with the rig at LN₂ temperatures was completed. The rig inlet pressure was maintained at 5900 to 6000 psig GN₂ except during pressure cycling. The leakages from the test are corrected to a nominal 6000 psig inlet pressure and are shown in figure 321.

Teardown inspection revealed the following:

1. The primary shaft lip seal had fatigue cracks and slight wear on the lip, as shown in figure 322.
2. The vent shaft lip seal exhibited little wear, as shown in figure 323.
3. The balance piston lip seal exhibited little wear, as shown in figure 324.

(2) Build 11

The primary and vent seals tested were TTTKK and the balance piston seal was TTK. The balance piston seal incorporated a thinner seal laminate and an increased seal lip as compared to the configuration tested in Build 10B.

A total of 10,000 shaft cycles and 500 pressure cycles with the rig at LN₂ temperatures was completed. The rig inlet pressure was maintained at 5900 to 6000 psig GN₂ except during pressure cycling. The leakages from the test are corrected to a nominal 6000 psig inlet pressure and are shown in figure 325.

Teardown inspection revealed the following:

1. The primary shaft lip seal showed moderate wear. (See figure 326.)
2. The vent shaft lip seal showed slight wear. (See figure 327.)
3. The balance piston lip seal showed very little wear. (See figure 328.)

(3) Build 12

The primary and vent seals tested were KKTTK and balance piston seal was KTK.

A total of 10,000 shaft cycles and 500 pressure cycles with the rig at LN₂ temperatures was completed. The rig inlet pressure was maintained at 5900 to 6000 psig GN₂ except during pressure cycling. The leakages from the test are shown in figure 329. At 7000 cycles the test was stopped and the rig allowed to warm to ambient. When the test was resumed, a step increase in the balance piston leakage was observed, which may have been caused by icing in the rig. At some points the vent leakage was above primary leakage indicating boiloff in the vent lines.

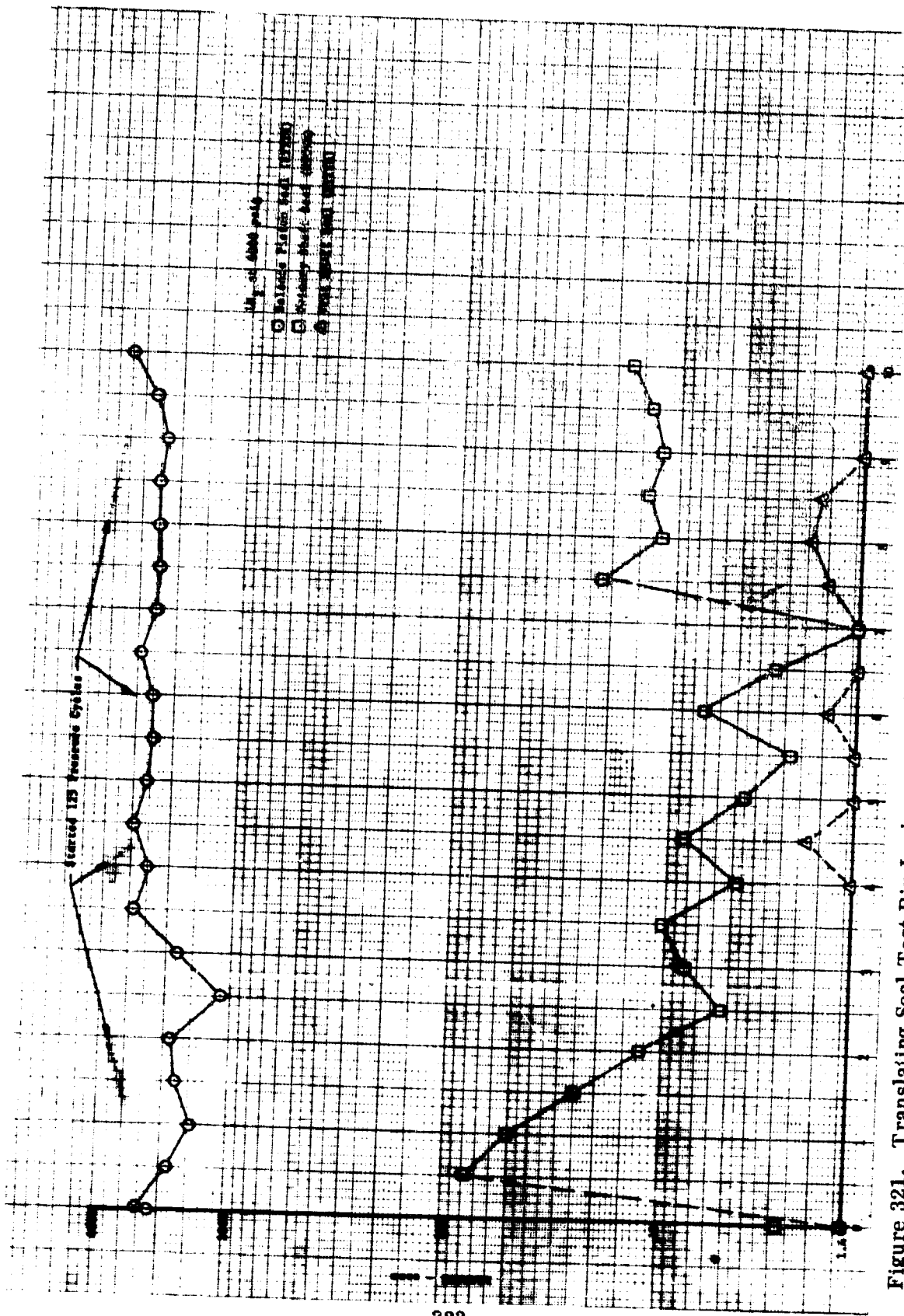


Figure 321. Translating Seal Test Rig Leakage vs Cycles for Build 10B

DF 62450



Figure 322. Primary Shaft Lip Seal After
Test of Build 10B

FE 76263

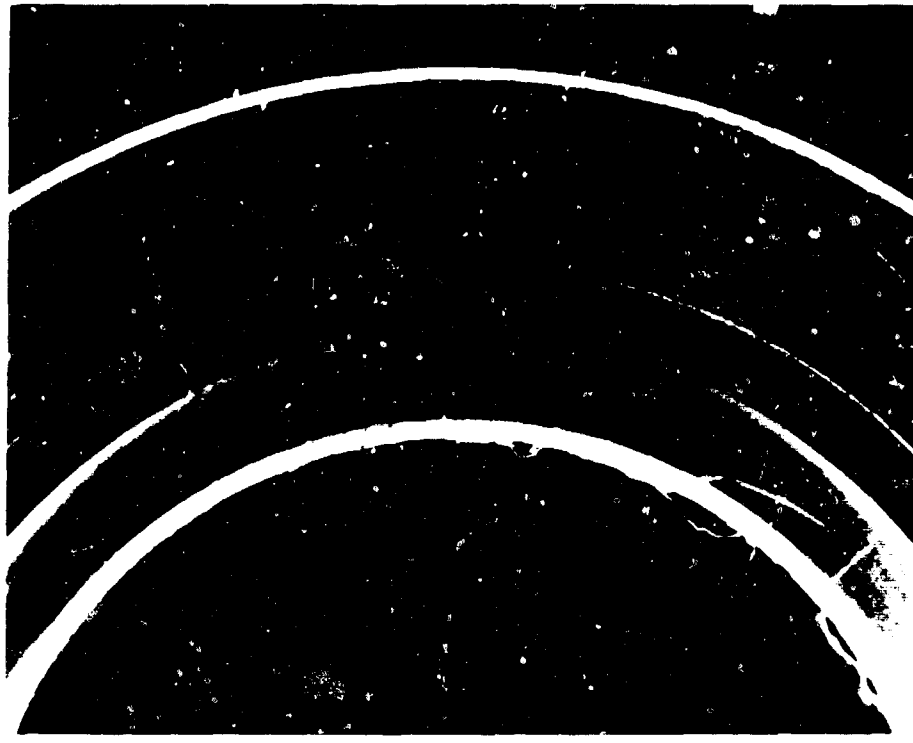


Figure 323. Vent Shaft Lip Seal After Test
of Build 10B

FE 76264

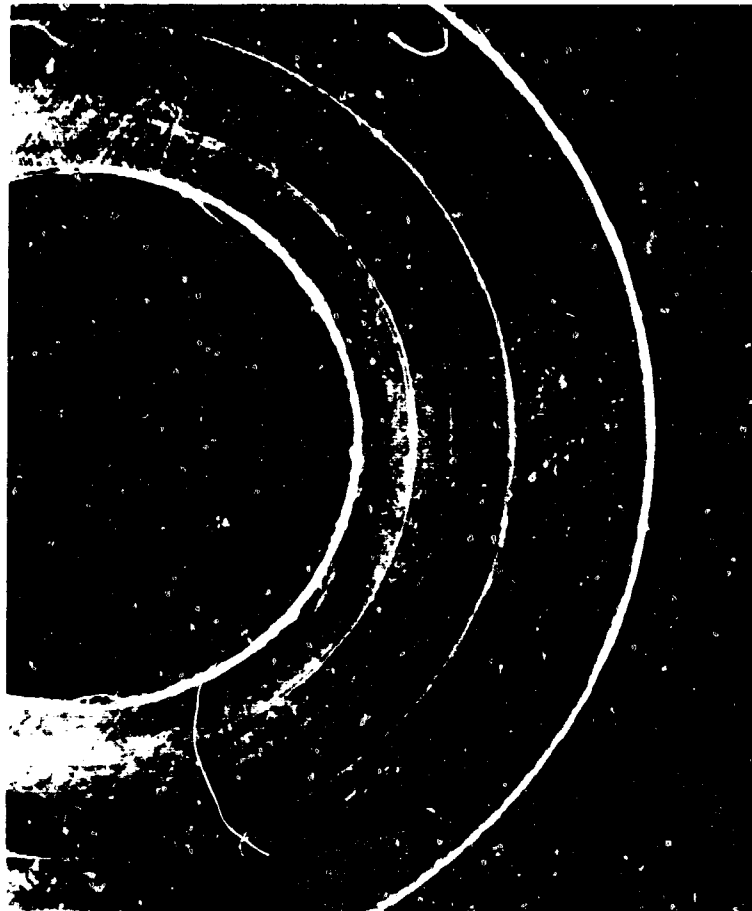


Figure 324. Balance Piston Lip Seal After Test
of Build 10B

FE 75832

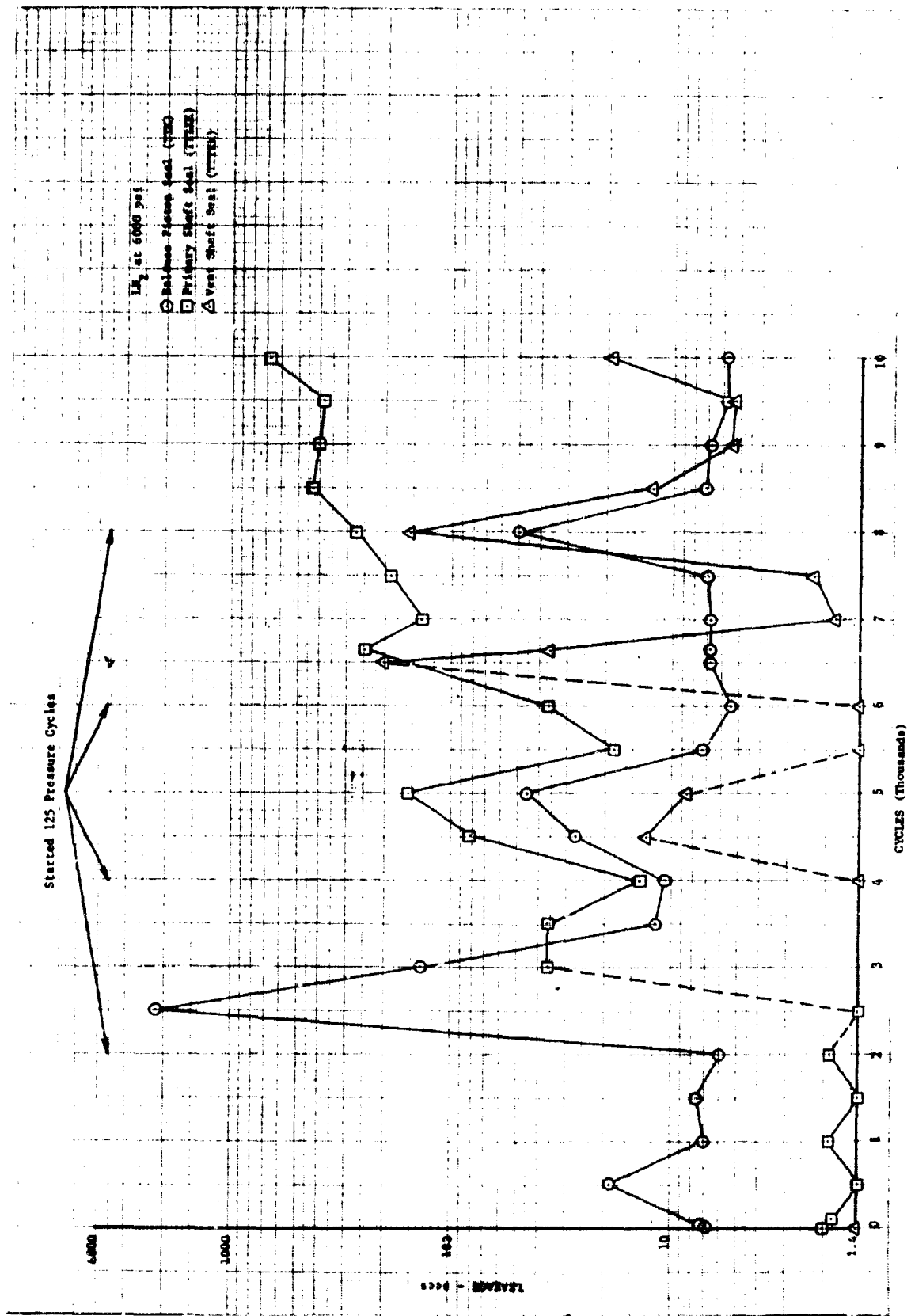


Figure 325. Translating Seal Test Rig Leakage vs Cycles for Build 11

DF 62451



Figure 326. Primary Shaft Lip Seal After Test
of Build 11

FE 75904

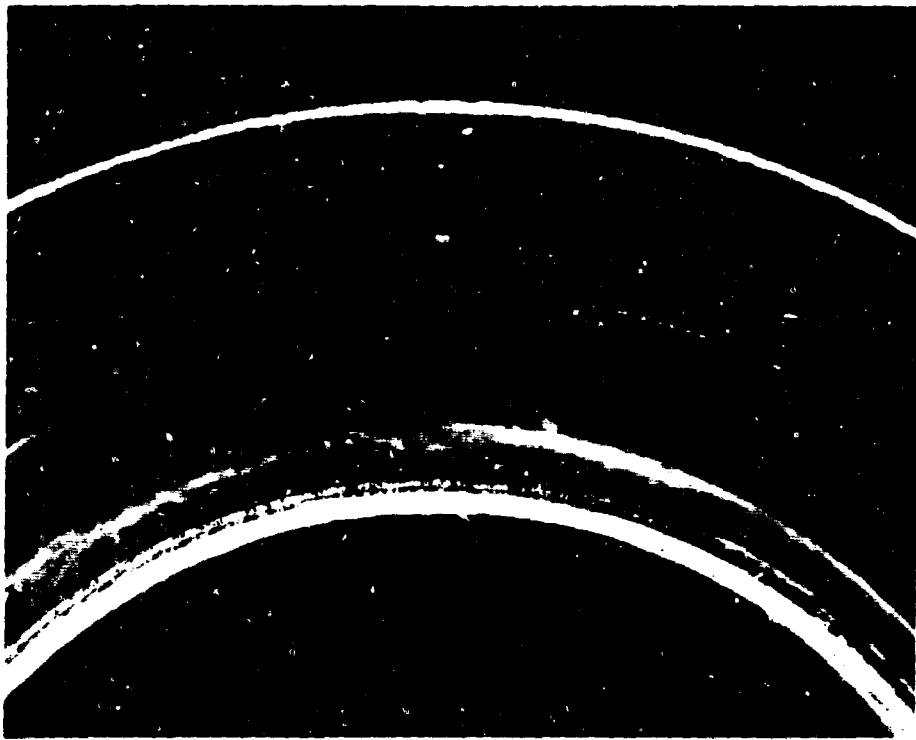


Figure 327. Vent Shaft Lip Seal After Test
of Build 11



Figure 328. Balance Piston Lip Seal After
Test of Build 11

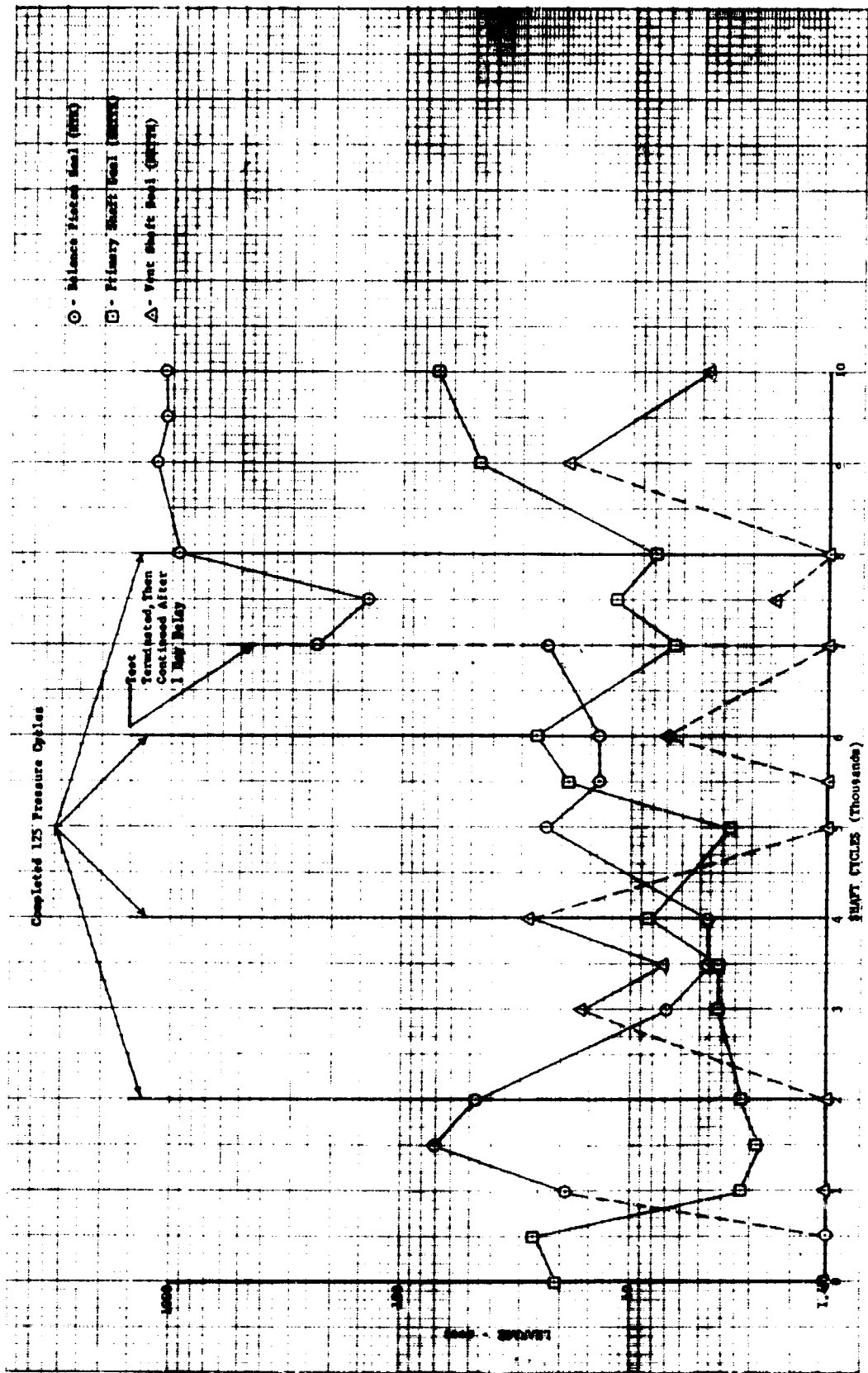


Figure 329. Translating Seal Test Rig Leakage vs Cycles for Build 12

A teardown inspection revealed the following:

1. The primary shaft lip seal showed moderate wear. (See figure 330.)
2. The vent shaft lip seal showed slight wear. (See figure 331.)
3. The balance piston lip seal showed moderate wear. (See figure 332.)

(4) Build 13

All seals tested were KTT laminate.

A total of 10,000 shaft cycles and 500 pressure cycles with the rig at LN₂ temperatures was completed. The rig inlet pressure was maintained at 5900 to 6000 psig GN₂ except during pressure cycling. The leakages from the test are shown in figure 333. Balance piston seal leakage shows a degradation as a function of cycles indicating the effects of wear. Vent seal leakage exceeded the 10 sccs limit at only one data point during the test.

A teardown inspection revealed the following:

1. The primary shaft lip seal showed moderate wear. (See figure 334.)
2. The vent shaft lip seal showed slight wear. (See figure 335.)
3. The balance piston lip seal showed heavy wear. (See figure 336.)

(5) Build 14

The primary and vent shaft seals tested were KTTTK and the balance piston was KTK. This test was conducted with the stand configuration as shown in figure 337. The test procedure prevents a buildup of liquid in the seal vent lines by maintaining a vacuum on the lines at all times.

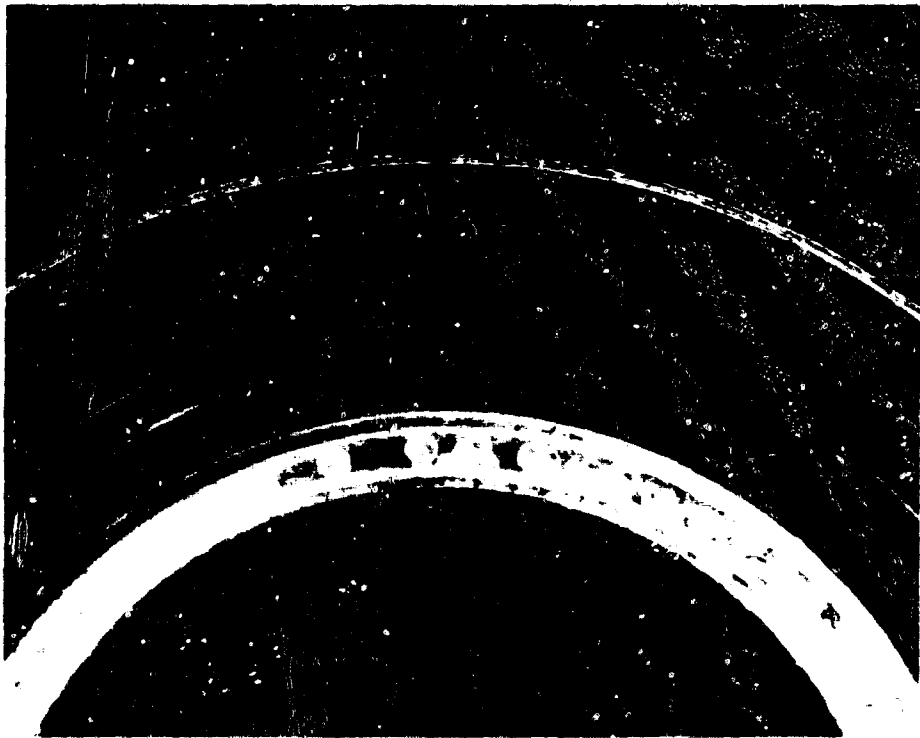


Figure 330. Primary Shaft Lip Seal After
Test of Build 12

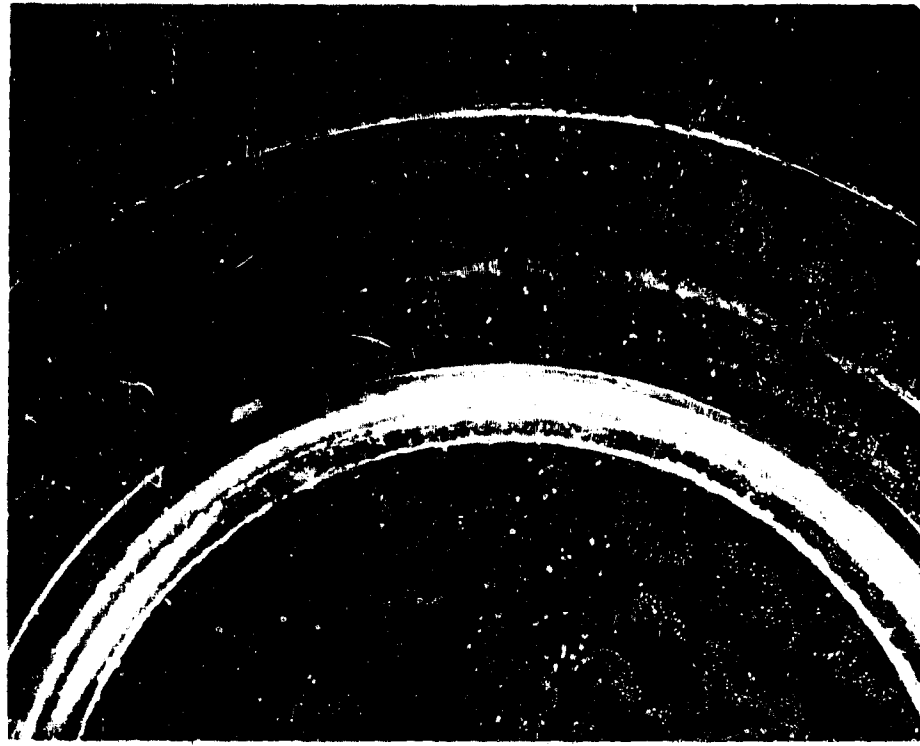


Figure 331. Vent Shaft Lip Seal After Test
of Build 12



Figure 332. Balance Piston Lip Seal After Test of FE 76477
Build 12

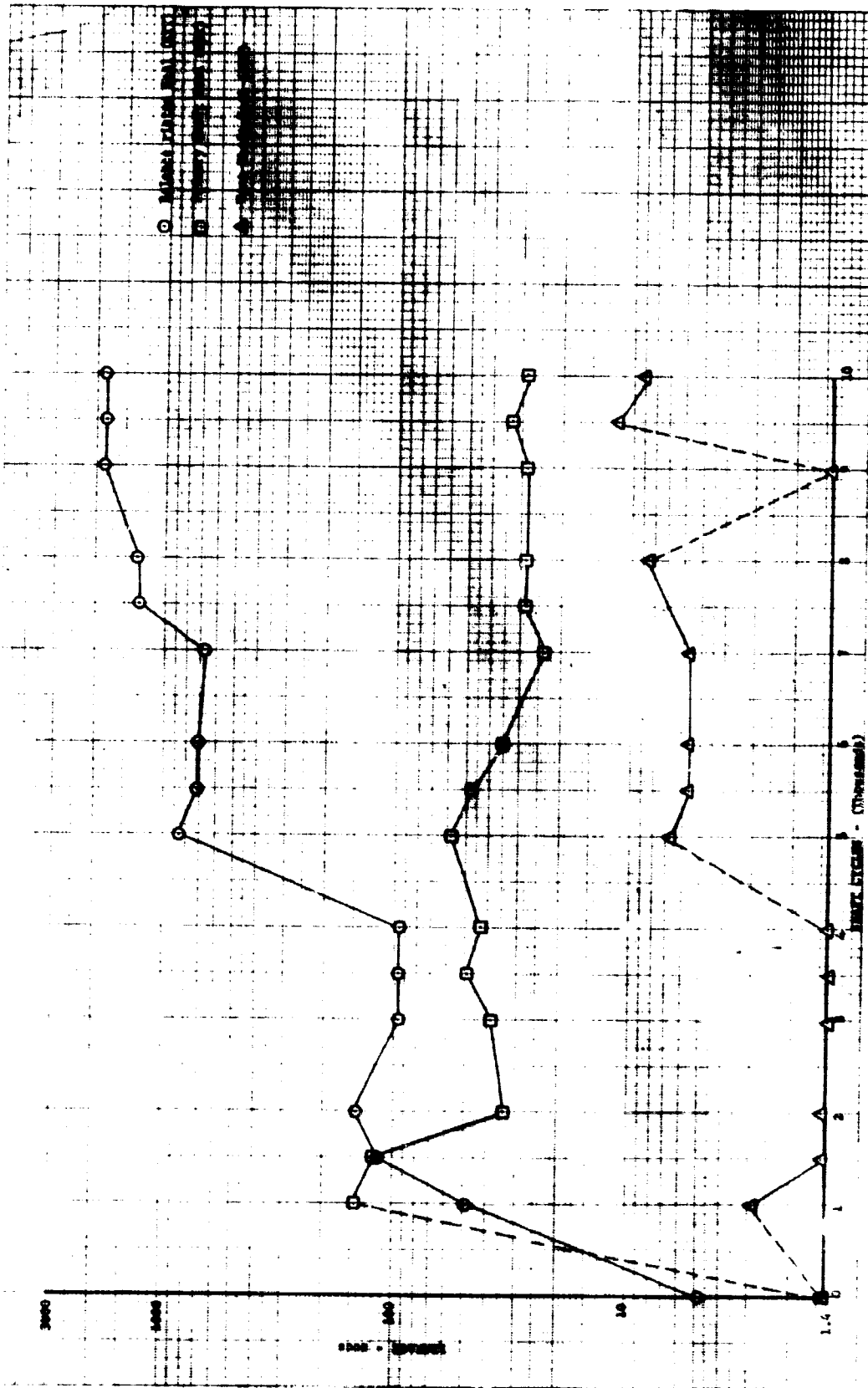


Figure 333. Translating Seal Test Rig Leakage vs Cycles for Build 13

DF 65296



Figure 334. Primary Shaft Lip Seal After
Test of Build 13

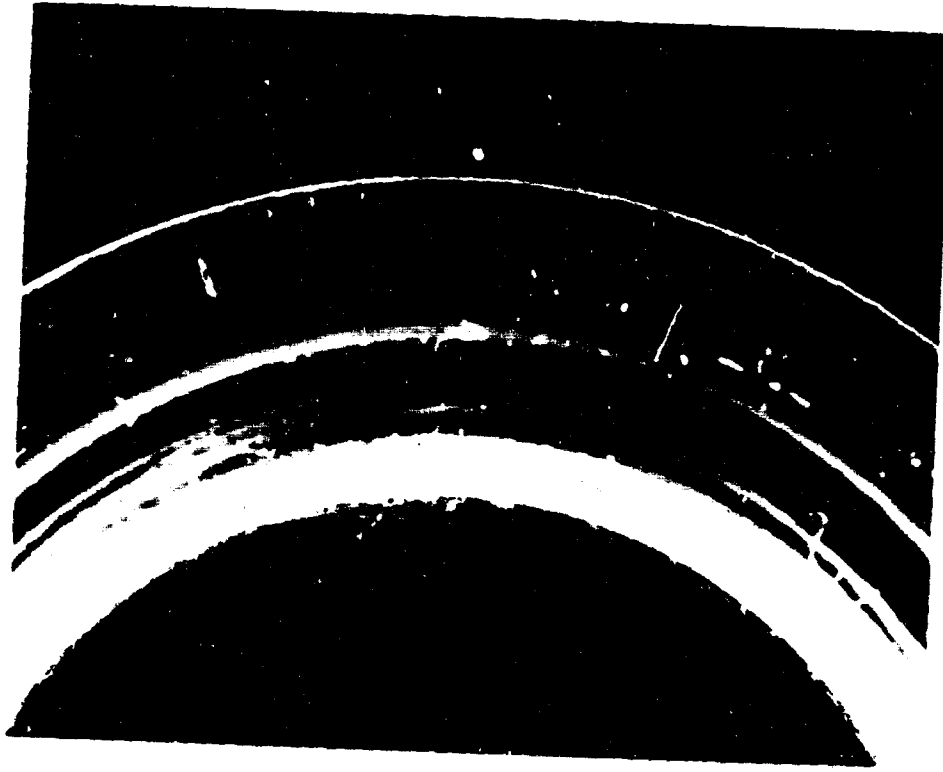


Figure 335. Vent Shaft Lip Seal After Test
of Build 13

FE 77096



Figure 336. Balance Piston Lip Seal After Test of FE 77098 Build 13

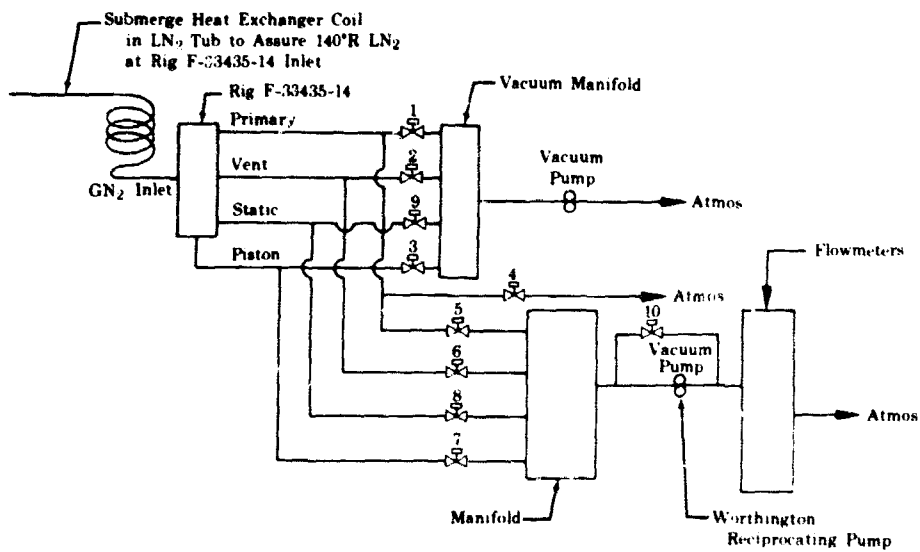


Figure 337. Plumbing Schematic for Testing Build 14 FD 24986A

f. Test Summary

A total of 10,000 shaft cycles and 375 pressure cycles with the rig at LN₂ temperatures was completed. The rig inlet pressure was maintained at 5900 to 6000 psig GN₂ except during pressure cycling. The pressure cycles at the 8000 cycle point were omitted because primary lip seal leakage was excessive (above 5000 secs) during pressured cycles. Seal wear produced some shredded material that lodged between the sealing surface and shaft during pressure cycling. The leakages are shown in figure 338.

A teardown inspection revealed the following:

1. The primary shaft lip seal showed heavy wear. (See figure 339.)
2. The vent shaft lip seal showed slight wear. (See figure 340.)
3. The balance piston lip seal showed heavy wear. (See figure 341.)

4. Static Seals

a. Introduction

During seal rig, component, and staged combustion rig testing conducted during Phase I (Contract AF04(611)-11401), excessive overboard static seal leakage was experienced. The measured overboard primary seal leakage at maximum thrust during the staged combustion rig test firings was equivalent to an impulse loss of approximately 2 sec, and some additional uncontrolled overboard leakage was visible. Static pressure tests on the main chamber oxidizer valve indicated that the leakage problem was aggravated by excessive flange separation and inadequate static seals.

During this report period, under the current demonstrator engine design program, hydrostatic test rigs with high-pressure joints were designed and tested. These rigs did not incorporate double seals with interseal vents because of the attendant weight penalty. The design goal for the rigs was for zero axial deflection at the seal diameter with 7500 psig internal pressures at liquid nitrogen temperature. Neither of the hydrostatic test rigs met the deflection criteria, but agreement with finite element computer program predictions was satisfactory. The computer program model was improved to provide a good stress and deflection analysis capability for the seal rigs to be designed under the component development phase of this program.

b. Summary, Conclusions, and Recommendations

Supporting data for satisfactory seal rig design was accomplished during this phase. The finite element computer program, as adapted to coupling analysis, will be satisfactory for optimizing coupling flanges.

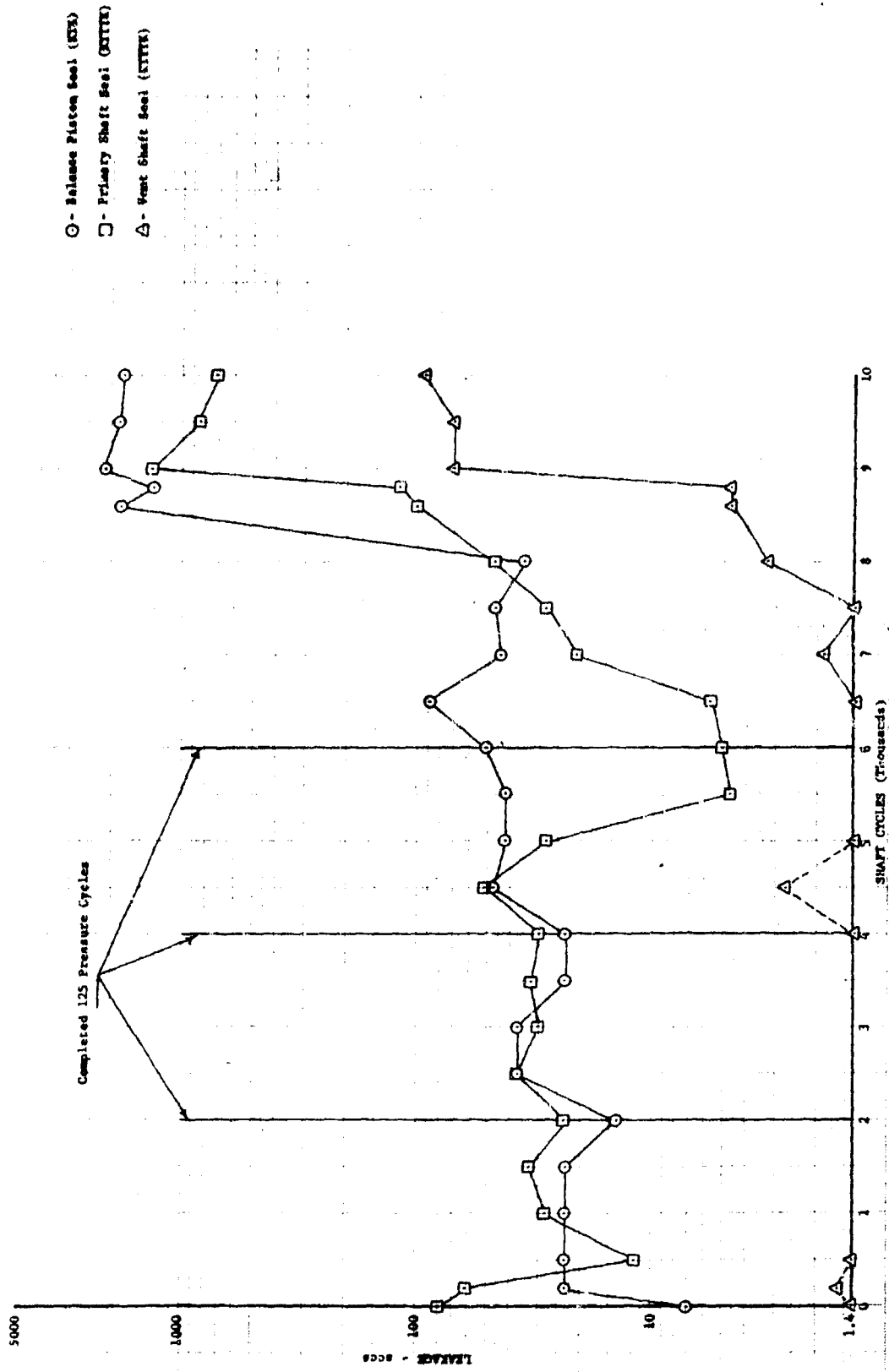


Figure 338. Translating Seal Test Rig Leakage vs Cycles for Build 14

DF 65297



FE 78204

Figure 340. Vent Shaft Lip Seal After
Test of Build 14



Figure 339. Primary Shaft Lip Seal After
Test of Build 14



Figure 341. Balance Piston Lip Seal After Test of FE 79205
Build 14

It is recommended that static seal test rigs be designed for the minimum deflection consistent with the demonstrator engine weight goals. The finite element computer program should be used to analyze all demonstrator engine flanges to limit deflection to the values selected for the static seal test rigs.

c. Design Analysis

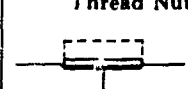
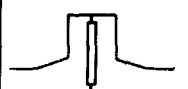
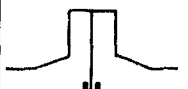
During this subtask, the primary effort was expended on obtaining information for a high pressure static seal rig design. Several initial configurations were sketched for specialized flange and seal combinations before calculation difficulties indicated that design effort should be concentrated on basic coupling configurations with analysis directed toward minimum weight and deflection with demonstrator engine materials.

A 6 in. diameter aluminum (AMS 4127) pipe coupling was chosen for analysis because of its relatively poor deflection characteristics when compared to those of the same diameter steel or smaller diameter aluminum or steel couplings. A high-pressure coupling design analysis of five basic coupling types

was completed. The configurations that were considered are shown as sketches A through E, in figure 342. Basic ground rules for the analyses were as follows:

1. Standard design criteria for the engine with regard to allowable stresses, weight, etc., were to be followed.
2. Pipe and coupling designs were based on stress limits for axial (blowoff) and hoop loads only. No vibration or mechanical bending load factors were added.
3. All couplings were assumed to have a perfect seal (not deflection limited) at the coupling inside diameter.

The results of the coupling spring rate deflection calculations, as shown in figure 343, indicated that increasing the number of bolts had a minor effect on bolted coupling overall spring rate, whereas weight increase was significant. Calculations to determine the initial clamping load required for each of the couplings to provide and maintain a minimum of 460 lb/in. seal load at 7500 psi resulted in the clamping load to blowoff load ratio (F_C/F_A) values shown in figure 342 (sketches A through E). Aside from the impracticality of attempting to obtain such high clamping loads, the numbers indicated that some method of improving the clamping load transfer to the seal area was required.

<p>(A) Large Bolt</p>  <p>Wt 22 to 28 lb Kc 0.067 to 0.065 in. Fc/Fa 7.6 to 25.8 Inconel 718 (AMS 5663) Bolts & Nuts</p>	<p>(B) Small Bolt</p>  <p>Wt 18.1 to 20.3 lb Kc 0.058 to 0.053 in. Fc/Fa 8.8 to 16.5 Inconel 718 (AMS 5663) Bolts & Nuts</p>	<p>(C) Pinned Joint</p>  <p>Wt 25.9 lb Kc 0.018 in. Fc/Fa -- Inconel 718 (AMS 5663) Pins & Clamp</p>	<p>(D) Double Thread Nut</p>  <p>Wt 17.3 lb Kc 0.015 in. Fc/Fa 10.6 Inconel 718 (AMS 5663) Nut</p>	<p>(E) Clamped</p>  <p>Wt 26.4 lb Kc 0.038 to 0.045 in. Fc/Fa 29.6 Inconel 718 (AMS 5663) Clamp & Bolts</p>
<p>(F) Single Thread Nut</p>  <p>Heavier than (D) More deflection than (D)</p>	<p>(G) Single Thread Nut Raised Face</p>  <p>Cantilever Beam load transfer to Seal</p>	<p>(H) Raised Face</p>  <p>Cantilever Beam load transfer from Bolt to Seal</p>	<p>(I) Undercut Face</p>  <p>Simple Beam load transfer from Bolt to Seal</p>	<p>(J) Flexible Lip</p>  <p>Reduced Deflection at Seal</p>

All calculations for 6-in. ID, 6 inch long open end aluminum (AMS 4130) pipe coupling.

Figure 342. Coupling Configurations

FD 25605A

Sketches F through I in figure 342 show some methods of providing this seal force, while sketch J shows a pressure assisted coupling intended to maintain seal load when flange deflection is present. Another method, not shown, of providing more effective seal loading would be to move the seal closer to the clamping load circle. In this case, part of the improved load transfer advantage would be lost because of the increased blowoff load. No detailed analyses of these or other variations from standard flat flange couplings have been completed, so no clear choice of coupling type for high pressure test was possible. The apparently obvious advantages and disadvantages of each coupling type for engine application were considered, and the small bolt flanged coupling was selected for

detailed analysis and initial seal rig design. Analysis required for optimizing the flange configuration or seal location to provide satisfactory seal load characteristics over the full pressure range was undertaken as primary effort.

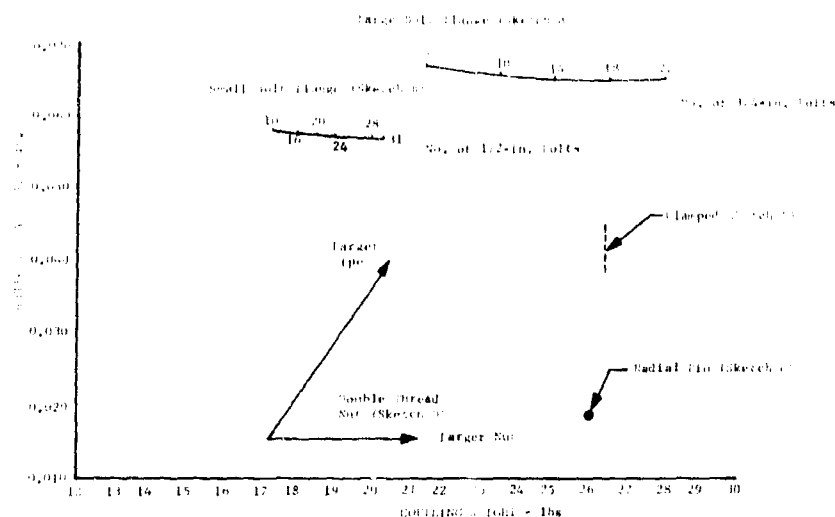


Figure 343. Predicted Coupling Deflection at Seal vs Weight

DF 68872

A study computer program was developed to analyze proposed coupling rig designs for stress and deflection characteristics. Initial rig designs were found to be unsuitable for the intended application. A 6 in. aluminum hydrostatic coupling stress and deflection test rig was then designed to evaluate the computer program predictions. Concurrently, a finite element computer program developed for disk analysis was modified for coupling analysis.

A reanalysis of the hydrostatic aluminum coupling layout using this deck on the IBM 360 computer resulted in lower predicted maximum flange stresses and higher deflections than the previous program.

Cantilever and simple beam flange seal loading schemes were then analyzed using the computer programs. This analysis indicated that the cantilever design would be lighter than the simple beam designs for the same deflection limit. A cantilever flange rework of the initial flat faced flange test rig was designed and added to the test rig layout.

As testing of the hydrostatic rig progressed, the computer programs were revised to improve agreement with the test results.

An additional flange design analysis based on shear center theory was completed. The application of this theory is that the load must pass through the shear center, or center of flexure to prevent twisting. Preliminary calculations indicated that the shear center design would improve flange stiffness but would probably be more bulky than a conventional flange design. Further analysis of the shear center flange design calculations indicated that effective coupling weight

reduction by removing flange material that is not highly stressed may be possible without significantly affecting flange stiffness.

d. Testing

(1) Flange Tests

Hydrostatic flange test rig housings and bolts were procured and delivered to the Materials Development Laboratory for assembly and testing. Rig 35120, Build 2 (Build 1 was used to test main chamber oxidizer valve inlet and outlet flange seals) was assembled as shown in figure 344. Stressecoat was used to determine strain gage locations. Sixteen biaxial strain gage rosettes were installed on the interior and exterior of the test rig according to the stresscoat patterns (figure 345). Preliminary Materials Development Laboratory tests indicated that X-ray inspection would be feasible to determine flange separation during the hydrostatic tests. A review of the X-ray techniques revealed that separation at various radii could be measured if actual separation was known at one or more points. Consequently, magnetic proximity probes (figure 346) were used to determine housing deflections at two points. The hydrostatic test rig was then assembled for testing. Six of the coupling bolts were strain gaged and calibrated for strain at the required load. All other bolts were then torqued sufficiently to obtain the average stretch obtained for the instrumented bolts. Assembly torque variation was too great to be useful for specific load application. During the test, readouts from all internal strain gages were lost due to potting material creep. The external strain gages and the proximity probes operated satisfactorily.

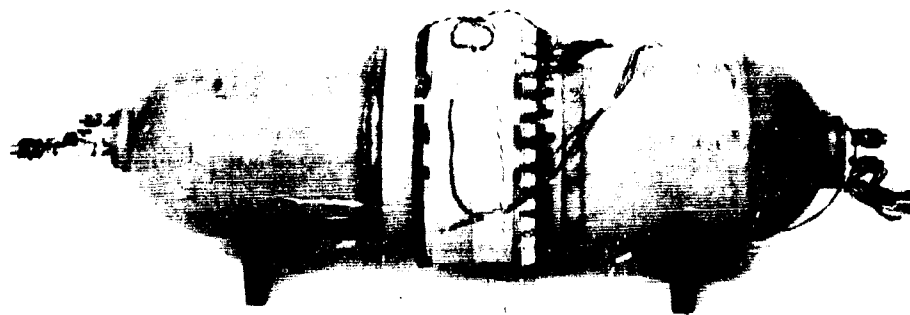


Figure 344. Flange Test Rig

FE 78045

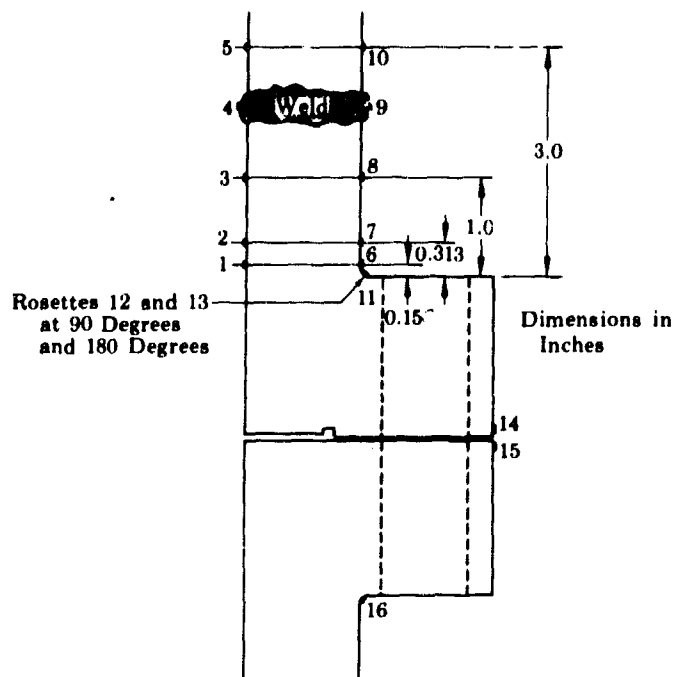


Figure 345. Locations of Strain Gage Rosettes

FD 25606

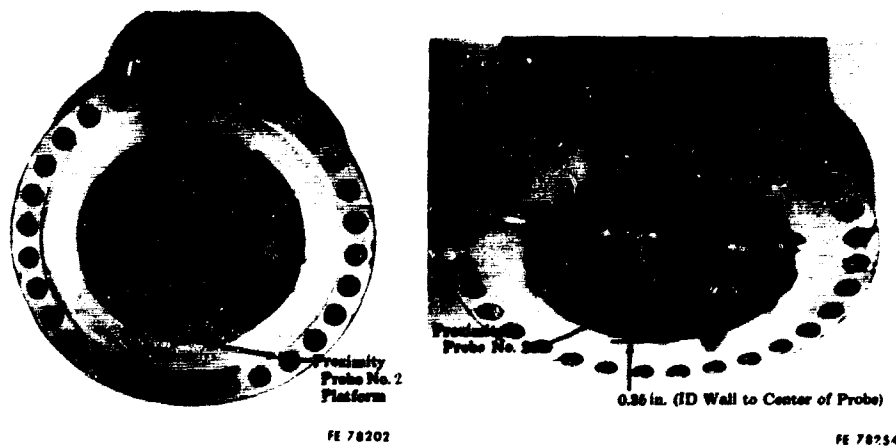


Figure 346. Magnetic Proximity Probe Locations
Rig 35120-2

FD 25607

Maximum axial tensile stress of 58,200 psi (0.9% strain) occurred in the flange radius at strain gage rosette location 11 (figure 345) under 5300 psig internal pressure. Maximum axial tensile stress of 31,700 psi (elastic) occurred in the straight wall section at strain gage rosette location 6 under 5300 psig internal pressure. Hoop stress at this point was 25,000 psi tension. The flanges began to separate at 2500 psig internal pressure where internal pressure blowoff load was approximately 25% of the assembly bolt load. Maximum flange separations at the inside diameter wall and seal groove were 0.025 in. and 0.018 in., respectively, under 5300 psig internal pressure.

The hydrostatic test rig data indicated reasonably good agreement with the finite element computer program predictions for both stress and deflection as shown in figure 347. The program was revised to improve matching by expansion to include both coupling members, multipoint bolt loading, and consideration of the effects of the bolt holes. The revised model was used to predict stress and deflection of a cantilevered flange coupling.

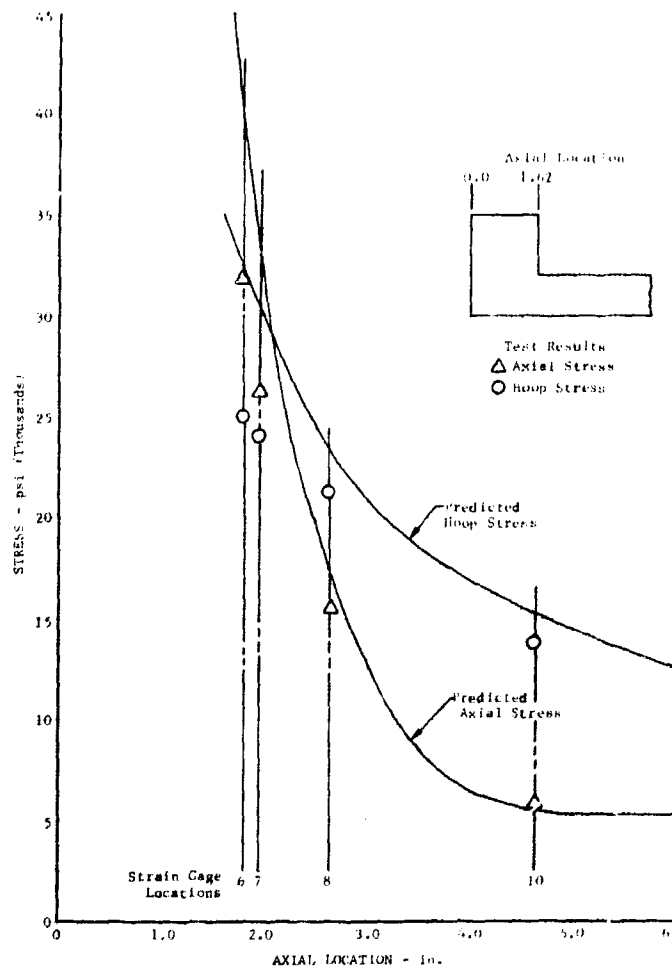


Figure 347. Finite Element Computer Program Predictions

DF 68871

The hydrostatic test rig flanges were reworked to the cantilevered design configuration for Rig 35120-3. Sixteen strain gages and six proximity probes were installed, as shown in figure 348, and the rig was assembled for test. Hydrostatic pressure testing was conducted at ambient temperature up to 5300 psig. Bolt loads were nearly constant and deflection at the inside diameter was essentially as predicted by the finite element program (figure 349).

Maximum indicated axial tensile stress (above yield) occurred in the flange radius at strain gage rosette location 5 (figure 348). The flanges did not separate under 5300 psig internal pressure but pivoted at the raised face outer diameter so that deflection at the seal diameter reached a value of approximately 0.004 in. Maximum flange separation at the inside diameter wall was 0.008 in. at this pressure.

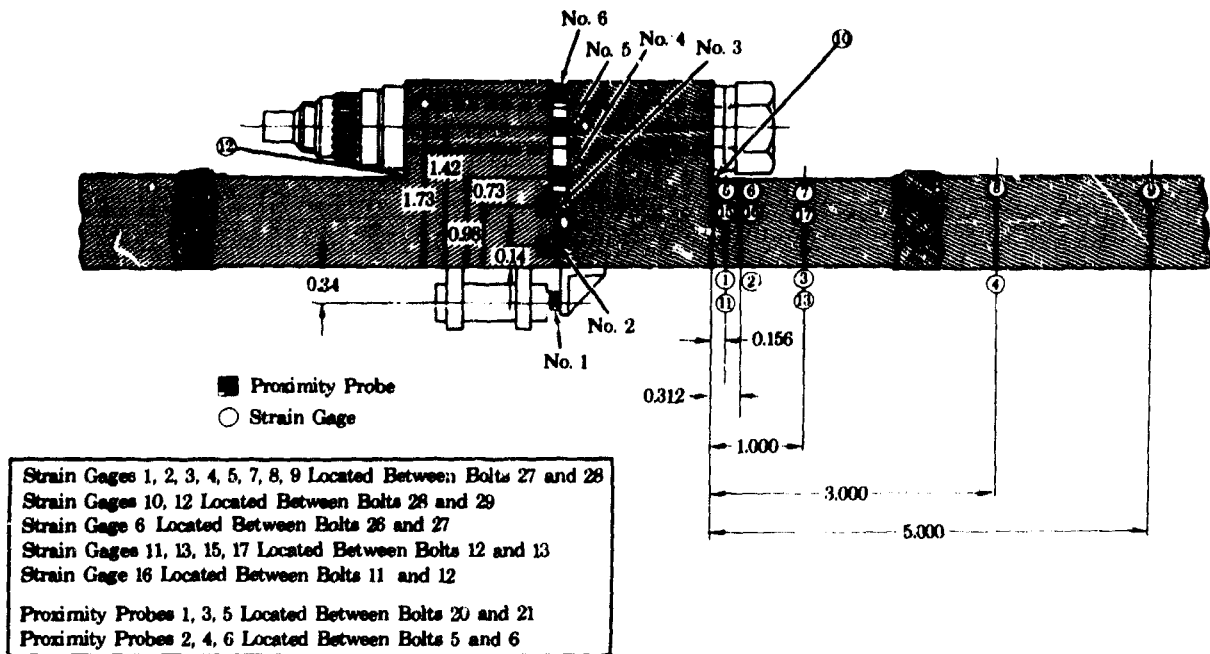


Figure 348. Instrumentation Locations Rig 35120-3 FD 25608

Review of the stress, load, and deflection curves for the cantilevered flange hydrostatic pressure test rig revealed that maximum surface stresses (below yield) near the flange were still somewhat below the finite element program predictions but agreement was improved as shown in figure 350. Both bolt loads and proximity probes indicated flange separation was imminent at the maximum pressure applied but bolt load was nearly constant up to that point. Bolt loads were then reduced to approximately 4000 pounds and the rig was pressurized to 3800 psig. Bolt loads remained essentially constant up to 3000 psig and calculated joint efficiency (blowoff load/bolt load) was essentially the same as in the previous test.

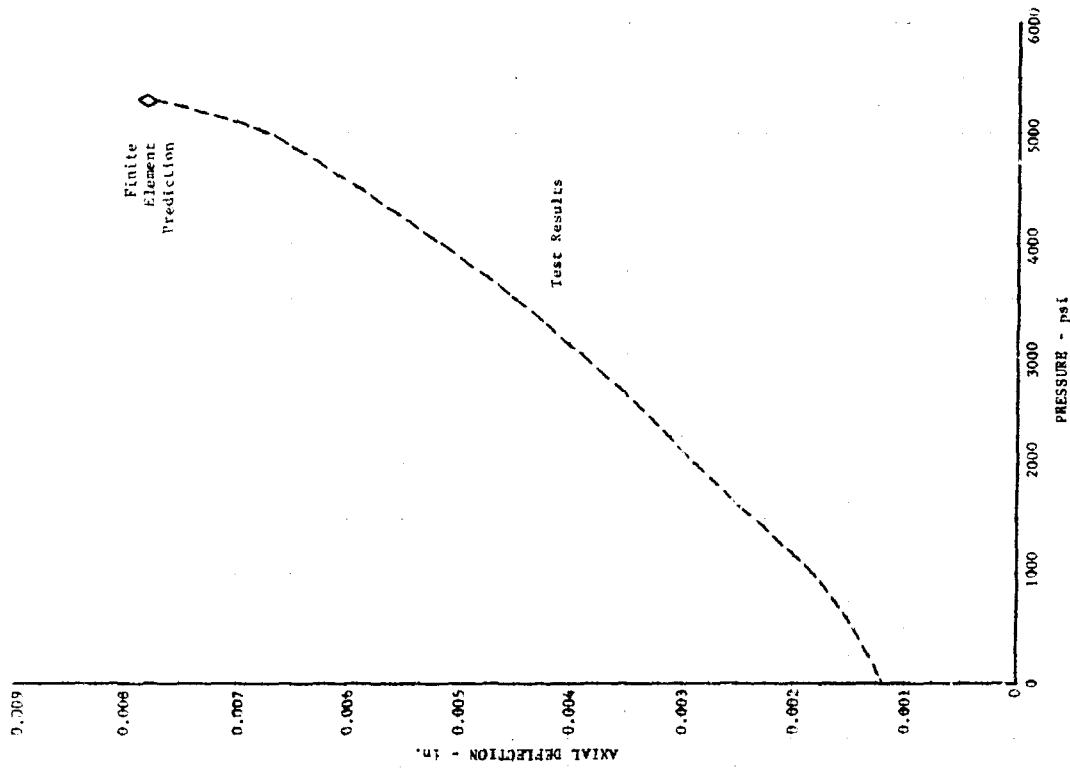


Figure 349. Axial Deflections at ID of Flange Rig 35120-3

DF 68870

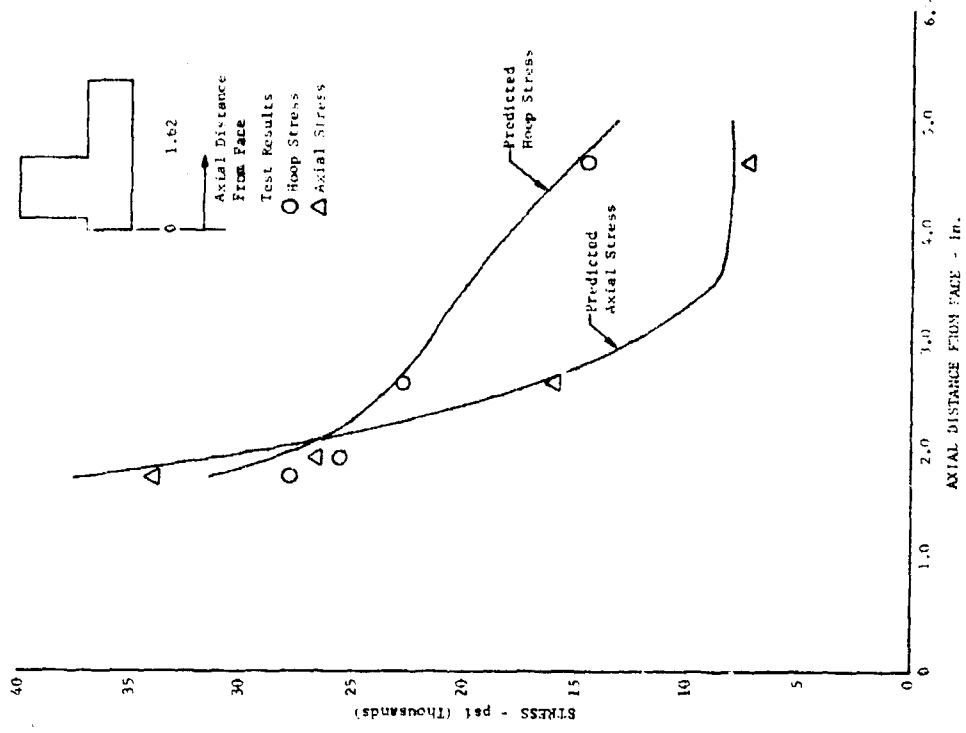


Figure 350. Comparison of Predicted and Measured Stresses on OD Wall Rig 35120-3

DF 68869